MATHEMATICAL MODELLING OF PHARMACEUTICAL UNIT OPERATIONS

Dr Zdeněk Grof

Habilitation Thesis

January 2021

Department of Chemical Engineering
University of Chemistry and Technology, Prague

Mathematical modelling of pharmaceutical unit operations

Habilitation thesis

Zdeněk Grof
January, 2021

zdenek.grof@vscht.cz

University of Chemistry and Technology, Prague
Department of Chemical Engineering
Technická 5
166 28, Prague 6
Czechia

This thesis contains reprints of articles that are protected by copyright laws. The articles are presented here by exercising author rights, granted according to respective publishing agreements, to include the reprints in a non-commercially published thesis. The copyright holders are:
©Elsevier B.V.
©Springer-Verlag
©American Physical Society
©American Association of Pharmaceutical Scientists

CONTENTS

PREFACE

This thesis presents author's selected results on the mathematical modelling of particulate and granular materials that can be found in the field of pharmaceutical products development. The results are presented as a commentary of twelve journal articles that were published in years 2006–2021 [1–12] and one recent study [13] that has not been published yet.

The research was carried out at the University of Chemistry and Technology, Prague, while the earliest contributions originated during author's postdoc stay at Imperial College London. Most of the computational work has been done using in-house developed software written by the author.

The research work was primarily supported by the Czech Science Foundation (GAČR) through the projects 104-08-P389, 15-05534S and 19-26127X.

ACKNOWLEDGEMENT

I thank all my co-authors for their contribution and hard work that enabled to publish the results summarised in this thesis. In particular, I am thankful to Prof František Štěpánek for his help, support and all the inspiring and motivating discussions on various topics we had during the years. Special thanks go to my students and postdocs: Tereza Choděrová, Veronika Lesáková, Martin Kalný, Dr David Smrčka and Dr Marek Schöngut who did a great deal of experimental and computational work in recently published papers.

LIST OF ABBREVIATIONS

API active pharmaceutical ingredient

CFD computational fluid dynamics

DNS direct numerical simulation

DEM distinct/discrete element method

EA evolutionary algorithm

GA genetic algorithm

PBM population balance model

PSD particle size distribution

Part I

COMMENTARY

1. INTRODUCTION

The basic chemical engineering concept is the division of an industrial plant or a complex manufacturing process into a sequence of unit operations classified into, for example, heat transfer, mass transfer, fluid dynamics, chemical reaction and other fields. For each type of unit operation there exist (i) the description of relevant processes by mathematical models, (ii) the list of model parameters characterising both the process itself and the processed material properties, and also, (iii) well developed and verified methods and procedures for evaluation of such parameters. From a mathematical modelling point of view, all these items are essential for reliable process simulations and design decisions.

Well established modelling methodologies (together with commercial process simulation software solutions) exist for traditional unit operations such as heat exchange, distillation, absorption, extraction, chemical reaction, transport of fluids, etc. In recent years, the focus of chemical engineering research has been therefore shifted from these traditional fields into fields where describing a particular operation by a mathematical model is more challenging and modelling tools for such unit operation are more scarce. The characteristics that stands out when one attempts to describe such challenging processes is the following: the properties of the system no longer depend on just material composition but also on material structure. The structure-property relationship must be therefore established—a task which can be difficult or even impossible when traditional modelling tools are used.

Unit operations involving particulate material are an obvious example of challenging processes. Let us illustrate applications in the area of pharmaceutical production development, where novel modelling tools could improve the traditional methods. First, there is an assembly of large aspect-ratio particles (e.g. fragile needle-shaped crystals) that changes its particle size distribution due to attrition and breakage during conveying, filtration or mixer-drying operations. The understanding of how particles behave when subjected to various types of stress fields encountered in these devices is mostly empirical. Second, wet granulation involves the wetting and evaporation taking place in porous media. This leads to a complex (and also only empirically understood) relationship between primary particles properties, operational conditions in a granulator and properties of resulting granules. Third, tablets are manufactured by a direct compression of particles as-

sembly consisting from different components (e.g. API[1], diluents, binders, disintegrants, etc.). The tablet properties such as mechanical stability or time–amount of API released profile depend on tablet structure which, in turn, is affected by both the primary particles assembly properties and by the tablet compression process parameters (the pressure in tablet press, for example). The software tools based design therefore requires models able to simulate the processes of tablet disintegration/dissolution and particles assembly compression in a tablet press.

This thesis contains a collection of research articles focused on the mathematical modelling of operations that are common in pharmaceutics production and for which a standard modelling methodology has yet to be established. The articles are arranged into three groups:

- Simulation of liquid–porous media or liquid–solid particles interactions [1–4].
- Simulation of particle–particle interactions and particle breakage [5–9].
- Simulation of tablet disintegration and dissolution processes [10–12].

The commentary part of the thesis is arranged in the same order.

[1] API—active pharmaceutical ingredient

2. CAPILLARY INTERACTIONS IN POROUS AND PARTICULATE MEDIA

Even a small amount of liquid phase present in granular media considerably changes its physical properties as is illustrated by a popular example of building sandcastles and very different properties of dry and wet sand [14]. These changes are caused by adhesive forces due to the liquid bridges between particles. Capillary force interactions (cf. Fig. 2.1) are also a primary cause of self-organisation effects, where components spontaneously form ordered aggregates [15].

Our work presented in this chapter focuses on a first-principle based modelling of capillary interactions and on the position tracking of liquid/gas and liquid/solid interfaces in particulate systems. These modelling methods can be applied to widely used industrial processes such as wet granulation, crystallization, drying, or other processes that involve the interaction between liquid and the granular material.

2.1 Fluid-particle interactions and DEM

The principle of Discrete element method (DEM), first demonstrated and applied for particle assembly by Cundal and Strack [17], is based on the discretization into distinct spherical or non-spherical elements. In each time step of the simulation, the mutual force interactions among elements are calculated and summed in order to obtain the total force and torque acting on each element. The movement of elements is governed by Newton's and Euler's laws for element translation and rotation, respectively.

The motion of particle assembly in the fluid is governed by coupling Navier-Stokes equation for the fluid and equations of motions for particles. Coupled particle-fluid flow problems can be solved by a direct numerical simulation of these equations (i.e. "DNS" approach) which can be computationally too difficult for a large number of particles.

Therefore, the approach using local mean variables such as fluid and solid phase velocity, fluid pressure, particle density and porosity has been formulated [18]. Since the solid phase is formally regarded as an additional fluid, this method is called the "two-fluid" or "Eulerian-Eulerian" approach.

Employing the combination of the locally averaged quantities method for fluid and the DEM for particles results into the "Eulerian-Lagrangian" approach that has been used, for example, to simulate fluidized-beds by

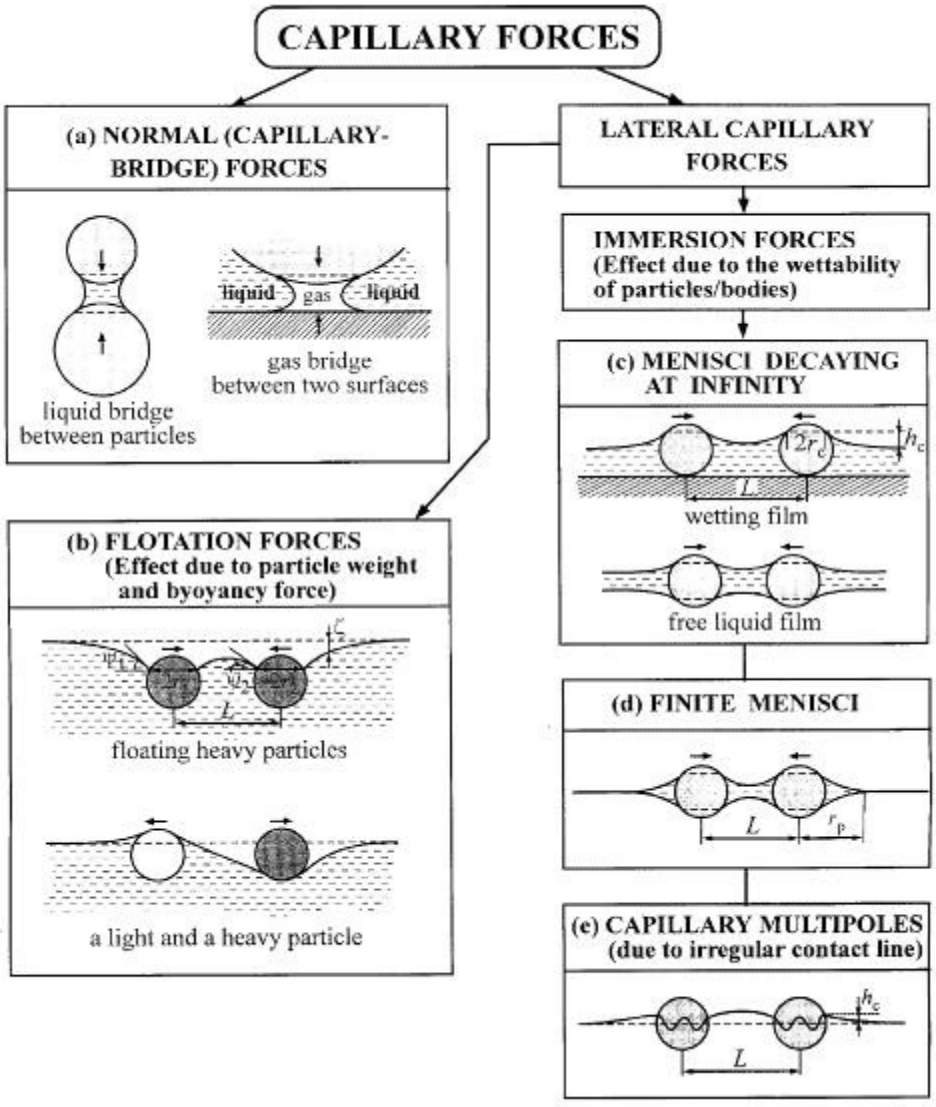

Fig. 2.1: Classification of capillary forces. (Figure reprinted from [16])

Tsuji *et al.* [19] or gas-particle flow phenomena [20, 21]. The fluid velocity field is resolved on a grid with a spatial discretization an order of magnitude larger than the average particle size and drag laws are used to estimate the hydrodynamic forces on each particle.

2.2 Capillary force interactions

DEM for cohesion-less particles and fluid flow problems considers the contact forces between particles (normal and friction) and the hydrodynamic drag force. Extending the employment of DEM to other applications (for example self-assembly of colloidal particles [22, 23]) requires the addition of other forces that become physically important: electrostatic, van der Waals, or capillary forces.

Capillary forces can be classified into two groups (cf. Fig. 2.1): (1) normal and (2) lateral capillary forces. The first type is present especially in wet granular materials in the form of liquid bridges in the pores between particles [24]. The normal capillary bridge force can be attractive or repulsive depending whether the capillary bridge is concave or convex. According to the amount of liquid in the granular material, the bridges are formed just at the contact points of grains if liquid content is low (pendular state), or both liquid bridges around contact points and liquid-filled pores coexist at higher liquid content (funicular or capillary states) [25]. On the other hand, lateral capillary force plays the role if the presence of particles on the liquid interface causes some perturbation of the shape of liquid surface [16]. These types of forces mediate the self-assembly of colloidal crystals as the partially immersed particles having the same wetting properties attract each other.

There exist various strategies of implementing capillary forces into DEM. For binary (pendular) liquid bridges, it is possible to derive analytical expressions for the force corresponding to a single bridge [26] or obtain a closed form approximation numerically [27] and use it as a part of the contact force calculation in the discrete particle model. The simulation of cohesive powder fludization [28] or our work [1] on particle entrainment is an example of such approach.

However, when the volume fraction of the liquid phase in the particle assembly increases such that the more complex liquid geometries than binary bridges are present (funicular or capillary state), the above mentioned approach is no longer possible and it is necessary to track the liquid phase topology explicitly. The situation is even more complicated for the lateral capillary forces between particles trapped in liquid films (e.g. during drying of colloidal crystal). The analytical solution for the force acting between two partially immersed objects is known [16], but it is difficult to use it in the case of a system of many bodies which are close to each other, and a number of approximations has to be made in order to include binary forces into DEM of self-assembly of colloid particles [22, 23]. Therefore, the explicit

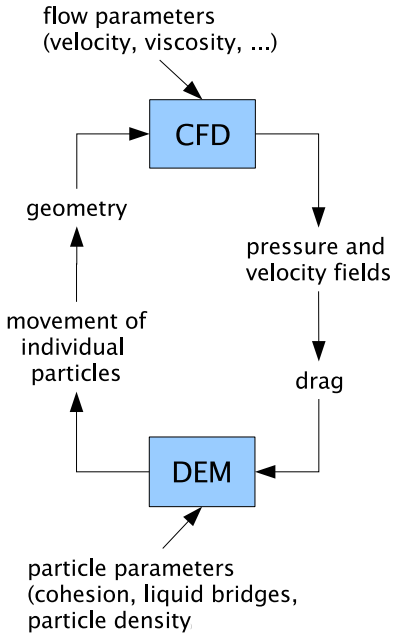

Fig. 2.2: Scheme for CFD-DEM coupling simulations.

simulation of the distribution of liquid phase is required for more rigorous modelling studies.

Several numerical methods capable to simulate the moving boundary or free interface problems have been described in the literature [29] such as the Level Set, Diffuse Interface, Volume of Fluid or the Marker and Cell method. However, these methods are not well suited for the calculation of the capillary bridge force due to the relative inaccuracy in the evaluation of the length of the three-phase contact line and of the interfacial area, in particular when there is a large difference between the characteristic sizes of the solid particles and liquid domains. Higher accuracy can be achieved by representing the interface as a moving polygonal mesh. This approach has been implemented, for example, in a well-known Surface Evolver software [30]. In order to simulate systems with topological changes such as those occurring during drying, condensation, or droplet coalescence, it is necessary to have a method that allows the merging and rupturing of interfaces.

2.3 Case studies involving liquid-particle interaction modelling

2.3.1 Coupled DEM/CFD approach

Paper [1] (cf. Section 7.1 on page 53) investigates sanding phenomena in well-bores by the numerical simulation of particle cluster entrainment due to fluid flow. The model (cf. Fig. 2.2) contains the following components:

- DEM to calculate solid particle cluster movement. The contact force is represented using a linear-elastic model, while the capillary bridge force is implemented by using a closed form approximation which was derived by curve-fitting to the numerical solution in [27].

- CFD part to calculate the fluid velocity and pressure fields by solving Navier-Stokes equations for an incompressible fluid followed by the calculation of the hydrodynamic drag on particles.

Two dimensionless parameters

$$\mathrm{Bo} = \frac{(\rho_\mathrm{s} - \rho_\mathrm{l}) R^2 g}{\gamma} \approx \frac{\text{gravitational}}{\text{capillary}} \tag{2.1}$$

$$\Psi = \frac{\eta u}{\gamma} \approx \frac{\text{hydrodynamic}}{\text{capillary}} \tag{2.2}$$

determine the ratio of the gravitational or the hydrodynamic force to the capillary force. In the previous equations, ρ_l and ρ_s are fluid and particle densities, R is the radius of particles, g is the gravitational acceleration, η is fluid viscosity, u is fluid superficial velocity and γ is the interface tension coefficient.

In terms of the parameters Bo, Φ and dimensionless liquid bridge volume V^*, regime maps were obtained by numerical simulations and the regions where cluster of particles holds or detaches were identified.

2.3.2 Liquid/Gas/Solid interface tracking

Papers [2] and [3] (cf. Sections 7.2 and 7.3 on pages 65 and 79) introduce a method for the simulation of liquid–gas interfaces in an arbitrary two dimensional granular media. The method has been inspired by the Surface Evolver software [30]. The geometry of wet granular system consisting of distinct solid and liquid objects is described by a set of liquid and solid polygons that represent the individual liquid domains and solid particles (cf. Fig. 2.3). The algorithm is organised as follows:

1. At the highest level of the algorithm, a small change, corresponding to the condensation/drying (i.e. liquid amount increase/decrease) or wet particle agglomerate deformation (i.e. solid particles movement), is made. For every step at this level, iterations on lower levels to find/re-establish the equilibrium state are performed. The equilibrium shape of liquid domains corresponding to the energy minimum should satisfy (i) constant mean curvature of all liquid–gas interfaces belonging to the same liquid domain and (ii) the equilibrium contact angle at all three-phase contact points.

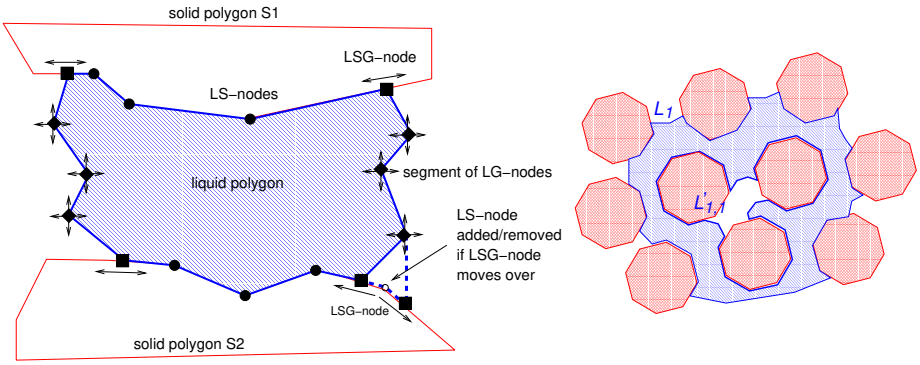

Fig. 2.3: Left image: A representation of an arbitrary three-phase system in two dimensions by a set of polygons and classification of its nodes: (i) LSG nodes can slide along the solid boundary (edges of polygon representing a solid particle) in order to meet the prescribed contact angle. (ii) LS nodes are fixed at vertices of solid polygon. They are inserted or removed as an LSG node (that represent a three-phase contact point) moves over them. (iii) LG nodes are free to move in any direction because they form a liquid-gas boundary. Right image: An example of a liquid polygon L_1 with an "anti-polygon" $L'_{1,1}$ that represents a topological case when solid particle(s) and gas bubble(s) are surrounded by a percolating cluster of liquid. (Figure reprinted from [2])

2. Polygon nodes are therefore iteratively moved in a direction that decreases the energy of the system. There are the following contributions to the displacement of nodes at the liquid–gas boundary (LS-nodes): (a) minimisation of total liquid–gas interface length, (b) convergence towards constant mean curvature, (c) preservation of uniform distribution of polygon nodes along the polygon boundary, and (d) preservation of the total polygon area. The movement of three-phase nodes (LSG-nodes) is confined to the edges of the solid polygon they are adjacent to.

3. In the course of nodes movement, it is also necessary to check if the topology of the system should be modified. For example, two liquid domains can coalesce into one or one liquid domain can be split in two when a narrow neck is formed. A wide range of additional possible topological changes involving liquid and solid polygons is extensively described in [2].

4. Once equilibrium positions of polygon nodes have been found, pseudo-static capillary force interaction between the solid particle and the liquid body is calculated. It consists of two contributions: (i) the first one is due to Laplace-Young pressure change across the curved

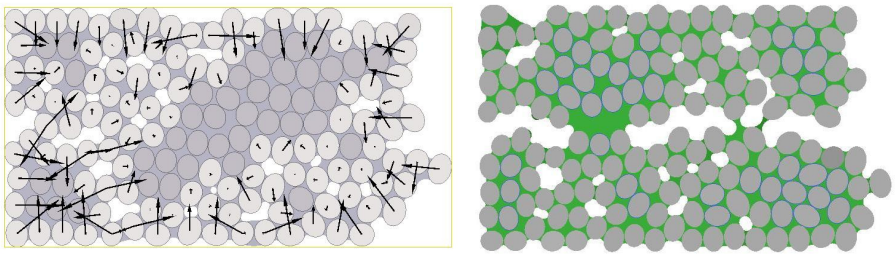

Fig. 2.4: Snap-shots of an three-phase system described by a set of polygons during capillary condensation simulation (left), or tensile strength experiment (right). Arrows show the capillary force acting on solid particles. (Figures reprinted from [2] and [3])

interface Δp

$$\Delta p = -\gamma \left(\frac{1}{R_1} + \frac{1}{R_2} \right), \tag{2.3}$$

where γ is the interface tension coefficient and R_1 and R_2 are the principal radii of curvature, and (ii) the second is the direct action of the surface tension of the liquid. Also global characteristics (e.g. total liquid–gas interface length, the tensile strength, liquid domain percolation state, etc.) corresponding to a particular value of an investigated parameter, such as liquid content or the extent of deformation, are calculated at this point. The simulation then moves in the loop back to point 1 and repeats the same procedure for a modified value of the parameter.

Computer simulations of the capillary condensation and tensile strength of a wet particle packing (cf. Fig. 2.4) were presented. The methodology allows to evaluate the tensile force as a function of relative liquid content and to compute the stress/elongation curve.

Taking into account the need to resolve all possible topological changes that could take place during the process of liquid phase spreading in porous media, the interface tracking by the polygon-based method is more difficult to implement than more traditional methods (e.g. Volume of Fluid [31, 32]). However, a substantial advantage of polygon tracking approach is the fact that the interfacial areas and the length of the contact lines can be evaluated more precisely. Such precision is needed when capillary forces have to be calculated in packings consisting from many solid particles.

2.3.3 Drying in porous media

Paper [4] (cf. Section 7.4 on page 93) combines experimental and computational work. The system of water and packing of cylindrical alumina

extrudates (1 mm diameter, 3–4 mm length) was used to observe the drying process. Extrudate particles were impregnated by dichlorodimethylsilane in order to obtain material with different wetting properties: hydrophilic (untreated particles) and neutral to hydrophobic (silanized particles). The porous media structure and the advance of the drying front have been observed using an X-ray micro-tomography scanner.

When the same porous medium structure as that obtained by a tomography scan was digitally encoded and the drying process was simulated numerically, a good agreement between the experiment and simulation was obtained. In numerical simulations, the Volume of Fluid method for tracking the liquid–gas interface has been used [32].

2.4 Conclusion and perspectives

The modelling approach presented in [2, 3] that is based on the explicit tracking of interfaces in a wet granular material is able to simulate liquid-particle interactions for any liquid bridge and solid particle arrangement. A high level of precision at which capillary forces can be calculated outweighs the implementation and extension to three-dimensional cases difficulties that are associated with this method.

In the field of pharmaceutical unit operations, liquid-particle interactions play an important role in the course of drying, granulation and coating processes. For example, in a fluid bed coating process [33], the knowledge of droplet drying rate is a necessary input to the process optimisation that attempts to avoid undesirable outcomes such as particle agglomeration or a non-uniform coating thickness. Also, assuming another example, liquid imbibition and evaporation rates affect binder spatial distribution inside produced granules. This distribution, in turn, determines the strength and disintegration/dissolution properties of the granule.

Therefore, the methodology able to describe liquid spreading and imbibition in a particulate or porous medium will be an essential part of multiscale simulation tools of these unit operations. The tools should be able, especially, to encode and predict the internal structure of products such as granules or coated particles.

3. INTERACTIONS AMONG PARTICLES AND PARTICLE BREAKAGE

Processes involving granular material handling present a challenging engineering problem. Probably no general formula can describe the enormous richness and complexity of granular motion [34]. There are no constitutive equations describing dense granular mechanics in an analogous way to Navier-Stokes equations that describe fluid dynamics. The understanding of process design and operations involving granular materials is mostly based on empirical knowledge rather than on predictions made from fundamental principles.

Let us take as an example particles in a pharmaceutical process. While their properties such as particle size distribution (PSD) can be well controlled in the granulation or crystallization step, further down-stream operations such as solids handling can often lead to an uncontrolled PSD change due to attrition and breakage. Also, as one component in a multi-component granule can be preferentially present on the surface of the granule [35], the granule size reduction and attrition has a potential to adversely affect the quality attributes of the final product [36]. This uncontrolled shift in granule composition can result in the pharmaceutical product not meeting specified requirements any more.

A general research framework regarding the operations with granular material is illustrated in Fig. 3.1. There are original particles with specific properties (e.g. granules of particular strength, structure, and composition; a bed of fragile crystals characterised by crystal size and strength distributions). The particles are subjected to a given stress-field such as uni-axial compression, shearing, impact or their combination. The result of the applied stress is the granular material with a modified structure (e.g. the granules broken up into fragments; the bed of particles with a different PSD due to particle breakage). The main research objective is the search for relationships between the structure of breakable granular material and dynamics of its change as a general stress-field is applied.

Our work presented in this chapter consists of: (i) the introduction of the algorithm that enables DEM simulations with breakable particles and (ii) the connection of DEM simulation results with population balance modelling (PBM).

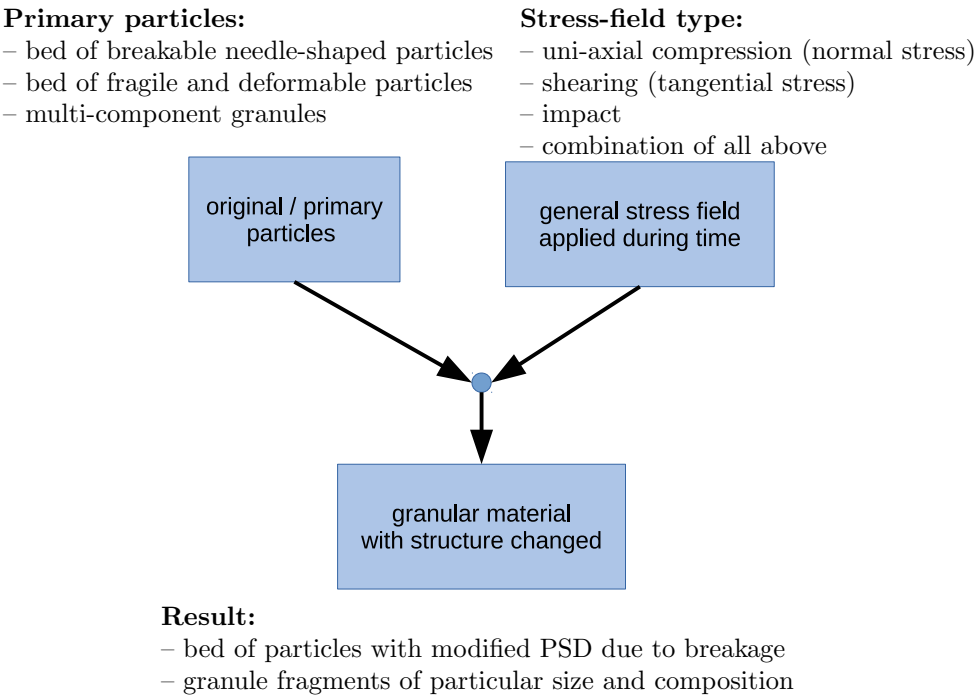

Fig. 3.1: General problem framework: What is the relationship between the primary particles, the applied stress and the resulting material structure? The problem can been studied either by experimental or by numerical computation techniques.

3.1 DEM and particle breakage

Discrete element method (DEM) is a well established methodology for the study of granular systems. It is based on simulating the movement of individual grains/particles by the integration of Newton's and Euler's equations for a translation and rotation of particles. If a proper force law for the particle–particle contact is used [37–39], the prediction of macroscopic properties of a granular system by DEM simulation agrees well with the experimental values. The DEM has been originally employed for cohesion-less grains only [17], however, by including the cohesion forces (e.g. a capillary force) and by connecting several primary particles together, also more complex systems such as non-spherical particle assemblies or granules can be modelled within a DEM framework.

For example, granules are modelled as clusters of individual particles. Particles represent either individual grains the granule is formed from, or just distinct parts of the granule in cases where the number of real grains is too large and the simulation with individual grains would be computationally unfeasible. The internal distribution of stress and strain build-up in the granule can be evaluated and crack formation or granule breakup can be

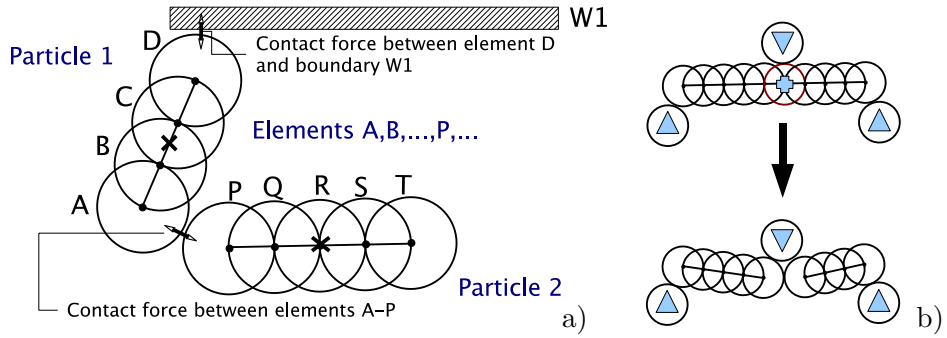

Fig. 3.2: Illustration of: (a) multi-element particle model, (b) breakage algorithm (Figure reprinted from [5])

simulated by DEM as has been demonstrated in several research papers [40–44].

Various DEM extension techniques to represent non-spherical particle systems have been reviewed in [45]. To represent elongated (needle-shaped) particles, multi-element particle model introduced in [46] has been used in our work. Each particle consists of several spherical elements whose positions are fixed relative to the positions of other elements within the particle (cf. Fig. 3.2a)—particles move as rigid bodies. In order to determine whether a particular particle breaks, it is necessary to calculate the internal loading within the particle. The particle can be viewed as a loaded beam and maximum shear and bending stresses are evaluated along its longest axis. If the maximum stress exceeds a particular threshold value then the particle is set to break in two daughter particles at the point of the maximum stress as is shown in Fig. 3.2b. This breakage algorithm for inertial particles (assuming that the particle reached a steady-state position before its loading state is evaluated) has been introduced in [5] and the generalisation also for non-inertial particles has been described in the Appendix of our follow-up paper [9]. An illustration of DEM simulation of an uni-axial compression of a bed of breakable particles is shown in Fig. 3.3. Such simulations with digitally encoded granular material can be viewed as *in-silico* experiments that, in comparison to physical (real-world) experiments, provide more detailed information about the breakage process (e.g. the list of breakage events, particle contacts topology, or stress distribution along force chains).

For non-rigid particles, a conceptually different approach such as bonded-sphere method [47–49] must be used to account for particle bending and associated dynamic phenomena like wave propagation. However, the introduction of particle deformations (i.e. when the elements a particle consists of can move separately and their movement is controlled also by the forces from intra-particle bonds) has its disadvantage. To still keep the particles stiff, the elastic moduli for the forces holding spherical elements together

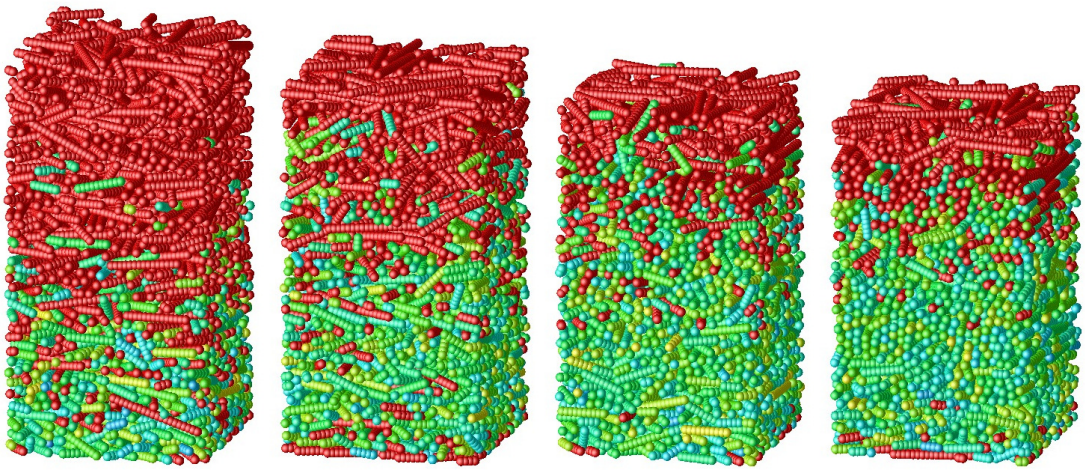

Fig. 3.3: Uni-axial compression of a bed of breakable particles using DEM simulation. The colour corresponds to the particle length. (Figure reprinted from [9])

and maintaining a defined bonding angle (intra-particle forces) must be set to values that are larger than the elastic modulus for the contact force between particles (inter-particle force). Taking into account that time-step size is inversely proportional to the largest modulus value, the simulation of both the movement and the bending of flexible particles requires a shorter time-step than the simulation with particles moving as rigid bodies. This difference increases with the required level of particle stiffness depending on material the actual particles are made from. Therefore, in terms of computation time requirements, a multi-element particle approach is more efficient for the simulation of stiff and brittle materials where the bending is small and can be neglected (e.g. needle-shaped crystals). On the other hand, a bonded sphere approach would be better suited for more flexible materials (e.g. spaghetti).

3.2 Population balance model

In the context of the mathematical modelling, DEM simulations provide computational experiments and can be viewed as a meso-scale model, while the population balance modelling (PBM) approach describes the breakage process at the macro-scopic level. Population balance equations define how populations of particular size classes develop over time. Two material and stress-field specific functions have to be supplied into PBM: the breakage kernel and the daughter distribution function. The breakage kernel determines the breakage rate of particles from each size class, while the daughter distribution function describes the size distribution of daughter particles

(fragments) that are formed once a particle from a given size class does break.

Assuming needle-shaped crystal particles as linear aggregates of primary units (elements), it is possible to correlate the particle length L_i with the number of units i

$$L_i \approx i,$$

where the subscript i also denotes a particular size class i. Particle size distribution is a discrete function with values n_i corresponding to the number concentration of particles consisting from i units, $i = 1, \ldots, N$, and N is the number of size classes.

The particle breakage and the change of particle size distribution $n_i(\tau)$ can be described by population balance equations [50, 51]

$$\frac{\mathrm{d}n_i}{\mathrm{d}\tau} = -r_i + \sum_{j=i+1}^{N} \beta_{ij} r_j, \tag{3.1}$$

where the first term on the right hand side is the rate of death of particles i to generate smaller fragments, while the second term is the birth of particles i due to the breakage of larger particles.

Particle breakage is the first order process with respect to particle concentration, the death rate can be therefore expressed as

$$r_i = k(L_i) n_i, \tag{3.2}$$

where $k(L_i)$ is the breakage kernel. The daughter distribution functions β_{ij} define the number of daughter fragments in class i produced upon breakup of a mother particle j. If only two fragments are formed during single breakage event, the following condition must be met

$$\sum_{i=1}^{j-1} \beta_{ij} = 2 \tag{3.3}$$

and the distribution β_{ij} is symmetrical about the middle of the mother particle $i = j/2$. If the breakage is self-similar, then a single daughter distribution function $\beta'(x)$, where $x = i/j$, characterises the breakage of mother particles of any length j.

The variable τ in population balance (3.1) usually corresponds to the grinding time. However, in the case of pseudo-stationary processes such as an uni-axial compression, population balance can be expressed also in terms of the relative displacement $y = (h - h_0)/h_0$, where h and h_0 is the actual and the initial bed height, respectively. Population balance (3.1) transforms into

$$\frac{\mathrm{d}n_i}{\mathrm{d}y} = -f(y) k(L_i) n_i + \sum_{j=i+1}^{N} \beta_{ij} f(y) k(L_j) n_j, \tag{3.4}$$

where

$$f(y) = \frac{2ya - y^2}{(a-y)^2}$$

and more details regarding the derivation of Eq (3.4) are provided in [6].

Evaluation of breakage kernel and daughter distribution function

The breakage kernel and the daughter distribution function can be determined experimentally, however a large number of experiments is required. There are attempts to partially replace laborious experiments by detailed mechanistic modelling of the breakage process using DEM [52–54], but methodologies linking the output of a meso-scale model (DEM) and input parameters of a macro-scale model (PBM) are still under development.

Let us illustrate an example of such DEM–PBM linking as is presented in [6]. The PSD and breakage events are recorded during the computational experiment and these results are used to identify both the breakage kernel and the daughter distribution function. Breakage events are grouped into M intervals $m = 0, \ldots, M$ according to the compression ratio y for which they occurred. A breakage probability $S_m(L_i)$ is defined as the probability that a particle of length L_i that was originally present in the system at compression ratio y_m was broken at some stage while the compression ratio y was in the range $(y_m; y_{m+1}\rangle$. This breakage probability is calculated according to

$$S_m(L_i) = \frac{n_i(y_m) - n_i(y_{m+1})}{n_i(y_m)}, \tag{3.5}$$

where $n_i(y_m)$ is the number of particles of length L_i present in the system at compression ratio y_m and $n_i(y_{m+1})$ is the number of such particles still "surviving" in the system at y_{m+1}. Note that any newly formed particles of length L_i are not counted into $n_i(y_{m+1})$ when evaluating $S_m(L_i)$.

DEM simulations [6] suggest that the breakage probability $S_m(L_i)$ can be fitted by the sigmoidal or power-law functions (cf. Fig. 3.4a):

$$S_m(L_i) = \frac{1}{1 + \exp(-\gamma_m(L_i - L_{0,m}))} \tag{3.6a}$$

$$S_m(L_i) = \alpha(L_i - L_{0,m})^{\gamma_m} \tag{3.6b}$$

and that an universal daughter distribution function can be fitted by the Gaussian function (cf. Fig. 3.4b)

$$\beta'(x) = \frac{2}{\sigma\sqrt{2\pi}} \exp\left(-\frac{(x-0.5)^2}{2\sigma^2}\right) \tag{3.7}$$

which confirms the self-similarity of particle breakage.

The results of DEM simulations can be then used for proposing suitable shapes of the breakage kernel and daughter distribution functions. The

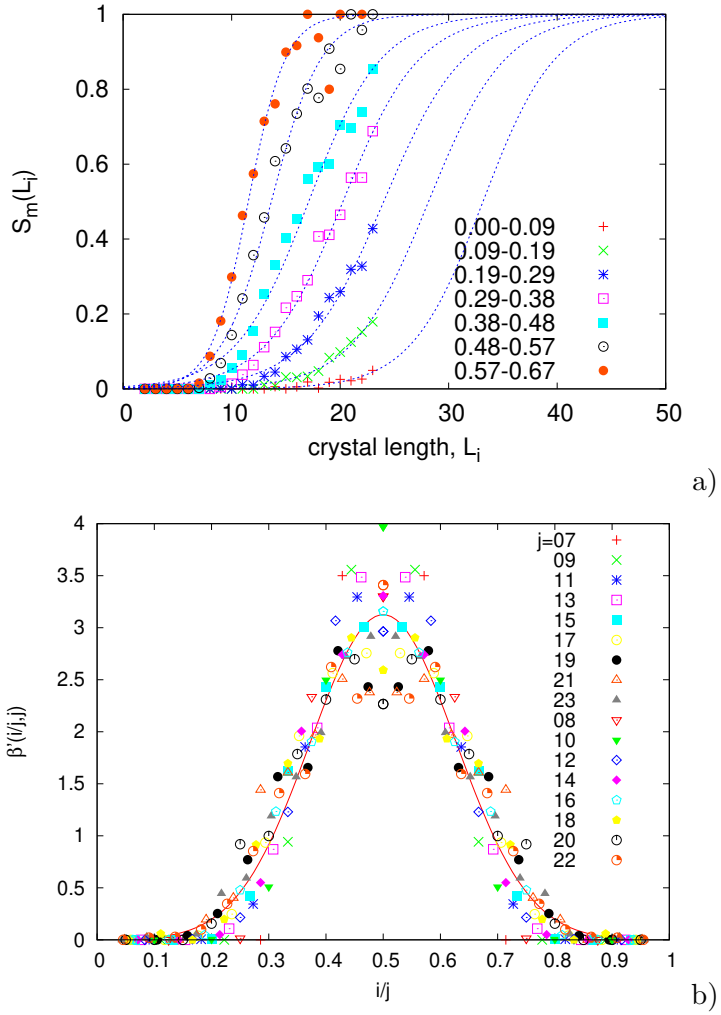

Fig. 3.4: Evaluation of the breakage kernel and the daughter distribution function from DEM computational experiments: (a) breakage probabilities $S_m(L_i)$ fitted by the sigmoidal function, (b) an universal (normalised) daughter distribution function fitted by Gaussian function. (Figure reprinted from [6])

parameters of those functions are then found by an optimisation to achieve the best match of particle size distribution predicted by PBM with DEM result. For example, if the power-law compression breakage kernel

$$k(L_i) = k_0(L_i - L_0)^\gamma \tag{3.8}$$

is introduced, the population balance (3.4) becomes

$$\frac{\mathrm{d}n_i}{\mathrm{d}y} = k_0 \frac{2ay - y^2}{(a-y)^2} \left(-(L_i - L_0)^\gamma n_i + \sum_{j=i+1}^{N} \beta_{ij} (L_j - L_0)^\gamma n_j \right), \tag{3.9a}$$

where

$$\beta_{ij} = \frac{2}{j\sigma\sqrt{2\pi}} \exp\left(-\frac{(i - j/2)^2}{2(j\sigma)^2} \right). \tag{3.9b}$$

This leads to five adjustable parameters in the model equations (3.9): the compression parameter a, the breakage constant k_0, the breakage exponent γ, the characteristic length L_0 and span of the Gaussian daughter distribution function σ. The parameter values can be obtained by finding the global minimum of objective function U

$$U = \sum_{m=1}^{M} \sum_{i=1}^{N} \left(n_i^{\mathrm{PBM}}(y_m) - n_i^{\mathrm{DEM}}(y_m) \right)^2. \tag{3.10}$$

3.3 Case studies involving particle breakage modelling

3.3.1 Methodology introduction

Paper [5] (cf. Section 8.1 on page 105) introduces the multi-element DEM with breakage algorithm and presents simulations of the breakage of needle-shaped particles in a bed of particles during uni-axial compression. A parametric study evaluating the porosity, polydispersity and average particle length as functions of particle strength and piston relative displacement y are presented. Recently, the computational simulations of uni-axial compression breakage [5, 7] were complemented by the actual experimental work done by our colleagues at the Institute of Chemical Process Fundamentals [55, 56].

3.3.2 Evaluation of breakage kernels for PBM

Paper [6] (cf. Section 8.2 on page 119) demonstrates how the results from computational experiments can be used to identify the breakage kernel and the daughter distribution function that have to be supplied into population balance equations. The methodology has been briefly summarised in Section 3.2. The paper also contains the experimental study of the breakage of real needle-shaped crystals under uni-axial compression and the comparison of PBM results with the experimental data.

3.3.3 Self-similarity of particle breakage during uni-axial compression

Paper [7] (cf. Section 8.3 on page 131) is a follow-up of paper [5] and presents a scaling relationship between the applied stress $\hat{\sigma}$ and the extent of breakage in a packed layer of needle-shaped particles $L^{-1}(\hat{\sigma})$.

The effective stress $\hat{\sigma}$ is defined by

$$\hat{\sigma} = (\sigma + w)/\sigma_{\mathrm{mat}}, \tag{3.11}$$

where σ is the compaction global stress, w is the correction factor to account for particle breakage due to own weight of the particle layer and σ_{mat} is the particle strength (i.e. the threshold stress required to break the particle). The extent of breakage $L^{-1}(\hat{\sigma})$ is inversely proportional to the number-mean particle length $L(\hat{\sigma})$

$$L(\hat{\sigma}) = \frac{\sum_{i=1}^{N} M_i(\hat{\sigma}) L_i}{\sum_{i=1}^{N} M_i(\hat{\sigma})} = \frac{M_0 L_0}{M(\hat{\sigma})}, \tag{3.12}$$

which gradually decreases as the compression stress $\hat{\sigma}$ increases. In Eq (3.12), M_i is the number of particles of length L_i and M is the total number of particles. It has been assumed that, as particles break during the compression, the overall length of the particles in the layer $\sum_{i=1}^{N} M_i(\hat{\sigma}) L_i = M_0 L_0$ remains unchanged.

The relationship between $\hat{\sigma}$ and the reciprocal number-mean particle length $L^{-1}(\hat{\sigma})$ calculated for a wide range of initial particle lengths L_0 and intrinsic particle strengths σ_{mat} is shown in Fig. 3.5 and can be interpreted as a phase map dividing the length-stress plane into two regions—a "forbidden" region in which particles of a given length cannot survive since they cannot withstand the local stress, and a "feasible" region in which particles of a given length can survive within the layer.

3.3.4 Compression of composite packings

Paper [8] (cf. Section 8.4 on page 139) investigates the breakage process that occurs during the uni-axial compression of composite packings formed from a mixture of fragile needle-shaped crystals and elastic spherical filler particles (cf. Fig. 3.6). The evolution of particle size distribution and particle contacts topology with the increasing stress was computed for different relative sizes R, volume fractions ϕ_{F} and elasticities of the filler particles within the packing.

Based on the parametric study results, it has been demonstrated that the breakage process in a composite packing under compression is related to the topology of the packing, especially to the number of inter-particle contacts. A larger number of contacts results in a larger number of force chains along which stress propagates through the packing, which reduces the

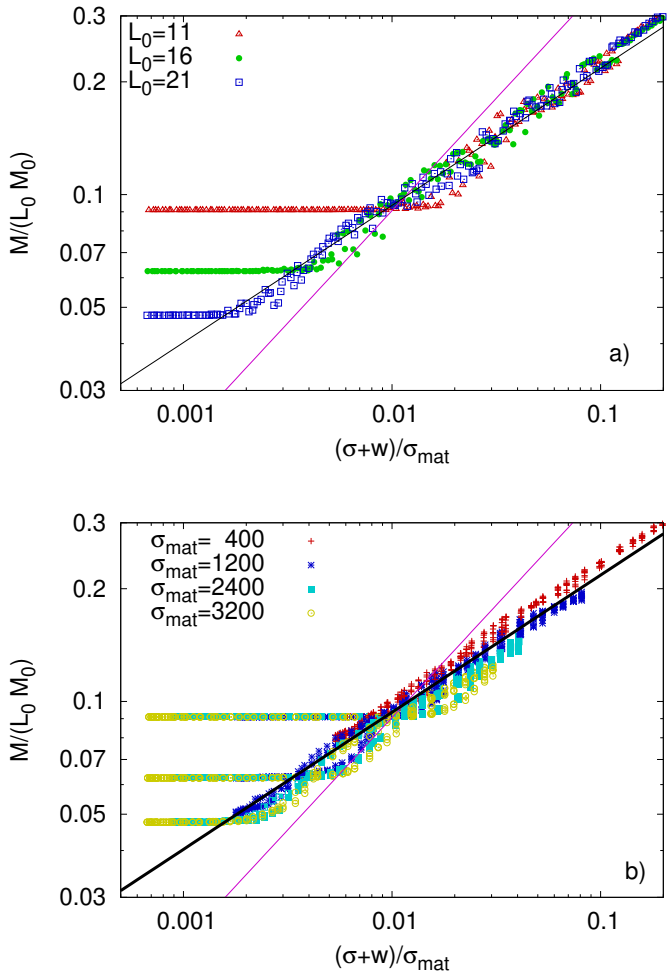

Fig. 3.5: Double-logarithmic plot showing the dependence of the reciprocal number-mean particle length $L^{-1} = M/(M_0 L_0)$ on the effective stress $\hat{\sigma} = (\sigma + w)/\sigma_{\mathrm{mat}}$. Data are annotated according to: (a) the initial particle length L_0 or to (b) the particle strength σ_{mat}. (Figure reprinted from [7])

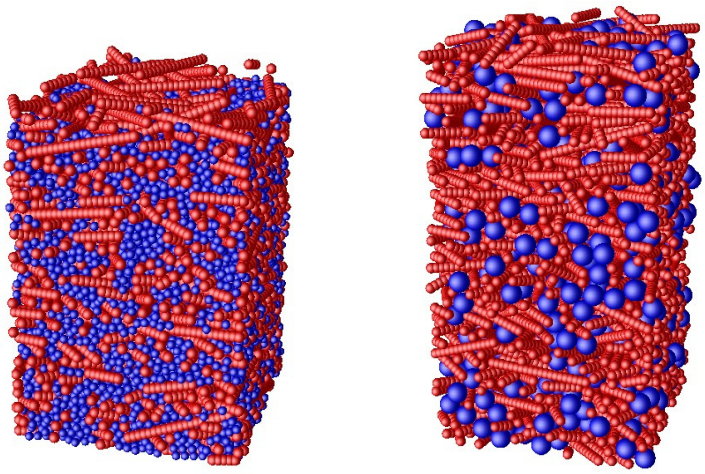

Fig. 3.6: Composite packings formed from needle-shaped crystals and spherical filler particles. Fillers relative size: $R = 0.8$ (left) and $R = 2$ (right), fillers volume fraction: $\phi_F = 0.4$ (Figure reprinted from [8]).

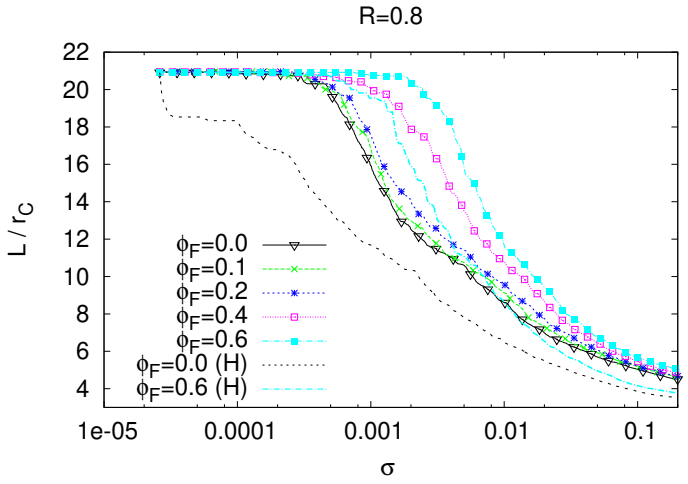

Fig. 3.7: The average relative crystal length as a function of the compaction stress σ. Note that the breakage is reduced as the volume fraction ϕ_F of filler particles increases. Lines denoted by "(H)" represent packings composed of week crystals (strength of week crystals is set to one half of the value for regular crystals). (Figure reprinted from [8])

loading stress experienced by individual particles. The addition of spherical elastic particles (fillers) to the packing of fragile crystals can therefore reduce the extent of crystal breakage if their addition increases the number of contacts; smaller fillers are more effective at reducing the breakage than larger fillers. For example, it can be seen from Fig. 3.7 that the extent by which the breakage is reduced increases as more filler particles are added to the packing; number-mean crystal length L at a particular value of compaction stress σ increases with the increase of volume fraction ϕ_{F} of filler particles in the packing.

3.3.5 Combination of shearing and compression

Paper [9] (cf. Section 8.5 on page 149) analyses the breakage patterns for a packing of needle-shaped particles that is confined between two parallel plates and subjected to a combination of compression and shearing. It presents computational experiments investigating the effect of particle strength, the compressive stress and the shear rate on the porosity, particle size distribution, particle orientation and particle velocity profile.

The results reveal that when the course of particle breakage is represented in the mean particle length L vs. polydispersity Z diagram (cf. Fig. 3.8), the breakage patterns for a slow shearing and a compression follow the same path that is close to the path constructed for an idealised breakage scenario assuming a progressive breaking of particles in half[1]

$$Z(L) = \frac{1}{2}(L_0/L)(3 - L_0/L). \tag{3.13}$$

On the other hand, the curves in a $L|Z$ diagram for a fast shearing deviate from the scenario towards higher polydispersities.

A possible cause of this deviation are higher velocity gradients that are observed at faster shearing rates. A large velocity gradient is a sign of the formation of a narrow zone between two layer parts that move at different velocities and the breaking of particles localised within the zone. Spatially localised breakage events are not consistent with an idealised breakage scenario assuming uniform distribution of breakages. A smaller gradient at a slower shearing rate suggests that the spatial distribution of breakage events is less localised than at faster shearing and therefore better corresponding to the scenario.

3.4 Conclusion and perspectives

When attempting to model unit operations that involve granular material, DEM is a primary tool that enables to carry out *en-silico* experiments and exhaustive parametric studies. Results of such studies are then used to map

[1] Derivation of Eq (3.13) is shown in Appendix A of [8] (page 139).

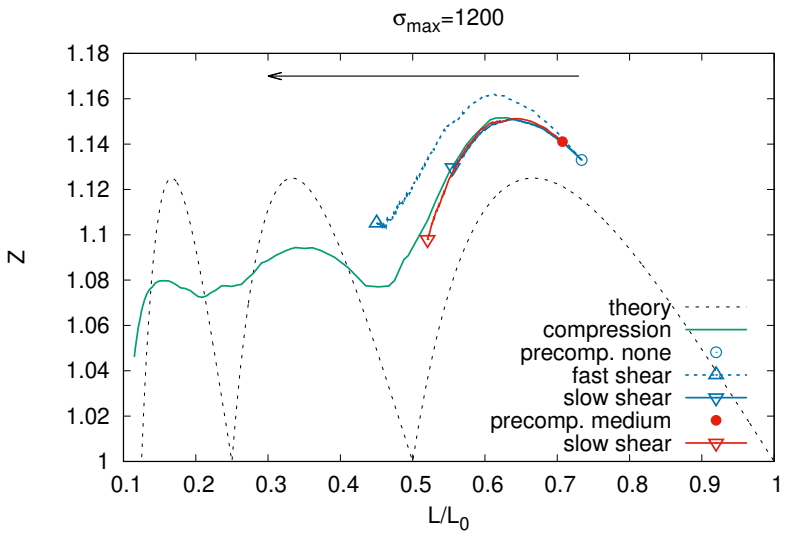

Fig. 3.8: The mean particle length L vs. polydispersity Z diagram for the following scenarios: (i) compression (green line), (ii) fast shearing (blue dashed line), (iii) slow shearing (blue line), (iv) partial layer compression followed by slow shearing (red line). (Figure reprinted from [9])

the material and process characteristics space (input parameters) with the characteristics of material resulting from the operation (output parameters).

DEM simulation is also essential when one tries to better understand the relationship between the structure and performance of the final product. For example, particle arrangement in a directly compressed pharmaceutical tablet determines the tablet porosity and the strength of inter-particle bonds which, in turn, determine the rate of tablet disintegration and API release. Only empirical or semi-empirical knowledge can be gained from purely experimental studies. However, when digitally encoded structures of granular material provided by DEM simulation are further analysed, structure-property relationships can be devised on a first principles basis.

4. DISINTEGRATION AND DISSOLUTION OF PHARMACEUTICAL TABLETS

Tableting (pelleting) is the process of compressing primary particles into the shape of a tablet (pellet) and it is widely used in the production of coal, iron ore or biomass pellets, detergents, food (e.g. cereals, pet food), fertilisers, and pharmaceutical products. These kinds of products are intended, at specific point during their lifetime, to disintegrate back into the primary particles and release their active component at a prescribed rate, cf. Fig. 4.1. They must therefore posses certain mechanical and chemical stability during handling, packaging and storing, while they must be able to timely disintegrate and dissolve during the application phase.

For pharmaceutical products such as tablets, the dosage and the release rate of an active pharmaceutical ingredient (API) is given by requirements based on the intended medicinal effect and related pharmacokinetics studies describing the API distribution and absorption within the body. API release curve is therefore one of the key prescribed parameters that must be met when a pharmaceutical tablet is designed and produced. The need for both immediate-release and sustained-release (i.e. drug release is delayed or the drug is being delivered for a prolonged period of time) tablets exists in the field of pharmaceutical products.

Many factors like the primary particle properties, composition, tableting

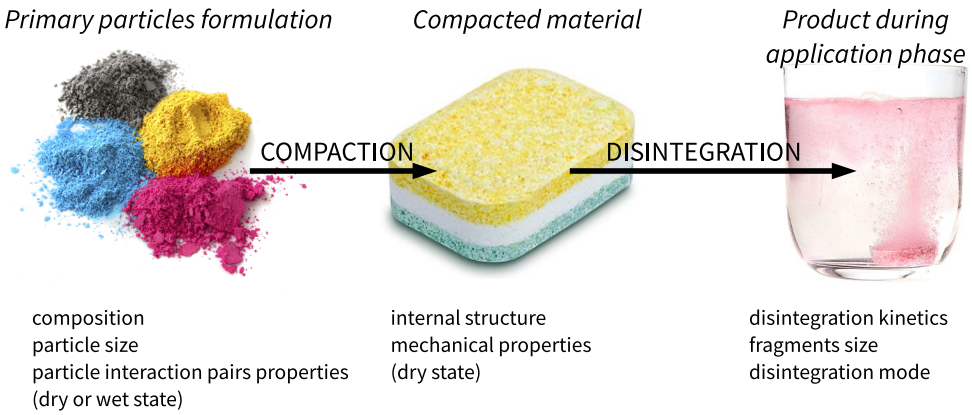

Fig. 4.1: The life cycle of pelleted products.

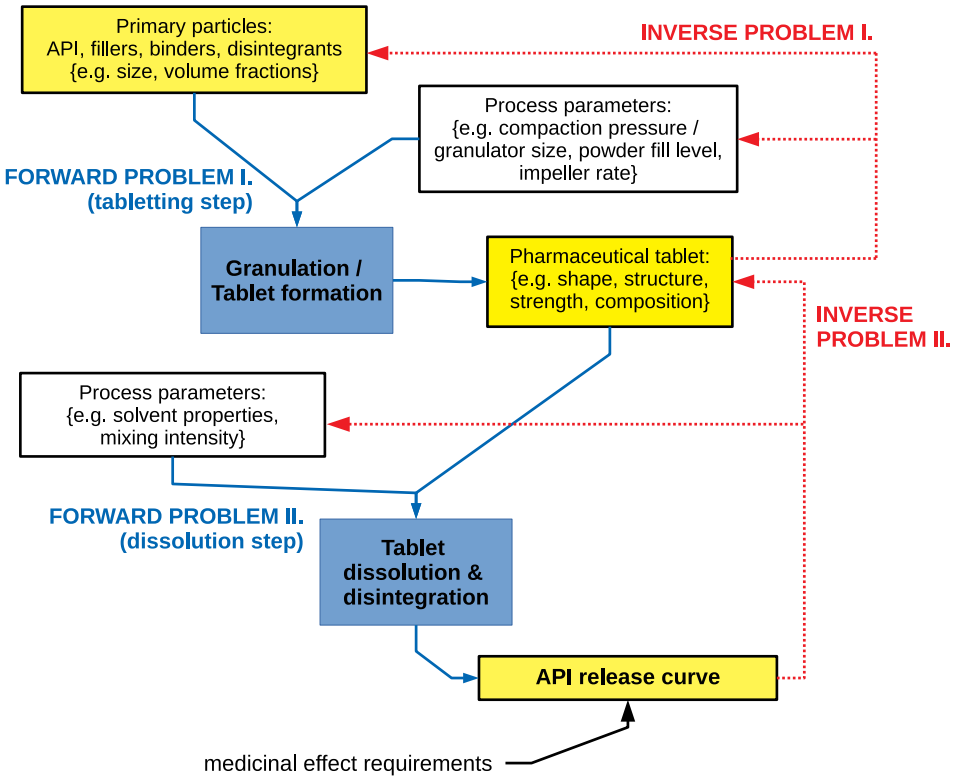

Fig. 4.2: Illustration of the forward and inverse problems in tablet development process.

conditions and material internal structure play an important role in the disintegration and dissolution behaviour. Standardised methods for measuring the rate of tablet disintegration and API dissolution exist and are routinely used to assess and compare different tablet formulations. Because a large number of formulations must be prepared and tested before an optimum formulation meeting the required API release curve is found, this approach to tablet design can be ineffective when taking into account the amount of laboratory worker's time spent and material consumed. Better approach uses *Quality by Design*, a methodology based on the understanding of how primary particle attributes and process parameters relate to product performance such as its disintegration and dissolution behaviour [57].

Diagram summarising tablet design and development is shown in Fig. 4.2. The process can be divided into two sub-problems: (i) Tableting step including the preparation of primary particles such as crystallization, sizing, blending, coating and granulation operations and particles compression in the tablet press. The output is a tablet with a particular composition, internal structure, shape and size, hardness, abrasion, friability, and API release properties. (ii) Tablet disintegration and dissolution behaviour at given

conditions which is characterised by the API release curve on the output.

Both these sub-problems can be viewed as **forward problems** and the mapping between input parameters (primary particles attributes and process operating conditions, or tablet attributes) and output parameters (tablet attributes, or API release curve) can be performed either by using experiments only or by combining experiments and simulations. The latter option is more effective because, compared to the purely experimental approach, it requires a smaller set of experiments that are used to validate the mathematical model and to set model parameter values that cannot be obtained from directly measurable quantities. Mathematical modelling and simulations therefore enable to perform extensive parametric mapping between input and output properties without the need for extensive consumption of valuable material.

After the methodology for solving forward problems is established, one can then focus on **inverse problems** as defined by the diagram in Fig. 4.2. The question that defines this problem is: How to search for, preferably using a systematic way, the set of tablet attributes that result into a tablet with the desired dose strength and drug release rate?

Let us illustrate the strategies for solving both forward and inverse problems in subsequent sections.

4.1 Modelling of the tableting step

This step involves a wide range of operations with particulate material such as crystallization, sizing, blending, coating, granulation and tablet compression. Discrete Element Modelling (DEM) can be therefore regarded as an universal tool that enables to carry out computational simulations of most of these operations [54, 58, 59].

Granulation is a unit operation that converts small fine or coarse particles to larger agglomerates called granules. Granules can be handled and compressed more easily than the source powders due to their free-flowing and dust-free behaviour. There exist experimental studies mapping high shear granulation parameters (impeller speed, wetting rate, granulation time, temperature) with several quality parameters of resulting tablets, e.g. [10, 60]. In order to test granules mechanical strength and its relation to the internal structure of granules characterised by binder amount and its distribution within the granule, DEM is often used to simulate a single granule compression and breakage [61]. The extent of intra-granule composition inhomogeneity [62] is another key property of produced granules that must be observed and controlled in the course of the granulation step.

To complete tablet manufacture, the particles are uni-axially compressed in a tablet press—the modelling of such operation has been already discussed in Chapter 3. DEM computational simulation provides an *in-silico* representation of the layer of particles for which a network of particle contacts can

be analysed. This analysis becomes valuable in the case of multi-component formulations that contain, for example, a mixture of API and excipient particles of different PSD and wetting properties. Assuming that the API is more hydrophobic while the excipient is more hydrophilic, tablet dissolution (disintegration) rate that is related to the rate of solvent uptake into the tablet will greatly depend on the percolation state of the hydrophilic phase. Therefore DEM simulations followed by connectivity analysis can help to establish the threshold volume fraction of excepient particles that leads to percolating excipient phase in the resulting tablet.

4.2 Modelling of the tablet disintegration and dissolution step

Mathematical models of drug dissolution were comprehensively reviewed [63–65] and they range from the simplest, diffusion based semi-empirical relations such as Noyes-Whitney, Higuchi or Peppas equations to more complex approaches considering also solvent uptake, swelling [66] and erosion processes that require the numerical solution of balance and transport equations [67]. In most cases the dissolution models are constructed by describing the tablet as a single-phase medium or an effective porous medium [68]. Also a DEM based approach can be used to model the swelling and dissolution in the case of extended release pharmaceutical tablets [69, 70].

As an example, let us introduce a single-phase tablet dissolution model that is formulated in [11] and can be viewed as an extension of Noyes-Whitney equation for irregular geometries. The simulation domain is discretized into cubical volume elements (voxels) with the spatial discretization step h. Tablet structure is encoded by the solid phase volume function $f_i \in \{0, 1\}$, where zero represents fluid-phase and one represents solid-phase voxels. The diffusion transport of the dissolved API is considered between each pair of neighbouring fluid-phase voxels within a boundary layer, up to a specified distance L from the nearest solid/fluid interface. The following dimensionless quantities are defined:

- dimensionless molar quantity $\hat{n} \equiv n/(h^3 c^\star)$,
- dimensionless concentration $\hat{c} \equiv c/c^\star$,
- dimensionless time $\hat{t} \equiv t/\tau_0$ and
- dimensionless distance $\hat{x} \equiv x/h$,

where n is the molar quantity of API component, c is the API molar concentration, $c^\star$ is the equilibrium solubility of the API and τ_0 is the characteristic time $\tau_0 = h^2/D$ where D is the diffusion coefficient of API in dissolution medium. The dimensionless analysis shows that, in addition to the tablet geometry, the model contains only three parameters: the characteristic time τ_0, the dimensionless boundary layer thickness $\delta = L/h$ and the relative API

Tab. 4.1: Effective scale model for tablet dissolution

API mass balance in fluid voxels	$(\mathrm{d}\hat{c}_i/\mathrm{d}\hat{t}) = -\sum_j (\hat{c}_i - \hat{c}_j)$	$\forall i : f_i = 0$
API mass balance in solid voxels	$(\mathrm{d}\hat{n}_i/\mathrm{d}\hat{t}) = -\sum_j (\hat{c}_i - \hat{c}_j)$	$\forall i : f_i > 0$
i.c. in fluid voxels	$\hat{c}_i(\hat{t} = 0) = 0$	$\forall i : f_i = 0$
i.c. in solid voxels	$\hat{n}_i(\hat{t} = 0) = \alpha$	$\forall i : f_i > 0$
b.c. at tablet/fluid interface	$\hat{c}_i(\hat{t}) = 1 \quad \forall i : f_i > 0$	
b.c. outside diffusion layer	$\hat{c}_i(\hat{t}) = 0 \quad \forall i : \lvert\hat{x}_i - \hat{x}_{\mathrm{solid}}\rvert > \delta$	

Note: The sum $\sum_j$ goes over all neighbouring voxels j of the voxel i.

solid-state concentration $\alpha = \rho/(M_w c^\star)$, where ρ and M_w is the API density and molar weight, respectively. The governing equations, initial conditions and boundary conditions are shown in Tab. 4.1. When the API amount n_i in a solid phase voxel i reaches zero, the voxel is reclassified as a fluid phase voxel and the shape of the tablet changes. The simulation continues until all solid phase voxels completely dissolve.

For an immediate release tablet to be able to disintegrate and fully dissolve within a short time after the application, disintegrants are often added to the tablet formulation. When contacted with physiological fluids, disintegrants increase their volume and promote the tablet disintegration into smaller fragments. This leads to a considerably higher drug release rate due to the increased surface area available for the dissolution [71–73]. Single-phase models cannot conveniently describe drug release and the classical modelling techniques must be extended. Several approaches able to model the disintegration part of drug release have been presented, e.g. using percolation theory [74] or cellular-automata [75]. Nevertheless, the DEM-based simulation approach [12] has been preferred in our research group. Our activities [76–79] include also testing of new experimental techniques for the observation of tablet disintegration—a task that must complement the development of mathematical modelling methods.

4.3 Methods for solving the inverse problem

Forward problem modelling techniques are able to predict API release curve for a tablet with given structure, while the inverse problem involves the search for an *unknown* structure that releases API in a manner as close as possible to the target API release curve. It is an optimisation problem maximising an objective function with respect to the decision variables subject to constraints and bounds on these variables. Here, the decision variables define tablet structure that is determined by, for example, a particular combination assigning APIs and excepient phase to sectors inside the tablet, API content in each sector and the intended interstitial dissolution rate of each sector. The objective function quantifies the match between the actual and the target release curves and an example of a constraint is the total API

amount in the tablet.

One can choose between deterministic and stochastic optimisation methods. It is expected that multiple solutions, probably with different objective function values, would exist for this problem. Even if a particular solution corresponds to the maximum value of the objective function, finding this global optimum (i.e. optimal solution) can be difficult due to an enormous space of the decision variable value combinations. Stochastic algorithms able to quickly produce good, although not necessarily optimal, solutions are therefore preferred in the present situation.

Stochastic optimisation methods [80] can be classified into the following groups:

- Random search techniques (adaptive random search, simulated annealing, tabu-search)
- Evolutionary methods (genetic algorithms, evolutionary programming, differential evolution)
- Swarm intelligence methods (ant colony optimisation, particle swarm optimisation)
- Other methods (harmony search, scatter search, tunnelling methods)

Genetic algorithm (GA) approach has been tested in our work [13]. GA is a population based search method inspired by features and processes of a biological evolution that seeks an improved performance by sampling the regions of solution space with a high probability for leading to good solutions. Starting from the initial set of random solutions (the initial population), new solutions (off-spring individuals) are generated by the combinations and modifications (cross-over and mutation operations) of the best solutions (parents) selected from the existing set of solutions (the actual population), while the worst solutions are discarded. The algorithm proceeds in an evolutionary manner where the most fit individuals survive in the population.

The computational time efficiency of GA depends on its ability to quickly asses the fitness of newly created individuals. More fit individuals are the tablet structures with their API release curve more closely matching the target API release curve. The classic simulation methods based on the numerical solutions of partial differential equations are too slow to be used within GA framework. The solution to this drawback might be a faster, event-driven dissolution algorithm for the computation of API release curve that is presented in [13].

4.4 Case-studies involving disintegration and dissolution modelling

4.4.1 Mapping of granulation parameters to the tablet structure

Paper [10] (cf. Section 9.1 on page 161) is an experimental study. Several batches of granules were prepared in a high-shear mixer granulator at different granulator volumes and Froude numbers. The internal structure of resulting granules was examined using an X-ray micro-tomography scanner and granule stiffness was tested by compressing the granule by a texture analyser.

Froude number Fr characterises the ratio between centrifugal and gravitational forces that act inside the granulator,

$$\mathrm{Fr} = \frac{n^2 d}{g} \approx \frac{\text{centrifugal force}}{\text{gravitational force}}. \tag{4.1}$$

In the previous equation, n is impeller rotation rate, d is impeller diameter and g is the gravitational acceleration.

The correlations between Froude number, granule porosity and granule stiffness that have been established suggest that, in general, the granulation at higher Froude numbers produces more compact and more stiff granules. However, a considerably high level of variation among mechanical properties of granules originating from a single batch was observed. This intra-batch variability increases with the increasing Froude number and makes this type of studies difficult and laborious as a large number of individual granules must be tested in order to obtain statistically representative results.

The work contains also the dissolution experiments with produced granules: a faster dissolution rate of less compact granules has been observed.

4.4.2 Dissolution modelling

Paper [11] (cf. Section 9.2 on page 175) studies the effect of tablet structure on its dissolution rate. It uses the diffusion layer-based mathematical model described in Section 4.2 to model drug release from tablets with an arbitrary geometry. Series of 3D-printed tablets with varying porosity was prepared and their drug release profiles were obtained experimentally and computationally. Thus a library of structural elements with known release kinetics was formed. Tablets with required drug release profiles were then designed and tested *in-silico* by the superposition of these structural elements as is illustrated in Fig. 4.3.

4.4.3 Disintegration and dissolution modelling

Paper [12] (cf. Section 9.3 on page 189) presents a method for the modelling of drug release from immediate-release tablets. These directly compressed tablets usually contain also a disintegrant component, for example

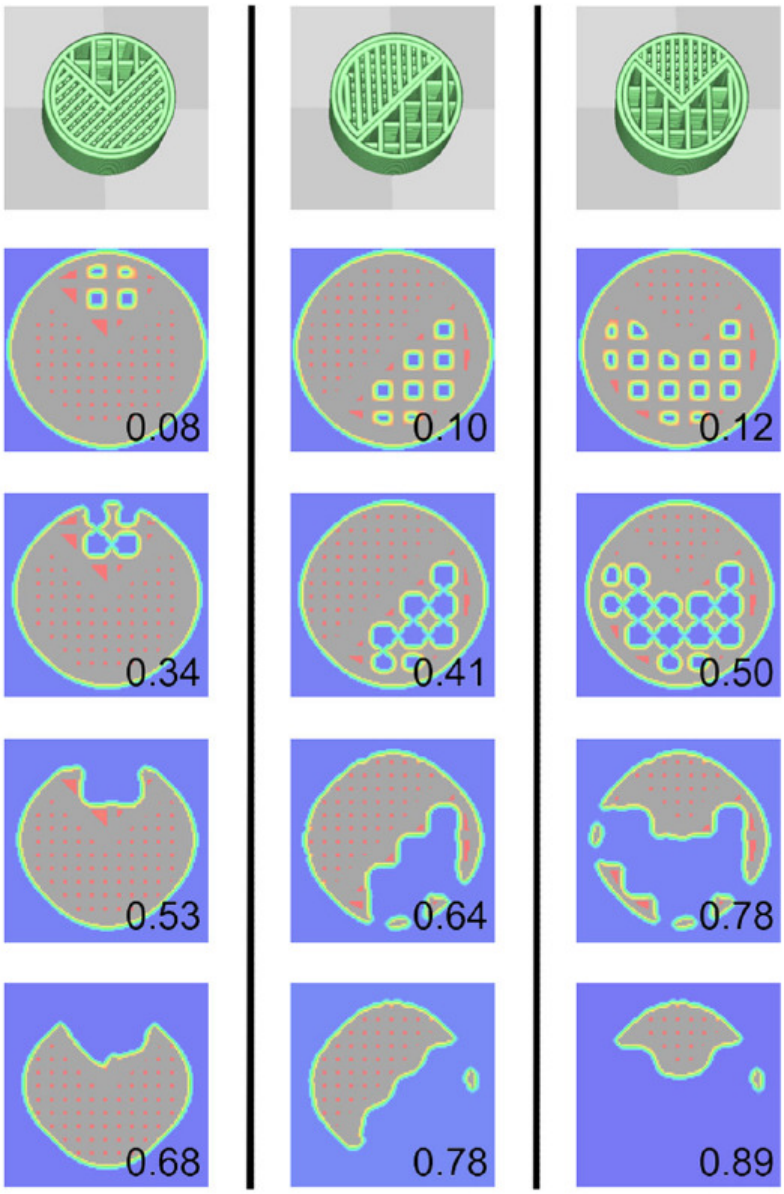

Fig. 4.3: Example of the *in silico* dissolution for composite 3D-printed tablets with combined 30 and 70 % infill at ratios 1:3, 1:1 and 3:1. (Figure reprinted from [11])

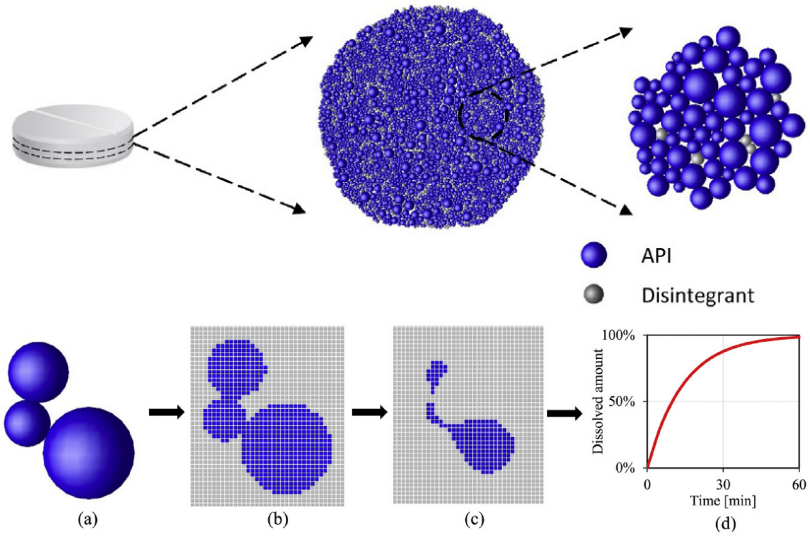

Fig. 4.4: Disintegration and dissolution modelling scheme: DEM simulation tablet disintegration into fragments (top row), dissolution of individual fragments (bottom row). (Figure reprinted from [12])

croscarmellose that swells rapidly in the presence of water and is able to increase its volume eight times when compared to its dry state. Disintegrant swelling therefore forms a mechanical stress within the tablet that promotes tablet disintegration into smaller fragments. The fragmentation process is modelled by a DEM-based model (cf. the top row of Fig. 4.4). Size distribution of primary particles the tablet is compressed from together with parameters characterising the repulsive and attractive forces among particles and the fraction of disintegrant particles in the tablet formulation are the inputs to the model. The result from the simulation is the fragment size distribution and the shape of individual fragments.

In the second part of the modelling procedure, individual fragments are discretized and superimposed on a rectangular elements grid and a boundary layer is created around the fragment. The fragment dissolution is simulated by the same diffusion layer-based model described in [11] (cf. the bottom row of Fig. 4.4). The complete dissolution curve of the modelled tablet is then reconstructed as a weighted sum of the fragment dissolution curves.

A proof-of-concept for this methodology has been successfully demonstrated: First, a parametric study investigating the effect of model parameters on tablet disintegration together with experimental data was used to find optimal parameter values. Let us note that only the experimental data for tablets of type A with 2% of disintegrant content were used to fit the model parameters. Secondly, size distribution of fragments formed by the disintegration of tablets containing varying disintegrant content (1%, 2%

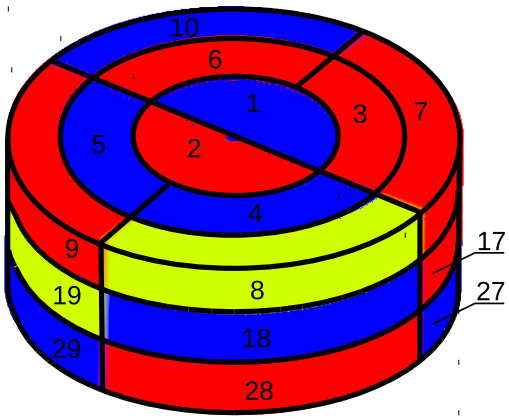

Fig. 4.5: Division of the tablet into sectors associated with particular building block types.

and 4%) and different primary particles size distribution (types A and B tablets) was predicted by numerical simulations using the same values of the parameters. These results were in a good agreement with experimental data without the need for any further parameter adjustment. Finally, the dissolution of individual fragments was simulated, and dissolution curves were constructed and compared with experiments.

4.4.4 Inverse problem solution by genetic algorithm

Our recent work [13] presented in Section 9.4 examines the possibility to use a genetic algorithm to optimise tablet configuration.

As is illustrated in Fig. 4.5, the tablet is spatially divided into sectors and every sector is associated with a particular segment type from a set of tablet building blocks. The set contains segments with a different combination of API component(s) concentrations and solid phase dissolution rates. For example, there are segments that contain API ("a","A") or do not contain any API ("b","B") and segments that dissolve fast ("A","B") or slowly ("a","b") in [13]. A particular assignment of segment types to individual sectors defines the tablet with a particular structure that leads to a particular API release curve.

The feasibility of the proposed algorithm to find the tablet structure that provides the release curve that is as close as possible to the arbitrarily given target release curve was evaluated in several scenarios. It has been demonstrated that this methodology indeed enables to solve the inverse problem and could be adopted as an useful tool in tablet design process.

4.5 Conclusion and perspectives

Let us summarise the key features and problems regarding the mathematical models able to reliable predict drug release profile from pharmaceutical tablets:

- Tablet microstructure determines the disintegration and dissolution behaviour—the model must operate with a digitally encoded structure discretized to a sufficiently detailed level. Unfortunately, microstructure variations leading to significant performance differences exist and make the computational and experimental studies laborious as a large number of samples must be processed to obtain statistically reliable conclusions.

- API release is a complex process involving several phenomena such as solvent up-take, swelling, fragmentation and dissolution. Full models incorporating all the phenomena are therefore difficult to develop. Nevertheless, simpler models are still useful despite their imperfections due to neglecting some phenomena.

- There is an enormous variety of tablet formulations and a wide range of API and excipients that are commonly used. Different models might be better suited for different tablet types.

- Analytical technologies for measuring mass transport and mechanical changes in the tablet during the disintegration and dissolution are scarce. This leads to the uncertainty in model parameter values and makes the identification and quantification of sources of discrepancies between model predictions and measurements difficult. Modelling methodologies should be therefore developed hand in hand with new measuring technologies.

5. CONCLUSIONS

This thesis summarises mathematical modelling approach that is used to study pharmaceutical unit operations including drying, granulation, coating, blending, and tablet compression. Also, the methods for solving the forward and inverse problem in the area of pharmaceutical products design and development are introduced.

Unlike empirical or semi-empirical studies, this approach is based on a first-principles description and quantification of particle–particle and liquid–particle interactions and other phenomena occurring within particulate materials. The modelling tools operate with digitally encoded structures and benefit from their ability to carry out computational (*in-silico*) experiments. They facilitate the search for and the finding of the true causes that determine the relationships between process conditions, material structure and material properties.

With respect to the manufacture and application of pharmaceutical tablets, there exist links between unit operations: the conditions during a granulation operation determine granule microstructure, a pharmaceutical formulation and tableting pressure determine tablet structure, and, consequently, this structure determines the disintegration and dissolution behaviour of the tablet. The presented modelling approach is able to take this into account and models developed for single unit operations can be linked together in the same way as the actual manufacturing process.

At present, the modelling of pharmaceutical processing operations is still largely under development and the existing models are far from perfect and complete. Although further effort is required to improve the models, it is a promising research field that is of an interest for both the academic and industrial areas. As regards the scope of further research, it is important to complement the modelling activities by novel (or yet mostly unused in the pharmaceutical engineering area) experimental techniques for a direct observation of material structure such as X-ray micro-tomography [4, 10], magnetic resonance imaging [76], microscopy or texture analysis [77–79].

6. REFERENCES

[1] Z. Grof, J. Cook, C. J. Lawrence, and F. Stepanek. The interaction between small clusters of cohesive particles and laminar flow: Coupled DEM/CFD approach. *J. Petrol. Sci. Eng.*, 66:24–32, 2009. doi:10.1016/j.petrol.2009.01.002.

[2] Z. Grof, C. J. Lawrence, and F. Stepanek. Computer simulation of evolving capillary bridges in granular media. *Granul. Matter*, 10:93–103, 2008. doi:10.1007/s10035-007-0071-1.

[3] Z. Grof, C. J. Lawrence, and F. Stepanek. The strength of liquid bridges in random granular materials. *J. Colloid Interf. Sci.*, 319:182–192, 2008. doi:10.1016/j.jcis.2007.11.055.

[4] M. Kohout, Z. Grof, and F. Stepanek. Pore-scale modelling and tomographic visualisation of drying in granular media. *J. Colloid Interf. Sci.*, 299:342–351, 2006. doi:10.1016/j.jcis.2006.01.074.

[5] Z. Grof, M. Kohout, and F. Stepanek. Multi-scale simulation of needle-shaped particle breakage under uniaxial compaction. *Chem. Eng. Sci.*, 62:1418–1429, 2007. doi:10.1016/j.ces.2006.11.033.

[6] Z. Grof, C. M. Schoellhammer, P. Rajniak, and F. Stepanek. Computational and experimental investigation of needle-shaped crystal breakage. *Int. J. Pharmaceut.*, 407:12–20, 2011. doi:10.1016/j.ijpharm.2010.12.031.

[7] Z. Grof and F. Stepanek. Distribution of breakage events in random packings of rodlike particles. *Phys. Rev. E*, 88:012205, 2013. doi:10.1103/PhysRevE.88.012205.

[8] Z. Grof and F. Stepanek. Quantifying the effect of fillers on the breakage behaviour of needle-shaped particles. *Adv. Powder Technol.*, 27:1093–1100, 2016. doi:10.1016/j.apt.2016.03.018.

[9] M. Schongut, Z. Grof, and F. Stepanek. Analysis of breakage patterns in a sheared layer of elongated particles. *Powder Technol.*, 345:682–691, 2019. doi:10.1016/j.powtec.2019.01.045.

[10] D. Smrcka, V. Lesakova, J. Dohnal, Z. Grof, and F. Stepanek. Experimental analysis of inter- and intra-batch variation of granule porosity, stiffness and dissolution rate. *Chem. Eng. Res. Des.*, 132:1131–1142, 2018. doi:10.1016/j.cherd.2018.02.014.

[11] M. Novak, T. Boleslavska, Z. Grof, A. Wanek, A. Zadrazil, J. Beranek, P. Kovacik, and F. Stepanek. Virtual prototyping and parametric design of 3D-printed tablets based on the solution of inverse problem. *AAPS PharmSciTech*, 19(8):3414–3424, 2018. doi:10.1208/s12249-018-1176-z.

[12] M. Kalny, Z. Grof, and F. Stepanek. Microstructure based simulation of the disintegration and dissolution of immediate release pharmaceutical tablets. *Powder Technol.*, 377:257–268, 2021. doi:10.1016/j.powtec.2020.08.093.

[13] Z. Grof and Stepanek F. The optimization of multi-component tablet internal structure by evolutionary agorithm. Unpublished manuscript draft, 2020.

[14] D. Hornbaker, R. Albert, I. Liestyo, A.-L. Barabasi, and P. Schiffer. What keeps sandcastles standing? *Nature*, 387:765–765, 06 1997. doi:10.1038/42831.

[15] G. M. Whitesides and M. Boncheva. Beyond molecules: Self-assembly of mesoscopic and macroscopic components. *P. Natl. Acad. Sci. USA*, 99:4769–4774, 2002. doi:10.1073/pnas.082065899.

[16] P. A. Kralchevsky and N. D. Denkov. Capillary forces and structuring in layers of colloid particles. *Curr. Opin. Colloid In.*, 6:383–401, 2001. doi:10.1016/S1359-0294(01)00105-4.

[17] P. A. Cundall and O. D. L. Strack. A discrete numerical model for granular assemblies. *Geotechnique*, 29:47–65, 1979. doi:10.1680/geot.1979.29.1.47.

[18] T. B. Anderson and R. Jackson. A fluid mechanical description of fluidized beds. *Ind. Eng. Chem. Fund.*, 6:527–539, 1967. doi:10.1021/i160024a007.

[19] Y. Tsuji, T. Kawaguchi, and T. Tanaka. Discrete particle simulation of two-dimensional fluidized bed. *Powder Technol.*, 77:79–87, 1993. doi:10.1016/0032-5910(93)85010-7.

[20] B. P. B. Hoomans, J. A. M. Kuipers, W. J. Briels, and W. P. M. Van Swaaij. Discrete particle simulation of bubble and slug formation in a two-dimensional gas-fluidised bed: A hard-sphere approach. *Chem. Eng. Sci.*, 51:99–118, 1996. doi:10.1016/0009-2509(95)00271-5.

[21] K. D. Kafui, C. Thornton, and M. J. Adams. Discrete particle-continuum fluid modelling of gas-solid fluidised beds. *Chem. Eng. Sci.*, 57:2395–2410, 2002. doi:10.1016/S0009-2509(02)00140-9.

[22] S. Maenosono, C. D. Dushkin, Y. Yamaguchi, K. Nagayama, and Y. Tsuji. Effect of growth conditions on the structure of two dimensional latex crystals: Modeling. *Colloid Polym. Sci.*, 277:1152–1161, 1999. doi:10.1007/s003960050504.

[23] H. Nishikawa, S. Maenosono, Y. Yamaguchi, and T. Okubo. Self-assembling process of colloidal particles into two-dimensional arrays induced by capillary immersion force: A simulation study with discrete element method. *J. Nanopart. Res.*, 5:103–110, 2003. doi:10.1023/A:1024489832472.

[24] N. Mitarai and F. Nori. Wet granular materials. *Adv. Phys.*, 55:1–45, 2006. doi:10.1080/00018730600626065.

[25] M. E. D. Urso, C. J. Lawrence, and M. J. Adams. Pendular, funicular, and capillary bridges: Results for two dimensions. *J. Colloid Interf. Sci.*, 220:42–56, 1999. doi:10.1006/jcis.1999.6512.

[26] F. Orr, L. Scriven, and A. Rivas. Pendular rings between solids: Meniscus properties and capillary force. *J. Fluid Mech.*, 67:723–742, 1975. doi:10.1017/S0022112075000572.

[27] C. D. Willett, M. J. Adams, S. A. Johnson, and J. P. K. Seville. Capillary bridges between two spherical bodies. *Langmuir*, 16:9396–9405, 2000. doi:10.1021/la000657y.

[28] T. Mikami, H. Kamiya, and M. Horio. Numerical simulation of cohesive powder behavior in a fluidized bed. *Chem. Eng. Sci.*, 53:1927–1940, 1998. doi:10.1016/S0009-2509(97)00325-4.

[29] R. Scardovelli and S. Zaleski. Direct numerical simulation of free-surface and interfacial flow. *Annu. Rev. Fluid Mech.*, 31:567–603, 1999. doi:10.1146/annurev.fluid.31.1.567.

[30] K. A. Brakke. The Surface Evolver. *Exp. Math.*, 1:141–165, 1992. doi:10.1080/10586458.1992.10504253.

[31] F. Stepanek, M. Marek, and P. M. Adler. Modeling capillary condensation hysteresis cycles in reconstructed porous media. *AIChE J*, 45: 1901–1912, 1999. doi:10.1002/aic.690450908.

[32] F. Stepanek and P. Rajniak. Droplet morphologies on particles with macroscopic surface roughness. *Langmuir*, 22:917–923, 2006. doi:10.1021/la051901u.

[33] J. Kolar, P. Kovacik, T. Choderova, Z. Grof, and F. Stepanek. Optimization of Wurster fluid bed coating: Mathematical model validated against pharmaceutical production data. Submitted to *Powder Technol.*, 2020.

[34] H. M. Jaeger, S. R. Nagel, and R. P. Behringer. Granular solids, liquids, and gases. *Rev. Mod. Phys.*, 68:1259–1273, 1996. doi:10.1103/RevModPhys.68.1259.

[35] P. Rajniak, C. Mancinelli, R. T. Chern, F. Stepanek, L. Farber, and B. T. Hill. Experimental study of wet granulation in fluidized bed: Impact of the binder properties on the granule morphology. *Int. J. Pharmaceut.*, 334:97–102, 2007. doi:10.1016/j.ijpharm.2006.10.040.

[36] P. Rajniak, K. Dhanasekharan, C. Sinka, N. MacPhail, and R. Chern. Modeling and measurement of granule attrition during pneumatic conveying in a laboratory scale system. *Powder Technol.*, 185:202–210, 2008. doi:10.1016/j.powtec.2007.10.017.

[37] J. Schafer, S. Dippel, and D. E. Wolf. Force schemes in simulations of granular materials. *J. Phys. I France*, 6:5–20, 1996.

[38] A. Di Renzo and F. P. Di Maio. Comparison of contact-force models for the simulation of collisions in DEM-based granular flow codes. *Chem. Eng. Sci.*, 59:525–541, 2004. doi:10.1016/j.ces.2003.09.037.

[39] H. Kruggel-Emden, E. Simsek, S. Rickelt, S. Wirtz, and V. Scherer. Review and extension of normal force models for the discrete element method. *Powder Technol.*, 171:157–173, 2007. doi:10.1016/j.powtec.2006.10.004.

[40] G. Lian, C. Thorntont, and M. J. Adams. Discrete particle simulation of agglomerate impact coalescence. *Chem. Eng. Sci.*, 53:3381–3391, 1998. doi:10.1016/S0009-2509(98)00152-3.

[41] K. D. Kafui and C. Thornton. Numerical simulations of impact breakage of a spherical crystalline agglomerate. *Powder Technol.*, 109:113–132, 2000. doi:10.1016/S0032-5910(99)00231-4.

[42] A. Hassanpour, C. C. Kwan, B. H. Ng, N. Rahmanian, Y. L. Ding, S. J. Antony, X. D. Jia, and M. Ghadiri. Effect of granulation scale-up on the strength of granules. *Powder Technol.*, 189:304–312, 2009. doi:10.1016/j.powtec.2008.04.023.

[43] R. Moreno-Atanasio and M. Ghadiri. Mechanistic analysis and computer simulation of impact breakage of agglomerates: Effect of surface energy. *Chem. Eng. Sci.*, 61:2476–2481, 2006. doi:10.1016/j.ces.2005.11.019.

[44] C. L. Martin, D. Bouvard, and G. Delette. Discrete element simulations of the compaction of aggregated ceramic powders. *J. Am. Ceram. Soc.*, 89:3379–3387, 2006. doi:10.1111/j.1551-2916.2006.01249.x.

[45] G. Lu, J. R. Third, and C. R. Muller. Discrete element models for non-spherical particle systems: From theoretical developments to applications. *Chem. Eng. Sci.*, 127:425–465, 2015. doi:10.1016/j.ces.2014.11.050.

[46] J. F. Favier, M. H. Abbaspour-Fard, M. Kremmer, and A. O. Raji. Shape representation of axi-symmetrical, non-spherical particles in discrete element simulation using multi-element model particles. *Eng. Computation*, 16:467–480, 1999. doi:10.1108/02644409910271894.

[47] D. O. Potyondy and P. A. Cundall. A bonded-particle model for rock. *Int. J. Rock Mech. Min.*, 41:1329–1364, 2004. doi:10.1016/j.ijrmms.2004.09.011.

[48] Z. Shen, M. Jiang, and C. Thornton. DEM simulation of bonded granular material. Part I: Contact model and application to cemented sand. *Comput. Geotech.*, 75:192–209, 2016. doi:10.1016/j.compgeo.2016.02.007.

[49] Y. Guo, C. Wassgren, B. Hancock, W. Ketterhagen, and J. Curtis. Predicting breakage of high aspect ratio particles in an agitated bed using crossmark the discrete element method. *Chem. Eng. Sci.*, 158: 314–327, 2017. doi:10.1016/j.ces.2016.10.043.

[50] M. Vanni. Approximate population balance equations for aggregation-breakage processes. *J. Colloid Interf. Sci.*, 221:143–160, 2000. doi:10.1006/jcis.1999.6571.

[51] D. W. Fuerstenau, A. De, and P. C. Kapur. Linear and nonlinear particle breakage processes in comminution systems. *Int. J. Miner. Process.*, 74S:S317–S327, 2004. doi:10.1016/j.minpro.2004.07.005.

[52] M. Khanal, W. Schubert, and Tomas J. DEM simulation of diametrical compression test on particle compounds. *Granul. Matter*, 7:83–90, 2005. doi:10.1007/s10035-005-0200-7.

[53] A. Bobet, A. Fakhimi, S. Johnson, J. Morris, F. Tonon, and M. R. Yeung. Numerical models in discontinuous media: Review of advances for rock mechanics applications. *J. Geotech. Geoenviron.*, 135:1547–1561, 2009. doi:10.1061/(ASCE)GT.1943-5606.0000133.

[54] W. R. Ketterhagen, M. T. Am Ende, and B. C. Hancock. Process modeling in the pharmaceutical industry using the discrete element method. *J. Pharm. Sci.*, 98:442–470, 2009. doi:10.1002/jps.21466.

[55] V. Penkavova, L. Kulaviak, M. C. Ruzicka, M. Puncochar, and P. Zamostny. Breakage of anisometric rod-shaped particles. *Particul. Sci. Technol.*, 36:432–437, 2018. doi:10.1080/02726351.2017.1347969.

[56] V. Penkavova, L. Kulaviak, M. C. Ruzicka, M. Puncochar, Z. Grof, F. Stepanek, M. Schongut, and P. Zamostny. Compression of anisometric granular materials. *Powder Technol.*, 342:887–898, 2019. doi:10.1016/j.powtec.2018.10.031.

[57] E. Tomba, P. Facco, F. Bezzo, and M. Barolo. Latent variable modeling to assist the implementation of Quality-by-Design paradigms in pharmaceutical development and manufacturing: A review. *Int. J. Pharmaceut.*, 457:283–297, 2013. doi:10.1016/j.ijpharm.2013.08.074.

[58] F. Bertrand, L. A. Leclaire, and G. Levecque. DEM-based models for the mixing of granular materials. *Chem. Eng. Sci.*, 60:2517–2531, 2005. doi:10.1016/j.ces.2004.11.048.

[59] W. R. Ketterhagen, M. P. Mullarney, J. Kresevic, and D. Blackwood. Computational approaches to predict the effect of shear during processing of lubricated pharmaceutical blends. *Powder Technol.*, 335:427–439, 2018. doi:10.1016/j.powtec.2018.05.023.

[60] D. T. Ring, J. C. O. Oliveira, and A. Crean. Evaluation of the influence of granulation processing parameters on the granule properties and dissolution characteristics of a modified release drug. *Adv. Powder Tech.*, 22:245–252, 2011. doi:10.1016/j.apt.2011.01.006.

[61] M. Dosta, S. Dale, S. Antonyuk, C. Wassgren, S. Heinrich, and J. D. Litster. Numerical and experimental analysis of influence of granule microstructure on its compression breakage. *Powder Tech.*, 299:87–97, 2016. doi:10.1016/j.powtec.2016.05.005.

[62] A. Kataria, S. Oka, D. Smrcka, Z. Grof, F. Stepanek, and R. Ramachandran. A quantitative analysis of drug migration during granule drying. *Chem. Eng. Res. Des.*, 136:199–206, 2018. doi:10.1016/j.cherd.2018.05.001.

[63] D. Caccavo. An overview on the mathematical modeling of hydrogels behavior for drug delivery systems. *Int. J. Pharmaceut.*, 560:175–190, 2019. doi:10.1016/j.ijpharm.2019.01.076.

[64] J. Siepmann and F. Siepmann. Mathematical modeling of drug dissolution. *Int. J. Pharmaceut.*, 453:12–24, 2013. doi:10.1016/j.ijpharm.2013.04.044.

[65] C. Mircioiu, V. Voicu, V. Anuta, A. Tudose, C. Celia, D. Paolino, M. Fresta, R. Sandulovici, and I. Mircioiu. Mathematical modeling of release kinetics from supramolecular drug delivery systems. *Pharmaceutics*, 11:140, 2019. doi:10.3390/pharmaceutics11030140.

[66] P. Borgquist, A. Korner, L. Piculell, A. Larsson, and A. Axelsson. A model for the drug release from a polymer matrix tableteffects of swelling and dissolution. *J. Control. Release*, 113:216–225, 2006. doi:10.1016/j.jconrel.2006.05.004.

[67] G. Lamberti, I. Galdi, and A. A. Barba. Controlled release from hydrogel-based solid matrices. A model accounting for water uptake, swelling and erosion. *Int. J. Pharmaceut.*, 407:78–86, 2011. doi:10.1016/j.ijpharm.2011.01.023.

[68] H. Zhu, A. Dhall, S. Mukherjee, and A. K. Datta. A model for flow and deformation in unsaturated swelling porous media. *Transp. Porous Med.*, 84:335–369, 2010. doi:10.1007/s11242-009-9505-z.

[69] J. A. Kimber, S. G. Kazarian, and F. Stepanek. Modelling of pharmaceutical tablet swelling and dissolution using discrete element method. *Chem. Eng. Sci.*, 69:394–403, 2012. doi:10.1016/j.ces.2011.10.066.

[70] J. A. Kimber, S. G. Kazarian, and F. Stepanek. Formulation design space analysis for drug release from swelling polymer tablets. *Powder Tech.*, 236:179–187, 2013. doi:10.1016/j.powtec.2012.02.027.

[71] D. Markl and A. Zeitler. A review of disintegration mechanisms and measurement technique. *Pharm. Res.*, 34:890–917, 2017. doi:10.1007/s11095-017-2129-z.

[72] P. M. Desai, C. V. Liew, and P. W. S. Heng. Review of disintegrants and the disintegration phenomena. *J. Pharm. Sci.*, 105:2545–2555, 2016. doi:10.1016/j.xphs.2015.12.019.

[73] J. Quodbach and P. Kleinebudde. A critical review on tablet disintegration. *Pharm. Dev. Technol.*, 21:763–774, 2016. doi:10.3109/10837450.2015.1045618.

[74] E. Krausbauer, M. Puchkov, G. Betz, and H. Leuenberger. Rational estimation of the optimum amount of non-fibrous disintegrant applying percolation theory for binary fast disintegrating formulation. *J. Pharm. Sci.*, 97:529–541, 2008. doi:10.1002/jps.21163.

[75] R. Yokoyama, G. Kimura, C. M. Schleputz, and M. Puchkov. Modeling of disintegration and dissolution behavior of mefenamic acid formulation using numeric solution of Noyes-Whitney equation with cellular

automata on microtomographic and algorithmically generated surfaces. *Pharmaceutics*, 10:259, 2018. doi:10.3390/pharmaceutics10040259.

[76] M. Gajdosova, D. Pecek, N. Sarvasova, Z. Grof, and F. Stepanek. Effect of hydrophobic inclusions on polymer swelling kinetics studied by magnetic resonance imaging. *Int. J. Pharmaceut.*, 500:136–143, 2016. doi:10.1016/j.ijpharm.2016.01.023.

[77] J. Tomas, M. Schongut, O. Dammer, J. Beranek, A. Zadrazil, and F. Stepanek. Probing the early stages of tablet disintegration by stress relaxation measurement. *Eur. J. Pharm. Sci.*, 124:145–152, 2018. doi:10.1016/j.ejps.2018.08.029.

[78] J. Dvorak, J. Tomas, D. Lizonova, M. Schongut, O. Dammer, T. Pekarek, J. Beranek, and F. Stepanek. Investigation of tablet disintegration pathways by the combined use of magnetic resonance imaging, texture analysis and static light scattering. *Int. J. Pharmaceut.*, 587: 119719, 2020. doi:10.1016/j.ijpharm.2020.119719.

[79] J. Tomas, J. Dvorak, O. Dammer, and F. Stepanek. Frequency analysis of stress relaxation patterns reveals the effect of formulation and process history on tablet disintegration. *Powder Technol.*, 379:438–446, 2021. doi:10.1016/j.powtec.2020.10.081.

[80] G. P. Rangaiah, editor. *Stochastic global optimization.* World Scientific, Singapore, 2010. ISBN 981-4299-20-0.

[81] J. Kosek, Z. Grof, A. Novak, F. Stepanek, and M. Marek. Dynamics of particle growth and overheating in gas-phase polymerization reactors. *Chem. Eng. Sci.*, 56:3951–3977, 2001. doi:10.1016/S0009-2509(01)00070-7.

[82] Z. Grof, J. Kosek, M. Marek, and P. M. Adler. Modeling of morphogenesis of polyolefin particles: Catalyst fragmentation. *AIChE J.*, 49: 1002–1013, 2003. doi:10.1002/aic.690490417.

[83] Z. Grof, J. Kosek, and M. Marek. Principles of the morphogenesis of polyolefin particles. *Ind. Eng. Chem. Res.*, 44:2389–2404, 2005. doi:10.1021/ie049106j.

[84] Z. Grof, J. Kosek, and M. Marek. Modeling of morphogenesis of growing polyolefin particles. *AIChE J.*, 51:2048–2067, 2005. doi:10.1002/aic.10549.

[85] B. Horackova, Z. Grof, and J. Kosek. Dynamics of fragmentation of catalyst carriers in catalytic polymerization of olefins. *Chem. Eng. Sci.*, 62:5264–5270, 2007. doi:10.1016/j.ces.2007.03.022.

[86] M. Marek, Z. Grof, P. Koci, M. Kohout, J. Kosek, and F. Stepanek. Multiscale modelling of transport, reaction and phase change in heterogeneous media. *J. Chem. Eng. Japan*, 40:879–889, 2007. doi:10.1252/jcej.07WE044.

[87] G. Frenkel, R. Blumenfeld, Z. Grof, and P. R. King. Structural characterization and statistical properties of two-dimensional granular systems. *Phys. Rev. E*, 77:041304, 2008. doi:10.1103/PhysRevE.77.041304.

[88] S. S. Manley, N. Graeber, Z. Grof, A. Menner, G. F. Hewitt, F. Stepanek, and A. Bismarck. New insights into the relationship between internal phase level of emulsion templates and gas-liquid permeability of interconnected macroporous polymers. *Soft Matter*, 5:4780–4787, 2009. doi:10.1039/b900426b.

[89] M. Schongut, Z. Grof, and F. Stepanek. Kinetics of dry neutralization of dodecyl-benzenesulfonic acid with respect to detergent granulation. *Ind. Eng. Chem. Res.*, 50:11576–11584, 2011. doi:10.1021/ie201047r.

[90] G. Salejova, Z. Grof, O. Solcova, P. Schneider, and J. Kosek. Strategy for predicting effective transport properties of complex porous structures. *Comput. Chem. Eng.*, 35:200–211, 2011. doi:10.1016/j.compchemeng.2010.06.002.

Publications included in the thesis: [1–13]
Other publications of the author: [33, 56, 62, 76, 81–90]

Part II

REPRINTS OF ARTICLES

7. ARTICLES ABOUT LIQUID–PARTICLE INTERACTIONS

7.1 The interaction between small clusters of cohesive particles and laminar flow: Coupled DEM/CFD approach

Zdeněk Grof
John Cook
Christopher J. Lawrence
František Štěpánek

Published in the *J. Petrol. Sci. Eng.*, Vol. 66, 2009, pp 24–32
DOI: 10.1016/j.petrol.2009.01.002.

Provided for non-commercial research and education use.
Not for reproduction, distribution or commercial use.

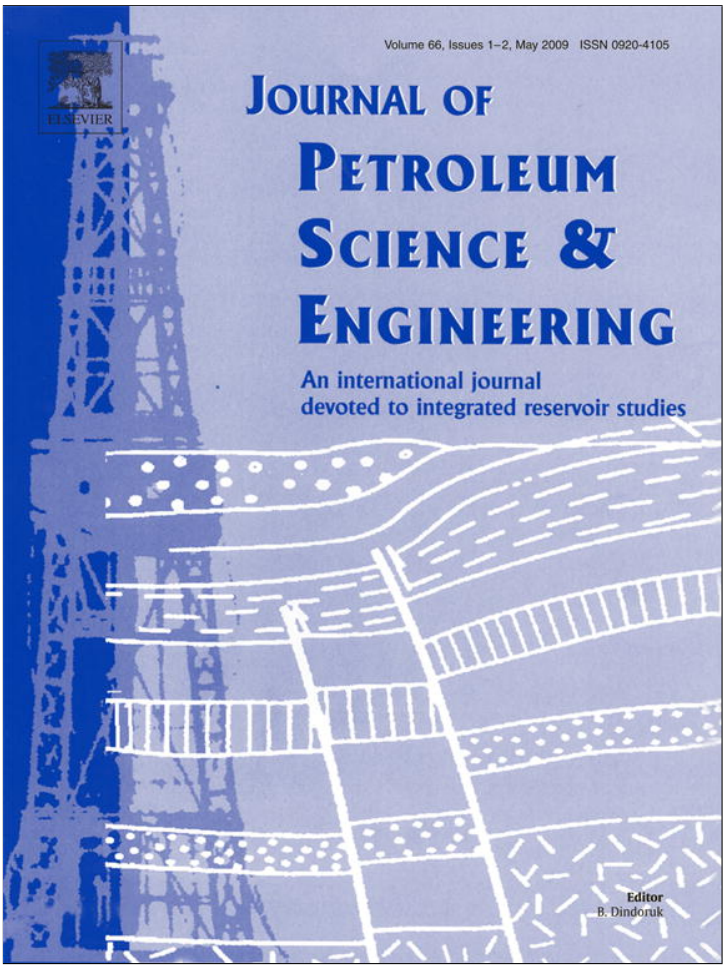

This article appeared in a journal published by Elsevier. The attached copy is furnished to the author for internal non-commercial research and education use, including for instruction at the authors institution and sharing with colleagues.

Other uses, including reproduction and distribution, or selling or licensing copies, or posting to personal, institutional or third party websites are prohibited.

In most cases authors are permitted to post their version of the article (e.g. in Word or Tex form) to their personal website or institutional repository. Authors requiring further information regarding Elsevier's archiving and manuscript policies are encouraged to visit:

http://www.elsevier.com/copyright

Author's personal copy

Journal of Petroleum Science and Engineering 66 (2009) 24–32

Contents lists available at ScienceDirect

Journal of Petroleum Science and Engineering

journal homepage: www.elsevier.com/locate/petrol

The interaction between small clusters of cohesive particles and laminar flow: Coupled DEM/CFD approach

Zdeněk Grof [c], John Cook [b], Christopher J. Lawrence [d], František Štěpánek [a,*]

[a] Department of Chemical Engineering, Imperial College London, South Kensington Campus, London SW7 2AZ, United Kingdom
[b] Schlumberger Cambridge Research, High Cross, Madingley Road, Cambridge CB3 OEL, United Kingdom
[c] Department of Chemical Engineering, Institute of Chemical Technology, Prague, Technicka 5, 166 28 Prague 6, Czech Republic
[d] Institutt for Energiteknikk, P.O. Box 40, 2027 Kjeller, Norway

ARTICLE INFO

Article history:
Received 19 July 2006
Accepted 23 January 2009

Keywords:
particle–fluid interaction
capillary forces
sand production
fluid flow
particle packing
erosion

ABSTRACT

A computational method for the simulation of systems where close coupling exists between a flowing fluid and mobile or stationary cohesive particles is presented in this work. The method is based on the solution of particle motion dynamics by the Discrete Element Method (DEM) coupled with the flow field calculation by a Computational Fluid Dynamics (CFD) approach. The method is demonstrated on two examples inspired by the problem of sand production in oil exploration, namely the stability of a random packed layer of cohesive particles under gravity and under laminar cross-flow. Regime maps suitable for the estimation of limiting conditions for the onset of particle erosion have been generated computationally.

© 2009 Elsevier B.V. All rights reserved.

1. Introduction

The interaction between a flowing liquid and a granular material is encountered in various geological applications such as river bed flows and soil erosion, in oil exploration (reservoir flows, pipeline flows), as well as in chemical engineering applications such as processing of particulate solids (granulation, crystallization). In oil production, the oil and/or water flow from the oil-reservoir through perforations into the main well-bore can be affected by the presence of sand particles and their clusters. Indeed, one of the most severe well–bore problems in the petroleum industry is the sand production which occurs when the reservoir sandstone fails under the in-situ stress (Acock et al., 2004; Nouri et al., 2006). The sand debris can then be transported by the flowing liquid and cause problems in the downstream operation such as the abrasion of equipment or flow obstruction by sand deposits. The exact mechanisms of sand production and transport are still not completely understood at the level of individual grains, where capillary forces between grains due to liquid bridges (oil/water wet systems) may play a significant role.

Sand production phenomena have traditionally been investigated by continuum-mechanics approaches whereby the consolidated sandstone reservoir is treated as a material with given effective-medium properties such as the bulk compression strength. Failure criteria are then obtained by resolving the stress field within the material and identifying the positions of failure planes. Once the location of cracks in the material is known, local erosion rates can be estimated by simultaneously solving the effective-medium fluid flow equation (Darcy's law), assuming an empirical coupling constant. Such an effective-medium model has been used e.g. by Papamichos et al. (2001) or Wang and Wan (2004). In this model, the local erosion rate is given by a constitutive equation for the generation of eroded solid mass, in the form $\dot{m}=\rho_s\lambda(1-\phi)\|\mathbf{q}\|$ where $(1-\phi)\|\mathbf{q}\|$ is the interstitial fluid velocity and λ is the so called "sand production coefficient", with units of area.

However, it has been often observed that rock or sandstone fracture does not necessarily represent the onset of sand production, due to the fact that loose sand particles or rock fragments can be held in place by various mechanisms such as arching, interlocking, or capillary forces (Vaziri et al., 2004). It has been reported (Vaziri et al., 2002) that increasing water cut significantly increases sanding potential as it reduces the capillary forces holding the dis-aggregated particles, and that changes in rock saturation or rock wettability can lead to instability and sand production (Han et al., 2002). These instabilities are also well known from sandpiles (or sand castles) where individual sand particles are held in place by capillary bridges; when these evaporate (i.e. the sand dries) the structure becomes unstable and fails (Albert et al., 1997). The castle will collapse as well when the tide displaces the gas from pores watering the bridges. Such particle-level phenomena are not captured by the effective-medium models mentioned above because a description of the discrete structure of the particle packing is required.

The objective of the present work, therefore, was to investigate sanding phenomena on the microscopic (particle) scale by numerical simulations taking into account capillary forces between individual

* Corresponding author. Tel.: +44 20 7594 5608; fax: +44 20 7594 5604.
E-mail address: f.stepanek@imperial.ac.uk (F. Štěpánek).

0920-4105/$ – see front matter © 2009 Elsevier B.V. All rights reserved.
doi:10.1016/j.petrol.2009.01.002

Author's personal copy

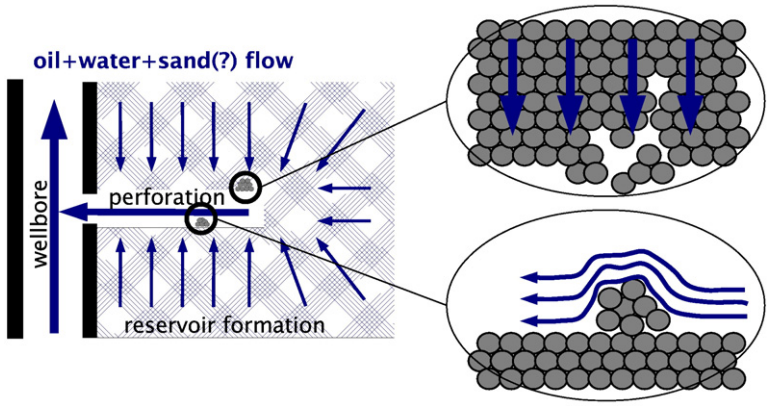

Fig. 1. Schematic illustration of the oil/water flow in a horizontal perforation (left) and two model arrangements corresponding to typical situations relevant to sand production phenomena considered in this work (right).

particles and the hydrodynamic force acting on the particles due to a flowing fluid. To this end, a coupled Discrete Element Method (DEM)–Computational Fluid Dynamics (CFD) approach has been adopted and used for the simulation of fluid–particle interactions under various scenarios and flow geometries characteristic of reservoir conditions. Specifically, two model situations have been studied: the stability of a particle packing under gravity, and the stability of a particle plug in a channel subjected to fluid flow. These two arrangements, illustrated in Fig. 1, have been chosen so as to correspond to common flow arrangements in a typical horizontal perforation (Acock et al., 2004). In both scenarios it is assumed that individual sand grains are loose (no solid bridges) and they are held together by capillary bridge forces only.

Coupled particle–fluid flow problems can in principle be solved by three different approaches (Ho et al., 2006).

(i) The two-fluid (Eulerian–Eulerian) approach, where the solid phase is formally regarded as an additional fluid and the governing equations are coupled to the Navier–Stokes equations of the "true" fluid via an inter-phase force.

(ii) The Eulerian–Lagrangian approach, where particles are treated as discrete entities and their trajectories obtained by solving Newton's law of motion for each particle. The fluid velocity field is resolved on a grid with a spatial discretisation an order of magnitude larger than the average particle size and simplified models (drag laws) are used to estimate the hydrodynamic forces on each particle. This approach is commonly used in the modelling of fluidisation or gas–particle flow phenomena (Tsuji et al., 1992; Hoomans et al., 1996; Kafui et al., 2002). Mikami et al. (1998) have included the cohesive force of pendular liquid bridges into the model in order to study wet powder fluidization.

(iii) The Direct Numerical Simulation approach, which differs from the previous one by the fact that the grid on which the Navier–Stokes equations are resolved has a resolution finer than the particle diameter. Particles present in the system therefore define boundary conditions for the fluid flow and the drag and lift forces acting on each particle are obtained by integration of the normal and tangential stresses over the particle surface.

For micro-level modelling of sand erosion, where clusters of cohesive particles with a priori unknown size distribution exist, the direct numerical simulation (DNS) appears to be the most suitable method. Different implementations of the DNS method can be found in the literature. The main differences are in the treatment of spatial discretisation (fixed vs. adaptive mesh) and the method for the solution of the fluid flow equations (Navier–Stokes equations, Lattice–Boltzmann method). In earlier work, Johnson and Tezduyar (1997) used an adaptive mesh (structured elements around the particles, unstructured mesh elsewhere) and performed 3D simulations with about 100 particles, whereas Glowinski et al. (1999) have used the Distributed Lagrange multiplier method on a fixed finite element mesh. An example of recent work using the lattice Boltzmann method can be found in Feng and Michaelides (2005). In the present work, a fixed mesh has been used with finite volume discretisation of the Navier–Stokes equations. The full details of the implementation are given in Section 2.

2. Method

The simulation proceeds by first creating a particle packing that represents the geometry of interest — e.g. a random packed bed, a cylindrical or rectangular duct, or an agglomerate. Subsequently, two computational modules are invoked in turn: a DEM module responsible for particle motion, and a CFD module responsible for fluid flow field calculation. These two modules are strongly coupled as can be seen in the scheme in Fig. 2; hydrodynamic forces acting on the particles in the DEM module are obtained from the flow field and at the same time, the instantaneous particle positions generate boundary conditions for the fluid flow. The two modules will now be described in more detail.

2.1. Discrete Element Method

The packed bed of particles (or other geometry of interest) is represented by spherical elements characterised by their positions $\boldsymbol{x}_i$,

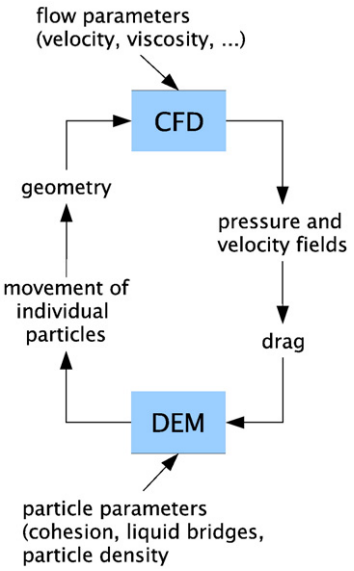

Fig. 2. Scheme for the coupling of CFD and DEM computations.

Author's personal copy

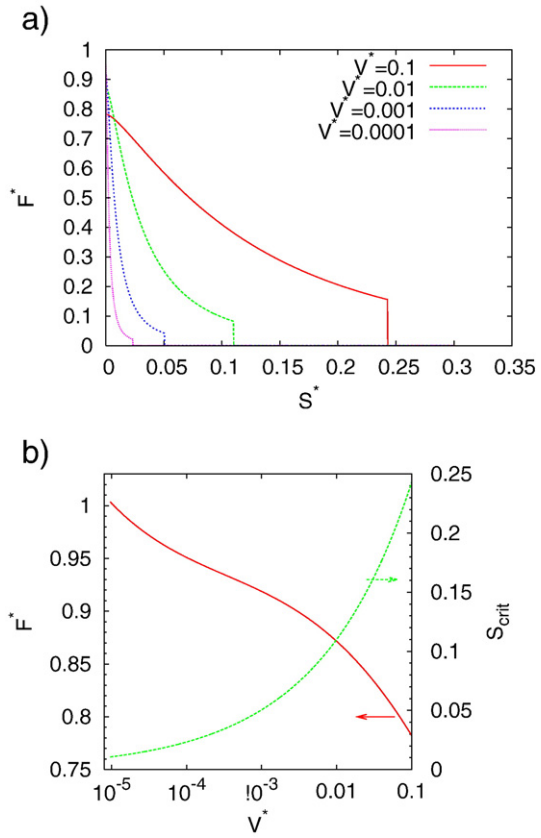

Fig. 3. a) Dimensionless force F^* of a liquid bridge between two spheres with the same radius as a function of the dimensionless distance S^* for different dimensionless bridge volumes V^*; b) Dimensionless force at $S^*=0$ (primary y-axis) and critical separation distance S_{crit} (secondary y-axis) as a function of V^*. The contact angle is zero in both panels. The curves have been calculated using closed form approximations from Willett et al. (2000).

radii r_i and velocities $\boldsymbol{v}_i$. Newton's equations of motion are used for the calculation of particle movements

$$\dot{\boldsymbol{x}}_i = \boldsymbol{v}_i \quad \frac{4}{3}\pi r_i^3 \rho_s \dot{\boldsymbol{v}}_i = \sum_j \left(\boldsymbol{F}_c^{ij} + \boldsymbol{F}_l^{ij}\right) + \boldsymbol{D}_i + \boldsymbol{G}_i \tag{1}$$

where the sum on the right hand side is over all elements j which are in contact with ith element; and, $\boldsymbol{F}_c$, $\boldsymbol{F}_l$, $\boldsymbol{D}$ and $\boldsymbol{G}$ are the contact, the capillary, the hydrodynamic and the gravitational forces, respectively.

The normal contact force between two elements is represented using a linear-elastic model (Cundall and Strack, 1979; Tsuji et al., 1992)

$$F_{cn}^{ij} = \begin{cases} E_n\left(1-e_{ij}\right) & \text{if } e_{ij}<1 \\ 0 & \text{if } e_{ij}\geq 1 \end{cases} \qquad e_{ij} = \frac{d_{ij}}{r_i + r_j} \tag{2}$$

where d_{ij} is the distance between element centers and E_n is the normal stiffness modulus. The tangential component of the contact force F_{ct}^{ij} depends on the history of each contact and cannot be calculated directly just from the knowledge of actual particle positions as, e.g. the normal contact force in Eq. (2). The tangential component of the contact force is set to zero at the formation of each contact and is then updated at every time step according to the relative velocity at the particle contact and the value of the tangential stiffness coefficient E_t. Coulomb type friction slider characterized by friction coefficient α is used in order to ensure that the tangential force is never larger than the friction force, $|F_{ct}^{ij}| \leq \tan\alpha |F_{cn}^{ij}|$. This is a standard method used in Cundall and Strack (1979). The algorithm for the calculation of the tangential force in a three-dimensional systems is fully described e.g. in Venugopal and Rajamani (2001) and Grof et al. (2007). The following values of parameters have been used in simulations: $E_n = E_t = 1$ N, $\alpha = 30°$ and $r = 1$ mm.

The other forces appearing in the model are the capillary, the gravitational force (corrected by the buoyancy), and the drag and lift forces due to fluid flow. These will be described in detail below. The boundary conditions for the DEM part of our model are implemented using static elements at the domain boundary.

Although there are no principal difficulties with simulations of poly-dispersed packings, a nearly mono-dispersed sphere packing is considered in the present work. A narrow Gaussian distribution ($\sigma/R = 0.05$) with the mean value $R = 1$ mm is used for the radii of elements. These small variations in the radius lead to natural-looking packings, and at the same time the particle assembly can still be considered as almost mono-disperse, for example when liquid bridge forces are calculated.

2.2. Capillary bridge forces

In this work we assume there are two liquids present, a wetting liquid forming binary (pendular) capillary bridges and a non-wetting liquid flowing in the interstitial space. The shape of the capillary bridges are assumed to be unaffected by gravity (Adams et al., 2002). The capillary force between two equal spheres is directed along line joining their centers, and its magnitude, F_l, is proportional to the sphere radius R and to the surface tension γ

$$F_l = 2\pi R\gamma F^*. \tag{3}$$

The dimensionless force F^* depends on the separation distance of the spheres $2S$, the volume of the liquid bridge V, and the contact angle φ of the wetting fluid at the surface of the spheres. To obtain its value it is necessary to solve the Laplace–Young equation numerically, or use analytical solutions in terms of elliptic integrals (Orr et al., 1975). However, for the purpose of the DEM calculations, it is more reasonable to use a closed form approximation which is derived by curve-fitting to the numerical solution presented by Willett et al. (2000)

$$F^* = f(V^*, S^*, \varphi) \tag{4}$$

$$V^* = \frac{V}{R^3}$$

$$S^* = \frac{S}{R} = \frac{\left(e_{ij}-1\right)\left(r_i + r_j\right)}{2R} \approx \left(e_{ij}-1\right).$$

The values of F^* as function of the dimensionless bridge volume and the separation distance ($S^*>0$) are plotted in Fig. 3a for $\varphi = 0°$. It can be seen that the capillary force has a maximum at $S^*=0$ (touching

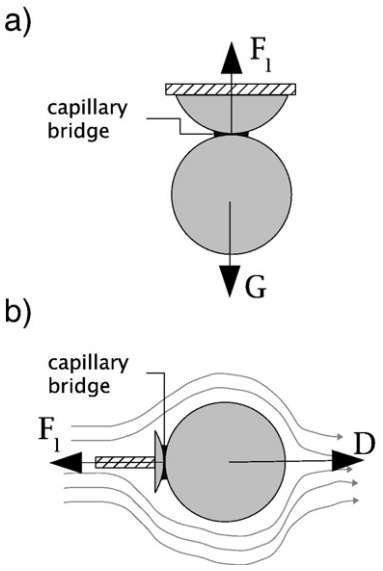

Fig. 4. Illustration of forces acting on a particle: a) gravitational and capillary forces; b) capillary and drag force.

Author's personal copy

Table 1
List of computational parameters.

		Basic value	Range
Radius of elements	r	1 mm	
Density of elements	ρ_s	2700 kg/m^3	
Fluid density	ρ_l	900 kg/m^3	
Fluid viscosity	η	0.02 Pa s	
Stiffness coefficient	E_n, E_t	1 N	
Friction angle	α	30°	
Surface tension	γ	0.023 N/m	
Contact (wetting) angle	φ	0°	
Gravitational acceleration	g	9.81 m/s^2	
Superficial velocity	u	1.1 cm/s	
Bond number	Bo	0.77	0.1–1.0
Drag/capillary number	Ψ	0.0096	0.005–0.025
Reynolds number	Re	1	0–10

spheres) and then monotonically decreases with increasing distance. The dependence on the volume of the liquid bridge V^* is not very strong, cf. Fig. 3b, where the value of F^* (at $S^*=0$) drops only from 1 to 0.75 while the volume varies over several orders of magnitude. The volume has a more important effect on the critical separation distance, i.e., the maximum distance before the rupture of the capillary bridge. This leads us to expect that as the volume of the liquid bridges decreases the clusters of particles could be more easily disintegrated by the action of even very small external forces. From the computational point of view this means that it is not feasible to make simulations with the volumes V^* smaller than approximately 10^{-5}–10^{-6}. To minimize the inaccuracy caused by discrete movements of particles, the distance particles are allowed to move in a single time-step should be considerably smaller than the critical separation distance and this requirement would result into unreasonably long computational times for very small volumes.

The upper limit of the validity of the closed form approximation of Willett et al. (2000) is $V^*=0.1$. Thus with the present model, no simulation for the liquid bridge volumes above this value has been done. Moreover the bridge character will change from the pendular to the funicular one. We have approximated that for the cubic close packing of monodispersed spheres with a uniform distribution of the liquid among all contacts, the value of V^* where pendular bridge become funicular is $V^*=0.06$, cf. Appendix A. The modeling of systems with funicular bridges would require a different model and this issue is beyond the scope of the present work.

Another approximation made in this work is that the liquid forming the capillary bridges is uniformly distributed among all elements and that a new liquid bridge is formed instantly between any two elements which touch each other. The bridge is removed when the separation distance exceeds the value of S_{crit}.

2.3. Calculation of the hydrodynamic force

During the CFD phase of the simulation the hydrodynamic force on each element, $\boldsymbol{D}$, required by the DEM part, has to be computed. In order to do this, the geometry of the system is first approximated by a discretisation on a regular mesh (the dimension of the grid used in this work is $210\times70\times70$ voxels, a single spherical particle is covered by 15 voxels in diameter) where the voxels occupied by any of the elements are assigned as a solid and all other voxels as a fluid. Then the stationary incompressible Navier–Stokes equations are solved using a pressure-correction implicit scheme on a collocated grid (Ferziger and Perić, 1999). The boundary conditions are no-slip velocity at the boundaries between the solid and the liquid voxels; velocity is prescribed at the inlet boundary; and finally a zero velocity gradient is applied at the outlet. The parameters of this system are (i) the geometry and (ii) the particle Reynolds number, $Re=uR\rho_l/\eta$, where u is the superficial velocity, and ρ_l and η are the fluid density and viscosity, respectively.

As soon as the velocity $\boldsymbol{u}$ and the pressure p profiles are known, the calculation of the total hydrodynamic force, i.e., the sum of hydrodynamic drag and lift forces $\boldsymbol{D}$ on each element is straightforward from the integration of forces acting on the particle surface:

$$\boldsymbol{D}=\int_A T\cdot\boldsymbol{n}_s\mathrm{d}A \quad T=pI+\eta\left(\nabla\boldsymbol{u}+(\nabla\boldsymbol{u})^T\right) \tag{5}$$

where I is the unit tensor and $\boldsymbol{n}_s$ is the surface normal vector. We define the dimensionless hydrodymamic force $K_D(Re)$

$$K_D=D/(6\pi\eta Ru) \tag{6}$$

where D is the magnitude of $\boldsymbol{D}$. As we are mostly considering the flow in a laminar regime, where the drag is proportional to the velocity, the

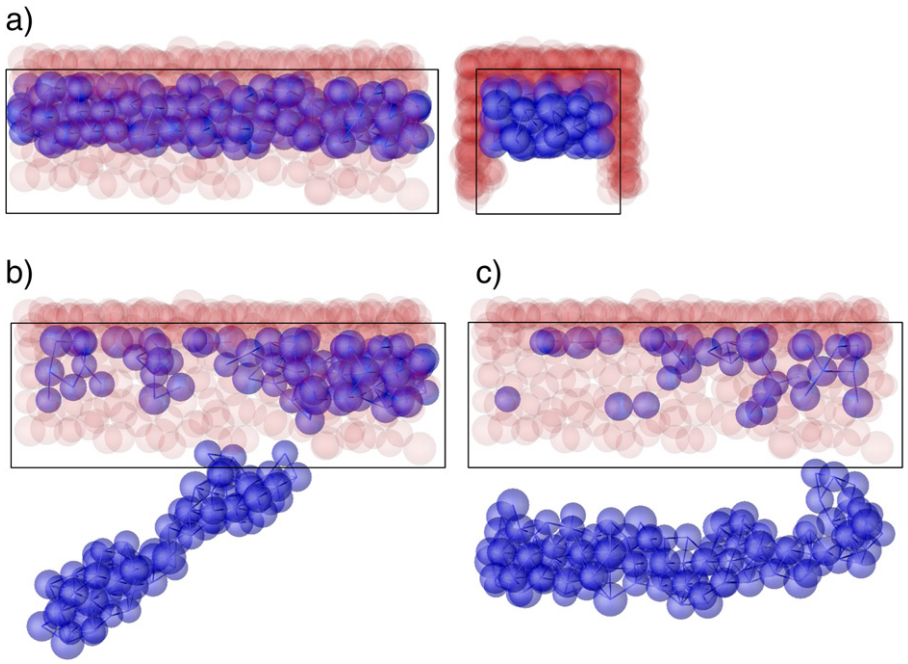

Fig. 5. Simulations with gravity as a principal force; a) the stable case (identical to the initial state), b) the detachment of a large cluster (the intermediate case) $Bo=0.32$, $V^*=0.02$; c) the detachment of all particles $Bo=0.32$, $V^*=0.01$.

Author's personal copy

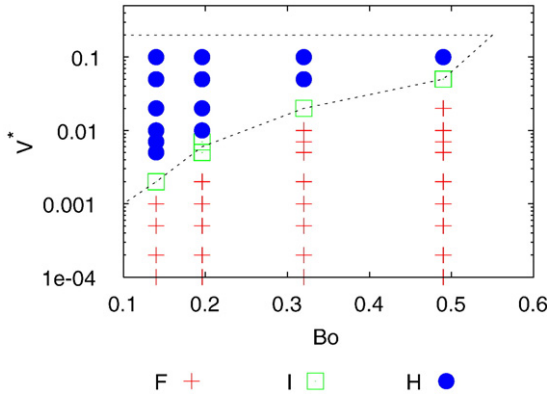

Fig. 6. Summary of the effect of parameters *Bo* and *V** on the detachment scenario of the geometry shown in Fig. 5a. Scenario H: the cluster of particles holds. Scenario I: partial detachment of particles (some particles detach and pull down more particles). Scenario F: the cluster of particles is detached at once.

parameter K_D is defined according to the Eq. (6) instead of the more common definition of the drag coefficient $C_D = 2D/(u^2\rho_l\pi R^2)$. For flows at very low Reynolds numbers around a single isolated sphere $K_D \approx 1$ (Stokes law).

2.4. Dimensionless criteria

As already discussed, we consider four kinds of forces acting on the particles:

(i) the gravitational force reduced by the buoyancy force, G, given by the formula

$$G = \frac{4}{3}\pi R^3(\rho_s - \rho_l)g; \tag{7}$$

(ii) the capillary force F_l;
(iii) the hydrodynamic (drag and lift) force D; and
(iv) the contact force F_c.

Let us consider the two simple geometrical configurations shown in Fig. 4. The condition for the rupture of the connection between the two spheres is

$$G > F_l \quad \text{or} \quad D > F_l \tag{8}$$

for cases a) or b), respectively. After making a substitution for the forces the rupture conditions become

$$\frac{2}{3}Bo > F^* \quad \text{and} \quad 3K_D\Psi > F^* \tag{9}$$

respectively, where the two dimensionless parameters, *Bo* (Bond number) and Ψ, determine the ratio of the gravitational or the hydrodynamic force to the capillary force

$$Bo = \frac{(\rho_s - \rho_l)R^2 g}{\gamma} \approx \frac{\text{gravitational}}{\text{capillary}} \qquad \Psi = \frac{\eta u}{\gamma} \approx \frac{\text{hydrodynamic}}{\text{capillary}}. \tag{10}$$

The direct use of the rupture criteria in Eq. (9) is of course limited as they are strictly valid only for the simple geometry of Fig. 4. However, they give a useful quick estimate of which forces prevail under given conditions. In order to determine these criteria for more complex geometries, a set of numerical simulations with parameters *Re*, *Bo*, Ψ and *V** has been carried out. Two examples will be presented in the next section. The remaining model parameters, E_n, E_t, α and φ have been kept constant during all simulations. The effect of the stiffness coefficients E_n or E_t is not significant as the ratio E_n/G in principle determines only the extent of the overlap of particles and the value of these parameters is set to such a value that particle overlap is as small as possible but the simulations are still computationally feasible. The increase of the friction angle α will increase the cohesiveness of the packing due to increased friction. The basic set of parameters is summarized in Table 1.

3. Results and discussion

3.1. Effect of gravity

As a first example, let us consider the case with no flow, i.e., $\Psi = 0$. The initial configuration, which has been created by the deposition of elements into the computational box, is shown in Fig. 5a. After the deposition, the boundary elements forming walls of the imaginary channel are fixed (transparent red elements in Fig. 5a) and the gravitation field is reversed.

The computational study testing the stability of this particular geometry for a combination of parameters *Bo* and *V** has been summarized in Fig. 6. Three qualitatively different scenarios have been identified by

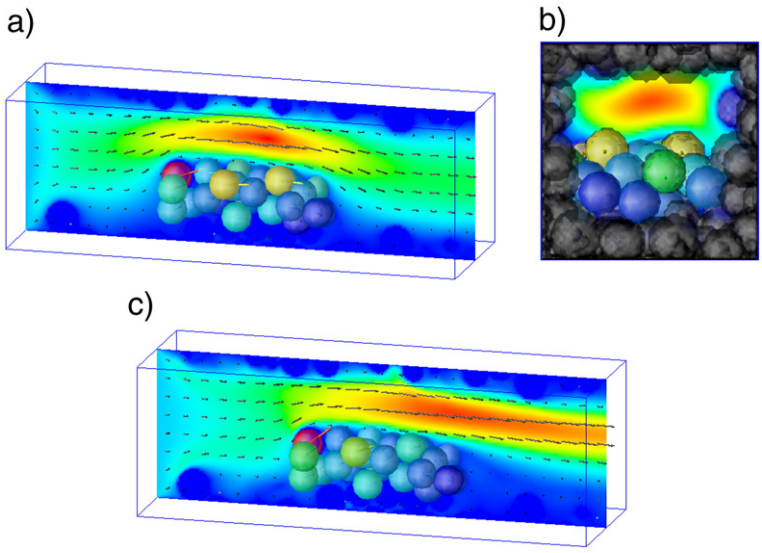

Fig. 7. Calculated velocity profile and hydrodynamic coefficient on the elements for two different Reynolds numbers: $Re = 0.1$ in panels a and b; $Re = 10$ in panel c. The boundary (static) elements are not shown in panels a and c. The color of elements represents the relative magnitude of the drag and lift acting on them.

Author's personal copy

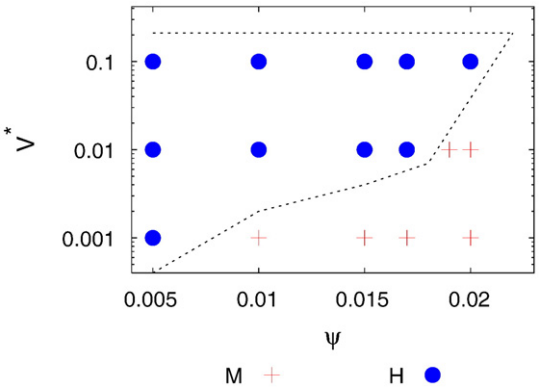

Fig. 8. Summary of the effect of parameters Ψ and V^* on the detachment scenario for the geometry shown in Fig. 9. Scenario H: the entire cluster of particles holds. Scenario M: particles detach and move due to flow.

observing the detachment of particles. Depending on the strength of the capillary forces the particles will either remain attached to the top wall (Scenario H) or they will fall down (Scenarios F and I). In the case of weak capillary forces (Scenario F, cf. Fig. 5c) a large cluster of particles detaches instantly from the whole of the top wall. On the other hand, in the intermediate case (Scenario I, cf. Fig. 5b) a few particles detach first from the top wall and as they start to fall down, they pull down the other particles with them. Fig. 6 defines regions in the Bo–V^* parameter space where behaviours of type H, I, and F have been observed. The graph can be used for judging the stability of a layer of particles held by capillary bridges as a function of the relative saturation by the wetting liquid (i.e., bridge volume).

The dotted line in Fig. 6 denotes the region of parameters where the packing is stable. Unfortunately the upper border of this region cannot be calculated by the present model taking account of pendular bridges only as it is outside of the allowed parametric range. For large values of V^* (when bridges will be funicular) the capillary force will decrease towards zero value at the complete saturation when bridges will disappear completely.

3.2. Effect of drag

The second geometry chosen for the illustration of our method is the flow through a duct with a cluster of particles partially obstructing

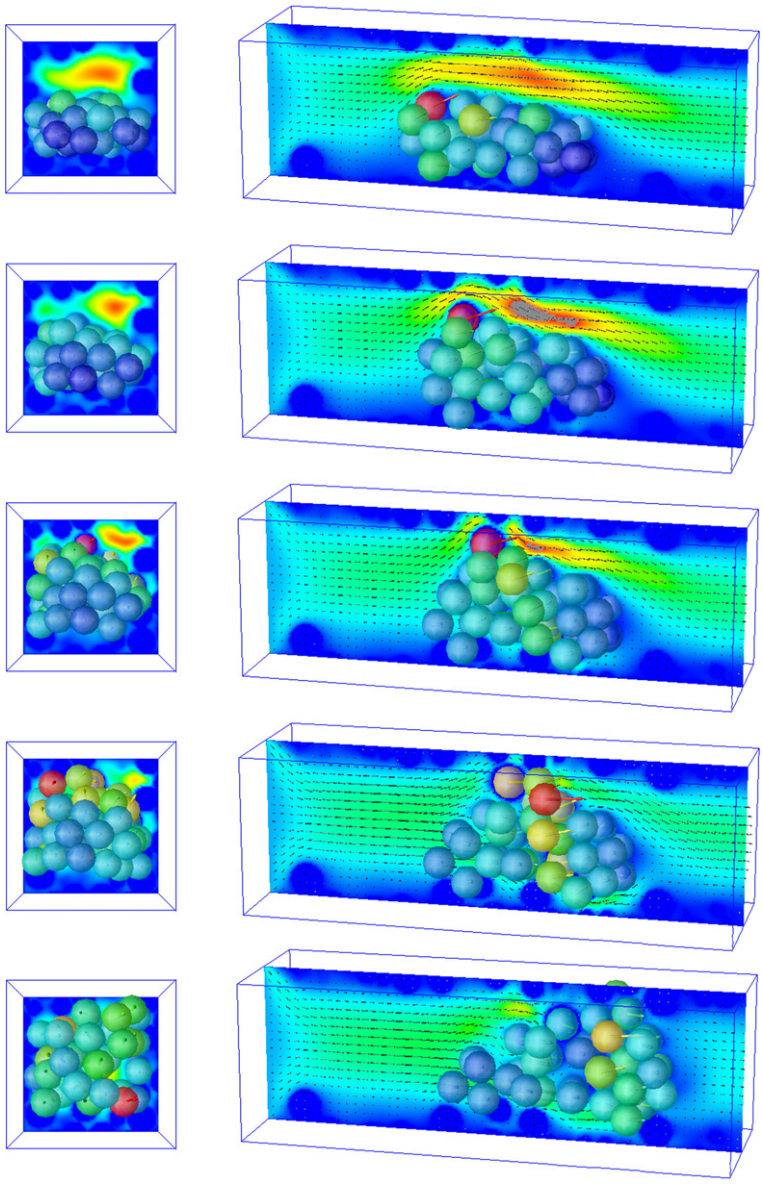

Fig. 9. Visualization of the course of particle detachment for parameters $\Psi = 0.015$, $V^* = 0.005$, and $Re = 1$.

Author's personal copy

the flow, cf. Fig. 7. The elements which form the walls of the duct are static and are shown in a darker shade (only in Fig. 7b). The other elements are held together (and to the walls of the duct) by the capillary forces. However, they can be moved by the drag and lift of the flowing fluid if it exceeds the cohesive capillary forces.

A visual comparison of velocity profiles for two different values of the particle Reynolds number is shown in Fig. 7a and c. The duct Reynolds number, i.e., Reynolds number related to the duct dimensions is 10 times larger than the particle Reynolds number for the current system. The profiles are qualitatively similar except in the region downstream of the obstacle. Also there are no significant differences in the relative magnitude or the direction of the hydrodynamic forces. The computational study for parameters Ψ and V^* is summarized in the flow map in Fig. 8. Two scenarios have been observed. (i) The cluster of particles becomes slightly deformed, but it will still hold (Scenario H) or (ii) the particles are detached from the wall and moved by the flow (Scenario M). Unlike in Fig. 6, no intermediate transition regime was observed in this case. This means that there is a sharp boundary between the H and M scenarios on the parameter map plotted in Fig. 8. Such behaviour would imply that the on-set of sanding on the microscopic level is a sudden event rather than a gradual erosion of individual grains. An example of the course of particle detachment is visualized in Fig. 9.

3.3. Parametric maps

The two regime maps obtained by numerical simulations and presented in Figs. 6 and 8 can be used for the prediction of the on-set of sanding for given conditions (flow velocity, capillary bridge volume, fluid viscosity, etc.).

It is useful to relate the dimensionless volume of the single liquid bridge V^* to a more recognisable parameter, namely the fraction of the relative pore space saturation by the wetting fluid ϕ

$$\phi = \frac{V_b}{V_\varepsilon} = \frac{n_b R^3 V^*}{\varepsilon V_{tot}} \tag{11}$$

where V_b and n_b are the total volume and the number of capillary bridges within an arbitrarily large packing of volume V_{tot}, respectively. In the previous equation, ε is the porosity and V_{tot} can be eliminated using the equation $V_{tot} = \varepsilon V_{tot} + (4/3)\pi R^3 n_s$ where n_s is the number of spherical grains within the volume V_{tot}. Eq. (11) therefore becomes

$$\phi = \frac{3}{4\pi}\frac{1-\varepsilon}{\varepsilon}(n_b / n_s)V^*. \tag{12}$$

Assuming that the capillary bridges are distributed uniformly over all contacts it is possible to write $(n_b/n_s) = (1/2)z$, where z is the coordination number (number of contacts per grain). For the random close packing of mono-dispersed grains with $\varepsilon = 0.36$ and $z \approx 10$, this results in the approximation

$$V^* \approx 0.47\phi. \tag{13}$$

Table 2
Calculated Bond number (Bo) using the range of typical parameter values in the case of oil production.

Bo			
r (mm)	γ (mN/m)		
	10	20	50
1.2	2.54	1.27	0.51
1.0	1.77	0.88	0.35
0.8	1.13	0.57	0.23
0.6	0.64	0.32	0.13
0.4	0.28	0.14	0.06

r is the radius of particles and γ is the interface tension of the water/oil system. Constant values of the density of the particles and the fluid, ρ_s and ρ_l, respectively, have been assumed in calculating the values for this table: $\rho_s = 2700$ kg/m^3, $\rho_l = 900$ kg/m^3.

Table 3
Dimensionless parameter Ψ calculated using the range of typical parameter values for the case of oil production.

Ψ				
η (mPa s)	u (cm/s)	γ (mN/m)		
		10	20	50
4.5	1	0.005	0.002	0.001
	2	0.009	0.005	0.002
	10	0.045	0.023	0.009
18	1	0.018	0.009	0.004
	2	0.036	0.018	0.007
	10	0.180	0.090	0.036
30	1	0.030	0.015	0.006
	2	0.060	0.030	0.012
	10	0.300	0.150	0.060

η is the fluid viscosity, u is superficial velocity and γ is the interface tension of the water/oil system.

The critical values of the dimensionless parameters Bo and Ψ defined by Eq. (10) for the case of sand particles subjected to oil/water flow using the range of typical (realistic) reservoir conditions are summarized in Tables 2 and 3. As these tables illustrate, the range of Bo and Ψ covered by the numerical simulations presented in the previous sections are wide enough to cover most combinations of dimensional parameters that can be expected in a real sand-production situation. The calculated regime maps can therefore be regarded as "universal" in the sense that when the likelihood of sanding is to be estimated for a concrete set of dimensional values, the dimensionless parameters Bo and Ψ can be evaluated and the appropriate region (stable, transition, unstable) on the regime map located.

4. Conclusions

In this work a methodology for coupling the Discrete Element Method with Computational Fluid Dynamics for the simulations of particle entrainment by fluid flow has been described. A parametric study in terms of dimensionless groups determining the strength of cohesive/capillary forces and, on the other hand, the magnitude of the drag (or gravitational) force has been presented. Parametric maps generated as the main output from the study allow a priori estimation of the critical conditions for the on-set of particle erosion (sanding) regimes.

The most significant limitation of the present model is the assumption of pendular capillary bridges which is not valid for a large saturation content of liquid forming the bridges (wetting fluid) where funicular bridges are prevailing. Improvement of the model by including the possibility to consider the funicular bridges as well is the subject of our future work. The situation considered in this work assumes that the only adhesion forces acting between particles are those caused by capillary bridges. The model can be extended by considering other interactions if required, for example electrostatic, or solid inter-particle bridges, by adding appropriate terms to Eq. (1).

The method presented in this work was illustrated on two relatively simple situations where gravitational and drag forces have been considered in isolation. However, more complex arrangements — both in terms of flow geometry and the simultaneous effects of flow and gravity — can be analysed using the method. Moreover, the method is applicable not only to sand production but also to other geological or engineering systems where the interplay between the

Author's personal copy

effect of capillary forces, the rate of the fluid flow and the system geometry determines phenomena such as agglomerate break-up, hard surface cleaning, or fluidisation of cohesive particles.

Notation

d_{ij}	distance between element centers, m
$\boldsymbol{D}_i$	hydrodynamic force (lift and drag) on *i*th element, N
e_{ij}	dimensionless distance between *i*th and *j*th elements, dimensionless
E_n	normal stiffness modulus, N
E_t	tangential stiffness modulus, N
$\boldsymbol{F}_c^{ij}$	contact force between *i*th and *j*th elements, N
F_{cn}^{ij}	the normal component of contact force, N
F_{ct}^{ij}	the tangential component of contact force, N
$\boldsymbol{F}_l^{ij}$	capillary force between *i*th and *j*th elements, N
F^*	dimensionless capillary force, dimensionless
g	gravitational acceleration coefficient, m s^{-2}
$\boldsymbol{G}_i$	gravitational force (reduced by the buoyancy force), N
K_D	dimensionless hydrodynamic force, dimensionless
p	fluid pressure, Pa
r_i	radius of the *i*th element, m
R	mean radius of particles, m
S	half-separation distance, m
S_{crit}	critical value of half-separation distance, m
u	superficial fluid velocity, m s^{-1}
$\boldsymbol{u}$	fluid velocity, m s^{-1}
$\boldsymbol{v}_i$	velocity of the *i*th element, m
V	volume of the liquid bridge, m^3
V^*	dimensionless volume of the liquid bridge, dimensionless
$\boldsymbol{x}_i$	position of the *i*th element, m

Greek letters

α	the friction angle, rad
γ	interface tension coefficient, N m^{-1}
η	fluid viscosity, Pa s
ε	porosity, dimensionless
φ	contact angle, rad
ϕ	relative pore space saturation, dimensionless
Ψ	ratio of the hydrodynamic to capillary force, dimensionless
ρ_l	density of the fluid, kg m^{-3}
ρ_s	density of the solid phase, kg m^{-3}

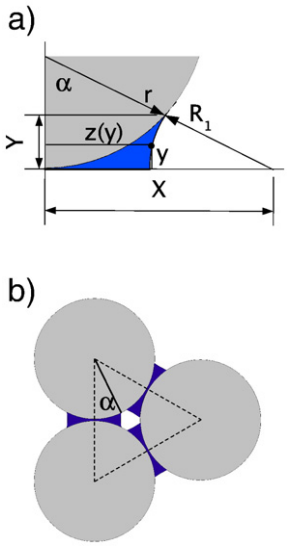

Fig. 10. Estimation of the funicular bridges threshold.

Table 4
Relation between the half-filling angle α and the dimensionless volume of pendular bridge V^* calculated from the circular-arc approximation (Eq. (14)) and from the analytical solution of Young–Laplace equation.

α	$V^{*,a}$	$V^{*,b}$
10°	0.0011	0.0011
20°	0.0144	0.0141
30°	0.0595	0.0578
40°	0.1569	0.1510
50°	0.3260	0.31
60°	0.5850	0.56

[a] From circle-arc approximation (Eq. (14)).
[b] From analytical solution Young–Laplace equation (Urso, 2001).

Other symbols

Bo	Bond number, dimensionless
Re	particle Reynolds number, dimensionless

Acknowledgments

Financial support from the EPSRC via grant no. GR/S82510/01 is gratefully acknowledged.

Appendix A. Transition threshold from pendular to funicular bridges

First, we need the relation between the volume of the single pendular bridge and the half-filling angle α, cf. Fig. 10a. The contact angle is $\varphi = 0°$ and we approximate the meridian profile of the bridge by a circular arc. The volume of the bridge is

$$V^{\text{bridge}} = 2V^{\text{torroid}} - 2V^{\text{cap}} = 2\pi \int_0^Y [Z(y)]^2 dy - \frac{2}{3}\pi Y^2(3r - Y) \quad (14)$$

where

$$Z(y) = X - \sqrt{R_1^2 - y^2} \quad X = \sqrt{R_1(2r + R_1)} \quad R_1 = \frac{r(1 - \cos\alpha)}{\cos\alpha}.$$

Taking into account that $V^* = V^{\text{bridge}}/r^3$ the relation between V^* and α has been calculated in Table 4. For comparison, we also report results of the volume calculated by the analytic solution of the Young–Laplace equation (Urso, 2001). As the difference is quite small we can conclude that the circular-arc approximation in Eq. (14) is satisfactory in the present situation.

Now it is possible to estimate at what V^* the prevailing pendular bridge configuration will change into the funicular mode. Assuming regular closed packing of monodisperse spheres and the uniform distribution of liquid among all particle contacts, it can be seen from Fig. 10b that pendular bridges at every particle contact remain separated until the half-filling angle α gets over 30°. Therefore, cf. Table 4, for $V^* < 0.06$ the liquid bridges remain pendular. For larger values of V^* the funicular character of bridges should to be taken into account when capillary force is calculated. No single threshold value can be derived for the case of random packing because at a particular value of V^* only some parts of the packing will contain funicular bridges while the remaining parts will be in the pendular mode. The threshold value of $V^* = 0.06$ can be still used for random packings, however in this case it is only an estimation.

References

Acock, A., et al., 2004. Practical approaches to sand management. Oilfield Rev. 16 (1), 10–27.
Adams, M.J., Johnson, S.A., Seville, J.P.K., Willett, C.D., 2002. Mapping the influence of gravity on pendular liquid bridges between rigid spheres. Langmuir 18, 6180–6184.

Author's personal copy

Albert, R., Albert, I., Hornbaker, D., Schiffer, P., Barabási, A.-L., 1997. Maximum angle of stability in wet and dry spherical granular media. Phys. Rev. E 56, 6271–6274.
Cundall, P.A., Strack, O.D.L., 1979. A discrete numerical model for granular assemblies. Géotechnique 29, 47–65.
Feng, Z.-G., Michaelides, E.E., 2005. *Proteus*: a direct forcing method in the simulations of particulate flows. J. Comput. Phys. 202, 20–51.
Ferziger, J.H., Perić, M., 1999. Computational Methods for Fluid Dynamics. Springer, Berlin.
Glowinski, R., Pan, T.-W., Hesla, T.I., Joseph, D.D., 1999. A distributed Lagrange multiplier/fictious domain method for particulate flows. Int. J. Multiph. Flow 25, 755–794.
Grof, Z., Kohout, M., Štěpánek, F., 2007. Multi-scale simulation of needle-shaped particle breakage under uniaxial compaction. Chem. Eng. Sci. 62, 1418–1429.
Han, G., Dusseault, M.B. and Cook, J., 2002. Quantifying rock capillary strength behavior in unconsolidated sandstones. SPE 78170.
Ho, T.X., Kosinski, P., Hoffmann, A.C., 2006. Direct numerical simulation of particle-fluid flow: the state-of-the-art. Proc. Fifth World Congress on Particle Technology (CD-ROM). New York, USA, AIChE.
Hoomans, B.P.B., Kuipers, J.A.M., Briels, W.J., Van Swaaij, W.P.M., 1996. Discrete particle simulation of bubble and slug formation in a two-dimensional gas-fluidised bed: a hard-sphere approach. Chem. Eng. Sci. 51, 99–118.
Johnson, A.A., Tezduyar, T.E., 1997. 3D simulation of fluid–particle interactions with the number of particles reaching 100. Comput. Methods Appl. Mech. Eng. 145, 301–321.
Kafui, K.D., Thornton, C., Adams, M.J., 2002. Discrete particle-continuum fluid modelling of gas–solid fluidised beds. Chem. Eng. Sci. 57, 2395–2410.
Mikami, T., Kamiya, H., Horio, M., 1998. Numerical simulation of cohesive powder behavior in a fluidized bed. Chem. Eng. Sci. 53, 1927–1940.
Nouri, A., Vaziri, H., Kuru, E., Islam, R., 2006. A comparison of two sanding criteria in physical and numerical modeling of sand production. J. Petrol. Sci. Eng. 50, 55–70.
Orr, F.M., Scriven, L.E., Rivas, A.P., 1975. Pendular rings between solids: meniscus properties and capillary force. J. Fluid Mech. 67, 723–742.
Papamichos, E., Vardoulakis, I., Tronvoll, J., Skjærstein, A., 2001. Volumetric sand production model and experiment. Int. J. Numer. Anal. Methods Geomech. 25, 789–808.
Tsuji, Y., Tanaka, T., Ishida, T., 1992. Lagrangian numerical simulation of plug flow of cohesionless particles in a horizontal pipe. Powder Technol. 71, 239–250.
Urso, M.E.D., 2001. Mechanics of granular interactions. PhD thesis, Imperial College London.
Vaziri, H., Barree, B., Xiai, Y., Palmer, I. and Kutas, M., 2002. What is the magic of water in producing sand? SPE 77683.
Vaziri, H., Allam, R., Kidd, G., Bennett, C., Grose, T., Robinson, P. and Malyn, J., 2004. Sanding: a rigorous examination of the interplay between drawdown, depletion, Start-up frequency and water cut. SPE 89895.
Venugopal, R., Rajamani, R.K., 2001. 3D simulation of charge motion in tumbling mills by the discrete element method. Powder Technol. 115, 157–166.
Wang, J., Wan, R.G., 2004. Computation of sand fluidization phenomena using stabilized finite elements. Finite Elem. Anal. Des. 40, 1681–1699.
Willett, C.D., Adams, M.J., Johnson, S.A., Seville, J.P.K., 2000. Capillary bridges between two spherical bodies. Langmuir 16, 9396–9405.

7.2 Computer simulation of evolving capillary bridges in granular media

Zdeněk Grof
Christopher J. Lawrence
František Štěpánek

Published in the *Granul. Matter*, Vol. 10, 2008, pp 93–103
DOI: 10.1007/s10035-007-0071-1.

Granular Matter
DOI 10.1007/s10035-007-0071-1

Computer simulation of evolving capillary bridges in granular media

Zdeněk Grof · Christopher J. Lawrence · František Štěpánek

Received: 1 February 2007
© Springer-Verlag 2007

Abstract A numerical method for the simulation of spatially evolving liquid–vapour interfaces in arbitrary two dimensional granular media is presented. Solid- and liquid-phase objects are described by polynomials whose edges evolve according to surface tension forces until a prescribed equilibrium contact angle at three-phase contact points and a constant mean curvature on two-phase contact lines is achieved. The main advantage of the method is the possibility to account for topological transitions (interface coalescence or rupture) and direct calculation of the force acting on solid interfaces due to liquid bridges. The method has been validated by comparing numerical and analytical results for a single pendular liquid bridge and then demonstrated on the simulation of transition from the pendular to funicular and capillary state in a wet particle assembly.

Keywords Liquid bridge · Capillary force · Contact angle · Surface tension · Topology · Condensation · Drying

1 Introduction

Wet granular media are found in many industrial applications such as cake filtration, wet granulation, spray drying, or colloid particle deposition. In order to model accurately processes such as flow or mixing of wet powders [5,7], breakage and coalescence of wet particle agglomerates [4], or pattern formation during the drying of colloidal suspensions [8], it is necessary to couple discrete particle models with continuum models of the liquid phase present in the system. At low relative moisture contents when only binary (pendular) liquid bridges prevail, it is possible to derive analytical expressions for the force of a single bridge [13,14] and use them as part of the contact force calculation in discrete particle model [2]. However, when the volume fraction of the liquid phase in the particle assembly increases such that more complex liquid domains than binary bridges are present (i.e., the funicular or capillary state), this approach is not possible and it is necessary to simulate the liquid phase topology explicitly.

Several numerical methods for the simulation of moving boundary or free interface problems have been described in the literature [9] such as the Level Set, Diffuse Interface, Volume of Fluid, or the Marker and Cell method. For example, the Volume of Fluid (VOF) method has been successfully applied to a number of problems involving wet granular systems such as drying [6], wet granulation [10], droplet spreading [11], or capillary condensation [12]. The VOF method, however, is not well suited for the calculation of capillary bridge force due to relative inaccuracy in the evaluation of the length of three-phase contact line and interfacial area, in particular when there is a large difference between the characteristic sizes of the solid particles and the liquid domains.

Higher accuracy can be achieved by representing the interface as a moving polynomial mesh. This approach has been implemented e.g. in the well-known Surface Evolver software [1]. In order to simulate systems with topological changes such as those occurring during drying, condensation or droplet coalescence, it is necessary to have a method that allows the merging and rupturing of interfaces. Therefore the objective of the present work was to implement such a method—initially in two dimensions—validate it against known analytical solution for simple geometries and then use it for the simulation of various scenarios involving liquid bridges in spatially complex granular media.

Z. Grof ( ) · C. J. Lawrence · F. Štěpánek
Department of Chemical Engineering,
Imperial College London, South Kensington Campus,
London SW7 2AZ, UK
e-mail: f.stepanek@imperial.ac.uk

2 Methodology

The geometry of any two dimensional wet granular system consisting of n_s and n_l topologically distinct solid and liquid objects, respectively, can be described by polygons $\mathscr{S}_i,\ i = 1, \ldots, n_s$ and $\mathscr{L}_i,\ i = 1, \ldots, n_l$ representing the individual solid particles and the liquid phase domains (cf. Fig. 1a). Each ith liquid polygon $\mathscr{L}_i$ can potentially contain a number of n'_i sub-polygons $\mathscr{L}'_{i,k} \in \mathscr{L}_i,\ k = 0, \ldots, n'_i$ corresponding to the "holes" within the parent liquid polygon. This hole can be either a single gas bubble, completely submerged solid, or the combination of the two, cf. Fig. 1b. Therefore the liquid sub-polygon should not be interpreted as the gas phase, but as a "not-a-liquid" phase, which is more general. For example, the sub-polygons in Fig. 1a represent two single gas inclusions, but, there are three solid particles inside the more complex sub-polygon in Fig. 1b. In the present model, we assume there are no holes within the solid phase but they could be easily included if necessary. In a correctly defined system, every sub-polygon $\mathscr{L}'_{i,k}$ must lie entirely inside its parent polygon $\mathscr{L}_i$. A solid $\mathscr{S}_j$ or liquid $\mathscr{L}_j$ polygon can be inside a liquid polygon $\mathscr{L}_i$ $(j \neq i)$ only if they lie fully inside one of its sub-polygons $\mathscr{L}'_{i,k}$. No part of a liquid or solid polygon may overlap with another polygon, i.e. all the polygons should be non-intersecting.

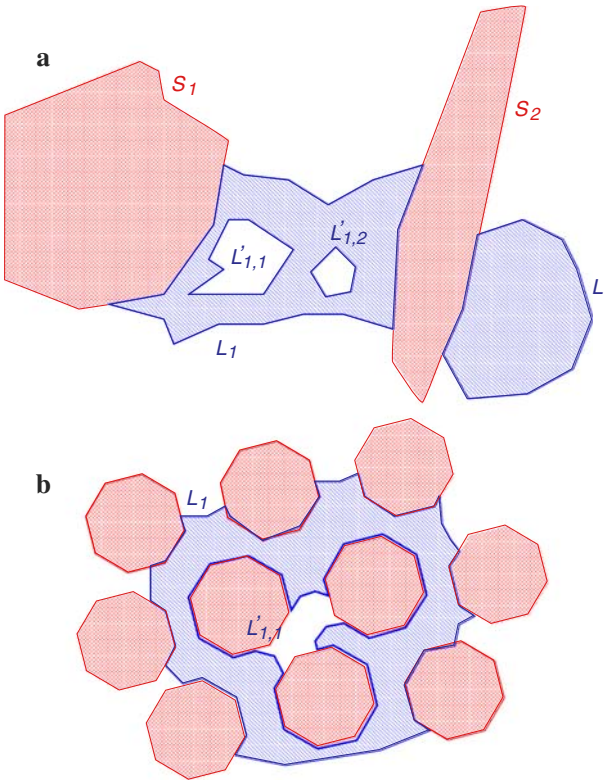

Fig. 1 Representation of an arbitrary three-phase system in two dimension by a set of polygons. The ith liquid domain is defined as the liquid polygon $\mathscr{L}_i$ from which all its sub-polygons $\mathscr{L}'_{i,k}$ are subtracted. Although sub-polygons $\mathscr{L}'_{1,1}$ and $\mathscr{L}'_{1,2}$ in panel "**a**" represent gas inclusions, the sub-polygons can be more complex. For example, in panel "**b**", there are three solid particles lying inside the sub-polygon $\mathscr{L}'_{1,1}$

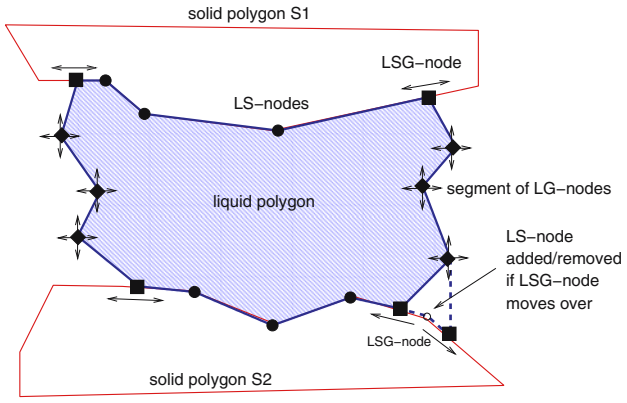

Fig. 2 Classification of nodes of the liquid polygon. While the segment of LG-nodes can move freely, the LSG-nodes are restricted to movements along the solid domain boundaries. The LS-nodes have the same positions as nodes of solid polygons

Every polygon $\mathscr{P}$ $(\mathscr{P} = \{\mathscr{L}, \mathscr{L}', \mathscr{S}\})$ is defined by m individual nodes $(t_k, \mathbf{x}_k) \in \mathscr{P},\ k = 1, \ldots, m$, characterized by their type t and position $\mathbf{x} = (x, y)$. From the node positions it is possible to calculate: the total area of the polygon A

$$A = \frac{1}{2}\sum_{k=1}^{m}(x_k y_{k+1} - x_{k+1} y_k) \quad x_{m+1} \equiv x_1,\ y_{m+1} \equiv y_1; \tag{1}$$

the normal vector $\mathbf{n}_k$ at every kth edge of the polygon

$$\mathbf{n}_k = -a_y \mathbf{i} + a_x \mathbf{j} \qquad \mathbf{a} = (\mathbf{x}_{k+1} - \mathbf{x}_k)/|\mathbf{x}_{k+1} - \mathbf{x}_k|; \tag{2}$$

and the local curvature κ_k at each node

$$\kappa_k = b_x + b_y \qquad \mathbf{b} = (\mathbf{n}_{k-1} - \mathbf{n}_k)/|\mathbf{x}'_{k-1} - \mathbf{x}'_k|, \tag{3}$$

where $\mathbf{x}'_k = (\mathbf{x}_{k+1} + \mathbf{x}_k)/2$ is the position of the middle of the corresponding edge. Note that, in order to obtain the area of the ith liquid domain, it is necessary to subtract the areas of sub-polygons $\mathscr{L}'_{i,k}$ (if any) from the area of parent liquid polygon $\mathscr{L}_i$.

The nodes of liquid polygon $\mathscr{L}$ (or its sub-polygon $\mathscr{L}'$) can be classified into three types t as is illustrated in Fig. 2: (i) nodes at the liquid–gas interface (t = LG), (ii) nodes at the liquid–solid interface (t = LS), and, (iii) nodes representing the three-phase contact points (t = LSG). For given fixed location of the solid phase and total area of the liquid phase, the equilibrium shape of the liquid phase polygons that minimises the energy of the system has to satisfy constant mean curvature of all liquid–gas interfaces belonging to the same liquid domain, and equilibrium contact angles at all three-phase points. In order to reach this state of minimum energy from an arbitrary initial shape of the liquid polygons,

the node positions are iteratively updated according to a set of rules which will now be discussed in detail for each node type.

2.1 Movement of LG-nodes

At every step the position of kth LG node belonging to the ith liquid polygon ($t_{i,k} = \mathrm{LG}$) is updated by

$$\mathbf{x}_{i,k}^{\mathrm{new}} = \mathbf{x}_{i,k}^{\mathrm{old}} + \Delta\mathbf{x}_{i,k}^{a} + \Delta\mathbf{x}_{i,k}^{b} + \Delta\mathbf{x}_{i,k}^{c} + \Delta\mathbf{x}_{i,k}^{d} \tag{4}$$

where the four terms with superscripts a, b, c, and d are contributions to the node displacement due to (a) minimisation of total liquid–gas interface length, (b) convergence towards constant mean curvature, (c) preservation of uniform distribution of nodes along the polygon boundary, and (d) preservation of the total polygon area, respectively.

The first contribution is calculated according to

$$\Delta\mathbf{x}_{i,k}^{a}/s_i^{a} = \mathbf{f}_{i,k}^{a} = \frac{-(l_x - l_0)}{\delta}\mathbf{i} + \frac{-(l_y - l_0)}{\delta}\mathbf{j}, \tag{5}$$

where

$$l_0 = |\mathbf{x}_{i,k} - \mathbf{x}_{i,k-1}| + |\mathbf{x}_{i,k+1} - \mathbf{x}_{i,k}|,$$
$$l_x = |(\mathbf{x}_{i,k}+\delta\mathbf{i}) - \mathbf{x}_{i,k-1}| + |\mathbf{x}_{i,k+1} - (\mathbf{x}_{i,k}+\delta\mathbf{i})|,$$
$$l_y = |(\mathbf{x}_{i,k}+\delta\mathbf{j}) - \mathbf{x}_{i,k-1}| + |\mathbf{x}_{i,k+1} - (\mathbf{x}_{i,k}+\delta\mathbf{j})|,$$

δ is a small arbitrary number and s_i^a is a scaling factor which will be described below. The geometrical meaning of the above expressions is that the node is moved in a direction against the gradient of liquid–gas interface length as function of node position, whereby the gradient is evaluated numerically using a small node displacement δ.

The second contribution moves every node in a direction normal to the liquid–gas interface by a distance proportional to the difference between the local curvature $\kappa_{i,k}$ (calculated according to Eq. 3) and the domain-average curvature $\bar{\kappa}_i$

$$\Delta\mathbf{x}_{i,k}^{b}/s_i^{b} = \mathbf{f}_{i,k}^{b} = (\kappa_{i,k} - \bar{\kappa}_i)\mathbf{n}_{i,k} \tag{6}$$

where $\bar{\kappa}_i = \sum_j \kappa_{i,j} / \sum_j 1,\ j \in \{1, \ldots, m_i : t_{i,j} = \mathrm{LG}\}$ and s_i^b is again a scaling factor which will be specified below.

The third contribution to the node displacement is included in order to maintain uniform coverage of the polygon shape by discretisation nodes, i.e., to prevent local "overstretching" or "overcrowding" of the polygon boundary. This contribution is calculated as

$$\Delta\mathbf{x}_{i,k}^{c}/s_i^{c} = \mathbf{f}_{i,k}^{c} = \left(|\mathbf{x}_{i,k+1} - \mathbf{x}_{i,k}| - l_{\mathrm{eq}}\right)\frac{(\mathbf{x}_{i,k+1} - \mathbf{x}_{i,k})}{|\mathbf{x}_{i,k+1} - \mathbf{x}_{i,k}|} \tag{7}$$

where the equidistant length l_{eq} is defined as the total length of the liquid–gas interface segment to which the kth node belongs, divided by the number of edges within this segment. The segment is formed by all consecutive LG-nodes bounded between LSG-nodes, all belonging to the same liquid polygon (cf. Fig. 2).

Finally, in order to ensure that the area of each liquid polygon A_i (calculated according to Eq. 1) is maintained after node displacements, the fourth term in Eq. 4 is set to

$$\Delta\mathbf{x}_{i,k}^{d} = s_i^{d}\mathbf{n}_{i,k} \tag{8}$$

where $\mathbf{n}_{i,k}$ is the interface normal vector at the kth node (Eq. 2) and the scaling factor s_i^d is adjusted so as to off-set any net change in polygon area that would be induced by the displacement contributions $\Delta\mathbf{x}_{i,k}^{l}$, $l \in \{a, b, c\}$. The required value of s_i^d is found iteratively by the Newton's method.

The scaling factors s_i^a, s_i^b and s_i^c introduced above are calculated in such a way that the distance by which any node is moved in a single step does not exceed a priori specified parameters ε^a, ε^b and ε^c, i.e.,

$$s_i^{l} = \varepsilon^{l} / \max_k |\mathbf{f}_{i,k}^{l}| \qquad l \in \{a, b, c\}. \tag{9}$$

The parameters ε^l, $l \in \{a, b, c\}$ control the speed and stability of convergence of the algorithm and in general have to be determined empirically.

2.2 Movement of LSG-nodes

The movement of three-phase points is confined to the edges of the solid polygon they are adjacent to. In every iteration step the position of the kth LSG node in the ith liquid polygon ($t_{i,k} = \mathrm{LSG}$) is updated according to

$$\mathbf{x}_{i,k}^{\mathrm{new}} = \mathbf{x}_{i,k}^{\mathrm{old}} + \Delta\mathbf{x}_{i,k} \tag{10}$$

where the displacement $\Delta\mathbf{x}_{i,k}$ is evaluated from

$$\Delta\mathbf{x}_{i,k} = s_{i,k}^{e}\,\mathrm{sign}\left((-n_y^S\mathbf{i} + n_x^S\mathbf{j}) \cdot \mathbf{n}^L\right)(-n_y^S\mathbf{i} + n_x^S\mathbf{j}) \tag{11}$$

In Eq. 11 above, $\mathbf{n}^S$ and $\mathbf{n}^L$ are the solid and liquid normal vectors at the LSG contact point, respectively. The scaling factor $s_{i,k}^e$ is adjuster iteratively by the Newton's method so as to locally satisfy the equilibrium contact angle ϑ^{eq}. The actual local contact angle can be calculated directly from the normal vectors, i.e.,

$$\vartheta = \arccos(\mathbf{n}^S \cdot \mathbf{n}^L). \tag{12}$$

As in the case of LG points, an upper limit on the node displacement in a single step is imposed in order to maintain the stability and convergence of the algorithm.

2.3 Movement of LS-nodes

In the current implementation the solid phase is considered stationary. Therefore, the positions of the LS-nodes on the liquid polygons are fixed as they coincide with the positions of solid polygon nodes. During the simulation, however, if a three-phase point (LSG-node) moves from one solid polygon edge to a neighbouring one then a LS-node is inserted

to (or removed from) the liquid polygon (cf. Fig. 2). This procedure ensures that the solid–liquid interface is correctly tracked down and there are no gaps or overlaps between adjacent liquid and solid polygons. If the evolution of liquid interfaces is coupled with the solid particle motion then translational and rotational movement of the solid polygons would be given by the dynamics of the corresponding discrete elements and hence dictate the LS node displacement.

2.4 Topological changes

The topology of the system can change in the course of the simulation. For example, if two different liquid domains come into contact they will coalesce into one (cf. Fig. 3a) and the polygons representing them—$\mathscr{L}_i$ and $\mathscr{L}_j$—should be joined. The opposite situation occurs when different liquid–gas interfaces of a single polygon $\mathscr{L}_i$ come close to each other forming a narrow neck. Eventually, the polygon intersects itself and when this happens it is split into two as is shown in Fig. 3b. The same operations can be carried out on the liquid sub-polygons $\mathscr{L}'_{i,k}$ as well; this corresponds to the bubble coalescence (Fig. 3c) and bubble rupture (Fig. 3d). If the liquid sub-polygon $\mathscr{L}'_{i,k}$ (i.e. bubble) comes into a contact with the boundary of its parent polygon $\mathscr{L}_i$ then they merge during an "opening" operation (Fig. 3e). There is a different type of an "opening" which occurs as a result of intersection of liquid $\mathscr{L}_j$ present inside a sub-polygon $\mathscr{L}'_{i,k}$ with its boundaries (Fig. 3g). Both types of "opening" operations have their counterparts in "closing" operations (Figs. 3f, h).

The topological transitions involving both liquid and solid polygons are summarised in Fig. 4. The "attachment" operation (Figs. 4a, c) is defined as the intersection of the liquid polygon $\mathscr{L}_i$ or sub-polygon $\mathscr{L}'_{i,k}$ with a non-wetted part of a solid polygon $\mathscr{S}$. When this occurs the following steps are carried out: (i) A pair of LSG-nodes are inserted into the liquid polygon at the position where the solid intersects with liquid polygon; (ii) All liquid polygon nodes lying inside solid polygon are removed; (iii) If LSG-nodes are not at the same solid polygon edge, LS-nodes are inserted between LSG-nodes so liquid polygon traces the solid boundary. The "detachment", i.e., the opposite operation (Fig. 4b, d) is detected when the length of wetted solid edge between the pair of LSG nodes becomes zero. The pair of LSG-nodes is then removed and the corresponding part of liquid polygon is detached from the solid polygon.

The group of operations in Fig. 3 involved splitting or joining liquid polygons, while in operations from Fig. 4 LSG-nodes have been inserted or deleted from polygons. The third group of topological changes shown in Fig. 5 can be regarded as a combination of the previous two groups. It consists of various "immersion" operations where two LSG-nodes meet

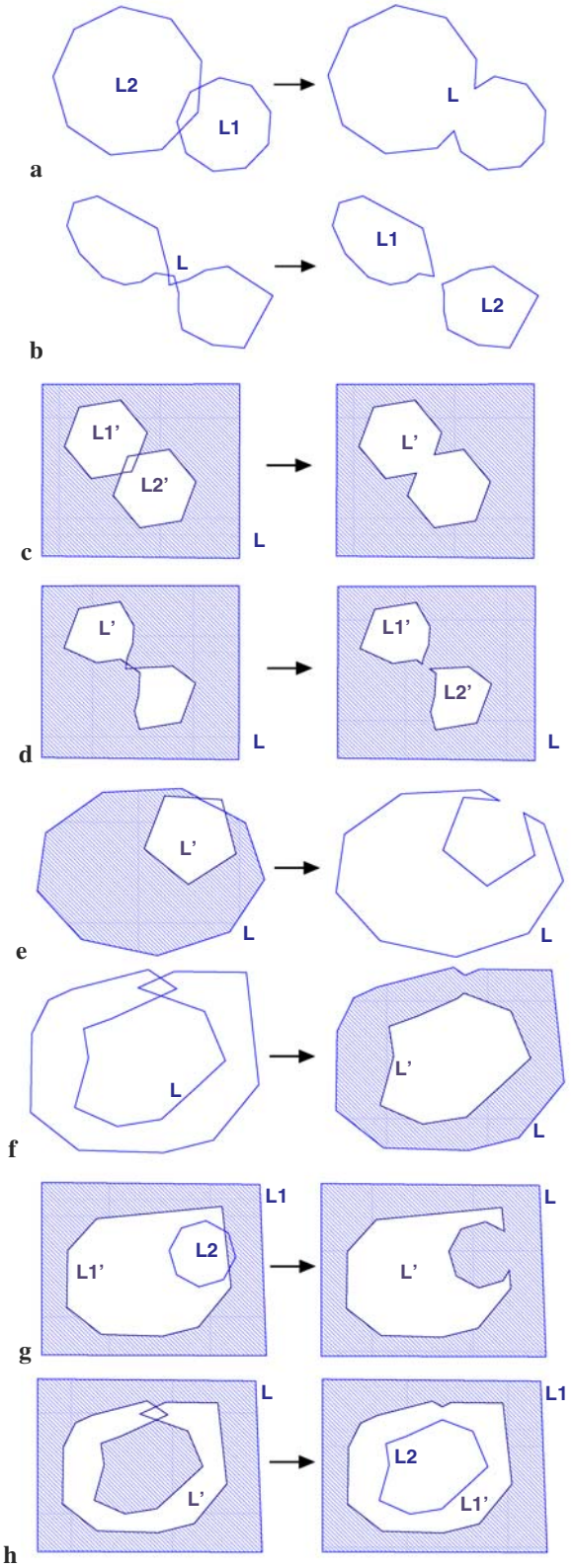

Fig. 3 Topological changes I (regarding intersections between liquid polygons only): **a** $\mathscr{L}_i\mathscr{L}_j$-coalescence, **b** $\mathscr{L}$-separation, **c** $\mathscr{L}'_{i,k}\mathscr{L}'_{i,l}$-coalescence, **d** $\mathscr{L}'$-separation, **e** $\mathscr{L}_i\mathscr{L}'_{i,k}$-opening, **f** $\mathscr{L}$-closing, **g** $\mathscr{L}'_{i,k}\mathscr{L}_j$-opening, **h** $\mathscr{L}'$-closing

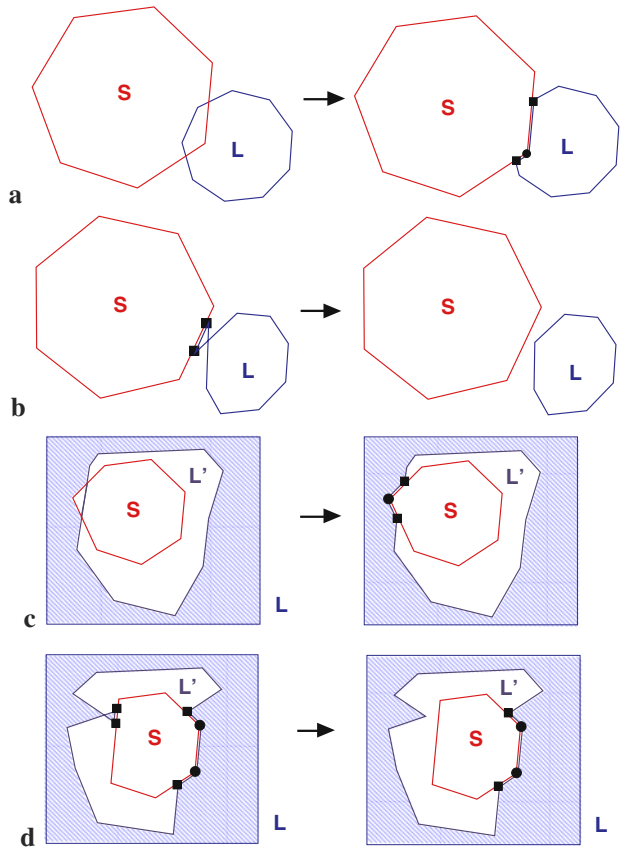

Fig. 4 Topological changes II (regarding intersections between liquid and solid polygons): **a** $\mathscr{L}$-attachment, **b** $\mathscr{L}$-detachment, **c** $\mathscr{L}'$-attachment, **d** $\mathscr{L}'$-detachment

and are deleted which corresponds to the disappearance of the non-wetted part of solid interface. If two LSG-nodes belong to different polygons $\mathscr{L}_i$ and $\mathscr{L}_j$ then the two polygons are joined together (Fig. 5a), while if LSG-nodes are from a single polygon $\mathscr{L}$ (Fig. 5c, e) the polygon splits into a sub-polygon $\mathscr{L}'_{i,k}$ and its parent polygon $\mathscr{L}_i$ similarly as in "closing" operations mentioned earlier. The distinction between situations in Fig. 5c, e is only in the type of polygon from which the LSG-nodes were deleted. The last kind of "immersion" operation takes place after the meeting of two LSG-nodes belonging to a liquid sub-polygon $\mathscr{L}'_{i,k}$ (Fig. 5g) leading to splitting of this liquid sub-polygon into two.

Every kind of the "immersion" operation has its counterpart "emersion". That is, liquid polygon $\mathscr{L}_i$ intersecting itself at liquid–solid interface splits into two polygons and, simultaneously, two LSG-nodes are created (Fig. 5b). Liquid sub-polygon $\mathscr{L}'_{i,k}$ intersecting its parent $\mathscr{L}_i$ at liquid–solid interface (Fig. 5d) or liquid polygon $\mathscr{L}_i$ intersecting its sub-polygon $\mathscr{L}'_{i,k}$ at liquid–solid interface (Fig. 5f) lead to the "emersion and opening" operation. Finally, sub-polygon $\mathscr{L}'_{i,k}$ intersecting another sub-polygon $\mathscr{L}'_{i,l}$ at liquid–solid interface results in joining the two sub-polygons (Fig. 5h).

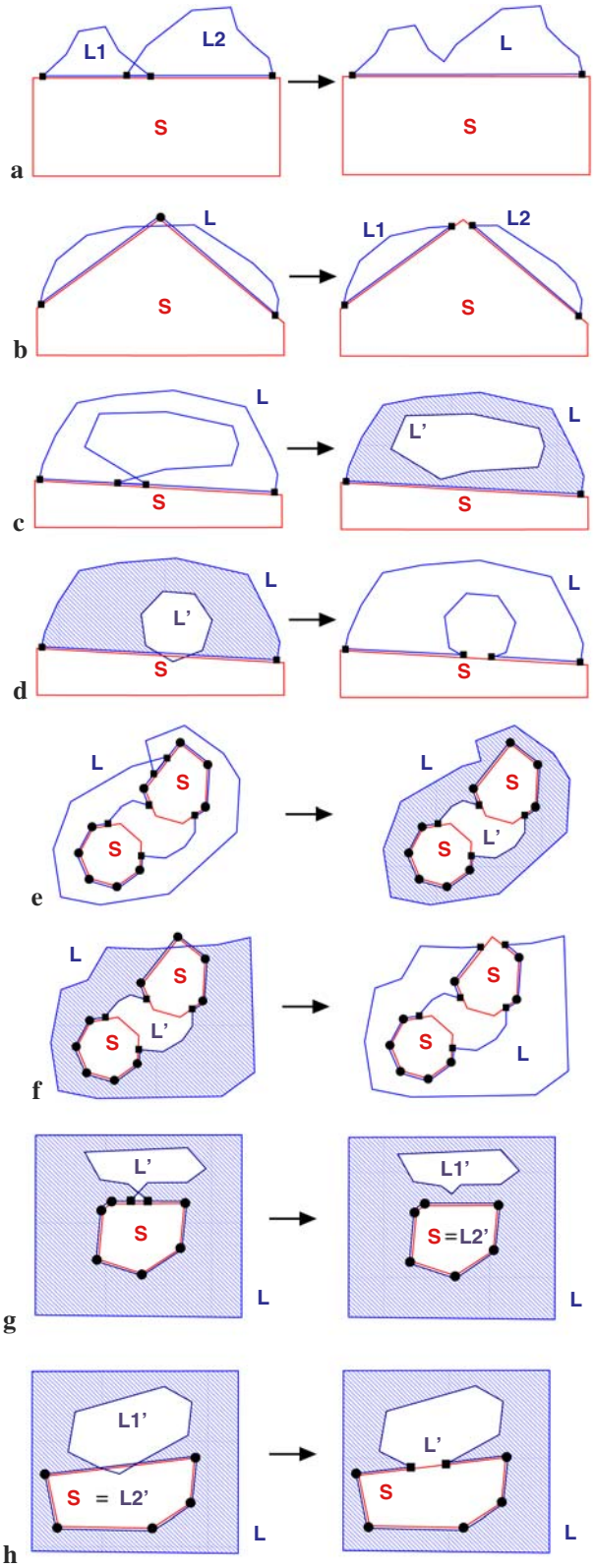

Fig. 5 Topological changes III (regarding intersections at liquid–solid interface and addition/removal of three-phase nodes): **a** immersion and coalescence, **b** emersion and separation, **c** $\mathscr{L}$-immersion and closing, **d** $\mathscr{L}'$-emersion and opening **e** $\mathscr{L}'$-immersion and closing, **f** $\mathscr{L}$-emersion and opening, **g** immersion and separation, **h** emersion and coalescence

2.5 Calculation of the capillary forces

Once the equilibrium positions of gas–liquid interfaces and three-phase points have been found as described above, the static capillary force interaction $\mathbf{F}_{ij}$ between particle $\mathscr{S}_i$ and liquid body $\mathscr{L}_j$ can be calculated. It consists of two contributions: the first one is due to Laplace–Young pressure difference $\Delta p = \gamma\bar{\kappa}$, and the second one is the direct action of the surface tension of the liquid

$$\mathbf{F}_{ij} = \mathbf{F}^p_{ij} + \mathbf{F}^t_{ij}. \tag{13}$$

The pressure component acts in the direction normal to liquid–solid interface and it is calculated by integration along this interface

$$\mathbf{F}^p_{ij} = -\gamma\bar{\kappa}_j \sum_e l_e \mathbf{n}^L_e \qquad e \in \mathscr{S}_i \cap \mathscr{L}_j, \tag{14}$$

where the subscript e in the sum goes for all the edges at the solid–liquid boundary, l_e is the length and $\mathbf{n}^L_e$ is the normal of the corresponding edge.

The surface tension component with a magnitude γ acts in the direction of the tangent to the liquid interface at the contact point and is calculated by summation of contributions from all contact points (LSG-nodes) between solid $\mathscr{S}_i$ and liquid $\mathscr{L}_j$ polygons

$$\mathbf{F}^t_{ij} = \sum_k \mathbf{F}^t_{ij,k} \qquad k \in (\mathscr{S}_i \cap \mathscr{L}_j) \cap (t_k = \mathrm{LSG}) \tag{15}$$

where

$$\mathbf{F}^t_{ij,k} = \gamma \ \mathrm{sign}\left((-n^L_y\mathbf{i} + n^L_x\mathbf{j}) \cdot \mathbf{n}^S\right)\left(-n^L_y\mathbf{i} + n^L_x\mathbf{j}\right). \tag{16}$$

In previous equations, $\mathbf{n}^L$ and $\mathbf{n}^S$ are the liquid and solid normals at the kth contact point (LSG node) and the sum in Eq. 15 runs over all LSG nodes common to polygons $\mathscr{S}_i$ and $\mathscr{L}_j$.

2.6 General organization of the algorithm

The flowchart of the algorithm is shown in Fig. 6. The algorithm consists of iteration loops at several levels. At the highest level, the simulation of a physical phenomenon such as condensation, drying, or deformation of a wet particle agglomerate is performed. For every step at this level, embedded iterations have to be performed in order to find the equilibrium liquid phase configuration which satisfies contact angle and mean curvature requirements, and hence enables the calculation of capillary forces. This "low-level" iteration itself consists of several nested loops as shown in Fig. 6. For every iteration updating the position of the LSG-nodes (i.e., of the contact points) approximately 50 steps of the LG-node movement are required in order to propagate this information along the whole liquid–gas interface. As the process of looking for polygon intersection and the eventual topological changes takes substantially more CPU-time than moving nodes, it is more effective to perform several node-moving steps before checking for topological change.

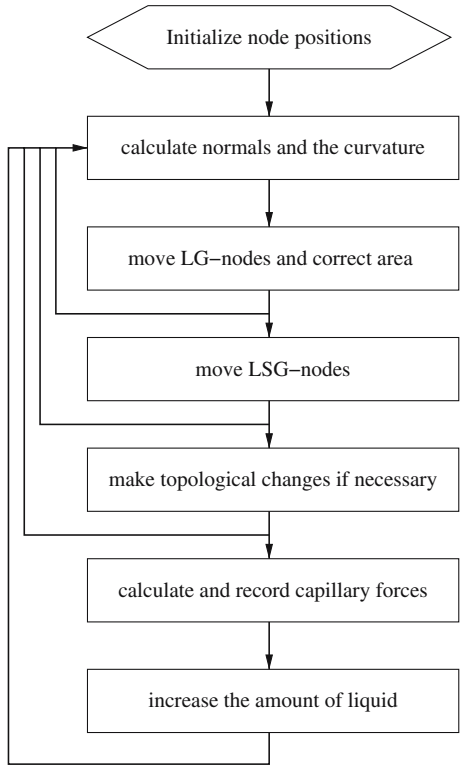

Fig. 6 Schematic flow-chart of the algorithm

3 Results and discussion

3.1 Validation of the model

In order to verify the accuracy of the method, the capillary force of a pendular liquid bridge between two discs of equal diameter was calculated and compared with analytical solution for the same geometry [13]. The results are presented in Fig. 7 for two different contact angles. The ratio b/a in Fig. 7 represents the dimensionless fraction of the liquid phase within the bridge; a is the radius of the solid circular discs and b is the radius of a circle having the same area as that of the liquid bridge. The force is made dimensionless by the liquid surface tension (in two dimensions the units are consistent). The circular discs are approximated by polygons consisting of 60 nodes and this approximation is the reason of the step-wise looking curves in Fig. 7a. Each step corresponds to a three-phase point (LSG-node) transferring from one solid polygon edge to another as the amount of liquid increases. The curve will flatten if the discretisation

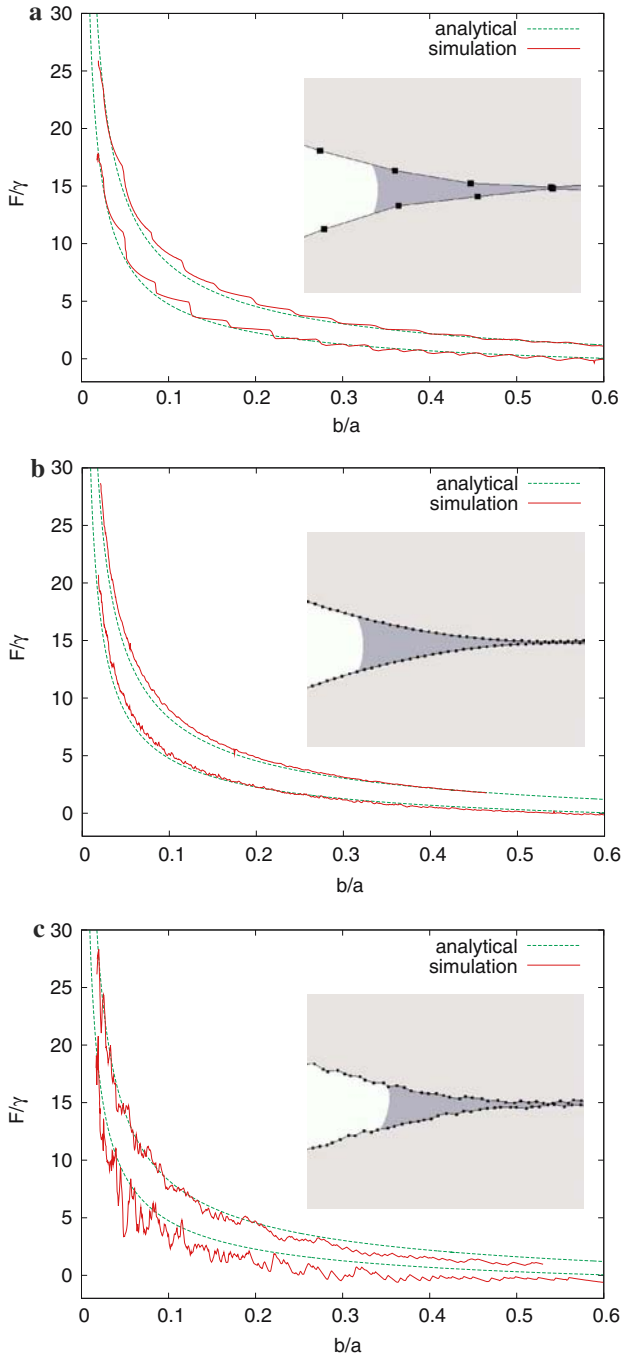

Fig. 7 Capillary force of a pendular liquid bridge. Comparison between analytical solution and simulation for values of contact angle $\vartheta = 26°$ (*upper curves*) and $\vartheta = 53°$ (*lower curves*). The ratio b/a represents the relative amount of liquid

is improved by adding more nodes to the solid polygons, cf. Fig. 7b where the number of nodes is 600.

As can be seen in the figure, the agreement between the analytical and numerical solution is acceptable, although the effect of surface roughness warrants further investigation. In Fig. 7c a random roughness has been introduced to the solid surface, and as a consequence there are fluctuations around the analytical solution for a smooth disc. At the same time, the simulations for rough surface provides confidence about the robustness and stability of the numerical algorithm because the solutions clearly follow the analytical ones.

3.2 Simulation of capillary condensation

In many applications the average capillary force acting on particles in a wet granular medium as function of the liquid content needs to be known (strength of agglomerates in wet granulation, wet powder flow, soil erosion, etc.). To this end, equilibrium distribution of liquid phase in a random granular medium has been found by the algorithm described above for increasing liquid saturations, and the capillary forces analysed. The particle packing was created by a multi-element DEM simulation of particle deposition into a rectangular domain [3]. The particles were modelled as ellipsoids with a small randomness introduced in the aspect ratio. A small initial amount of liquid has been placed at the particle coordination points and the ellipsoids representing solid particles were shrinked in order to remove intersections among them. The equilibrium contact angle used in the simulation was 26° for all particles. The relative amount of the liquid is characterized by a variable $\phi = A_{\text{liq}}/(A_{\text{tot}} - A_{\text{sol}})$, where A_{liq}, A_{sol} and A_{tot} are the area of the liquid, the solid and the total area of the system within the simulation box, respectively.

Figure 8 shows the distribution of liquid among particles and capillary force exerted on particles by the liquid bridges for increasing liquid content in the system. A detailed view of the shape of liquid–gas interface for three selected liquid fractions is then presented in Fig. 9 where each connected liquid cluster is shown in a different color. The following four regimes of liquid content have been distinguished in wet granular media: pendular, funicular, capillary and slurry state [7]. In the pendular state, particles are held together by binary liquid bridges at their contacts as can be seen in Fig. 8a. The force chains existing in the particle packing are clearly apparent in this state as the bridges exist at particle coordination points, i.e. at the same location where force transmission took place in the random particle packing created by DEM simulation.

According to analytical solutions (both two and three dimensional) and several experimental works, e.g. [14], the cohesive capillary force slowly decreases with increasing liquid content. The transition to the funicular state occurs when the liquid bridges start to coalesce and fill the voids between particles. The different stages of this state are illustrated in Fig. 9. In Fig. 9a one can still find the binary liquid bridges (i.e., pendular regions), while the funicular bridges exist among at most three particles. The number of binary bridges rapidly decreases at the intermediate stage (Fig. 9b) where most of the liquid domains are adjacent to 3–5 particles.

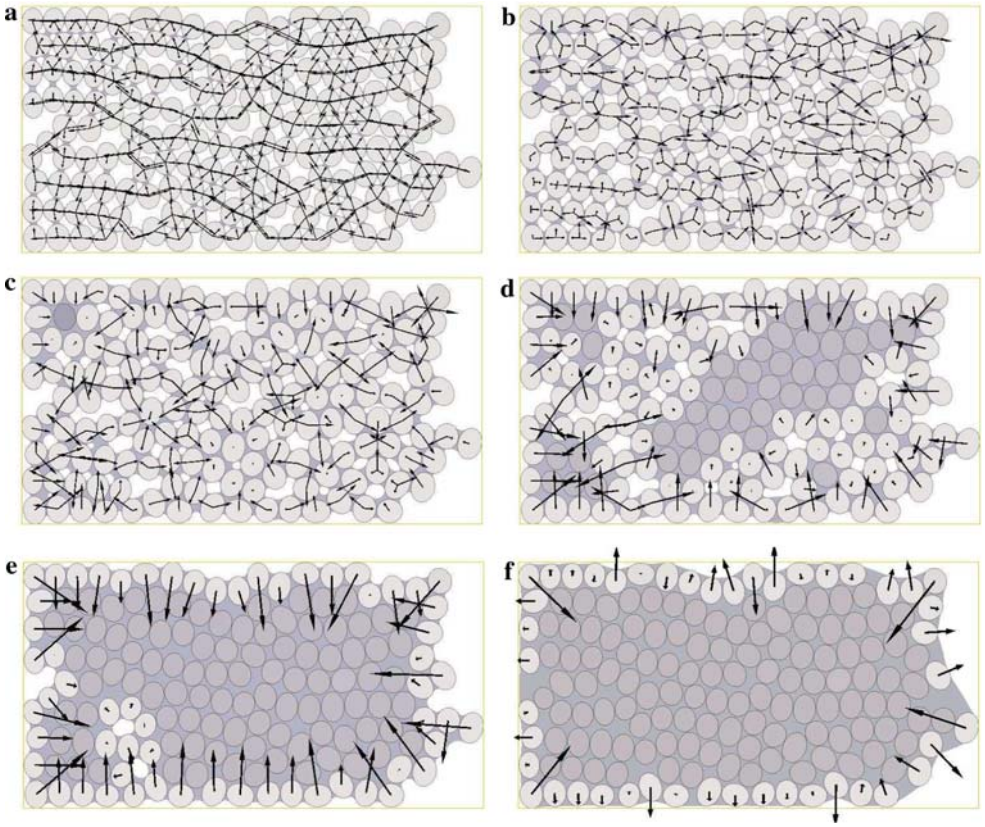

Fig. 8 Series of images illustrating the structure during the capillary condensation. **a** $\phi = 0.18$, **b** $\phi = 0.46$, **c** $\phi = 0.66$, **d** $\phi = 0.80$, **e** $\phi = 0.93$, **f** $\phi = 1.14$

These domains become larger at the stage which is near to the transition to a capillary state in Fig. 9c. It can also be seen that the structure of force chains that existed at low liquid contents has nearly disappeared. If the solid particles were free to move, rearrangements would be likely to take place. When the liquid content increases even further (Fig. 8d), many particles become completely submerged and no capillary force acts on them anymore.

In Fig. 8e the system is practically in the capillary state (except two small voids in the lower left corner of the image). The capillary force acts now solely on particles at the boundary with the surrounding gas phase. Initially, these interactions are cohesive, i.e., the particles are being pulled toward the center of the system. As the boundary particles become almost completely wetted for the highest saturation, shown in Fig. 8f, the forces become repulsive and most of the particles are pushed away from the center of mass of the system. This is due to the chosen value of the equilibrium contact angle (26°), which causes the particles to be present at the gas–liquid interface rather than being totally submerged in the droplet (the same principle is also sometimes used for emulsion stabilisation). Interestingly, there are still few particles which are drawn inwards in Fig. 8f, these particles lie at the corners of the system. Moreover, after a close examination of the previous snapshot (Fig. 8e) one can see that the force drawing particles inward is larger in the "corners" than at the "sides" of the system rectangle. This suggests that if the particles were free to move then the whole cluster of particles would transform from the rectangular into the circular shape as a result of capillary forces. The last regime, i.e., the slurry state occurs when all particles are fully immersed and no capillary interaction appears among particles.

The evolution of several characteristics during the simulation of the capillary condensation is presented in Fig. 10 for three different random realizations of the initial particle packing. Figure 10a shows the number of liquid domains n_l per number of grains n_s in the system as function of the liquid content. Initially, n_l/n_s remains constant for ϕ smaller than approximately 0.25 and then monotonously decreases. This threshold corresponds to the transition between pendular and funicular states. For a three dimensional system, this transition has been reported to occur around 10% of liquid content in the literature [5]. The number of liquid domains eventually drops to $1/n_s$ which occurs just before the transition into the capillary state.

The average number of liquid–particle contacts per liquid domain (n_b/n_l) is shown in Fig. 10b. The contacts between a liquid and a completely immersed particle are excluded

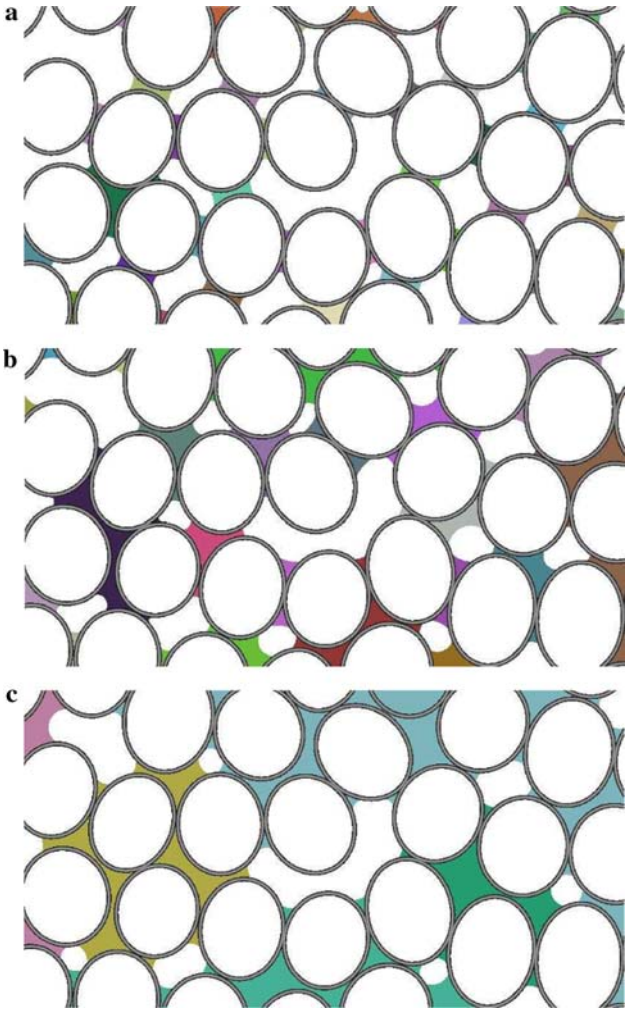

Fig. 9 Details of the system structure. **a** $\phi = 0.33$, **b** $\phi = 0.57$, **c** $\phi = 0.74$

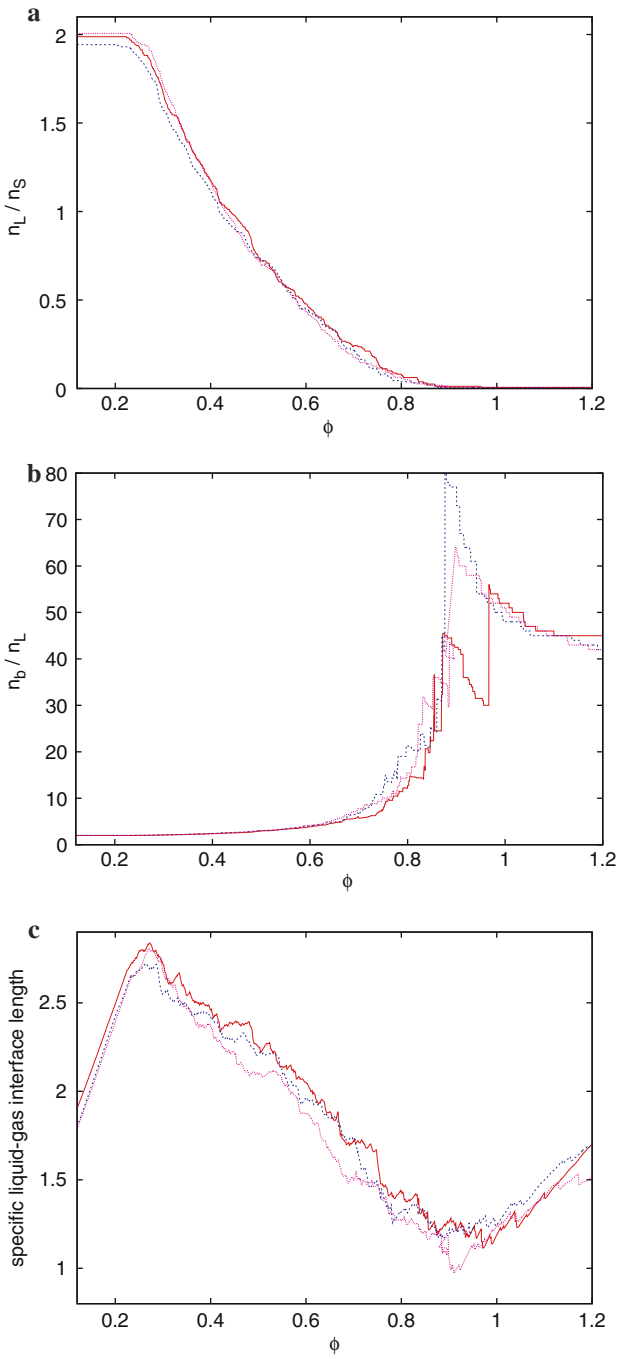

Fig. 10 Global characteristics during capillary condensation. **a** Number of liquid domains per solid particle, n_l/n_s, **b** number of liquid–solid contacts per liquid domain, **c** specific length of the liquid–gas interface

during counting the number of liquid–particle contacts. The ratio n_b/n_l is 2 in the pendular state, implying that each liquid domain is in direct contact with two particles. It slowly increases with increasing liquid content as the pendular liquid bridges coalesce into funicular ones. Near the transition from funicular to the capillary state where the number of liquid domains n_l becomes close to 1, the ratio n_b/n_l raises shortly up to the value 80 (the number of particles on the boundary) but then starts decreasing because the number of contacts n_b decreases as the individual particles, including those at the boundary, are eventually immersed. Although not seen in Fig. 10b, the n_b/n_l will eventually drop to zero, when all particles are immersed. After reaching this slurry state, there will be no capillary interactions among particles.

The dependence of the total length of the liquid–gas interface divided by the total area of the system on the liquid content ϕ is shown in Fig. 10c. The specific liquid–gas interface length in Fig. 10c is a two dimensional analog to specific surface area in three dimensions. The curve contains a maximum and a minimum and these two extreme points can be used as clear boundaries dividing the system into pendular, funicular, and capillary regimes. With increasing liquid content, the liquid–gas interface length is growing in the pendular, decreasing in the funicular, and then again increasing in the capillary and droplet (slurry) regimes. Another interesting

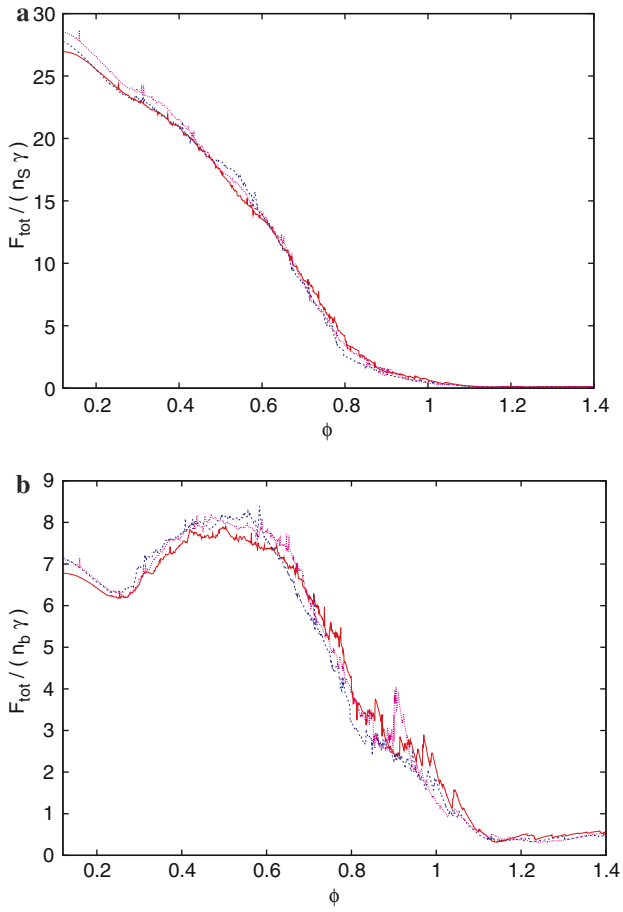

Fig. 11 Evolution of the capillary force during capillary condensation. **a** Sum of capillary forces over all contacts per solid particle $F_{\text{tot}}/(n_s\gamma)$, **b** force averaged per liquid contact $F_{\text{tot}}/(n_b\gamma)$

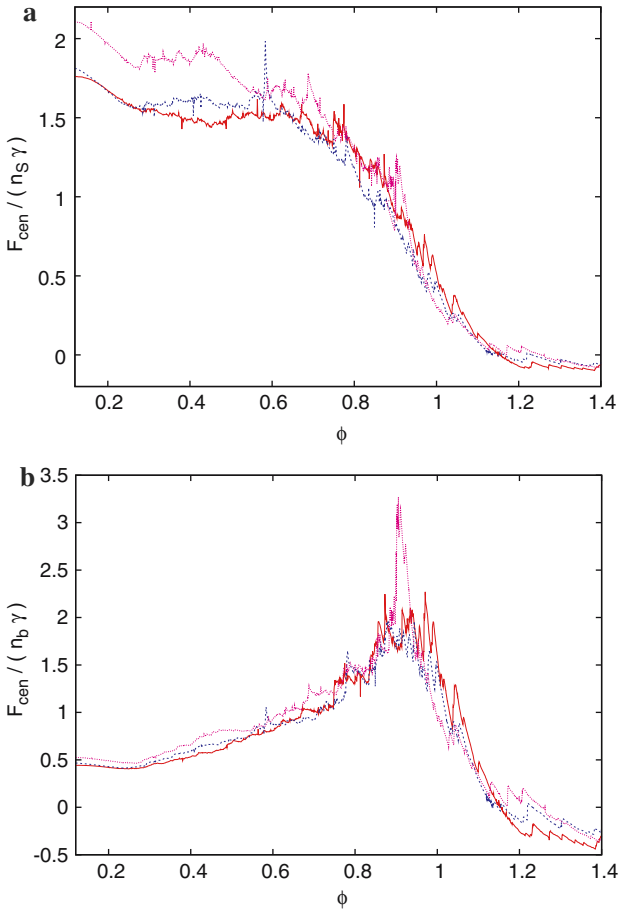

Fig. 12 Evolution of the capillary force projected into the centre of the system. **a** Sum over all contacts per solid particle $F_{\text{cen}}/(n_s\gamma)$, **b** force averaged per liquid contact $F_{\text{cen}}/(n_b\gamma)$

thing to notice in Fig. 10 is that the spread between the three curves for different random initial realisations is much larger in certain regimes than in others—for example, in Fig. 10b, the number of solid particles per liquid domain is almost unaffected during the pendular and funicular states, but as the transition to the capillary state approaches at $\phi \approx 0.7$, the "noise to signal" ratio becomes much more significant.

The dependence of the sum of all capillary forces in the system per solid particle $F_{\text{tot}}/n_s = (1/n_s)\sum_{i,j}|\mathbf{F}_{ij}|$, where $\mathbf{F}_{ij}$ was calculated according to Eq. 13, and the average force per liquid–solid contact F_{tot}/n_b on the liquid-content ϕ is shown in Fig. 11. The sum of forces is decreasing monotonously, however the average force (Fig. 11b) goes through a local minimum followed by a local maximum. Initially (i.e., in the pendular state) the average force decreases in the same way as the force of a single bridge between two discs in Fig. 7. The local minimum corresponds to the transition to the funicular state and the average force then increases toward a maximum and decreases again. The reason for this behaviour is that number of contacts n_b is decreasing faster than the sum of capillary forces, hence the average force is increasing.

The fact that the individual cohesive forces have a large magnitude at low liquid content cannot be directly interpreted in terms of the macroscopic cohesive strength of a wet particle agglomerate, though. Although at low liquid content the force of an individual capillary bridge is stronger, it has to be considered that the distance particles have to be pulled apart in order to break a liquid bridge is shorter. Therefore, the particle assembly is more susceptible to breakage due to small vibrations or particle dislocations when the liquid content is low.

An alternative way to express the cohesive capillary force which holds the cluster of particles together is by considering the projection of the capillary force at every liquid–particle contact into the direction toward the center of mass of the system, i.e.,

$$F_{\text{cen}} = \sum_{i,j}\left(\mathbf{F}_{ij}\cdot(\mathbf{x}_c - \mathbf{x}_{ij})\right), \tag{17}$$

where $\mathbf{x}_{ij}$ is the position where the capillary force $\mathbf{F}_{ij}$ acts and $\mathbf{x}_c$ is the center of mass of the particle cluster. The total central force per solid particle F_{cen}/n_s and its average value F_{cen}/n_b are plotted in Fig. 12. Notice that the F_{cen} is substantially smaller than F_{tot} because apart from particles present at the outer boundaries of the system, the capillary forces acting from different directions tend to cancel each other out. The F_{cen}/n_b curve has a maximum near the transition from funicular to capillary state where the remaining contacts are at the boundary. The force then decreases and becomes negative when the boundary particles are pushed away from the center of the system.

4 Conclusions and future work

In this work a numerical method for tracking liquid interfaces in arbitrary two dimensional granular medium has been described, validated and used for the calculation of global characteristics such as the number of particles per liquid domain, interface length, and the total and average capillary force as function of liquid content. The implementation of the basic algorithm opens up ways for the direct numerical simulation of many industrially important processes involving wet granular media, such as droplet penetration into powder bed, coating of porous particles and granules, calculation of wet agglomerate deformation and tensile strength, condensation, drying, etc. When the simulation of evolving liquid bridges is coupled with DEM simulation of the solid particle motion, further phenomena such as wet granule consolidation, or crack formation during drying of suspensions or slurries can be modelled. Finally, the extension of the numerical procedure to three dimensions will be the subject of our future work.

Acknowledgments Financial support from EPSRC through grant no. GR/S82510/01 is gratefully acknowledged.

References

1. Brakke, K.A.: The surface evolver. Exp. Math. **1**, 141–165 (1992)
2. Grof, Z., Cook, J., Lawrence, C.J., Štěpánek, F.: The interaction between small clusters of cohesive particles and laminar flow: a coupled DEM/CFD approach. J. Petrol. Sci. Eng. (2006) (submitted)
3. Grof, Z., Kohout, M., Štěpánek, F.: Multi-scale simulation of needle-shaped particle breakage under uniaxial compaction. Chem. Eng. Sci. **62**, 1418–1429 (2007)
4. Iveson, S.M., Litster, J.D., Hapgood, K.P.: Nucleation, growth and breakage phenomena in agitated wet granulation processes: a review. Powder Technol. **117**, 3–39 (2001)
5. Herminghaus, S.: Dynamics of wet granular matterr. Adv. Phys. **54**, 221–261 (2005)
6. Kohout, M., Grof, Z., Štěpánek, F.: Pore-scale modelling and tomographic visualisation of drying in granular media. J. Colloid Interface Sci. **299**, 342–351 (2006)
7. Mitarai, N., Nori, F.: Wet granular materials. Adv. Phys. **55**, 1–45 (2006)
8. Park, J., Moon, J.: Control of colloidal particle deposit patterns within picoliter droplets ejected by ink-jet printing. Langmuir **22**, 3506–3513 (2006)
9. Scardovelli, R., Zaleski, S.: Direct numerical simulation of free-surface and interfacial flow. Ann. Rev. Fluid Mech. **31**, 567–603 (1999)
10. Štěpánek, F., Ansari, M.A.: Computer simulation of granule microstructure formation. Chem. Eng. Sci. **60**, 4019–4029 (2005)
11. Štěpánek, F., Rajniak, P.: Droplet morphologies on particles with macroscopic surface roughness. Langmuir **22**, 917–923 (2006)
12. Štěpánek, F., Šoós, M., Rajniak, P.: Characterization of porous media by the virtual capillary condensation method. Colloids Surf. A Physicochem. Eng. Asp. **300**, 11–20 (2007)
13. Urso, M.E.D., Lawrence, C.J., Adams, M.J.: Pendular, funicular, and capillary bridges: results for two dimensions. J. Colloid Interface Sci. **220**, 42–56 (1999)
14. Willett, C.D., Adams, M.J., Johnson, S.A., Seville, J.P.K.: Capillary bridges between two spherical bodies. Langmuir **16**, 9396–9405 (2000)

7.3 The strength of liquid bridges in random granular materials

Zdeněk Grof
Christopher J. Lawrence
František Štěpánek

Published in the *J. Colloid Interf. Sci.*, Vol. 319, 2008, pp 182–192
DOI: 10.1016/j.jcis.2007.11.055.

Provided for non-commercial research and education use.
Not for reproduction, distribution or commercial use.

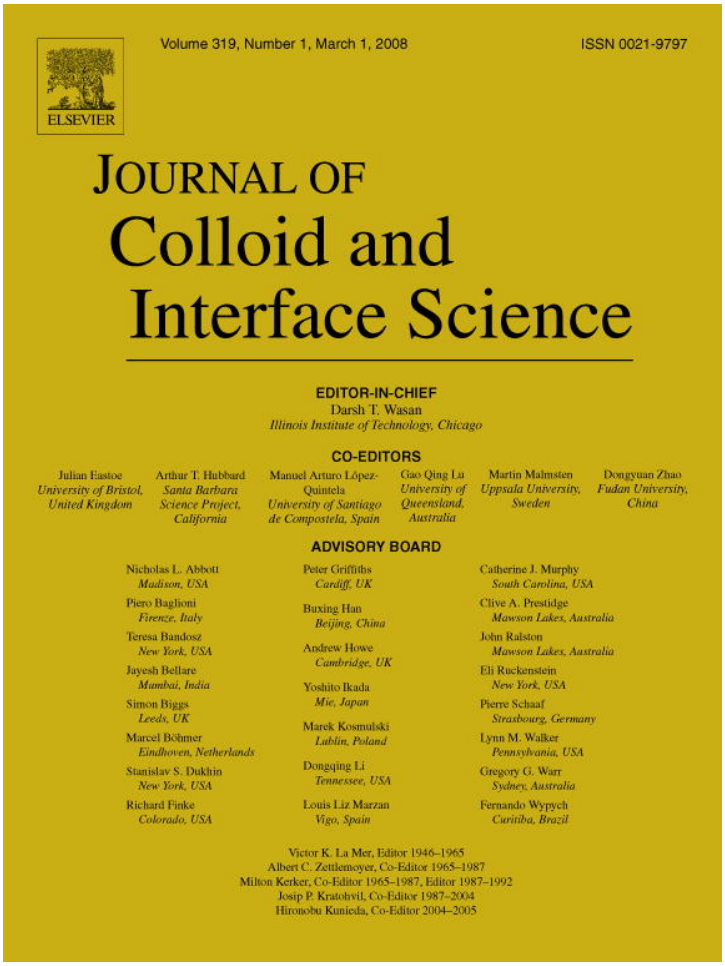

This article was published in an Elsevier journal. The attached copy is furnished to the author for non-commercial research and education use, including for instruction at the author's institution, sharing with colleagues and providing to institution administration.

Other uses, including reproduction and distribution, or selling or licensing copies, or posting to personal, institutional or third party websites are prohibited.

In most cases authors are permitted to post their version of the article (e.g. in Word or Tex form) to their personal website or institutional repository. Authors requiring further information regarding Elsevier's archiving and manuscript policies are encouraged to visit:

http://www.elsevier.com/copyright

Author's personal copy

Available online at www.sciencedirect.com
ScienceDirect
Journal of Colloid and Interface Science 319 (2008) 182–192
JOURNAL OF Colloid and Interface Science
www.elsevier.com/locate/jcis

The strength of liquid bridges in random granular materials

Zdeněk Grof, Christopher J. Lawrence, František Štěpánek *

Department of Chemical Engineering, Imperial College London, South Kensington Campus, SW7 2AZ London, UK

Received 30 September 2007; accepted 29 November 2007

Available online 8 December 2007

Abstract

The strength of capillary bridges in randomly packed granular media was analyzed by means of computer simulations. A novel simulation method, based on the tracking of moving interfaces, has been implemented and used for determining the equilibrium shape of capillary bridges in a granular medium under a range of liquid saturations and solid-phase geometry. The net force acting on each grain due to the capillary bridges was evaluated, as well as the aggregate force acting between two wet granular media during their separation in the normal directions. The simulation results are consistent with previous experimental observations and reveal interesting phenomena such as the existence of a maximum in the tensile strength of a wet granular medium as function of liquid saturation.
© 2007 Elsevier Inc. All rights reserved.

Keywords: Capillary force; Wetting; Pendular and funicular regime; Modeling; Tensile strength; Surface tension; Contact angle

1. Introduction

Wet granular materials play an important role in a range of natural as well engineering systems; for instance, the stability of wet land masses (landslides), the erosion of soil or the entrainment of sand particles during reservoir flows are examples of naturally occurring phenomena where the cohesion forces between grains due to capillary interactions are important [1]. In industry, processes such as wet granulation [2], deep-bed filtration, arching and rat-holing during granular flows in silos, etc., can all be related to the mechanical behavior of wet granular media. In order to understand and eventually predict the behavior of such systems, it is key to know the relationship between micro-scale parameters of the granular medium, such as grain shape and size distribution and packing density, the pore-space saturation, the contact angle and surface tension of the wetting fluid on the one hand, and the effective macroscopic properties on the other hand. Of these, the tensile strength of a wet granular material is one of the most important, as it determines whether the system is stable or will break/collapse under applied external or internal stress.

The measurement of the tensile strength of wet granular media has been subject to several studies [3–5], where the stress-strain curves of a granular medium were obtained under well-defined conditions—such as on a string of beads or in artificially prepared sand-packs. The main qualitative conclusion from these studies is that the tensile strength (force per unit area at the rupture point) as function of liquid saturation may have a maximum, despite the fact that the strength of a single pendular bridge between two particles decreases monotonously with increasing volume. However, the precise location of the maximum can vary widely [6] depending on the material used (particle size, etc.), and can even disappear in some cases. Situations where two local extrema of tensile strength exist have also been observed [7]. The behavior of wet granular media is still far from understood. Let us cite from Ref. [6]: "In the funicular state, the cohesive stress dependence on the liquid content is not clearly understood. The cohesive stress may either increase or decrease with saturation in the funicular state. There would be at least one maximum of the cohesive stress at a certain liquid content, though it is not clear, a priori, the location of the peak."

The exact geometrical configuration of capillary bridges at the microscopic (individual grain) length-scale is experimentally accessible for pendular bridges between two particles [8], but in the funicular state in a randomly packed structure it is

* Corresponding author. Fax: +44 20 7594 5638.
E-mail address: f.stepanek@imperial.ac.uk (F. Štěpánek).

0021-9797/$ – see front matter © 2007 Elsevier Inc. All rights reserved.
doi:10.1016/j.jcis.2007.11.055

Author's personal copy

much more difficult to observe directly [2]. Hence, computer simulations lend themselves as a useful tool for investigating the relationship between the geometry of liquid menisci at the grain-level and the overall macroscopic properties of the granular medium. Systems containing only pendular (binary) capillary bridges can be simulated using the discrete element method (DEM) extended by taking into account additional attractive interaction between particles due to the capillary force [9–11]. However, for higher liquid saturations where funicular bridges and more complicated liquid clusters begin to form, this simplified approach is no longer possible.

The objective of the present work, therefore, was to develop a new methodology for computer simulation of static and dynamic capillary bridges in arbitrary liquid saturation in granular media (as well as other geometries), and then use it for the computational study of the force acting on particles under various scenarios. The paper is structured as follows: first the computer simulation algorithm is described and its validity shown by comparing the numerical solution for a single pendular bridge with analytical solution. A study of the effect of pore saturation on the force acting on particles in a simple four-grain cluster is carried out next, followed by simulated tensile strength tests for both regular and random assemblies containing a statistically large number of grains.

2. Methodology

The numerical method used for simulation of the interface was described in detail in our recent work [12], here the main principles are outlined. The geometry of the wet granular system is defined by polygons $\mathcal{S}_i$ and $\mathcal{L}_j$, representing the individual solid particles and the liquid phase domains. Each liquid polygon can potentially contain a number of sub-polygons $\mathcal{L}'$ corresponding to the "holes" within the parent liquid polygon. These sub-polygons can either represent a single gas bubble, a completely submerged solid particle, or the combination of the two, cf. Fig. 1a.

Every polygon $\mathcal{S}$, $\mathcal{L}$ or $\mathcal{L}'$ is defined by a number of nodes, characterized by their type and position. From the node positions it is possible to calculate: the total area of the polygon, the normal vector at every polygon edge and the local curvature at each node. The nodes of liquid polygon (or its sub-polygon) can be classified into three types as is illustrated in Fig. 1b: (i) nodes at the liquid–gas interface, (ii) nodes at the liquid–solid interface, and (iii) nodes representing the three-phase contact points. For given fixed location of the solid phase and the total area of the liquid phase, the equilibrium shape of the liquid phase polygons that minimizes the energy of the system has to satisfy constant mean curvature of all liquid–gas interfaces belonging to the same liquid domain, and the equilibrium contact angle at all three-phase points. In order to reach this state of minimum energy from an arbitrary initial shape of the liquid polygons, the node positions are iteratively updated according to the following set of rules (further details can be found in reference [12]).

The nodes at the liquid–gas interface (LG-nodes) can move without any constraints, the movement consists of the following steps: (a) minimization of total liquid–gas interface length,

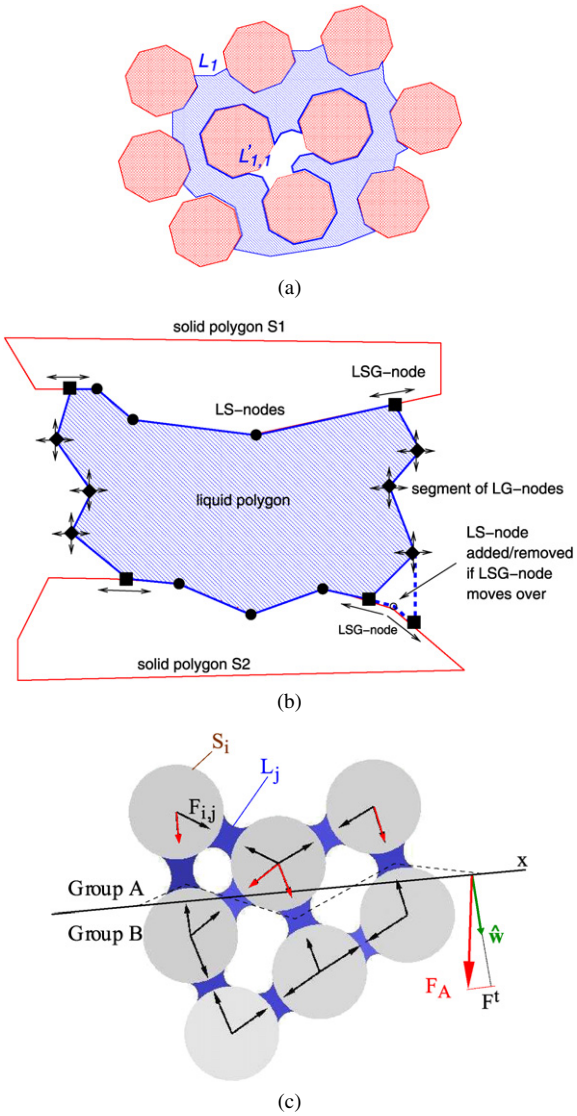

Fig. 1. Representation of an arbitrary three-phase system in 2-D by a set of polygons.

(b) convergence toward constant mean curvature, (c) preservation of uniform distribution of nodes along the polygon boundary, and (d) preservation of the total polygon area. The movement of three-phase points (LSG-nodes) is confined to the edges of the solid polygon they are adjacent to. The displacement is adjusted iteratively by the Newton's method so as to locally satisfy the equilibrium contact angle. Finally, position of nodes at liquid–solid interface (LS-nodes) is fixed to the position of solid polygon nodes. During the simulation a LS-node can be inserted to (or removed from) liquid polygon whenever a three-phase point moves from one solid polygon edge to a neighboring one. This procedure ensures that the solid–liquid interface is correctly tracked down and there are no gaps or overlaps between adjacent liquid and solid polygons [12]. During the movement of the LG- and LSG-nodes, topological changes such as the merging or separation of interfaces are also taken into account. The solid polygons can move step-wise in a prescribed direction in order to simulate processes such as the deformation or separation of a granular medium.

Author's personal copy

2.1. Calculation of the capillary forces

As soon as the equilibrium positions of gas–liquid interfaces and three-phase points have been found the static capillary interaction $\boldsymbol{F}_{ij}$ between particle $\mathcal{S}_i$ and liquid body $\mathcal{L}_j$ can be calculated. It consists of two contributions: the first one is due to Laplace–Young pressure difference and the second one is the direct action of the surface tension of the liquid. The pressure component acts in the direction normal to liquid–solid interface and it is calculated by integration along this interface. The surface tension component with a magnitude γ acts in the direction of the tangent to the liquid interface at the contact point and is calculated by summation of contributions from all contact points (LSG-nodes) between the solid and the liquid polygons.

The capillary force acting on a solid particle $\mathcal{S}_i$ is calculated by summation of contributions from all liquid domains $\mathcal{L}_j$

$$\boldsymbol{F}_i = \sum_j \boldsymbol{F}_{ij}. \tag{1}$$

Upon definition that if particle $\mathcal{S}_i$ and liquid domain $\mathcal{L}_j$ are not in contact then $\boldsymbol{F}_{ij} = 0$, one can write the sum running over all liquids j in the above equation which simplifies the notation.

In order to calculate the tensile strength of a wet granular medium, the solid particles are divided by a line x into two groups, A and B, as shown in Fig. 1c. The capillary force acting on group A and B is

$$\boldsymbol{F}_A = \sum_{i\in A}\sum_j \boldsymbol{F}_{ij}, \qquad \boldsymbol{F}_B = \sum_{i\in B}\sum_j \boldsymbol{F}_{ij}. \tag{2}$$

It can be simply proved that at the equilibrium $\boldsymbol{F}_A + \boldsymbol{F}_B = 0$ by writing

$$\boldsymbol{F}_A + \boldsymbol{F}_B = \sum_i\sum_j \boldsymbol{F}_{ij} = \sum_j\left(\sum_i \boldsymbol{F}_{ij}\right) = 0 \tag{3}$$

and noticing that the term in brackets is the total capillary force on every liquid domain which must be zero at the equilibrium. The tensile force is defined as a normal component of the force holding the groups A and B together

$$F^t = \boldsymbol{F}_A \cdot \hat{\boldsymbol{w}}, \tag{4}$$

where $\hat{\boldsymbol{w}}$ is a unit vector perpendicular to line x and pointing in the direction from group A to B (Fig. 1c).

As well as the force F^t, let us define two additional integral quantities which will be used for the characterization of the system: (i) the specific liquid–gas interface, defined as the total length of all liquid–gas interfaces, divided by the area of the smallest convex envelope of the system of interest (solid, liquid, and gas phases combined); (ii) the wetted solid fraction, defined as the length of all solid–liquid interfaces, divided by the total length of solid interfaces in contact with either liquid or gas phase.

3. Results and discussion

3.1. Validation of the model

In order to validate the model, the theoretical force of pendular bridge between two equal disks has been calculated analytically [13] and compared with results of our numerical procedure. The equations for the analytic calculation for this simple geometry are listed in Appendix A. The capillary force as a function of the separation of disks is shown in Fig. 2a. The calculated results are close to the theoretical values, except the fact that the curves in Fig. 2a are not smooth and they are shifted slightly above the analytical solution. This error is well below 5% so it can be neglected in the practical applications.

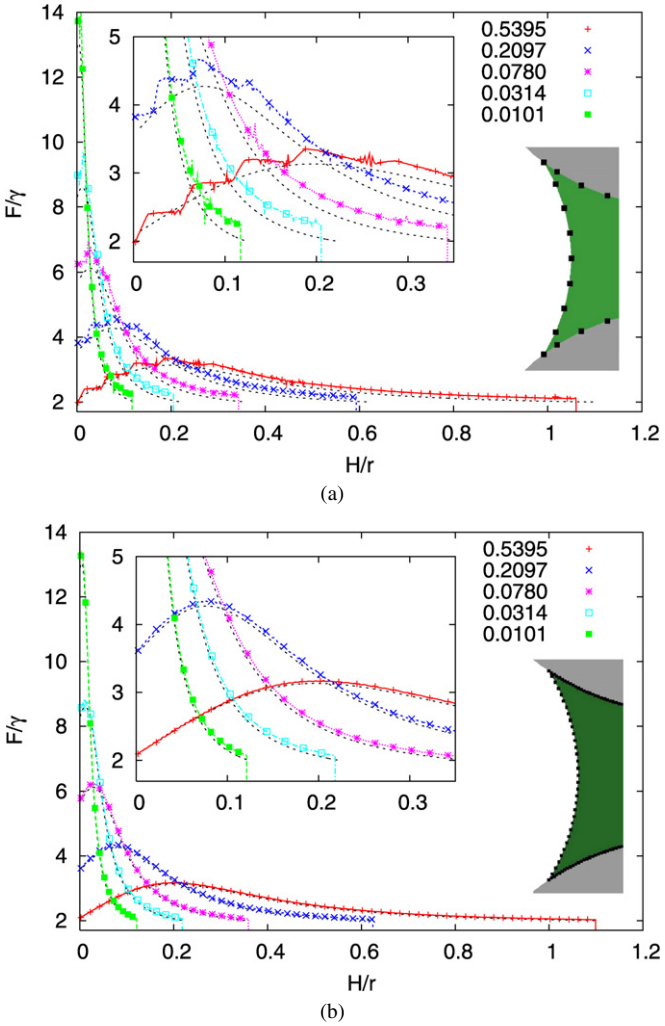

Fig. 2. The dependence of the liquid bridge force F on the half-separation distance H between two disks having radius r. Comparison between analytical solution (dotted lines) and numerical simulation. The liquid content (area A/r^2) is 0.5395, 0.2097, 0.0780, 0.0314, and 0.0101, which at $H = 0$ corresponds to the half-filling angle α of 61°, 43°, 29°, 22°, and 15°, respectively. Compared to panel (a), a finer discretization has been used for simulations in panel (b).

The differences are caused by the discretization nature of the algorithm. When the number of nodes representing solid disks has been increased from 50 to 500 the "step-wise" looking features disappeared. The increase of the number of nodes at the liquid–gas interface resulted in decreasing the difference between numerical and analytical results significantly, as shown in Fig. 2b. In calculations containing many solid particles and liquid interfaces this would lead to the unnecessary increase of the calculation time. Therefore, in the rest of the simulations

Author's personal copy

presented in this paper we used the same extent of discretization as in Fig. 2a, accepting an error of approximately 5%.

3.2. Simple four-particle geometry

Before investigating the tensile strength of granular material in which the effect of many liquid bridges is combined, let us analyze the behavior of liquid bridges in a simpler arrangement. Dependencies of the capillary force on the liquid amount and the separation distance for a pendular liquid bridge between two particles have been already presented in Fig. 2. When particles are separated the liquid bridge force $F(H, A)$ increases toward a maximum $F_{\max}(H_{\max}, A)$ and then decreases until reaching the critical separation H_{cr} at which bridge ruptures. When one decreases the amount of liquid A, both the $H_{\max}$ and H_{cr} shift toward smaller separation distances H and the maximum capillary force increases. Let us point out that the capillary force of a three-dimensional pendular bridge decreases monotonously with separation distance [14] and that the capillary force at the zero separation is relatively less influenced by the amount of liquid than in its two-dimensional counterpart discussed in the present paper.

At least three particles are necessary for the presence of a funicular bridge. The liquid distribution between triplets of particles including $F(H, A)$ dependencies calculated analytically have been presented in earlier publication by Urso et al. [15]. In the present paper a group of four particles was chosen because this geometry can be regarded as the basic structural unit of a granular material with periodic cubic arrangement. This structure is shown in Fig. 3. The simulation started with the system in the capillary state, i.e., the space between particles was filled completely, and evaporation was simulated by subsequently removing small amounts of liquid. Each liquid removal step was followed by approximately 4000 iterative node movements in order to find new minimum energy configuration. In the course of simulation shown in Fig. 3 both the transitions to funicular and pendular regimes take place. The first transition can be seen when the liquid looses the symmetry just after the menisci of liquid–gas interfaces pass through the narrowest part of the gap between particles. As one of four liquid–gas interfaces appears inside the cavity among particles, this situation can be regarded as the funicular regime. The second transition is the split of the single funicular liquid bridge into three pendular ones.

The cohesive effect of capillary forces on the four particles can be quantified best as the sum of capillary forces projected into the center of the system, F_{cen}

$$F_{\mathrm{cen}} = \sum_{i=1}^{4} (\boldsymbol{x}_i - \boldsymbol{x}_0) \cdot \boldsymbol{F}_i, \tag{5}$$

where $\boldsymbol{F}_i$ and $\boldsymbol{x}_i$ are the capillary force on the ith particle and its position, respectively and $\boldsymbol{x}_0$ is the center of the system. The value of F_{cen} can be negative which means that capillary forces among particles are repulsive. The change of the capillary cohesion force F_{cen} during liquid evaporation is illustrated in Fig. 4a. The relative liquid content ϕ on the x-axis is defined as $\phi = A_{\mathrm{liq}}/(A_{\mathrm{tot}} - A_{\mathrm{sol}})$ where A_{liq} and A_{sol} are the areas of liquid and solid phases, respectively, and A_{tot} is area of the black rectangle in Fig. 3. The action of capillary forces is symmetrical in the capillary regime and during evaporation its magnitude increases toward a maximum as the curvature of liquid–gas interface menisci grows. The F_{cen} at this maximum is larger for smaller contact angle and its actual value depends on the system geometry, i.e., the ratio between gap and particle size, δ/r, which is 0.2 in the presented example. The transition to the funicular regime is characterized by an instant drop of the cohesive force, the drop is larger for smaller contact angles. As evaporation continues the cohesion slowly decreases until another drop which marks the separation of funicular bridge into three pendular ones. The position and size of this drop depends on the contact angle. Finally, the capillary force has a flat maximum in the pendular region before it decreases to the point where the bridges eventually rupture. It is interesting to note that the dependence of the cohesion on the contact angle is less significant in funicular than in pendular or capillary regimes for contact angles smaller than 72°.

The curves for specific liquid–gas interface length (Fig. 4b) have minimum just before the capillary to funicular transition at $\phi \approx 0.3$ regardless of the contact angle. On the other hand, the position of the transition between funicular and pendular states marked by the drop of the interface length, moves to lower liquid content as the contact angle increases. The above mentioned transitions can be seen also in the dependencies of wetted solid fraction in Fig. 4c. It can be surprising at first, that the curves for different contact angles at no point intersect each other, although they become close when contact points are near narrowest part of the gap between particles. However, the explanation is simple. Regardless of the liquid content, the wetted fraction of the solid phase should monotonously increase with decreasing contact angle.

If the evaporation is stopped just before any of the three pendular bridges rupture and the process is reversed, i.e., one

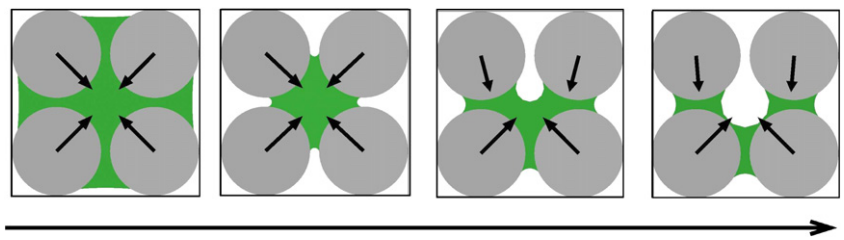

Fig. 3. Simulation of liquid evaporation from cluster of four particles. Contact angle is 26° and liquid content ϕ is 0.6514, 0.3215, 0.3052, and 0.2060.

Author's personal copy

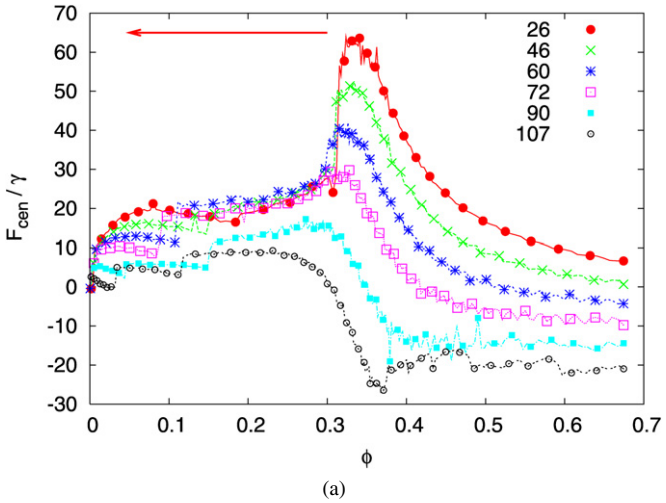

(a)

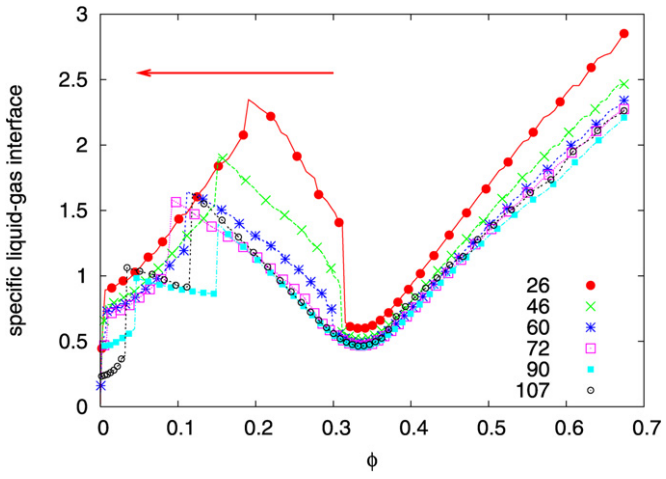

(b)

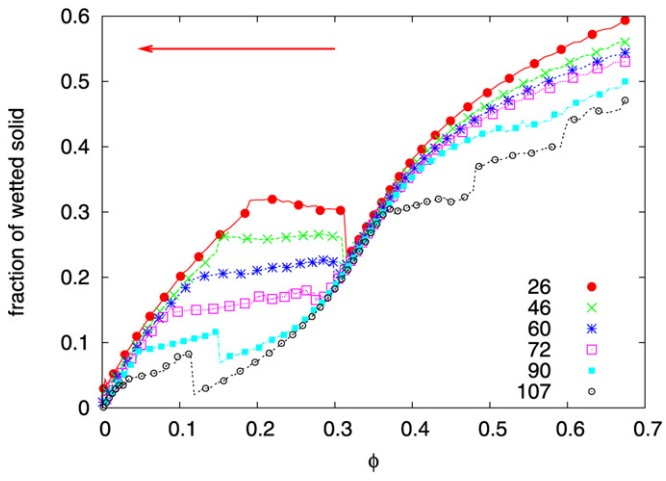

(c)

Fig. 4. Liquid evaporation from cluster of four particles. The evolution of cohesiveness force, specific liquid–gas interface length and the fraction of wetted solid interface length. The numbers denote the contact angle.

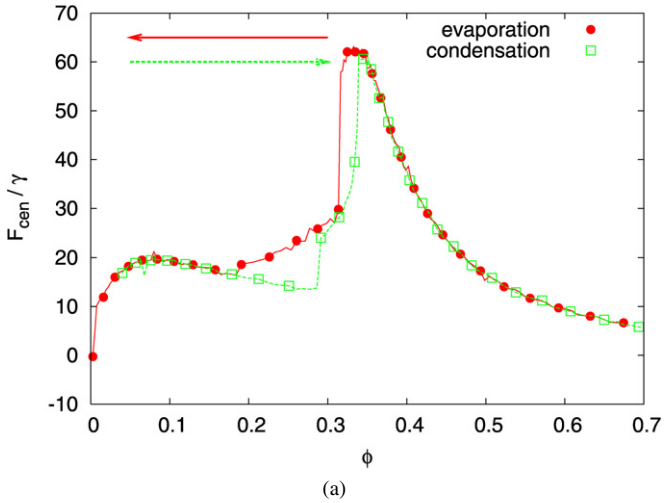

(a)

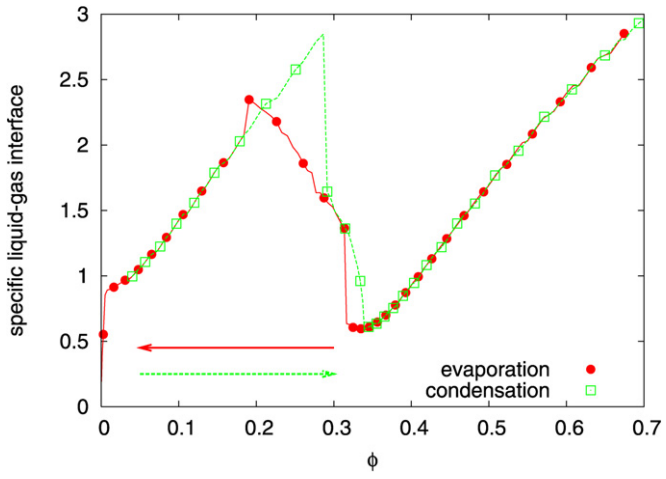

(b)

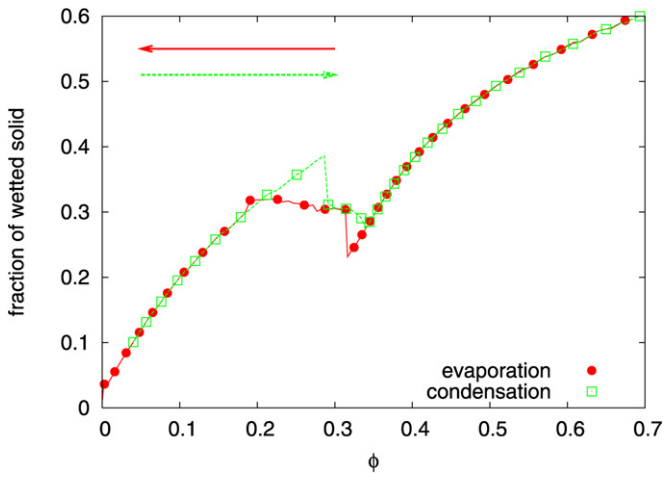

(c)

Fig. 5. Illustration of the hysteresis through evaporation/condensation of liquid from a cluster of four particles. Contact angle 26°.

starts to gradually add liquid, then hysteresis occurs in funicular state as shown in Fig. 5. The quantities follow the same paths in the pendular and capillary states, however, the transitions to the funicular regime occur at different liquid content ϕ. The most profound difference is the pendular/funicular transition, which during condensation occurs at larger ϕ than during evaporation. Compared to the evaporation, the cohesion force F_{cen} is lower and both the liquid–gas interface and the wetted solid fraction are larger during condensation.

Author's personal copy

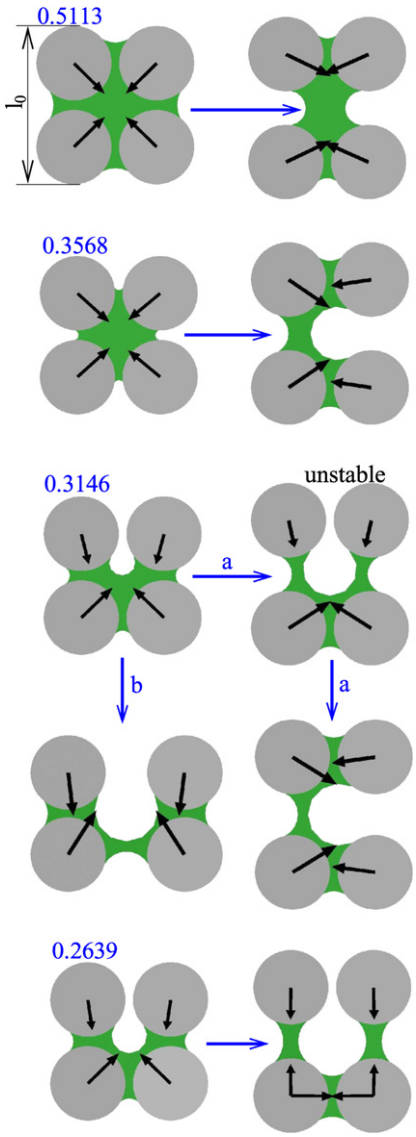

Fig. 6. Simulation of tensile strength testing experiments. Contact angle is 26° and numbers denote the initial relative liquid content ϕ.

Now let us discuss the tensile strength of the system of four particles at different liquid content ϕ. During simulations the pairs of particles were sequentially moved apart as illustrated in Fig. 6 and the capillary force acting between the pairs recorded until the bridge ruptured. This type of computer simulation is analogous to experiment for tensile strength measurement. The simulated stress/strain curves are shown in Figs. 7a and 7b. The curves can be classified into two groups depending whether the force initially increases or decreases. In the capillary state (high values of ϕ) the force initially increases until a maximum (Fig. 7a) and the tensile strength of the particle quartet can be defined as this maximum. For systems in funicular or pendular states there is no maximum on the stress-strain curve for the current geometry used, but it would appear if the gap size was smaller. Experimental evidence for two-particle [14,16] or three-particle [17] systems shows a monotonous decrease in capillary force only, however, these measurements have been carried for a 3-D liquid bridge geometry. Because the funicular

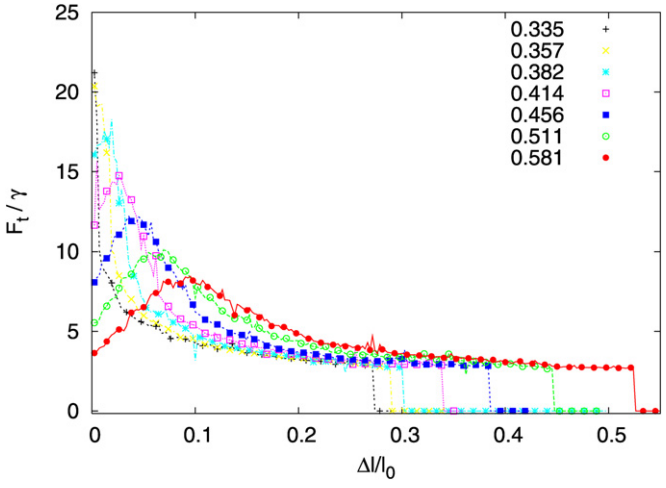

(a)

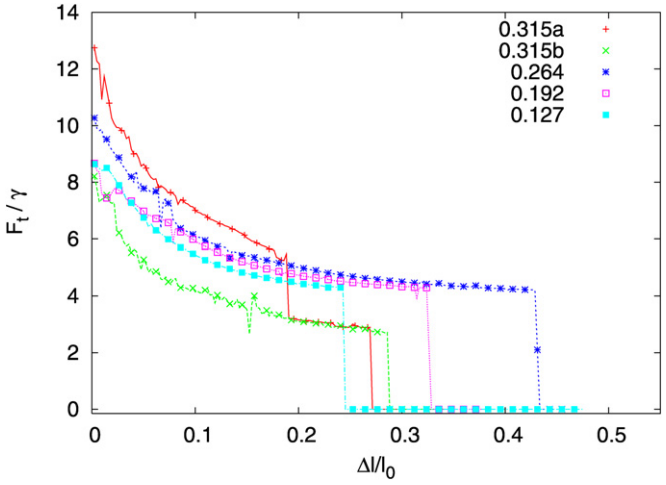

(b)

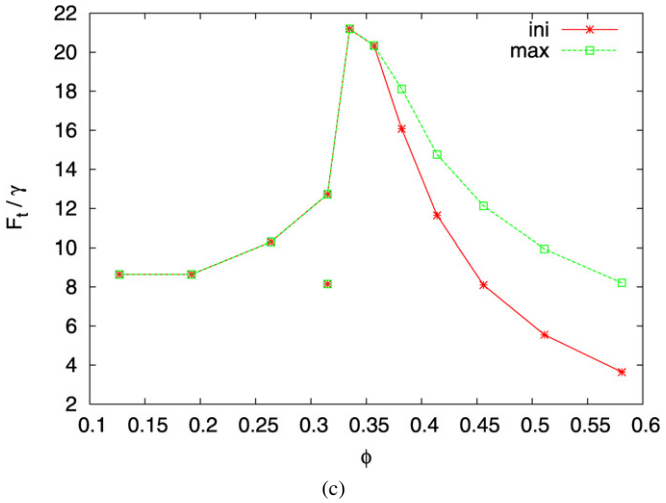

(c)

Fig. 7. (a and b) Simulated stress/elongation curves of quartet of particles. The number denote the relative liquid content ϕ. (c) Initial (at $\Delta l/l_0 = 0$) and maximal tensile force as a function of the relative liquid content ϕ.

bridge is non-symmetric the tensile strength is anisotropic. The two lines denoted as $\phi = 0.315$a and 0.315b in Fig. 7b are the result of vertical and horizontal movement, respectively. (Let us note that no volume forces—gravity in particular—were con-

Author's personal copy

sidered during the simulations, i.e., the interfaces move solely due to surface tension.) The force is considerably larger in the case a, but as particles are pulled vertically an unstable configuration shown in Fig. 6 develops. The liquid bridge then rearranges spontaneously into the identical configuration one would obtain by horizontal movement, cf. case b. The unstable configuration followed by spontaneous rearrangement discussed in the previous example exists only for a narrow range of ϕ in the funicular regime. For example, when ϕ is lowered to 0.264, the funicular bridge splits into pendular ones before the unstable configuration can develop.

Fig. 7c summarizes the dependence of the tensile strength on the liquid content ϕ. There is a clear maximum located at the capillary/funicular transition. The size and position of the maximum depends on the system geometry, e.g., the maximum would be larger if the particle distances were smaller. It has already been noted that tensile strength initially increases with the strain toward a local maximum in the capillary state system. This is demonstrated by the maximum tensile force curve ("max") being above the tensile force at the zero strain ("ini") for ϕ larger than 0.36 (capillary state). In pendular or funicular state both curves coincide. The single point at $\phi = 0.315$ illustrates the anisotropicity of tensile strength and is for the weaker orientation (the case "b" in Figs. 6 and 7).

3.3. Hexagonally packed geometry

Increasing the complexity of the problem, the next geometry being analyzed is the regular hexagonal packing of uniform particles. The simulations have been carried in a 30×10 block of circular particles. The distance between particles was the same as in the case of the four-particle cluster discussed in the previous section ($\delta = 0.2r$). Pendular bridges have been regularly placed between particles so every particle (except those at the boundary) was in contact with six pendular bridges. The condensation was simulated first. The amount of liquid subsequently added to every liquid domain was proportional to the total length of its liquid–gas interface. Results of this simulation were the distributions of liquid among particles at different liquid contents. These configurations have then been used as an initial configuration for the simulations of the tensile strength measurement. While keeping liquid content constant, one group of particles has been gradually moved apart and the tensile force between the groups of particles has been calculated (cf. Fig. 1c). Results of these simulations are presented in Figs. 8 and 9. It has to be noted that the relative position of particles within each group have been fixed. This is an approximation, and a more rigorous approach would require the relative particle movement within the groups to be considered as well, governed by capillary and contact forces among individual particles.

The tensile strength F_t in the course of the condensation simulation is shown in Fig. 8a. The force is divided by the number of particles n_x along the division line ($n_x = 30$ in Fig. 8). The curve denoted as "max" has been obtained later from stress/strain curves as the maximum value of the tensile force during tearing simulation. The dotted vertical lines correspond to system configurations in Fig. 9. The graph of specific

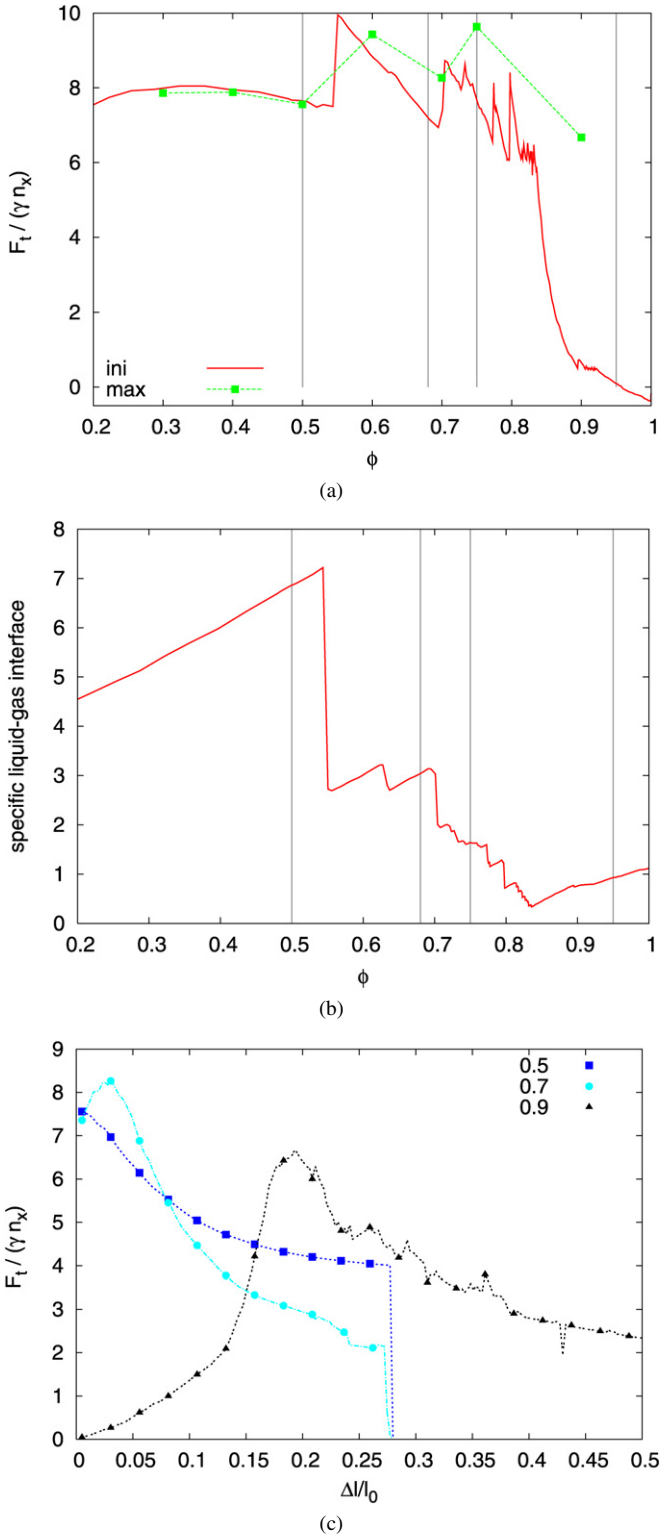

Fig. 8. Hexagonal packing of particles. (a) Initial and maximal tensile force as function of relative liquid content ϕ. (b) Evolution of specific liquid–gas area during liquid condensation. (c) Simulated stress/elongation curves for different liquid content ϕ.

liquid–gas interface length, Fig. 8b, illustrates best the topological transitions of the system during condensation. First, in pendular state, it is possible to observe a flat maximum on the tensile strength curve together with a monotonously growing

Author's personal copy

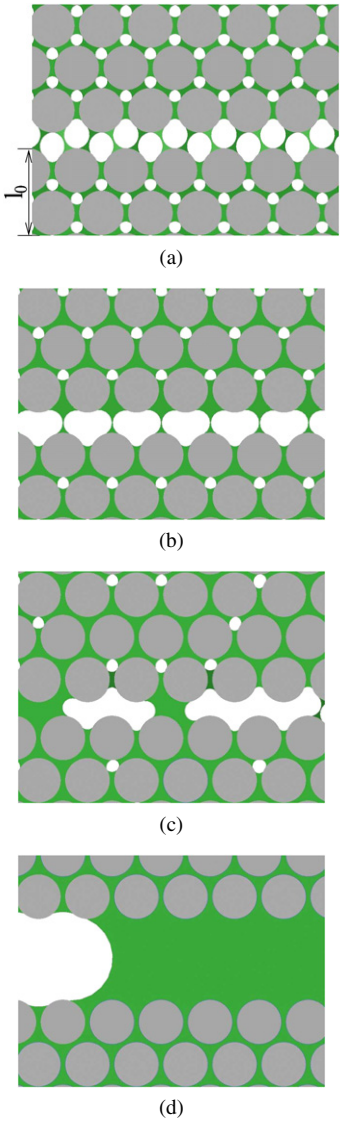

Fig. 9. Hexagonal packing of particles. Simulation of tensile strength experiments. The initial relative liquid content ϕ in the samples was 0.50, 0.68, 0.75, and 0.95, respectively, and corresponds to dotted vertical lines in Figs. 8a and 8b.

liquid–gas interface for liquid saturation ϕ bellow 0.54. This behavior is merely the summation of single pendular bridges and, for example, can be compared with the appropriate part of curves in Figs. 5a and 5b. At $\phi \approx 0.54$ the pendular bridges (Fig. 9a) coalesce at once and form funicular bridges among triplets of particles (Fig. 9b) sharply reducing the liquid–gas interface length (and total energy of system) while tensile force increases significantly.

As ϕ increases, the liquid force decreases again because of decreasing menisci curvature and at $\phi \approx 0.7$ the funicular bridges among triplets of particles start to coalesce and form larger liquid domains. The force abruptly increases once more while the liquid–gas interface length curve contains another drop at this point. However, as a result of small numerical fluctuations, the trivalent bridges do not all coalesce at once, which leads to the termination of uniformity. There are gas inclusions randomly located within the system, cf. Fig. 9c. From this point on, the individual liquid domains coalesce non-uniformly, the tensile force curve oscillates while liquid–gas interface length decreases in step-wise manner but monotonously.

When most of gas inclusions inside the system disappeared by liquid coalescence, the global characteristics are determined by the state at the boundary where the remaining menisci are. The tensile force is predominantly due the pressure difference depending on the curvature of menisci at the boundary. The pressure difference is largest when the menisci are located in the narrowest part of the gap between particles and this location is marked by the local minimum on the liquid–gas interface length curve at $\phi \approx 0.85$, cf. Fig. 8b. It can be seen that although there are no liquid–gas interfaces inside the packing, cohesive force is still relatively important. This liquid–gas interface minimum can be regarded as marking the funicular/capillary state transition.

The behavior of system in capillary state is then analogous to that observed in a cluster of four particles, cf. Fig. 5. The liquid–gas interface increases while the tensile force decreases, reaching zero when menisci are flat (zero curvature). If liquid content is increased even more the cohesion force becomes negative. Note that compared to the system of four particles where the "boundary effects" were relatively strong, the global characteristics (e.g., F_t) change to smaller extent within capillary state than within the whole range of ϕ. This can be verified by comparing parts of curves corresponding to capillary state in Figs. 5 and 8.

The characteristics shapes of stress-strain curves for three different values of ϕ are shown in Fig. 8c. It can be seen their shape is qualitatively similar to the stress-strain curves discussed previously in the context of a four-particle system (shown in Fig. 7c). At a high liquid content corresponding to the capillary state ($\phi = 0.9$) the force is very small initially but as the strain $\Delta l / l_0$ increases, the force reaches a maximum. For a lower liquid contents ($\phi = 0.7$) the position of this maximum shifts toward lower separation distances, and also the force at zero separation is higher in this case, due to the higher strength of the funicular state compared to the capillary one. Eventually, as the liquid content decreases even further ($\phi = 0.5$), the maximum disappears and a monotonously decreasing stress-strain curve is obtained.

3.4. Complex granular media

Finally, let us investigate the stress-strain response of a random packing of non-uniform particles as function of liquid content. Several different random packings of elliptical particles (aspect ratio 1.075–1.325, minor axis 0.2) of the same packing density have been generated in order to investigate the sensitivity of the results on the packing structure. The liquid content in each of the random particle packings has been gradually increased, and the stress-strain curves obtained by the simulated tensile strength test, same as in the cases discussed above (four particles and hexagonal packing). The results are summarized in Fig. 10: the stress-strain curves for two random realizations, called samples C and F, are shown in Fig. 10b and Fig. 10c, respectively. In each case, curves for four different values of liq-

Author's personal copy

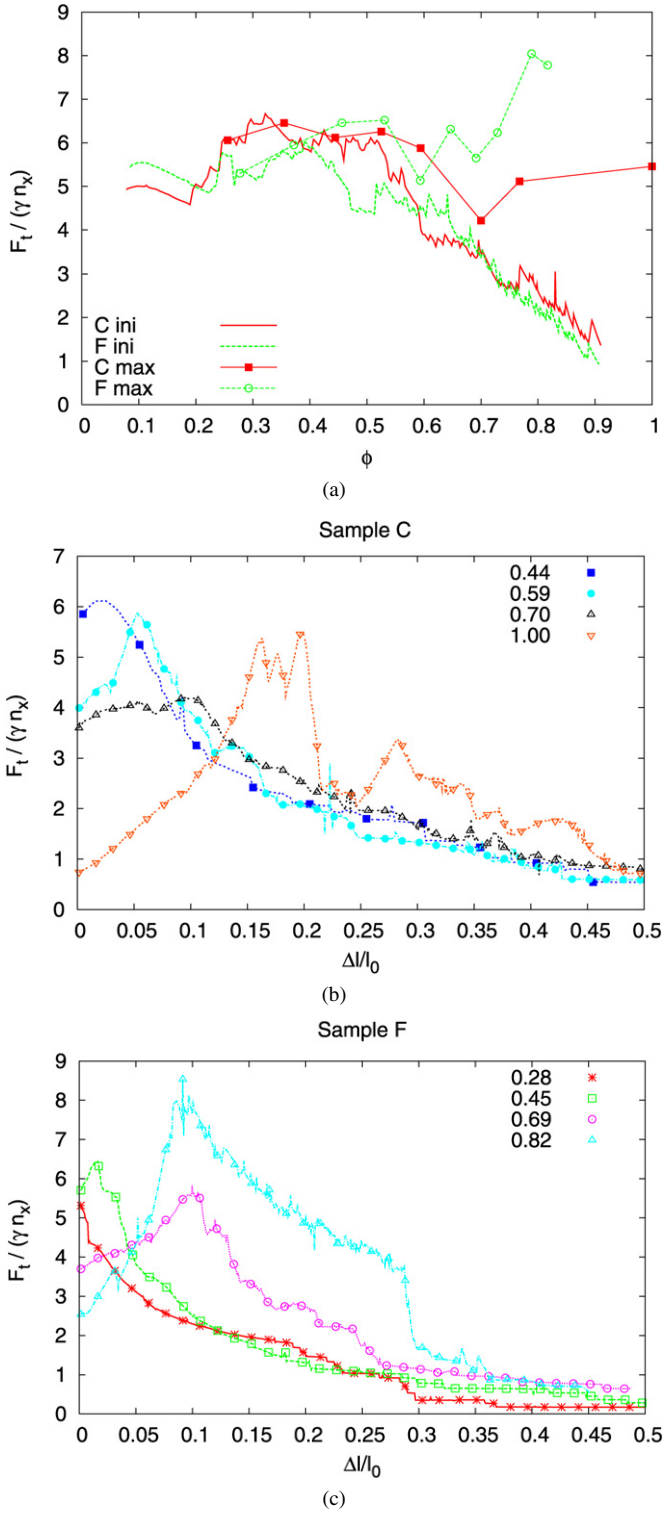

Fig. 10. Packing of elliptic particles. (a) Initial and maximal tensile force as a function of relative liquid content for two different packing realizations (Samples C and F). (b) Simulated stress/elongation curves of Sample C for different liquid content ϕ. (c) Same as in panel b but for Sample F. For both samples: $n_x = 20$, $l_0 = 0.4$. Size of particles: minor axis is 0.2 and aspect ratio in the range 1.075–1.325.

uid content ϕ are shown, covering the cases of maximum being present (higher ϕ–capillary state), maximum shifting toward lower separation distances (medium ϕ–funicular state), and monotonously decreasing stress-strain curve (low ϕ–pendular liquid bridges). Qualitatively, the same regimes as in the hexagonal and the four-particle system have been covered. The shape of stress-strain curves in funicular or capillary state with a local maximum is similar to measured tensile stress-strain curves of moist limestone agglomerates, reported in [5].

As in the cases of the four-particle and the hexagonal packing, the initial and maximum force evaluated from the stress-strain curves are plotted as function of the liquid content ϕ in Fig. 10a. Notice that the curves of maximum force for two different random realizations of the packing (C and F) are relatively close to each other for lower liquid content, but deviate more substantially as ϕ is increased. The explanation of this behavior follows from considering the number of individual liquid bridges that contribute to the aggregate force acting between the two halves of the granular medium during its separation in the course of the simulated tensile strength test. At low liquid contents, there is a large number of pendular or funicular bridges (Figs. 11a and 11b), the statistics is good and the difference between two random realizations of the particle packing is small. However for higher ϕ as the capillary state is approached, only a few liquid clusters comparable to the size of the entire system dominate the interaction (Figs. 11c and 11d), and this causes larger fluctuations between different random realizations of the particle packing. The evolution of the liquid bridges at a higher liquid content ($\phi = 0.69$) during stress-strain simulation is illustrated in detail in Fig. 12. As can be seen, only three large liquid bridges exist in the later stages despite the large number of solid particles; the rupture of one such bridge then naturally leads to a larger step on the stress-strain curve. This problem could be reduced by simulating a larger system, with the associated higher computational costs.

4. Summary

The tensile strength of a granular medium due to liquid bridges has been investigated by computer simulations in two dimensions. Starting from geometrically simple arrangements (group of four spherical particles, hexagonal packing) through to more complex (random packing of ellipsoidal particles), it has been shown that the dependence of the cohesive force on the separation distance—i.e., the stress-strain curve—can have qualitatively different behavior depending on the liquid content in the granular medium: at high liquid saturations, a clear maximum of tensile strength as function of separation distance exists; at intermediate liquid saturations, this maximum shifts toward lower separation distances until it eventually disappears at low liquid contents. Our computational results are consistent with experimental observations and they help explain and unify the range of apparently contradicting trends observed in previously published experimental works. As can be appreciated, e.g., from Fig. 8c, depending on the range of liquid saturations and separation distances investigated, completely opposing trends can be observed: existence of a maximum, monotonously decreasing or monotonously increasing tensile strength as function of separation distance.

Author's personal copy

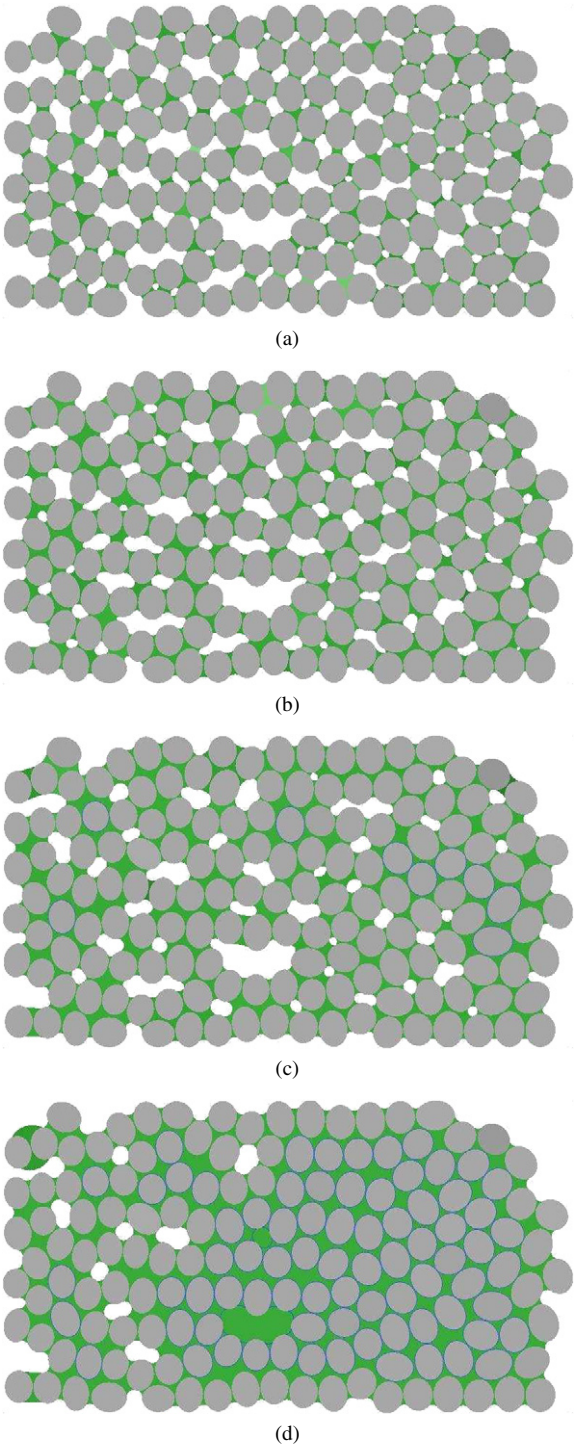

Fig. 11. The illustration of the course of liquid condensation of elliptic particles packing (Sample C). Relative amount of liquid ϕ is 0.25, 0.44, 0.59, and 0.77, respectively.

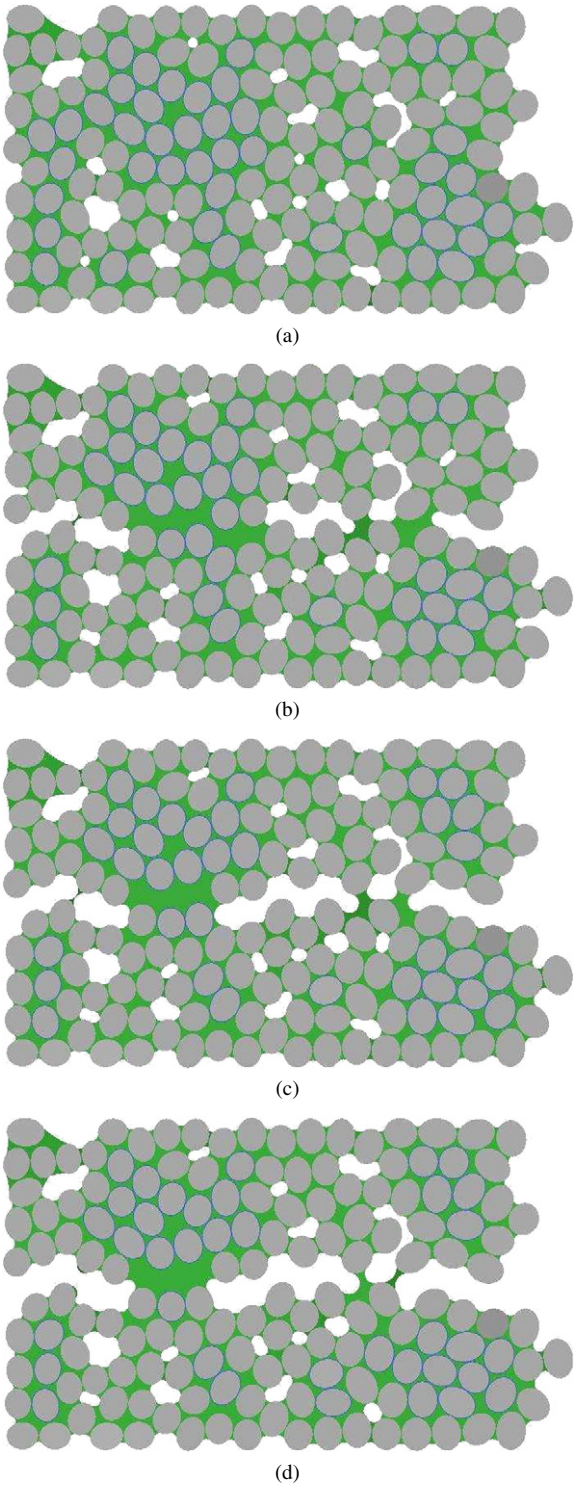

Fig. 12. The course of tensile strength experiment of Sample F. Initial relative liquid content ϕ was 0.69.

The understanding of the strength of capillary force interactions is practically important in several domains of science and engineering at varying length-scales: from geological systems (soil erosion), through particle technology (wet agglomeration of pharmaceutical powders) to nano-technology (e.g., the formation of defects during drying of photonic crystal layers). Further research will focus on the investigation of particle heterogeneity (bi-modal particle size distribution, distribution of particle surface properties—hence contact angles), and on extending the simulation methodology to three-dimensional systems.

Acknowledgments

Support from EPSRC through Grant No. GR/S82510/01 is gratefully acknowledged.

Author's personal copy

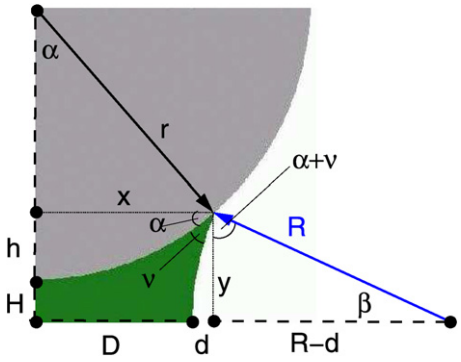

Fig. 13. Pendular capillary bridge.

Appendix A. Capillary force of 2-D pendular bridge

In this appendix we derive the analytical solution for the force of a two-dimensional liquid bridge between two equal circular particles with radius r. When the parameters wetting angle ν, half-filling angle α, and half-separation distance H, are specified (see Fig. 13 for definitions), the remaining quantities can be calculated as follows. The position of the three-phase contact point is

$$x = r\sin\alpha, \qquad y = H + r(1-\cos\alpha), \tag{A.1}$$

and the meniscus radius R and the half of neck thickness D are

$$R = \frac{y}{\cos(\nu+\alpha)}, \qquad d = R\big(1-\sin(\nu+\alpha)\big),$$
$$D = x - d. \tag{A.2}$$

Then the area of the bridge is

$$A = A(\alpha, H, \nu) = 4(A_1 - A_2 - A_3), \tag{A.3}$$

where

$$A_1 = xy, \qquad A_2 = \frac{r^2}{4}(2\alpha - \sin 2\alpha),$$

$$A_3 = \frac{R^2}{4}(2\beta - \sin 2\beta), \tag{A.4}$$

and $\beta = \pi/2 - \nu - \alpha$ is the half-spanning angle of the meniscus. Finally, the capillary force is calculated from

$$\frac{F}{\gamma} = 2\cos(\pi/2 - \alpha - \nu) + \frac{2x}{R} = 2 + \frac{2D}{R}. \tag{A.5}$$

In Eq. (A.5), the terms on the right-hand side are the contributions of the surface tension and the pressure difference due to curved liquid–gas interface, respectively. Also it can be seen that the magnitude of the capillary force does not depend on the particle radius r.

References

[1] S. Herminghaus, Adv. Phys. 54 (2005) 221.
[2] S.J.R. Simons, in: A.D. Salman, M.J. Hounslow, J.P.K. Seville (Eds.), Handbook of Powder Technology: Granulation, vol. 11, Elsevier, Amsterdam, 2007, p. 1257.
[3] P. Pierrat, H.S. Caram, Powder Technol. 91 (1997) 83.
[4] H. Schubert, Powder Technol. 11 (1975) 107.
[5] H. Schubert, W. Herrmann, H. Rumpf, Powder Technol. 11 (1975) 121.
[6] N. Mitarai, F. Nori, Adv. Phys. 55 (2006) 1.
[7] N. Lu, B.L. Wu, C.P. Tan, J. Geotech. Geoenviron. Eng. 133 (2007) 144.
[8] Z. Fournier, D. Geromichalos, S. Herminghaus, M.M. Kohonen, F. Mugele, M. Scheel, M. Schulz, B. Schulz, Ch. Schier, R. Seemann, A. Skudelny, J. Phys. Condens. Matter 17 (2005) S477.
[9] T. Gröger, U. Tüzün, D.M. Heyes, Powder Technol. 133 (2003) 203.
[10] V. Richefeu, M.S. El Youssoufi, F. Radjaï, Phys. Rev. E 73 (2006) 051304.
[11] F. Soulie, F. Cherblanc, M.S. El Youssoufi, C. Saix, Int. J. Numer. Anal. Meth. Geomech. 30 (2006) 213.
[12] Z. Grof, C.J. Lawrence, F. Štěpánek, Granul. Matter (2007), doi:10.1007/s10035-007-0071-1.
[13] M.E.D. Urso, C.J. Lawrence, M.J. Adams, J. Colloid Interface Sci. 220 (1999) 42.
[14] C.D. Willett, M.J. Adams, S.A. Johnson, J.P.K. Seville, Langmuir 16 (2000) 9396.
[15] M.E.D. Urso, C.J. Lawrence, M.J. Adams, Chem. Eng. Sci. 57 (2002) 677.
[16] G. Mason, W.C. Clark, Chem. Eng. Sci. 20 (1965) 859.
[17] K. Murase, T. Mochida, H. Sugama, Granul. Matter 6 (2004) 111.

7.4 Pore-scale modelling and tomographic visualisation of drying in granular media

Martin Kohout
Zdeněk Grof
František Štěpánek

Published in the *J. Colloid Interf. Sci.*, Vol. 299, 2006, pp 342–351
DOI: 10.1016/j.jcis.2006.01.074.

Available online at www.sciencedirect.com
SCIENCE DIRECT®
Journal of Colloid and Interface Science 299 (2006) 342–351
JOURNAL OF Colloid and Interface Science
www.elsevier.com/locate/jcis

Pore-scale modelling and tomographic visualisation of drying in granular media

Martin Kohout, Zdeněk Grof, František Štěpánek *

Department of Chemical Engineering, Imperial College London, South Kensington Campus, London, SW7 2AZ, UK

Received 19 December 2005; accepted 31 January 2006
Available online 2 March 2006

Abstract

Spatio-temporal evolution of liquid phase clusters during drying of a granular medium (realised by random packing of cylindrical particles) has been investigated at the length-scale of individual pores. X-ray microtomography has been used to explicitly resolve the three-dimensional spatial distribution of the solid, liquid, and gas phases within the wet particle assemblies. The propagation of liquid menisci through the granular medium during drying was dynamically followed. The effect of contact angle on the degree of dispersion of the drying front has been studied by observing drying in a layer of untreated (hydrophilic) and silanised particles; the drying front was found to be sharper in the case of the silanised (less hydrophilic) particles. This observation was confirmed by direct numerical simulations of drying in a digitally encoded porous medium identical in structure to the experimental one. The simulations also revealed that the average gas–liquid interfacial area in a given porous microstructure strongly depends on the contact angle.
© 2006 Elsevier Inc. All rights reserved.

Keywords: Drying front; Porous media; Particle packing; Contact angle; Meniscus; Interfacial area; X-ray microtomography; Volume-of-fluid method

1. Introduction

Drying is a widely used industrial process, employed in applications such as isolation of particulate solids [1] or dewatering of foods and other bio-materials. Drying can be described on several length-scales [2], as shown in Fig. 1. At the process unit length-scale, aggregate quantities such as the total heat transfer rate into a process vessel and the total moisture removal rate are of interest. At the so-called effective medium length-scale, spatial distribution of moisture content and temperature within the material are resolved. Finally, details of the wet material microstructure (packed bed of particles, porous solid, etc.) and the morphology of liquid menisci within the individual pores are revealed at the pore space length-scale.

Mathematical modelling of drying at the effective medium length-scale involves the solution of volume-averaged transport equations—the Fourier's law for heat conduction, the Fick's law for diffusion, and the Darcy's law for fluid flow [3,4]. Knowledge of the dependence of effective transport coefficients (effective thermal conductivity, effective vapour-phase diffusivity, and liquid-phase permeability) on the microstructure and the moisture content of the porous medium is required as input information [5] and can be obtained by simulations at the pore space length-scale [6,7]. Published models of drying at the pore space length-scale have traditionally been based on approximating the porous microstructure by a two- or three-dimensional capillary network and the solution of vapour diffusion and capillary flow problems on that network [8–10]. This approach is methodologically similar to that used for network-based modelling of imbibition phenomena in porous media [11]. Drying can be regarded as an invasion percolation phenomenon, and indeed drying fronts with fractal structure have been shown to evolve [12,13].

An alternative approach to pore-scale modelling of drying is to construct "realistic" three-dimensional models of the porous medium, such as regular or random packings of spheres [14–16], and to determine liquid menisci configuration in the structural model either analytically (if possible) or numerically [17]. The objective of the present work is to take this

* Corresponding author. Fax: +44 20 7594 5604.
E-mail address: f.stepanek@imperial.ac.uk (F. Štěpánek).

0021-9797/$ – see front matter © 2006 Elsevier Inc. All rights reserved.
doi:10.1016/j.jcis.2006.01.074

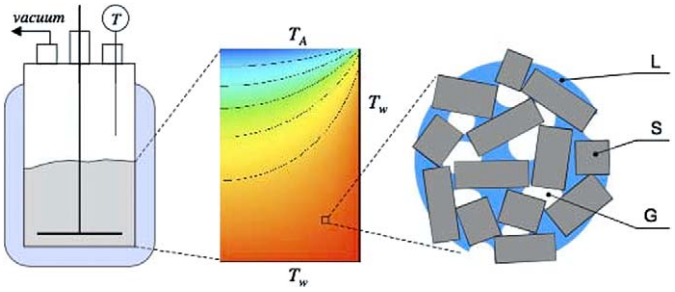

Fig. 1. Hierarchy of length-scales at which drying processes can be described: unit operation length-scale (left), effective medium length-scale (middle), and pore space length-scale (right).

approach one step further and perform numerical simulation of liquid menisci propagation through digitally encoded porous structures [18] obtained by X-ray microtomography and therefore identical to a physical granular medium in which drying experiments have been carried out. The numerical procedure is based on the volume-of-fluid (VOF) method which has been used in the past for the simulation of other processes involving liquid interface propagation in spatially complex structures, such as capillary condensation [19], bubble nucleation in porous media [20], or coating of rough particle surfaces [21].

Experimental techniques suitable for non-invasive monitoring of fluid-phase profiles in porous media include laser-induced fluorescence [22], magnetic resonance imaging [23–27], and X-ray computed tomography [28,29]. The latter two have been used for the visualisation of drying phenomena at the effective medium length-scale. While information about moisture distribution in the bulk material was obtained, neither the microstructure of the porous medium nor the individual liquid menisci within the pores were explicitly resolved. The objective of the present work is to use X-ray microtomography to visualise individual liquid–vapour interfaces within the pores, and to compare the experimental liquid-phase morphologies with those obtained numerically in identical microstructures. Furthermore, the effect of particle surface wettability on the shape of the drying front will be investigated.

2. Materials and methods

2.1. Drying experiments set-up

For the observation of the drying process, the system of water and cylindrical alumina extrudates (Criterion Catalysts and Technologies, USA) with the diameter 1 mm and the length 3–4 mm has been chosen. In order to change the wetting properties of the extrudate particles from hydrophilic to neutral, they have been impregnated in a 5% solution of dichlorodimethylsilane in trichloroethylene according to a procedure described in [30]. The reaction taking place at the surface of alumina is the condensation of the dichlorodimethylsilane with the surface hydroxyl groups. Both the untreated (hydrophilic) and the silanised (neutral) particles have been then used in the drying experiments.

The sample of extrudates was placed into a cylindrical plastic container with the diameter 12 mm, forming a packed bed of particles of the height approximately 10 mm. The sample was completely saturated by water. During the drying stage the container was placed inside a heated vessel and kept either at 150 mbar or (for certain experiments) at atmospheric pressure for a period of time varying from 15 to 30 min. Heat inflow to the sample occurred by conduction through the bottom of the container, which was kept at a constant temperature of 65 °C.

At the end of each drying step, the sample was weighted determining the amount of water evaporated during this step. The container was then closed and the geometry of the liquid and the solid phase of the sample was analysed by an X-ray microtomography scanner, as will be described in Section 2.2. Even if great care was taken during the manipulation with the container in order to minimise the movement of the solid phase due to small shakes, it was not possible to completely avoid small dislocations of particles between scans. The dislocations became more pronounced near the end of experiment when the liquid content was very low and the cohesive forces of capillary liquid bridges between particles disappeared.

2.2. Tomography scanning and image processing

A portable X-ray microtomography instrument Skyscan 1074HR (SkyScan, Belgium) equipped with 40 kV, 1 mA X-ray tube and a 768 × 576 pixels X-ray camera with pixel size of 22 μm [31] has been used. The volume of the sample which can be analysed is about 1 cm^3. The principle of X-ray microtomography is illustrated in Fig. 2a. The sample is placed between the X-ray source and the detector. The X-rays are attenuated as they pass through the sample, the extent of this attenuation is proportional to the local density, creating a transmission image (cf. Fig. 2b). The sample is placed on a rotation holder and transmission images obtained from different angles are used for the reconstruction of a three-dimensional map of the attenuation coefficient within the sample [32]. An example of a section of the 3D image obtained by the scanner is shown in Fig. 3a.

Frequency distributions (histograms) of the attenuation coefficient for two experiments are shown in Figs. 4a and 4b. Each curve in these graphs represents one scan; between two consecutive scans the sample was subjected to drying stage as described in Section 2.1. The attenuation coefficient is proportional to the density of the material: the first peak from the right in Fig. 4 represents the solid phase, the second peak from the right is the liquid phase (this peak is disappearing as the content of water in the sample decreases during drying), finally, the two remaining peaks at the left are for the wall of the plastic container and for the gas phase, respectively.

To continue the analysis of the geometry of the sample after scanning, it is necessary to segment the image, i.e., to separate the solid, liquid and gas phases. Two threshold values of the attenuation coefficient were found: a_1 at the local minimum of the frequency distribution between peaks for a container wall and the liquid (i.e., $a_1 \approx 0.14$ in Fig. 4a) and a_2 at the minimum between liquid and solid phase peaks (i.e., $a_2 \approx 0.4$ in Fig. 4a). The solid, the liquid and the gas phases are then distinguished as follows: (i) voxels with the attenuation coefficient lower than a_1 are assigned to the gas phase, (ii) voxels with

the attenuation coefficient between a_1 and a_2 are assigned to the liquid phase, and finally, (iii) the remaining voxels with the attenuation coefficient higher than a_2 are assigned to the solid phase. The result of the thresholding applied to image in Fig. 3a is shown in Fig. 3b.

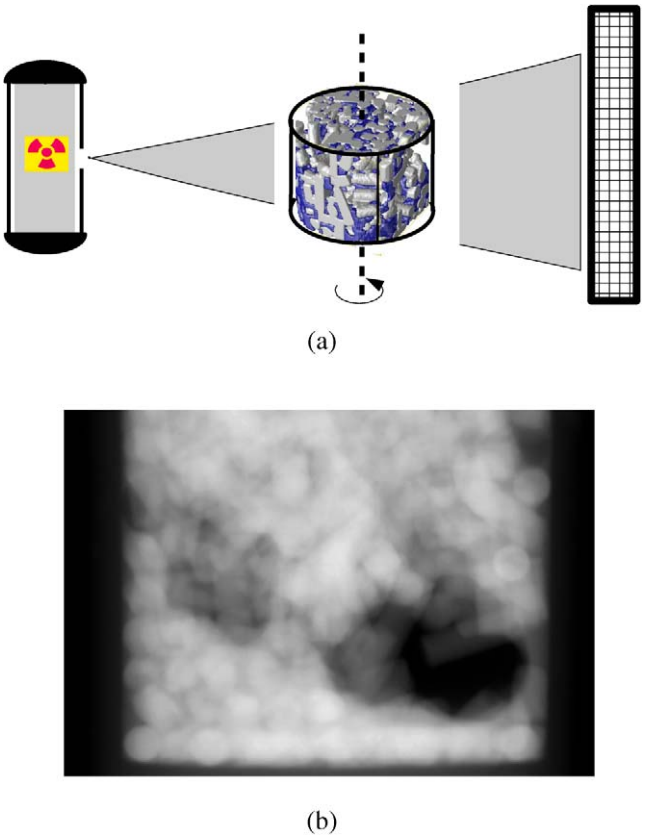

Fig. 2. Illustration of the principles of the tomography analysis: (a) set-up of the microtomography scanner, (b) example of a transmission image.

To ensure the feasibility of calculations the size of the system was subsequently reduced. Only a part of the sample was selected and used as the input for the simulations (cf. black rectangle in Fig. 3b). The image also needs to be filtered in order to remove the thin artificial layer of liquid at the solid–gas interface which can be seen in Fig. 3c. This artifact appears even in the completely dry sample and is caused by the application of the segmentation algorithm (there is a gradual transition between the solid and gas attenuation coefficient). Unfortunately, it is then not possible to detect the genuine liquid layer thinner than the feature resolution of the scanner, i.e., approximately 50–80 μm in this case. The filtration algorithm used in order to remove the artificial liquid layer can be described as follows: (i) Morphological closing and opening operations were performed independently on both the solid and the liquid phases. (ii) Voxels which were occasionally assigned to both the liquid and the solid phases were assigned to be part of solid phase only. (iii) Gas phase was identified as the complement of the liquid and solid phases. The image at this stage of the filtration is shown in Fig. 3d. (iv) Morphological opening and closing operations were performed on the gas phase in order to identify the gas voxels which possibly may form artificial gas gaps at the liquid–solid interface. These gas voxels which at the same time had a liquid voxel neighbour were changed to liquid. The final result of the filtration algorithm is shown in Fig. 3e.

2.3. Computational

The spatial distribution of the solid (S), liquid (L), and gas (G) phase was encoded on a unit cell consisting of a cubic

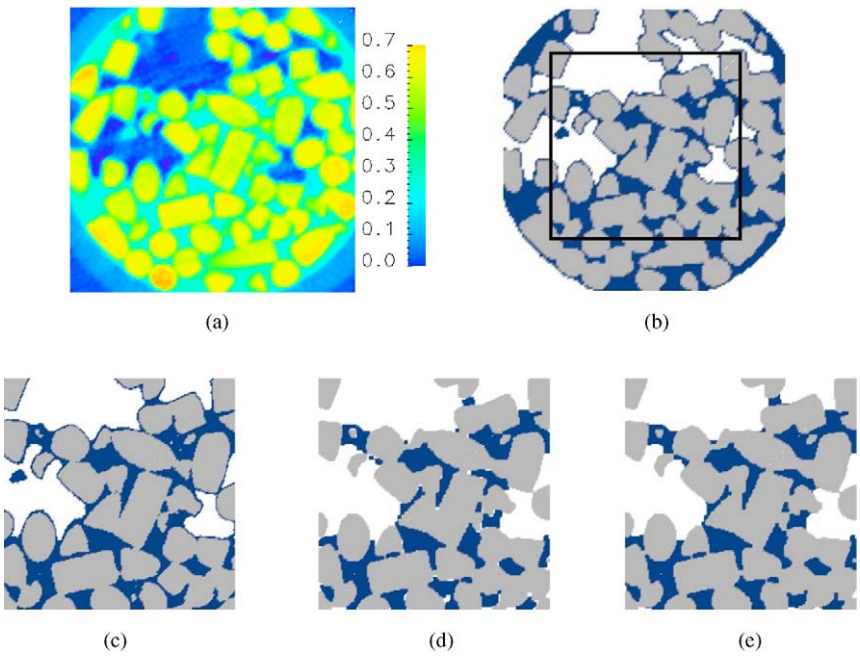

Fig. 3. Processing of the output from the tomography scanner: (a) section of the attenuation coefficient image; (b) identification of the solid and the liquid phases (rectangle shows the region of interest); (c) morphology of the sample before filtration; (d) intermediate result after applying steps i–iii of the filtration algorithm (see text); (e) final result of the filtration algorithm.

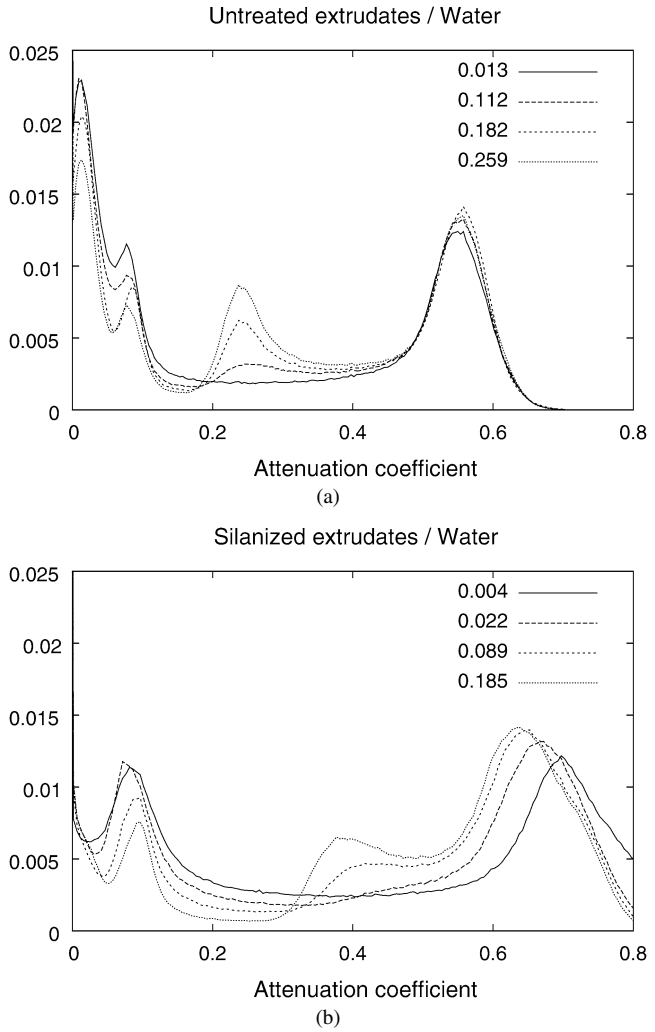

Fig. 4. Example of frequency distribution of the attenuation coefficient. The peaks in each panel correspond (from left to right) to the air, the wall of sample container, water and alumina extrudate particles. The curves are labelled by the liquid-phase volume fraction in the sample.

grid of $N_x \times N_y \times N_z$ volume elements (voxels) of size h. The phase volume functions, $f_k(\mathbf{r}, t)$, defined as the volume fraction of each voxel occupied by phase $k \in \{S, L, G\}$, were specified on the grid; here $\mathbf{r} = [x, y, z]$ denotes the spatial coordinate of the voxel and t is simulation time. The solid phase was assumed to be static throughout the simulation, and the gas phase volume fraction can be calculated from the binding condition $f_S + f_L + f_G = 1$. Therefore the only phase function whose spatio-temporal evolution needs to be tracked is the liquid-phase one, f_L. The simulation proceeds by specifying an initial liquid-phase distribution, $f_L(\mathbf{r}, t_0)$, and then evolving the liquid-phase volume function in all liquid–vapour interface points according to

$$\frac{\partial f_L(\mathbf{r})}{\partial t} = -\frac{1}{h}\frac{\dot{m}_{\mathrm{LG}}(\mathbf{r}, t)}{\rho_L} \tag{1}$$

where $\dot{m}_{\mathrm{LG}}$ is the mass evaporation rate per unit of liquid–vapour interface area. In the general case $\dot{m}_{\mathrm{LG}}$ would be a function of both space and time and depend on the heat and mass transfer rates at the effective medium length-scale, at a point represented by the unit cell [4]. In the pore-scale simulation at steady state (constant-rate period of drying), $\dot{m}_{\mathrm{LG}}$ is a constant.

In between each time advancement step of Eq. (1), the liquid–vapour interfaces are allowed to relax to a position satisfying the condition of constant mean curvature of all menisci belonging to the same liquid-phase cluster, and contact angles at all three-phase contact lines being equal to the equilibrium contact angle, θ_{eq}. During this relaxation, which corresponds to liquid-phase redistribution due to capillary forces, the phase volume functions are updated iteratively according to

$$\frac{\partial f_L(\mathbf{r})}{\partial \tau} = \begin{cases} \alpha[\kappa(\mathbf{r}) - \bar{\kappa}], & \forall \mathbf{r} \in \Omega_2, \\ \beta[\cos\theta_{\mathrm{eq}} - \cos\theta(\mathbf{r})], & \forall \mathbf{r} \in \Omega_3, \end{cases} \tag{2}$$

where τ is pseudo-time, α and β are numerical parameters determining the speed and stability of the relaxation, Ω_2 and Ω_3 are the sets of two- and three-phase points in the unit cell, respectively. The interface relaxation is stopped when $\max \|\partial f_L(\mathbf{r})/\partial\tau\| < \epsilon$, where ϵ is a chosen error tolerance. It should be noted that while Eq. (1) represents the dynamics of drying, Eq. (2) is a geometrical scheme only, i.e., the simulation time t is not advanced during the iterative evolution of f_L due to Eq. (2).

The local contact angle $\theta(\mathbf{r})$ and interface curvature $\kappa(\mathbf{r})$ appearing in Eq. (2) are calculated from their geometrical definitions, i.e.,

$$\cos\theta = \mathbf{n}_S \cdot \mathbf{n}_L \tag{3}$$

and

$$\kappa = -\nabla \cdot \mathbf{n}_L. \tag{4}$$

The solid and liquid interface normal vectors are calculated from the corresponding phase volume functions according to

$$\mathbf{n}_k = -\frac{\nabla \tilde{f}_k}{\|\nabla \tilde{f}_k\|}, \quad k \in L, S, \tag{5}$$

where $\tilde{f}_k$ is a smoothed phase volume function obtained from f_k by the application of the "1-6-1" kernel and renormalisation.

The numerical integration of Eq. (1) produces three-dimensional spatio-temporal profiles of liquid phase volume function in the unit cell. These can be either used for direct visualisation by 3D rendering or further processed by evaluating integral characteristics. We will use in particular the xy-averaged relative liquid-phase volume fraction, defined by

$$x_L(z, t) = \frac{\sum f_L(z, t)}{\sum(1 - f_S(z))}, \tag{6}$$

where the sums are over all voxels within an x–y plane with given z coordinate. The profiles $x_L(z/Z)$ where $Z = N_z h$ is the vertical dimension of the unit cell will be used to study the propagation of the drying front through the unit cell. The position and shape of the drying front will be expressed by the quantiles z_{10}, z_{50}, and z_{90}, defined as z coordinates such that 10, 50 and 90% of the overall liquid phase volume, respectively, is contained below this z coordinate. Finally, we will follow the

dimensionless gas–liquid interfacial area, defined as

$$A_{\mathrm{rel}} = \frac{\sum_{\mathbf{r}\in\Omega_2}(1 - f_S(\mathbf{r}))}{\epsilon N_x N_y}, \tag{7}$$

where ϵ is the void fraction of the unit cell, i.e., $\epsilon = \sum(1 - f_s(\mathbf{r}))/(N_x N_y N_z)$. The sum in the numerator of Eq. (7) represents the total number of voxels containing a gas–liquid interface, while the denominator is the free cross-sectional area of the unit cell averaged over Z.

3. Results and discussion

The experimental and computer simulation results are presented as follows: first, a direct comparison between simulations and experiments is carried out for the case of untreated particles under two drying conditions—vacuum drying which has lead to the formation of a cavity in the particle layer and drying under atmospheric pressure in which case a compact particle layer has been retained. Drying in a layer of silanised particles is studied next both tomographically and by simulations. Finally, a computational study of the effect of contact angle on the shape of a drying front will be presented.

3.1. Drying of untreated particles

The solid-phase microstructure and the evolution of the liquid phase during drying of random packed layer of untreated (hydrophilic) particles at 150 mbar and 65 °C is shown in Fig. 5. The top row of Fig. 5 shows experimental data from X-ray microtomography, while simulation results using identical initial conditions (solid-phase microstructure and liquid-phase distribution) can be seen in the bottom row. The three sets of liquid-phase profiles always have the same total moisture content x_L. The solid phase is only shown for the initial conditions in order not to obscure the 3D view of the liquid phase in subsequent panels. Due to the application of vacuum, a cavity has formed in the packed layer of particles as can be seen in the left panel of Fig. 5. The solid phase volume fraction is equal to $x_S = 0.48$.

A direct visual comparison of the simulation and experimental results would suggest that the liquid phase is more dispersed in the experimental case. However, this is most likely an artifact of the spatial discretisation; to render the problem computationally feasible, the original spatial resolution of the experimental data (voxel size $h_{\mathrm{exp}} = 22$ μm, $N_x = N_y = 358$, $N_z = 442$) has been diluted by a factor of four for the simulation (hence $h_{\mathrm{sim}} = 88$ μm). This means that the liquid clusters below a certain size which are still visible in the experimental images cannot be seen in the simulation ones. The second noticeable difference between simulations and experiments is that the simulation unit cell contains several larger liquid-phase clusters near the cell boundaries (faces or edges) which do not evaporate. This is caused by the boundary conditions: while the pore space containing this liquid is connected to the surface in the actual packed bed from which the unit cell is a cut-out (cf. Fig. 3b), in the simulations all walls of the unit cell with the exception of the top one are considered impermeable.

A quantitative comparison between the experimental and simulation results can be made by considering the liquid-phase profiles in the z direction, as defined by Eq. (6). The evolution of these profiles is plotted in Fig. 6 for experiments (panel a) and simulations (panel b). Relatively good agreement between experiments and simulations can be seen. For further studies, however, the cavity which demonstrates itself as the "dip" in the middle section of the graphs in Fig. 6 is not a suitable feature. The cavity has been formed due to drying in vacuum. Therefore, the experiment with untreated particles has been repeated under atmospheric pressure—in that case, the packed particle layer remained compact ($x_S = 0.60$)

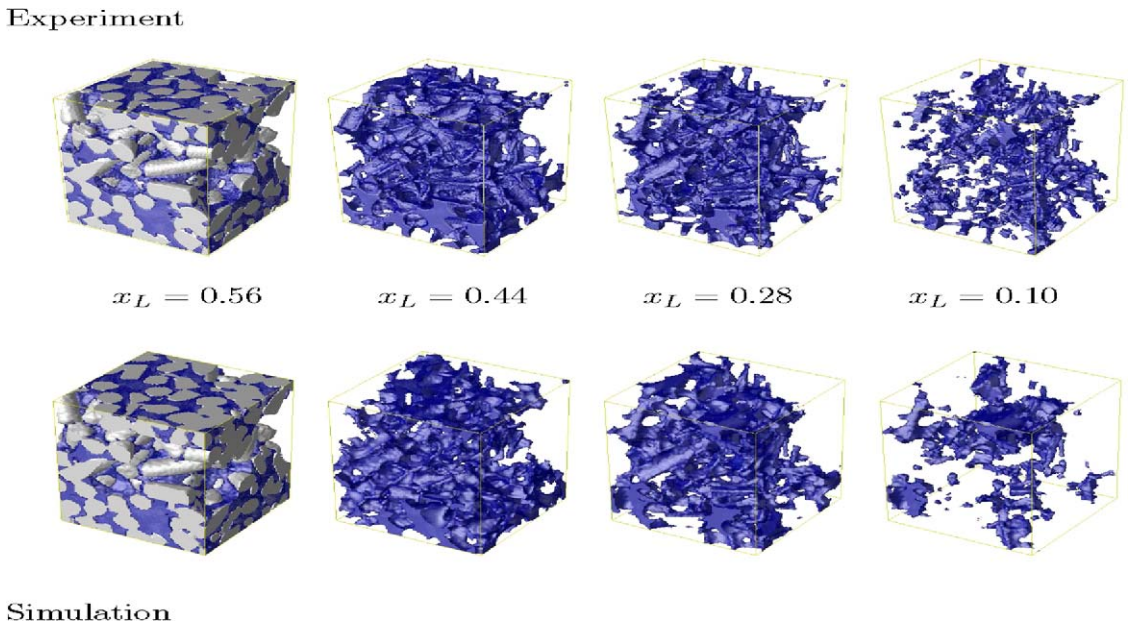

Fig. 5. Morphology of the packing of untreated particles dried in vacuum forming a microscopic cavity. Comparison of the experiment with the simulation. Only the liquid phase is shown in all columns except the first one for the purpose of better readability.

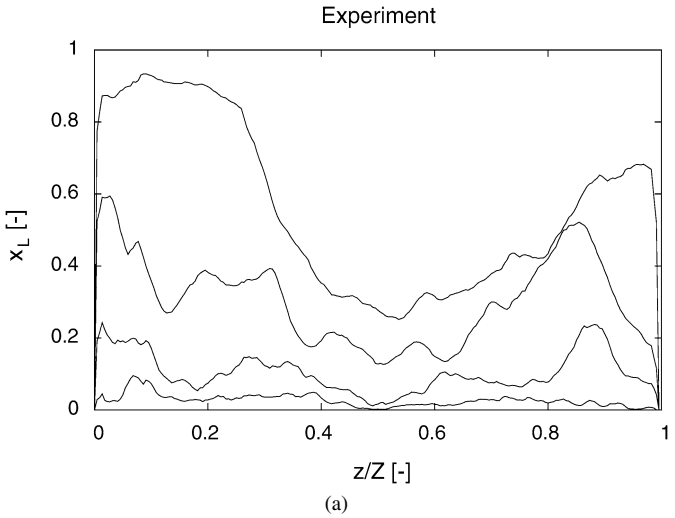

(a)

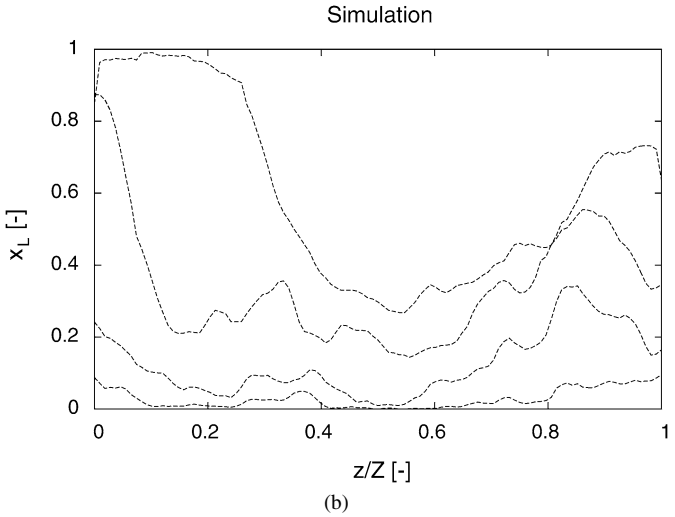

(b)

Fig. 6. Evolution of xy-averaged relative liquid-phase volume fraction during drying of a packed layer of untreated particles with a cavity at 150 mbar and 65 °C. (a) Experimental data; (b) simulation results.

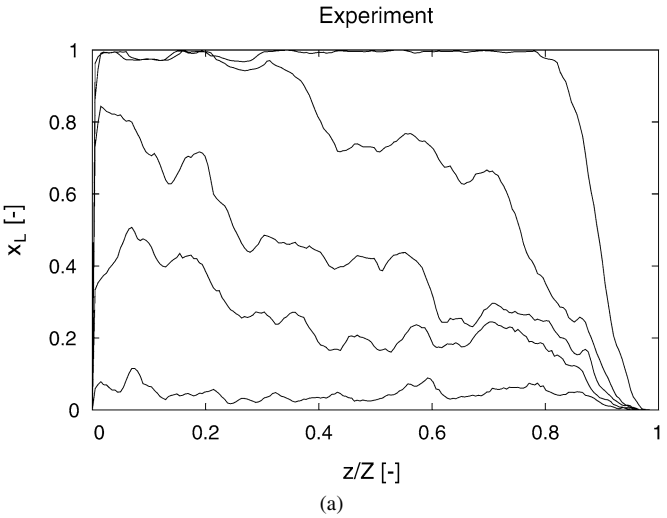

(a)

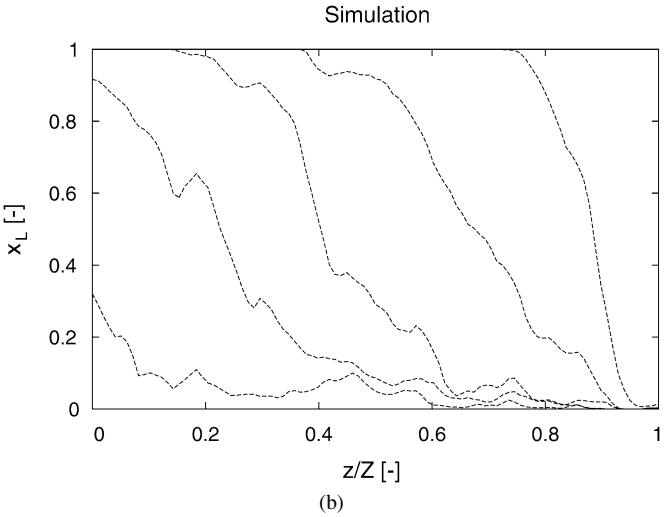

(b)

Fig. 7. Evolution of xy-averaged relative liquid-phase volume fraction during drying of a compact packed layer of untreated particles at atmospheric pressure. (a) Experimental data; (b) simulation results.

and a single drying front propagated from the top. Although the drying at atmospheric pressure was slower then under vacuum, the drying rate is not expected to have any significant effect on the liquid-phase distribution within the porous structure at any given x_L because in both cases the characteristic time of reaching equilibrium meniscus shape due to capillary forces is much shorter than that of meniscus motion due to evaporation. Moreover, even the samples dried under vacuum are exposed to atmospheric pressure during scanning.

A comparison between experimental and simulation liquid-phase profiles during drying at atmospheric pressure can be seen in Fig. 7. For brevity the three-dimensional images of this system are not shown. The simulations suggest the existence of a drying front which propagates from the top of the unit cell (i.e., from the right in Fig. 7b) and at the same time becomes more diffused. This trend can also be seen on the experimental profiles, however, the dispersion of the front is stronger than that seen in the simulations, to the extent that the drying "front" eventually spans the entire width of the region of interest. This difference between experiments and simulations may be caused by the spatial discretisation, i.e., the lack of the simulations to capture the capillary action of the smallest pores which are responsible for the retention of the liquid in otherwise dry upper sections of the particle packing. However, it should also be noted that the formation of a diffused drying front is characteristic of an invasion percolation process, whereby larger pores empty preferentially while small ones retain the liquid. This leads to the dispersion of the drying front as shown in [13,33]. Due to the relatively small size of our sample, the asymptotic width of a drying front that would develop in an infinite porous medium may be larger than our unit cell, hence the observed liquid phase profiles.

3.2. Drying of silanised particles

The dispersion of the drying front mentioned above is due to capillary forces which depend on the wettability of the solid phase, i.e., on the equilibrium contact angle. Capillary forces tend to pull the liquid from larger pores to small ones when

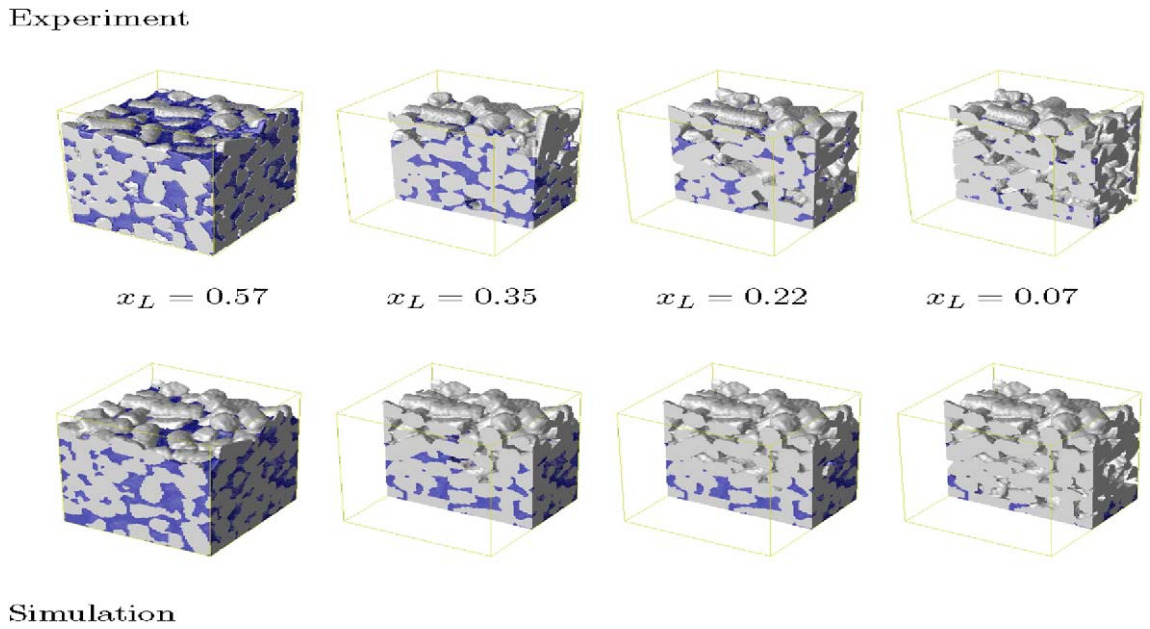

Fig. 8. Comparison of simulation and experimental liquid phase morphologies in a compact packing of silanised particles dried at 150 mbar and 65 °C.

the equilibrium contact angle is less than 90° (hydrophilic particles) and vice versa if $\theta_{eq} > 90°$. In order to realise a system where all morphological parameters of the random packed layer remain the same (particle size and shape) but the surface wettability is modified to increase the contact angle, the alumina particles were treated by silanisation as described in Section 2.1.

The evolution of the liquid phase in the close packed structure of silanised particles is shown in Fig. 8 both for experiments and simulations. Rather than showing only the liquid-phase profiles as was done in Fig. 5, sections including the solid phase are displayed in order to be able to compare liquid-phase morphology in exactly the same portions of the porous medium. The solid phase volume fraction in this case is equal to $x_S = 0.54$. The corresponding xy-averaged liquid phase profiles are plotted in Fig. 9. The contact angle used for the simulations was 60°; this value was chosen to give the best agreement (within ±10°) between simulated and measured liquid-phase profiles. The agreement between the profiles is indeed relatively good with the exception of the peak appearing in the middle of the sample in the later stage of the experiment. This peak may be due to local restructuring of the solid phase which causes the presence of un-evaporated liquid in the pore space—see panels corresponding to $x_L = 0.22$ in Fig. 8 which clearly shows that while evaporation occurs in the bottom part of the unit cell in the experimental system, the same portion of the pore space remains filled by liquid in the simulations. On the other hand, some liquid is retained in smaller pores in the upper sections of the experimental structure, while these pores are empty in the simulations. A possible explanation for this difference could either be non-uniform silanisation of the particles, i.e., the existence of more hydrophilic regions in the experimental structure that tend to retain the liquid phase. Another possible effect is that liquid-phase clusters that appear to be isolated in the simulation do in fact percolate in the physical system, however, the connecting path lies outside of the boundaries of the unit cell.

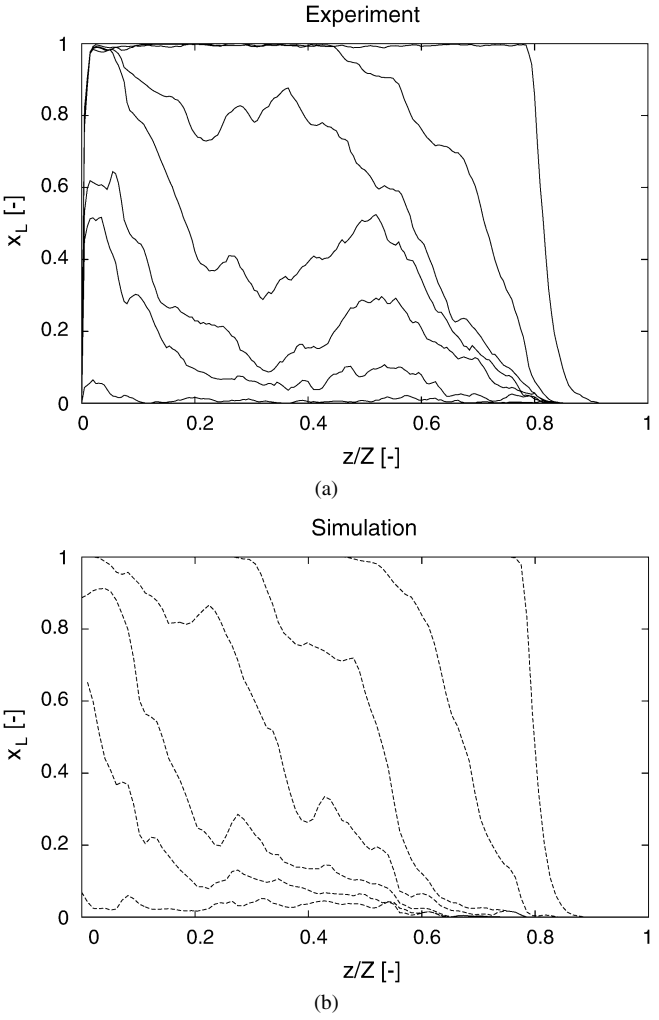

Fig. 9. Evolution of xy-averaged relative liquid-phase volume fraction during drying of a packed layer of silanised particles at 150 mbar and 65 °C. (a) Experimental data; (b) simulation results.

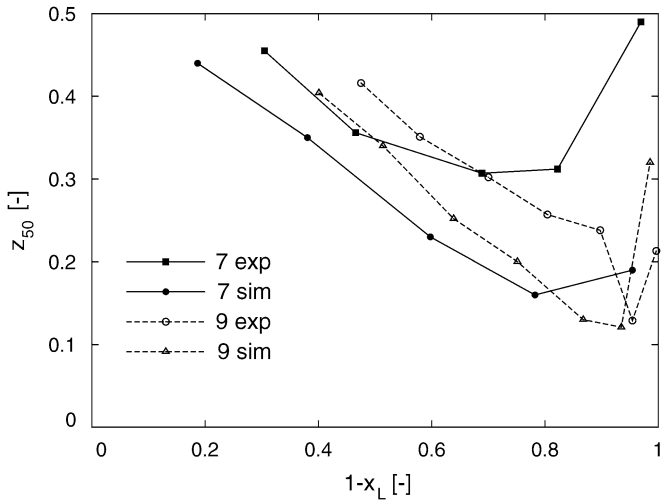

Fig. 10. Direct comparison of the evolution of drying front position expressed by z_{50} (see text for definition) for the experimental and simulation fronts shown in Figs. 7 and 9. The legend refers to the source figure.

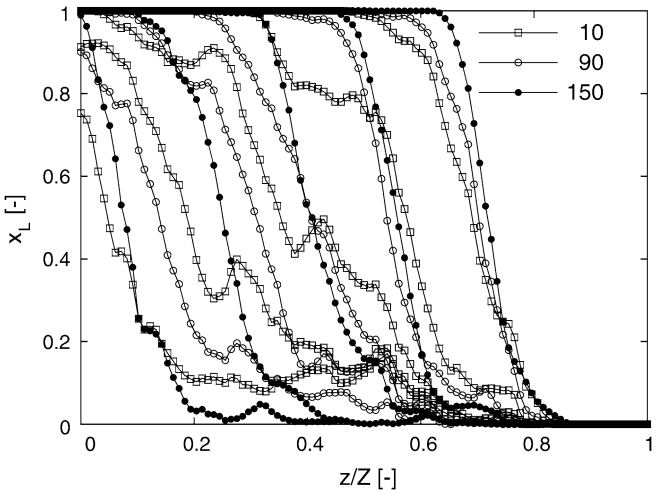

Fig. 11. Shape and position of the drying front at five values of overall moisture content $x_L = 0.75, 0.62, 0.51, 0.39, 0.26$ (from right to left) for three different equilibrium contact angles as indicated in the legend).

Figs. 7 and 9 allow qualitative comparison of the experimental and simulation profiles. In order to assess the accuracy of the simulations also quantitatively, let us compare the average front positions, z_{50}, as function of the relative liquid phase volume fraction, x_L, for each case. This comparison is shown in Fig. 10. It can be seen that the agreement between simulations and experiments in the case of silanised particles (Fig. 9) is better.

Compared with the untreated particles (cf. Fig. 7), the drying front in the silanised particles appears to be sharper both in the experimental and the computational graphs. In order to investigate the effect of contact angle on the degree of dispersion of the drying front more systematically, a computational parametric study has been performed and will be discussed in the following section.

3.3. *Effect of contact angle on drying front*

Using identical solid-phase microstructure as in Section 3.2, the effect of contact angle on the spatial distribution of the liquid phase in the granular medium during drying was investigated computationally. Four values of the equilibrium contact angle have been considered, namely $\theta_{eq} = 10, 60, 90$, and $150°$. The initial conditions as well as the evaporation rate $\dot{m}_{LG}$ appearing in Eq. (1) were kept constant. The temporal evolution of relative liquid-phase volume fraction profiles in the z direction is plotted in Fig. 11 for three of the four cases. It is possible to see that while the drying front for $\theta_{eq} = 150°$ tends to attain an asymptotic shape and remains relatively sharp, as the equilibrium contact angle decreases (i.e., the particles become more hydrophilic), the drying front becomes more diffused. In the case of $\theta_{eq} = 10°$, the drying front seems to span across almost the entire unit cell.

In order to compare the "sharpness" of the drying front in each of the four cases in a more quantitative way, the quantities z_{10}, z_{50}, and z_{90} that were defined following Eq. (6), are plotted in Fig. 12. First, let us note that the drying front velocity, which is expressed by the slope of the z_{50} line, is identical in

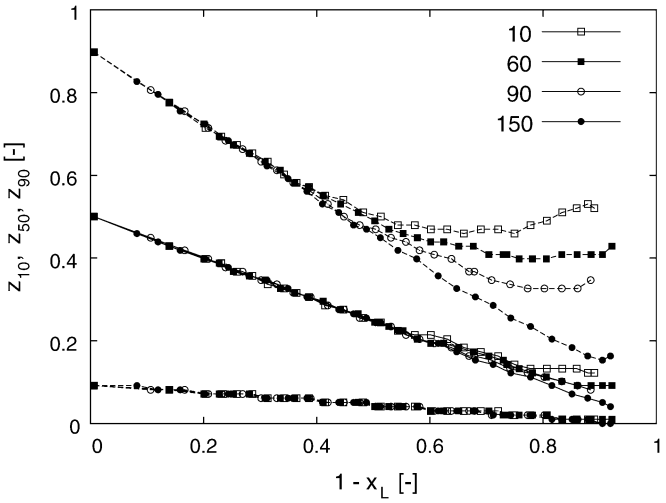

Fig. 12. Effect of contact angle on the propagation of drying front; z_{50} is a measure of the front position, the spread between z_{90} and z_{10} is a measure of the front sharpness (see text for exact definitions).

all four cases—as it should be since $\dot{m}_{LG}$ was the same. However, the width of the drying front, which can be defined as the difference between z_{90} and z_{10}, progressively increases with increasing hydrophilic character of the particles (lower values of θ_{eq}). Initially (large values of x_L), the difference between the four cases is not noticeable, but as we move to lover moisture contents and the drying front has had a chance to develop, the differences become clearly apparent. The eventual increase in z_{90} as $x_L \to 0$ is caused by the fact that as more liquid in the bottom part of the unit cell dries out, one actually has to sample a larger proportion of the unit cell in order to cover 90% of the liquid.

The reason why the drying front is more diffused in the case of more hydrophilic particles is the capillary rise—i.e., the tendency of the small pores to pull liquid from the large ones, which therefore appear to be evaporating faster. This situation is shown on a cross section of a particle layer with contact angle

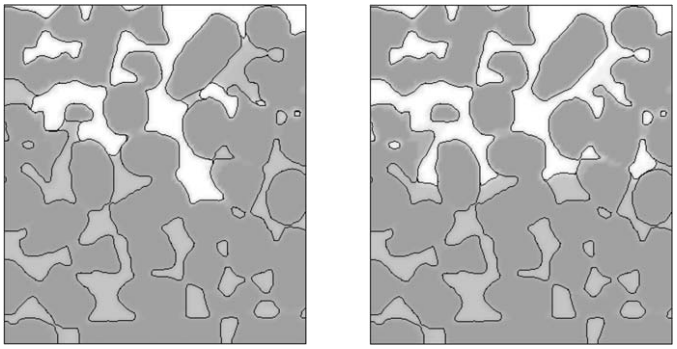

(a) (b)

Fig. 13. Cross sections of the particle layer showing the difference in liquid-phase distribution in (a) hydrophilic ($\theta_{eq} = 10°$) and (b) hydrophobic ($\theta_{eq} = 150°$) cases—simulation results.

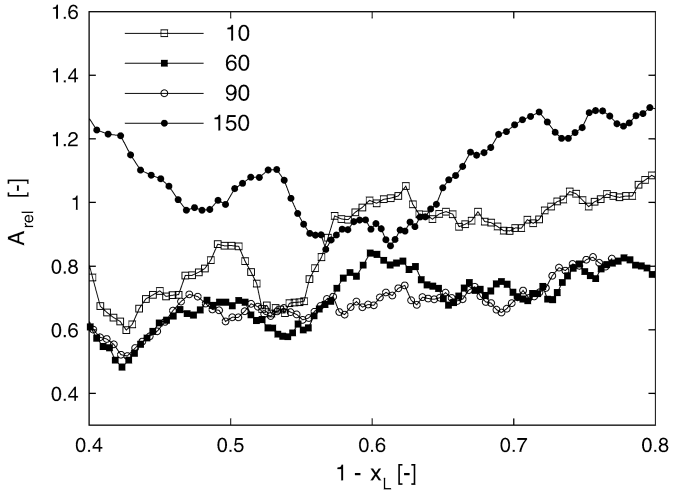

Fig. 14. Effect of contact angle on the evolution of gas–liquid interfacial area during drying (simulation results).

$\theta_{eq} = 10°$ in Fig. 13a where characteristic U-shaped menisci are clearly visible. In contrast, Fig. 13b shows a cross section of the same solid microstructure with the same overall liquid content x_L, but for a contact angle of $\theta_{eq} = 150°$. All the liquid menisci appear to be more-or-less at the same height as implied by the sharp front seen in Fig. 11.

Finally, let us investigate the evolution of the gas–liquid interfacial area in the unit cell during drying. A plot of the relative interfacial area defined by Eq. (7) as function of the gas-phase relative volume fraction in the unit cell is shown in Fig. 14, again for four different values of the equilibrium contact angle. Interesting—and perhaps initially not entirely intuitive—trends can be seen: notice that the interfacial area in the case of $\theta_{eq} = 150°$ is systematically higher than in any of the other cases in the initial stages of drying. This can be explained by the preferential evaporation from larger pores in the hydrophilic cases; the remaining liquid is then located in pores with narrow "necks," therefore having smaller interfacial area with the gas phase.

Otherwise both low (10°) and high (150°) values of contact angle lead to higher interfacial area then the intermediate (60° and 90°) values. This is because both low and high contact angles cause the formation of curved menisci as opposed to flat liquid interface in the intermediate wettability cases. The apparent fluctuations in A_{rel} which can be seen in Fig. 14 are due to the randomness of the solid microstructure through which the drying front propagates. As the liquid–vapour interface moves through different regions of the particle packing, the interfacial area is affected by the local pore-space morphology and therefore fluctuates to some extent. This is in part caused by the relatively small cross section area of our sample—in a larger sample these fluctuations would be smoothed out. Fig. 14 also reveals that the interfacial area fluctuates much more in the extreme hydrophilic and extreme hydrophobic cases than in the intermediate cases where it remains practically constant. This can be explained by the fact that the propagating menisci are "copying" the shape of the pore space much more closely when the solid is either very hydrophilic or very hydrophobic than in the neutral case of 90° when flat liquid–gas interface moves through the porous medium without any influence of the solid phase.

4. Summary

X-ray microtomography was shown to be a powerful technique for the observation of dynamic processes with phase change in porous media—drying in this case. The ability to directly visualise the three-dimensional structure of both the solid and liquid phases gave the opportunity to "observe" capillary phenomena in complex porous microstructures and compare them with computer simulations. In this study the effect of particle surface wettability on the shape of drying front propagating through a random close packing of cylindrical particles during drying was investigated. It was shown that hydrophilic surfaces lead to relatively dispersed fronts due to strong interaction between the solid and the liquid menisci; on the other hand, sharp drying front tends to form in and around the neutral wetting case.

References

[1] R.B. Keey, Drying of Loose and Particulate Materials, Hemisphere Publishing, New York, 1992.
[2] M. Kohout, A.P. Collier, F. Štěpánek, in: A. Barbosa-Povoa, H. Matos (Eds.), Computer Aided Process Engineering, vol. 14, Elsevier, Amsterdam, 2004, p. 1075.
[3] S. Whitaker, The Method of Volume Averaging, Springer-Verlag, Heidelberg, 1999.
[4] M. Kohout, A.P. Collier, F. Štěpánek, Chem. Eng. Sci. (2006), in press.
[5] S.C. Nowicki, H.T. Davis, L.E. Scriven, Drying Technol. 10 (1992) 925.
[6] M. Kohout, A.P. Collier, F. Štěpánek, Int. J. Heat Mass Transfer 47 (2004) 5565.
[7] M. Kohout, A.P. Collier, F. Štěpánek, Powder Technol. 156 (2005) 120.
[8] Y. Le Bray, M. Prat, Int. J. Heat Mass Transfer 42 (1999) 4207.
[9] M. Prat, Chem. Eng. J. 86 (2002) 153.
[10] L.A. Segura, P.G. Toledo, Drying Technol. 23 (2005) 2007.
[11] D.W. Bousfield, G. Karles, J. Colloid Interface Sci. 270 (2004) 396.
[12] H.P. Huinink, L. Pel, M.A.J. Michels, Phys. Rev. E 68 (2003) 056114.
[13] A.G. Yiotis, A.K. Stubos, A.G. Boudouvis, I.N. Tsimpanogiannis, Y.C. Yortsos, Transp. Porous Media 58 (2005) 63.
[14] S. Bryant, A. Johnson, J. Colloid Interface Sci. 263 (2003) 572.
[15] M. Gladkikh, S. Bryant, J. Colloid Interface Sci. 288 (2005) 526.
[16] R.P. Mayer, R.A. Stowe, J. Colloid Interface Sci. 294 (2006) 139.

[17] F.M. Orr, R.A. Brown, L.E. Scriven, J. Colloid Interface Sci. 60 (1977) 137.
[18] P.M. Adler, Porous Media: Geometry and Transports, Butterworth–Heinemann, Boston, 1992.
[19] F. Štěpánek, M. Marek, P.M. Adler, AIChE J. 45 (1999) 1901.
[20] F. Štěpánek, M. Marek, P.M. Adler, Chem. Eng. Sci. 56 (2001) 467.
[21] F. Štěpánek, P. Rajniak, Langmuir 22 (2006) 917.
[22] M.M. Fontenot, R.D. Vigil, J. Colloid Interface Sci. 247 (2002) 481.
[23] G. Guillot, A. Trokiner, L. Darrasse, H. Saint-Jalmes, J. Phys. D Appl. Phys. 22 (1989) 1646.
[24] I.V. Koptyug, V.B. Fenelonov, L.Y. Khitrina, R.Z. Sagdeev, V.N. Parmon, J. Phys. Chem. B 102 (1998) 3090.
[25] I.V. Koptyug, S.I. Kabanikhin, K.T. Iskakov, V.B. Fenelonov, L.Y. Khitrina, R.Z. Sagdeev, V.N. Parmon, Chem. Eng. Sci. 55 (2000) 1559.
[26] M.P. Hollewand, L.F. Gladden, Magn. Reson. Imaging 12 (1994) 291.
[27] M.D. Mantle, N.C. Reis, R.F. Griffiths, L.F. Gladden, Magn. Reson. Imaging 21 (2003) 293.
[28] A. Léonard, S. Blacher, P. Marchot, J.-P. Pirard, M. Crine, J. Microsc. 212 (2003) 197.
[29] A. Léonard, S. Blacher, P. Marchot, J.-P. Pirard, M. Crine, Can. J. Chem. Eng. 83 (2005) 127.
[30] S.A.M. Al-Chalabi, A.R. Jones, P.F. Luckham, J. Aerosol. Sci. 21 (1990) 821.
[31] A. Sasov, D. van Dyck, J. Microsc. 191 (1998) 151.
[32] A.C. Kak, M. Slaney, Principles of Computerised Tomographic Imaging, IEEE Press, New York, 1988.
[33] I.N. Tsimpanogiannis, Y.C. Yortsos, S. Poulou, N. Kanellopoulos, A.K. Stubos, Phys. Rev. E 59 (1999) 4353.

8. ARTICLES ABOUT PARTICLE BREAKAGE

8.1 Multi-scale simulation of needle-shaped particle breakage under uniaxial compaction

Zdeněk Grof
Martin Kohout
František Štěpánek

Published in the *Chem. Eng. Sci.*, Vol 62, 2007, pp 1418–1429
DOI: 10.1016/j.ces.2006.11.033.

ELSEVIER

Chemical Engineering Science 62 (2007) 1418–1429

Chemical Engineering Science

www.elsevier.com/locate/ces

Multi-scale simulation of needle-shaped particle breakage under uniaxial compaction

Zdeněk Grof[a], Martin Kohout[b], František Štěpánek[a,*]

[a]*Department of Chemical Engineering, Imperial College London, South Kensington Campus, London SW7 2AZ, UK*
[b]*Department of Chemical Engineering, Institute of Chemical Technology, Technická 5, 166 28 Prague, Czech Republic*

Received 29 June 2006; received in revised form 17 October 2006; accepted 8 November 2006
Available online 22 November 2006

Abstract

The breakage of needle-shaped particles within a random packed bed subjected to uni-directional compaction has been simulated using the discrete element method (DEM). Elongated particles with a chosen aspect ratio have been created by linking individual spherical discrete elements by rigid bonds, characterized by a given ultimate bending strength. A randomly packed bed of these elongated particles has been formed and gradually compressed between two infinite parallel solid planes. The particle size distribution as function of the compaction ratio has been studied in dependence on the individual particle strength, the initial particle length, and their distribution. The simulations have shown that the fragmentation generally follows the sequential halving kinetics and that the formation of fines is most profound in systems with a distribution of particle strengths, both within and between individual particles.
© 2006 Elsevier Ltd. All rights reserved.

Keywords: DEM; Fragmentation; Compaction; Crushing; Mathematical modelling; Particle

1. Introduction

Many chemical products and intermediaries are manufactured in the form of crystals that, depending on the molecular properties of the particular compound, can have several internal structures (polymorphism) or external shapes (crystal habit). Although crystal habit can sometimes be controlled by the hydrodynamic conditions in the crystallizer or by the addition of a surface active compound that selectively hinders crystal growth along a particular facet, this is not always possible (specific chemistry) or desirable (contamination). Hence, one is often faced with the need to process crystals with large aspect ratio, either in one (needles) or two (flakes) directions. Such crystal shapes are specific in that "downstream" unit operations such as filtration, drying (Lekhal et al., 2004), or conveying (Salman et al., 2002) may lead to significant (and often uncontrolled) changes in particle size distribution (PSD) due to attrition and breakage. In order to be able to understand and eventually predict the effect of a given unit operation on the PSD, it is necessary to understand the response of a particle assembly to a well-defined stress field such as uni-axial compaction or shear. This knowledge combined with the distribution of stresses in a particular unit operation, obtained e.g., by means of a CFD simulation (Zumaeta et al., 2005), can then be used for the prediction of the overall effect of this unit operation on the PSD.

The objective of the present work is to demonstrate computational methodology for calculating the PSD as function of compaction ratio in a randomly packed bed of needle-shaped particles with specified initial size and intrinsic strength (either constant for all particles or following a given distribution) subjected to uni-axial compaction. We will first describe the computational methodology, based on the discrete element method (DEM), and then demonstrate its use in a computational parametric study of the effect of initial particle size, particle strength, and its distribution both within and between individual particles, on PSD under uni-axial compaction.

The DEM has been used in the past for the simulation of particle breakage due to impact (Thornton et al., 1999) or compaction (Golchert et al., 2004; Khanal et al., 2005) in the case of a single spherical agglomerate. However, for practical industrial applications, the behaviour of a bulk particle assembly

* Corresponding author. Tel.: +44 20 7594 5608; fax: +44 20 7594 5604.
E-mail address: f.stepanek@imperial.ac.uk (F. Štěpánek).

0009-2509/$ - see front matter © 2006 Elsevier Ltd. All rights reserved.
doi:10.1016/j.ces.2006.11.033

is mostly of interest (Kou et al., 2001). In situations where a distribution of properties (particle size, strength) is present, an extension from single-particle breakage to that of an entire population is not obvious because particle assembly (packing) effects are convoluted with single-particle effects (distribution of stresses within a particle). Such multi-scale problems can be addressed by direct numerical simulation, as presented in this work. Single-parameter sensitivity studies then make it possible to deconvolute the assembly- and particle-level phenomena, and help us to understand the role of particle size and strength distributions on breakage patterns.

2. Methodology

The method used in this work belongs to the class of discrete element models, which were pioneered by Cundall and Strack (1979). A multi-element particle model (Favier et al., 1999) is used for the representation of elongated particles, as illustrated in Fig. 1. Each particle consists of several spherical elements whose positions are fixed relative to positions of other elements within the particle. In the simulation, the state of each particle is characterized by the position of its centre of mass $\boldsymbol{X}_i$, the translational and the angular velocity $\boldsymbol{V}_i$ and $\boldsymbol{\omega}_i$, respectively, and the Euler angles ϕ_i, θ_i and ψ_i describing its orientation. The position $\boldsymbol{x}_j$, the velocity $\boldsymbol{v}_j$ and the angular velocity $\boldsymbol{\omega}_j$ of each spherical element j are derived directly from the state of the particle i they belong to

$$\boldsymbol{x}_j = \boldsymbol{X}_i + \boldsymbol{x}_j^d, \quad \boldsymbol{v}_j = \boldsymbol{V}_i + (\boldsymbol{\omega}_i \times \boldsymbol{x}_j^d), \quad \boldsymbol{\omega}_j = \boldsymbol{\omega}_i, \tag{1}$$

where $\boldsymbol{x}_j^d$ is the relative position of the element within the particle. (The angular velocity of the element j is the same as that of the whole particle i, thus, regarding the vector $\boldsymbol{\omega}$, no distinctive notation between the particle and the element has been used.)

The equations for translational movement of the ith particle are

$$\dot{\boldsymbol{X}}_i = \boldsymbol{V}_i, \quad \dot{\boldsymbol{V}}_i m_i^p = \boldsymbol{F}_i - \eta_t \boldsymbol{V}_i, \tag{2}$$

where $m_i^p = \sum_j m_j^e$ is the particle mass and $\boldsymbol{F}_i$ is sum of all forces acting on the ith particle. The rotation of the particle is governed by Euler equations for rigid body motion

$$\begin{aligned} I_{i,1}\dot{\omega}'_{i,1} &= M'_{i,1} + (I_{i,2} - I_{i,3})\omega'_{i,2}\omega'_{i,3} - \eta_r \omega'_{i,1}, \\ I_{i,2}\dot{\omega}'_{i,2} &= M'_{i,2} + (I_{i,3} - I_{i,1})\omega'_{i,3}\omega'_{i,1} - \eta_r \omega'_{i,2}, \\ I_{i,3}\dot{\omega}'_{i,3} &= M'_{i,3} + (I_{i,1} - I_{i,2})\omega'_{i,1}\omega'_{i,2} - \eta_r \omega'_{i,3}, \end{aligned} \tag{3}$$

where $I_{i,k}$ are the principal moments of inertia, $\omega'_{i,k}$ are components of the angular velocity and $M'_{i,k}$ are the components of the total moment on the ith particle. A global damping of the translational movement and the rotation of particles is used in order to allow the system to reach a stationary state, i.e., the kinetic energy is dissipated. The damping is controlled by the computational parameters η_t and η_r in Eqs. (2) and (3).

The axes of the coordinate system for components of vectors $\boldsymbol{M}$ and $\boldsymbol{\omega}$ in Eq. (3) are aligned with the principal axes of the inertia of the particle, i.e., the components M'_k and ω'_k are in particle local coordinates. The orientation of particle local coordinates with respect to the global coordinates is determined by the Euler angles. The components can be transformed between the particle local and global coordinate systems by a rotation matrix $\mathrm{R}_i(\phi_i, \theta_i, \psi_i)$ which is a function of the Euler angles

$$\mathrm{R}_i = \begin{bmatrix} \cos\psi_i \cos\phi_i - \cos\theta_i \sin\phi_i \sin\psi_i & \cos\psi_i \sin\phi_i + \cos\theta_i \cos\phi_i \sin\psi_i & \sin\psi_i \sin\theta_i \\ -\sin\psi_i \cos\phi_i - \cos\theta_i \sin\phi_i \cos\psi_i & -\sin\psi_i \sin\phi_i + \cos\theta_i \cos\phi_i \cos\psi_i & \cos\psi_i \sin\theta_i \\ \sin\theta_i \sin\phi_i & -\sin\theta_i \cos\phi_i & \cos\theta_i \end{bmatrix}. \tag{4}$$

Hence, the coordinate transformation is carried out in the following way:

$$c_j = R_{jk}^{\mathrm{T}} c'_k, \quad c'_j = R_{jk} c_k, \tag{5}$$

where c_j and c'_j are components of an arbitrary vector $\boldsymbol{c}$ written for global and local coordinate systems, respectively, and the superscript T denotes the matrix transpose. Finally, to complete the system of differential equations we need the relation between components of angular velocities and the time derivatives of Euler angles (Arya, 1990)

$$\begin{aligned} \dot{\phi}_i \sin\theta_i &= \omega'_{i,1} \sin\psi_i + \omega'_{i,2} \cos\psi_i, \\ \dot{\theta}_i &= \omega'_{i,1} \cos\psi_i - \omega'_{i,2} \sin\psi_i, \\ \dot{\psi}_i \sin\theta_i &= \omega'_{i,3} \sin\theta_i - \omega'_{i,1} \cos\theta_i \sin\psi_i \\ &\quad - \omega'_{i,2} \cos\theta_i \cos\psi_i. \end{aligned} \tag{6}$$

2.1. Calculation of forces between particles

The total force $\boldsymbol{F}_i$ on each individual particle and the total moment about its centre of mass $\boldsymbol{M}_i$ are calculated as a sum of forces and moments on its elements

$$\boldsymbol{F}_i = \sum_{j=1}^{N_i} \boldsymbol{f}_j, \quad \boldsymbol{M}_i = \sum_{j=1}^{N_i} [(\boldsymbol{x}_j^d \times \boldsymbol{f}_j) + \boldsymbol{m}_j], \tag{7}$$

where $\boldsymbol{f}_j$ and $\boldsymbol{m}_j$ are the total force and the total moment on element j, respectively; $\boldsymbol{x}_j^d = \boldsymbol{x}_j - \boldsymbol{X}_i$ is the relative position of

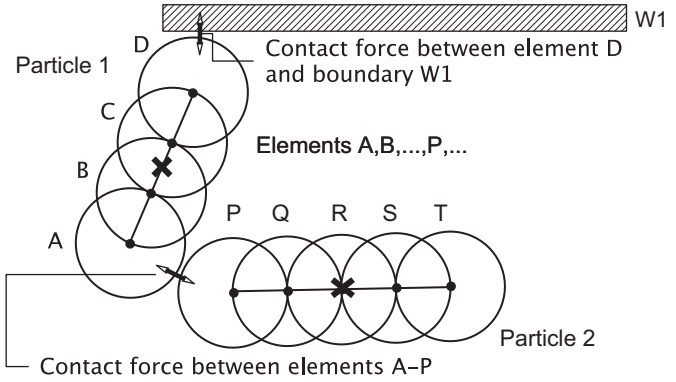

Fig. 1. Illustration of the multi-element particle model.

element j with respect to the centre of mass of the particle it belongs to and, finally, N_i is number of elements within the ith particle.

The total force $\boldsymbol{f}_j$ and the total moment $\boldsymbol{m}_j$ on individual element j is the result of: (i) normal and tangential contact forces with other elements, $\boldsymbol{f}^n_{jp}$ and $\boldsymbol{f}^t_{jp}$; (ii) normal and tangential contact forces with boundaries, $\boldsymbol{f}^n_{jw}$ and $\boldsymbol{f}^t_{jw}$; and (iii) the gravitational force

$$\boldsymbol{f}_j = \sum_p \boldsymbol{f}^n_{jp} + \sum_p \boldsymbol{f}^t_{jp} + \sum_w \boldsymbol{f}^n_{jw} + \sum_w \boldsymbol{f}^t_{jw} + m^e_j \boldsymbol{g},$$
$$\boldsymbol{m}_j = \sum_p \boldsymbol{m}^t_{jp} + \sum_w \boldsymbol{m}^t_{jw}. \tag{8}$$

In Eqs. (8) the sums run over all elements p or walls w which have a contact with the jth element. Let us note that the contact forces between elements belonging to the same particle are assumed to be zero as their relative positions are fixed.

In order to calculate the contact forces we use the linear spring model with a Coulomb-type friction slider for the tangential force (Cundall and Strack, 1979; Venugopal and Rajamani, 2001). Contact forces are described by three parameters; the normal and the tangential stiffness coefficients, E_n and E_t, and the friction angle α. Let us define the dimensionless distance e_{ap} and the unit distance vector $\boldsymbol{d}_{ap}$ between elements A and P

$$e_{ap} = \frac{|\boldsymbol{x}_p - \boldsymbol{x}_a|}{r_a + r_p}, \quad \boldsymbol{d}_{ap} = \frac{\boldsymbol{x}_p - \boldsymbol{x}_a}{|\boldsymbol{x}_p - \boldsymbol{x}_a|}, \tag{9}$$

where $|\boldsymbol{x}_p - \boldsymbol{x}_a|$ is the distance between centres of elements and r_a and r_p are the radii of the elements. Then the normal repulsive contact force between elements A and P acting on elements A and P, respectively, is

$$\boldsymbol{f}^n_{ap} = \begin{cases} E_n(e_{ap} - 1)\boldsymbol{d}_{ap} & \text{if } e_{ap} < 1, \\ 0 & \text{if } e_{ap} \geqslant 1, \end{cases} \quad \boldsymbol{f}^n_{pa} = -\boldsymbol{f}^n_{ap}. \tag{10}$$

Unlike the normal force, the friction (tangential) force $\boldsymbol{f}^t_{ap} = -\boldsymbol{f}^t_{pa}$ cannot be directly calculated from the actual position of elements but its value has to be saved for each contact pair and updated in the course of the simulation. At the beginning of each contact the friction force is set to zero. The tangential component of the velocity of the element P relative to element A is

$$\boldsymbol{v}^t_{ap} = \boldsymbol{v}_{ap} - (\boldsymbol{v}_{ap} \cdot \boldsymbol{d}_{ap})\boldsymbol{d}_{ap}, \quad \boldsymbol{v}_{ap} = \boldsymbol{v}_p - \boldsymbol{v}_a \tag{11}$$

and the shear velocity at the contact point is

$$\boldsymbol{v}^s_{ap} = \boldsymbol{v}^t_{ap} - r_a(\boldsymbol{\omega}_a \times \boldsymbol{d}_{ap}) - r_p(\boldsymbol{\omega}_p \times \boldsymbol{d}_{ap}). \tag{12}$$

Two operations have to be made in order to update the actual tangential force $\boldsymbol{f}^t_{ap}$ to a value which will be used in the next computation step, $\boldsymbol{f}^t_{ap}(t+\Delta t)$. In the first operation, the friction force changes according to the incremental shear displacement across the contact $\boldsymbol{v}^s_{ap}\Delta t$:

$$\boldsymbol{f}^*_{ap} = \boldsymbol{f}^t_{ap} + \frac{2E_t}{r_a + r_p}\boldsymbol{v}^s_{ap}\Delta t, \quad \max|\boldsymbol{f}^*_{ap}| = \tan\alpha|\boldsymbol{f}^n_{ap}|, \tag{13}$$

where Δt is the time step and $\boldsymbol{f}^*_{ap}$ is the intermediate value of the tangential force. If $|\boldsymbol{f}^*_{ap}|$ becomes larger than the maximum allowed friction force $\tan\alpha|\boldsymbol{f}^n_{ap}|$ then the magnitude of $\boldsymbol{f}^*_{ap}$ is reduced accordingly at this moment (Coulomb-type friction slider). If $\boldsymbol{v}^t_{ap} \neq \boldsymbol{0}$ then the contact normal is rotating as the elements A and P move. Therefore, in the second operation the vector $\boldsymbol{f}^*_{ap}$ is rotated in such a way that its direction remains perpendicular to the contact normal $\boldsymbol{d}_{ap}$ during the simulation. The rotation of the contact normal plane is described by the vector $\boldsymbol{\omega}_{ap}$

$$\boldsymbol{\omega}_{ap} = (1/|\boldsymbol{x}_p - \boldsymbol{x}_a|)\boldsymbol{d}_{ap} \times \boldsymbol{v}^t_{ap}. \tag{14}$$

An arbitrary vector $\boldsymbol{a}$ after rotation through angle β about an axis $\boldsymbol{n}$ becomes $\boldsymbol{a}'$ (Sayer and Bones, 1990)

$$\boldsymbol{a}' = (\cos\beta)\boldsymbol{a} + (1 - \cos\beta)(\boldsymbol{n} \cdot \boldsymbol{a})\boldsymbol{n} + (\sin\beta)\boldsymbol{n} \times \boldsymbol{a}. \tag{15}$$

One can substitute $\beta = |\boldsymbol{\omega}_{ap}|\Delta t$, $\boldsymbol{n} = \boldsymbol{\omega}_{ap}/|\boldsymbol{\omega}_{ap}|$ and $\boldsymbol{a} = \boldsymbol{f}^*_{ap}$ to the rotation formula Eq. (15). Note that the middle term of the RHS then becomes zero as vectors $\boldsymbol{f}^*_{ap}$ and $\boldsymbol{\omega}_{ap}$ are perpendicular to each other. The resulting formula for the updated tangential force $\boldsymbol{f}^t_{ap}(t + \Delta t)$ is therefore:

$$\boldsymbol{f}^t_{ap}(t + \Delta t) = \cos(|\boldsymbol{\omega}_{ap}|\Delta t)\boldsymbol{f}^*_{ap} + \sin(|\boldsymbol{\omega}_{ap}|\Delta t)\frac{\boldsymbol{\omega}_{ap}}{|\boldsymbol{\omega}_{ap}|} \times \boldsymbol{f}^*_{ap}. \tag{16}$$

If Δt is small Eq. (16) simplifies to

$$\boldsymbol{f}^t_{ap}(t + \Delta t) \doteq \boldsymbol{f}^*_{ap} + \Delta t\boldsymbol{\omega}_{ap} \times \boldsymbol{f}^*_{ap}. \tag{17}$$

The boundary walls are realized by solid planes with the unit normal vector $\boldsymbol{n}_w$ and position $\boldsymbol{x}_w$. The contact forces with the boundary walls are calculated in the same way as with elements, except that the dimensionless distance e_{aw} and unit distance vector $\boldsymbol{d}_{aw}$ between wall W and element A are defined by

$$e_{aw} = \frac{\boldsymbol{n}_w \cdot (\boldsymbol{x}_a - \boldsymbol{x}_w)}{r_a}, \quad \boldsymbol{d}_{aw} = -\boldsymbol{n}_w. \tag{18}$$

With this definition, the normal and friction contact forces on element A, $\boldsymbol{f}^n_{aw}$ and $\boldsymbol{f}^t_{aw}$, respectively, are calculated using Eqs. (10)–(16) where the subscript p is replaced by w; the last term in Eq. (12) is ignored; the term $2E_t/(r_a + r_p)$ in Eq. (13) is replaced by E_t/r_a; and $\boldsymbol{\omega}_{aw}$ is set to $\boldsymbol{0}$ in Eq. (14).

The moment on the particles A and P due to frictional force is

$$\boldsymbol{m}^t_{ap} = r_a\boldsymbol{d}_{ap} \times \boldsymbol{f}^t_{ap}, \quad \boldsymbol{m}^t_{pa} = \boldsymbol{m}^t_{ap}. \tag{19}$$

2.2. Algorithm of particle breakage

The movement of particles is modelled using the equations described above. If the boundary walls are static and the energy is dissipated by the global damping the particles will reach a static equilibrium. In order to determine whether the ith particle breaks it is necessary to calculate the internal loading within the particle. To do so, the method of section is used; a particle is imaginary cut by a plane passing through any of the non-end elements and perpendicular to the main particle axis—cf.

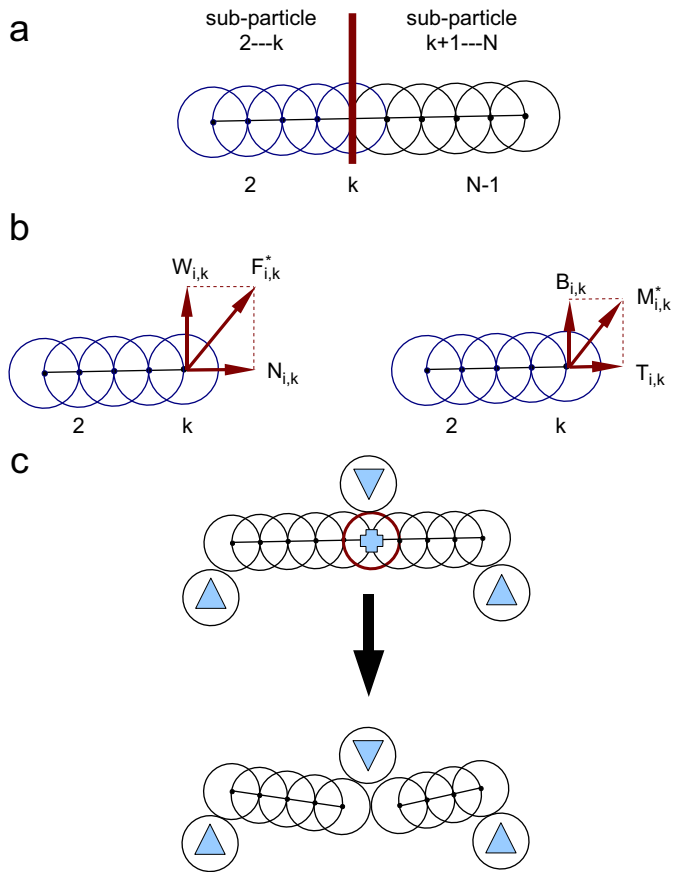

Fig. 2. Breakage of particles: (a) method of sections to calculate the particle internal loading; (b) decomposition of internal force and internal moment; (c) illustration of the breakage algorithm. If the stress at the position "+" exceeds a threshold value b the particle will break. The element marked by "+" is removed and the particle is divided into two.

Fig. 2a. This plane separates the particle into two sub-particles. In the static equilibrium, the total force and the total moment exerted on any sub-particle (and the whole particle as well) are zero. Therefore, the internal loading at this imaginary interface k between the sub-particles characterized by internal force $\boldsymbol{F}^*_{i,k}$ and moment $\boldsymbol{M}^*_{i,k}$ can be calculated from

$$\sum_{j=1}^{k} \boldsymbol{f}_j + \boldsymbol{F}^*_{i,k} = 0, \quad k = 2, \ldots, N_i - 1, \tag{20}$$

$$\sum_{j=1}^{k} ((\boldsymbol{r}_j - \boldsymbol{r}_k) \times \boldsymbol{f}_j + \boldsymbol{m}_j) + \boldsymbol{M}^*_{i,k} = 0, \quad k = 2, \ldots, N_i - 1, \tag{21}$$

where N_i is number of elements within the particle i. The internal loading calculated by Eqs. (20) and (21) is the actual force and moment holding the sub-particles together. They can be resolved into two components, one parallel and the other perpendicular to the main axis of the particle, cf. Fig. 2b,

$$\boldsymbol{F}^*_{i,k} = \boldsymbol{N}_{i,k} + \boldsymbol{W}_{i,k}, \quad \boldsymbol{M}^*_{i,k} = \boldsymbol{T}_{i,k} + \boldsymbol{B}_{i,k}, \tag{22}$$

where $\boldsymbol{N}$ and $\boldsymbol{W}$ are the normal (axial) and the shear force, respectively, $\boldsymbol{T}$ is the torsional moment and $\boldsymbol{B}$ is the bending moment. For the sake of simplicity, we do not consider the breakage of particles as a result of the axial loading or the torsion, leaving us with the bending as the only mechanism which can lead to breakage. Therefore, the particles are treated as loaded beams in order to calculate the maximum longitudinal (bending) stress σ and the maximum transverse (shear) stress τ along the particle. For a beam with circular cross-section of radius r the flexure and shear formulae (Hibbeler, 2005; Sayer and Bones, 1990) are

$$\sigma_{i,k} = \frac{4}{\pi r^3}|\boldsymbol{B}_{i,k}|, \quad \tau_{i,k} = \frac{4}{3\pi r^2}|\boldsymbol{W}_{i,k}|,$$
$$\sigma_i^{\max} = \max_k(\sigma_{i,k}), \quad \tau_i^{\max} = \max_k(\tau_{i,k}). \tag{23}$$

If the maximum stress due to these internal forces and internal moments $\max(\tau_i^{\max}, \sigma_i^{\max})$ exceeds a particular threshold value b then particle will break at the point of this maximum stress, as is illustrated in Fig. 2c. The element marked "+" is removed and the particle is divided into two fragments. The mass of the removed element is distributed among the remaining elements in the two fragments. The dimensionless length of the ith particle L_i is calculated from the number of elements within this particle by $L_i = l/r = (N_i + 1)$. Therefore, the sum of lengths of the two fragments is the same as the length of the mother particle.

2.3. Set-up of computational experiments

First, 200–300 particles with given initial particle length distribution are generated within a computational domain having periodic boundary conditions in the x and y principal directions and a stationary bottom wall w_1 at $z = 0$. The position and orientation of particles is completely random and they are not in contact. A random particle packing is created by applying a gravitational field $\boldsymbol{g} = (0, 0, -g)$ and by letting particles to settle down, cf. Fig. 3. Eventually, each particle moves to its equilibrium position where its weight is counter-balanced by the contact forces from neighbouring particles in the bed and/or from the bottom wall. The particle will oscillate around this position, however these oscillations will decrease in the course of the simulation because of the damping coefficients in Eqs. (2) and (3). Note that unlike many packing algorithms where the particles are deposited sequentially, in our simulation we move all particles at once. So particles at the bottom layers are allowed to move even though this movement are just small oscillations around the equilibrium position. The advantage of our algorithm over the sequential one is the fact we do not need to define a stability criterion determining when to fix the particle during the assembly of the bed. Particles are not allowed to break during the formation of the packing. We denote the height of the initial packed bed by h_0.

In the second phase, a wall w_2 is added above the packing and the bed of particles is gradually compressed as this wall is moving downward. When it moves a distance $\Delta h = r/10$ the wall is stopped and bed of particles is allowed to continue to

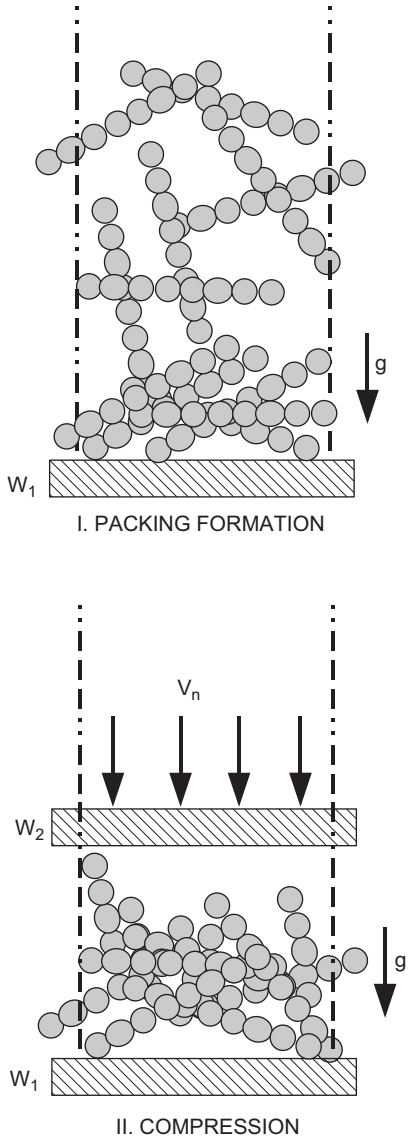

Fig. 3. Scheme of the set-up for computational experiments. The vertical dashed lines represent periodic boundary conditions.

move in order to reach the static situation. After the calculation of the stress and eventually fragmentation as described above, the w_2 boundary wall is continued to shift again. This computational cycle is repeated and the evolution of particle length distribution is recorded as a function of the position of the w_2 wall, i.e., the compression ratio h/h_0. Here h is defined as the actual distance between the horizontal plates w_1 and w_2.

The values of fixed numerical parameters used in the simulations, as well as the ranges of variable physical parameters are listed in Table 1. The radius of elements r has been chosen so the size and shape of particles is similar to typical alumina extrudates used as catalyst supports in packed bed reactors. Let us discuss how other parameter have been chosen. The stiffness and damping coefficients should be interpreted more as numerical than the physical parameters. As we are not investigating the real time-scale of our simulation, the value of damping coefficients which determines how fast the

Table 1
Values of parameters used in the simulations

η_r	global damping of the rotation	$3000\,\mathrm{kg\,m^2\,s^{-1}}$
η_t	global damping of the translation	$3000\,\mathrm{kg\,s^{-1}}$
g	gravitational acceleration	$9.81\,\mathrm{m\,s^{-2}}$
m^e	mass of element	0.417 mg
r	radius of element	0.405 mm
E_n	normal stiffness coefficient	1 N
E_t	tangential stiffness coefficient	1 N
α	friction angle	10°
b	maximum stress	3–30 kPa

mechanical energy of the system is dissipated can be set to any arbitrary value. It means, for example, that the terminal velocity of falling particles can be controlled by the damping coefficient η_t.

Real particles relevant to this study are made from a stiff, non-elastic material and one would therefore require as large stiffness as possible. However, if one uses a very large stiffness coefficient (e.g., that corresponding to the Young modulus of a real material) then the distance a particle is allowed to move in one step will be extremely small resulting in unfeasible long computational times. Therefore, the normal stiffness coefficient is treated as a numerical parameter which controls the extent of the overlap between elements. If this overlap remains small then the topology of the contacts between particles in the bed is similar for both the "real" and the "computational" packings although the stiffness coefficient differs several orders of magnitude. It is the topology of contacts not the extent of overlaps which will affect how the particles will be loaded and their fragmentation patterns.

Let us illustrate the value of the stiffness coefficient used in this study on a simple example. Assume single element lying on the bottom wall, the magnitude of the contact force is same as the weight of the element. Therefore, the extent of the overlap between the bottom wall and the element will be $(1-e)r = (m^e g/E_n)r \approx (4\times10^{-6})r$ for the values of parameters used in our simulations (cf. Table 1). Although the extent of the overlap in a bed of particles cannot be determined beforehand, it can be calculated after a particular bed has been assembled. The fraction of the overlapped volume of non-compressed packings was below 5×10^{-4} in our simulations. Therefore, the particles in simulations can be still considered to be stiff as are the real materials.

The parameter which remains to be discussed is the maximum strength b. It will affect the magnitude of forces the particle can withstand under a particular loading pattern before it breaks. Assume that $|\boldsymbol{f}^{\max}|$ is such a maximum force the particle withstands. Then from the computational point of view one can differentiate between the two situations: (i) for small b the $|\boldsymbol{f}^{\max}|$ will be less or on the same order of magnitude as the weight of the particles meaning that particles are so fragile that they break by their own weight; (ii) for large b the particles are firm and their weight is negligible so it will not affect the fragmentation. Therefore, only the contact forces $|\boldsymbol{f}^n| = E_n(1-e) \geqslant |\boldsymbol{f}^{\max}|$ are able to break the particles (cf. Eq. (10)). It is possible to calculate the overlap between

elements required to break the particle: $(1-e)^{\max} = |f^{\max}|/E_n$. From this equation one can see that if b is too large the particle is computationally "non-breakable" as it does not break until the overlap is unrealistically large (or it does not break at all). We have selected the value of b so it lies between the two above-mentioned limiting cases, i.e., the particles in the bed do not break until the bed is compressed, but they will break before the overlap between particles becomes unreasonably high. For the parameter values used in this study, the overlap at breakage during a simulated three-point bending test (cf. Fig. 2c) was of the order of $\approx (1\text{–}10 \times 10^{-4})r$.

3. Results and discussion

In this section we present a parametric study of breakage of particles under compression stress. The load is applied gradually so that the rate of rearrangement of individual particles is much faster than the rate at which the stress is increased. No attempt was made to describe the dynamics of the process nor to study the breakage of particles due to impact. It is assumed that the bed of particles is in a pseudo-stationary state at all times during the compaction.

There are four different kinds of parameters which will affect the fragmentation of a bed of particles: (i) the initial random realization of the bed as determined by the positions and orientations of particles; (ii) the maximum bending stress a single particle can sustain before it breaks, i.e., the strength of particles; (iii) the initial length of particles as characterized by the particle length distribution; (iv) the inter-particle friction, which will affect the transmission of forces between particles. The advantage of computations over physical experiments is that the effects of the above parameters can be easily separated and studied individually. We will discuss the effects of parameters (i)–(iii) in the remainder of this section.

Simulations with increased friction coefficient result in beds with higher porosity. In the quasi-stationary case treated in this work, the effect of varying the friction coefficient (iv) between 0° and 30° has been found to be less significant than effects (ii) and (iii). The variations of the average particle length were on the same order as variations due to randomness of the packing (i). Therefore, a constant value of the friction coefficient will be kept throughout the simulations presented below.

3.1. Effect of initial particle packing

For a random packed bed containing a sufficiently large number of particles, the evolution of particle length distribution as function of compaction ratio should not depend on the initial realization of the packed bed. At the same time, it is desirable to work with the smallest possible number of particles in order to maintain reasonable computational times. The number of particles used in this study was approximately 200–300 in each simulation. In this section we will demonstrate that this number is sufficiently large so as not to influence the simulation results. This will be done by comparing the breakage patterns obtained for several random initial realizations of the packed bed and constant values of other parameters.

An example of a single computational experiment is visualized in Fig. 4. Initially, the bed consists of particles of a uniform length of $L = 15$ and the depth of the bed is h_0. The distance between two solid walls w_1 and w_2 (cf. Fig. 3) is h and $h > h_0$ at the beginning of the simulation. As the upper solid wall w_2 is moving downward the particles are breaking and the particle length distribution begins to evolve. This can be seen in the histogram in Fig. 5 where the amount of shorter particles is gradually increasing. The absence of particles of the length 11–14 is implying that particles prefer to break approximately in the middle. The color of particles in Fig. 4 indicates their length.

The statistical characteristics of the particle length distribution are shown in Fig. 6 as function of the compaction ratio h/h_0. The number-average particle length L_n and the polydispersity index Z are calculated from the moments of the distribution μ_k as

$$L_n = \frac{\mu_1}{\mu_0}, \quad Z = \frac{\mu_2\mu_0}{\mu_1\mu_1}, \quad \mu_k = \sum_{i=1}^{\infty} i^k N(i), \tag{24}$$

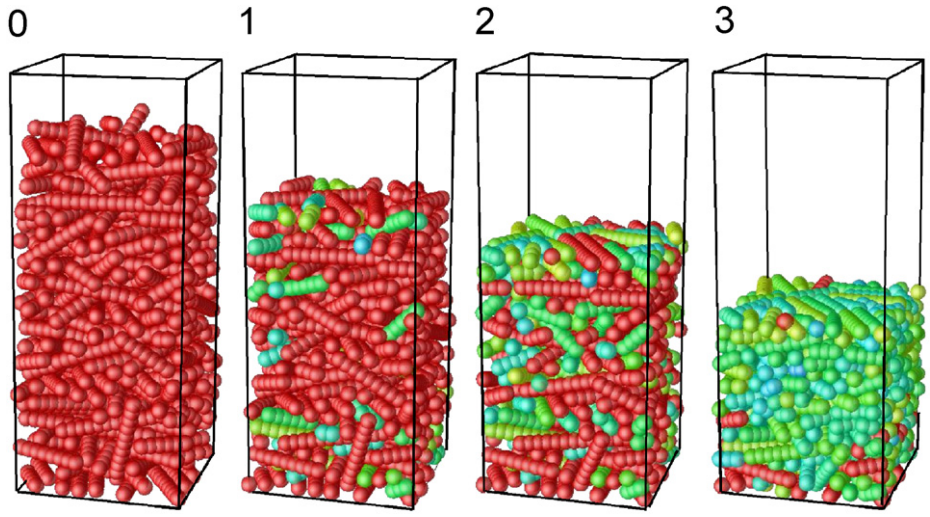

Fig. 4. Visualization of the process of particle breakage under compaction.

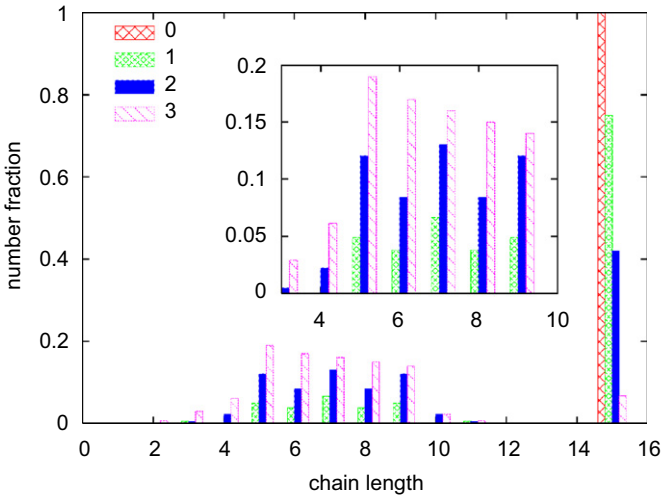

Fig. 5. Histogram of the particle length distribution corresponding to packings shown in Fig. 4.

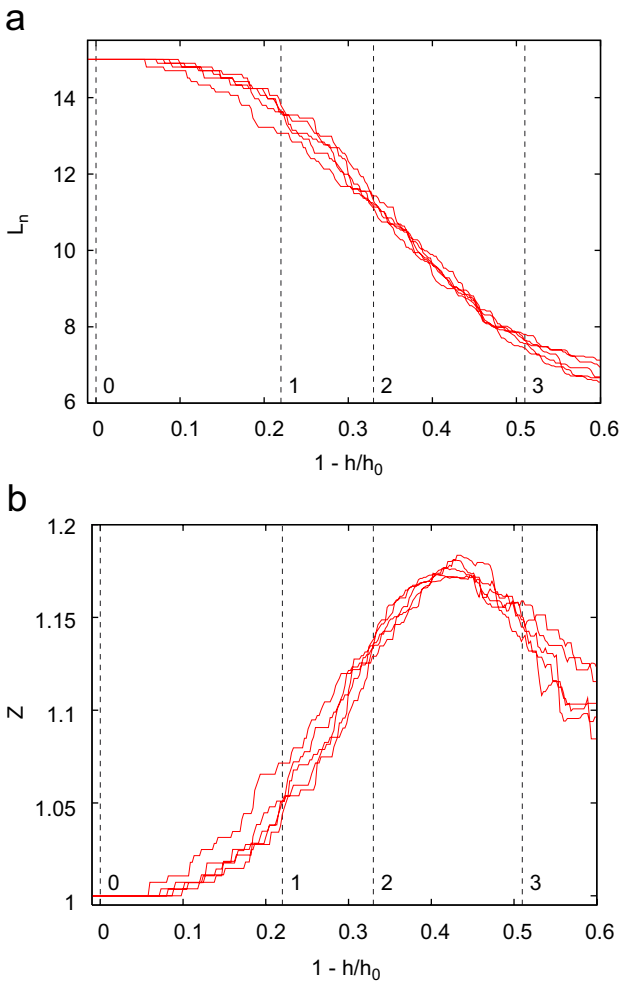

Fig. 6. Effect of the initial random realization of the packed bed on the properties of the particle length distribution: (a) number-average particle length L_n; (b) polydispersity index Z. Vertical lines correspond to the stage of the compression shown in Figs. 4 and 5.

where $N(i)$ is the number of particles of length i. The individual curves in Fig. 6 are for different random initial realizations of the packed bed where all other parameters (i.e., particle strength and friction) have been kept constant. It can be seen that variations due to randomness of the packing are not significant. Specifically, the standard deviation calculated on the basis of the five random realization does not exceed 4%, and is 1.6% on average (average over all h/h_0 values). Therefore, the number of particles in the order of 200–300 (about 3000–4000 elements) is considered sufficient and will be used throughout this study.

The polydispersity index Z, plotted as function of the compaction ratio in Fig. 6b, goes through a characteristic maximum. The maximum corresponds to a situation when some particles are still unbroken, while there are some very short fragments ($L_n \to 1$) already present in the bed. This gives the widest possible size distribution, hence a large value of the polydispersity index. The polydispersity index plotted in Fig. 6b can be compared with the full histograms at the corresponding states of breakage, denoted 0, 1, 2, 3 in Fig. 5.

The particle volume fraction ϕ_1 has been calculated as a sum of volumes of all particles within the region of the bed having volume V^{reg}. In order to eliminate the wall effect this region has been obtained from the whole bed by removing 10% of its top and bottom part

$$\phi_1 = \left(\sum_i V^{\mathrm{part}}(N_i)\right) \Big/ V^{\mathrm{reg}},$$
$$V^{\mathrm{part}}(N_i) = \left(\frac{11}{16}N_i + \frac{5}{16}\right) V^{\mathrm{sp}}, \tag{25}$$

where $V^{\mathrm{sp}} = (4/3)\pi r^3$ is the volume of an element and index i goes over all particles within region V^{reg}. Alternatively, the particle volume fraction ϕ_2 can be defined as a fraction ϕ_1 reduced by the volume of interparticle overlaps

$$\phi_2 = \phi_1 - \left(\sum_{ij} V_{ij}^{\mathrm{overlap}}\right) \Big/ V^{\mathrm{reg}},$$
$$V_{ij}^{\mathrm{overlap}} = \frac{2}{3}\pi\left(r - \frac{d_{ij}}{2}\right)^2 \left(2r + \frac{d_{ij}}{2}\right), \tag{26}$$

where ij runs over all interparticle contacts within region V^{reg} and d_{ij} is the distance between elements i and j.

The evolution of the volume fraction during the typical compression step is reported in Table 2. The difference $\phi_1 - \phi_2$ in Table 2 confirms that the assumption of the stiffness of "computational" particles is valid for more than the first half of the compression phase when the overlaps between particles remain well below 0.01. However, particle stiffness becomes more questionable at later stages of the compression as the fraction of overlaps eventually grows up to the value 0.10.

3.2. Effect of intrinsic particle strength

In the first parametric study, let us focus on the effect of the strength of individual particles determined by the parameter b

Table 2
Volume of fraction of a typical packing during compression

$1-h/h_0$	ϕ_1	ϕ_2
0.00	0.43	0.43
0.12	0.47	0.47
0.33	0.61	0.60
0.56	0.90	0.80

ϕ_1 is the volume of fraction of the particles.
$\phi_2 = \phi_1 - \phi_0$ where ϕ_0 is the volume fraction of interparticle overlaps.
h/h_0 is the compression ratio.

defined in Section 2.2 following Eq. (23). Initially, all particles have the same length $L = 15$ and all simulations start from the same realization of the packed bed. All bonds in all particles in the bed are initially given the same strength b. The number-mean particle size L_n as function of the compaction ratio h/h_0 for three values of the intrinsic particle strength, namely $b = 3$, 12, and 30 kPa, is shown in Fig. 7a, and the particle length distribution corresponding to a single point at a later stage of compaction is shown in Fig. 7b. It is possible to identify three regions for each curve in Fig. 7a.

Firstly, in the region where $h > h_0$ the upper plate w_2 (cf. Fig. 3) has not approached the top of the packing yet and any fragmentation of particles at this stage occurs only due to the weight of the particle layers above them. This is the case for the simulation with $b = 3$ kPa where the particles are extremely fragile and the average chain length drops instantly from 15 to 8 before compaction as such even begins. At the same time the height of the bed h decreases significantly (as was shown in Williams and Philipse, 2003, the packing density increases from 0.35 to 0.53 as the aspect ratio decreases from 10 to 4).

For higher (more realistic) values of b the particles are strong enough not to break until the compression load is applied. If the strength of particles is increased to $b = 12$ kPa only a small fraction of particles will break by the weight of the bed (cf. a small drop of L_n from 15 to 14 in Fig. 7a), and for $b = 30$ kPa there is practically no observable breakage during the pre-compaction stage.

The second region on the breakage–compaction curves is a plateau starting at $h = h_0$. The stress has been applied, but particles are still relatively free to rearrange their positions without fragmentation. Finally, in the third region, particles begin to break and their average length is decreasing. An example of PSD for $h/h_0 = 0.55$ is shown in Fig. 7b. The histogram shows that the number fraction of unbroken long particles is the largest in the case of the strongest particles ($b = 30$ kPa).

For a bed of real particles the strength of individual particles can be obtained experimentally (e.g., by three-point bending experiments) and the strength is usually not uniform but can follow the Weibull distribution (Li et al., 2000). In order to investigate the effect of strength distribution on breakage patterns, a simulation starting with a bed consisting of a mixture of particles of different intrinsic strengths has been performed. The results for a 1:1:1 mixture of particles with strength $b = 18$, 24, 30 kPa are shown in Figs. 8 and 9. In Figs. 8a and 9a, the breakage curves for weaker-than-average ($b = 18$) and

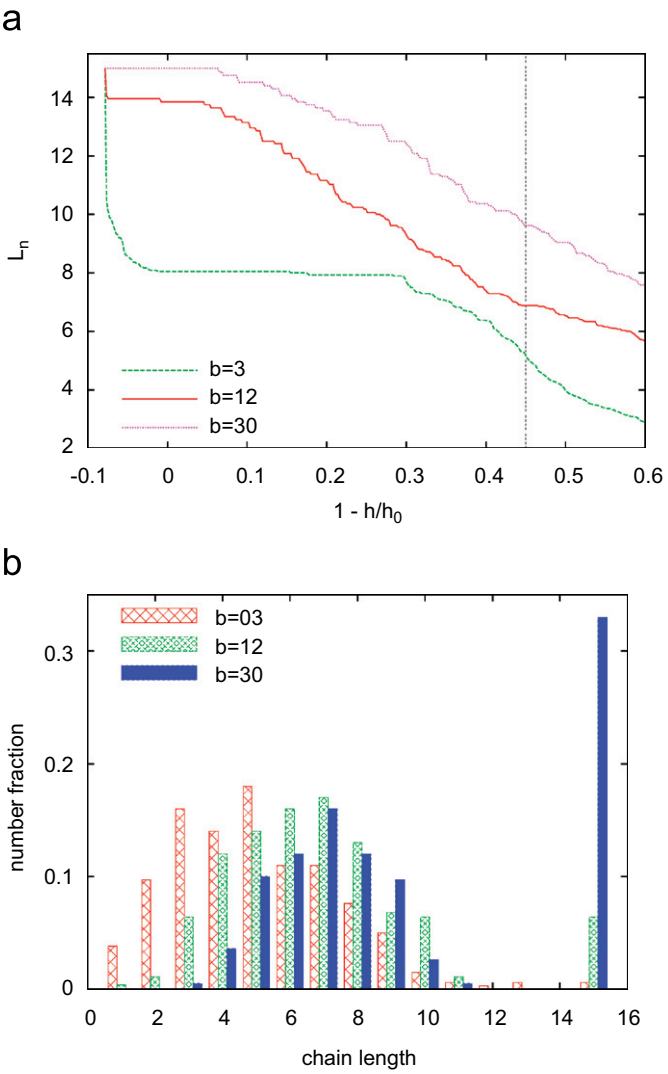

Fig. 7. Effect of particle strength on fragmentation during compaction: (a) number-average chain length; (b) histogram of particle length distribution at a later stage of the compaction (as denoted by the vertical line in the panel (a)).

stronger-than-average ($b = 30$) particles obtained when those particles are within the mixed bed are compared with breakage curves of "pure" $b = 18$ and 30 particles. The results are very interesting: both curves for the "pure" case are closer to average than for the mixed case. This means that the weak particles tend to break more when admixed with stronger particles, and on the other hand, the strong particles tend to break less when they are part of a mixture also containing the weaker particles. As a measure of the difference between each pair of curves, we can again compare the maximum and the mean deviation, which is 12% and 3.4%, respectively, in the $b = 18$ case, and 11% and 2.8%, respectively, in the $b = 30$ case.

This behaviour has a practical significance as it means that when stronger particles are present in a mixture with weaker ones, the fragmentation of the weaker particles will be aggravated under otherwise identical conditions. Such phenomena as fines formation in agitated vacuum drying or

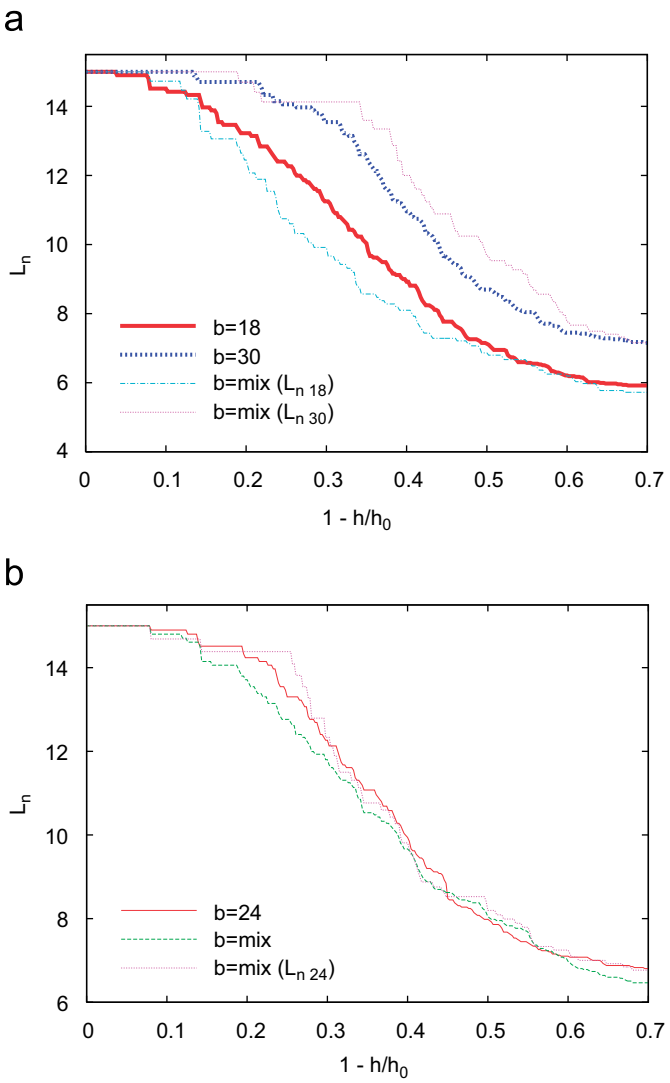

Fig. 8. Breakage curves for a bed composed of a 1:1:1 mixture of particles with intrinsic strength $b = 18$, 24, and 30 kPa: (a) comparison of strong ($b = 30$ kPa) and weak ($b = 18$ kPa) particle breakage in a mixture and when compacted alone; (b) comparison of the average chain length L_n calculated for the whole sample, for particles of the median strength when in the mixture, and for median-strength particles when compacted alone.

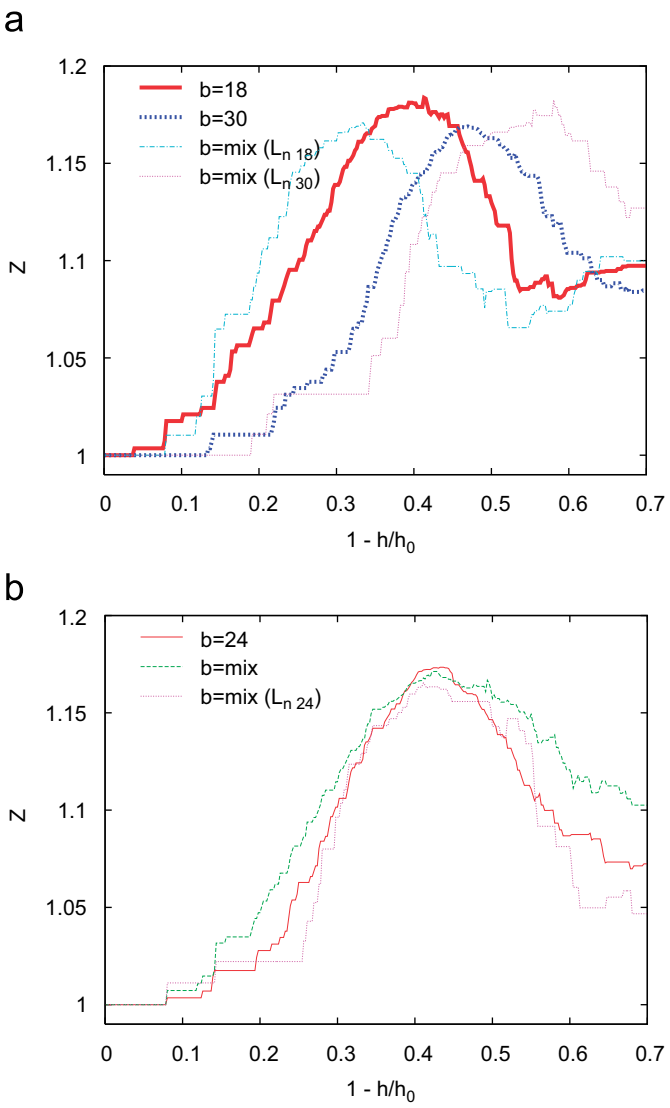

Fig. 9. Polydispersity Z of mixtures corresponding to Fig. 8.

higher-than-expected increase of filter cake resistance during pressure filtration could be attributed to this effect. In the extreme case of a very large difference between the intrinsic strength of the "weak" and the "strong" particles, the system would effectively behave as a media mill.

However, when the breakage curve of the average particles ($b = 24$) for the pure case is compared with that for the mixed case, as is shown in Figs. 8b and 9b, we can see that they are not only almost identical, but also closely coincide with the number-mean breakage curve of the entire mixture. The maximum and the mean standard deviation calculated for the three curves in Fig. 8b is 6% and 1.9%, respectively, which is comparable to the "natural" variance that was seen as a result of different random realizations. Hence, one can conclude that for a symmetrical initial particle strength distribution, the evolution of the mean particle length during compaction can be predicted by considering the mean strength of the initial distribution. The fraction of fines, however, will be higher in the case of a wide initial distribution of particle strength, as illustrated by the higher values of the polydispersity index in Fig. 9b.

3.3. Effect of intra-particle heterogeneity

So far the strength of all bonds present in a single particle was considered constant and heterogeneity in the bulk mixture was realized by admixing particles with a different value of the intrinsic bond strength. Let us now consider a situation where bond strengths are distributed randomly within each particle in the bed, rather than among the particles. This distribution would mimic, e.g., the presence of defects at different locations of actual particles made of the same material. The strengths, b_j, allocated to individual bonds were distributed

according to

$$b_j = \bar{b}(1 + s y_j), \tag{27}$$

where $\bar{b}$ is the mean bond strength, y_j is a uniformly distributed random variable contained in $[-0.5; +0.5]$, and $s > 0$ is a parameter characterizing the prescribed width of the intra-particle bond strength distribution.

The value of the mean bond strength was chosen to be $\bar{b} = 24$ kPa, i.e., the same as in the previous case. The evolution of the mean particle length and the polydispersity index for cases of $s = 0.05$ and 1.00 is plotted in Fig. 10a and b, respectively. In each case, three different random realizations of the intra-particle bond strength distribution (i.e., of the random variables y_j) were generated in order to obtain an estimate of the statistical spread similarly to Fig. 6. As can be seen, the case with a wider strength distribution ($s = 1.0$) yields a smaller mean particle size for all compaction ratios, i.e., the extent of particle breakage is larger on average. The difference between the two sets of curves is clearly greater than the spread within each set, and can therefore be regarded as statistically significant.

When discussing Fig. 7, it was noted that the fragment size distribution is symmetrical and has a maximum at half of the original particle length, which indicated that the particles with uniform intra-particle bond strength tend to break in the middle. However, this is not necessarily the case when the intra-particle bond strengths are no longer uniform. The fragment size distributions corresponding to several compaction ratios as indicated in Fig. 10a by the numbers 1,2, and 3 are plotted in Fig. 10c for both cases, i.e., $s = 0.05$ and 1.0. As can be seen, the $s = 0.05$ case is not qualitatively different from the behaviour already observed for uniform particles: the fragment size distributions are symmetrical and have a maximum at a chain length equal to half of that of the mother particle. However, the fragment size distributions for the wider variation of intra-particle bond strengths ($s = 1.0$) show interesting deviations.

Firstly, it can be seen that although at early stages the mean fragment size is still around the half of the mother particle, the distribution is no longer monomodal. This is because although the particles still tend to break near the centre, the exact breaking point may be off-set from the central location depending on the position of the "locally weakest" bond within the mother particle. The second noticeable effect is that for higher compaction ratios, the fragment size distribution looses symmetry and becomes skewed toward smaller particle size compared with the $s = 0.05$ case. This means that on average the extent of breakage will be larger when intra-particle strength heterogeneity is present.

3.4. Effect of particle length

Another important parameter that can be expected to affect the fragmentation patterns is the initial particle length. The initial particle volume fractions of packings assembled from particles of different lengths are summarized in the Table 3 and compared with values reported in Williams and Philipse (2003).

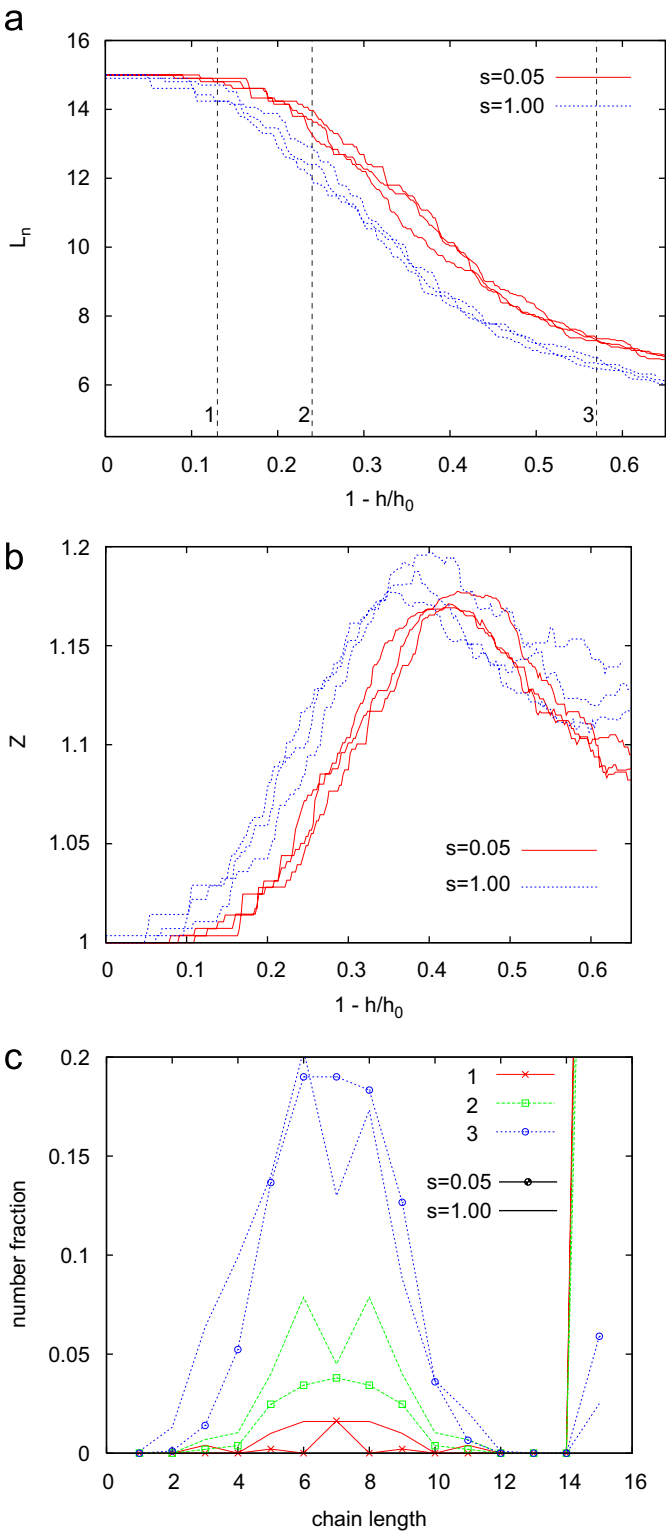

Fig. 10. Breakage in packings with a non-uniform intraparticle strength distribution: (a), (b) effect of different random realizations on the number-average chain length L_n and the polydispersity Z; (c) evolution of the particle size distribution for packings with different levels of intraparticle strength variations s (lines with symbols are for $s = 0.05$, lines without symbols are for $s = 1.00$). The individual compression steps 1–3 correspond to the compaction ratios denoted by the vertical lines in the panel (a)).

Table 3
Initial particle volume fraction of packings from particles of different lengths

N	α	ϕ	ϕ_3
5	3.0	0.65	0.58
10	5.5	0.54	0.49
15	8.0	0.43/0.31[a]	0.42
20	10.5	0.35	0.35

N is number of elements in one particle.
$\alpha = (N + 1)/2$ is the aspect ratio.
ϕ is the initial particle volume fraction of particles in the bed.
ϕ_3 are volume fractions reported in Williams and Philipse (2003).
[a]With friction coefficient 30°, for other beds the friction was 10°.

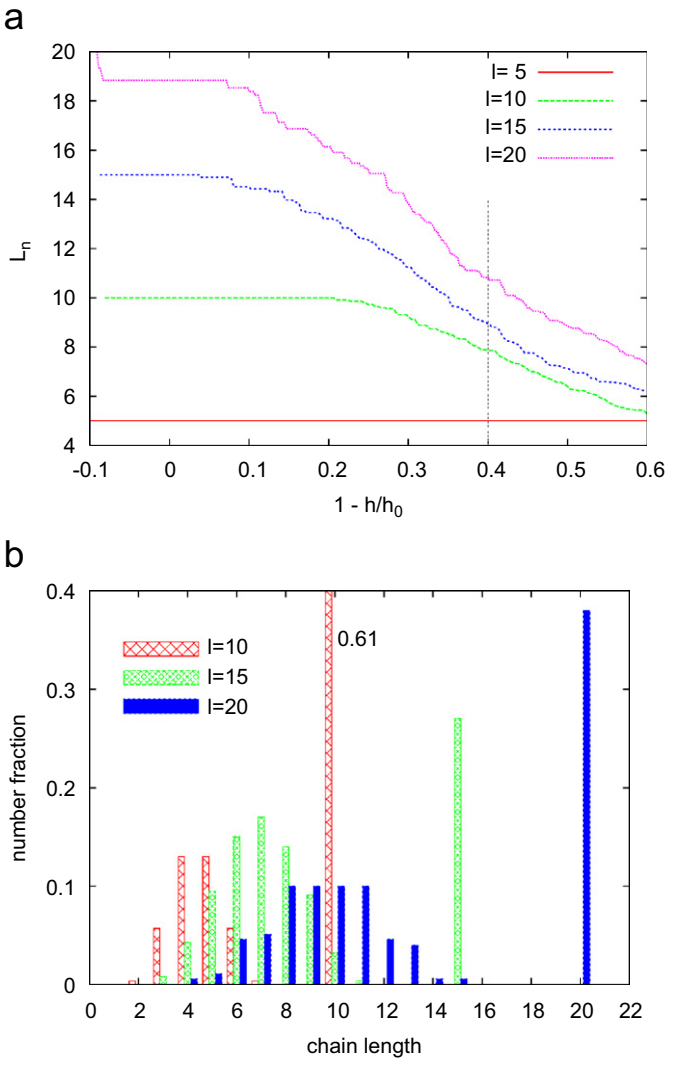

Fig. 11. Effect of the initial length of particles in the bed on their compaction: (a) number-average chain length; (b) histogram of particle length distribution in the later stage of the compaction (as denoted by the vertical line in the panel (a)).

In that work Williams and Philipse (2003) used "mechanical contraction" method to obtain a packing of spherocylinders of the range of aspect ratios up to 180. There is a good agreement for packings of longer particles ($N = 15$ and 20) while packings of shorter particles ($N = 5$ and 10) have larger particle volume fraction than packings from Williams and Philipse (2003). Breakage curves obtained when starting with a random packing of particles of different lengths are plotted in Fig. 11. All remaining parameters of the particles were kept constant and equal for all particles. Two trends are clearly apparent from these results. Firstly, longer particles begin to fragment at lower compaction ratios than shorter ones; this is indicated by a shorter plateau of L_n plot in Fig. 11a. This is most likely caused by the fact that longer particles can be less easily rearranged to fill the remaining space as the bed is compressed without being broken. Also, the bending moment is larger in longer particles. Secondly, it can be observed from the histogram of the length distribution in Fig. 11b that particles break approximately in the middle regardless of their absolute size. This result is an important confirmation, through a computational experiment, of assumptions often made in statistical–mechanical models of particle breakage phenomena (McCoy and Wang, 1994).

4. Conclusions

A methodology for the simulation of random packing of elongated particles and their fragmentation under uni-axial compaction has been developed and implemented. Computational studies of the effect of initial bed randomness, particle strength and its distribution both within the bed and inside individual particles, and of particle length on the fragmentation patterns have been carried out. Several interesting phenomena have been revealed by the computational studies: the formation of fines from relatively weaker particles tends to be more significant when stronger particles are also present in the mixture, and inversely, the on-set of fragmentation of these stronger particles is delayed when they are mixed with weaker particles compared to when they are compacted on their own. Similarly, when strength heterogeneity is present within the particles, the extent of breakage is larger than in the case of homogeneous particles with the same mean strength. The analysis of the effect of initial particle length on fragmentation revealed that although longer particles tend to break at lower compaction ratio than shorter particles of identical strength due to the combined effect of lower packing density (larger excluded volume) and higher bending moment acting on each particle, there is a size-invariant behaviour—namely, that on average the particles tend to break preferentially in the middle rather than asymmetrically. The computational method presented in this work can also be applied to other means of particle loading, such as fragmentation under shear.

Notation

b	maximum internal stress, kPa
$\boldsymbol{B}_{i,k}$	bending moment at the kth element of ith particle, N m
$\boldsymbol{d}_{ap}$	the normal direction unit vector of the contact AP, dimensionless

e_{ap} dimensionless distance between particles A and P, dimensionless
E_t, E_n stiffness modulus of the tangential and normal contact force, N
$\boldsymbol{f}_j$ force on the jth element, N
$\boldsymbol{f}^n_{ap}$,$\boldsymbol{f}^t_{ap}$ normal and tangential force on the ath element due to contact AP, N
$\boldsymbol{F}_i$ force on the ith particle, N
$\boldsymbol{F}^*_{i,k}$ internal force at the kth element of ith particle, N
$I_{i,k}$ the principal moments of inertia of the ith particle, kg m^2
L_n number-average particle length, dimensionless
$\boldsymbol{m}_j$ moment on the jth element, N m
m^p_i mass of the ith particle, kg
m^e_j mass of the jth element, kg
$\boldsymbol{M}_i$ moment on the ith particle, N m
$\boldsymbol{M}^*_{i,k}$ internal moment at the kth element of ith particle, N m
$M_{i,k}$ kth component of the vector $\boldsymbol{M}_i$ in global co-ordinates, N m
$M'_{i,k}$ kth component of the vector $\boldsymbol{M}_i$ in particle (local) co-ordinates, N m
N_i number of elements of the ith particle, dimensionless
r_j radius of the jth element, m
R_i rotation matrix for ith particle, dimensionless
$\boldsymbol{v}_j$ translational velocity of the jth element, m s^{-1}
$\boldsymbol{v}^s_{ap}$ shearing velocity across the contact AP, m s^{-1}
$\boldsymbol{v}^t_{ap}$ tangential component of the vector $(\boldsymbol{v}_p - \boldsymbol{v}_a)$, m s^{-1}
$\boldsymbol{V}_i$ translational velocity of the ith particle, m s^{-1}
$\boldsymbol{W}_{i,k}$ internal shearing stress at the kth element of ith particle, N
$\boldsymbol{x}_j$ position of the jth element, m
$\boldsymbol{x}^d_j$ relative position of the jth element, m
$\boldsymbol{X}_i$ position of the centre of mass of the ith particle, m

Greek letters

α friction angle, rad
η_r damping coefficient of the rotation, kg m^2 s^{-1}
η_t damping coefficient of the translation, kg s^{-1}
θ_i second Euler angle of the ith particle, rad
σ bending stress (longitudinal stress), Pa
τ shearing stress (transversal stress), Pa
ϕ_i first Euler angle of the ith particle, rad
ψ_i third Euler angle of the ith particle, rad
$\boldsymbol{\omega}_i$, $\boldsymbol{\omega}_j$ angular velocity of the ith particle or the jth element, s^{-1}
$\boldsymbol{\omega}_{ap}$ rotation of the contact normal $\boldsymbol{d}_{ap}$, s^{-1}
$\omega_{i,k}$ kth component of the vector $\boldsymbol{\omega}_i$ in global co-ordinates, s^{-1}
$\omega'_{i,k}$ kth component of the vector $\boldsymbol{\omega}_i$ in particle (local) co-ordinates, s^{-1}

References

Arya, A.P., 1990. Introduction to Classical Mechanics. Allyn & Bacon, Boston.

Cundall, P.A., Strack, O.D.L., 1979. A discrete numerical model for granular assemblies. Gèotechnique 29, 47–65.

Favier, J.F., Abbaspour-Fard, M.H., Kremmer, M., Raji, A.O., 1999. Shape representation of axi-symmetrical, non-spherical particles in discrete element simulation using multi-element model particles. Engineering Computations 16, 467–480.

Golchert, D., Moreno, R., Ghadiri, M., Litster, J., 2004. Effect of granule morphology on breakage behaviour during compression. Powder Technology 143–144, 84–96.

Hibbeler, R.C., 2005. Mechanics of Materials. Prentice Hall, Singapore.

Khanal, M., Schubert, W., Tomas, J., 2005. DEM simulation of diametrical compression test on particle compounds. Granular Matter 7, 83–90.

Kou, S.Q., Liu, H.Y., Lindqvist, P.-A., Tang, C.A., Xu, X.H., 2001. Numerical investigation of particle breakage as applied to mechanical crushing—part II: interparticle breakage. International Journal of Rock Mechanics and Mining Sciences 38, 1163–1172.

Lekhal, A., Girard, K.P., Brown, M.A., Kiang, S., Khinast, J.G., Glasser, B.J., 2004. The effect of agitated drying on the morphology of L-threonine (needle-like) crystals. International Journal of Pharmaceutics 270, 263–277.

Li, Y.D., Wu, D.F., Zhang, J.P., Chang, L., Wu, D.H., Fang, Z.P., Shi, Y.H., 2000. Measurement and statistics of single pellet mechanical strength of differently shaped catalysts. Powder Technology 113, 176–184.

McCoy, B.J., Wang, M., 1994. Continuous-mixture fragmentation kinetics: particle size reduction and molecular cracking. Chemical Engineering Science 49, 3773–3785.

Salman, A.D., Hounslow, M.J., Verba, A., 2002. Particle fragmentation in dilute phase pneumatic conveying. Powder Technology 126, 109–115.

Sayer, F.P., Bones, J.A., 1990. Applied Mechanics: A Modern Approach. Chapman & Hall, London.

Thornton, C., Ciomocos, M.T., Adams, M.J., 1999. Numerical simulation of agglomerate impact breakage. Powder Technology 105, 74–82.

Venugopal, R., Rajamani, R.K., 2001. 3D simulation of charge motion in tumbling mills by the discrete element method. Powder Technology 115, 157–166.

Williams, S.R., Philipse, A.P., 2003. Random packings of spheres and spherocylinders simulated by mechanical contraction. Physical Review E 67, 051301.

Zumaeta, N., Cartland-Glover, G.M., Heffernan, S.P., Byrne, E.P., Fitzpatrick, J.J., 2005. Breakage model development and application with CFD for predicting breakage of whey protein precipitate particles. Chemical Engineering Science 60, 3443–3452.

8.2 Computational and experimental investigation of needle-shaped crystal breakage

Zdeněk Grof
Carl M. Schoellhammer
Pavol Rajniak
František Štěpánek

Published in the *Int. J. Pharmaceut.*, Vol. 407, 2011, pp. 12–20
DOI: 10.1016/j.ijpharm.2010.12.031.

Provided for non-commercial research and education use.
Not for reproduction, distribution or commercial use.

This article appeared in a journal published by Elsevier. The attached copy is furnished to the author for internal non-commercial research and education use, including for instruction at the authors institution and sharing with colleagues.

Other uses, including reproduction and distribution, or selling or licensing copies, or posting to personal, institutional or third party websites are prohibited.

In most cases authors are permitted to post their version of the article (e.g. in Word or Tex form) to their personal website or institutional repository. Authors requiring further information regarding Elsevier's archiving and manuscript policies are encouraged to visit:

http://www.elsevier.com/copyright

Author's personal copy

International Journal of Pharmaceutics 407 (2011) 12–20

Contents lists available at ScienceDirect

International Journal of Pharmaceutics

journal homepage: www.elsevier.com/locate/ijpharm

Computational and experimental investigation of needle-shaped crystal breakage

Zdeněk Grof[a], Carl M. Schoellhammer[b], Pavol Rajniak[b], František Štěpánek[a,*]

[a] Department of Chemical Engineering, Institute of Chemical Technology, Technická 5 166 28 Prague, Czech Republic
[b] Merck & Co., Inc., West Point, PA, USA

ARTICLE INFO

Article history:
Received 14 June 2010
Accepted 29 December 2010
Available online 11 January 2011

Keywords:
DEM
Population balance modeling
Fragmentation
Daughter length distribution
Breakage kernel

ABSTRACT

Needle-shaped crystals are a common occurrence in many pharmaceutical and fine chemicals processes. Even if the particle size distribution (PSD) obtained in a crystallization step can be controlled by the crystal growth kinetics and hydrodynamic conditions, further fluid–solid separation steps such as filtration, filter washing, drying, and subsequent solids handling can often lead to uncontrolled changes in the PSD due to breakage. In this contribution we present a combined computational and experimental methodology for determining the breakage kernel and the daughter distribution functions of needle-shaped crystals, and for population balance modeling of their breakage. A discrete element model (DEM) of needle-shaped particle breakage was first used in order to find out the appropriate types of the breakage kernel and the daughter distribution functions. A population balance model of breakage was then formulated and used in conjunction with experimental data in order to determine the material-specific parameters appearing in the breakage functions. Quantitative agreement between simulation and experiment has been obtained.

© 2011 Elsevier B.V. All rights reserved.

1. Introduction

Needle-shaped crystals (crystals with a large aspect ratio) are commonly encountered in pharmaceutical processes. While the particle size distribution (PSD) can nowadays be controlled relatively precisely in the crystallization step by adjusting the supersaturation, seeding, and hydrodynamic conditions in the crystallizer (Yu et al., 2007), further downstream fluid-solid separation steps such as filtration, filter washing, drying, and subsequent solids handling can often lead to uncontrolled changes in the PSD due to attrition and breakage (Müller et al., 2006; Kalman, 2000). The effect of breakage on the particle size distribution can be described by population balances (Hill and Ng, 1997; Kostoglou, 2007). For population balance models of breakage to be effective, two material- and stress-field specific functions need to be known: the breakage kernel (selection function) and the daughter distribution function (breakage function) (Austin, 1971; Kelly and Spottiswood, 1990). The breakage kernel determines the breakage rate of particles from each size fraction, while the daughter distribution function describes the size distribution of daughter particles (fragments) that are formed once a particle of a given size does break.

Although methodologies for experimental determination of the breakage kernel and daughter distribution functions are known (Gupta et al., 1981), they either require a relatively large number of experiments or the solution of an inverse problem (Sathyagal et al., 1995). An alternative approach is based on trying to determine the functions theoretically (Hill, 2004) or computationally by detailed mechanistic modeling of the breakage of single particles (Khanal et al., 2005) or particle ensembles (Bobet et al., 2009; Ketterhagen et al., 2008). Grof et al. (2007) recently demonstrated the feasibility of detailed numerical simulation of the breakage of needle-shaped particles within a random packed bed subjected to uni-directional compaction, using the discrete element method (DEM). Elongated particles with a chosen aspect ratio have been created by linking individual spherical discrete elements by rigid bonds, characterized by a given bending stiffness and ultimate bending strength. A randomly packed bed of these elongated particles has been formed and gradually compressed between two infinite parallel solid planes. The particle size distribution as a function of the compaction ratio has been studied while systematically varying the individual particle strength, the initial particle length, and its distribution.

The aim of the present work is to develop and validate a novel methodology for the determination of the breakage kernel and daughter distribution functions, based on the combination of computational and experimental techniques. The methodology consists of four parts: *(i)* the DEM simulation of needle-shaped particle breakage under uni-axial compaction as described in (Grof et al., 2007); *(ii)* post-processing of the DEM simulation outputs using population balance models and explicit evaluation of the appropriate types of the breakage functions; *(iii)* experimental study of the breakage of real needle-shaped crystals under uni-axial

* Corresponding author. Tel.: +420 220 443 236; fax: +420 220 444 320.
E-mail address: Frantisek.Stepanek@vscht.cz (F. Štěpánek).

0378-5173/$ – see front matter © 2011 Elsevier B.V. All rights reserved.
doi:10.1016/j.ijpharm.2010.12.031

Author's personal copy

Nomenclature

a	compression parameter (dimensionless)
A	die cross-section area (m^2)
C	span of Gaussian function (dimensionless)
E	specific energy input (J/kg)
F	compaction force (N)
$f(y)$	compression function ($m\,s^{-2}$)
$g(F)$	alternative form of compression function (m/kg)
h	bed height (m)
$k(L_i)$	breakage kernel (kg/J)
k_0	breakage constant (dimensionless)
L_i	length of a crystal from the ith size class (m)
L_0	characteristic length (m)
m	sample mass (kg)
N	number of size classes (dimensionless)
n_i	number concentration of crystals from the ith size class (kg^{-1})
P	compaction pressure (Pa)
r_i	breakage rate (J^{-1})
$S_m(L_i)$	breakage probability (dimensionless)
U	objective function (kg^{-2})
y	relative piston position (dimensionless)
z	piston travel distance (m)

Greek letters

$\beta(i,j)$	daughter distribution function (dimensionless)
$\beta'(x)$	transformed (universal) daughter distribution function (dimensionless)
γ	breakage exponent (dimensionless)

compaction; *(iv)* fitting of the population balance models to the experimental data and evaluation of the material-specific parameters in the breakage functions.

2. Population balance model

When applying the rigorous population balance model (Vanni, 2000) to needle-shaped crystals we assume that the crystals are linear aggregates of primary particles (or "monomers") of equal size. Such a description is consistent with the multi-element particle model (Favier et al., 1999; Grof et al., 2007) used for the representation of elongated (needle-shaped) particles or crystals. This assumption makes it possible to correlate the length L_i of a crystal with the number of primary particles i that form it as:

$$L_i \approx i. \tag{1}$$

The particle size distribution is then a discrete function, whose values n_i, $i = 1, \ldots, N$ are the number concentrations of the particles consisting of i monomers and N is the number of size classes.

Theoretical treatments of Weichert (1992), Fuerstenau et al. (1996, 2004), lead to expressing the population balance equations for the breakage under uni-axial compression in terms of the specific energy expended rather than in grinding time as follows

$$\frac{dn_i}{dE} = -r_i + \sum_{j=i+1}^{N} \beta_{ij} r_j. \tag{2}$$

The first term on the right side of Eq. (2) is the rate of death of particles i to generate smaller fragments, while the second one is the birth of particles i due to rupture of larger particles.

The specific energy input E can be equated with the work of compression per unit feed mass (Fuerstenau et al., 1996)

$$E \approx \frac{APz}{m} = \frac{Fz}{m}, \tag{3}$$

where A is the die cross-sectional area, P is the compaction pressure, F is the compaction force, m is the sample mass which is proportional to the initial bed height

$$m \approx h_0 \tag{4}$$

and z is the piston travel distance which may be expressed in terms of h_0 and h, the initial and instantaneous bed heights

$$z = h_0 - h. \tag{5}$$

Kawakita and Lüdde (1971) listed 15 equations of compaction that relate pressure with volume (or bed height). For example the Kawakita piston compression equation has the form

$$\frac{z}{m} \approx y = \frac{h_0 - h}{h_0} = \frac{abP}{1 + bP} = \frac{acF}{1 + cF} \tag{6}$$

or

$$P = \frac{y}{b(a - y)}, \tag{7}$$

where y is the degree of volume reduction (or relative piston position) and a and b are parameters characterizing the powder. The parameter a is equal to the initial porosity in the case of piston compression. By combining relations (3)–(7) and lumping all proportionality constants, the specific energy may be expressed as

$$E \approx Py \approx \frac{y^2}{a - y} \tag{8}$$

and consequently

$$dE \approx \frac{2ay - y^2}{(a - y)^2} dy = f(y)\,dy. \tag{9}$$

Breakup is usually a first order process with respect to particle concentration, since it generally depends on the local stress field acting on the particles. It is convenient to express the death rate as

$$r_i = k(L_i) n_i, \tag{10}$$

where $k(L_i)$ is the breakage kernel. There is a strong dependence of the breakage kernel on particle size, L_i. Different breakage kernels are summarized in (Vanni, 2000; Rajniak et al., 2008).

Finally, introducing (9) and (10) into the rigorous population balances (2) and lumping different proportionality factors together we get the population balance equations in terms of the relative piston position y

$$\frac{dn_i}{dy} = -f(y)k(L_i)n_i + \sum_{j=i+1}^{N} \beta_{ij} f(y) k(L_j) n_j \tag{11}$$

with $f(y)$ defined by Eq. (9).

There exist many different fragment (daughter) distribution functions β_{ij} defining the number of daughter fragments in class i produced upon breakup of a mother particle j (Vanni, 2000; Rajniak et al., 2008). Here we have considered only the formation of two fragments during every breakage event, i.e. corresponding binary breakage distribution functions are normalized with respect to condition (12)

$$\sum_{i=1}^{j-1} \beta_{ij} = 2. \tag{12}$$

Author's personal copy

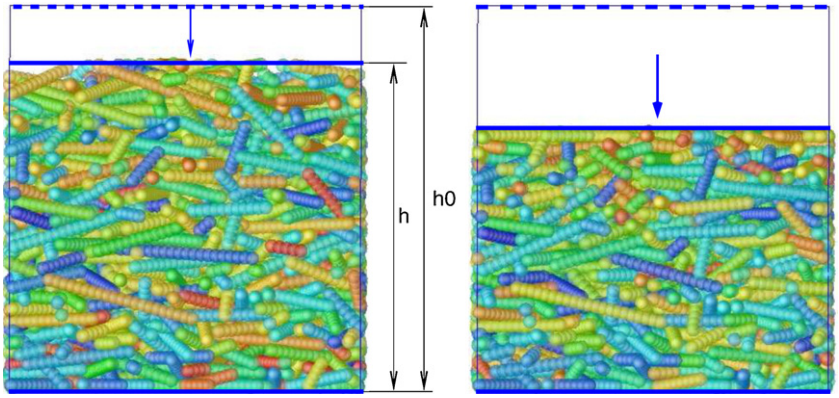

Fig. 1. Simulation setup for discrete element modelling of uniaxial compression and breakage of needle-shape particles.

An alternative form of the model equations are based on expression (6) with the compression force F as the independent variable. For the specific energy input we can write

$$E \approx Fy \approx \frac{cF^2}{1+cF} \tag{13}$$

and consequently

$$\mathrm{d}E \approx \frac{2F+cF^2}{(1+cF)^2}\mathrm{d}F = g(F)\,\mathrm{d}F. \tag{14}$$

The alternative population balance equations then have the following form

$$\frac{\mathrm{d}n_i}{\mathrm{d}F} = -g(F)k(L_i)n_i + \sum_{j=i+1}^{N}\beta_{ij}g(F)k(L_j)n_j. \tag{15}$$

In the next chapter we will discuss how the discrete element methodology helps elucidate appropriate expressions for the breakage kernel and daughter distribution functions.

3. Discrete element method

3.1. Simulation of the compression and breakage of a layer of particles

A methodology based on the discrete element method (Cundall and Strack, 1979) modified to treat non-spherical particles by the multi-element model (Favier et al., 1999) has been used to simulate the movement and breakage of individual needle-shaped particles. The magnitude and the location of contact forces at each particle determine the load on the particle. Particles are treated as loaded beams in order to calculate bending and shear stresses along the particle. When a set threshold value anywhere along a particle is exceeded the particle breaks into two daughter particles at the point of maximum stress. A full description of the algorithm has been given in our earlier work (Grof et al., 2007).

In order to determine the breakage kernel and the daughter distribution function for a sample of needle-shaped particles, the computational breakage experiment has been carried out in the following way. First, a population of 800 particles with a specified size distribution was generated inside the computational box with periodic boundary conditions in the direction of the x- and y-axes and a fixed wall perpendicular to the xy-plane (at the bottom boundary of the box). The particles were allowed to settle down due to gravitational forces in the direction of the z-axis thus forming the initial random packing desired. A second wall parallel with the xy-plane was then placed above the packing and compression was simulated by a stepwise movement of this piston (cf. Fig. 1). After each step of the piston, the particles were allowed to move and rearrange in the packed layer until a static state was achieved. The stress on every particle was then calculated and particle breakage carried out where required.

Every breakage event encountered during the simulated compression experiment has been recorded and the following data collected: *(i)* the relative piston position (compression ratio) $y = (h_0 - h)/h_0$, where h and h_0 are the current and the initial packing heights, respectively, determined by the piston position; *(ii)* the length L_i of the (mother) particle before breakage; *(iii)* if the particle broke during a given compression step, the length of the shorter daughter particle. The results collected from simulated compression experiments of five different particle packings are shown in Fig. 2, where each curve represents the particle length distribution at a given compression ratio y. The error bars indicate the standard deviations due to the five different random realizations of the initial particle packing. The gradual particle breakage is clearly demonstrated as the particle size distribution shifts towards shorter particles and the number of longer particles diminishes with increasing y.

3.2. Breakage kernel

The breakage kernel is obtained by post-processing of the breakage events recorded during the computational experiment. The breakage events were first grouped into M intervals $m = 0, \ldots, M$ according to the compression ratio y for which they occurred. A

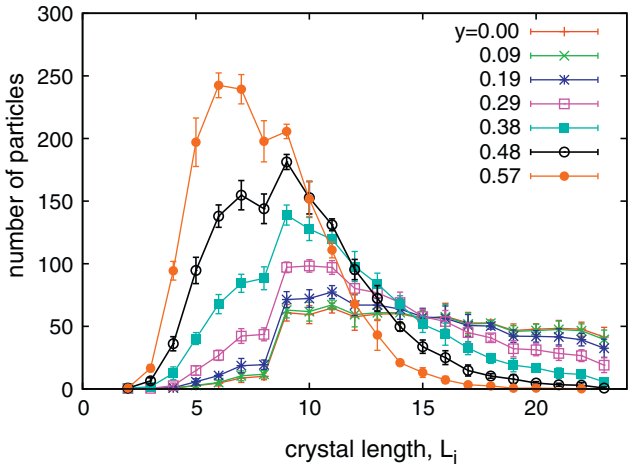

Fig. 2. Evolution of PSD with compression ratio y in a DEM simulation. The error bars represent the standard deviation obtained by compounding the results of compressing five different random realizations of the initial particle packings.

Author's personal copy

breakage probability $S_m(L_i)$ is defined as the probability that a particle of length L_i that was originally present in the system at compression ratio y_m disappeared from the system (i.e., it was broken) at some stage while the compression ratio y was in the range $\langle y_m\,;y_{m+1}\rangle$. This breakage probability was calculated according to

$$S_m(L_i) = 1 - \frac{n_i(y_{m+1})}{n_i(y_m)}, \tag{16}$$

where $n_i(y_m)$ is the number of particles of length L_i present in the system at compression ratio y_m and $n_i(y_{m+1})$ is the number of such particles still "surviving" in the system at y_{m+1}. Note that any newly formed particles of length L_i are not counted into $n_i(y_{m+1})$ when evaluating $S_m(L_i)$.

Let us derive the relation between the breakage probability $S_m(L_i)$ and the breakage kernel $k(L_i)$, introduced above. From Eq. (11), the number of particles undergoing breakage during the interval $\langle y_m\,;y_{m+1}\rangle$ is

$$\Delta n_i = (n_i(y_m) - n_i(y_{m+1})) = k(L_i)f(\overline{y})\Delta y\overline{n_i}. \tag{17}$$

Assuming that $\overline{n_i}\doteq n_i(y_m)$ and substituting Eq. (17) into the relation for S_m (16) one obtains

$$S_m(L_i) = k(L_i)f(\overline{y})(y_{m+1} - y_m). \tag{18}$$

The breakage probability $S_m(L_i)$ evaluated from DEM simulations is shown in Fig. 3a. Then, as shown in Fig. 3b and c the curves can be fitted by the sigmoidal and power-law functions of the form:

$$S_m(L_i) = \frac{1}{1+\exp(-\gamma_m(L_i - L_{0,m}))} \text{ and} \tag{19a}$$

$$S_m(L_i) = \alpha(L_i - L_{0,m})^{\gamma_m}. \tag{19b}$$

It can be seen from Fig. 3b and c that the sigmoidal function provides a better fit of the breakage probability obtained by DEM simulation than the power law function. In particular, the sigmoidal function satisfies the property that in the limit for large particles, the breakage probability approaches unity, while the power law function diverges. Using a single parameter α for the entire range of the compression ratio, the power law is able to fit the DEM data well only at small compression ratio y, but fails for the two curves at $y > 0.48$. A better fit could be obtained by using three parameters in the power law, i.e., by allowing the value of α to depend on the compression ratio. On the other hand, the sigmoidal function is able to fit the data well over the entire range of y with only two adjustable parameters.

3.3. Daughter distribution function

To evaluate the daughter distribution function $\beta(i,j)$, the entire set of breakage events recorded for compression in the range $\langle y_0\,;y_M\rangle$ was used. Unlike the breakage probability $S_m(L_i)$, there is no reason to assume that the daughter distribution $\beta(i,j)$ would depend on the compression ratio. Moreover, the larger number of breakage events analyzed reduces the variations of data points in the evaluated function. Let $D_{i,j}$ be the number of breakage events where the particle of length j breaks into particles of length i and $j-i$, respectively, and let $i<j-i$ (i.e. the shorter of the two fragments is given the index i). Then the points in the the daughter distribution $\beta(i,j)$ are calculated as

$$\beta(i,j) = \frac{D_{i,j}}{\sum_{k=1}^{j/2} D_{k,j}}, \quad i = 1,\ldots,j/2 \tag{20a}$$

and the other half can be completed employing the symmetry of the distribution

$$\beta(i,j) = \beta(j-i,j) \quad i = j/2,\ldots,j. \tag{20b}$$

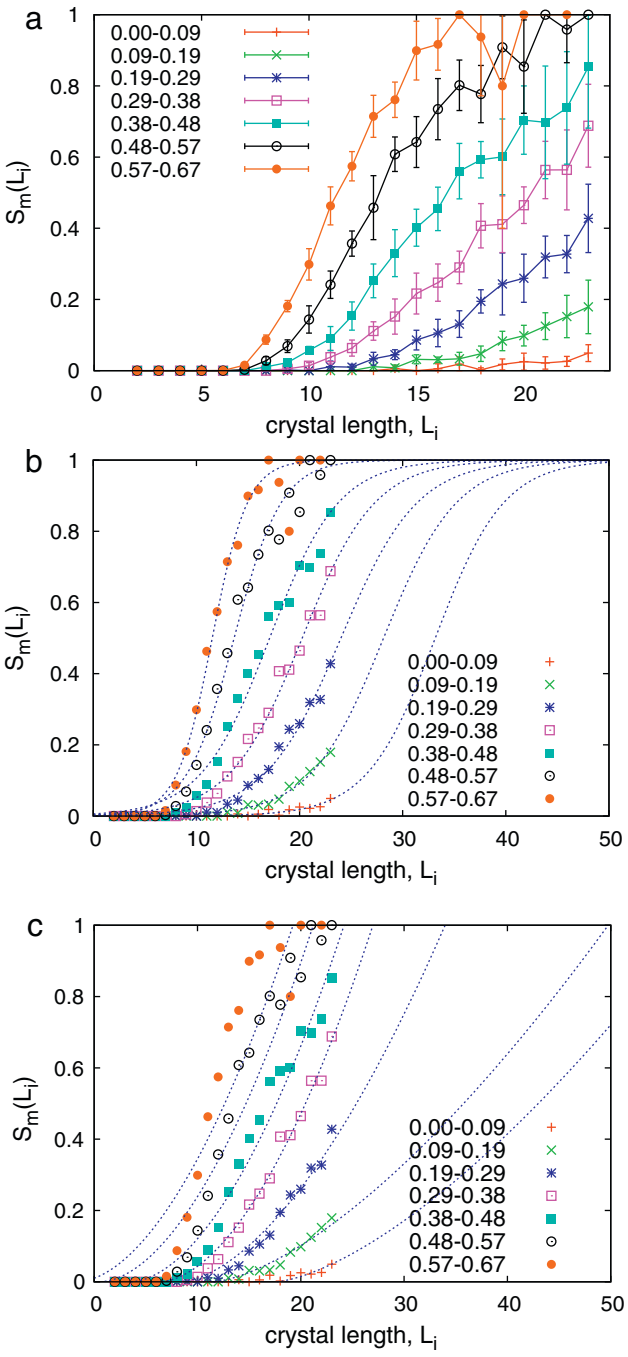

Fig. 3. Compression-dependent breakage kernel from DEM simulation: (a) computation data with error bars representing the standard deviation obtained from five simulation runs, (b) fit of data by a sigmoidal function (19a), (c) fit of data by a power-law function (19b).

If the breakage is self-similar, then a single daughter distribution function $\beta'(x)$, where $x = i/j$, characterizes the breakage of mother particles of any length j. For binary breakage (two fragments from a single breakage event) the daughter distribution functions are normalized to 2:

$$\sum_{i=1}^{j}\beta(i,j) = \int_0^1 \beta'(x)\,\mathrm{d}x = 2. \tag{21}$$

The normalized daughter distribution $\beta'(x)$ obtained from the DEM simulations is shown in Fig. 4. Based on DEM simulation data analysis, it has been confirmed the breakage is indeed self-similar,

Author's personal copy

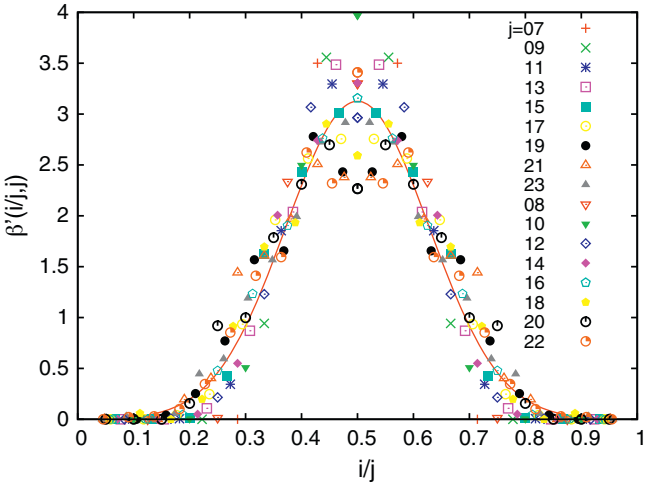

Fig. 4. Normalized (universal) daughter distribution $\beta'(i/j,j)$. Mean values evaluated from five different random sample realizations are displayed and fitted by a Gaussian function (22).

as breakage functions for particles of different lengths superimpose on a single master curve that can be fitted by the Gaussian function

$$\beta'(x) = \frac{2}{\sigma\sqrt{2\pi}} \exp\left(-\frac{(x-\mu)^2}{2\sigma^2}\right) \tag{22}$$

with parameters $\mu = 0.5$ and $\sigma = 0.1276 \pm 0.0016$. Therefore, the daughter distribution for mother particle of length L_j is

$$\beta(i,j) = \frac{2}{j\sigma\sqrt{2\pi}} \exp\left(-\frac{(i-j/2)^2}{2(j\sigma)^2}\right), \tag{23}$$

where the linear dependence of distribution width on mother particle length is described by the proportional parameter σ.

4. Fitting of computational DEM results by PBM

In the previous section, it has been demonstrated that the two *a priory* unknown functions required in the population balance equations (11) – i.e. the breakage kernel $f(y)k(L_i)$ and the daughter distribution β_{ij} – can be directly evaluated by post-processing of DEM simulation results. There are two ways of utilizing the results from Sections 3.2 and 3.3. The breakage kernel and the daughter distribution can be constructed directly by finding an arbitrary function able to provide a good approximation of $f(y)k(L_i)$ or β_{ij} data, then performing a least-square regression of those data and evaluating the function's parameters. The other option is to use DEM results for proposing suitable shapes of the breakage kernel and daughter distribution functions. The parameters of those functions are then found by optimization to achieve the best match of particle size distribution predicted by PBM with DEM result. The latter method will be demonstrated in this section. Its main advantage is that it only requires the PSD at several compression ratios as its input, which is also the format in which experimental data are available (unlike in DEM simulations, the recording and post-processing of single breakage events is not feasible in a real experiment). Thus, the estimation method for PBM functions and parameters can be the same, but the input data can originate either from a computational or from a physical experiment.

The key observations from the evaluation of the DEM simulations discussed in section 3 are that the breakage kernels can be more or less successfully fitted by power-law and sigmoidal functions

$$k(L_i) = k_0(L_i - L_0)^\gamma \tag{24a}$$

$$k(L_i) = \frac{k_0}{1 + \exp(\gamma(L_i - L_0))} \tag{24b}$$

and that the daughter distribution function is self-similar and can be fitted by the Gaussian function. Let us now find the values of parameters appearing in the breakage kernel and daughter distribution function by fitting a population balance model (PBM) introduced in Section 2 to the DEM results.

After introducing the power-law compression breakage kernel (24a) into the PB equations (11) with relative piston position y as the independent variable, the following final form of PBE for each size class i is

$$\frac{dn_i}{dy} = k_0 \frac{2ay - y^2}{(a-y)^2} \left(-(L_i - L_0)^\gamma n_i + \sum_{j=i+1}^{N} \beta_{ij}(L_j - L_0)^\gamma n_j \right) \tag{25}$$

and similarly also for the sigmoidal breakage kernel (24b). The parameters β_{ij} are calculated from the Gaussian daughter distribution function

$$\beta_{ij} \approx \exp\left(-\frac{(i-j/2)^2}{(NC)^2}\right). \tag{26}$$

There are five adjustable parameters in the model equations (25) and (26), i.e., the compression parameter a, the breakage constant k_0, the breakage exponent γ, the characteristic length L_0 and span of the Gaussian daughter distribution function C.

A customized (Compaq Visual Fortran) version of the DIRECT optimization algorithm (Perttunen et al., 1993; Bjorkmann and Holmstrom, 1999) was employed for finding the global minimum of the objective function U

$$U = \sum_{m=1}^{7} \sum_{i=1}^{N} \left(n_i^{\exp}(y_m) - n_i^{\mathrm{cal}}(y_m)\right)^2 \tag{27}$$

constrained by the population balances (25). $n_i(y_m)$ is the calculated or experimental number concentration of crystals of the class i at the piston position y_m.

The optimized parameter values and the corresponding objective functions are compared in Table 1 and a graphical comparison with the DEM simulation results is shown in Fig. 5. Please note that the DEM data in Fig. 5 are the same as those in Fig. 2 but they are shown in the cumulative rather than differential form for clarity. It can be concluded that the fit is visually satisfactory for both the power-law and sigmoidal function. The objective function at optimum ($U = 0.0113$) is slightly better when employing the power-law breakage kernel than for the sigmoidal kernel ($U = 0.0168$). A possible reason is that the functions calculated from DEM results (Fig. 3) have a sigmoidal shape only for the highest compressions (at piston positions y_6 and y_7) as it was already discussed in relation to Fig. 3. It is interesting to note that the value of the compression

Table 1
Fitting of the DEM results by PBM.

Breakage kernel, $f(y)k(L_i)$	$f(y)$	a	k_0	γ	L_0	C	U
$f(y)(L_i - L_0)^\gamma$	Eq. (9)	0.730	0.0185	1.75	6	0.081	0.0113
$\frac{f(y)}{1+\exp(-\gamma(L_i - L_0))}$	Eq. (9)	0.733	1.35	0.667	12.7	0.07	0.0168

Author's personal copy

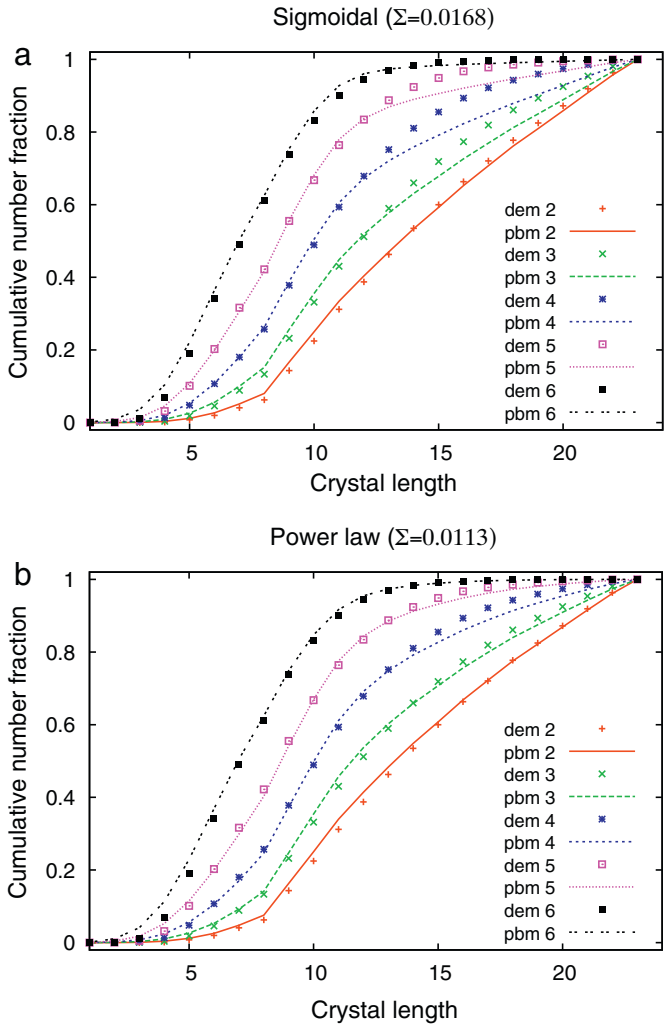

Fig. 5. Comparison of size distribution obtained by the DEM simulation with the distribution calculated by PB model using (a) sigmoidal and (b) power-law form of the breakage kernel in the PB equations.

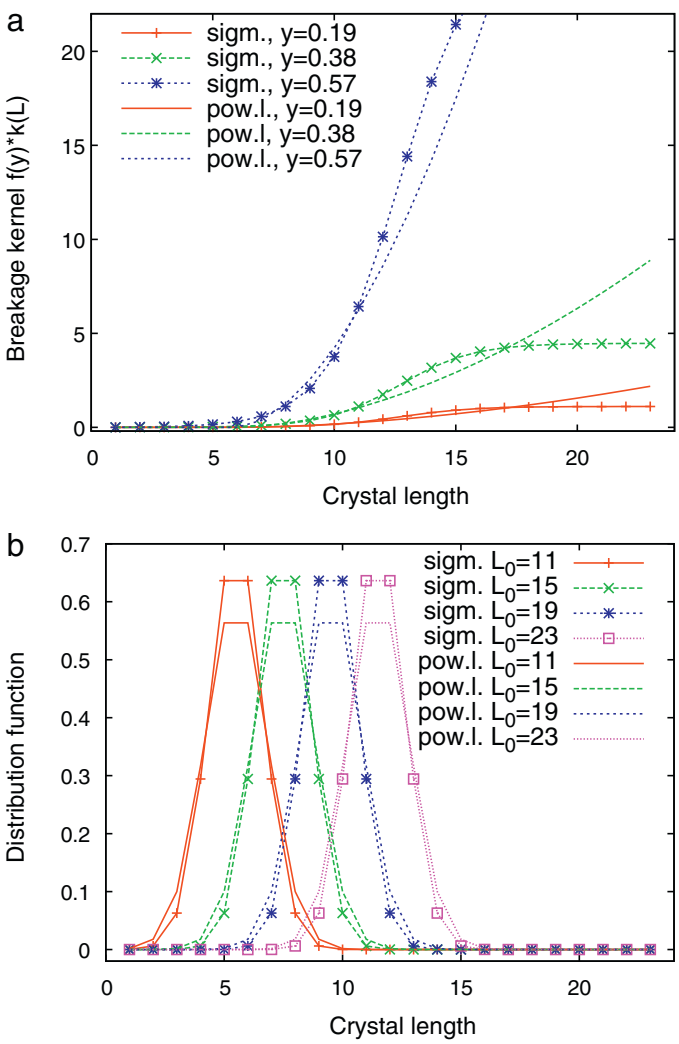

Fig. 6. (a) The breakage kernel and (b) the daughter distribution functions in PB equations.

parameter is almost exactly the same for both kernels ($a = 0.730$ vs. 0.733) and is also close to the theoretical value of the initial porosity ($\varepsilon_0 = 0.77$) of the needle-shape crystals in the DEM simulation sample. Also the optimum span of the self-similar Gaussian daughter distribution function is comparable for both cases as it is also illustrated in Fig. 6b. The values of other optimum parameters are different because of the different mathematical expressions used for the breakage kernels.

5. Experimental study

The experimental breakage study was carried out using crystals of a pharmaceutical compound, a white crystalline solid composed of needle-shaped particles with a mean length of approximately 31 μm and an aspect ratio of 70. These crystals were chosen for this study because their size, shape and fragility are characteristic of typical materials encountered during the process development for active pharmaceutical ingredients (APIs).

The uni-axial compaction breakage experiment was carried out as follows. First, approximately 4 mg of the powder was weighed out and loaded into a 3.8 mm diameter stainless steel die. The top punch was placed gently into the die, resting on top of the sample. An automatic texture analyzer (Stable Micro Systems TA.XT2i) was then used to apply force on the sample and measure the force-displacement curve. Each sample was compacted once under a normal load of 200, 400, 800, and 1600 g (corresponding to pressures of 0.173, 0.346, 0.692 and 1.381 MPa, respectively) with the punch displacement rate set to 0.1 mm/s. Once the specified compression load was achieved, the upper punch was immediately raised away from the sample. An example of typical force–displacement curves obtained in the course of a single experiment is shown in Fig. 7.

Once the sample had been compacted, it was gently pushed out of the die and into a sonication vial where it was dispersed in Isopar G with 0.25% Lecithin, which the sample is not soluble in. The sample was sonicated for 30 s intervals until the pellet was evenly dispersed in the fluid. A microscope slide was cleaned, and using a dropper, one drop was placed on the slide from approximately 1 cm above the slide. The liquid was allowed to air-dry and then the sample was visualized using an Olympus SZX16 Stereo Microscope. Ten images were randomly selected from across the width of the slide and analyzed using the Image Pro Plus software. The length, aspect ratio, and projected area were the three statistics taken from each image. From this data, particle size distributions were created and compared to an uncompacted standard.

Representative images of samples compacted to various forces can be seen in Fig. 8. The evolution of the PSD with increasing compaction load is shown in Fig. 9 and the mean particle size as a function of the compaction load is summarized in Fig. 10. It can

Author's personal copy

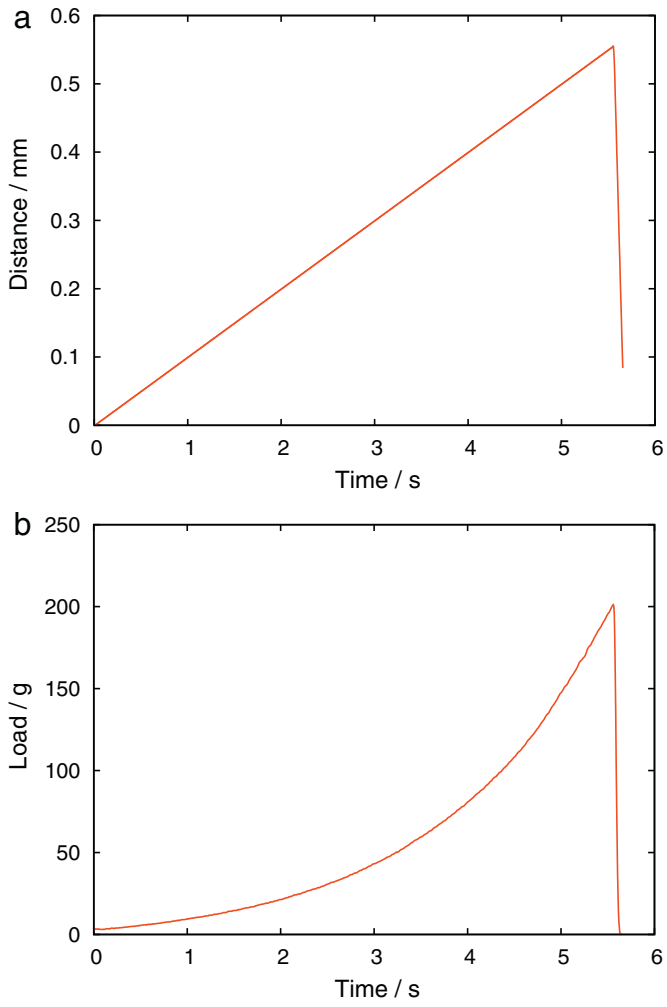

Fig. 7. Example of force displacement curves obtained in the 200 g load experiment.

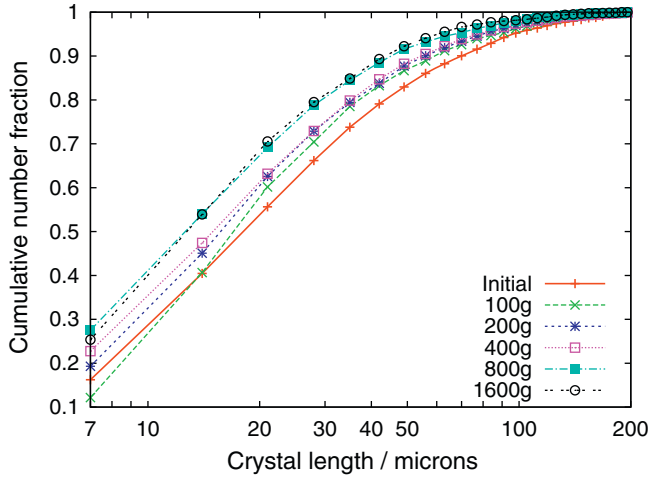

Fig. 9. Experimental PSD at different breakage forces evaluated from image analysis.

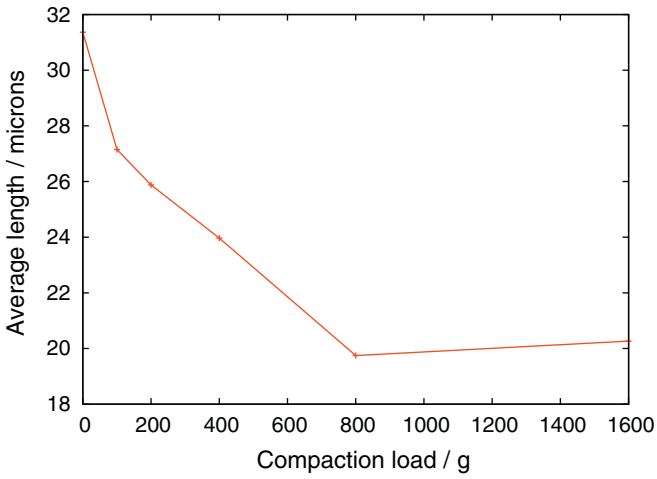

Fig. 10. Average particle size evaluated from experimental data.

Fig. 8. Images of particles used for the evaluation of particle size distribution.

Author's personal copy

Table 2
Fitting of the experimental data by PBM.

Breakage kernel, $g(F)k(L_i)$	$g(F)$	c	k_0	γ	L_0	C	U
$g(F)(L_i - L_0)^\gamma$	Eq. (14)	3.90	0.0079	1.75	0	1.1	0.0793
$\frac{g(F)}{1+\exp(-\gamma(L_i - L_0))}$	Eq. (14)	10.5	0.81	0.75	4	1.2	0.0218

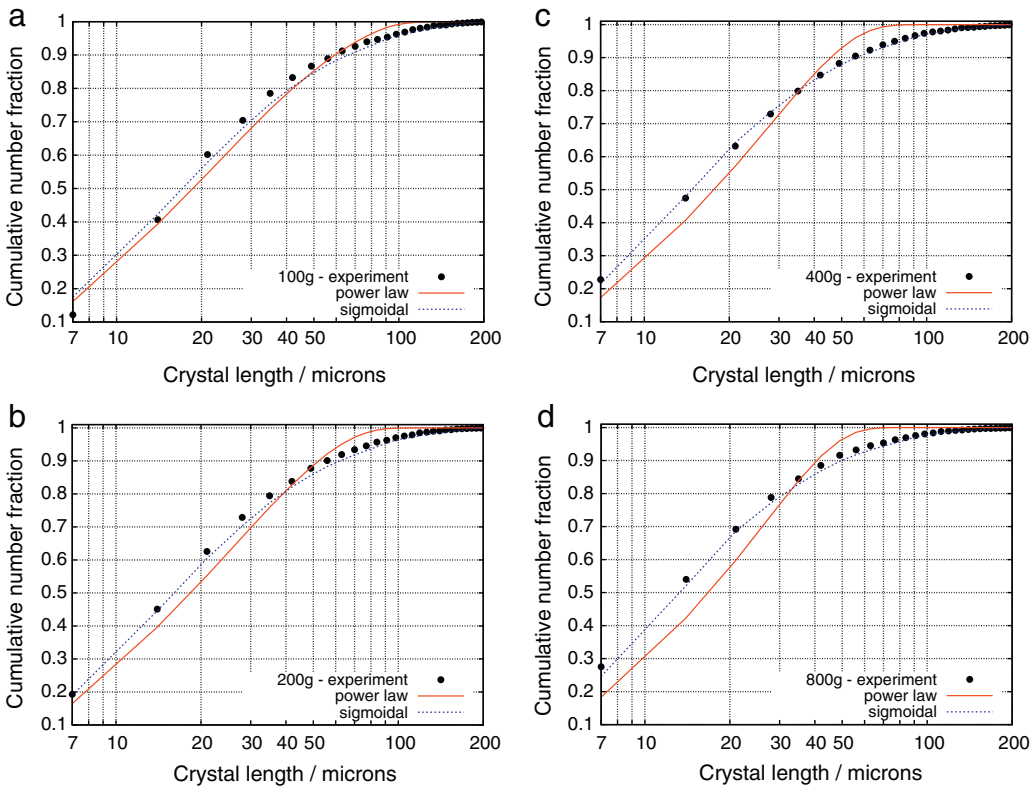

Fig. 11. Comparison of PBM with experiment.

be observed that particle size plateaus with increased compaction force, suggesting that the particles are no longer susceptible to uni-axial compaction breakage past a certain point.

6. Fitting of experimental results by PBM

The experimental data discussed in Section 5 were analyzed by the same optimization procedure that was used for the DEM data evaluation as described in Section 4. The population balance equations (15) with the compression force F as the independent variable were employed for the calculation of the number concentrations at different compressions.

After introducing the sigmoidal compression breakage kernels (24b) into the PB equations (15) with the compression force F as the independent variable, we obtain the following form of the population balance model for each size class i

$$\frac{dn_i}{dF} = k_0 \frac{2F + cF^2}{(1+cF)^2} \times \left(\frac{-n_i}{1+\exp(\gamma(L_i - L_0))} + \sum_{j=i+1}^{N} \frac{\beta_{ij} n_j}{1+\exp(\gamma(L_j - L_0))} \right). \quad (28)$$

The values of the optimum parameters and objective functions are compared in Table 2 and their graphical comparison with experimental data is shown in Fig. 11. In this case the fit is significantly better when employing the sigmoidal function. This can be explained by the particle size plateau at higher compaction forces (Fig. 10) suggesting that the particles are no longer breaking beyond a certain point and the corresponding breakage kernel indeed has a sigmoidal shape, as was observed also in the computational "experiments" by DEM.

7. Conclusions

It has been shown that computational and experimental techniques can be combined successfully into a single methodology that allows the identification of the breakage kernel and the daughter distribution functions for needle-shaped crystals, and of material-specific parameters appearing therein. A single-pass uni-axial compaction experiment has been shown to be sufficient, with no need for repeated differential breakage experiments. This approach can significantly reduce the experimental effort and therefore the time needed for the identification of the breakage kernel and daughter distribution functions and of material-specific parameters when the breakage properties of a new chemical entity (NCE) are to be determined. The approach combining modeling with experiment is particularly valuable in early-phase pharmaceutical process development when only small quantities of the NCE are often available and it is desirable to maximize the information gain from a limited number of experiments. By the combination of small-scale experimental analysis, population balance modeling, and DEM simulation, the information needed for the estimation of

Author's personal copy

in-process behavior of the powder can be obtained. Challenge areas for future research include the simulation of other modes of breakage – such as breakage under shear and breakage in the presence of capillary liquid bridges – as well as the integration of particle breakage models with large-scale CFD or DEM simulations of entire process vessels in order to predict the overall extent of breakage as a function of process-level parameters.

Acknowledgments

Financial support from the Czech Science Foundation (grant GA/104/08/P389) and the Czech Ministry of Education (project MSM 6046137306) is gratefully acknowledged.

References

Austin, L.G., 1971. Introduction to the mathematical description of grinding as a rate process. Powder Technol. 72, 1–17.
Bjorkmann, M., Holmstrom, K., 1999. Global optimization using the DIRECT algorithm in Matlab. Adv. Modell. Optimization 1, 17–36.
Bobet, A., Fakhimi, A., Johnson, S., Morris, J., Tonon, F., Yeung, R.M., 2009. Numerical models in discontinuous media: Review of advances for rock mechanics applications. J. Geotech. Geoenviron. Eng. 135, 1547–1561.
Cundall, P.A., Strack, O.D.L., 1979. A discrete numerical model for granular assemblies. Géotechnique 29, 47–65.
Favier, J.F., Abbaspour-Fard, M.H., Kremmer, M., Raji, A.O., 1999. Shape representation of axi-symmetrical, non-spherical particles in discrete element simulation using multi-element model particles. Eng. Comput. 16, 467–480.
Fuerstenau, D.W., Gutsche, O., Kapur, P.C., 1996. Confined particle bed comminution under compressive loads. Int. J. Miner. Process. 44-45, 521–537.
Fuerstenau, D.W., De, A., Kapur, P.C., 2004. Linear and nonlinear particle breakage processes in comminution systems. Int. J. Miner. Process. 74S, S317–S327.
Grof, Z., Kohout, M., Stepanek, F., 2007. Multi-scale simulation of needle-shaped particle breakage under uniaxial compaction. Chem. Eng. Sci. 62, 1418–1429.
Gupta, V.K., Hodouin, D., Berube, E.A., Everell, M.D., 1981. The estimation of rate and breakage distribution parameters from batch grinding data for a complex pyritic ore using a back-calculation method. Powder Technol. 28, 97–106.
Hill, P.J., Ng, K.M., 1997. Simulation of solids processes accounting for particle-size distribution. AIChE J. 43, 715–726.
Hill, P.J., 2004. Statistics of multiple particle breakage accounting for particle shape. AIChE J. 50, 937–952.
Kalman, H., 2000. Particle breakage and attrition. Kona 18, 108–120.
Kawakita, K., Lüdde, K.H., 1971. Some considerations on powder compression equations. Powder Technol. 4, 61–68.
Kelly, E.G., Spottiswood, D.J., 1990. The breakage function: what is it really? Minerals Eng. 3, 405–414.
Ketterhagen, W.R., am Ende, M.T., Hancock BC, 2008. Process modeling in the pharmaceutical industry using the discrete element method. J. Pharm. Sci. 98, 442–470.
Khanal, M., Schubert, W., Tomas, J., 2005. DEM simulation of diametrical compression test on particle compounds. Granul. Matter 7, 83–90.
Kostoglou, M., 2007. The linear breakage equation: from fundamental issues to numerical solution techniques. In: Salman, A.D., Ghadiri, M., Hounslow, M.J. (Eds.), Handbook of Powder Technology, vol. 12 – Particle Breakage. Elsevier, Amsterdam, pp. 793–835.
Müller, M., Meier, U., Wieckhusen, D., Beck, R., Pfeffer-Hennig, S., Schneeberger, R., 2006. Process development strategy to ascertain reproducible API polymorph manufacture. Cryst. Growth Des. 6, 946–954.
Perttunen, C.D., Jones, D.R., Stuckman, B.E., 1993. Lipschitzian optimization without the lipschitz constant. J. Optimiz. Theory App. 79, 157–181.
Rajniak, P., Dhanasekharan, K., Sinka, C., MacPhail, N., Chern, R., 2008. Modeling and measurement of granule attrition during pneumatic conveying in a laboratory scale system. Powder Technol. 185, 202–210.
Sathyagal, A.N., Ramkrishna, D., Narsimhan, G., 1995. Solutions of inverse problems in population balances: II. Particle break-up. Comput. Chem. Eng. 19, 437–451.
Vanni, M., 2000. Approximate population balance equations for aggregation-breakage processes. J. Colloid Interf. Sci. 221, 143–160.
Weichert, R., 1992. Application of defect statistics and fracture mechanics for describing comminution processes. Zement-Kalk-Gips Int. 3, 51–57.
Yu, Z.Q., Chew, J.W., Chow, P.S., Tan, R.B.H., 2007. Recent advances in crystallization control: an industrial perspective. Chem. Eng. Res. Des. 85 (A7), 893–905.

8.3 Distribution of breakage events in random packings of rodlike particles

Zdeněk Grof
František Štěpánek

Published in the *Phys. Rev. E*, Vol. 88, 2013, art.no. 012205
DOI: 10.1103/PhysRevE.88.012205.

Distribution of breakage events in random packings of rodlike particles

Zdeněk Grof and František Štěpánek
Department of Chemical Engineering, Institute of Chemical Technology Prague, Technická 5, 166 28 Prague 6, Czech Republic
(Received 19 December 2012; published 18 July 2013)

Uniaxial compaction and breakage of rodlike particle packing has been studied using a discrete element method simulation. A scaling relationship between the applied stress, the number of breakage events, and the number-mean particle length has been derived and compared with computational experiments. Based on results for a wide range of intrinsic particle strengths and initial particle lengths, it seems that a single universal relation can be used to describe the incidence of breakage events during compaction of rodlike particle layers.

DOI: 10.1103/PhysRevE.88.012205 PACS number(s): 81.05.Rm, 45.50.Jf, 45.70.−n, 46.50.+a

I. INTRODUCTION

Birds' nests, anthills, or haystacks are examples of structurally stable pseudorandom packings of rodlike particles—that is, particles with a large aspect ratio. Packings of rodlike particles are also found in diverse man-made systems, such as filter cakes of needle-shaped crystals often encountered in the pharmaceutical industry [1]. When a randomly packed layer of rodlike particles is subjected to stress either due to its own weight or due to an externally applied force, it is of both fundamental and practical interest to establish the relationship between the magnitude of the applied stress and the degree of compaction of the layer. If the underlying particles are fragile, a complex cascade of breakage events can occur in response to the applied stress [2], leading to an evolution of the particle length distribution. This, in turn, affects the structure and porosity of the packing. The transmission of forces in the layer [3–5] and the distribution of the breakage events depend on a number of factors including the length distribution of the particles, their intrinsic strength, and the degree of disorder in the packing. In this paper, a scaling relationship between the number of breakage events and the applied stress is derived and compared with numerical experiments using the discrete element method (DEM).

II. METHODOLOGY

Let us first derive a scaling relationship between the applied stress and the extent of breakage in a packed layer of rodlike particles. Consider a layer of unit horizontal area initially containing M_0 particles of the same length L_0, compacted from the top by a steadily increasing global stress σ. Breaking all particles at once into two equal fragments creates the next generation of the packing. The number and length of particles in the nth generation are

$$M_n = 2^n M_0 \quad \text{and} \quad L_n = L_0/2^n. \tag{1}$$

A particle will break [6] if the local bending moment acting on it, $F_{\mathrm{loc},n}L_n$, exceeds the strength of the particle, σ_{mat}, i.e., if $F_{\mathrm{loc},n} = \alpha\sigma_{\mathrm{mat}}/L_n$, where the proportionality constant α depends on the particle loading pattern. Our earlier simulations and experiments confirmed that rodlike particles in a random packing break preferentially in the middle during pseudostationary compaction [7]. This is not necessarily true in cases where particles are flexible enough to be able to bend to a large extent, e.g., spaghetti [8], or when fragmentation is the result of dynamic rather than pseudostationary loading forces, as in impact fragmentation [9–12].

Let C_n denote the number of force chains per horizontal area that mediate the transmission of the compacting vertical stress $\sigma(n)$ through the packing. Then, on average, the local force will be $F_{\mathrm{loc},n} = \sigma(n)/C_n$. Assuming that the packing topology remains self-similar, the number of force chains scales with the number of particles according to $C_n = \beta M_n^{2/3}$ (cf. the Appendix). Combining the above relations eliminates $F_{\mathrm{loc},n}$ and results in a relationship between the breakage generation and the loading stress,

$$\sigma(n)/\sigma_{\mathrm{mat}} = (2^n)^{5/3}\alpha\beta M_0^{2/3} L_0^{-1}. \tag{2}$$

Assuming that particles break as soon as the local stress exceeds their strength, allowing noninteger particle generation and expressing the actual number of particles in the packing $M(n)$ instead of the generation number n completes the derivation:

$$M(n) = M_0 + (L_0 M_0)^{3/5}(\alpha\beta)^{-3/5}[\sigma(n)/\sigma_{\mathrm{mat}}]^{3/5}. \tag{3}$$

This scaling law has been derived on the assumption that, as particle length decreases, the packing structure remains self-similar. However, this assumption cannot be justified in the whole range of applied stresses and will not be valid for too small or too large stresses. Starting with small stresses, one can expect particle rearrangement and layer compaction to take place instead of particle breakage. Below a certain $\sigma/\sigma_{\mathrm{mat}}$ limit, the number of particles and their length will not depend on the applied stress at all. The self-similarity assumption cannot hold at too large relative stresses either. If the aspect ratio of rodlike particles decreases beyond a threshold, the number of contacts per rod is no longer constant [13]. Therefore, the parameter β related to the number of force chains will not be constant any longer. Furthermore, other fracture mechanisms than a "clean" breakage into two fragments, e.g., crushing or denting, become more significant at larger stresses. In the course of computational experiments a wide range of stresses has to be used in order to both verify the scaling law exponent and identify an appropriate interval of stresses for the scaling law. Another relationship would hold outside the interval.

To verify the scaling relationship, a discrete element method simulation using multielement particles [14] has been applied in computational *in silico* experiments. Rodlike particles are approximated by a string of spherical elements and the

 ©2013 American Physical Society

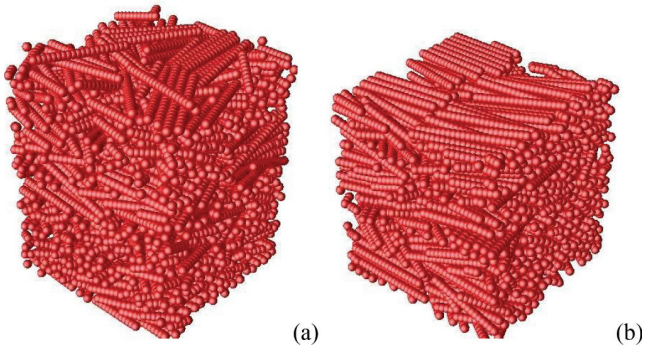

FIG. 1. (Color online) Rodlike particle packing before compression with random $\lambda = 0$ (a) and uniaxial $\lambda = 1$ (b) orientation.

particles move according to Newton's laws of motion in response to the interparticle contact forces, contact forces with external boundaries, and the gravitational force. At each time step, the stress acting on each particle is evaluated and the particle is broken at a point where the local stress exceeds the particle strength σ_{mat} if such a point exists. Two daughter particles are created from one mother particle during a breakage event. A detailed description of the computational algorithm has been given in [15].

The computational experiment proceeds as follows: (i) A packing of 760, 1140, or 1520 rodlike particles each consisting of 20, 15, or 10 elements (depending on the required initial particle length) is created by depositing the particles into a computational box with periodic boundary conditions in the x and the y directions and a flat horizontal bottom wall at a fixed z position. In addition to random packings, also uniaxially oriented packings have been created by applying a torque to a fraction λ of the particles during their deposition into the layer. The magnitude of the torque has been deliberately set small to allow imperfection in the particle alignment even for cases when $\lambda = 1$. The structure of the packing is illustrated in Fig. 1 and the obtained degree of uniaxial orientation is shown in Table I. As can be seen from the table and subsequent results, only packings with $\lambda \geqslant 0.75$ can be considered to have partially uniaxial orientation. (ii) A second wall free to move along the z axis is placed above the packing and its mass is slowly increased, which gradually increases the stress acting on the packing and leads to sequential particle breakage. (iii) The change of particle size (length) distribution is recorded during the simulation and can be conveniently described by the number-mean particle length L which gradually decreases as the compression stress σ increases. The number-mean particle length is related to the number of breakage events $[M(\sigma) - M_0]$ that have occurred since the initial state by $L(\sigma) = M_0 L_0 / M(\sigma)$. In this paper we focus on the number of breakage events from which the number-mean particle length can be obtained.

TABLE I. Degree of uniaxial orientation (fraction of particles deviating from the alignment axis by less than 12°).

λ	0.00	0.25	0.50	0.75	1.00
Fraction (%)	8.1	8.5	11.1	14.8	39.5

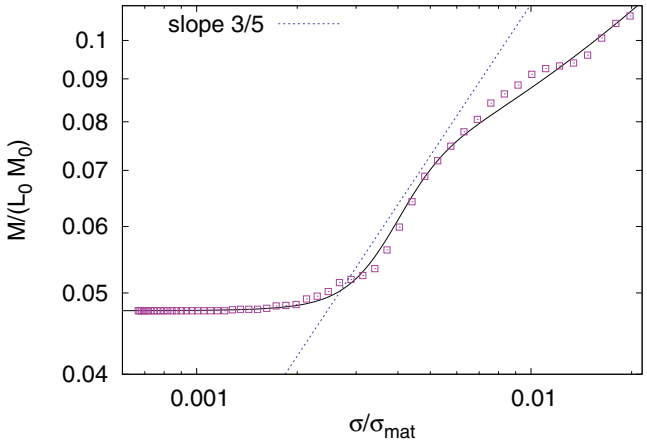

FIG. 2. (Color online) Illustration of progress of breakage events during a single numerical experiment.

III. RESULTS AND DISCUSSION

The progress of breakage events recorded within a random packing during a single numerical experiment is shown in Fig. 2. Initially, the particle layer responds to increasing stress by consolidation without breakage [16]. Once a certain critical value of the compaction stress is exceeded, breakage occurs and the number of particles starts to increase significantly. However, the rate of breakage then decreases and an asymptotic dependence of the number of particles on the applied stress is approached.

The data points for various values of σ_{mat} can be brought closer together if an effective stress $\hat{\sigma}$ defined by

$$\hat{\sigma} = (\sigma + w)/\sigma_{\text{mat}} \tag{4}$$

is used instead of $\sigma/\sigma_{\text{mat}}$. In the previous equation, w is a correction factor to account for breakage due to its own weight of the particle layer, i.e., the mean stress due to particle weight. The value of $w = 1.269$ has been calculated as one-half of the layer weight divided by the horizontal cross-section area. The effect of this correction is demonstrated in Fig. 3. The correction is significant only for particles with small σ_{mat}: as σ_{mat} increases, the effect of the weight of the packing on particle breakage diminishes.

In order to compare the theoretical scaling law with numerical experiments, simulations of compaction and breakage starting from packings of three different lengths L_0 and a broad range of intrinsic particle strength σ_{mat} have been carried out. The results are summarized in a double logarithmic plot in Fig. 4. Figure 4(a) is color coded according to the initial particle length and Fig. 4(b) according to the particle strength. As can be seen, all initially distinct data point groups approach a single trend line at higher effective stress $\hat{\sigma}$.

Recalling that the physical meaning of $M(\hat{\sigma})/(M_0 L_0)$ on the y axis is a reciprocal value of the number-mean particle length $1/L(\hat{\sigma})$, the results indicate that at sufficiently high $\hat{\sigma}$, the packing behavior is no longer dependent on the initial state and a single value of the mean-particle length can be assigned to a particular value of $\hat{\sigma}$. This "equilibrium" length will further be denoted by $L^*(\hat{\sigma})$. The transient behavior at low $\hat{\sigma}$ will be discussed later; let us now focus on the asymptotic

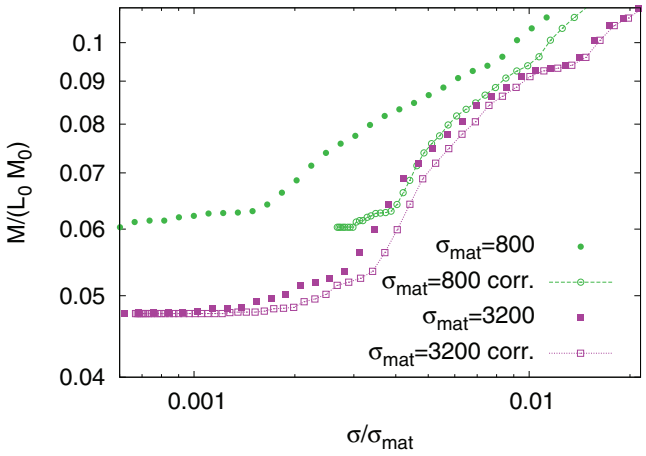

FIG. 3. (Color online) Correction to account for the breakage due to its own weight of the particle layer. The closed unconnected symbols represent uncorrected data ($\sigma/\sigma_{\rm mat}$), while open connected symbols represent data with correction $[(\sigma + w)/\sigma_{\rm mat}]$. It can be seen that the correction is significant for particles with small $\sigma_{\rm mat}$ only.

scaling behavior at large $\hat{\sigma}$ and compare the numerical results with the theoretical derivation presented above. The scaling law evaluated from the simulations is

$$M(\hat{\sigma})/(M_0 L_0) = 1/L^*(\hat{\sigma}) \approx q\hat{\sigma}^{0.37} \quad \text{at high } \hat{\sigma} \qquad (5)$$

where there is a small dependence of q on $\sigma_{\rm mat}$. As Fig. 4 demonstrates, there is a scaling between the number-mean particle length and the applied stress, but the scaling exponent has a value of 0.37 rather than the theoretically expected slope of 3/5. The derivation of the theoretical scaling law was based on the assumption of a self-similar particle packing, and hence a constant number of force chains per particle. However, as the layer is compacted and the length (and thus aspect ratio) of the particles changes, this assumption may not be valid. Indeed, Philipse [13] has shown that a constant value of the coordination number of 10.8 is reached in packings of rodlike particles in the limit of high aspect ratios, but deviates from this value when the aspect ratio is lower. For an aspect ratio of 1 (i.e., spheres, which may be considered as the ultimate stage of breakage), the probability that a particle is part of a force chain approaches unity [17] for high applied stress. Thus, if the theoretical equation (3) is rederived using a general relationship between the number of force chains and the number of particles of the form $C_n = \beta M_n^a$ then Eq. (3) becomes

$$M(n) = M_0 + (L_0 M_0)^b (\alpha\beta)^{-b} [\sigma(n)/\sigma_{\rm mat}]^b, \qquad (6)$$

where $b = 1/(a+1)$. The exponent $b = 0.37$ evaluated from the numerical simulation would then correspond to $a = 1.70$, which is higher than the theoretical value of $a = 2/3$ for self-similar packings.

A more detailed view of the evolution of the number of breakage events and the resulting particle length during the compression of the particle packing is given in Fig. 5, which also illustrates the initial transients. The number of breakage events $[M(\hat{\sigma}) - M_0]$ can be described by a sigmoidal

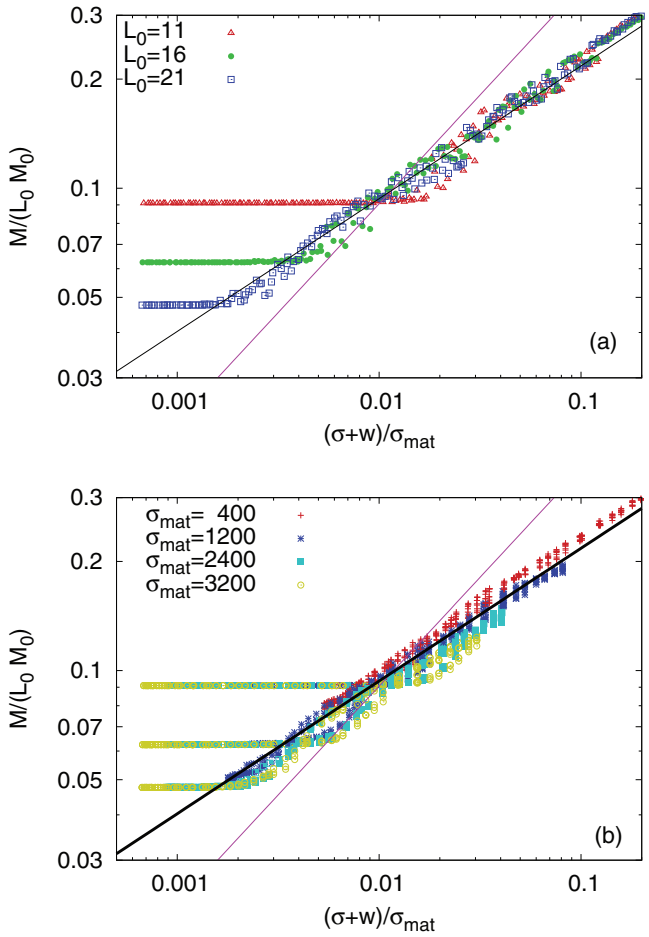

FIG. 4. (Color online) Double-logarithmic plot showing the dependence of the reciprocal number-mean particle length $1/L = M/(M_0 L_0)$ on the effective stress $\hat{\sigma} = (\sigma + w)/\sigma_{\rm mat}$. Data are annotated according to (a) the initial particle length L_0 or to (b) the particle strength $\sigma_{\rm mat}$. The two solid lines have slopes 0.37 and 3/5.

function

$$\frac{M - M_0}{(L_0 M_0)^{3/5}} = \frac{p_1 \hat{\sigma}^{3/5}}{1 + \exp[p_3(p_2 - \hat{\sigma}^{3/5})]}, \qquad (7)$$

where the parameters p_1, p_2, and p_3 have been set individually for each value of $\sigma_{\rm mat}$ and are summarized in Table II. Three regions can be identified in the dependence of the breakage number on the compaction stress: (i) a constant value of M or L at low effective stress $\hat{\sigma}$ where no breakage occurs, only consolidation of the layer; (ii) a transition region at medium stress ($\hat{\sigma} \approx 0.03$–$0.05$) characterized by intensified breakage, and (iii) a constant-slope region at a higher stress where breakage events proceed at a slower rate than in the transition

TABLE II. Values of parameters p_1, p_2, and p_3 in Eq. (7) obtained by a nonlinear fit of random packing data.

$\sigma_{\rm mat}$	3200	2400	1600	1200	800	400
p_1	30	32	34	34	35	38
$p_2/10^{-2}$	3.5	3.4	3.2	3.0	2.9	
p_3	270	260	230	210	170	

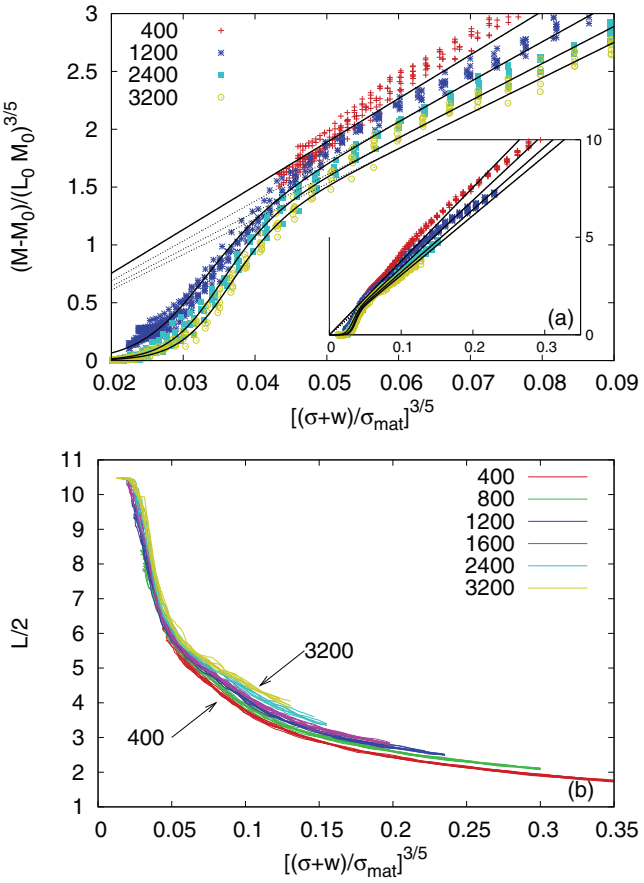

FIG. 5. (Color online) (a) Number of breakage events $M - M_0$ and (b) particle aspect ratio $L/2$ dependence on the effective compression stress $\hat{\sigma} = (\sigma + w)/\sigma_{\mathrm{mat}}$ for random packings of various particle strengths σ_{mat} and initial particle length $L_0 = 21$. The solid lines in (a) correspond to the sigmoidal function defined by Eq. (7).

region (this is the asymptotic scaling behavior discussed above).

It is interesting to note that while the scaling exponent in the asymptotic region deviates from the theoretical one, a detailed view of the transition region (Fig. 2) reveals good agreement with the theoretical value of $3/5$. Thus, it can be concluded that the assumptions under which the theoretical scaling law has been derived are valid only in this transition region. The transition region is characterized by a high incidence of breakage events—it follows a phase where the layer has been compacted without breakage due to the low value of the applied stress. Once a certain critical value of the applied stress is exceeded, a rapid cascade of breakage events occurs, as can be seen in Fig. 5(b). Since particle breakage rather than layer consolidation is the predominant response to the applied stress in this region, the conditions of self-similar packing structure on which the theoretical derivation was based are most accurately satisfied.

It can be expected that the number of contacts per particle may change depending on the orientation of the particles in the layer [18]. A comparison of random and uniaxially oriented packings is shown in Fig. 6. On average, particles in a uniaxially oriented packing break at a higher stress than those in a random packing under otherwise identical conditions. It

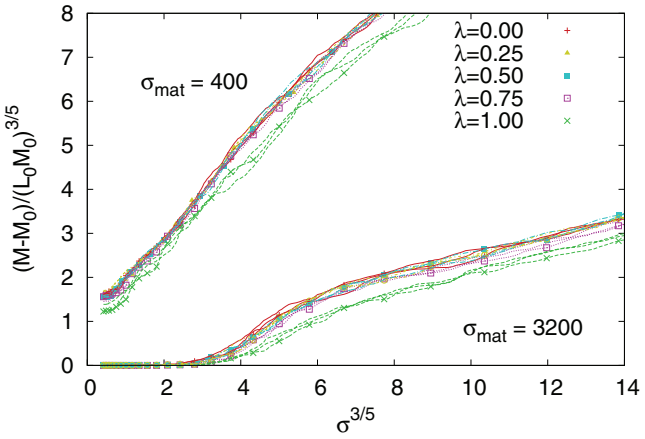

FIG. 6. (Color online) Dependence of the number of breakage events $M - M_0$ on the stress σ for packings of various degrees of particle orientation λ.

means that at the same stress, the length of particles in a more ordered packing will be larger. This effect can be explained by the fact that, on average, there are more particle contacts in ordered than in random packings. As the effective stress σ is distributed among a larger number of contacts, the local stress at each contact is smaller, making ordered packing less susceptible to breakage than a random one.

IV. CONCLUSIONS

The relationship between the extent of breakage and the applied stress [Fig. 4 or 5(b)] can be interpreted as a phase map dividing the length-stress plane into two regions—a "forbidden" region in which particles of a given length cannot survive since they cannot withstand the local stress, and a "feasible" region, in which particles of a given length can survive within the layer. Since this relationship has been expressed using dimensionless variables (the dimensionless stress $\hat{\sigma}$ and particle aspect ratio) and has been calculated for a wide range of initial particle lengths and intrinsic particle strengths, it can be regarded as universal. As such, it can be used for the prediction of particle breakage rates and breakage kernels for population balances in a diversity of situations where rodlike particle packings are exposed to uniaxial stress.

ACKNOWLEDGMENT

F.S. would like to acknowledge support from MSMT via Grant No. LH12115 (MultiGRAN).

APPENDIX: DERIVATION OF THE RELATIONSHIP BETWEEN THE NUMBER OF PARTICLES AND THE NUMBER OF FORCE CHAINS

Let us suppose a particle layer at rest between two infinite parallel horizontal planes, supporting a vertical stress exerted on the layer by the upper plane. Let us place a representative cube with side δ into the layer. The number of force chains C through which stress propagates from the top to the bottom layer will be proportional to the horizontal area of

the representative cube, i.e., $C \propto \delta^2$. The number of particles present in the cube M will be proportional to the volume of the cube, i.e., $M \propto \delta^3$ or $\delta \propto M^{1/3}$. Consequently, the relation between the number of particles and the number of force chains in a vertically stressed particle layer will scale as $C \propto (M^{1/3})^2$ and therefore

$$C = \beta M^{2/3} \tag{A1}$$

where β is a constant dependent on the structure of the packing. This justifies the $2/3$ exponent used for a derivation in Sec. II.

[1] C. S. MacLeod and F. L. Muller, Org. Process Res. Dev. **16**, 425 (2012).
[2] N. V. Mantzaris, J. Phys. A **38**, 5111 (2005).
[3] T. S. Majmudar and R. P. Behringer, Nature (London) **435**, 1079 (2005).
[4] J. F. Peters, M. Muthuswamy, J. Wibowo, and A. Tordesillas, Phys. Rev. E **72**, 041307 (2005).
[5] M. E. Cates, J. P. Wittmer, J.-P. Bouchaud, and P. Claudin, Phys. Rev. Lett. **81**, 1841 (1998).
[6] G. R. McDowell and M. D. Bolton, Geotechnique **48**, 667 (1998).
[7] Z. Grof, C. M. Schoellhammer, P. Rajniak, and F. Stepanek, Int. J. Pharm. **407**, 12 (2011).
[8] B. Audoly and S. Neukirch, Phys. Rev. Lett. **95**, 095505 (2005).
[9] J. R. Gladden, N. Z. Handzy, A. Belmonte, and E. Villermaux, Phys. Rev. Lett. **94**, 035503 (2005).
[10] L. Pauchard and J. Meunier, Phys. Rev. Lett. **70**, 3565 (1993).
[11] G. Timar, F. Kun, H. A. Carmona, and H. J. Herrmann, Phys. Rev. E **86**, 016113 (2012).
[12] H. Katsuragi, D. Sugino, and H. Honjo, Phys. Rev. E **68**, 046105 (2003).
[13] A. P. Philipse, Langmuir **12**, 1127 (1996).
[14] J. F. Favier, M. H. Abbaspour-Fard, M. Kremmer, and A. O. Raji, Eng. Comput. **16**, 467 (1999).
[15] Z. Grof, M. Kohout, and F. Stepanek, Chem. Eng. Sci. **62**, 1418 (2007).
[16] P. Richard, Nat. Mater. **4**, 121 (2005).
[17] H. A. Makse, D. L. Johnson, and L. M. Schwartz, Phys. Rev. Lett. **84**, 4160 (2000).
[18] F. X. Villarruel, B. E. Lauderdale, D. M. Mueth, and H. M. Jaeger, Phys. Rev. E **61**, 6914 (2000).

8.4 Quantifying the effect of fillers on the breakage behaviour of needle-shaped particles

Zdeněk Grof
František Štěpánek

Published in the *Adv. Powder Technol.*, Vol 27, 2016, pp. 1093–1100
DOI: 10.1016/j.apt.2016.03.018.

Advanced Powder Technology 27 (2016) 1093–1100

Contents lists available at ScienceDirect

Advanced Powder Technology

journal homepage: www.elsevier.com/locate/apt

Original Research Paper

Quantifying the effect of fillers on the breakage behaviour of needle-shaped particles

Zdeněk Grof*, František Štěpánek

Department of Chemical Engineering, University of Chemistry and Technology Prague, Technická 5, 166 28 Prague 6, Czech Republic

ARTICLE INFO

Article history:
Received 27 July 2015
Received in revised form 10 March 2016
Accepted 18 March 2016
Available online 26 March 2016

Keywords:
DEM
Composite packings
Compaction
Force chains
Breakage

ABSTRACT

Understanding the relationship between the applied stress and the behaviour of packings of breakable granular particles is required in many chemical engineering applications. A pharmaceutical tablet is an example where a composite packing (a packing containing a mixture of several kinds of particles) is compacted in the process of tablet formation. In this work, the unidirectional compaction and the breakage processes in composite packings formed from a mixture of breakable needle-shaped crystals and elastic spherical filler particles were studied using a Discrete Element Method (DEM) simulation. The evolution of crystal size distribution and contacts topology with the increasing stress was computed for different relative size, volume fraction and elasticity of filler particles inside the packing. We show that crystals breakability in a packing is directly related to the number of contacts among particles and that it can be significantly influenced by an appropriate choice of added filler particles. The results can be used for the development of mathematical models that describe the pharmaceutical tablet production and other processes involving composite packings of fragile particles.

© 2016 The Society of Powder Technology Japan. Published by Elsevier B.V. and The Society of Powder Technology Japan. All rights reserved.

1. Introduction

Packings of breakable granular particles are often present in both nature and various industrial processes, including pharmaceutics, food, cosmetics and fertilizers. Because of the enormous richness and complexity of granular motion [1], processes involving the handling of granular materials still present a challenging engineering problem. To design such processes, it is necessary to understand and be able to quantitatively describe how the particle packing responds to various kinds of stress fields and how the particle size distribution changes as a result of external stress fields (particle breakage).

When a particle packing is subjected to stress, the breakage of individual particles depends on the way the forces are transmitted through the packing. It is known that the stress propagates along force chains [2,3], i.e., through just a fraction of contacts that form a percolating network in the packing. The force chains have been observed by both experimental [4,5] and computational [6–9] techniques. The relationship between an externally applied stress and the magnitude of local forces, which are experienced by the particles and eventually cause them to break, is not clear, but most probably strongly depends on the particle coordination number and the contacts topology. The topology changes as particles rearrange and break inside the packing during its compaction. In granular physics research, packings of spheres have been well studied, while considerably less attention has been given to packings of anisotropic particles [10–16] or packings containing a mixture of several different kinds of particles (composite packings) [17,18].

An example of a composite particle packing can be found in a pharmaceutical tablet. Before tablet compaction, the active pharmaceutical ingredient (API), often present in the form of fragile needle-shaped crystals [19], is mixed with other particles called excipients that have different roles in the tablet (e.g. fillers, disintegrants, controlled release polymers, etc.). In order to maintain consistent product properties and defined dissolution profiles of the API, it is essential to understand the changes of particle size distribution that may occur during the material handling and tableting steps. The properties of single-component needle-shaped particle packings, including an investigation of particle breakage, were discussed in our previous papers [20–22]. The presence of an additional kind of particle in the packing can alter its compaction and breakage properties, but the extent of such change is currently not well understood.

Therefore, the aim of the present work is to investigate the breakage processes that occur during the unidirectional compaction of composite packings formed from a mixture of

* Corresponding author.
E-mail addresses: zdenek.grof@vscht.cz (Z. Grof), frantisek.stepanek@vscht.cz (F. Štěpánek).

http://dx.doi.org/10.1016/j.apt.2016.03.018
0921-8831/© 2016 The Society of Powder Technology Japan. Published by Elsevier B.V. and The Society of Powder Technology Japan. All rights reserved.

fragile needle-shaped crystals and elastic spherical filler particles. Using a Discrete Element Method (DEM) simulation, the evolution of particle size distribution and contacts topology with increasing stress was computed for different relative sizes, volume fractions and elasticities of the filler particles within the packing. We show that the susceptibility of particles to break in a packing is directly related to the number of contacts among the particles and that this parameter can be significantly influenced by an appropriate choice of added filler particles. The results can be used for the development of mathematical models that describe the pharmaceutical tablet production and other processes involving composite packing of fragile particles subjected to external stress fields.

2. Methodology

DEM was used for the preparation of granular packings and for the simulation of their unidirectional compaction between two parallel walls. The packing was formed from two kinds of particles: needle-shaped breakable crystals and spherical non-breakable fillers. The needle-shaped crystals were represented by the multi-element method [23] as compound particles consisting of overlapping spherical elements with radius r_C; relative positions among elements were fixed so the particle moves as a rigid body. During a simulation, the load on the particle is regularly updated and when it exceeds a set threshold, the particle is divided (broken) into two. The algorithm details are presented in our earlier paper [20] and the values of model parameters are reported in Table 1. The second kind of particles, further called fillers, are just spherical particles with a radius r_F and can have different mechanical properties (such as elastic modulus) than the crystals.

The mixed packings were prepared by placing crystals and fillers at random position (but in such a way they initially do not overlap) inside a simulation box and letting the particles settle to the bottom wall under gravity acting along the z axis. Periodic boundary conditions were applied along the x and y axes. The mixed packing can be characterised by two parameters: (i) the relative size of fillers compared to the size of crystals, $R = r_F/r_C$ and (ii) the volume fraction of fillers in the packing $\phi_F = V_F/(V_F + V_C)$, where V_F and V_C represent the volume of all filler and crystal particles in the packing, respectively.

Examples of mixed packings with various parameters R and ϕ_F are shown in Fig. 1. When forming the packings, the initial number of crystals n_{C0} and fillers n_F were chosen in such a way that the prescribed packing parameters are met and also that the volume of all particles $V_F + V_C$ is similar in all packings. Thus, the number of crystals n_{C0} varied between 450 and 1150 for packings with high and low filler volume ratio ϕ_F, respectively, and the number of filler particles n_F varied between 0 and 45000. All crystals initially consisted of $N_0 = 20$ elements and had the same initial length $L_0 = (N_0 + 1)r_C$. The ratio between the simulation box size and the initial length of crystal particles is 2. Therefore, even with periodic boundary condition, the boundary effect between longest crystals in prepared packings cannot be completely excluded. The segregation was also observed in packings with some particular combination of R and ϕ_F: the extent of segregation effect will be discussed separately at the end of the Results & discussion section.

Table 1
Parameter values used in simulations.

η_t	Global damping of the translation	158 s^{-1}
g	Gravitational acceleration	10 m/s^2
m_C	Mass of element	8.4 mg
r_C	Radius of element	1 mm
k	Elastic modulus	2005 N/m
b	Particle strength: maximum stress	641.68 or 320.84 kPa

The packing compaction and crystals breakage was then simulated by placing a top wall above the packing. The packing was compressed between the top and bottom walls by gradually increasing the weight of the top wall while keeping the position of the bottom wall fixed. As the stress propagating through the packing increased, the load on individual crystals increased as well, eventually leading to their breakage.

The following parameters were recorded at every time step i during the computational experiment: the number of crystals n_{Ci}, the number of contacts between various kinds of particles (m_{CCi}, m_{CFi} and m_{FFi} for crystal-crystal, crystal-filler and filler-filler contacts, respectively), the mean and the variance of local forces acting at particle contacts, the polydispersity index Z_i which characterises the width of the crystal length distribution, the void fraction (porosity) of the packing ε_i, and the overall dimensionless stress σ_i acting on the packing

$$\sigma_i = \left(\frac{F_i^{top}}{k_{CC} r_C}\right) \Big/ A \qquad A = A'/r_C^2. \tag{1}$$

The symbols F_i^{top} and A' in Eq. (1) are the weight and the area of the top wall and k_{CC} is the elastic modulus (stiffness) of the linear spring characterising the local force at contacts between crystals.

In addition, several packing characteristics independent of the packing size and comparable between different packings were also calculated: The average crystal length L_i

$$L_i = \left(\frac{N_0 n_{C0}}{n_{Ci}} + 1\right) r_C, \tag{2}$$

which is inversely proportional to the number of crystal breakage events ($n_{Ci} - n_{C0}$). The average length between two contacts supporting the crystals, d_i, which is defined as

$$d_i = \frac{(N_0 + 1)\, n_{C0}\, r_C}{2m_{CCi} + m_{CFi}}, \tag{3}$$

where the numerator corresponds to the total length of all crystals and the denominator is the number of crystal contacts. Finally, the filler coordination number

$$E_i = \frac{2m_{FFi} + m_{CFi}}{n_F} \tag{4}$$

characterises the contact network among the filler particles.

3. Results & discussion

The effect of two packing parameters, namely the relative size $R = r_F/r_C$ and the volume fraction $\phi_F = V_F/(V_F + V_C)$ of spherical filler particles admixed to a random packing of needle-shaped crystals, was studied in the course of DEM computational experiments. The maximum stress (shear or bending) a crystal is able to withstand before it breaks was first set to a value that ensured the crystals did not break just due to their own weight in the packing, but were sufficiently fragile to undergo fragmentation during uniaxial compaction of the packing. Apart from packings with the default setting of the crystal strength, also packings consisting of "weak" crystals whose breakage threshold was set to one half of the threshold for regular crystals were prepared.

The results (Fig. 2) show that the addition of fillers into the packing generally postpones crystal breakage to higher compaction stresses σ; the average crystal length L starts to decrease at higher values of σ. In other words, the crystals of a particular length can hold up until higher stresses in composite packings containing fillers than in the packings of crystals only. This difference increases with increasing volume fraction of the fillers and decreasing relative filler size. It can be seen, for example, that weak crystals can withstand similar stresses as regular crystals if they

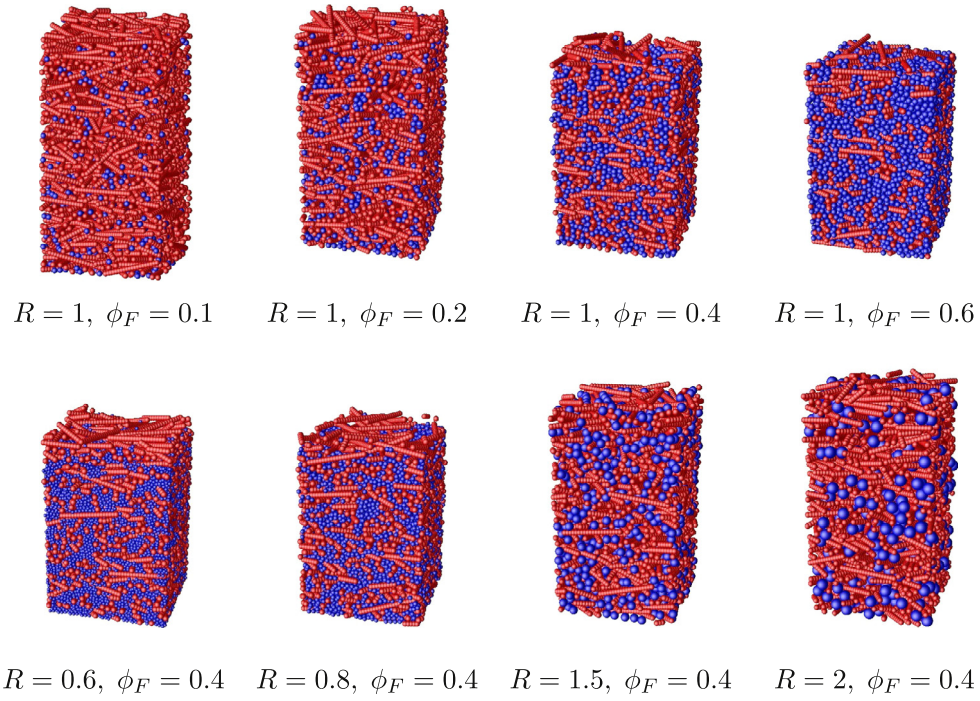

Fig. 1. Illustration of different composite packings before compaction. Crystals are pictured in red and fillers in blue colour. Packing parameters are the relative size $R = r_F/r_C$ and volume fraction ϕ_F of filler particles. (For interpretation of the references to colour in this figure legend, the reader is referred to the web version of this article.)

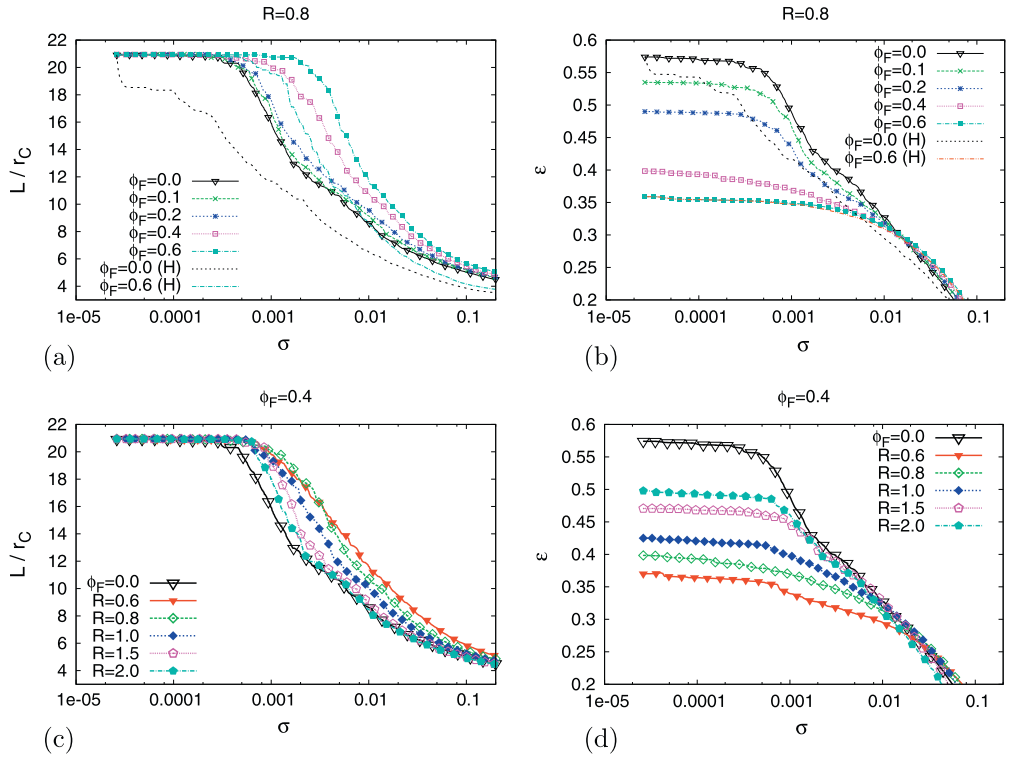

Fig. 2. The average relative crystal length L/r_C and porosity ε as function of compaction stress σ in packings with different packing parameters R and ϕ_F. Lines denoted by "(H)" represent packings composed of weak crystals (all other lines represent packings of regular crystals). For the weak crystals, the maximum load the crystals are able to withstand before breakage is set to one half of the value for regular crystals.

are mixed with fillers in a composite packing (cf. curves "$\phi_F = 0.6(H)$" and "$\phi_F = 0$" in Fig. 2a).

A key to the explanation of this effect might be the number of contacts in the packings. A crystal breaks if the local stress at an individual contact exceeds a set threshold (the crystal strength). The local bending stress is the product of the local force and the distance between contacts. A higher number of contacts means that (i) more force chains that transmit the compression stress can exist and that, consecutively, the local forces are smaller; and (ii) the average distance between contacts is shorter. The average distance

d between contacts that support the crystal particles (Fig. 3) is shorter in packings with higher ϕ_F and smaller R (smaller filler radius means that there is a larger number of fillers for a particular filler volume fraction). As can be seen by comparing the curves of corresponding packings in Figs. 2 and 3, the decrease of d corresponds well with the postponement of the breakage onset to higher stresses.

The contacts network can also be shown from the viewpoint of the fillers rather than crystals, and characterised by the average coordination number E of the fillers (Fig. 4). The coordination number is initially higher for fillers in packings with higher ϕ_F and further increases as the packing gets more compacted during the course of compression.

The relation between the compaction stress σ and the local force F at the particle contacts depends on the topology of contacts. It has been reported [24,25] that there can be a relatively wide distribution of the magnitude of local forces within a packing, which is confirmed by our simulations as well. The mean and the standard deviation of the local force are presented in Fig. 5. For small stresses σ at the early stages of bed consolidation, both the mean and the variance of the local forces are higher for crystal-crystal (CC) than for crystal-filler (CF) or filler-filler (FF) contacts. As the compaction progresses, this difference diminishes and at higher values of σ there is no more difference between the contact types. The higher variation of local forces for CC contacts can be explained by the fact that elongated crystals are able to rearrange less easily than spherical fillers inside the packing. Therefore, a larger difference in F_{CC} can arise. Fillers, on the other hand, can move relatively freely (their coordination number is low) and, unlike crystals, are less likely to jam [26,27]. The difference between the relative mobility of crystals and fillers diminished at later stages of the compaction process as the crystals become smaller due to breakage and simultaneously the filler coordination number increases as the entire packing becomes denser.

The last property to be discussed is the evolution of the polydispersity index Z (Fig. 6). Let us first imagine a simple scenario of crystal breakage: Starting with n_0 particles of identical length L_0, the particles gradually break into identical fragments of length $\frac{L_0}{2}$ (symmetric binary breakage). The first-generation fragments only start breaking once all original L_0 particles are consumed. This leads to $2n_0$ particles of length $\frac{L_0}{2}$, at which point the breakage scenario can repeat itself to form crystals of length $\frac{L_0}{4}$, then $\frac{L_0}{8}$ and so on. Assuming this scenario, the following relation between the polydispersity Z and the mean crystal length L can be derived

$$Z(L) = \frac{1}{2}(L_0/L)(3 - L_0/L), \tag{5}$$

where the function $Z(L)$ has a maximum $Z = \frac{9}{8}$ at $L = \frac{2}{3}L_0$. The derivation of Eq. (5) is shown in Appendix A.

A comparison of the theoretically derived function $Z(L)$ with Z and L values obtained from computational experiments, as shown in Fig. 6, makes it possible to assess the difference between a random breakage mechanism and the simple scenario described above. A relatively good qualitative (though not quantitative) agreement with the theory is clearly visible. This suggests that even in a random packing the crystals tend to undergo predominantly symmetrical binary breakage, and that the breakage proceeds through individual "generations" of daughter particles that do not break further until the previous generation is consumed. However, due to the discrete element representation of the crystals in the computer simulation, the number of breakage generations is limited and the computer simulation data eventually diverge from the theoretical values.

An interesting observation can be made by examining the result for composite packings and comparing them with the result for a packing without fillers ($\phi_F = 0$): If $R \geqslant 1$, the filler volume fraction ϕ_F has little effect on the breakage pattern, the results are very

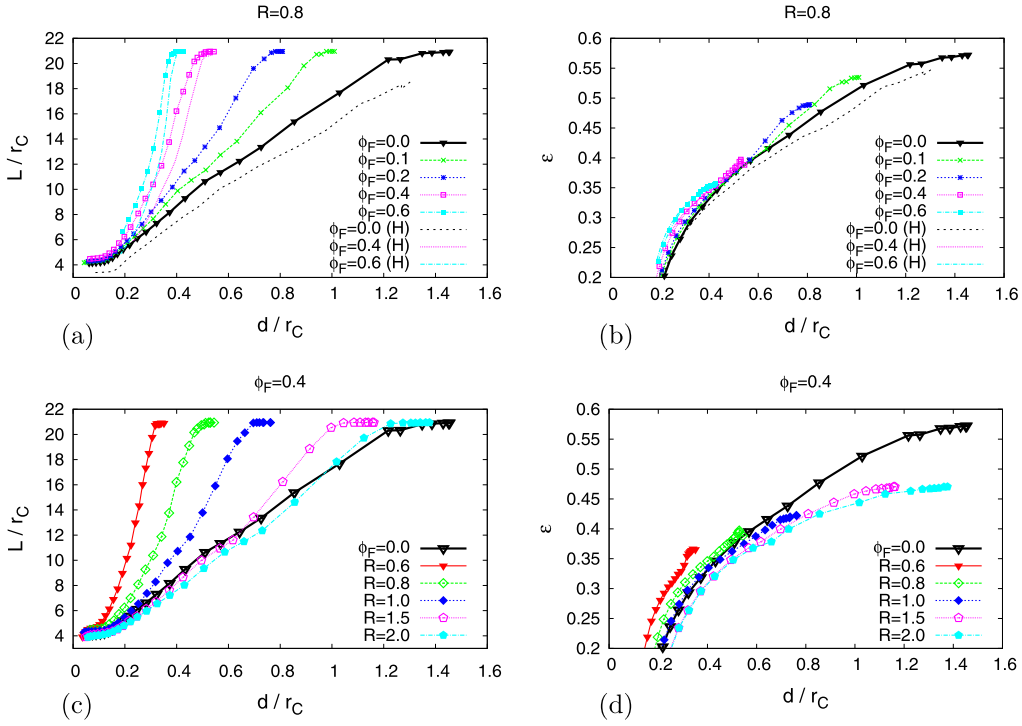

Fig. 3. Correlation between the average distance d between contacts that support crystal particle and the average crystal length L (and porosity ε) in packings with different packing parameters R and ϕ_F. The meaning of "(H)" lines is explained in the caption of Fig. 2.

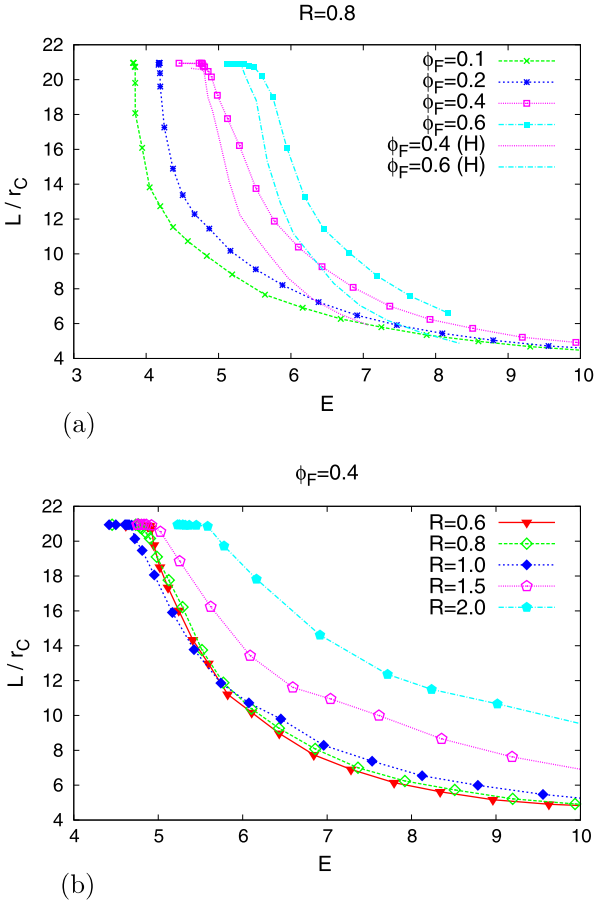

Fig. 4. The coordination number of filler particles E increasing with decreasing average crystal length L as packings with different parameters R and ϕ_F are compressed. The meaning of "(H)" lines is explained in the caption of Fig. 2.

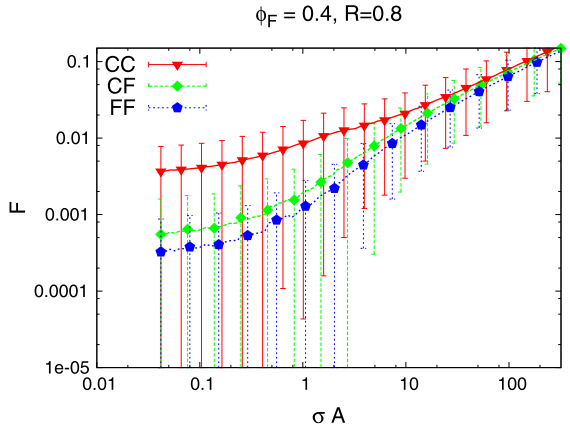

Fig. 5. Evolution of the local forces at inter-particle contacts with increasing dimensionless global force σA: crystal–crystal contacts (CC), crystal–filler contacts (CF) and filler–filler contacts (FF). The curve corresponds to the mean value, the bars above and bellow the data-points indicate the standard deviation of the forces. F is a dimensionless local force $F = F^{loc}/(k_{CC} r_C)$.

close to each other and there is little difference between composite and crystal-only packings. On the other hand, if R is small and ϕ_F is high (e.g. $R = 0.6$ and $\phi_F = 0.4$) the difference becomes clearly visible. It seems that the presence of small filler particles at larger volume fraction not only postpones crystal breakage to larger stress

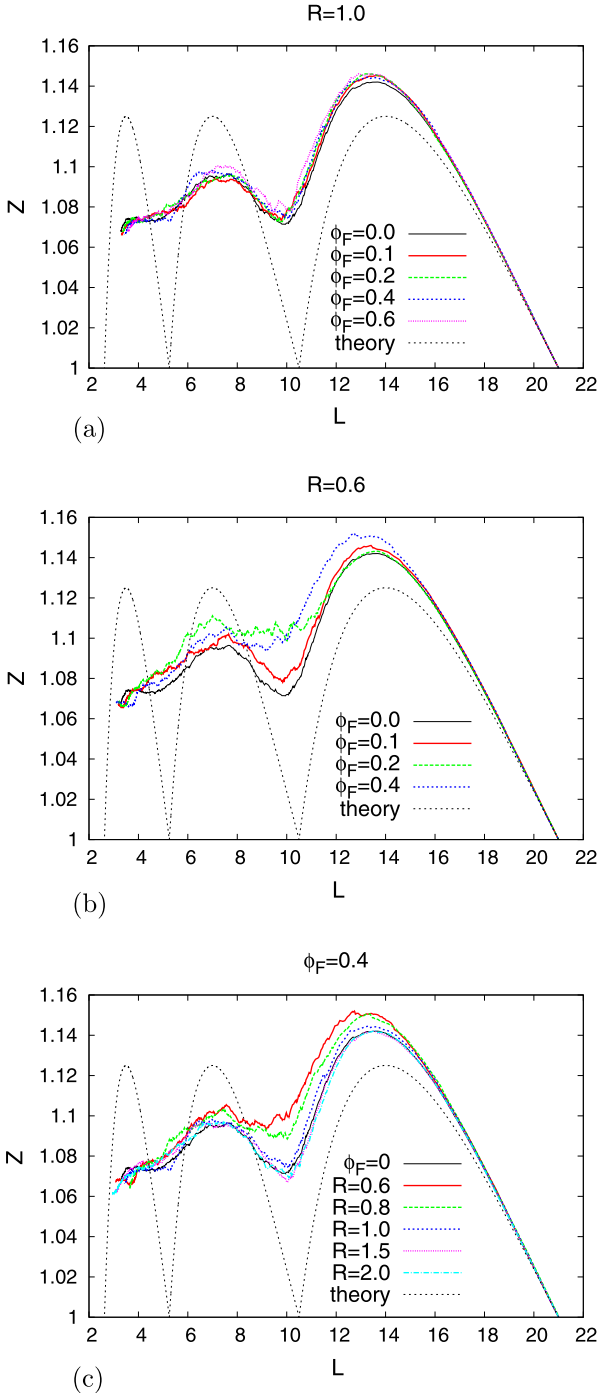

Fig. 6. Evolution of the polydispersity index Z with decreasing mean crystal size L as the packing undergoes compression. Packings with different packing properties R and ϕ_F are compared. The theoretical evolution of the polydispersity corresponds to the idealised sequential binary breakage model where all particles of the initial length L_0 break to the length $\frac{L_0}{2}$ before breaking further to $\frac{L_0}{4}$ and so on.

values σ (as is demonstrated in Fig. 2), but also shifts the breakage pattern further from the theoretical one (a larger number of small crystal fragments will be formed).

3.1. The effect of filler elasticity

In all results presented thus far, the particle elasticity was the same for both crystal and filler particles, i.e. the stiffness of linear

springs was the same for all contact pair types: $k_{CC} = k_{CF} = k_{FF}$. In order to observe the compaction behaviour of packings containing fillers that are softer or harder than crystals, an additional packing parameter $\kappa = k_{FF}/k_{CC}$ was investigated. This parameter corresponds to the relative elasticity of filler with respect to crystal particles: the values $\kappa < 1$ and $\kappa > 1$ correspond to softer and harder fillers, respectively.

Results (Fig. 7) indicate, that the effect of filler elasticity on the susceptibility of crystals to break is actually smaller than the effect of other packing parameters ϕ_F and R. It can be seen that the crystals break more in mixtures with harder fillers ($\kappa = 10$) than in mixtures with softer fillers ($\kappa = 0.1$). However this difference is subtle in comparison to the difference made by changing the parameter ϕ_F. More significant effect of filler elasticity on crystal breakage would be expected if the compaction would be carried out as a dynamic and not as a static process. In static compaction, the smaller elasticity (spring stiffness) k_{FF} will result only in larger overlaps between spherical elements leading to a larger number of contacts and shorter average distance d between contacts.

3.2. The effect of local inhomogeneities

The properties presented in this paper are averaged over the whole packing, but the breakage behaviour can be different in various parts of a packing. In order to be able to assess these differences, the packing was virtually divided from the top to the bottom into four sections having the same size. (The section $j = 1$ is the top section, while the section $j = 4$ is the bottom section.) Every particle and every contact were assigned to one section according to their position: a particle was assigned to a section according to its centre of mass, the fact that the particle can also exceed into other section was, for the simplicity, neglected. Local variations of packing characteristics, $L_{i,j}, d_{i,j}$ and $\phi_{F,j}$, defined in the Methodology section, were then evaluated for each section j.

Let us begin with results for packings without filler particles. As is illustrated in Fig. 8, the crystal particles break initially more at the bottom than at the top of the packing. As the compaction proceeds, the difference between local average crystal length among packing sections diminishes. The different breakage behaviour in the early stages of the compaction can be explained by spatial inhomogeneities in the packing. While responding to the compaction stress, the crystals in the top sections can rearrange more easily than those in the bottom sections and therefore the crystals at the top can better avoid the local stress building up at particle contacts and leading to the breakage.

The presence of filler particles in packings brings up the segregation as another possible cause for spatially different breakage behaviour. Local relative volume fraction of filler particles, $\phi_{F,j}$, shown in Table 2 can be used to analyse the segregation in packings. It seems that the segregation can be significant in packings, where the size of fillers is smaller than the size of crystal elements (i.e. $R = 0.6$ or 0.8) and the volume fraction of fillers is small ($\phi_F = 0.1$ or 0.2). The reason is that small filler particles can easily go through the gaps between the crystals. The local value of $\phi_{F,j}$ is therefore larger in the bottom section, and consequently, $\phi_{F,j}$ is smaller in the top section of the packing.

The effect of inhomogeneities caused by the segregation on the breakage behaviour is consistent with conclusions already drawn from the analysis of the whole packings: the crystal particles break less in the bottom section where the local volume fraction of fillers is higher, and break more in the top section with a lower local volume fraction of fillers. This is clearly shown in Fig. 9a for a packing where the segregation is especially high ($R = 0.6, \phi_F = 0.2$). Correspondingly smaller spatial breakage differences were observed in packings with a smaller extent of segregation. It is also interesting to note that the $L|d$ curves in Fig. 9b for different packing sections (with different values of local $\phi_{F,j}$) within a single packing are consistent with the $L|d$ curves in Fig. 3 obtained by parametric study of the ϕ_F parameter. The answer to the question, how the variation of filler volume fraction changes the breakage, is therefore the same, regardless of whether the analysis is made over the whole packing or locally,

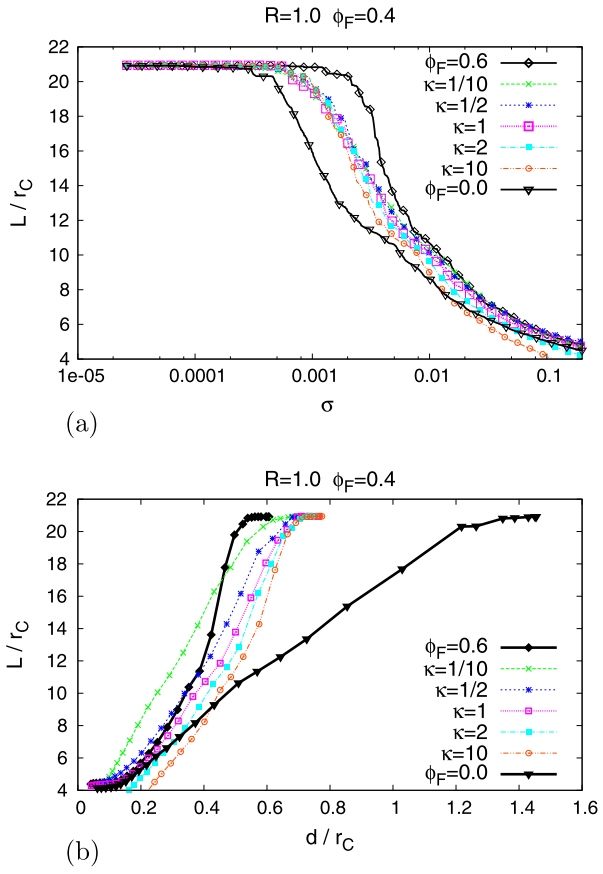

Fig. 7. The effect of parameter $\kappa = k_{FF}/k_{CC}$ (softer or harder fillers) on crystal breakage. The value $\kappa = 1$ is used also for lines denoted "$\phi_F = 0$" and "$\phi_F = 0.6$" drawn just to compare the sensitivity to parameter κ with the sensitivity to parameter ϕ_F.

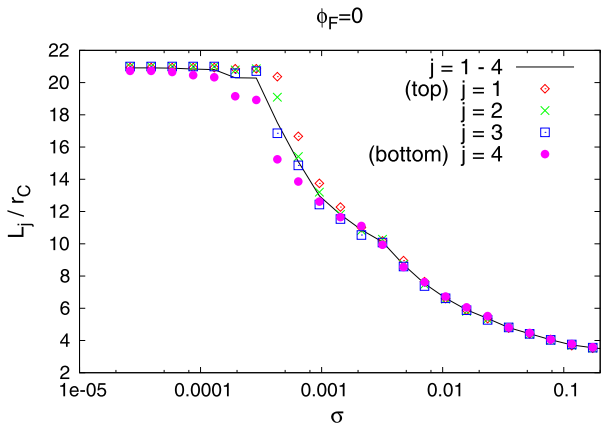

Fig. 8. Breakage inhomogeneities in a packing without filler particles. The local average crystal length L_j/r_C as function of compaction stress σ.

Table 2
Local relative volume fraction (in %) of filler particles in different sections of the packing, $\phi_{F,j}$. Numbers displayed in bold show the overall volume fraction evaluated over the whole packing (j = 1–4).

	$\phi_F = 0.1$	$\phi_F = 0.2$	$\phi_F = 0.4$	$\phi_F = 0.6$	j
$R = 0.6$	**10.4**	**19.0**	**38.1**		**overall**
	5.5	6.6	27.9		1 (top)
	9.3	17.4	39.5		2
	9.1	15.2	38.9		3
	16.6	32.4	43.6		4 (bottom)
$R = 0.8$	**10.4**	**18.7**	**41.4**	**58.4**	**overall**
	6.9	11.9	37.4	59.4	1 (top)
	11.2	19.4	41.4	57.5	2
	9.5	17.4	41.0	57.9	3
	13.5	24.7	45.0	58.7	4 (bottom)
$R = 1$	**9.3**	**19.4**	**39.5**	**59.9**	**overall**
	8.0	14.6	39.3	57.4	1 (top)
	8.7	21.0	40.1	60.1	2
	9.6	18.6	39.2	62.9	3
	10.7	22.7	39.6	58.9	4 (bottom)
$R = 1.5$	**10.0**	**19.9**	**40.9**	**61.0**	**overall**
	9.7	17.7	39.3	57.0	1 (top)
	8.9	22.8	38.6	64.3	2
	10.2	23.4	41.0	59.5	3
	11.2	23.6	44.5	62.8	4 (bottom)
$R = 2$	**11.2**	**20.7**	**40.8**		**overall**
	11.2	19.5	40.1		1 (top)
	11.1	20.5	37.5		2
	10.1	20.2	43.5		3
	12.6	22.4	41.8		4 (bottom)

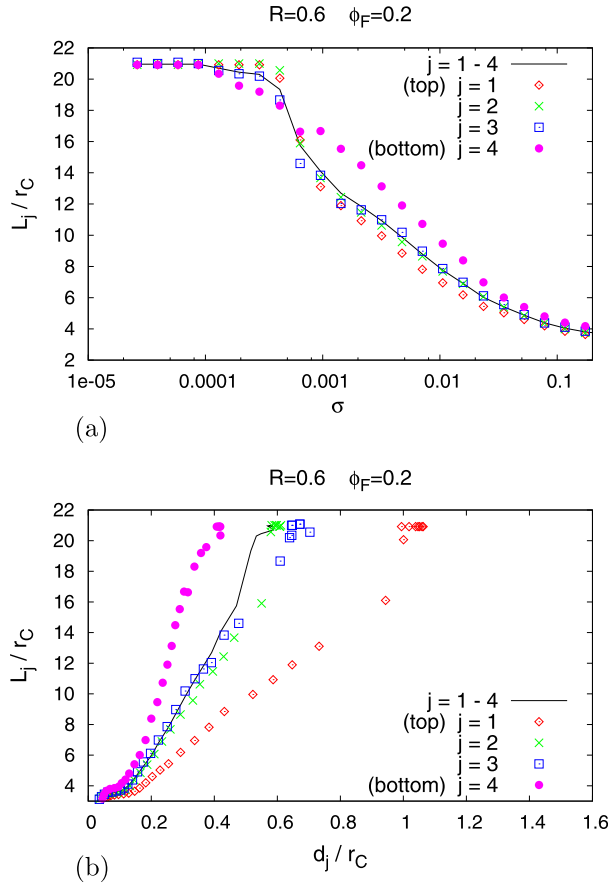

Fig. 9. Breakage inhomogeneities due to segregation. (a) The local average crystal length L_j/r_C as function of compaction stress σ. (b) The correlation between the local average distance d_j between contacts that support crystal particle with the local average crystal length L_j.

4. Conclusions

The breakage patterns that emerge in composite packings of fragile crystal particles and spherical filler particles, subjected to uniaxial compaction stress, have been explored by computer simulations. An extensive parametric study reveals that the breakage process in a composite packing under compression is related to the topology of the packing, especially to the number of inter-particle contacts. A larger number of contacts results in a larger number of force chains along which stress propagates through the packing, which reduces the loading stress experienced by individual particles. The addition of spherical elastic particles (fillers) to the packing of fragile crystals can reduce the extent of crystal breakage only if their addition increases the number of contacts; smaller fillers are more effective at reducing the breakage than larger fillers. The effect of other packing properties, such as filler elasticity, crystal elasticity and filler volume fraction can be explained in the same way: there is a direct link between the packing topology and particle breakage. These results have a potential practical significance e.g. in the pharmaceutical industry, where tablets are formed by the compaction of a mixture of crystals of the active substance with various auxiliary components (fillers) whose size and material properties can often be selected from several choices. Knowledge of general trends that govern the breakage patterns of the crystals during compaction can help in the rational selection of such components, such that predictable product properties be obtained.

Acknowledgement

Support from Czech Science Foundation through Grant No. 15-05534S is gratefully acknowledged.

Appendix A. Derivation of the relation between polydispersity Z and average particle length L

Let us assume the following breakage scenario: Starting with n_0 identical particles of length L_0, the particles gradually break into fragments of length $L_0/2$, which themselves do not break further until all the L_0 particles are consumed. Let us denote n_1 and n_2 the current number of L_0 and $L_0/2$ particles, respectively. As every breakage event decreases n_1 by one and increases n_2 by two, n_1 and n_2 can be calculated from the number of breakage events, β, as follows

$$n_1 = n_0 - \beta \qquad \text{and} \qquad n_2 = 2\beta.$$

The distribution moments are therefore

$$\mu_0 = n_1 + n_2 = n_0 + \beta \tag{A.1}$$

$$\mu_1 = L_0 n_1 + (L_0/2) n_2 = L_0 n_0 \tag{A.2}$$

$$\mu_2 = L_0^2 n_1 + (L_0/2)^2 n_2 = L_0^2 (n_0 - \beta/2). \tag{A.3}$$

Now it is possible to calculate the dependence of the polydispersity Z on the mean particle length L. Polydispersity and the mean particle length are defined using the distribution moments

$$Z = \frac{\mu_0 \mu_2}{\mu_1^2} \qquad \text{and} \qquad L = \frac{\mu_1}{\mu_0}$$

and, after substitution from Eqs. (A.1)–(A.3), the equations become

$$Z = (1 + \beta/n_0)\left(1 - \frac{1}{2}\beta/n_0\right) \tag{A.4}$$

$$L = \frac{L_0}{1 + \beta/n_0}. \tag{A.5}$$

The term containing the number of breakage event, β/n_0, can be eliminated by combining Eqs. (A.4) and (A.5) to obtain Eq. (5).

References

[1] H.M. Jaeger, S.R. Nagel, Granular solids, liquids, and gases, Rev. Modern Phys. 68 (4) (1996) 1259–1273.
[2] R.P. Behringer et al., Science in the sandbox: fluctuations, friction and instabilities, Lecture Notes Phys. 567 (2001) 351–391.
[3] M. Muthuswamy, A. Tordesillas, How do interparticle contact friction, packing density and degree of polydispersity affect force propagation in particulate assemblies?, J Stat. Mech. (2006) P09003.
[4] T.S. Majmudar, R.P. Behringer, Contact force measurements and stress-induced anisotropy in granular materials, Nature 435 (2005) 1079–1082.
[5] R.C. Hidalgo, C.U. Grosse, F. Kun, H.W. Reinhardt, H.J. Herrmann, Evolution of percolating force chains in compressed granular media, Phys. Rev. Let. 89 (20) (2002) 205501.
[6] F. Radjai, M. Jean, J.J. Moreau, S. Roux, Force distributions in dense two-dimensional granular systems, Phys. Rev. Let. 77 (2) (1996) 274–276.
[7] J.F. Peters, M. Muthuswamy, J. Wibowo, A. Tordesillas, Characterization of force chains in granular material, Phys. Rev. E 72 (2005) 041307.
[8] A.A. Pena, A. Lizcano, F. Alonso-Marroquin, H.J. Herrmann, Biaxial test simulations using a packing of polygonal particles, Int. J. Numer. Anal. Meth. Geomech. 32 (2008) 143–160.
[9] E. Azema, F. Radjai, Internal structure of inertial granular flows, Phys. Rev. Let. 112 (2014) 078001.
[10] G. Lumay, N. Vandewalle, Compaction of anisotropic granular materials: experiments and simulations, Phys. Rev. E 70 (2004) 051314.
[11] G. Lumay, N. Vandewalle, Experimental study of the compaction dynamics for two-dimensional anisotropic granular materials, Phys. Rev. E 74 (2006) 021301.
[12] E. Azema, F. Radjai, Force chains and contact network topology in sheared packings of elongated particles, Phys. Rev. E 85 (2012) 031303.
[13] R.C. Hidalgo, D. Kadau, T. Kanzaki, H.J. Herrmann, Granular packings of cohesive elongated particles, Granular Matter 14 (2012) 191–196.
[14] T. Borzsonyi, R. Stannarius, Granular materials composed of shape-anisotropic grains, Soft Matter 9 (2013) 7401–7418.
[15] G. Lu, J.R. Third, C.R. Muller, Effect of particle shape on domino wave propagation: a perspective from 3d, anisotropic discrete element simulations, Granular Matter 16 (2014) 107–114.
[16] W. Nan, Y. Wang, Y. Ge, J. Wang, Effect of shape parameters of fiber on the packing structure, Powder Technol. 261 (2014) 210–218.
[17] R.S. Ransing, R.W. Lewis, D.T. Gethin, Using a deformable discrete-element technique to model the compaction behaviour of mixed ductile and brittle particulate systems, Phil. Trans. R. Soc. Lond. A 362 (2004) 1867–1884.
[18] F.M. Sanchez-Arevalo, H. Tapia-McClung, G. Pulos, R. Zenit, Reduction of compaction force in a confined bidisperse granular media, Phys. Rev. E 87 (2013) 052210.
[19] C.S. MacLeod, F.L. Muller, On the fracture of pharmaceutical needle-shaped crystals during pressure filtration: case studies and mechanistic understanding, Org. Process Res. Dev. 16 (2012) 425–434.
[20] Z. Grof, M. Kohout, F. Stepanek, Multi-scale simulation of needle-shaped particle breakage under uniaxial compaction, Chem. Eng. Sci. 62 (5) (2007) 1418–1429.
[21] Z. Grof, C.M. Schoellhammer, P. Rajniak, F. Stepanek, Computational and experimental investigation of needle-shaped crystal breakage, Int. J. Pharmaceutics 407 (1–2) (2011) 12–20.
[22] Z. Grof, F. Stepanek, Distribution of breakage events in random packings of rodlike particles, Phys. Rev. E 88 (2013) 012205.
[23] J.F. Favier, M.H. Abbaspour-Fard, M. Kremmer, A.O. Raji, Shape representation of axisymmetrical, non-spherical particles in discrete element simulation using multi-element model particles, Eng. Comput. 16 (4) (1999) 467–480.
[24] R.C. Hidalgo, I. Zuriguel, D. Maza, I. Pagonabarraga, Role of particle shape on the stress propagation in granular packings, Phys. Rev. Let. 103 (2009) 118001.
[25] H.A. Makse, D.L. Johnson, L.M. Schwartz, Packing of compressible granular materials, Phys. Rev. Let. 84 (18) (2000) 4160–4163.
[26] M.E. Cates, J.P. Wittmer, J.-P. Bouchaud, P. Claudin, Jamming, force chains, and fragile matter, Phys. Rev. Let. 81 (9) (1998) 1841–1844.
[27] F. Ludewig, N. Vandewalle, Strong interlocking of nonconvex particles in random packings, Phys. Rev. E 85 (2012) 051307.

8.5 Analysis of breakage patterns in a sheared layer of elongated particles

Marek Schöngut
Zdeněk Grof
František Štěpánek

Published in the *Powder Technol.*, Vol. 345, 2019, pp. 682–691
DOI: 10.1016/j.powtec.2019.01.045.

Powder Technology 345 (2019) 682–691

Contents lists available at ScienceDirect

Powder Technology

journal homepage: www.elsevier.com/locate/powtec

Analysis of breakage patterns in a sheared layer of elongated particles

Marek Schöngut, Zdeněk Grof *, František Štěpánek

Department of Chemical Engineering, University of Chemistry and Technology, Prague, Technická 5, 166 28 Prague 6, Czech Republic

ARTICLE INFO

Article history:
Received 17 August 2018
Received in revised form 19 December 2018
Accepted 20 January 2019
Available online 24 January 2019

Keywords:
DEM
Needle-shaped particles
Breakage
PSD

ABSTRACT

Discrete Element Method (DEM) simulations of elongated (i.e. needle-shaped) particles breakage in a shear field confined between two parallel plates, in analogy with processes occurring in a powder shear cell tester, were carried out. Effects of particle strength, shear rate and the compressive stress were investigated. The breakage patterns occurring in a layer of particles due to compressive and shearing stress fields are analysed in detail and compared. The results of these computational experiments reveal that when the course of particle breakage is represented in the mean particle length vs. polydispersity diagram, the breakage patterns for slow shearing and compression follow the same path that is close to the path constructed for an idealized breakage scenario, while curves for fast shearing deviate from the scenario towards higher polydispersities.

© 2019 Elsevier B.V. All rights reserved.

1. Introduction

In the field of pharmaceutical production, granular materials and their transformation are ubiquitous. As an example, the active pharmaceutical ingredient (API) is often present in the form of needle-shaped crystals of well defined particle size distribution (PSD) formed during the initial crystallisation step. However, uncontrolled changes of PSD due to particle breakage often occur in subsequent steps of the manufacturing process such as drying, granulation or compaction where the particles encounter mechanical stress. The understanding of how particles behave when subjected to various types of stress fields (e.g. normal load or shear) is necessary for the modelling, design and optimisation of pharmaceutical unit operations. Population balance modelling (PBM), e.g. [1,2], is a common method for the modelling of PSD changes due to particle breakage. However, the method requires a suitable kernel with a set of parameters that specify the breakage rate of individual particles and the size distribution of the breakage fragments — information that is not *a priori* known.

This information can be extracted from experimental data or by the post-processing of computer simulations of granular flow using the Discrete Element Method (DEM). Experimental observations of breakage and attrition of needle-shaped pharmaceutical particles subjected to shear stress were presented in the work of Agrawal et al. [3] or Hare and Ghadiri [4]. A slight disadvantage of the experimental evaluation of breakage patterns is that the stress and breakage history of individual particles is nearly impossible to trace, and the analysis of PSD generally requires off-line measurement, i.e., in order to measure PSD, particles have to be transported from the shearing cell to another apparatus thus interrupting the actual shearing experiment that cannot be then resumed from the identical particle arrangement as before the PSD measurement. In contrast, DEM simulations make it possible to evaluate breakage kernels from the analysis of a statistically large number of individual breakage events that occur within the powder bed. This methodology was first demonstrated for the case of elongated particle breakage due to normal load [5–7]. The DEM modelling of elongated particle breakage in other configurations such as breakage due to the action of an impeller embedded in the powder bed [8,9] or breakage of elongated particles admixed with spherical fillers [10] were recently reported in the literature. DEM has been also employed in studies analysing the structure evolution of elongated particle packings in sheared beds [11–13] or in piles [14]. The combination of DEM and PBM was used for the modelling of a granulation process [15].

The subject of the present work is the use of computational experiments for the analysis of particle breakage patterns in a shear field confined between two parallel plates, in analogy with processes occurring in a powder shear cell tester. The aim is to compare qualitatively and quantitatively the breakage patterns of elongated particles during compressive and shearing stress fields and to investigate how the specific particle breakage sequence scales with the shear rate and particle size.

2. Methodology

2.1. DEM simulation

Computational experiments with a sheared layer of breakable needle-shaped particles were carried out using the DEM approach, which is based on the numerical solution of equations of motion [16]. The particles are composed of overlapping spherical elements [17]

* Corresponding author.
E-mail addresses: zdenek.grof@vscht.cz (Z. Grof), frantisek.stepanek@vscht.cz (F. Štěpánek).

https://doi.org/10.1016/j.powtec.2019.01.045
0032-5910/© 2019 Elsevier B.V. All rights reserved.

whose relative positions with respect to the particle center of mass are kept fixed so that the particles move as rigid bodies. For every particle, the contact forces acting on its elements from other particle elements and the gravitational forces are added to obtain the overall force and torque acting on the particle, which then determine the particle movement for the next time step. A method of section is used in order to evaluate the internal force and torque that hold elements within a particle connected. By assuming that a particle is imaginarly divided into two parts, adding element forces separately for each part and by using kinematic constraints that keep the relative position of the parts fixed, formulae for the internal force and torque at each possible breakage position within the particle can be derived (the course of derivation is described in detail in Appendix A). Therefore, it is possible to quantify the internal stress acting within the particle and to determine whether a set threshold for particle strength, denoted σ_{max}, is exceeded between any two neighbouring spherical elements within the particle in each time step. If this happens anytime during the simulation, the particle is broken into two parts at the point of the maximum internal load as described by [5].

There exists a conceptually different approach for joining spherical elements into aggregates that represent non-spherically shaped particles. Intra-particle bonds connecting the elements are employed [18] which allows bending or other deformations of particles. Literature review reveals many numerical simulation studies, where this approach has been used, for example, to study the deformation and the breakage of granules [19], or to evaluate the load-displacement curves during agglomerates crushing [20]. However, taking into account the computational time, the simulation of both the moving and the deformation of particles is more demanding than the simulation with particles moving as rigid bodies. This difference increases with the required level of particle stiffness regarding the actual material properties. Therefore, the approach presented in this work is more efficient for the simulation of stiff and brittle materials where the bending is small and can be neglected (e.g. needle-shaped crystals). On the other hand, the bonding sphere approach would be better suited for more flexible materials.

The computational experiments proceed as follows (see also Fig. 1). First, a layer of particles is created by inserting the required number of non-overlapping particles with a random initial orientation and position into the simulation domain and allowing the particles to settle on the bottom wall by gravity. The particles are confined from the top and the bottom along the Z-axis by horizontal, flat, rigid walls, while periodic boundary conditions are applied along the X- and the Y-axes. Layers of particles with different particle strength σ_{max} were prepared. They are illustrated in Fig. 2, where the color represents either the particle length or the loading of individual particles within the layer. Particles with a uniform initial length were used. However, in the case of low σ_{max} (weak particles), some particles at the bottom of the layer broke due to the weight of the layer of particles above them. As the value of σ_{max} increases, the number of broken particles decreases and there was no initial particle breakage in layers with high value of σ_{max} (strong particles).

In the next phase, the top wall is inserted and the layer of particles is pre-compressed by steadily increasing the mass of the top wall M_i until reaching a pre-defined stress in the layer, $S_i = M_i/(\Delta x \Delta y s_0)$, where Δx and Δy denote the dimensions of the computational domain and s_0 is the scaling unit of stress. An example of the layer compression is shown in Fig. 3. After pre-compressing the layer, the simulation proceeds by applying shear. The shearing motion in the layer is created by assigning a constant velocity in the direction of the X-axis to all particles within a defined distance from the top and the bottom walls. Particles near the top wall were set to move at velocity $v_x = v/2$ while the velocity of particles near the bottom wall was set to $v_x = -v/2$. It has to be noted that while the mass of top wall is constant during shearing, its vertical position remains unconstrained, thus allowing expansion or contraction of the particle layer as required by the evolving particle orientation and particle length distribution, which jointly determine the packing density. Also, the velocities in the y and z directions, the

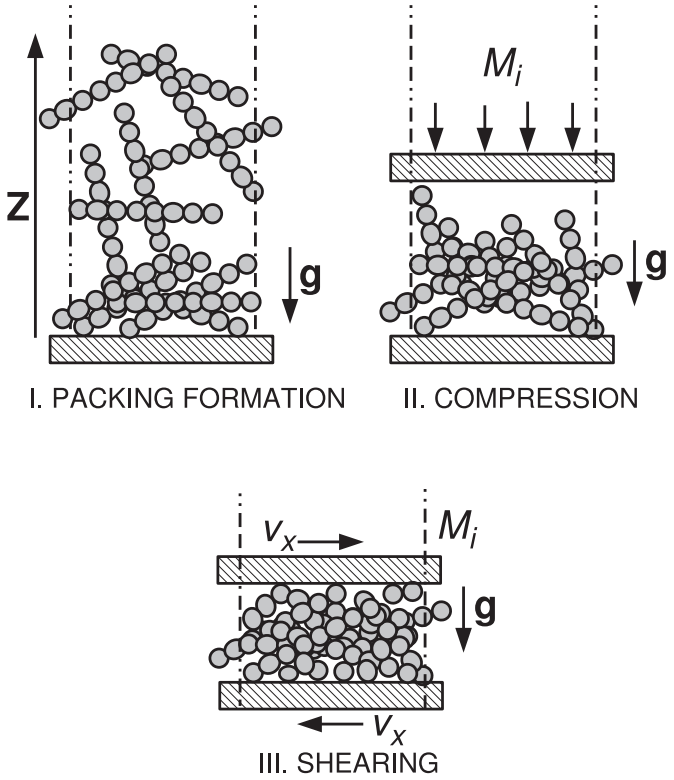

Fig. 1. Scheme of computational experiments set-up.

position, orientation and rotation rate of particles in the near wall regions are not constrained in any way. Assuming that the vertical position of the bottom and top walls is $z = 0$ and $z = h$, the groups of particles with constrained velocity $v_x = -v/2$ and $v_x = +v/2$ are defined by the position of their center of mass at $0 \le z < 0.1h$ and $0.9h < z \le h$, respectively. During the simulation, the velocity constraint is imposed or released dynamically as soon as the particle enters or leaves the near wall region.

In order to characterize the particle layer, the following parameters are recorded at every time step i during the simulation: the number of particles n_i, the porosity of the particle layer ε_i, the mean particle length $L_i = \mu_1(i)/\mu_0(i)$ and the polydispersity index $Z_i = [\mu_0(i)\mu_2(i)]/[\mu_1(i)^2]$ that characterizes the width of particle length distribution. The distribution moments required for the calculation of the mean length L_i and the polydispersity Z_i are calculated as

$$\mu_0(i) = \sum_{j=1}^{j_{max}} n(i,j) = n_i,$$

$$\mu_1(i) = \sum_{j=1}^{j_{max}} L(j) n(i,j),$$

$$\mu_2(i) = \sum_{j=1}^{j_{max}} L(j)^2 n(i,j),$$

where $n(i,j)$ is the number of particles of the length $L(j)$ at time step i. A complete set of simulation parameters is reported in Table 1.

2.2. Theoretical breaking scenario

As a reference analytical solution to be compared with the outcomes of numerical simulations, let us consider the following scenario. Beginning with a layer containing n_0 particles of identical length L_0, the scenario assumes that as the layer is subjected to the compressive or shearing stress, the particles progressively break, forming particles of

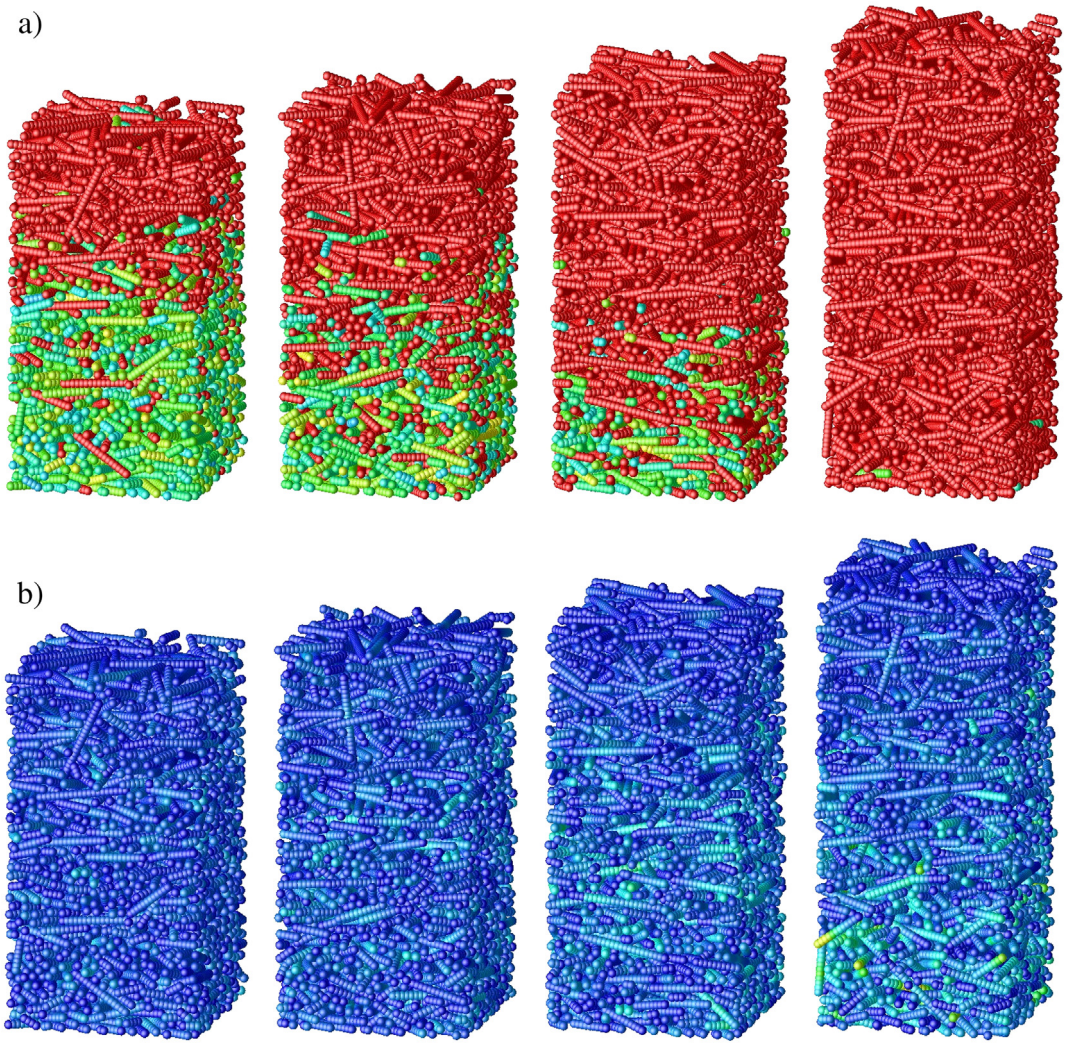

Fig. 2. Illustration of initial packing structures of particles with σ_{max} of 400, 800, 1600 and 2400. The color represents: a) the particle length or b) the loading of individual particles within the layer.

length $L_0/2$. It is also assumed that the $L_0/2$ particles do not break further as long as there still exist some L_0 particles in the layer. In other words, there is a transition from a layer of n_0 particles having the same length L_0, through a mixture of L_0 and $L_0/2$ long particles to a layer of $2n_0$ particles having once again the same length $L_0/2$. The breakage then continues to further generations of particles of length $L_0/4$, $L_0/8$, etc. Assuming this scenario, the following relation between the polydispersity Z and the mean particle length L can be derived [10].

$$Z(L) = \frac{1}{2}(L_0/L)(3-L_0/L), \tag{1}$$

where the $Z(L)$ function has a maximum $Z = \frac{9}{8}$ at $L = \frac{2}{3}L_0$. In the following text we will compare the $Z(L)$ function determined from computational experiments of a sheared particle layer with the theoretical expression given by Eq. (1) to assess the difference between this simple scenario and the actual breakage pattern during compression and shearing.

3. Results and discussion

3.1. Effect of particle strength and shear rate on breakage pattern

The evolution of the mean particle length and polydispersity during pre-compression of the particle layer is summarized in Fig. 4. In general, the mean particle length L decreases with increasing compressive stress S; however, in layers of particles with higher strength σ_{max} there is an initial period where the particles do not start to break until a specific level of stress S is reached. The $L \mid Z$ diagram represents the breaking pattern and shows how the actual PSD differs from PSD that would be obtained if the breakage proceeded according to the idealized breakage scenario described in Section 2.2. It can be seen that qualitatively the curves from numerical experiments in Fig. 4b follow a similar path as the theoretical one. There is a good agreement for minima positions that separate the individual breakage generations (L_0, $L_0/2$, $L_0/4$, …) in the theoretical scenario. However, the polydispersity is higher because the real breakage does not completely follow the theoretical scenario and there is a co-existence of more than two generations of breakage fragments. The extent of this difference is increased in layers of weak particles (low σ_{max}) where some particles at the bottom break just due to the weight of particles above them. An additional reason for higher polydispersities observed in numerical experiments is the fact that the breakage location is not in the particle middle. It actually follows a Gaussian distribution that was evaluated in [6]; only the mean of this distribution is located in the particle middle.

The breakage due to shearing the layer of particles is shown in Fig. 5 for two different shear rates (slow and fast), and for three different particle strengths. The velocity v was ten times higher in simulations denoted as “fast shear” than in “slow shear”. Comparing points

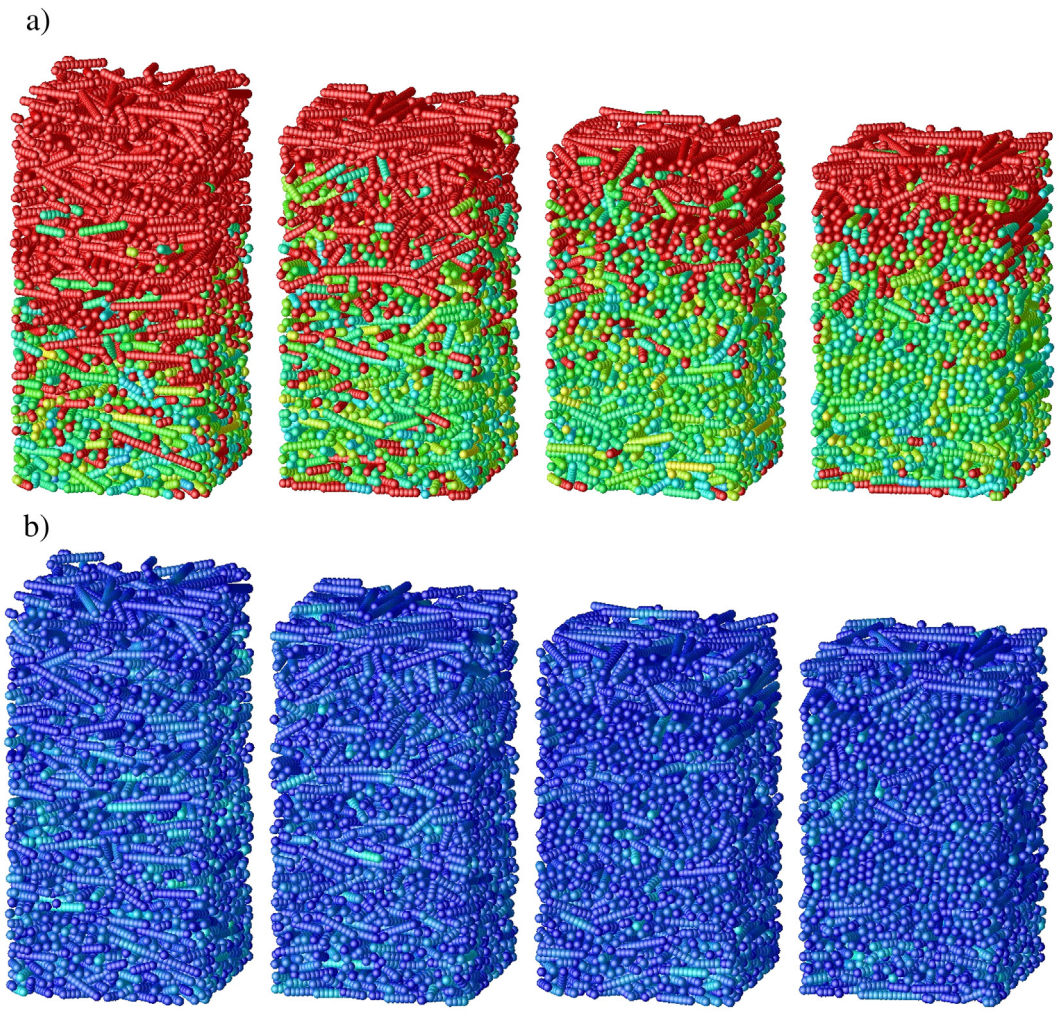

Fig. 3. Illustration of packing structure change during the compression phase ($\sigma_{max} = 1200$). The mass of the top wall M (and also the compressive stress S) increases from left to right. (The value of S/σ_{max} is 1.9×10^{-4}, 8.7×10^{-4}, 18.4×10^{-4} and 27.9×10^{-4}, respectively.) The color represents: a) the particle length or b) the loading of individual particles within the layer.

with the same sheared distance δ in Fig. 5a, there is either no visible difference of the mean length L between different shear rates, or L is lower at the faster shear. Also, it can be seen that particle breakage during shearing can be viewed as a random process: the probability that a particle gets jammed and that it breaks due to the contact forces decreases with decreasing particle size. As particles get shorter, the incidence of breakage events decreases. It can be expected, that at a sufficiently long shearing distance, the breakage probability becomes so low that the steady state is reached. There exists an irreducible particle size that depends on particle strength and on the value of a maximum force that can occur inside the layer. However, significantly longer simulation times would be necessary to actually see the mean particle length approaching to a constant value (note that the x-axis scale in Fig. 5a is logarithmic).

The course of breakage pictured in the $L \mid Z$ diagram reveals that the polydispersity (and the deviation from theoretical scenario) is higher for the faster shear rate and for weaker particles.

Table 1
Parameter values used in simulations.

η_{lt}	Global damping of the translation	158 s^{-1}
g	Gravitational acceleration	10 m/s^2
m_C	Mass of spherical element	8.4 mg
r_C	Radius of spherical element	1 mm
k	Contact force elastic modulus	2005 N/m
s_0	Scaling unit of stress	0.2005 kPa
L_0	Initial particle length	21 mm
v	shearing velocity	1.58 or 15.8 mm/s

3.2. Comparison between compression and shear breakage patterns

There are two variables that can quantify the extent of stress a layer of particles is exposed to: the compressive stress S during pre-compression, and the sheared distance δ during shearing. A direct comparison of breakage patterns caused by these two modes of applying stress (cf. Figs. 4a and 5a) is therefore difficult. On the other hand, the $L \mid Z$ diagrams can be constructed from both compression and shearing simulations. The diagrams in Fig. 6 show a combination of the following modes of applying stress: (i) compression only, (ii) fast and slow shearing, and (iii) partial compression followed by slow shearing. The combination shows an interesting result: the curves follow the same trajectory for compression and slow shearing. For fast shearing, the curves deviate to higher polydispersity levels. In order to elaborate on this result, let us recall the breakage pattern hypothesis that assumes preferential breakage of the longest particles in the layer while shorter particles do not break until all longer particles are broken. There appears to be little difference between the breakage mode during compression and slow shearing and, as the experimental curves are not too far

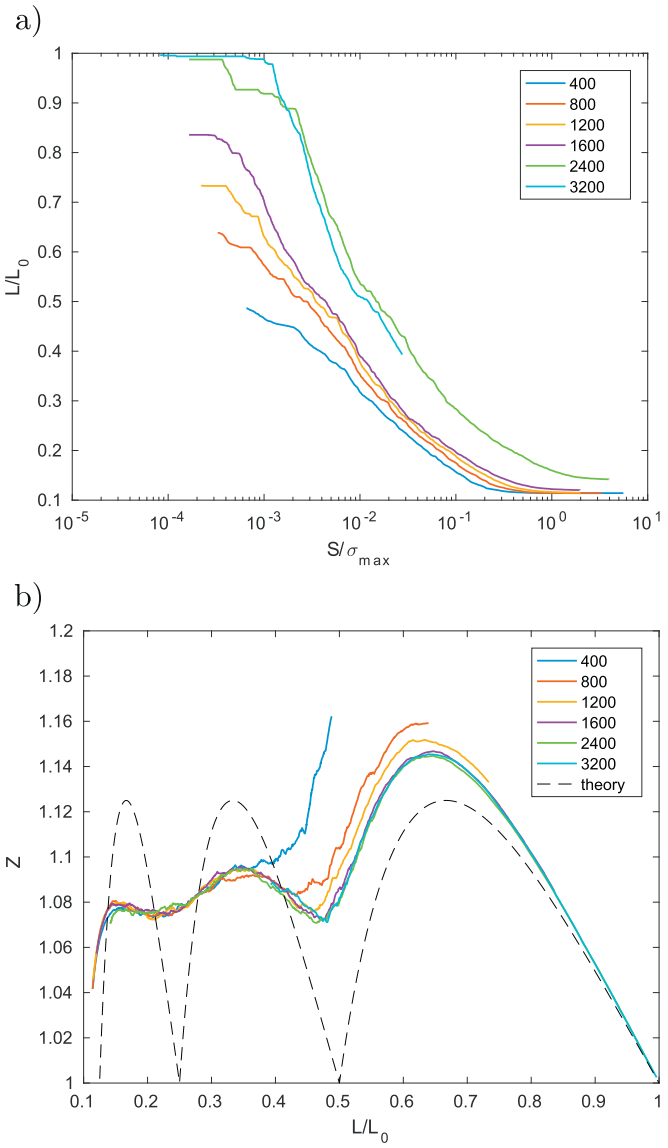

Fig. 4. Compression of the layer of particles with different particle strength σ_{max}: a) the average particle length (L/L_0) dependence on relative compressive stress (S/σ_{max}), b) the relation between polydispersity Z and average particle length L/L_0. The number in the legend denotes particle strength σ_{max}.

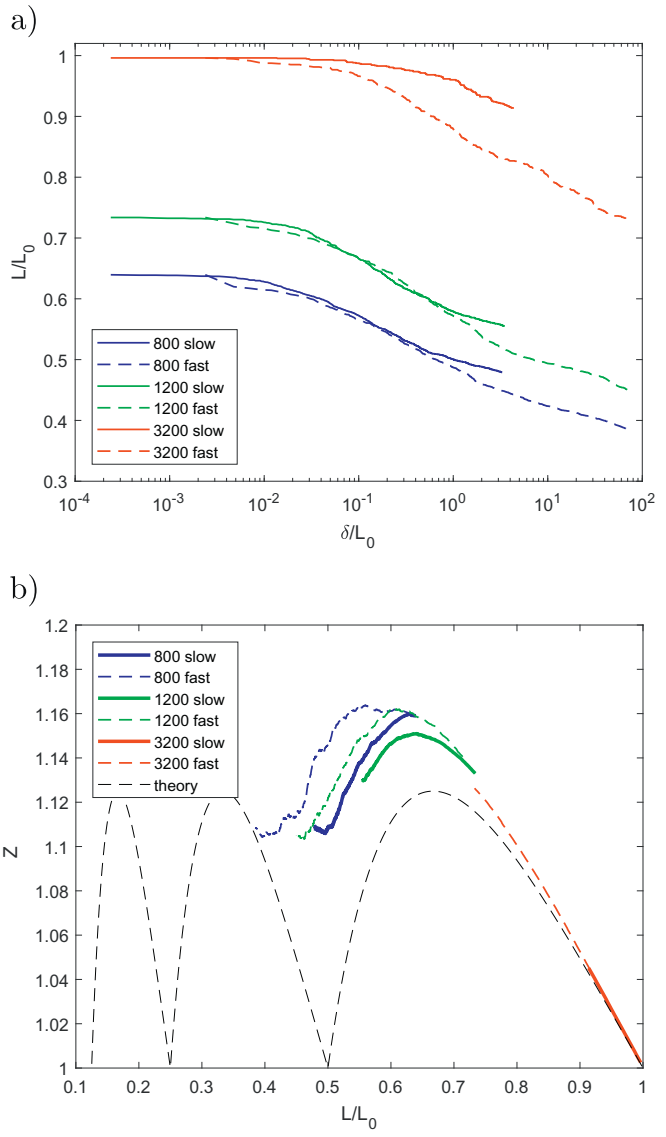

Fig. 5. Shearing of the layer of particles. In the legend, the number denotes particle strength σ_{max} and the text indicates the slow or fast shearing rate: a) the average particle length (L/L_0) dependence on the relative sheared distance (δ/L_0), b) the relation between polydispersity Z and average particle length L/L_0.

from the theoretical one, both patterns follow the above-mentioned hypothesis. On the other hand, during fast shearing there is a larger number of shorter particles forced to break because they have less time to decrease the local load they are exposed to by rearranging their orientation within the layer.

The shearing of partially compressed layers breaks more particles than the shearing of uncompressed layers (cf. Fig. 7). The breakage is enhanced with higher compression level as the result of reduced opportunities for particle rearrangements in partially compressed layers. Hence, the porosity of the layer was investigated in more detail.

3.3. Porosity and stored elastic energy within the layer

Fig. 8 shows the relationship between the mean particle length and the layer porosity. During pre-compression, which can be viewed as a pseudo-static process, the porosity decreases monotonously with decreasing particle length. The relationship is more interesting for shearing process. Looking at the porosity during shearing, the porosity initially increases above and then drops bellow the compression curve. The shearing of particles raises the top wall thus increasing the layer height and the porosity. The increase of porosity in sheared beds of particles has been observed in DEM simulations focused on the detailed structure analysis, e.g. [11,21]. This increase is more significant for higher shearing rate and smaller compressive stress. As particles become shorter due to breakage and as the shearing promotes particle rearrangement, the layer becomes more compact and less porous than during compression for the same mean particle length. This is consistent with the fact that the porosity of particle packing decreases for particles with lower aspect ratio (i.e. for shorter particles) [22].

In the area of comminiution, the breakage event occurs when stored elastic energy exceeds the critical breakage energy which results into the relaxation of local contact forces and also unjamming of particles [23]. Particle rearrangement during shearing also leads to the relaxation of elastic energy that would be accumulated during compression. This is

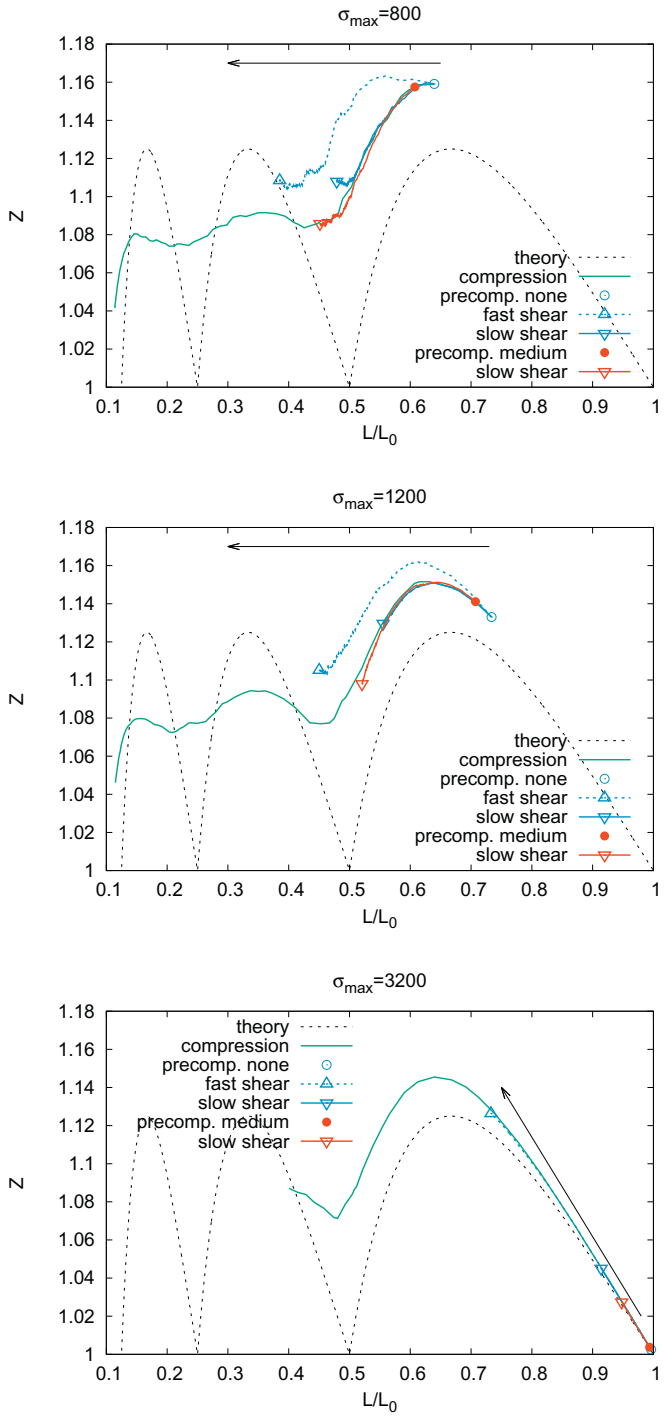

Fig. 6. Comparison of compression and shearing scenarios for particles of different strength. The following scenarios are shown in the diagrams: (i) compression (green line), (ii) fast shearing (blue dashed line), (iii) slow shearing (blue line) and (iv) partial layer compression followed by slow shearing (red line). (For interpretation of the references to color in this figure legend, the reader is referred to the web version of this article.)

shown in Fig. 9. The total energy E_{elast} is calculated as the sum of elastic energies over all particle contacts. While it steadily increases during compression, its value remains considerably lower during shearing due to the possibility of individual particles to rearrange and change orientation. This possibility decreases when partial compression is applied during shearing and the stored elastic energy increases with increasing value of compressive stress.

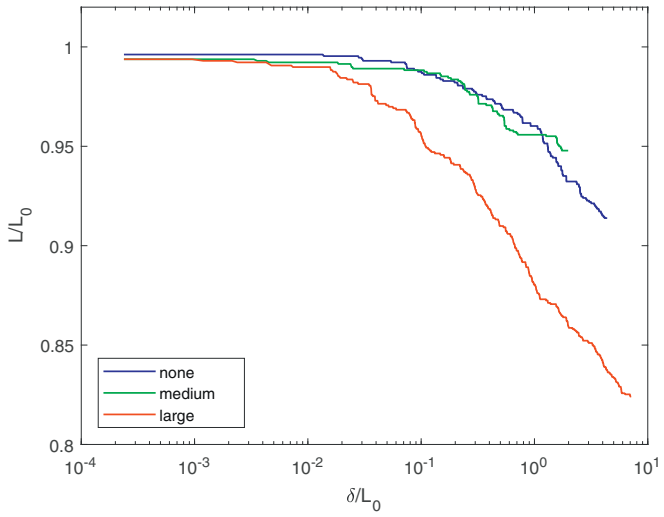

Fig. 7. The average particle length (L/L_0) change during shearing that follows a partial compression. This example is for particle strength $\sigma_{max} = 3200$. In the legend, labels "none", "medium" and "large" denote compressive stress S/σ_{max} equal 0, 1.5×10^{-4} and 3.2×10^{-4}, respectively.

3.4. Particle size distribution

Although the mean particle length and the polydispersity contain information about the bulk layer, additional details can be conveyed by analysing the full particle size distribution (PSD). A typical course of PSD evolution during pre-compression is shown in Fig. 10. For small values of compressive stress, a small difference is visible between the top and the bottom layer due to the additional stress at the bottom, caused by the weight of the layer. This difference disappears as the compressive stress increases.

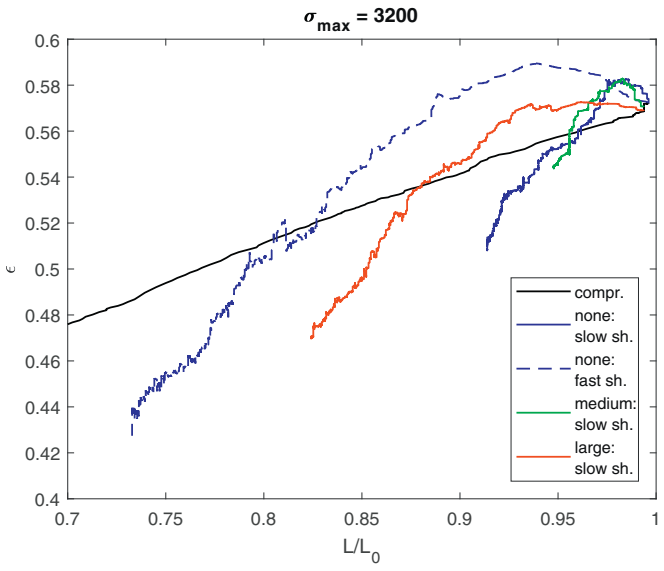

Fig. 8. Relation between average particle length (L/L_0) and the porosity of the layer ε. Comparison between compression ("compr." label, black line), slow/fast shearing without compressive stress ("none:slow/fast sh." labels, blue lines) and partial compression with medium (1.5×10^{-4}) and large (3.2×10^{-4}) compressive stress followed by slow shearing ("medium:slow sh." label, green line and "large:slow sh." label, red line). (For interpretation of the references to color in this figure legend, the reader is referred to the web version of this article.)

For the shearing mode (cf. Fig. 11), the course is similar to PSD evolution during compression and no difference between the two modes is visible. Additionally, the comparison of Fig. 11a and b reveals that also the shearing rate does not have an effect on the appearance of the PSD.

3.5. Particle orientation and velocity profile

Another interesting consequence of shear is the change of particle orientation from random to oriented [21,24,25]. During the course of shearing, particles become oriented preferentially along the shearing direction as is demonstrated in Fig. 12. The angle between the particle axis and the shearing direction has been calculated for every particle in the layer and the orientation distribution has been plotted at different stages of shearing. It can be seen that the initial distribution is uniformly random, while distributions at higher shearing distance contain a clear peak at low angle (i.e. particles oriented along the shearing distance) that increases with longer shearing distance.

Finally, the velocity profile has been analysed by calculating the mean particle velocity along the shearing direction at several vertical positions (Fig. 13). The typical velocity profile is qualitatively different for slow and fast shearing rates. At slow shearing, the velocity profile is more uniform (almost linear) and stable, while at fast shearing the profile is "S"-shaped and is fluctuating rapidly during shearing. The large velocity gradient is a sign of the formation of a narrow zone between two layer parts that move at different velocities and the breaking of particles localized within the zone. The smaller gradient at slower shearing rate suggests that the spatial distribution of breakage events is less localized than at faster shearing.

4. Conclusion

The breakage patterns occurring in a layer of needle-shaped particles during compression and shearing have been analysed in detail and compared. The results of computational experiments reveal that when the course of particle breakage is represented in the $L \mid Z$ diagram (mean particle length vs. polydispersity), the breakage patterns for slow shearing and compression follow the same path that is close to the path

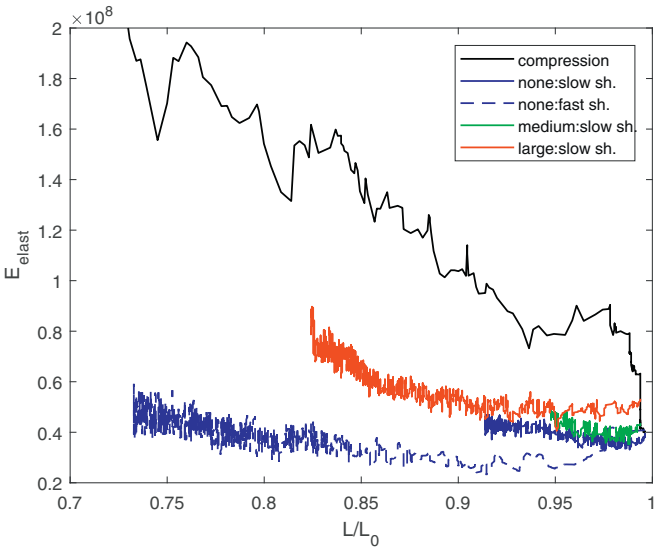

Fig. 9. Relation between average particle length (L/L_0) and stored elastic energy E_{elast} during different scenarios. The label and color notation is the same as in Fig. 8.

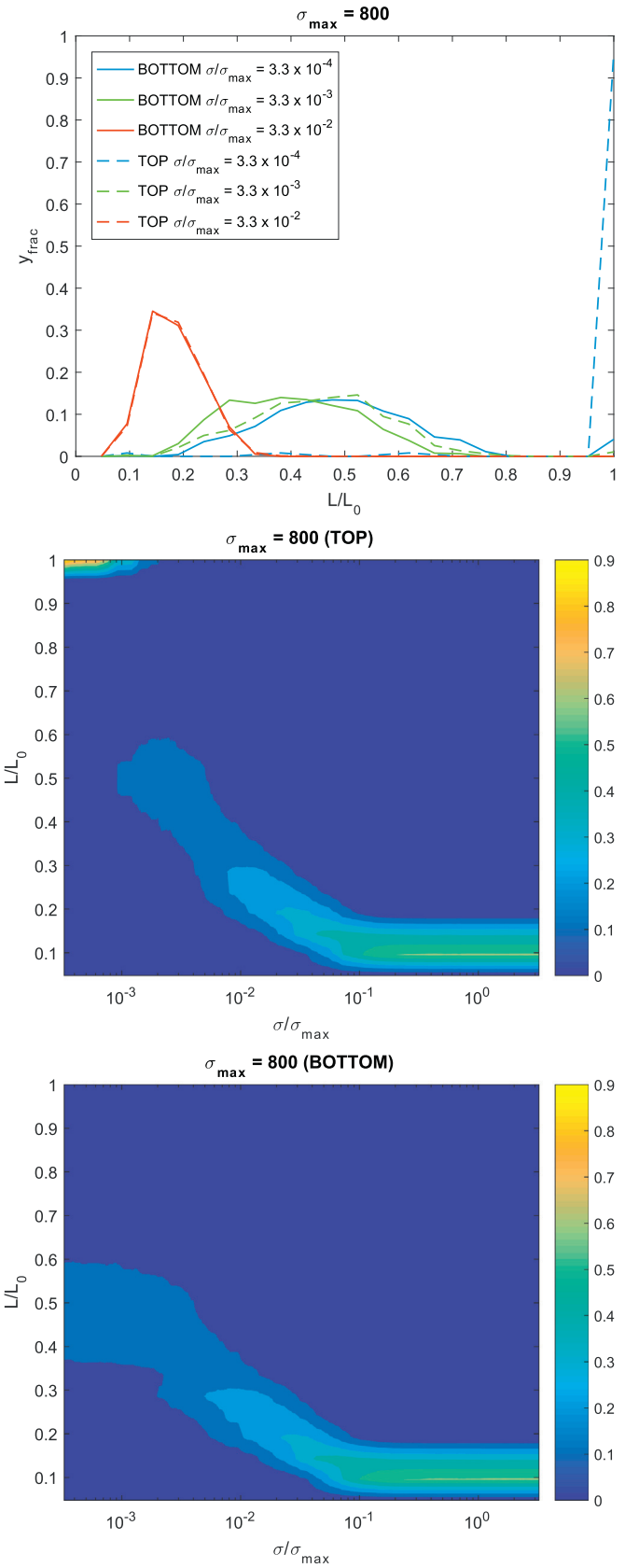

Fig. 10. Particle size distribution during compression in the top and bottom part of the layer. Example for particle strength $\sigma_{max} = 800$.

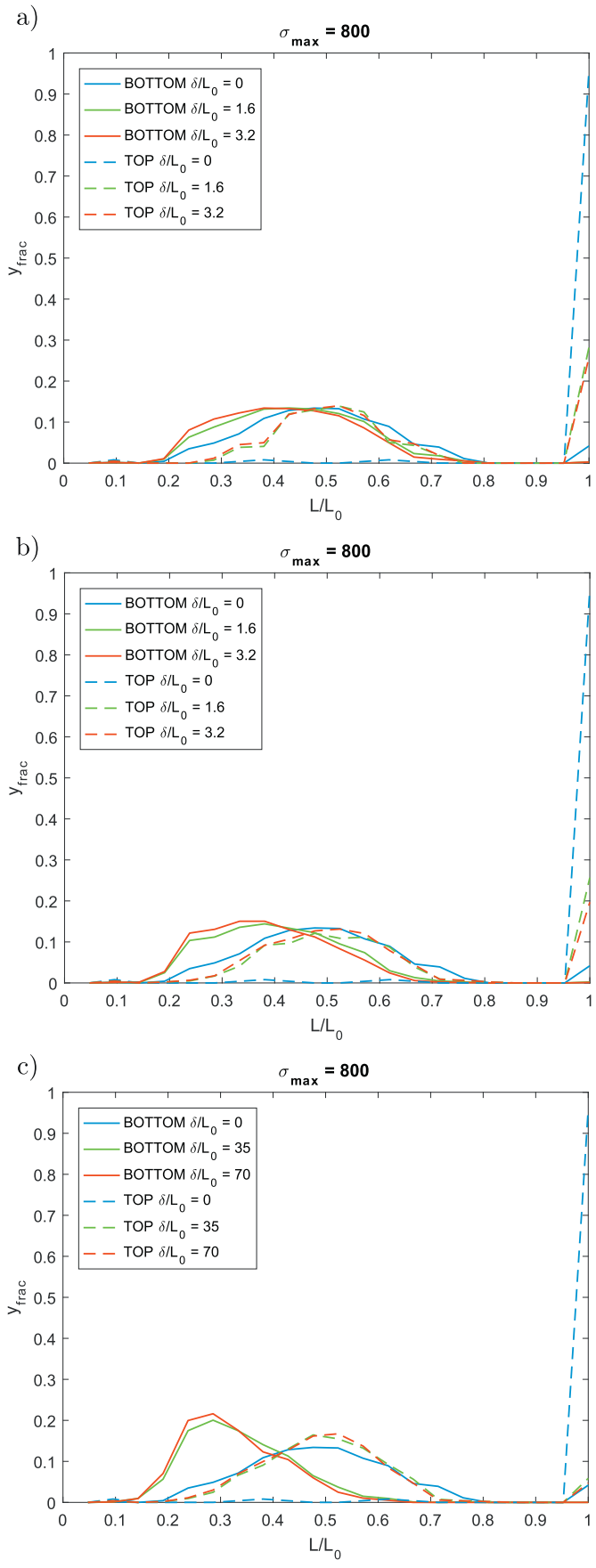

Fig. 11. Particle size distribution during shear in the top and bottom part of the layer. a) Slow shear, b) fast shear at the same sheared distance as in panel a, c) fast shear at longer sheared distance.

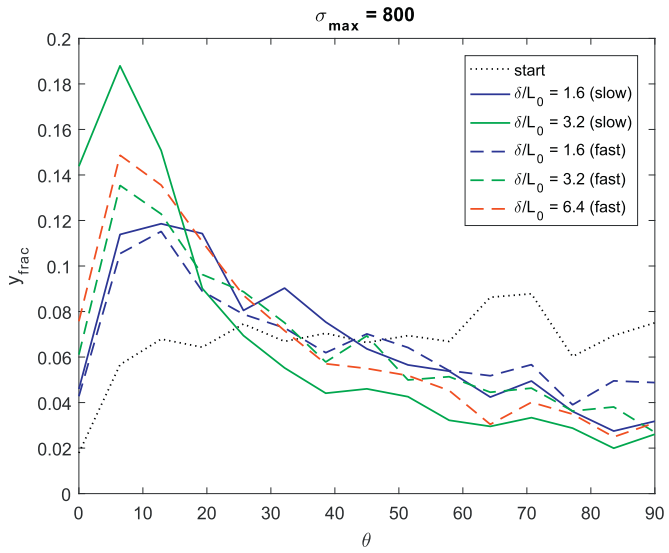

Fig. 12. Orientation distribution change during shearing.

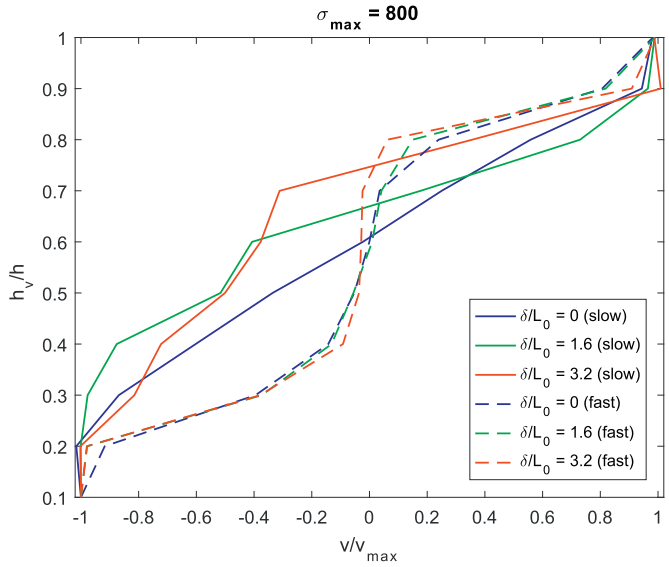

Fig. 13. Velocity profile in sheared layers.

constructed for an idealized breakage scenario, while curves for fast shearing deviate from the scenario towards higher polydispersities. Higher velocity gradients and localization of breakage events in a narrower zone that has been observed at faster shearing rates is a possible cause of this deviation. Therefore, we believe that the idealized breakage scenario can be used for the construction of population balance kernels describing the breakage process for both the compression and sufficiently slow shearing rates, with a possible extension also to faster shearing rates by introducing an additional parameter quantifying the localisation of the shear zone.

Notation

δ	sheared distance, m
E_{elas}	sum of elastic energies over particle contacts, J
ε	bed porosity, dimensionless
h	bed height, m
L	mean particle length, m

L_0	initial particle length, m
M	mass of the top wall, kg
n	number of particles, dimensionless
S	compressive stress in the bed, dimensionless
s_0	scaling unit of stress, Pa
σ_{max}	particle strength threshold, dimensionless
v	shearing velocity, m/s
Δx	computational domain size, m
Δy	computational domain size, m
y_{frac}	number fraction of particles in distribution plots, dimensionless
Z	polydispersity index, dimensionless

Acknowledgment

Support from Czech Science Foundation through Grant No. 15-05534S is gratefully acknowledged.

Appendix A. Breakage algorithm for non-inertial particles

Rigid body motion is described by Newton

$$\ddot{\mathbf{r}} = \mathbf{F}/m \tag{A.1}$$

and Euler equations

$$I_{xx}\dot{\omega}_x = T_x + (I_{yy} - I_{zz})\omega_y\omega_z \tag{A.2a}$$

$$I_{yy}\dot{\omega}_y = T_y + (I_{zz} - I_{xx})\omega_z\omega_x \tag{A.2b}$$

$$I_{zz}\dot{\omega}_z = T_z + (I_{xx} - I_{yy})\omega_x\omega_y. \tag{A.2c}$$

Please note that the vector components of $\mathbf{T}$ and $\boldsymbol{\omega}$ vectors should be for a particle coordinate system (particle coordinate system is chosen in such a way that the off-diagonal components of inertia tensor become zero).

An algorithm for the decision if and at what position a particle breaks will be described here in Appendix. It is based on the method of section: the particle AB is imaginarly divided into two sub-particles A and B (as shown in Fig. **A1**) and the internal force $\mathbf{F}^*$ and the internal torque $\mathbf{T}^*$ holding the sub-particles together is evaluated. An algorithm based on this concept was used in simulations of gradual compression of the layer of breakable needle-shaped particles [5]. As a steady-state could be reached after each compression step, it was possible to use the assumption that when the internal force and torque were evaluated, the particles were stationary (i.e. inertial). In the case of shearing, this assumption is no longer valid. Therefore, the algorithm has to be modified so it can account for non-inertial particles as well.

Let $\mathbf{f}_i$ be the sum of contact forces and gravitational force on i-th spherical element within particle AB located at the position $\mathbf{r}_i$. Then

$$\mathbf{F}_A = \sum_{i\in A} \mathbf{f}_i \tag{A.3a}$$

$$\mathbf{F}_B = \sum_{i\in B} \mathbf{f}_i \tag{A.3b}$$

$$\mathbf{F}_{AB} = \mathbf{F}_A + \mathbf{F}_B, \tag{A.3c}$$

where $\mathbf{F}_A$, $\mathbf{F}_B$ and $\mathbf{F}_{AB}$ are sums of forces acting on sub-particles A and B and particle AB, respectively. If $\mathbf{r}_A$, $\mathbf{r}_B$ and $\mathbf{r}_{AB}$ are center of mass positions of sub-particles A and B and particle AB, respectively, the torque acting on sub-particles A and B and particle AB can be calculated as

$$\mathbf{T}_A = \sum_{i\in A}((\mathbf{r}_i - \mathbf{r}_A) \times \mathbf{f}_i) \tag{A.4a}$$

$$\mathbf{T}_B = \sum_{i\in B}((\mathbf{r}_i - \mathbf{r}_B) \times \mathbf{f}_i) \tag{A.4b}$$

$$\mathbf{T}_{AB} = (\mathbf{r}_A - \mathbf{r}_{AB}) \times \mathbf{F}_A + (\mathbf{r}_B - \mathbf{r}_{AB}) \times \mathbf{F}_B + \mathbf{T}_A + \mathbf{T}_B. \tag{A.4c}$$

The movement of sub-particle A will follow Eqs. A.1 and A.2, yet the internal force $\mathbf{F}^*$ and torque $\mathbf{T}^*$ due to the connection with sub-particle B must be added to $\mathbf{F}_A$ and $\mathbf{T}_A$. Equations of motion for sub-particle A will be therefore

$$\ddot{\mathbf{r}}_A = (\mathbf{F}_A + \mathbf{F}^*)/m_A \tag{A.5}$$

and

$$I_{xx,A}\dot{\omega}_{x,A} = U_x + T_x^* + (I_{yy,A} - I_{zz,A})\omega_{y,A}\omega_{z,A} \tag{A.6a}$$

$$I_{yy,A}\dot{\omega}_{y,A} = U_y + T_y^* + (I_{zz,A} - I_{xx,A})\omega_{z,A}\omega_{x,A} \tag{A.6b}$$

$$I_{zz,A}\dot{\omega}_{z,A} = U_z + T_z^* + (I_{xx,A} - I_{yy,A})\omega_{x,A}\omega_{y,A}. \tag{A.6c}$$

In previous equations, $\mathbf{U} = [U_x, U_y, U_z]$ is a short-hand notation for

$$\mathbf{U} = \mathbf{T}_A + (\mathbf{r}_d - \mathbf{r}_A) \times \mathbf{F}^*,$$

where $\mathbf{r}_d$ is the position of the boundary between sub-particles.

Because relative position of sub-particles do not change, the following kinematic relations must also hold

$$\dot{\mathbf{r}}_A = \dot{\mathbf{r}}_{AB} + \boldsymbol{\omega}_{AB} \times (\mathbf{r}_A - \mathbf{r}_{AB}) \tag{A.7}$$

$$\boldsymbol{\omega}_{AB} = \boldsymbol{\omega}_A = \boldsymbol{\omega}. \tag{A.8}$$

Making the derivatives with respect to time of Eqs. A.7 and A.8 leads to

$$\ddot{\mathbf{r}}_A = \ddot{\mathbf{r}}_{AB} + \dot{\boldsymbol{\omega}}_{AB} \times (\mathbf{r}_A - \mathbf{r}_{AB}) + \boldsymbol{\omega}_{AB} \times (\boldsymbol{\omega}_{AB} \times (\mathbf{r}_A - \mathbf{r}_{AB})) \tag{A.9}$$

and

$$\dot{\boldsymbol{\omega}}_{AB} = \dot{\boldsymbol{\omega}}_A. \tag{A.10}$$

Finally, by writing Newton equation A.1 for particle AB and substituting it, together with Eq. A.5, to the kinematic relation, Eq. A.9, the internal force $\mathbf{F}^*$ can be explicitly evaluated

$$\frac{\mathbf{F}^*}{m_A} = -\frac{\mathbf{F}_A}{m_A} + \frac{\mathbf{F}_{AB}}{m_{AB}} + \dot{\boldsymbol{\omega}}_{AB} \times (\mathbf{r}_A - \mathbf{r}_{AB}) + \boldsymbol{\omega}_{AB} \times (\boldsymbol{\omega}_{AB} \times (\mathbf{r}_A - \mathbf{r}_{AB})) \tag{A.11}$$

Let us note, that for an inertial particle (e.g. during a steady-state compression), Eq. A.11 reduces to $\mathbf{F}^* + \mathbf{F}_A = \mathbf{0}$, which is an expression that can be found in classical textbooks dealing with shearing stress and bending moment evaluation for loaded beams. The three additional terms in Eq. A.11 correspond to corrections that have to be considered for non-inertial particles, namely due to (i) the translational acceleration, (ii) the rotational acceleration and (iii) the centrifugal force.

The internal torque $\mathbf{T}^*$ can be evaluated in an analogous way: Euler equations written for sub-particle A (Eqs. A.6) and for particle AB are substituted into Eq. A.10, Eq. A.8 is considered and the resulting formulas are rearranged to obtain:

$$\frac{T_x^* + U_x}{I_{xx,A}} = \frac{T_{x,AB}}{I_{xx,AB}} + \left(\frac{I_{yy,AB} - I_{zz,AB}}{I_{xx,AB}} - \frac{I_{yy,A} - I_{zz,A}}{I_{xx,A}}\right)\omega_y\omega_z \tag{A.12a}$$

$$\frac{T_y^* + U_y}{I_{yy,A}} = \frac{T_{y,AB}}{I_{yy,AB}} + \left(\frac{I_{zz,AB} - I_{xx,AB}}{I_{yy,AB}} - \frac{I_{zz,A} - I_{xx,A}}{I_{yy,A}}\right)\omega_z\omega_x \tag{A.12b}$$

$$\frac{T_z^* + U_z}{I_{zz,A}} = \frac{T_{z,AB}}{I_{zz,AB}} + \left(\frac{I_{xx,AB} - I_{yy,AB}}{I_{zz,AB}} - \frac{I_{xx,A} - I_{yy,A}}{I_{zz,A}}\right)\omega_x\omega_y. \tag{A.12c}$$

The remaining part of the algorithm is the same as has been already described in [5]: The internal loading calculated by Eqs. A.11 and A.12 is the actual force and torque holding the sub-particles together. They can be resolved into two components, one parallel and the other perpendicular to the main axis of the particle, cf. Fig. **A1**,

$$\mathbf{F}^* = \mathbf{N} + \mathbf{W} \qquad \mathbf{T}^* = \mathbf{R} + \mathbf{Y}, \tag{A.13}$$

where **N** and **W** are the axial and the shear force, respectively, **R** is the torsional moment and **Y** is the bending moment. As breakage of particle as a result of the axial loading or the torsion is not considered, bending is the only mechanism that can lead to breakage. The maximum transverse (shear) stress τ and maximum longitudal (bending) stress ρ along the particle is calculated. The flexure and shear formulae for a beam with circular cross-section of radius r_C are

$$\rho = \max_{\mathbf{r}_d} \frac{4}{\pi r_C^3} |\, \mathbf{Y}(\mathbf{r}_d)\,|, \qquad \tau = \max_{\mathbf{r}_d} \frac{4}{3\pi r_C^2} |\, \mathbf{W}(\mathbf{r}_d)\,|\,. \tag{A.14}$$

If the maximum stress due to this internal loading $\max(\rho,\tau)$ exceeds a particular threshold value $s_{max} = \sigma_{max}/s_0$, then the particle will break at the point of this maximum stress. Additional details can be found in [5].

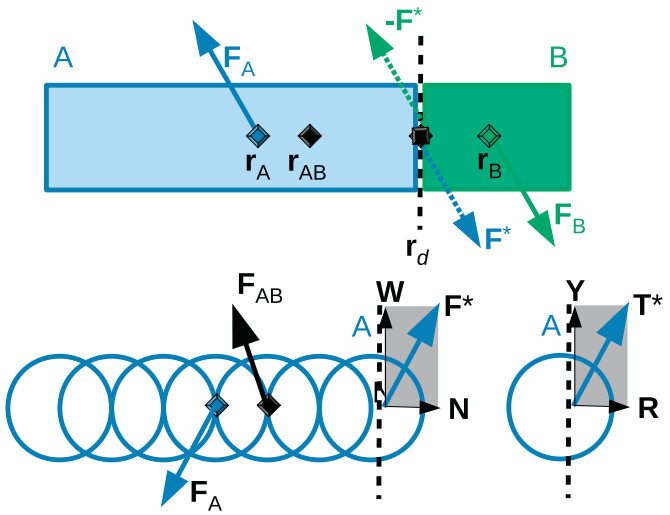

Fig. A1. Illustration of the breakage algorithm.

References

[1] B. Szilágyi, P.S. Agachi, B.G. Lakatos, Numerical analysis of crystalization of high aspect ratio crystals with breakage, Powder Technol. 283 (2015) 152–162.
[2] B. Szilágyi, B.G. Lakatos, Model-based analysis of stirred cooling crystalizer of high aspect ratio crystals with linear and nonlinear breakage, Comput. Chem. Eng. 98 (2017) 180–196.
[3] S.G. Agrawal, A. Balandier, A.H.J. Paterson, J.R. Jones, Study on lactose attrition inside the mixing cell of a laser difraction particle sizer using a novel attrition index, Powder Technol. 208 (2011) 669–675.
[4] C. Hare, M. Ghadiri, Attrition of paracetamol and aspirin under bulk shear deformation, Chem. Eng. Sci. 125 (2015) 13–19.
[5] Z. Grof, M. Kohout, F. Stepanek, Multi-scale simulation of needle-shaped particle breakage under uniaxial compaction, Chem. Eng. Sci. 62 (2007) 1418–1429.
[6] Z. Grof, C.M. Schoellhammer, P. Rajniak, F. Stepanek, Computational and experimental investigation of needle-shaped crystal breakage, Int. J. Pharm. 407 (2011) 12–20.
[7] Z. Grof, F. Stepanek, Distribution of breakage events in random packings of rodlike particles, Phys. Rev. E 88 (2013) 012205.
[8] X. Hua, J. Curtis, Y. Guo, B. Hancock, W. Ketterhagen, C. Wassgren, The internal loads, moments, and stresses in rod-like particles in a low-speed, vertical axis mixer, Chem. Eng. Sci. 134 (2015) 581–598.
[9] Y. Guo, C. Wassgren, B. Hancock, W. Ketterhagen, J. Curtis, Predicting breakage of high aspect ratio particles in an agitated bed using the discrete element method, Chem. Eng. Sci. 158 (2017) 314–327.
[10] Z. Grof, F. Stepanek, Quantifying the effect of fillers on the breakage behaviour of needle-shaped particles, Adv. Powder Technol. 27 (2016) 1093–1100.
[11] P. Fu, Y.F. Dafalias, Fabric evolution within shear bands of granular materials and its relation to critical state theory, Int. J. Numer. Anal. Methods Geomech. 35 (2011) 1918–1948.
[12] W.M. Yan, L. Zhang, Fabric and the critical state of idealized granular assemblages subject to biaxial shear, Comput. Geotech. 49 (2013) 43–52.
[13] Y. Yang, Y.M. Cheng, J.A. Wang, Exploring the contact types within mixtures of different shapes at the steady state by DEM, Powder Technol. 301 (2016) 440–448.
[14] H. Zhao, X. An, D. Gou, B. Zhao, R. Yang, Attenuation of pressure dips underneath piles of spherocylinders, Soft Matter 14 (2018) 4404–4410.
[15] T. Kulju, M. Paavola, H. Spittka, R.L. Keiski, E. Juuso, Modeling continuous high-shear wet granulation with DEM-PB, Chem. Eng. Sci. 142 (2016) 190–200.
[16] P.A. Cundall, O.D.L. Strack, Discrete numerical-model for granular assemblies, Geotechnique 29 (1979) 47–65.
[17] J.F. Favier, M.H. Abbaspour-Fard, M. Kremmer, A.O. Raji, Shape representation of axisymmetrical, non-spherical particles in discrete element simulation using multi-element model particles, Eng. Comput. 16 (1999) 467–480.
[18] D.O. Potyondy, P.A. Cundall, A bonded-particle model for rock, Int. J. Rock Mech. Min. Sci. 41 (2004) 1329–1364.
[19] D. Golchert, R. Moreno, M. Ghadiri, J. Litster, Effect of granule morphology on breakage behaviour during compression, Powder Technol. 143–144 (2004) 84–96.
[20] T. Afshar, M.M. Disfani, A. Arulrajah, G.A. Narsilio, S. Emam, Impact of particle shape on breakage of recycled construction and demolition aggregates, Powder Technol. 308 (2017) 1–12.
[21] J. Tian, E. Liu, Effect of particle shape on micro- and mesostructure evolution of granular assemblies under biaxial loading conditions, C. R. Mécanique 346 (2018) 1233–1252.
[22] S.R. Williams, A.P. Philipse, Random packings of spheres and spherocylinders simulated by mechanical contraction, Phys. Rev. E 67 (2003) 051301.
[23] I. Einav, Fracture propagation in brittle granular matter, Proc. R. Soc. A 436 (2007) 3021–3035.
[24] R.C. Hidalgo, B. Szabo, K. Gillemot, T. Borzsonyi, T. Weinhart, Rheological response of nonspherical granular flows down an in cline, Phys. Rev. Fluids 3 (2018) 074301.
[25] A. Sufian, A.R. Russell, A.J. Whittle, Evolving pore orientation, shape and size in sheared granular assemblies, Granul. Matter 21 (2019) 4.

9. ARTICLES ABOUT TABLET DISSOLUTION

9.1 Experimental analysis of inter- and intra-batch variation of granule porosity, stiffness and dissolution rate

David Smrčka
Veronika Lesáková
Jiří Dohnal
Zdeněk Grof
František Štěpánek

Published in the *Chem. Eng. Res. Des.*, Vol. 132, 2018, pp. 1131–1142
DOI: 10.1016/j.cherd.2018.02.014.

Contents lists available at ScienceDirect

Chemical Engineering Research and Design

journal homepage: www.elsevier.com/locate/cherd

Experimental analysis of inter- and intra-batch variation of granule porosity, stiffness and dissolution rate

David Smrčka[a,b], Veronika Lesáková[a], Jiří Dohnal[b], Zdeněk Grof[a], František Štěpánek[a,*]

[a] Department of Chemical Engineering, University of Chemistry and Technology Prague, Technická 3, 166 28 Praha 6, Czech Republic

[b] Zentiva k.s., U Kabelovny 130, 102 00 Praha 10, Czech Republic

ARTICLE INFO

Article history:
Received 30 September 2017
Received in revised form 9 January 2018
Accepted 6 February 2018
Available online 14 February 2018

Keywords:
Porosity
X-ray micro-tomography
High-shear wet granulation
Texture analysis
Single granule dissolution
Froude number

ABSTRACT

Using a pharmaceutical formulation, granule batches were produced at a range of granulator volumes from 0.5 L to 400 L and process conditions, characterised by the Froude number in the range from Fr = 0.26 to Fr = 1.63. The mean values and the standard deviations of granule porosity, granule stiffness and granule dissolution rate evaluated from each batch using the 400–1000 μm sieve fraction were compared in order to establish structure–property correlations. Both granule stiffness and granule dissolution rate were found linearly correlated with the Froude number. A significant intra-batch variability of all investigated granule properties was observed. The relative standard deviation of granule stiffness also increased linearly with the Froude number. Coupled experiments relating the microstructure of granules with their individual compression and dissolution curves were carried out for the first time. A surprising diversity of intra-batch granule structures and their associated dissolution rates was found in batches produced at both low and high Froude numbers, highlighting the importance of avoiding granule segregation in downstream unit operations in order to maintain consistent drug release profiles from the investigated formulation.

© 2018 Institution of Chemical Engineers. Published by Elsevier B.V. All rights reserved.

1. Introduction

In high-shear wet granulation, each individual granule experiences a unique sequence of collision events and intervals of exposure to a range of shear and normal stresses, depending on the circulation pattern of the granular mass in the vessel (Gantt et al., 2006; Nakamura et al., 2013; Khalilitehrani et al., 2014). The distribution of local conditions, such as velocity or shear rate, in a typical pharmaceutical high-shear mixer granulator can be rather broad (Reynolds et al., 2008). Parameters such as the bowl diameter, the impeller rotation rate, or the powder fill level jointly determine the distribution of local conditions that individual granules are exposed to during the granulation process. The specific sequence of collision events and stress history that each granule experiences during its residence time in the granulator then determines the resulting granule properties such as porosity (Farber et al., 2003; Rajniak et al., 2007; Hafsa et al., 2014), strength (Rahmanian et al., 2009; Wade et al., 2015) or dissolution rate (Mangwandi et al., 2010; Ring et al., 2011). Since the ensemble properties of the granular matter are a superposition of the individual granule properties, the distribution of these properties within a granule population directly determines the end-use properties of the bulk.

Despite a large body of literature dealing with the high-shear wet granulation process and its sensitivity to various process- and formulation-related parameters, in most cases the only commonly measured distributed property is particle size (PSD), whereas the intra-batch variation of other granule properties is rarely reported. Only a few studies that focus

* Corresponding author.
E-mail address: Frantisek.Stepanek@vscht.cz (F. Štěpánek).
https://doi.org/10.1016/j.cherd.2018.02.014
0263-8762/© 2018 Institution of Chemical Engineers. Published by Elsevier B.V. All rights reserved.

Table 1 – Granulation process conditions.

Granulator volume (L)	Impeller diameter (m)	Impeller rotation rate (rpm)	Froude number (–)	Impeller tip speed (m/s)
400	1.0	95	0.26	4.97
0.5	0.14	361	0.52	2.65
400	1.0	135	0.52	7.07
4	0.21	455	1.23	5.00
0.5	0.14	642	1.63	4.71
0.5	0.14	642	1.63	4.71

on the statistical distribution of other properties than particle size can be found in the literature. These include studies of binder distribution (Reynolds et al., 2004), porosity distribution (Ramachandran et al., 2008), or solid component distribution across granule size classes (Ramachandran et al., 2012; Oka et al., 2015), as well as studies of the statistical distribution of individual granule dissolution rates in relationship to that of the bulk (Kochba et al., 1994). A few studies relating the microstructure of individual granules to their end-use properties can also be found. These include a study relating individual granule microstructure to its stiffness under normal load (Dosta et al., 2016), or studies relating the component distribution within a granule to its release rate during dissolution (Ansari and Štěpánek, 2008; Kašpar et al.,2013).

However, quantitative studies correlating all three properties (porosity, stiffness, dissolution) for a single formulation processed at different granulator scales are very rare. Consequently, there is a gap in our understanding of how the process–structure–property relationships at the individual particle level project into the collective properties of the granule population as a whole. Hence, the aim of the present work is to provide an experimental data set that systematically compares the properties of individual granules (porosity, stiffness, dissolution rate) produced under different conditions (impeller rpm and granulator scale) with the population averages. Using a pharmaceutical formulation (Smrčka et al., 2015) we explore the contribution of individual granule subpopulations within a batch to the bulk properties. For the first time, we compare structure–property correlations obtained at individual granule level with those obtained at the bulk level.

2. Experimental

2.1. Granule formulation and process

Six batches of granules were prepared by high-shear mixer granulation at various combinations of granulator volume and main impeller rotation rate, as specified in Table 1. These conditions represent a sub-set of a parametric sensitivity and scale-up study reported in our earlier work (Smrčka et al., 2015, 2016). The Glatt TMG (0.5 L and 4.0 L vessel), Glatt VG (25.0 L vessel) and the Aeromatic Fielder PMA (400 L vessel) granulators were used. The granulator bowels were geometrically similar and used a 3-blade angled main impeller (so-called Z-impeller). The granulation protocol consisted of 3 min of dry mixing, followed by 3 min of water addition and 3 min of wet massing. Water was added by means of a hose without any spraying or atomisation. Thus, the granulator was operated in the mechanical dispersion regime according to the classification described in Iveson et al. (2001). The granules were dried on a tray under ambient conditions, resulting in a residual moisture content (Loss on Drying – LOD) of $2.74 \pm 0.04\%$. For purpose of this work, granules belonging to the size range from 400 μm to 1 mm were retained for further investigation.

Table 2 – Granule formulation.

Component	Mass fraction (–)	$d_{4,3}$ (μm)
API	0.58	3
Prosolv SMCC 90	0.24	64
Neosorb P100T	0.07	97
Povidone K25	0.05	73
Sodium lauryl sulfate	0.01	43
Crospovidone	0.05	74

This size range was chosen as a statistically highly represented granule fraction, which at the same time enables reasonable manipulation with individual granules, especially in the context of coupled experiments (Section 2.5).

The granule composition, which is based on an actual pharmaceutical formulation specified in Table 2, was kept constant throughout the study. The Active Pharmaceutical Ingredient (API) represented more than half of the formulation by weight. Since the API was micronized ($d_{4,3} = 3$ μm), a relatively large binder/solids ratio (0.39, w/w) was required for the granulation. The roles of individual formulation components can be briefly described as follows. Povidone acts as a binder together with water. Prosolv is silicified microcrystalline cellulose, which improves the physical properties of the powder, such as flowability. Neosorb is a crystallised sorbitol powder, which has good tableting properties as well as a cool taste and a pleasant mouth-feel. Sodium lauryl sulfate is a surface-active agent that improves wettability. Crospovidone has good swelling characteristics and acts as a disintegrant.

2.2. Evaluation of granule stiffness

The sieved granules (size fraction 400–1000 μm) were subjected to a compression test using the CT3 Texture Analyzer (Brookfield). A cylindrical steel probe with a diameter of 4 mm was used for the compression of individual granules, which were fixed on a steel base table by a two-sided adhesive tape. The probe speed was fixed at 0.3 mm/s. The granule stiffness was evaluated by linear regression of the recorded load–displacement curve up to the first failure point. The stiffness of at least 25 granules from each batch was measured.

2.3. Micro CT analysis

The inner structure of the granules was examined via X-ray micro tomography using the SkyScan microCT attachment hosted in a Jeol JCM-5700 Scanning Electron Microscope. Using a Peltier-cooled CCD camera with 512×512 pixel resolution, a 180° scan was applied with 3 frames averaging. The field of view was set to 1.6 mm, which corresponds to a 3 μm per pixel resolution. The SkyScan/Bruker NRecon software (version 1.7.1.0) was used for the cone-beam reconstruction. The granule porosity was calculated from image analysis by using the ImageJ software. A cube was inscribed within the 3D recon-

Table 3 – Summary of granule properties from independent measurement of porosity and stiffness.

Granulator volume (L)	Froude number (–)	Granule porosity (%)	Granule stiffness (g/mm)	RSD of stiffness (%)
400	0.26	35.1 ± 10.4	248 ± 109	44
0.5	0.52	33.1 ± 7.2	352 ± 119	34
400	0.52	32.2 ± 5.1	361 ± 226	63
4	1.23	30.1 ± 2.4	744 ± 482	65
0.5	1.63	30.1 ± 2.4	803 ± 713	89
0.5	1.63	28.1 ± 6.3	710 ± 540	76

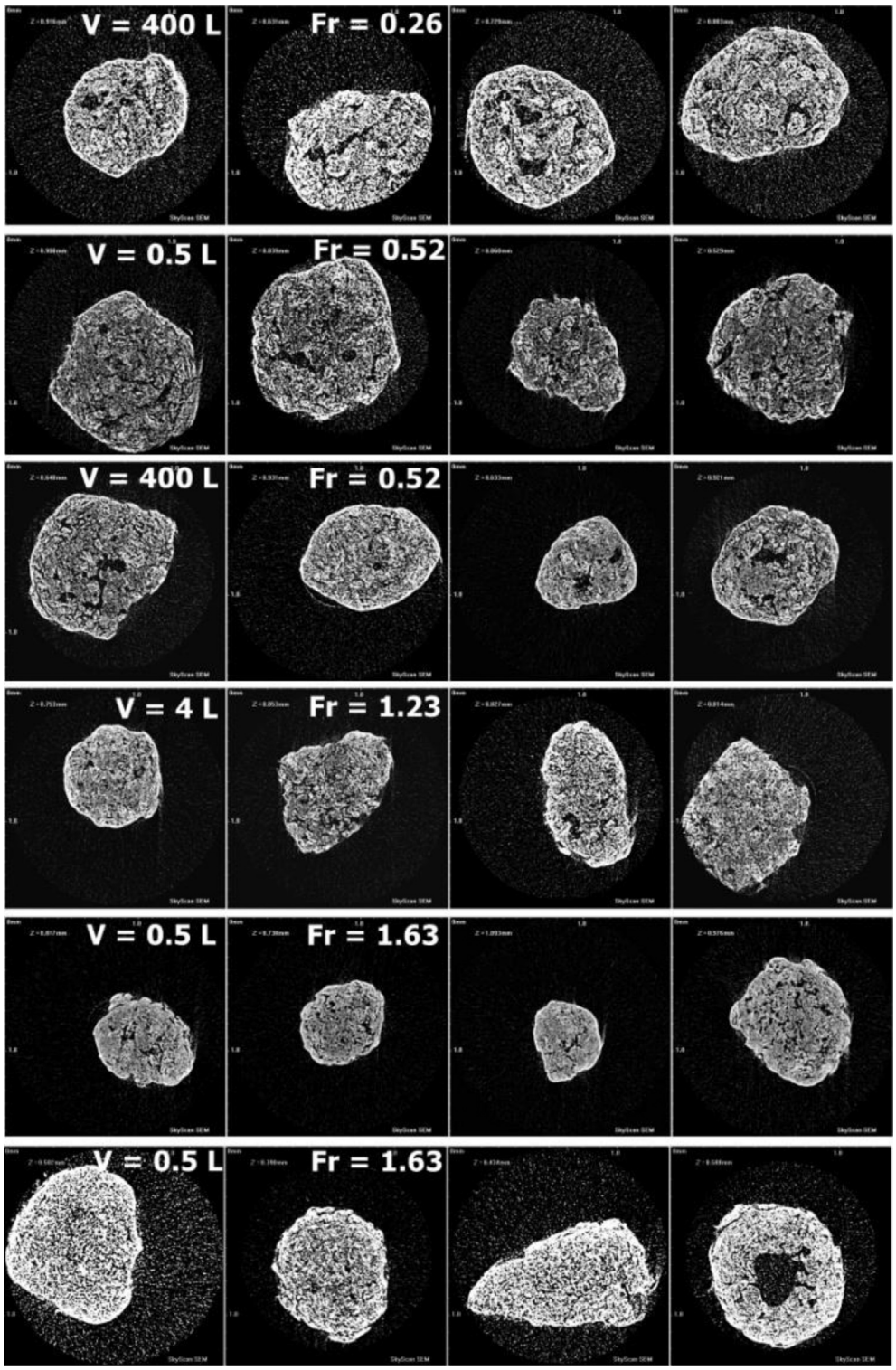

Fig. 1 – Examples of the inner structures of granules from the six batches specified in Table 1. Four granules per batch are shown in each row. The images show slices of 3D reconstructed micro CT images in the *x*–*y* plane located approximately in the middle of the granules along the *z*-axis.

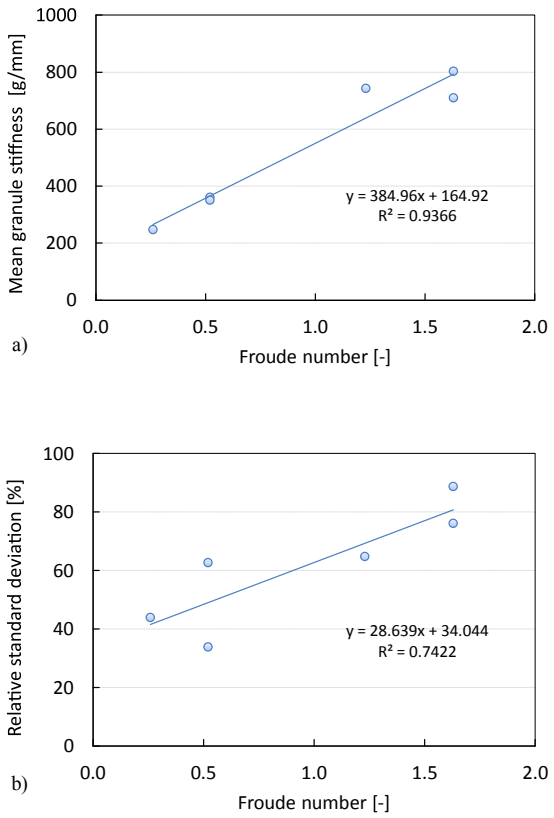

Fig. 2 – (a) Correlation between Froude number and the mean granule stiffness based on the six batches specified in Table 1. (b) Correlation between Froude number and the relative standard deviation (RSD) of granule stiffness based on the six batches specified in Table 1.

structed granule as a Region Of Interest. Image thresholding was done by the Otsu algorithm and porosity was evaluated as the fraction of voxels belonging to the pore space after image binarisation.

2.4. *Granule dissolution tests*

2.4.1. *Single granule dissolution*

A phosphate buffer (pH 4.5) at 37 °C was used as the dissolution medium. Each individual granule was weighed and its dissolution rate was then measured in a test tube filled by 2 ml of buffer with a micro magnetic stirrer (200 rpm) using the Pion μDISS Profiler apparatus equipped with fibre-optic UV/vis probes with 1 cm path-length tips. Absorbance at 250 nm was recorded as function of time for 60 min, yielding a dissolution curve for each granule. Typically, between 10 and 15 individual granules per batch were analysed.

2.4.2. *Bulk granule dissolution*

Dissolution was conducted in stirred vessels (100 rpm) containing 500 ml of buffer (pH 4.5 phosphate buffer at 37 °C). The API concentration as function of time was detected by UV spectrophotometry at 250 nm. The dissolution test was conducted either using a representative sample of granules from the entire batch in order to compare granule batches produced under different conditions (inter-batch variation), or using narrower size fractions (0–71 μm, 71–100 μm, 100–140 μm, 140–250 μm, 250–500 μm, and 500–1000 μm) in order to assess intra-batch variation of dissolution rate.

2.5. *Coupled methods*

In order to quantify the intra-batch variation of individual granule properties, coupled methods investigating the inner structure, mechanical properties and dissolution were used. The purpose of this coupling is to move from correlations between averaged values at the population level to paired information about the inner structure and an "external quality" (dissolution rate, granule stiffness) at the individual granule level. For coupled porosity-stiffness measurement, each granule was first weighed and scanned as described in Section 2.3. A double-sided adhesive tape with the granule was then carefully transferred from the sample stage of the micro-CT apparatus to the table kit of the Texture Analyzer and subjected to a compression test as described in Section 2.2. Information about the inner structure coupled with a load–displacement curve for each individual granule was obtained in this way. For coupled porosity-dissolution measurement, each granule was first weighed and then scanned as described in Section 2.3. After micro-CT scanning, the granule was gently removed from the adhesive tape and transferred to the dissolution test tube in which a single granule dissolution experiment was conducted as described in Section 2.4.1. The outcome of this coupling is information about the mass of the granule, its outer and inner 3D structure, and its dissolution profile.

3. Results and discussion

3.1. *Granule structure and porosity*

The results from micro CT measurements have shown a trend of decreasing mean granule porosity with increasing Froude number (Table 3). This is consistent with the expectation that a higher degree of consolidation should reduce the amount of cavities or voids within the granules. However, the difference in the mean porosity of granules produced at the lowest and the highest Froude number is only 7% (Table 3). This is comparable with the range of individual granule porosities that could be found within each batch, as manifested by the large standard deviations of porosity values (Table 3).

As can be seen from the micro CT images in Fig. 1, the granule structures produced at the highest and the lowest Froude numbers exhibit qualitative differences even though the quantitative differences in porosity values are small. In the case of low Froude numbers, the pores are generally wider, and a few larger pores are connected across the granule. Almost every granule had at least one larger rupture or defect. For higher Froude numbers, the pores are narrower and usually more evenly distributed across the granule. The granule inner structure appears to be formed by a more continuous, consolidated solid phase. It will be shown below that this may have a profound effect on both granule stiffness and dissolution rate. Interestingly, a few cases of hollow-core granules could also be found among the granules formed at higher Froude numbers, created probably by the arching of primary particles around a liquid droplet during the nucleation stage. A similar mechanism has been reported for in situ melt fluid bed granulation (Ansari and Štěpánek, 2006) and for the granulation of hydrophobic powders (Hapgood and Khanmohammadi, 2009).

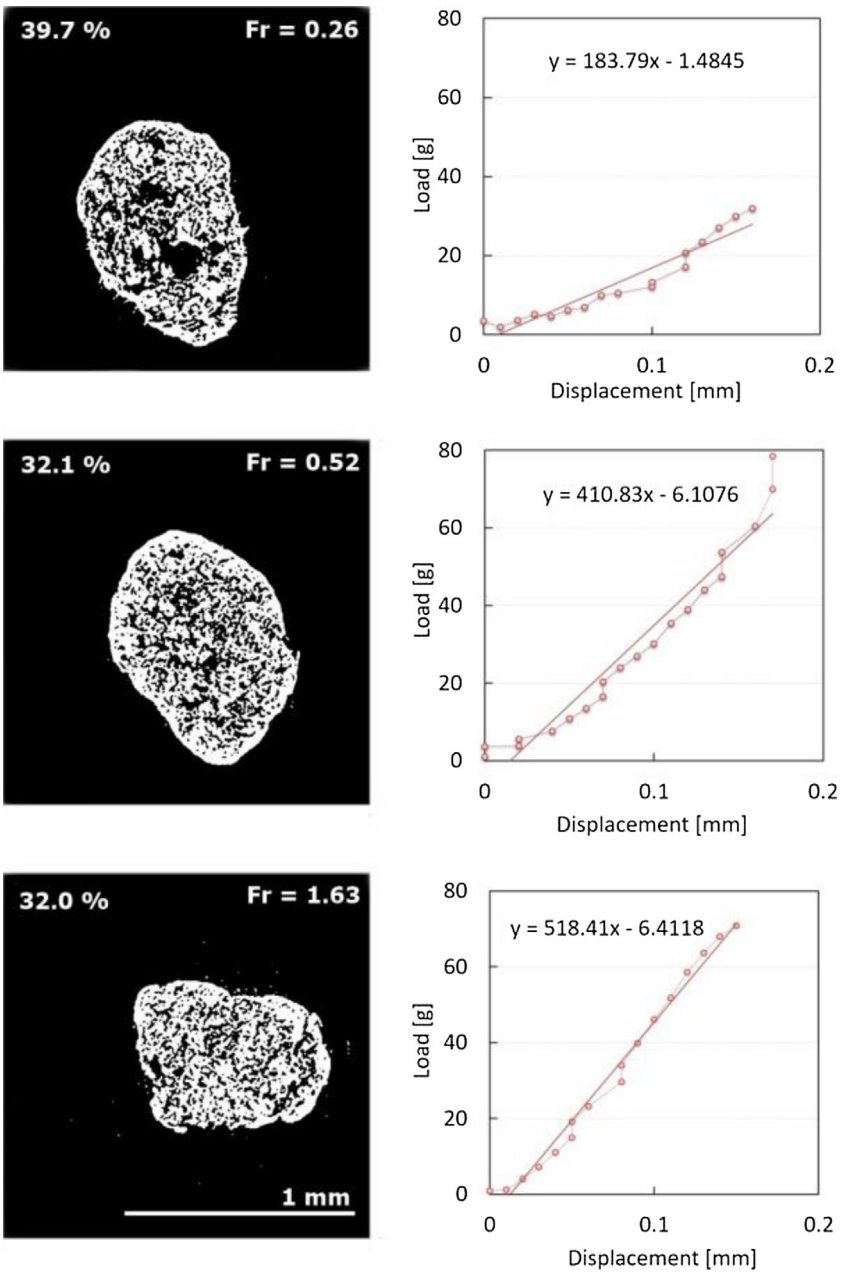

Fig. 3 – Example of inter-batch variation of granule structures and their load–displacement curves. The three granules were produced under different Froude numbers as indicated by each structure.

3.2. *Granule stiffness*

3.2.1. *Inter- and intra-batch variation*

Preliminary measurement of granule stiffness revealed a high level of variation among the mechanical properties of granules originating from a single batch. Hence, the number of tested granules was increased to 25 per batch in order to obtain statistically more robust data sets. When all data were recorded and the granule stiffness (slope of the initial linear part of the load–displacement curve) was plotted against the Froude number of the corresponding granulation experiment, a relatively strong correlation between those two parameters was obtained (see Fig. 2a). It can be reasoned that the connection between the Froude number and granule stiffness is via granule porosity and inner structure. As can be seen in Table 3, granule porosity systematically decreases with increasing Froude number, probably due to increased granule consolidation. Examples of individual granule structures and their corresponding load–displacement curves are shown in Figs. 3 and 4 for the inter- and intra-batch variation, respectively.

While the inter-batch comparison of granule stiffness revealed a linear correlation between the Froude number and granule stiffness, the intra-batch insight reveals a significant variation of stiffness among individual granules. The relative standard deviation (RSD) of granule stiffness for granules within one batch was found to be systematically increasing with increasing Froude number, as shown in Fig. 2b. Thus, it can be stated that granulation conditions characterised by a high Froude number result not only in a higher mean granule stiffness, but also in a broader distribution of granule stiffness within the granule population from the same batch.

For a fixed formulation and liquid to solid ratio, the main factor determining the extent of granule consolidation at the individual granule level is the individual history of kinetic energy, shear and normal stresses that the granule expe-

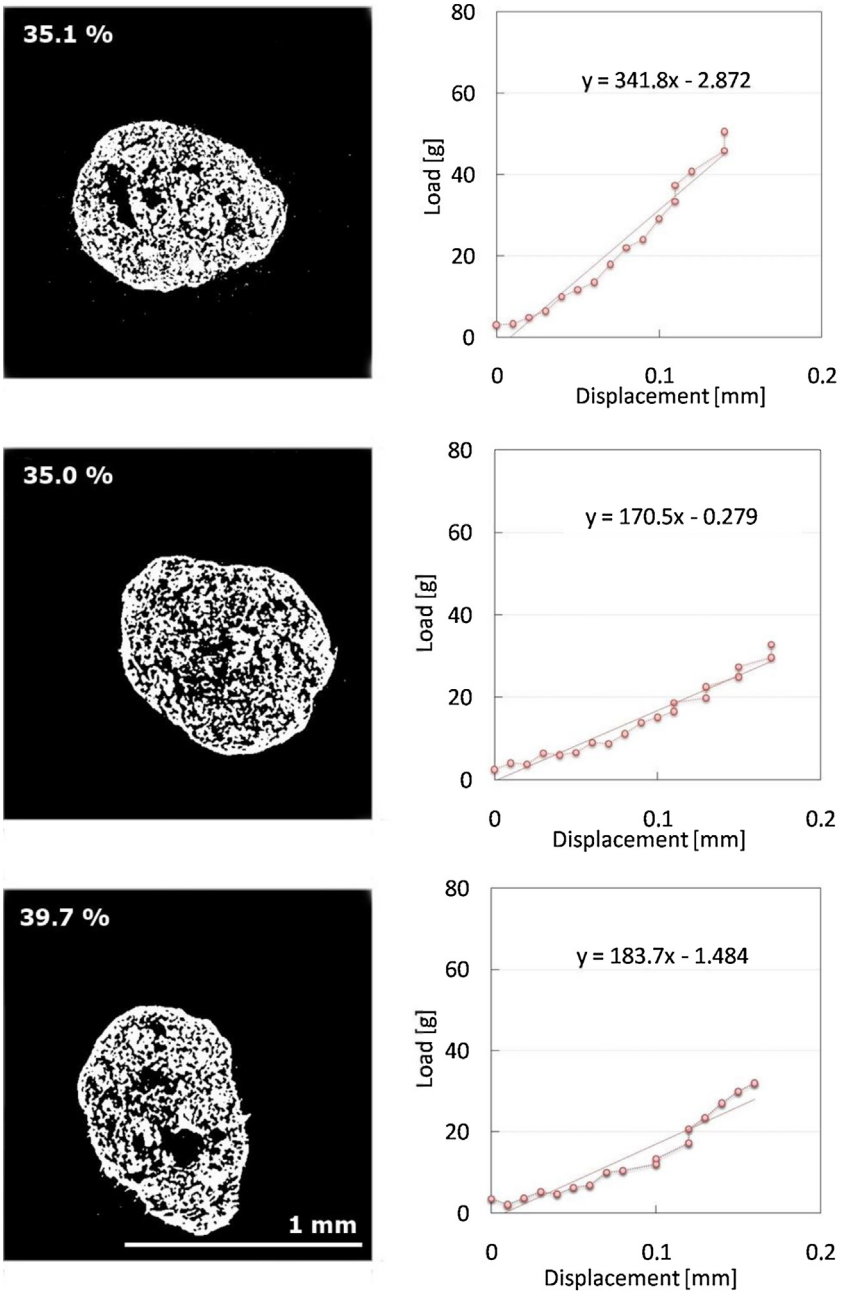

Fig. 4 – Example of intra-batch variation of granule structures and their load–displacement curves. The three granules originate from the same batch, i.e. they were produced under identical conditions (Fr = 0.26).

riences as it undergoes a quasi-periodic motion between high-velocity regions near the periphery and low-velocity regions closer to the centre of the granulation vessel. Therefore, the variation of granule properties at the intra-batch level could be affected by two factors: (i) the maximum tangential velocity of the impeller and thus the theoretical velocity range; and (ii) the flow pattern of the wet mass in the granulator, which determines the width of the "corridor" for particle trajectories.

In the specific case considered in this work, the lowest relative standard deviation (RSD) of 34% was found for granules produced at Fr = 0.52 and V = 0.5 L. An increase of impeller rpm in the same vessel (Fr = 1.63, V = 0.5 L) resulted in an increase of RSD to 89% (see Table 3 and Fig. 2b). Keeping constant Froude number (Fr = 0.52) but increasing the vessel volume from 0.5 L to 400 L resulted in a less dramatic increase of RSD, from 34% to 63%. Finally, when the impeller tip speed is kept constant (4.97–5.00 m/s) but the vessel diameter increases from 4.0 L to 400 L, the RSD of granule stiffness actually decreases from 64% to 44%, in line with a decrease in the Froude number from Fr = 1.23 to Fr = 0.26. Hence, it can be stated that for the formulation investigated in this work, the granule stiffness and its RSD are correlated with the Froude number as shown in Fig. 2, and not with the tip speed.

3.2.2. *Coupled experiments*

In order to confirm trends observed using mean values of granule populations, coupled experiments were performed on granules prepared at Froude numbers 0.26, 0.52 and 1.63 as described in Section 2.5. The results are summarised in Table 4 and the examples of granule structures with evaluated porosity and the corresponding load–displacement curve are shown in Fig. 3. With increasing Froude number the porosity of the granules dropped from 39.7% to 32.1%, while the granule stiffness increased from 184 g/mm to 518 g/mm. The granule produced at Fr = 0.26 contains large pores, which may explain

Table 4 – Summary of granule properties from coupled measurement of porosity and stiffness.

Froude number (–)	Granule porosity (%)	Granule stiffness (g/mm)
0.26	39.5	247
0.52	32.3	559
1.63	31.4	601

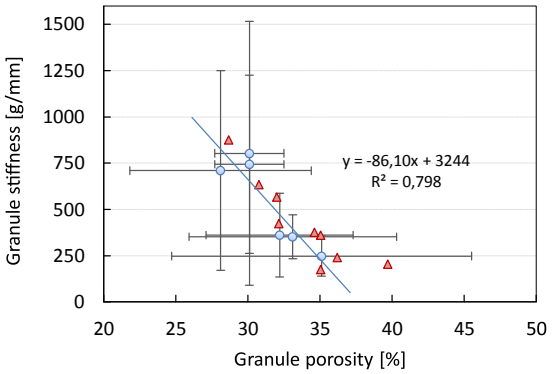

Fig. 5 – Correlation between granule stiffness and granule porosity. The circles represent mean values from the six batches specified in Table 1, where porosity and stiffness were measured independently as described in Sections 2.2 and 2.3, respectively. The triangles represent the results from a coupled experiment (Section 2.5), where porosity and stiffness were measured on the same granules.

its easy deformability (low gradient of the load–displacement curve). From these results it might seem that trend for inter-batch variation of granule properties is clear. However, there is still a significant variation within each batch and the porosity values of individual granules often overlay across batches produced under different Froude numbers.

An illustration of this behaviour is shown in Fig. 4, where three different granule structures belonging to the same batch (Fr = 0.26) are shown, along with their load displacement curves measured during the coupled experiment. The first and the second granule have a comparable porosity (35.1% and 35.0%, respectively) but the difference of their stiffness is huge (342 g/mm and 171 g/mm, respectively) due to qualitatively different inner structure. The first granule appears to be more solid with a few cavities contributing to the porosity, while the second granule has a sponge-like structure. Despite the fact that the third granule in Fig. 4 has a significantly higher porosity (39.7%), its stiffness is still higher (184 g/mm) than the second granule. From that point of view, the granule skeleton probably plays an important role and once it is solid enough, it provides the granules with a higher stiffness no matter if there are some cavities within.

3.2.3. *Structure–property correlation*

The overall relationship between granule porosity and stiffness, based on all experiments (both inter- and intra-batch analysis), is summarised in Fig. 5. It is interesting to observe that a relatively small increase of the mean granule porosity (from 28% to 35%) was responsible for a rather large decrease in the mean granule stiffness (from 710 g/mm to 248 g/mm). However, both granule porosity and granule stiffness exhibited rather broad intra-batch variation, as demonstrated by their standard deviations (Table 3) and discussed above. In order to test whether the correlation between granule stiffness and porosity seen in the mean values is not coincidental, data from coupled experiments (cf. Section 2.5) were also included in Fig. 5 (red triangles). As can be seen, they follow the same trend as the mean values of stiffness and porosity obtained from independent measurements. It can be concluded that a small change in porosity is generally associated with a large change in granule stiffness, and that this trend is valid both intra-batch for individual granules, and inter-batch for the mean values of granule populations. However, the inter- and intra-batch distributions of porosity and stiffness span across similarly broad intervals.

3.3. *Granule dissolution*

3.3.1. *Effect of Froude number*

Apart from granule stiffness, which is important mainly from the processing point of view (granule storage, handling, compression), a very important end-use property of pharmaceutical granules is the release rate of the active pharmaceutical ingredient (API). Granules from all batches were subjected to standard USP-type dissolution tests (Section 2.4.2) and the overall results are summarised in Fig. 6. It was found that the dissolution behaviour is strongly correlated with the Froude number under which the granules were produced, regardless of the granulator scale (Fig. 6b). It was also found that the correlation holds regardless of which time point on the dissolution curve is chosen as an integral measure of the API release, i.e. 5 min, 30 min, or 45 min (Fig. 6a and b).

For a given formulation, the release rate of the API from granules depends mainly on two factors: (i) the granule size, because the characteristic diffusion time is proportional to the square the of diffusion distance; and (ii) the granule inner structure, because the effective diffusion coefficient depends on the porosity and tortuosity of the porous medium. Thus, any inter- and intra-batch variation of dissolution rate should be analysed with these two factors in mind. The effect of granule size on the release rate of the API from granules belonging to the same batch is shown in Fig. 7. In order to isolate the effect of granule inner structure alone, further analyses were performed using only granules taken from the 400 to 1000 μm sieve fraction. However, even when comparing granules from the same size class, individual size variations will inevitably exist. Therefore, it is important to always record the granule weight before conducting single-granule measurements of dissolution.

3.3.2. *Inter- and intra-batch variation*

To assess the inter- and intra-batch variation of granule dissolution due to the inner granule structure, granules produced at the lowest (Fr = 0.26) and the highest (Fr = 1.63) value of the Froude number were compared. Note that the impeller tip speed in these two cases is comparable, 4.97 vs. 4.71 m/s (Table 1). It was shown above that granules produced under these conditions reveal the most significant differences in both inner structure (Section 3.1) and stiffness (Section 3.2). For each batch, 13 granules were weighed and dissolved as described in Section 2.4.1. The results are summarised in Fig. 8. There is a clear trend of a decrease of the fraction of dissolved API with increasing granule weight. For really big granules (0.7 mg) only a few percent of the API was released, while on the other side of the weight range almost 60% of dissolved API was reached over the same time interval (30 min). It can be seen that although a non-negligible intra-batch variation exists in both granule populations (Fig. 8a), the intra-batch variation of dissolution rate is not as huge as it was in the

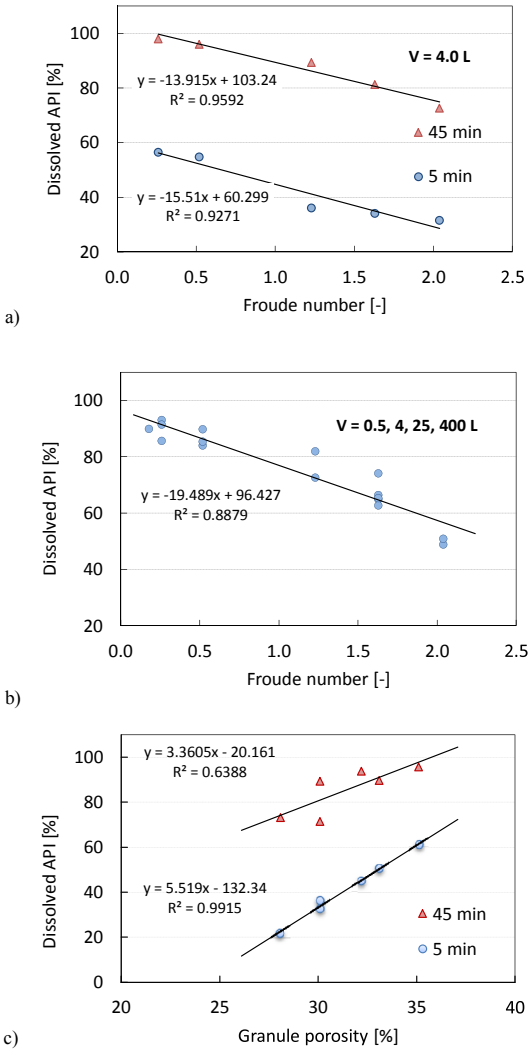

Fig. 6 – Correlation between the dissolved API percentage and Froude number. (a) Percentage of API dissolved after 5 min and 45 min for granules produced in a 4 L granulator at various Froude numbers. (b) Percentage of API dissolved after 30 min for all investigated combinations of Froude number and granulator volume (0.5, 4, 25 and 400 L). (c) Percentage of API dissolved after 5 and 45 min for granule batches specified in Table 1, plotted as function of granule porosity.

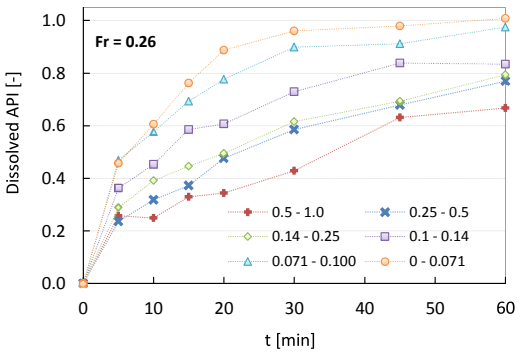

Fig. 7 – Dissolution profiles of granule size fractions belonging to a batch produced at Fr = 0.26, showing the contribution of individual size classes to the overall dissolution behaviour.

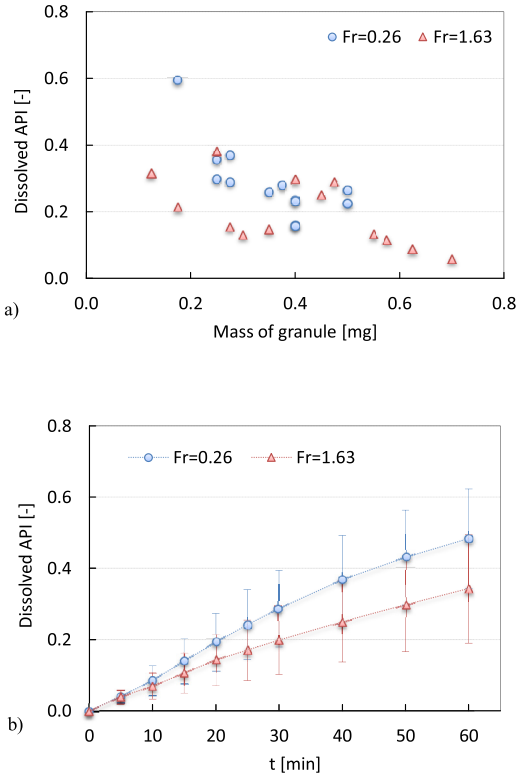

Fig. 8 – Summary of single granule dissolution tests for granules produced at the lowest and the highest Froude number. (a) Correlation between the fraction of dissolved API after 30 min and the individual granule mass. (b) Averaged dissolution curves based on all tested individual granules for each Froude number. All granules were taken from the 400 to 1000 μm size range.

case of granule stiffness (Table 3). Also, the overlap between the two populations is not so high and the separation between the two granule populations is clearer. Most of the Fr = 0.26 granules dissolved more API than the Fr = 1.63 granules. The mean release curves differ by approx. one standard deviation (Fig. 8b), which means the inter-batch variation can be regarded as statistically significant. On average, the lower Froude number granules released 48% of API after 60 min, while the higher Froude number granules released 34%.

The mechanistic explanation for a faster dissolution of granules produced at lower Froude number could be their higher porosity (thus higher effective diffusion coefficient) and weaker mechanical structure (thus potential contribution of granule disintegration to purely diffusion-controlled API release). On the other hand, higher Froude number implies tougher granules, which are able survive longer in dissolution bath. While the inter-batch variation of average properties is given by different magnitude of forces acting on the powder in the granulator, the intra-batch variation is given by the distribution of those forces acting on individual granules. It was shown that for granule stiffness the relative standard deviation (RSD) reached 44% for Fr = 0.26 (Section 3.2), while the RSD for dissolution was 39%. Granules produced at Fr = 1.63 exhibited RSD of up to 89% for stiffness, but only 49% for dissolution profiles, despite the fact that the statistical sample for single granule dissolution experiments was 13 granules per batch compared to 25 granules per sample for granule stiffness. It was shown recently (Smrčka et al., 2016) that in case of higher Froude number, the prevailing mechanism of API release is leaching or surface erosion. Since the granule breakage does

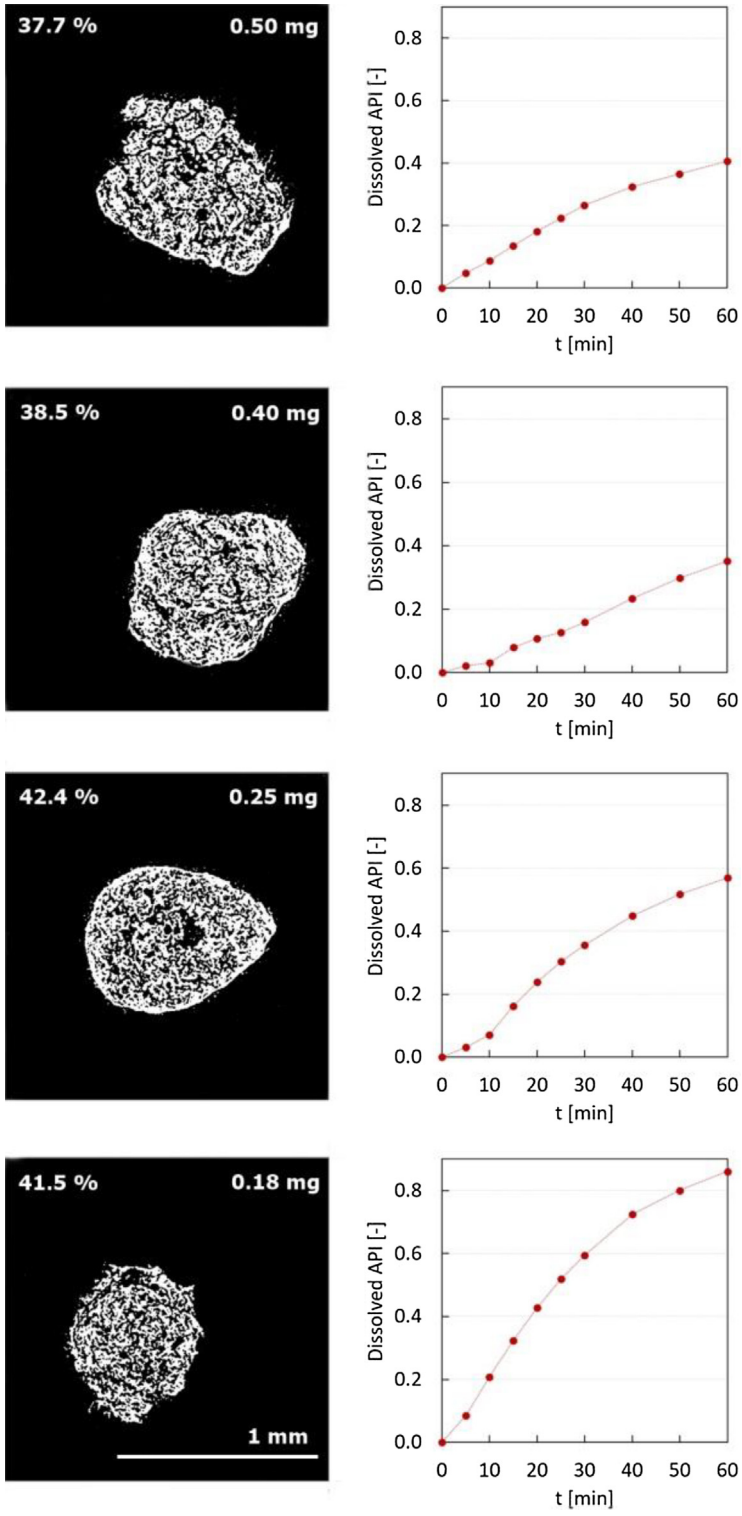

Fig. 9 – Example of intra-batch variation of individual granule structures (left column) and their dissolution profiles (right column) for granules produced at Fr = 0.26 and V = 400 L. The values of individual granule porosity and mass are indicated for each structure. All granules were taken from the 400 to 1000 μm size range.

not play such a significant role, granule porosity is more important than the granule stiffness in this case, and therefore the RSD is lower for dissolution profiles.

3.3.3. *Coupled experiments*

Four granules from each batch were scanned by micro CT and then dissolved as described in Section 2.5. The results are summarised in Figs. 9 and 10 for granules produced at low (Fr = 0.26) and high (Fr = 1.63) values of the Froude number, respectively. The fraction of dissolved API after 60 min was generally given by mass of the granule, as seen in Fig. 8a. However, there were interesting differences caused by variations of individual granule structures. For example, the first granule in Fig. 9 has a very similar porosity as the second granule (37.7% and 38.5%, respectively) and is 25% heavier (0.5 mg and 0.4 mg, respectively), but it dissolved faster – especially in the first 30 min. A difference in the two granule structures could be observed. The first granule has rugged edges with some discontinuities and several open pores connected directly to the surface, while the second granule is much smoother and compact near the

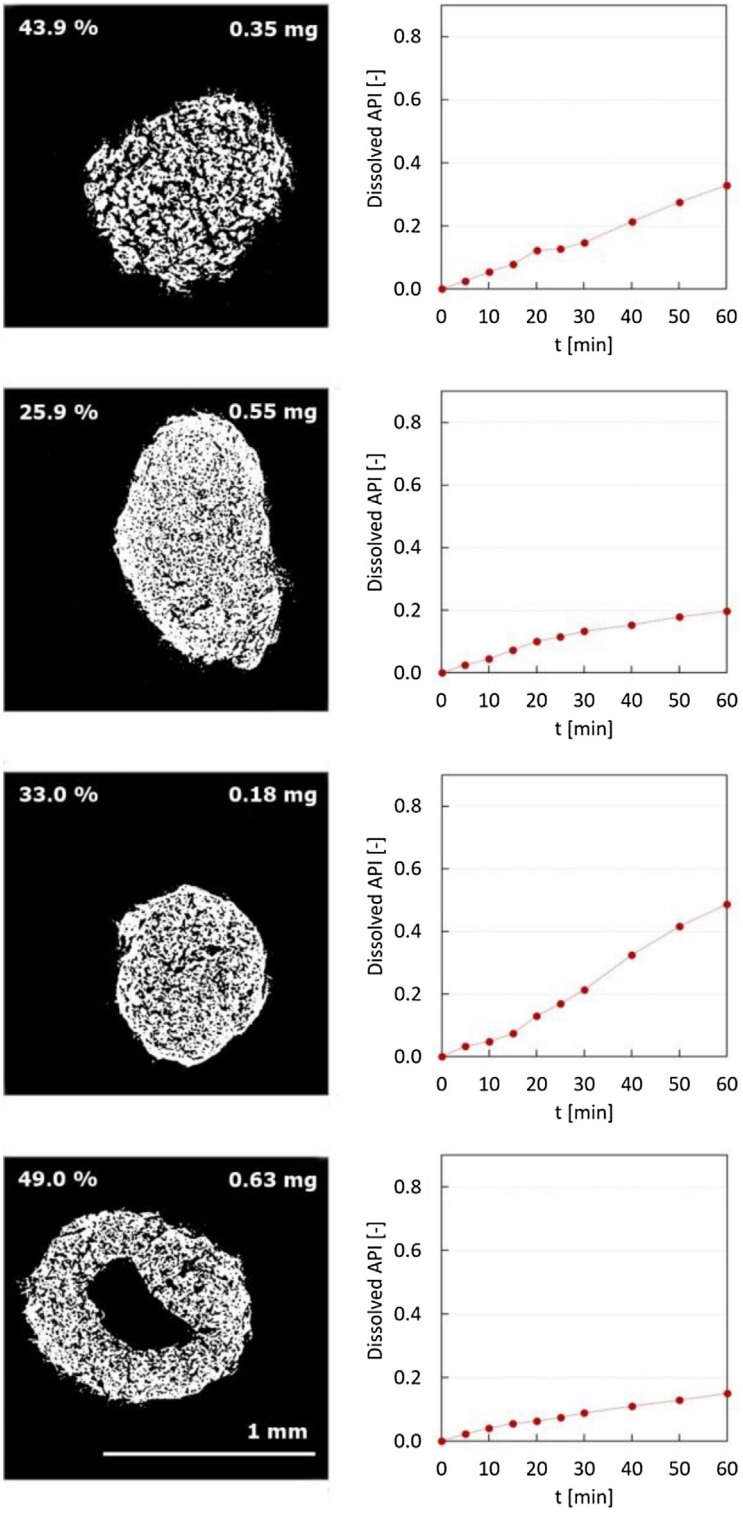

Fig. 10 – Example of intra-batch variation of individual granule structures (left column) and their dissolution profiles (right column) for granules produced at Fr = 1.63 and V = 0.5 L. The values of individual granule porosity and mass are indicated for each structure. All granules were taken from the 400 to 1000 μm size range.

surface. It is easy to imagine that the dissolution media could percolate into the pore space much easier in the case of the first granule. It is the same in the case of the fourth granule in Fig. 9, with perhaps even rougher surface. Granules with a closed, smooth surface exhibit a lag phase in the early stages of dissolution (2nd and 3rd granule in Fig. 9), while granule with a more open surface structure enhance the API release from early on (1st and 4th granule in Fig. 9). Interestingly, these qualitatively different granule structures originate from the same batch. Clearly, their individual collision and stress histories must have been very different despite spending together 6 min at 95 rpm in the same granulator (cf. Table 1). Detailed X-ray micro CT scans of these granule structures are provided in Fig. 11 and in the Supplementary Material.

Granules produced at the high value of Froude number (Fr = 1.63) also revealed some interesting behaviour (Fig. 10), especially when compared with their low-Froude counterparts possessing similar characteristics (porosity or mass). By chance, there is an 18.0 mg granule in each batch, which makes it possible to directly compare the effect of porosity

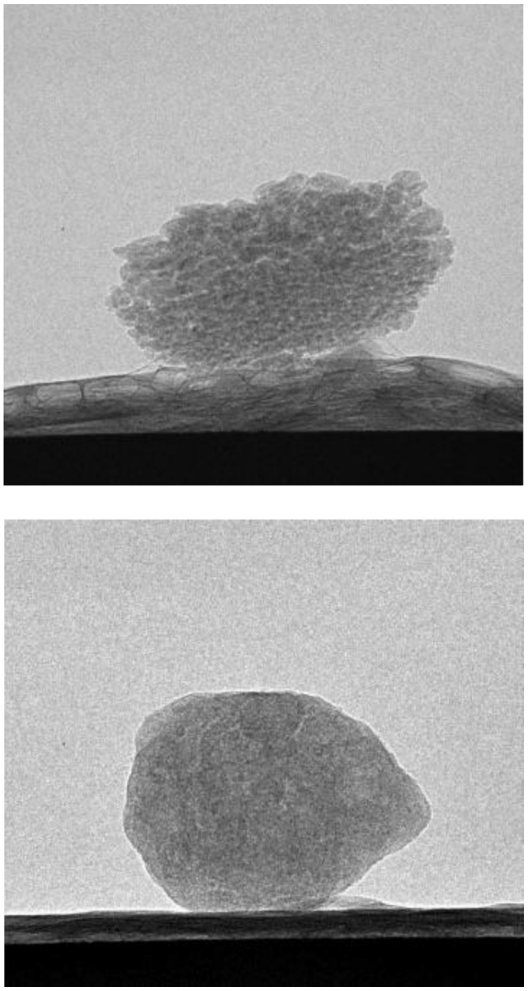

Fig. 11 – X-ray transmission images of two qualitatively different granule structures from the same batch. (a) Grape-like structure with open pores connected to the surface; (b) smooth structure with smaller, disconnected pores. The 3D micro CT scans of these granules can be found as Supplementary Material.

and pore structure. The granule produced at Fr = 1.63 has a lower overall porosity than the granule produced at Fr = 0.26 (33.0% against 41.5%) and has a characteristic dense, smooth surface, which manifests itself by the initial lag phase and a generally lower dissolution rate. This effect therefore holds not only for granules from the same batch as discussed in the previous paragraph, but also across batches produced under different conditions. Now if we compare the 1st granule from Fig. 10 (Fr = 1.63) with the 1st granule from Fig. 9 (Fr = 0.26), we can see that both granules have a similar open-pore structure, and the high-Froude granule from Fig. 10 has both higher porosity (43.9% against 37.7%) and lower mass (0.35 mg against 0.50 mg), so it should theoretically dissolve faster. However, it actually dissolves slower than its low-Froude counterpart.

This could possibly be explained by the structure of the apparently solid-state segments of the granule, which in reality are probably also porous (but their pore size is below the spatial resolution of the micro-CT instrument used in this work). It can be hypothesised that these granule segments are denser in the high-Froude granule, and therefore the release rate of the API is slower. Thus, granule porosity alone cannot be taken as a reliable predictive measure of dissolution rate. This is underlined by the 4th granule shown in Fig. 10. Although it has a high overall porosity of 49.0%, this porosity is mainly due to the hollow core structure whereas the shell is relatively dense and the pores are disconnected. Consequently, the API release is extremely slow. As in the case of the low Froude number (Fr = 0.26, V = 400 L) discussed above, we can see that at the opposite end of the granulator scale (Fr = 1.63, V = 0.5 L), the variety of granule structures that co-exist within the same batch is no less diverse.

4. Conclusions

Using a pharmaceutical formulation, we have investigated the variation of granule microstructure formed under a range of conditions (Froude numbers) at granulator scales from small laboratory units (0.5 L volume) to the manufacturing scale (400 L volume). Both inter- and intra-batch variation of granule porosity, evaluated from X-ray micro CT scans, granule stiffness, and granule dissolution rate was analysed. We have compared structure–property correlations not only for population averages but also for individual granules. For the first time, the results form coupled experiments – i.e. the scanning of granule microstructure followed by single-granule measurement of stiffness or dissolution of the very same granule – have been reported.

For the formulation investigated in this work, both granule stiffness and granule dissolution rate were found to correlate well with the Froude number, regardless of the granulator volume. However, granules from a single batch exhibited a significant variation of stiffness. The intra-batch relative standard deviation of granule stiffness was found to increase linearly with increasing Froude number. This can be explained by the relatively broad distribution of stress and shear conditions that individual granules experience, especially in granulation vessels with larger dimensions along with the fact that due the method binder addition available at the manufacturing scale, the granulator is operated in the mechanical dispersion regime. Thus, non-uniform initial particle wetting and therefore binder distribution can be expected. If a more uniform intra-batch distribution of granule properties were to be obtained, two conditions would have to be met: (i) more uniform initial binder distribution (e.g. using an atomisation nozzle), and (ii) narrower distribution of normal and shear stresses in the granulation vessel (e.g. using a Couette-type device).

The micro CT scans revealed an increasing level of granule consolidation with increasing Froude number. Granule porosity also exhibited intra-batch variation, but to a lower extent than in the case of granule stiffness. The granule stiffness could be correlated with porosity, and the same correlation was obtained for population averages as well as for individual granules. The Froude number was shown to be a parameter determining granule dissolution properties at the inter-batch level. At the intra-batch level, granules follow general trends, but the concrete behaviour is given by a specific combination of granule size and inner structure. In the case of inner structure, the overall porosity was not necessarily the controlling parameter. Surface consolidation was found to be an important parameter affecting the dissolution profiles.

Although it could be expected that granules exposed to the same granulation conditions for a sufficient period of time (e.g. 6 min of granulation at 642 rpm, as was the case in the experiment with Fr = 1.63) should all experience statistically the same conditions, a surprising diversity of granule structures was found within the same batch. From the practical point

of view in pharmaceutical manufacturing, this highlights the importance of avoiding granule segregation in subsequent unit operations such as capsule filling, blending or tabletting. If granules segregate according to size, surface roughness or density, the consequence can be large deviations in the release rate of the API from the final dosage form.

As a topic for future work, it will be important to find out how the differences in individual granule behaviour translate into the behaviour of tablets (disintegration time, dissolution rate) compressed from granules produced under different Froude numbers. In particular, it remains to be seen whether the tablet compaction pressure diminished any differences caused by different tablet porosity, and whether the tablets disintegrate into the granules they are compressed from, or into disintegration fragments of different size distribution.

Acknowledgments

We would like to thank Zentiva, k.s., for supporting this work, providing pharmaceutical grade materials and granting access to laboratory and pilot plant facilities. D. Smrčka would like to acknowledge support from Specific University Research (MŠMT no. 20-SVV/2017). Z. Grof and F. Štěpánek would like to acknowledge support from GAČR project no. 15-05534S.

References

Ansari, M.A., Štěpánek, F., 2006. Formation of hollow core granules by fluid bed in-situ melt granulation: modelling and experiments. Int. J. Pharm. 321, 108–116.

Ansari, M.A., Štěpánek, F., 2008. The effect of granule microstructure on dissolution rate. Powder Technol. 181, 104–114.

Dosta, M., Dale, S., Antonyuk, S., Wassgren, C., Heinrich, S., Litster, J.D., 2016. Numerical and experimental analysis of influence of granule microstructure on its compression breakage. Powder Technol. 299, 87–97.

Farber, L., Tardos, G., Michaels, J.N., 2003. Use of X-ray tomography to study the porosity and morphology of granules. Powder Technol. 132, 57–63.

Gantt, J.A., Cameron, I.T., Litster, J.D., Gatzke, E.P., 2006. Determination of coalescence kernels for high-shear granulation using DEM simulations. Powder Technol. 170, 53–63.

Hafsa, I., Cuq, B., Kim, S.J., Le Bail, A., Ruiz, T., Chevallier, S., 2014. Description of internal microstructure of agglomerated cereal powders using X-ray microtomography to study of process–structure relationships. Powder Technol. 256, 512–521.

Hapgood, K.P., Khanmohammadi, B., 2009. Granulation of hydrophobic powders. Powder Technol. 189, 253–262.

Iveson, S.M., Litster, J.D., Hapgood, K., Ennis, B.J., 2001. Nucleation, growth and breakage phenomena in agitated wet granulation processes: a review. Powder Technol. 117, 3–39.

Kašpar, O., Tokárová, V., Oka, S., Sowrirajan, K., Ramachandran, R., Štěpánek, F., 2013. Combined UV/Vis and micro-tomography investigation of acetaminophen dissolution from granules. Int. J. Pharm. 458, 272–281.

Khalilitehrani, M., Abrahamsson, P.J., Rasmuson, A., 2014. Modeling dilute and dense granular flows in a high shear granulator. Powder Technol. 263, 45–49.

Kochba, M., Ayalon, O., Avnimelech, Y., 1994. Slow release rate: individual granules and population behaviour. Fert. Res. 39, 39–42.

Mangwandi, C., Adams, M.J., Hounslow, M.J., Salman, A.D., 2010. Effect of impeller speed on mechanical and dissolution properties of high-shear granules. Chem. Eng. J. 164, 305–315.

Nakamura, H., Fujii, H., Watano, S., 2013. Scale-up of high shear mixer-granulator based on discrete element analysis. Powder Technol. 236, 149–156.

Oka, S., Emady, H., Kašpar, O., Tokárová, V., Muzzio, F.J., Štěpánek, F., Ramachandran, R., 2015. The effects of improper mixing and preferential wetting of active and excipient ingredients on content uniformity in high shear wet granulation. Powder Technol. 278, 266–277.

Rahmanian, N., Ghadiri, M., Jia, X., Stepanek, F., 2009. Characterisation of granule structure and strength made in a high shear granulator. Powder Technol. 192, 184–194.

Rajniak, P., Mancinelli, C., Chern, R., Štěpánek, F., Farber, L., Hill, B.T., 2007. Experimental study of wet granulation in fluidized bed: impact of the binder properties on the granule morphology. Int. J. Pharm. 334, 92–102.

Ramachandran, R., Poon, J.M.H., Sanders, C.F.W., Glaser, T., Immanuel, C.D., Doyle, F.J., Litster, J.D., Stepanek, F., Wang, F.Y., Cameron, I.T., 2008. Experimental studies on distributions of granule size, binder content and porosity in batch drum granulation: inferences on process modelling requirements and process sensitivities. Powder Technol. 188, 89–101.

Ramachandran, R., Ansari, M.A., Chaudhury, A., Kapadia, A., Prakash, A.V., Stepanek, F., 2012. A quantitative assessment of the influence of primary particle size polydispersity on granule inhomogeneity. Chem. Eng. Sci. 71, 104–110.

Reynolds, G.K., Biggs, C.A., Salman, A.D., Hounslow, M.J., 2004. Non-uniformity of binder distribution in high-shear granulation. Powder Technol. 140, 203–208.

Reynolds, G.K., Nilpawar, A.M., Salman, A.D., Hounslow, M.J., 2008. Direct measurement of surface granular temperature in a high shear granulator. Powder Technol. 182, 211–217.

Ring, D.T., Oliveira, J.C.O., Crean, A., 2011. Evaluation of the influence of granulation processing parameters on the granule properties and dissolution characteristics of a modified release drug. Adv. Powder Technol. 22, 245–252.

Smrčka, D., Dohnal, J., Štěpánek, F., 2015. Effect of process scale-up on the dissolution of granules with a high content of active pharmaceutical ingredient. Powder Technol. 285, 88–95.

Smrčka, D., Dohnal, J., Štěpánek, F., 2016. Dissolution and disintegration kinetics of high-active pharmaceutical granules produced at laboratory and manufacturing scale. Eur. J. Pharm. Biopharm. 106, 107–116.

Wade, J.B., Martin, G.P., Long, D.F., 2015. The evolution of granule fracture strength as a function of impeller tip speed and granule size for a novel reverse-phase wet granulation process. Int. J. Pharm. 488, 95–101.

9.2 Virtual prototyping and parametric design of 3D-printed tablets based on the solution of inverse problem

Matěj Novák
Tereza Boleslavská
Zdeněk Grof
Adam Waněk
Aleš Zadražil
Josef Beránek
Pavel Kovačík
František Štěpánek

Published in the *AAPS PharmSciTech*, Vol. 19, 2018, pp. 3414–3424
DOI: 10.1208/s12249-018-1176-z.

AAPS PharmSciTech, Vol. 19, No. 8, November 2018 (© 2018)
DOI: 10.1208/s12249-018-1176-z

Research Article

Theme: Printing and Additive Manufacturing
Guest Editors: Niklas Sandler and Jukka Rantanen

Virtual Prototyping and Parametric Design of 3D-Printed Tablets Based on the Solution of Inverse Problem

Matěj Novák,[1,2] Tereza Boleslavská,[1,2] Zdeněk Grof,[1] Adam Waněk,[1] Aleš Zadražil,[1] Josef Beránek,[2] Pavel Kovačík,[2] and František Štěpánek[1,3]

Received 29 May 2018; accepted 5 September 2018; published online 25 September 2018

Abstract. The problem of designing tablet geometry and its internal structure that results into a specified release profile of the drug during dissolution was considered. A solution method based on parametric programming, inspired by CAD (computer-aided design) approaches currently used in other fields of engineering, was proposed and demonstrated. The solution of the forward problem using a parametric series of structural motifs was first carried out in order to generate a library of drug release profiles associated with each structural motif. The inverse problem was then solved in three steps: first, the combination of basic structural motifs whose superposition provides the closest approximation of the required drug release profile was found by a linear combination of pre-calculated release profiles. In the next step, the final tablet design was constructed and its dissolution curve found computationally. Finally, the proposed design was 3D printed and its dissolution profile was confirmed experimentally. The computational method was based on the numerical solution of drug diffusion in a boundary layer surrounding the tablet, coupled with erosion of the tablet structure encoded by the phase volume function. The tablets were 3D printed by fused deposition modelling (FDM) from filaments produced by hot-melt extrusion. It was found that the drug release profile could be effectively controlled by modifying the tablet porosity. Custom release profiles were obtained by combining multiple porosity regions in the same tablet. The computational method yielded accurate predictions of the drug release rate for both single- and multi-porosity tablets.

KEY WORDS: 3D printing; hot-melt extrusion; parametric programming; dissolution; mathematical modelling.

INTRODUCTION

One of the most significant trends in contemporary medicine is its inclination towards personalised treatment. Advances in the fields of pharmacogenomics, diagnostics, and clinical trials enable to optimise each treatment according to the needs of a specific patient, taking into account individual physical and genetic characteristics and previous medication (1) to prescribe an optimum drug administration regime (2,3). While a personalised drug absorption profile can be calculated with relatively good accuracy, in reality it can be achieved only partially by prescribing the drug in one of the available dosage strengths. The patient is often forced to take multiple tablets with different drugs throughout the day, which may lead to reduced compliance or even accidental under- or overdose.

To address these problems, new drug formulation technologies are being developed. In particular, the application of additive manufacturing methods could enable the design and production of patient-specific dosage forms with the desired combination of dose strength and drug release rate. For example, syringe-based 3D printing of a drug-containing paste was employed to produce polypills, containing up to five different drugs with both immediate and extended release profiles (4,5). Stereolithographic 3D printing was used to create drug-loaded hydrogel tablets where the release profile could be modified by water content in the formulation (6). Ink-jet 3D printing coupled with a hot-melt extruded chamber was successfully used to produce tablets with varying internal geometries in order to modify the release rate (7).

Guest Editors: Niklas Sandler and Jukka Rantanen

[1] Department of Chemical Engineering, University of Chemistry and Technology, Prague, Technická 5, 166 28, Prague 6, Czech Republic.
[2] Zentiva, k.s, U Kabelovny 130, 102 00, Prague 10, Czech Republic.
[3] To whom correspondence should be addressed. (e–mail: Frantisek.Stepanek@vscht.cz)

Perhaps, the most widespread 3D printing technology is Fused Deposition Modelling (FDM), which uses solid polymeric filaments as the feed material. It has been demonstrated that drug release kinetics from FDM dosage forms can be controlled in multiple ways. Tablets of different shapes (cylinder, cube, torus) were printed, while a chosen key characteristic remained constant (tablet weight, surface area or surface/volume ratio), successfully altering the dissolution kinetics (8). Tablets containing acetaminophen were printed with varying inner core fill density and outside shell thickness, and their geometry was correlated with the dissolution and drug release rates (9). In another study, caplets containing hydrochlorothiazide as a model drug were produced containing perforated channels of varying geometry and the effect on drug release rate and tablet disintegration mechanism was observed (10). It was also demonstrated that FDM can yield tablets for immediate release by using drugs with a good solubility, adding dissolution enhancing excipients, or non-melting fillers to the filaments and keeping the printing temperature under the melting point of the drugs (11,12). In order to assess the potential of additive manufacturing in terms of patient acceptability, a randomised pilot study was conducted on 50 participants, observing their subjective response to printed dosage forms of different colours, sizes and shapes (13).

However, the apparently endless possibilities offered by FDM to customise the tablet geometry, composition and inner structure, also raise an important question: how to choose, in a systematic way, the final set of tablet design parameters?

The drug release rate from FDM-printed dosage forms can be affected by the composition of the filament (drug content, specific ratio of polymers and fillers) and by controlling the inner structure of the dosage form (spatial distribution of porosity or combination of regions printed from different filaments). Since these characteristics depend solely on the supplied 3D drawing of the object to be printed, they can be rapidly adjusted before the final production step of the dosage form. The design of a personalised dosage form can therefore be considered an inverse problem, since the result (the required drug release profile, optimised for a specific patient) is prescribed and the task at hand is to find the structural parameters of the dosage form that are necessary to achieve this result. The engineering concept of finding the solution of an inverse problem using known correlations between the initial parameters and the end results is a prevalent algorithm in many fields of product development (14). For example, in aeronautics, wings are designed using a database of airfoils, where the airflow and the resulting aerodynamic force are pre-calculated (15–17). In chemical engineering, problems such as the optimization of heat transfer in large-scale systems (18) can be solved in a similar fashion, as well as the design of “classical” (non-3D printed) dosage forms such as granules and tablets (19,20).

In the present work, we apply the concept of inverse problem solution by parametric design to pharmaceutical tablets produced by 3D printing. As a model substance, we chose a hypertension drug from the classification group BCS II (Biopharmaceutical Classification System). In order to solve the inverse problem, a series of tablets with varying porosity has been printed, and their drug release profiles were obtained experimentally and computationally. After the formation of a database of drug release profiles for 3D-printed tablets with systematically varying porosities, a computational approach, based on the numerical solution of the drug diffusion in the dissolution medium coupled with the erosion of the tablet structure, was employed. Tablets with the required drug release profiles were then designed and tested *in silico* by the superposition of structural elements with known release kinetics, before physically 3D printing the final tablet and confirming its dissolution profile by a USP (United States Pharmacopoeia) method.

MATERIALS AND METHODS

Materials

The Active Pharmaceutical Ingredient (API), polymeric excipients (Polymer 1, Polymer 2), and a plasticiser were kindly donated by Zentiva, k.s. The desiccant (also serving as an additional plasticiser) and a lubricant were purchased from Merck. The API was supplied in the form of a powder with a mean particle size of around 100 μm. Polymer 1 was a graft copolymer based on polyethylene glycol while Polymer 2 was a cellulose-based excipient. The Plasticiser was a polyether with a uniform chain length. The Desiccant was an organic acid with the ability to bind water during the extrusion process. The lubricant was an insoluble organic salt. All the substances were chosen so as to be commercially available approved pharmaceutical-grade excipients, frequently used in solid-state formulation development.

Production of Filaments for 3D Printing

The composition of filaments was optimised to achieve mechanical and rheological properties that ensure reproducible printability. The API load was fixed at 10% (*w*/*w*) and the proportion of the matrix polymers (Polymer 1, Polymer 2), the plasticiser, desiccant and lubricant was systematically varied until acceptable mechanical properties were achieved. The matrix polymers Polymer 1 and Polymer 2 at the right concentrations enable uniform dispersion of the API and provide sufficient mechanical durability of the filaments during FDM 3D printing, the Plasticiser increases the filament elasticity and the Lubricant facilitates continuous powder flow during hot-melt extrusion while also preventing powder aggregation, acting as an anticaking agent. The investigated composition ranges are specified in Table I. To produce the filaments, approximately 8 g of the mixture was added gradually to a co-rotating twin-screw hot melt extruder, Three-Tec ZE 12 HMI (Seon, Switzerland) with an automatic volumetric feeder. The filament extrusion rate was kept at 0.4 g/min, the temperatures of the heated segments were set to 70, 135, 140 and 118 °C and the torque was between 0.4–1.2 Nm at 120 rpm. The lower temperature of the last segment allowed the homogenised filament to emerge from the extruder in an almost solid state. Furthermore, an external fan, focused on the nozzle of the extruder, facilitated rapid cooling of the filament, leading to its solidification and ensuring

Table I. Range of Investigated Compositions to Determine Filament Printability

Component	Mass fraction (%)
API	10–40
Polymer 1	20–80
Polymer 2	0–55
Plasticiser	1–8
Desiccant	0–3
Lubricant	0–8

homogeneity of its diameter. Before 3D printing, the filaments were stored in sealed plastic bags at room temperature.

Characterisation of Filaments

The mechanical properties of the filaments were characterised by using CT3 Texture Analyser (Brookfield Engineering). The bending modulus was measured by a three-point bending test. A 5-cm sample of the filament was placed on a holder (denoted TPB, Brookfield Engineering) with two stationary supports placed 15 mm apart, and the force-displacement curve was recorded using a dull knife probe (denoted TA7, Brookfield Engineering). The indentation hardness was measured by a needle probe (denoted TA9, Brookfield Engineering) pushed into a filament positioned horizontally on a flat support base table. In both cases, the force-distance curve was acquired in at least three repeat measurements. the Modulus of (bending) elasticity and the indentation hardness were obtained by linear regression of the force-distance curves.

Rheological properties of the filaments were characterised by a rotational rheometer with a cylindrical plate probe Ares G2 (TA instruments). To obtain representative values of viscosity, the values of dynamic viscosity at the temperature of 145 °C (the same temperature used for printing) were measured at shear rates from 0.1 s^{-1} to 10 s^{-1}, and averaged from four independently measured samples of the filaments. Newton's power law was used to model the experimentally obtained dependence of viscosity on shear rate. The reference (normalised) viscosity for the filaments was obtained from the formula $\eta = k\ \gamma^{a-1}$, where η is the dynamic viscosity, γ is the shear rate, k is the normalised viscosity and a is the rate index.

To evaluate content uniformity, five samples (around 3 μg) were taken from separate portions of each filament, dissolved in 2 ml of phosphate buffer (pH = 6.8) and analysed by a UV/VIS spectrometer Specord 205 (Analytik Jena) by comparing the absorption of the samples to a calibration curve of the pure drug.

Tablet Design and FDM 3D Printing

The tablet template with a variable infill level was based on a cylinder with a diameter of 10 mm and a height of 5 mm. The tablet structures were designed using 3DS MAX DESIGN (Autodesk, Inc., USA) and imported to the 3D printer's interface software, Cura 2.6.21. Tablets were produced using a commercial FDM 3D printer LulzBot TAZ6 (Aleph Objects Inc., Colorado), with a 0.5-mm nozzle, using modified settings for ABS (acrylonitrile butadiene styrene) filaments. The infill pattern was set to "lines" in order to print one set of straight parallel lines in each layer, shifting their orientation by 90° for each new layer. This setting lead to the formation of a grid made of orthogonal lines. The layer height (vertical resolution) was set to 200 μm. The horizontal thickness of the printed lines was partially limited by the diameter of the printer nozzle (500 μm), the tablet shell thickness was therefore set to 490 μm. The base and the top solid layer thickness was set to 0 μm in order to produce tablets with open pores and allow the API to diffuse into the dissolution medium. The print speed was set to 20 mm/s, resulting in a shear-rate at the nozzle exit approximately 40 s^{-1}. The optimum printing nozzle temperature was found to be 145 °C and, to ensure proper adhesion of the first printed layer, the build plate was heated to 60 °C.

Tablet Characterisation

Digital images of the tablets were obtained using a Pylon 4 UBS camera with an additional 2.5″ lens. For the acquisition of close-up images of whole tablets, Dino-Lite Pro AM3113T Mounted WD Digital Camera and the software DinoCapture 2.0 were used. Microscopic imaging of tablet surface was done using a digital camera Canon EOS 1100D with a close-up lens. Pore size of the printed tablets was evaluated by analysing the images using the public domain software ImageJ. To obtain the mean pore size, images from two tablets of each design were converted to a binary format, the area of four to six randomly selected pores was evaluated and the mean square root of those values was taken as the representative pore size.

In vitro Dissolution of Tablets

In vitro dissolution tests were performed using a USP 2 apparatus (Sotax AT7). The tablets were placed into a USP compliant Japanese Pharmacopoeia sinker basket 13 (purchased from Agilent) to decrease the variability of the results caused by potential floating of the tablets. All dissolution tests were performed under sink conditions. The dissolution medium was 500 mL of 50 mM phosphate buffer pH 6.8 at 37 ± 0.5 °C and 75 rpm. Samples (1.5 mL) were taken every 30 min, filtered through a 2.5-μm filter and analysed by liquid chromatography. All samples were analysed using the Waters Acquity UPLC system equipped with Xselect HSS C18 SB column (50 × 4.6 mm; 3.5 μm) and a PDA detector. The following gradient of 30 mM $NH_4H_2PO_4$/acetonitrile at flow rate 0.8 mL/min was used: linear change from 60/40 to 30/70 (0–1 min) followed by steady state (1–2 min) and a linear change to starting conditions (2–2.25 min) followed by steady state for 1.25 to re-equilibrate. Data were

processed using the Empower software. The concentration at each data point was calculated as the mean value from three separate measurements. The final dissolution curves (and their standard deviations) were the result of averaging individual dissolution curves of 4–5 independently printed and dissolved tablets for each of the specific tablet geometry/design.

Mathematical Model of Tablet Dissolution and Disintegration

Taking the CAD (computer-aided design) model of the tablet as an input, the simulation domain was discretised by the finite volume method into $108 \times 108 \times 60$ cubical volume elements (voxels) with a spatial discretisation step h, and the tablet structure was encoded by the solid phase volume function $f_i \in \langle 0;1 \rangle$, where 0's represent fluid-phase voxels and 1's represent solid-phase voxels. The spatial discretisation step was chosen such that the numerical solution no longer changed with further grid refinement. The diffusion transport of the dissolved API is considered between each pair of neighbouring fluid-phase voxels within a boundary layer, up to a specified distance L from the nearest solid/fluid interface, with sink conditions applied outside this boundary layer and equilibrium API solubility at the solid/fluid interface.

The model was solved in a dimensionless form by defining the dimensionless molar quantity $\hat{n} = n/(h^3 c^*)$, the dimensionless concentration $\hat{c} = c/c^*$, the dimensionless time $\hat{t} = t/\tau_0$ and the dimensionless distance $\hat{x} = x/h$, where n is the molar quantity of API, c is the API molar concentration, c^* is the equilibrium solubility of the API and τ_0 is characteristic time defined by $\tau_0 = h^2/D$ where D is the diffusion coefficient of API in the dissolution medium. The dimensional analysis shows that, in addition to the system geometry, the model contains only three parameters: the characteristic time τ_0, the dimensionless boundary layer thickness $\delta = L/h$ and the relative API solid-state concentration $\alpha = \rho / (M_w c^*)$, where ρ and M_w is the API density and molar weight, respectively.

The governing equations, initial conditions (i.c.) and boundary conditions (b.c.) can be summarised as follows:

$$\text{API mass balance in fluid voxels} \quad \frac{d\hat{c}_i}{d\hat{t}} = -\sum_j (\hat{c}_i - \hat{c}_j) \tag{1a}$$

$$\text{API mass balance in solid voxels} \quad \frac{d\hat{n}_i}{d\hat{t}} = -\sum_j (\hat{c}_i - \hat{c}_j) \tag{1b}$$

$$\text{i.c. in fluid voxels } \hat{c}_i(\hat{t} = 0) = 0 \; \forall i : f_i = 0 \tag{2a}$$

$$\text{i.c. in solid voxels } \hat{n}_i(\hat{t} = 0) = \alpha \; \forall i : f_i > 0 \tag{2b}$$

$$\text{b.c. at tablet/fluid interface } \hat{c}_i(\hat{t}) = 1 \; \forall i : f_i > 0 \tag{3a}$$

$$\text{b.c. at diffusion layer } \hat{c}_i(\hat{t}) = 0 \; \forall i : \|\hat{x}_i - \hat{x}_{\text{solid}}\| > \delta \tag{3b}$$

The rate of tablet dissolution is controlled primarily by the diffusion of dissolved API from the tablet surface through a stagnant layer of the dissolution medium (the boundary layer). Its width L depends on the hydrodynamic conditions around the tablet and could be calculated rigorously by solving the Navier-Stokes equations in the fluid phase surrounding the tablet. In the present work, a simplified approach was taken by assuming a constant width of the diffusion boundary layer and setting its value such that the numerical solution and experimentally measured dissolution profiles for reference cases were in quantitative agreement. Since all dissolution experiments were done under identical hydrodynamic conditions, the parameter δ is a "global" parameter that must have the same value for the regression of all dissolution experiments. Likewise, since all tablets were printed from the same material containing the same API (hence, the same density, molar weight, solubility and diffusion coefficient), the parameters α and τ_0 must also be identical for all tablets. The only differentiating factor between individual tablets was the infill level and its spatial distribution. As stated in the previous section, the dissolution experiments were done using a sample of 4–5 tablets for each infill level. A sample mean dissolution curve was calculated from these measurements for each infill level and then a single set of parameter values was found iteratively so as to minimise the global error between simulation and experiment.

RESULTS AND DISCUSSION

Filament and Tablet Characteristics

Solid filaments containing 10% (*w*/*w*) of the API were produced by hot-melt extrusion as specified in section "Production of Filaments for 3D Printing". The degree of filament "printability" depends on its mechanical properties—elasticity, hardness and cohesivity—in the solid state, and on the rheology (shear-rate dependent dynamic viscosity) of the melt at the printing temperature. Furthermore, sufficient uniformity of filament diameter and composition had to be achieved in order to enable defined mass flow during 3D printing. All these factors were shown to be dependent on the proportion of components in the formulation (the API, matrix polymers, plasticizers, lubricant) and settings of the extrusion conditions (temperature of the heated segments, screw rotation speed, powder feed rate, filament cooling and conveying rate). While the content of the API could be up to 30% (*w*/*w*) without losing printability, at high API loadings the reproducibility of the printing process was slightly reduced due to higher viscosity of the filament, which led to occasional clogging of the printer nozzle. Therefore, 10% (*w*/*w*) API content was chosen for the purpose of further tablet design experiments. It should

Table II. Material and Rheological Properties of the Final Printable Filaments

Property	Value and units	Method
Elasticity modulus	55.65 ± 3.31 kN/m	Three-point bending test
Indentation hardness	62.58 ± 5.07 kN/m	Needle-probe test
Normalised viscosity at 145 °C	10,658 ± 1308 Pa.s	Rotational rheometry
Thickness uniformity	2911 ± 31 μm	Digital calliper
API content uniformity	9.96 ± 0.53 wt.%	HPLC + UV spectroscopy

also be noted, that the values of the elasticity modulus are also strongly dependent on the thickness of the filaments, as observed in past research (21); therefore, the value is only relevant for a given filament diameter, but can still be used as a comparative characteristic. The final filament properties are summarised in Table II. The rate index a for the modified Newton's power law (from which the normalised viscosity k was obtained) was 0.434 ± 0.037.

Following the successful extrusion of filaments, tablets were printed as specified in section "Tablet Design and FDM 3D Printing". The CAD drawings of 3D tablet templates with variable infill density, and a detail of the FDM print-head, are shown in Fig. 1. The infill level was systematically varied from 25 to 100% (*i.e.*, completely filled tablet with no voids) while the shell thickness was kept constant. Furthermore, tablets with two different infill levels (70% and 30%) were printed by combining two sections as separate models and aligning them into the printer interface either in a stack or a pie arrangement (see "Solution of the Inverse Problem" and "Experimental Verification of Inverse Problem Solution" below). The actual printed tablet porosity ε was calculated from the formula $\varepsilon = 1 - m_x / m_{100}$ where m_x is the mass of a tablet with the infill level of x and m_{100} is the mass of tablet with a 100% infill level. The properties of the printed tablets are summarised in Table III.

While reproducible tablet structures were achieved, the actual horizontal distance between the infill lines was smaller than the value set in the CAD models (Table II). This was due to a slight overlap of the printed layers as shown in Fig. 2. In reality, the single layers deposited during FDM do not have the form of rectangular stripes but rather flattened cylinders (11,12,22). Therefore, the pore size evaluated from the microscopic images of the tablet upper surface only yields information about the minimum distance of the infill lines, not taking into account the vertical curvature of the deposited layers. Microscopic images of the tablets (Fig. 2) showed that in the case of 70% infill, the pores were partially blocked (regardless of the tablet orientation under the microscope or the illumination used).

The results of USP dissolution experiments of tablets with a systematically varying infill are shown in Fig. 3. Tablets with a 70% infill showed no significant increase of dissolution rate compared to non-porous tablets with a 100% of infill, presumably due to pore blocking. In the case of 50% infill, an increase of the API release rate was observable due to the fact that all pores were already accessible and the surface area in contact with the dissolution medium was therefore higher. By reducing the infill level to 40%, 35% and 30% (*i.e.*, by increasing tablet porosity and pore size), the API release rate was further accelerated, most probably due to increased contribution of convective transport through the pores, as opposed to diffusion-limited transport that occurs in smaller pores whose diameter is comparable with the thickness of the

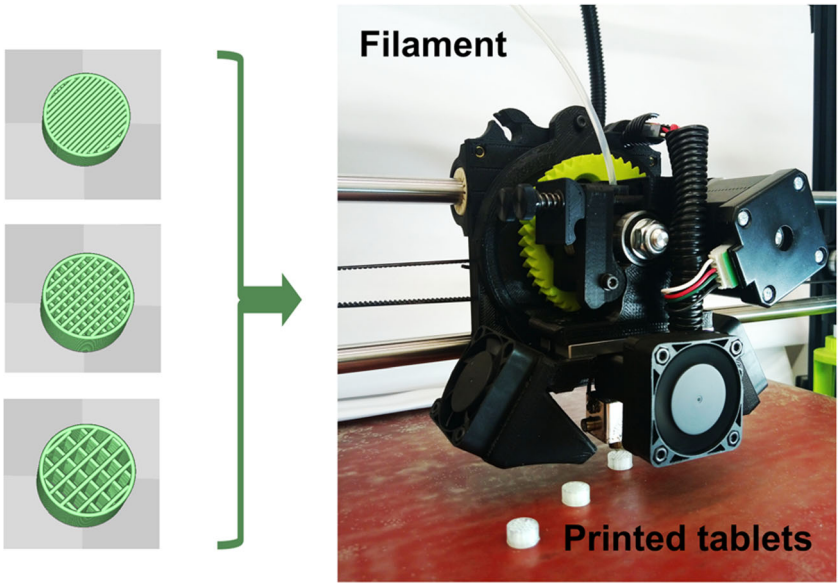

Fig. 1. CAD drawings of cylindrical tablets with a single infill density that serve as input templates for 3D printing (left). Detail of the FDM print-head used in this work (right)

Table III. Summary of Bulk Properties of 3D-Printed Tablets

Infill density set (%)	Tablet mass measured (mg)	Pore size set (mm)	Mean pore size measured (mm)	Tablet porosity calculated (%)
100	479.4 ± 8.7	0.00	0.00	0.0
70	387.1 ± 8.1	0.21	–*	19.3
50	301.8 ± 9.5	0.50	0.45	37.1
40	245.6 ± 6.5	0.75	0.79	48.8
35	243.5 ± 4.7	0.93	1.00	49.2
30	218.0 ± 5.0	1.17	1.20	54.5
25	202.6 ± 4.9	1.49	1.54	57.7
70/30 pie (3:1)	369.3 ± 4.7	–	–	23.0
70/30 pie (1:1)	332.7 ± 4.0	–	–	30.6
70/30 pie (1:3)	351.0 ± 13.0	–	–	26.8
70/30 stack (1:1)	286.4 ± 1.8	–	–	40.3

* The pore mouths were partially blocked

diffusion boundary layer. By reaching an infill level of 25%, no further increase of API release rate was observed because further increase of the pore size no longer enhanced the convective contribution to mass transfer. These findings are consistent with previous work where channels of varying size and position were implemented into 3D-printed tablets and it was found that in order for the pores to actively contribute to the dissolution rate enhancement, their size has to exceed a certain threshold (approx. 0.6 mm in that specific case) (10). However, it should be kept in mind that the exact value or even the existence of any limiting tablet infill level depends on the tablet composition and the specific arrangement of the dissolution experiment (*e.g.*, the tablet orientation with respect to the flow field, which affects the relative contribution of convective and diffusive mass transfer in the pores) (23).

Computational Dissolution Studies

Having experimentally established the limiting cases for the fastest and the slowest API release, the dissolution of tablets was simulated computationally using the procedure described in "Mathematical Model of Tablet Dissolution and Disintegration". The parameter α was set based on the known physico-chemical properties of the API, while the diffusion layer thickness δ and the characteristic time τ_0 were adjusted iteratively such that a quantitative agreement between the measured and the computed API release curves was achieved for two reference cases, chosen to be 30% and 70% infill level. The eroding tablet structures obtained from the numerical simulation for these two infill levels are shown in Fig. 4. Note that in the case of the 70% infill tablet, the pores contain a saturated solution of the API because the pores are smaller than the diffusion boundary layer

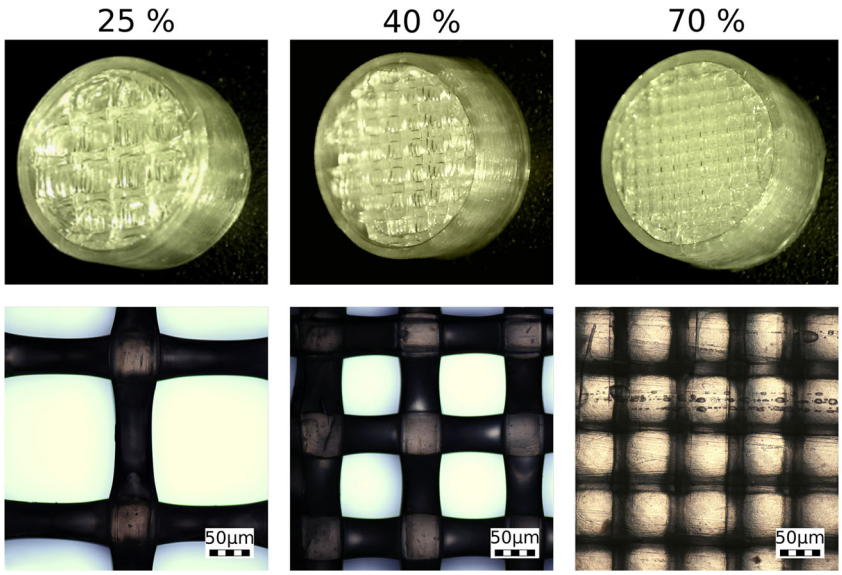

Fig. 2. Photographs of 3D-printed tablets and micro-scale details of their pore structure for tablets with a varying infill density of 25, 40, and 70% as indicated

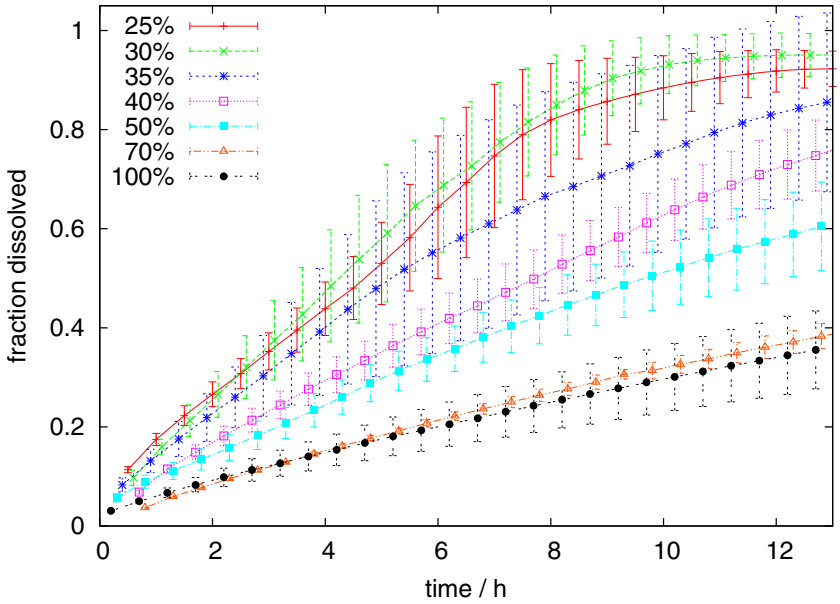

Fig. 3. Experimentally measured dissolution curves of 3D-printed tablets with a single value of infill density, ranging from 25 to 100% as indicated. The data points represent the mean values and the error bars standard deviations ($n = 4$)

thickness, and the tablet only erodes from the external surfaces. On the other hand, pores in the 30% infill tablet are accessible to the dissolution medium and the internal surfaces effectively contribute to the drug release. Consequently, the tablet eventually loses its integrity and breaks up into smaller fragments during the final stages of dissolution.

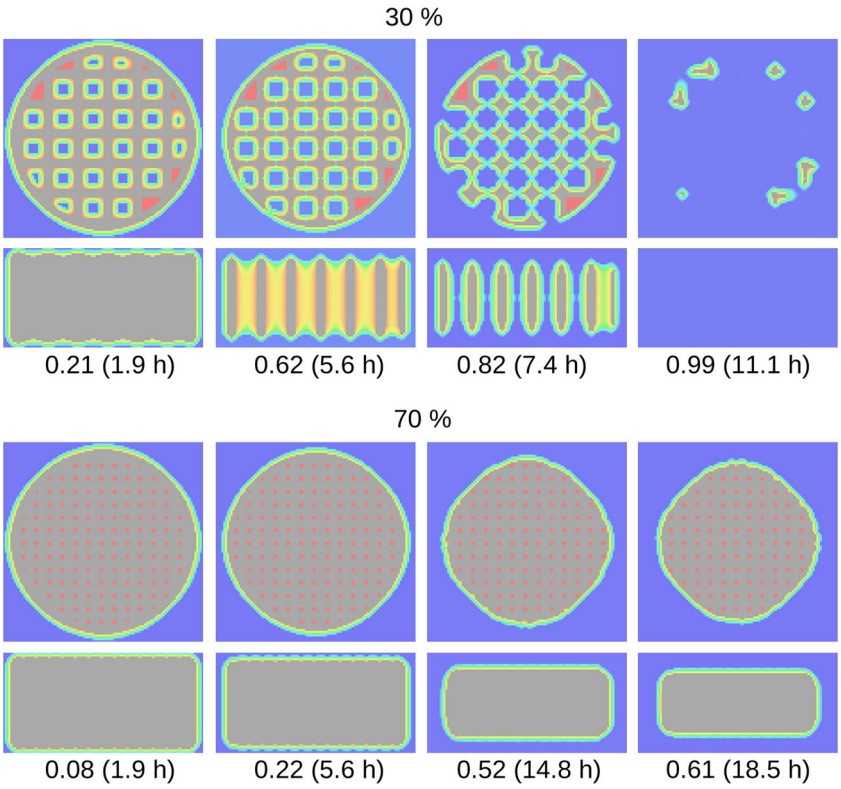

Fig. 4. Evolution of tablet structure and concentration profiles of the API in the diffusion boundary layer during the three-dimensional simulated dissolution of tablets with the infill density of 30 and 70% (top and side view). The numbers below the figures indicate the fraction of the dissolved API at the corresponding times

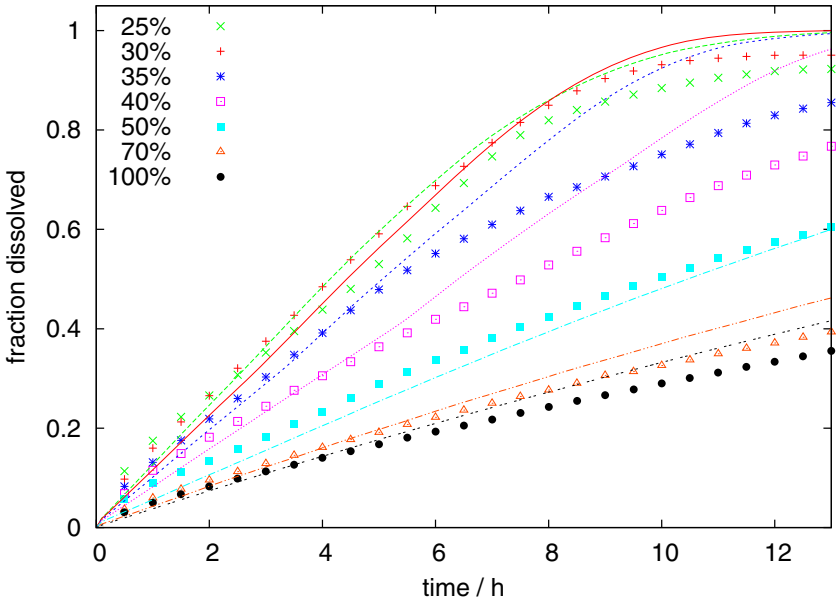

Fig. 5. Direct comparison of experimentally (represented by points, reproduced from Fig. 3) and computationally (represented by curves of corresponding colour) obtained dissolution profiles of 3D-printed tablets with a single value of infill density ranging from 25 to 100%

Once the model parameters (τ_0, α and δ) were fixed, simulations for the intermediate infill levels were carried out and compared with the experimentally measured API release curves. This comparison is shown in Fig. 5. While the agreement between simulations and experiment is very good in many cases, there are some systematic deviations in the case of 35% and 40% infills, particularly in the later stages of the dissolution experiment. This can be caused by a physical re-structuring of the tablets that is not captured by the model, as in this region of infill levels, the sensitivity to pore size is very high. A small degree of tablet swelling may lead to partial blocking of some pores in the later stages of dissolution, which results in a lower than predicted API release. In the early stages of dissolution when the tablet geometry and structure is still well defined, the agreement between the model and the experiment is good.

Solution of the Inverse Problem

Let us now consider the inverse problem, *i.e.*, the design of a composite tablet composed of regions with a different structure and therefore different local release rate of the API. Conceptually, this problem can be approached by using pre-calculated release profiles from single-infill tablets located at opposite ends of the design space—in this case we select the fast (30% infill) and the slow (70% infill) release cases as the basis—and then finding such combination of these basic structures that results in a prescribed overall release curve. To test this concept, let us consider composite tablets with a "pie" structure as shown in Fig. 6, consisting of regions with a 30% and a 70% infill at varying proportions (1:3, 1:1, and 3:1). The API release curves obtained by computer simulation from these composite structures are shown in Fig. 7 as lines, while the points in Fig. 7 denote the

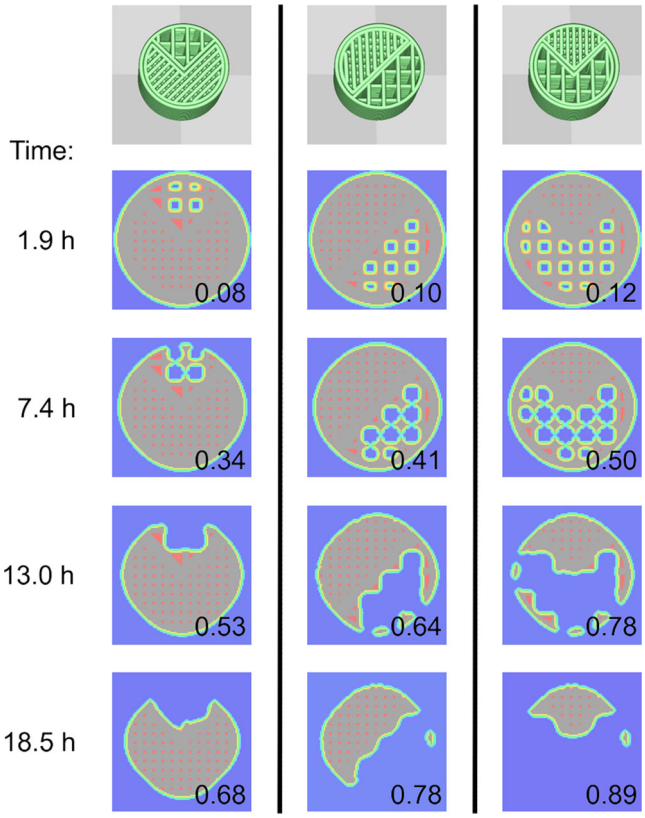

Fig. 6. Evolution of tablet structure during the *in silico* dissolution for composite pie-type tablets with combined infill of 30 and 70% combined at ratios 1:3, 1:1, and 3:1. The values in the bottom-right corners of each image represent the fraction of API released at the corresponding time

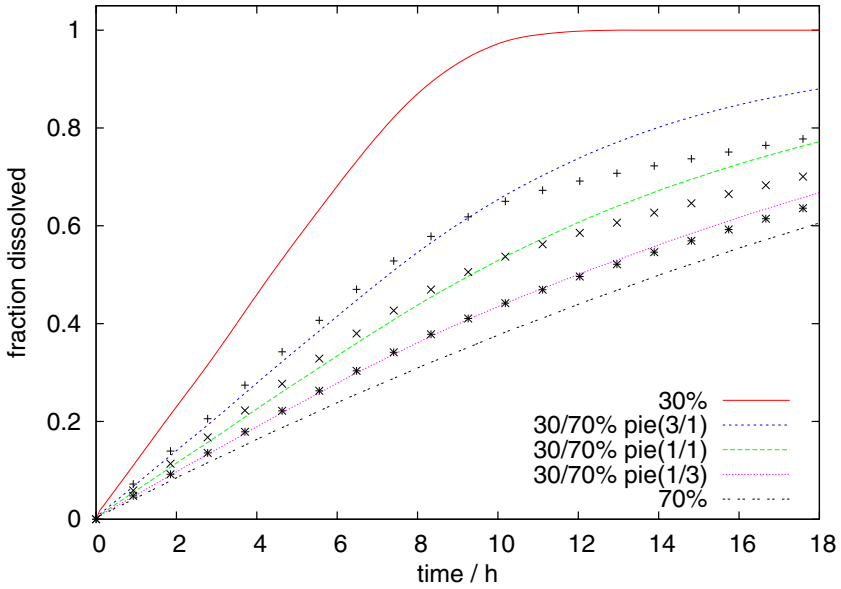

Fig. 7. Comparison of interpolated dissolution curves calculated according to Eq. (4), shown as discrete data points, with dissolution curves obtained by full 3D *in silico* dissolution simulations of composite pie-type tablets, shown as lines. The dissolution curves of single infill tablets (30 and 70%) are reproduced from Fig. 5 for reference

interpolation of single infill tablet simulations, calculated according to the formula

$$y_{\text{pie}} = \lambda\, y_{30} + (1-\lambda)\, y_{70} \tag{4}$$

The interpolation parameter λ has been calculated from the relation

$$\lambda = \left(\varphi_{70} - \varphi_{\text{pie}}\right) / (\varphi_{70} - \varphi_{30}) \tag{5}$$

where φ denotes the solid phase volume fraction in the tablet (Table III). The value of λ for the 3:1, 1:1 and 1:3 pies is 0.452, 0.265 and 0.107, respectively. As can be seen in Fig. 7, although the interpolation approach does not provide a perfect match with the full simulation of the composite structure dissolution, a reasonable agreement is obtained. The main advantage of interpolation from pre-calculated release profiles is its simplicity and speed, since no additional simulations are required and the calculation can be done using a simple spreadsheet or even by hand.

Experimental Verification of Inverse Problem Solution

As the final step of the design methodology, the composite structures were 3D printed (Fig. 8a), the API release curves were measured by the USP method (Fig. 8b) and compared with the release profiles obtained computationally (Fig. 9). The direct comparison of computationally predicted and experimentally measured API release profiles shows a very good agreement (the root mean square error between simulations and experiments was only 0.024, 0.013, and 0.026 for the 3:1, 1:1, and 1:3 composites, respectively), which confirms the viability of the *in silico* design methodology.

It should be noted that due to the structure of the model, the methodology could also be applied for the prediction of dissolution profiles of tablets containing multiple APIs (multi-drug formulations). Once the diffusion coefficients of each component and the thicknesses of the diffusion layer are provided by a small set of experimental data using single-API tablets, and as long as there is no irregularity such as excessive swelling of one of the APIs that could alter the tablet pore morphology, the prediction of the release of each API separately from a combined tablet should be possible.

One practical aspect to consider is that combining regions with different infill levels in a pie structure is not the only possibility; another option is to form a stack, simply layering regions with different infill levels on top of each other while preserving the overall tablet height. Such structure was 3D printed in the case of 1:1 ratio of the 30% and 70% infill regions, and indeed its dissolution curve is nearly identical to that of a pie arrangement with identical composition (Fig. 8b). While this approach might work well for binary composites (*i.e.*, tablets containing only two regions with different infill level or two different APIs), when the number of sub-regions is three or more, a stack geometry would no longer allow independent release from all regions since the top and the bottom layer would control the access of dissolution medium and diffusion of the API from the intermediate sandwiched layers. The pie geometry (or the combination of a 2-layer stack with a pie on each side) would therefore be required to enable independent release when three or more regions are required in the composite tablet.

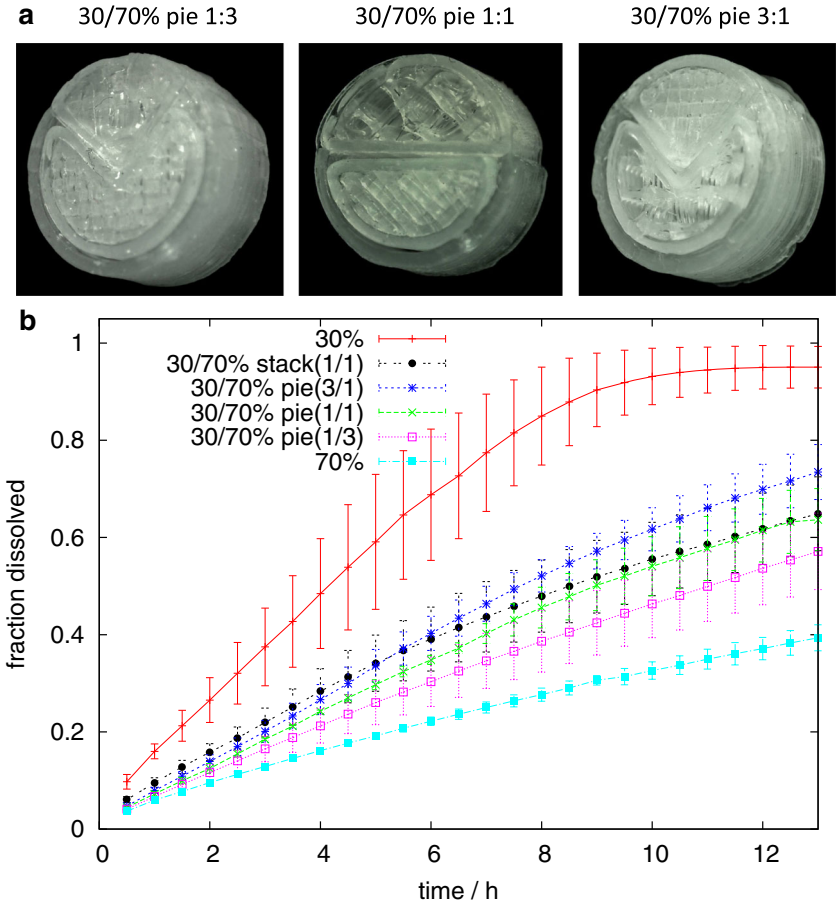

Fig. 8. **a**) Photographs of 3D-printed pie-type tablets with combinations of 30 and 70% infill at ratios 1:3, 1:1, and 3:1. **b**) Experimentally measured dissolution curves of the pie-type tablets and a 1:1 stack-type tablet; the single infill dissolution curves (30 and 70%) are reproduced from Fig. 3 for reference. The data points represent the mean values and the error bars standard deviations ($n = 4$)

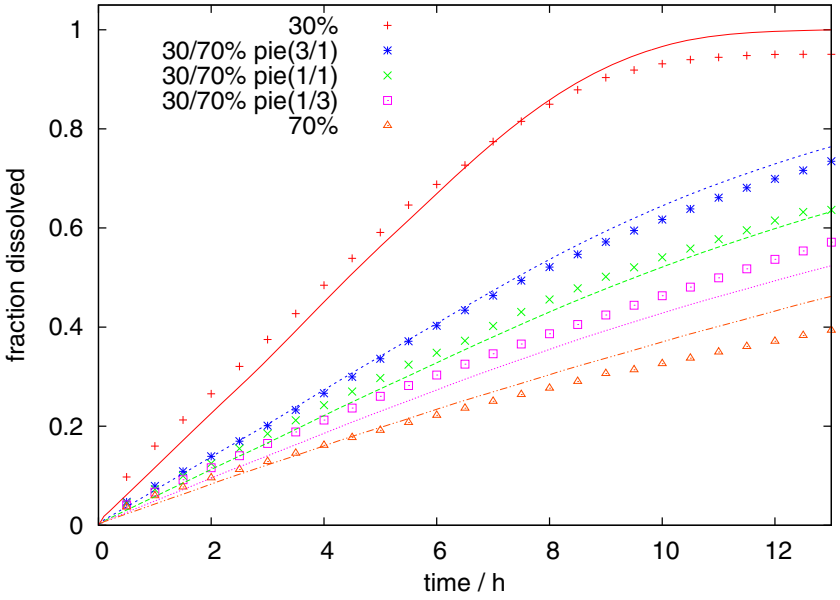

Fig. 9. Direct comparison of experimentally (represented by points, reproduced from Fig. 8) and computationally (represented by curves of corresponding colour) obtained dissolution profiles of 3D-printed pie-type tablets with two different values of infill density (30 and 70%) combined at ratios 1:3, 1:1, and 3:1. The dissolution curves of single infill tablets (30 and 70%) are reproduced from Fig. 5 for reference

CONCLUSIONS

A methodology for *in silico* design of tablet structure for 3D printing by FDM was proposed and demonstrated. The method is based on the solution of the inverse problem by the combination of pre-calculated structure-dissolution relationships obtained for simple structural motifs (in this case tablets containing a single infill level) into more complex structures that satisfy the condition of additive behaviour (in this case a pie or a 2-layer stack structure). Through methods of parametric programming, a three-dimensional mathematical model of tablet dissolution was formulated and validated for tablets with a single value of infill density. While the tablet geometry and initial drug content were given as inputs, the diffusion coefficient and the thickness of the diffusion boundary layer were adjusted for the simulation to quantitatively agree with experimental data. Although changing infill density (porosity) of the tablets by modifying their printing settings and the supplied 3D template has been shown to affect their dissolution rate, this trend is not linear. As observed also in other recent work (10), the enhancement of dissolution by increasing the surface area through the introduction of porosity into the tablet is only possible if the pore size exceeds a certain threshold. The exact value of the threshold depends on the thickness of the diffusion boundary layer and in the case of swellable formulations, also on the degree of swelling of the tablet.

Amongst the most frequently mentioned potential advantages of 3D-printed drug forms is the possibility to incorporate multiple drugs with varying release profiles (5,12,24,25). In order to test the applicability of the method of adjusted dissolution for future tablets containing multiple drugs with varying release profiles, composite tablets with two different values of infill density were printed. The model was able to predict the dissolution kinetics of the composite pie-type tablets and the simulated release profiles agreed well with those measured experimentally by the physical dissolution of real 3D-printed composite tablets.

FUNDING INFORMATION

The authors would like to thank Zentiva, k.s., for supporting this work. M.N. ant T.B. would like to acknowledge financial support by Specific University Research (MSMT 21-SVV/2018).

REFERENCES

1. Meyer UA, Zanger UM, Schwab M. Omics and drug response. Annu Rev Pharmacol Toxicol. 2013;53:475–502.
2. Momper JD, Wagner JA. Therapeutic drug monitoring as a component of personalized medicine: applications in pediatric drug development. Clin Pharmacol Ther. 2014;95:138–40.
3. Koudijs KKM, Moes DJ, Hartigh J. Interfacing MW\Pharm to a laboratory information system calculates AUCs of immunosuppressants with fewer errors and in less time. Pharm Weekbl. 2015;150:250–2.
4. Khaled SA, Burley JC, Alexander MR, Yang J, Roberts CJ. 3D printing of five-in-one dose combination polypill with defined immediate and sustained release profiles. J Control Release. 2015;217:308–14.
5. Khaled SA, Burley JC, Alexander MR, Yang J, Roberts CJ. 3D printing of tablets containing multiple drugs with defined release profiles. Int J Pharm. 2015;494:643–50.
6. Martinez PR, Goyanes A, Basit AW, Gaisford S. Fabrication of drug-loaded hydrogels with stereolithographic 3D printing. Int J Pharm. 2017;532:313–7.
7. Kyobula M, Adedeji A, Alexander MR, Saleh E, Wildman R, Ashcroft I, et al. 3D inkjet printing of tablets exploiting bespoke complex geometries for controlled and tuneable drug release. J Control Release. 2017;261:207–15.
8. Goyanes A, Robles Martinez P, Buanz A, Basit AW, Gaisford S. Effect of geometry on drug release from 3D printed tablets. Int J Pharm. 2015;494:657–63.
9. Zhang J, Yang W, Vo AQ, Feng X, Ye X, Kim DW, et al. Hydroxypropyl methylcellulose-based controlled release dosage by melt extrusion and 3D printing: structure and drug release correlation. Carbohydr Polym. 2017;177:49–57.
10. Sadia M, Arafat B, Ahmed W, Forbes RT, Alhnan MA. Channelled tablets: an innovative approach to accelerating drug release from 3D printed tablets. J Control Release. 2018;269:355–63.
11. Okwuosa TC, Stefaniak D, Arafat B, Isreb A, Wan KW, Alhnan MA. A lower temperature FDM 3D printing for the manufacture of patient-specific immediate release tablets. Pharm Res. 2016;33:2704–12.
12. Sadia M, Sośnicka A, Arafat B, Isreb A, Ahmed W, Kelarakis A, et al. Adaptation of pharmaceutical excipients to FDM 3D printing for the fabrication of patient-tailored immediate release tablets. Int J Pharm. 2016;513:659–68.
13. Goyanes A, Scarpa M, Kamlow M, Gaisford S, Basit AW, Orlu M. Patient acceptability of 3D printed medicines. Int J Pharm. 2017;530:71–8.
14. Tanaka M. Inverse problems in engineering mechanics IV. International symposium on inverse problems in engineering mechanics 2003. Nagano: Elsevier; 2003.
15. Malone JB, Vadyak J, Sankar LN. Inverse aerodynamic design method for aircraft components. J Aircr. 1987;24:8–9.
16. Matsushima K, Iwamiya T. An aerodynamic design method for multi-element wings using inverse problems A2. In: Tanaka M, Dulikravich GS, editors. Inverse problems in engineering mechanics. Oxford: Elsevier Science Ltd; 1998. p. 417–25.
17. Leifsson L, Koziel S. Multi-fidelity design optimization of transonic airfoils using physics-based surrogate modeling and shape-preserving response prediction. Journal of Computational Science. 2010;1:98–106.
18. Woodbury KA. Inverse Engineering Handbook. Boca Raton: CRC press; 2002.
19. Štěpánek F. Computer-aided product design: Granule dissolution. Chem Eng Res Des. 2004;82:1458–66.
20. Kimber JA, Kazarian SG, Štěpánek F. DEM simulation of drug release from structurally heterogeneous swelling tablets. Powder Technol. 2013;248:68–76.
21. Zhang J, Feng X, Patil H, Tiwari RV, Repka MA. Coupling 3D printing with hot-melt extrusion to produce controlled-release tablets. Int J Pharm. 2017;519:186–97.
22. Chai X, Chai H, Wang X, Yang J, Li J, Zhao Y, et al. Fused deposition modeling (FDM) 3D printed tablets for intragastric floating delivery of domperidone. Sci Rep. 2017;7:2829.
23. Korte C, Quodbach J. 3D-printed network structures as controlled-release drug delivery systems: dose adjustment, API release analysis and prediction. AAPS PharmSciTech. 2018, accepted. https://doi.org/10.1208/s12249-018-1017-0.
24. Norman J, Madurawe RD, Moore CMV, Khan MA, Khairuzzaman A. A new chapter in pharmaceutical manufacturing: 3D-printed drug products. Adv Drug Deliv Rev. 2017;108:39–50.
25. Palo M, Holländer J, Suominen J, Yliruusi J, Sandler N. 3D printed drug delivery devices: perspectives and technical challenges. Expert Rev Med Devices. 2017;14:685–96.

9.3 Microstructure based simulation of the disintegration and dissolution of immediate release pharmaceutical tablets

Martin Kalný
Zdeněk Grof
František Štěpánek

Published in the *Powder Technol.*, Vol. 377, 2021, pp. 257–268
DOI: 10.1016/j.powtec.2020.08.093.

Powder Technology 377 (2021) 257–268

Contents lists available at ScienceDirect

Powder Technology

journal homepage: www.elsevier.com/locate/powtec

Microstructure based simulation of the disintegration and dissolution of immediate release pharmaceutical tablets

Martin Kalný, Zdeněk Grof *, František Štěpánek

Department of Chemical Engineering, University of Chemistry and Technology, Technická 5, Prague 166 28, Czech Republic

ARTICLE INFO

Article history:
Received 4 October 2019
Received in revised form 28 July 2020
Accepted 28 August 2020
Available online 01 September 2020

Keywords:
Drug dissolution modelling
Disintegrant
Discrete element method
Croscarmellose sodium
Ibuprofen

ABSTRACT

The design of pharmaceutical tablets involves the determination of formulation parameters that define the tablet composition and internal microstructure. These parameters must be chosen so that the release of an active pharmaceutical ingredient (API) from the tablet follows a prescribed dissolution curve. In the case of immediate release formulations, the dissolution process typically consists of tablet disintegration, followed by the dissolution of the disintegration fragments. In order to find the appropriate values of formulation parameters, numerous experiments are typically required. In the present work, we propose a computational methodology for in silico design of tablet formulations with the aim of reducing the amount experimental work required during tablet design. The methodology is based on the coupling of two modelling approaches: *(i)* tablet fragmentation triggered by the swelling of the disintegrant is simulated by the discrete element method (DEM), and *(ii)* the dissolution of the resulting population of disintegration fragments is simulated using a finite volume grid-based model. The final API release curve is then obtained by the superposition of dissolution curves originating from the individual disintegration fragments. Using directly compressed tablets containing ibuprofen as the API and croscarmellose sodium as the disintegrant, the model was validated against experimental data. The fragment size distribution was evaluated by static light scattering and the dissolution profiles were obtained by a standard dissolution apparatus with UV/Vis spectroscopic detection. We demonstrate that the computational methodology is able to quantitatively predict the effect of disintegrant content and API primary particle size on the fragment size distribution and the final dissolution profiles, and is therefore useful as a tool for computer-assisted tablet formulation design.

© 2020 Elsevier B.V. All rights reserved.

1. Introduction

Pharmaceutical tablets are the most convenient and used dosage forms for oral administration of drugs to patients. Tablets are typically compacted from heterogeneous powders or granules that consist of an active pharmaceutical ingredient (API) and a range of excipients such as diluents, binders, glidants, lubricants, or disintegrants. According to the desired release rate and the body location where API is supposed to be released from the tablet, tablets are classified as immediate or sustained release tablets [1]. For an immediate release tablet to be able to disintegrate and fully dissolve within a short time after administration, disintegrants are often added to the tablet formulation. Chemically, these are typically crosslinked polymers (crospovidone) or cellulose-based materials (croscarmellose sodium). When contacted with physiological fluids, these components increase their volume and promote the tablet disintegration into smaller fragments. This leads to a considerably higher dissolution rate of the API due to increased surface area available for dissolution [2]. Both the disintegration and subsequent dissolution processes therefore determine the API release rate, one of the most important pharmaceutical tablet behaviour characteristics affecting the drug bioavailability and its medicinal effects.

The development of tablets includes an interesting design problem: what values of formulation parameters that define the tablet internal microstructure and composition should be used in order to meet certain requirements on the release profile of the API? Examples of such formulation parameters include the size distribution of API primary particles, the grade of excipients, the type and amount of distintegrant, the location of the disintegrant (intra-granular vs. extra-granular), etc. Finding the appropriate values of these parameters is often a semi-empirical procedure requiring numerous experiments. The design process could be improved, and the number of required experiments possibly reduced by using computational simulations of tablet disintegration and dissolution processes and by determining the effects of formulation parameters on the resulting tablet behaviour computationally.

Mathematical models of drug dissolution were comprehensively reviewed [3,4] and they range from the simplest, diffusion based semi-empirical relations such as Noyes-Whitney, Higuchi or Peppas

* Corresponding author.
E-mail address: zdenek.grof@vscht.cz (Z. Grof).

https://doi.org/10.1016/j.powtec.2020.08.093
0032-5910/© 2020 Elsevier B.V. All rights reserved.

equations to more complex approaches considering also solvent uptake, swelling and erosion processes that require the numerical solution of balance and transport equations [5]. In most cases the dissolution models are constructed by describing the tablet as a single-phase medium or an effective porous medium [6].

For tablets containing a disintegrant, single-phase models cannot conveniently describe drug release due to the heterogeneous nature of disintegration mechanism [2,7,8] and the classical modelling techniques must be modified for this case. In a recent work, Yokoyama presents a method that uses cellular automata-supported disintegration [9]. However, also other approaches able to model the disintegration part of drug release are available. Discrete-element model (DEM) is a well-established methodology for the modelling of processes involving granular materials [10–12]. When extending its application scope, DEM is also able to model reaction-transport problems taking place in evolving multi-phase media as was presented, for example, for the catalyst fragmentation and the particle growth during polymerization of olefins [13–15], or for the swelling and dissolution [16–18] processes in the case of extended release pharmaceutical tablets. The need for the development of more complex models of dissolution can be illustrated by the fact that the state of the art modelling products such as “gPROMS FormulatedProducts” do not possess fragmentation size predictability.

In this work, DEM based model able to simulate the disintegration of a directly compressed immediate-release tablet is presented and validated against experimental data. Tablets containing ibuprofen as the API and croscarmellose sodium as the disintegrant were considered. The effect of primary particle size and the amount of disintegrant in the tablet on the resulting fragment size distribution was evaluated. In the second part of the simulation process, the obtained disintegration fragments were used as an input to a dissolution model [19]. Drug release was modelled by the dissolution of individual fragments and summation of the individual release curves. In order to validate the presented approach, also the resulting dissolution curves were compared with experimentally measured ones.

2. Experimental part

In order to validate the modelling approach and test its predictive power, the simulation results must be compared with experimental data. The disintegration and dissolution behaviour of directly compressed immediate-release tablets has been investigated experimentally in our recent work [20,21]. The prepared tablets contain ibuprofen (Hubei Biocause Pharmaceuticals Co. Ltd., China) as the active pharmaceutical ingredient, croscarmellose sodium (FMC Health and Nutrition) as a disintegrant and lactose monohydrate (Friesland Foods Domo, Netherlands) as a filler. The tablets are flat-faced cylindrical tablets (diameter is 13 mm, mass is 500 mg) and were prepared using a compression force of 20 kN with a hold of 3 s in a single-punch hydraulic tablet press (Carver 4530 L). The tablets contain 90 per cent by weight of ibuprofen and a varying amount of croscarmellose sodium (disintegrant): 1, 2 and 4 per cent by weight. Lactose forms the remaining mass of the tablet, i.e. 6–9 per cent by weight. Using ibuprofen crystals with different particle size distribution (PSD), two tablet types were prepared. The PSD of the ibuprofen crystals used for the preparation of the tablets denoted as "type A" is characterized by the following quantiles: $d_{10} = 45$ μm, $d_{50} = 130$ μm and $d_{90} = 274$ μm, while the quantiles for "type B" tablets are $d_{10} = 67$ μm, $d_{50} = 102$ μm and $d_{90} = 144$ μm.

Both disintegration and dissolution of the prepared tablets was measured. Phosphate buffer saline of pH 7.4 (PBS 7.4) with ionic strength of 0.15 mol/l was used as the disintegration medium. The disintegration experiment was carried out by placing a single tablet in an unstirred beaker containing 18 ml of PBS 7.4. In order to eliminate the effect of dissolution of the individual substances which could affect the measurement of particle size distribution of the disintegration fragments, the PBS 7.4 was saturated with ibuprofen and lactose prior to the disintegration experiments. When the tablet fully disintegrated, the resulting fragment size distribution was measured using static light scattering in a Horiba Partica LA-950 S2 unit and verified by optical microscopy. The dissolution experiments were carried out separately by dissolving a single tablet in 900 ml of PBS 7.4 solution (without ibuprofen and lactose in this case) in a beaker with magnetic stirrer [20,22] stirred at 600 rpm. Samples of the solution were taken at regular intervals and the ibuprofen concentration was determined using liquid chromatography. The dissolution test was repeated at least three times for every tablet.

3. Mathematical model

To model the disintegration process, the discrete elements method (DEM) was used [23]. At the start of the simulation, each element was described by its mass m, radius R, position and velocity vectors $\boldsymbol{r}$ and $\boldsymbol{v}$, orientation specified by Euler angle $\boldsymbol{\varphi}$ and angular velocity $\boldsymbol{\omega}$. At every step of the simulation, contact forces among individual particles were calculated and the change of particle position and velocity vectors was obtained according to Newton's law:

$$\frac{d^2\boldsymbol{r}}{dt^2} = \frac{d\boldsymbol{v}}{dt} = \frac{\sum_i \boldsymbol{F}_i}{m} \tag{1}$$

$$\frac{d^2\boldsymbol{\varphi}}{dt^2} = \frac{d\boldsymbol{\omega}}{dt} = \frac{\sum_i \boldsymbol{M}_i}{J} \tag{2}$$

where t is time, $\sum \boldsymbol{F}_i$ and $\sum \boldsymbol{M}_i$ are the overall force and torque acting on the element and J is the moment of inertia. Particle positions and their time derivatives were updated in each step using the Gear predictor-corrector algorithm, a method that is well suited for DEM due to its numerical integration stability [24].

Three force types were considered in our model: (i) contact force, which represents a repulsive force at the contact between two loose particles; (ii) attractive force, which represents the cohesion between two neighbouring particles prior to disintegration; and (iii) damping force, which represents the fluid resistance to particle movement. The forces are described in the following section.

3.1. Force scheme

The contact force is considered as a repulsive force between the pair of overlapping particles. There are several approaches that can approximate the contact force between particles. In our model, the soft-sphere approach originally developed by Cundall and Strack [25] able to describe the viscoelastic deformation of particles is used. This force applies only if the particles are overlapping and its magnitude is proportional to the extent of the overlap. To identify if two spherical particles are overlapping, following equation is used:

$$\varepsilon_{i,j} = R_i + R_j - \left|\boldsymbol{r}_i - \boldsymbol{r}_j\right| \tag{3}$$

where $\varepsilon_{i,j}$ is the overlap between i-th and j-th particle, R_i and $\boldsymbol{r}_i$ are the i-th particle radius and position. Then the contact force is calculated as:

$$\boldsymbol{F}_{i,j} = \begin{cases} \boldsymbol{F}^n_{i,j} + \boldsymbol{F}^t_{i,j} & \varepsilon_{i,j} > 0 \\ \boldsymbol{0} & \varepsilon_{i,j} \le 0 \end{cases} \tag{4}$$

where superscripts n and t denote the normal and the tangential component of the force. The contact force is equal to zero if the particles do not overlap.

The normal force consists of a dissipative (viscous) and a conservative (elastic) part. This can be described by the Kelvin-Voigt model for viscoelastic materials, which is represented as a combination of elastic spring and viscous damper connected in parallel as shown in Fig. 1.

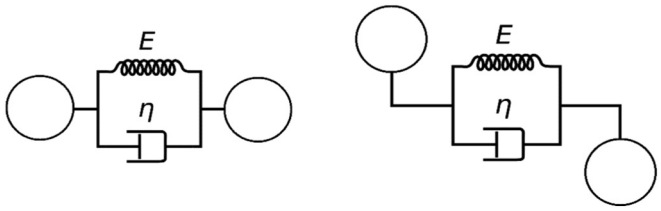

Fig. 1. Kelvin-Voigt model for viscoelastic materials describing the normal and tangential contact forces.

Using this model, the equation describing the contact of two viscoelastic spheres according to Tsuji [26] becomes:

$$\boldsymbol{F}_{i,j}^{n} = \left(-k_n \varepsilon_{i,j}^{\frac{3}{2}} - \eta_n \varepsilon_{i,j}^{\frac{1}{2}} \dot{\varepsilon}_{i,j}\right) \boldsymbol{n}_{ij} \tag{5}$$

where k_n is the normal stiffness coefficient evaluated from Eq. (6), η_n is the damping coefficient evaluated from Eq. (8) and $\boldsymbol{n}_{ij}$ is the unit vector pointing from i-th to j-th particle centers. The normal stiffness coefficient k_n is given by the Hertzian theory [27] for elastic deformation as a function of material parameters E (Young modulus) and ν (Poisson ratio):

$$k_n = \frac{E\sqrt{2R_{eff}}}{3(1-\nu^2)} \tag{6}$$

where R_{eff} is the effective radius calculated from the following equation:

$$\frac{1}{R_{eff}} = \frac{1}{R_i} + \frac{1}{R_j} \tag{7}$$

The damping coefficient η_n in Eq. (5) can be calculated by the following equation:

$$\eta_n = \sqrt{2 m_{eff} k_n} \tag{8}$$

where m_{eff} is the effective mass of the two particles calculated from the following equation:

$$\frac{1}{m_{eff}} = \frac{1}{m_i} + \frac{1}{m_j} \tag{9}$$

The Kelvin-Voigt model is used also for the tangential part of the contact force. Similarly, as for the normal force, it is represented by a combination of a spring and damper connected in parallel, its orientation is however perpendicular to the surface of the particles in contact. The tangential force is described by the following equation:

$$\boldsymbol{F}_{i,j}^{t} = -k_t \boldsymbol{\zeta} - \eta_t \boldsymbol{v}_{rel} \tag{10}$$

where $\boldsymbol{\zeta}$ is the displacement in tangential direction described by Eq. (12), k_t is the tangential stiffness given by Eq. (13), η_t is the tangential damping coefficient described by Eq. (14) and $\boldsymbol{v}_{rel}$ is the relative velocity of spheres at their point of contact as described by following equation:

$$\boldsymbol{v}_{rel} = \boldsymbol{v}_{ij} - (\boldsymbol{v}_{ij}\, \boldsymbol{n}_{ij})\boldsymbol{n}_{ij} + (R_i \boldsymbol{\omega}_i + R_j \boldsymbol{\omega}_j) \times \boldsymbol{n}_{ij} \tag{11}$$

where $\boldsymbol{v}_{ij}$ is the velocity of the i-th particle relative to the j-th particle and $\boldsymbol{\omega}$ is the angular velocity. The tangential displacement $\boldsymbol{\zeta}$ is described as follows:

$$\boldsymbol{\zeta}(t) = \int_{t_c}^{t} \boldsymbol{v}_{rel}(t')dt' \tag{12}$$

where t_c is the time when the particles touched each other. The tangential stiffness k_t and the tangential damping η_t coefficients are described similarly as their normal counterparts:

$$k_t = \frac{2E\sqrt{2R_{eff}}}{2(1+\nu)(2-\nu)} \tag{13}$$

$$\eta_t = \sqrt{2 m_{eff} k_t} \tag{14}$$

As is shown above, the contact force between two particles in our model is explicitly evaluated and depends only on the actual positions, velocities and the two material constants of contacting particles.

The attractive force in our model is active even if the particles do not overlap. In theory, this interparticular cohesive force should represent a combination of a wide range of forces such as intermolecular bonds, solid bridges and mechanical interlocking [2]. In order to simplify the calculations, these forces are combined and modelled as a single attractive force that acts between the points on the surface of two neighboring particles.

The attractive force is empirically defined by the following equation:

$$\boldsymbol{F}_{i,j}^{a} = \alpha \varepsilon_{i,j}^{a} \boldsymbol{n}_{ij}^{a} \tag{15}$$

where α is the attractive force strength coefficient, $\boldsymbol{n}_{ij}^{a}$ is the unit vector between two points on the surfaces of the i-th an j-th particle and $\varepsilon_{i,j}^{\alpha}$ is the current distance between these two points, which is expressed as:

$$\boldsymbol{\varepsilon}_{ij}^{a} = \left|\boldsymbol{r}_j^{a} - \boldsymbol{r}_i^{a}\right| \tag{16}$$

where $\boldsymbol{r}_j^{a}$ and $\boldsymbol{r}_i^{a}$ are the coordinates that specify the bond between particles and correspond to the points on the surface of particles i and j, that were closest to each other when the bond formed. The position of a point on particle surface is stored using the particle local coordinates system. Therefore the bond position and orientation is tracked correctly regardless of the particles rotation. The transformation from the local to the global coordinates system and the determination of particle orientation is conveniently resolved using quaternions that are comprehensively described in [23,24]. The strength of the bond between two particles is determined by the attractive force strength coefficient α. As it has no direct physical meaning, it must be tuned using the comparison of simulations with experimental data.

The attractive force in our model is assumed to represent adhesive bonds that form between individual API or disintegrant particles when the tablet is compressed. The bond between two particles is created only if the distance between particles is smaller than certain minimal distance ($\varepsilon_{i,j} < d_{min}$) at the time before the disintegration begins. No new bonds are created later during the disintegration phase of the simulation as the bond breakage during the disintegration is permanent. In the simulation, the bond breaks and the attractive force will no longer apply to this pair of particles if the distance between two points on the surface of the particle exceeds a certain limit ($\varepsilon_{i,j}^{a} > d_{max}$).

The damping force has been added to our model to keep the simulation numerically stable and to ensure that the emerging fragments do not move too fast by damping the particles movement. It has the same effect as a drag force of a fluid medium and could be therefore replaced by equations describing more rigorously the fluid resistance, such as the Stokes equation. The damping force is proportional to the particle velocity and mass, as described by Eq. (17), where b is the damping force parameter.

$$\boldsymbol{F}_i^{d} = -b \boldsymbol{v}_i m_i \tag{17}$$

3.2. Disintegration simulation

To test the disintegration simulation, a directly compressed tablet containing ibuprofen (API), croscarmellose sodium (disintegrant) and lactose (filler) was used. Croscarmellose is commonly used as a disintegrant, because it swells rapidly in the presence of water and is able to increase its volume eight times (compared to its dry state volume) [28]. Its main disintegration mechanism is multiaxial swelling, which is advantageous for the modelling, as the orientation of the disintegrant particles does not have to be considered during the swelling.

To model the disintegration of this tablet using the DEM approach described in the previous section, the tablet is first discretized into circular elements. In this work, the simulations were done only for two dimensions in order to minimize computational time. The number of elements used for each simulation was 8100 and multiple simulations were run for each set of parameters. Each element is classified either as an API or a disintegrant element. The content of lactose in the tablet was small (<10 %) and therefore its effect on the size of the fragments created by disintegration is negligible, which was also confirmed by experiments. The size of a typical lactose particle is very small and therefore the simulation time step would have to be considerably decreased, which would increase the computational cost of the simulations. The size and type of elements and their number is chosen according to the particle size distribution and composition of real tablets. The modelling domain and the DEM discretization is shown in Fig. 2.

To create the tablet representation, the particles are placed on a regular grid to ensure that they do not overlap. In the initial simulation phase, the "gravitational" force pointing towards the centre of the grid is enabled, which leads to the formation of a circular structure that is similar to the tablet. When the steady-state is reached, single cluster of particles is created by connecting adjacent elements by bonds (enabling attractive forces) as described in the previous section. The gravitational force forming the tablet is disabled and no longer considered.

The next simulation phase is the tablet disintegration that is caused by the growth of the disintegrant particles. The size of disintegrant particles is gradually increased, the growth of the disintegrant particles is linear in time and is described by the following equation:

$$\frac{dR_i}{dt} = \begin{cases} R_i(0)Q, & R_i < qR_i(0) \\ 0, & R_i \geq qR_i(0) \end{cases} \tag{18}$$

where Q is the rate of growth of the disintegrant particles, q is the maximum increase in radius of the particle and $R_i(0)$ is the particle's initial radius. The rate of growth Q is constant and its value is set in such a way that the simulation results no longer change when Q is decreased. This means, the parameter's value has to be small enough, so that the structure can reach equilibrium before the next increase in size of the disintegrant particles. The maximum increase factor q depends on the swelling properties of the disintegrant and its maximum water uptake.

The growth of disintegrant elements leads to the repulsion of the adjoining elements, the breakage of the bonds between particles and the disintegration of tablet into fragments. The simulation is stopped when disintegrant particles reach their final size (eightfold increase of their initial volume) and no more fragments can form. The size and shape of each fragment is analysed and stored; particle size distribution of the fragments is calculated. The arithmetic mean of Feret diameters along x and y axes directions is used to characterize the fragment size. The bins for particle size distributions are chosen to be the same as the bins used to report the light scattering measurement results. The simulation phases are illustrated in Fig. 3. When comparing the experimental and simulation results, the relative difference between cumulative PSD curves z can be calculated as

$$z = \sqrt{\frac{1}{N}\sum_{i=1}^{N}\left(F_i^{exp} - F_i^{sim}\right)^2} \tag{19}$$

where F_i is the cumulative distribution function at i-th size class bin.

A parametric study was done in order to determine the effect of the attractive force parameters α and d_{max} on the resulting structures and to find their optimal values. Once the optimal parameter values were found, the effect of disintegrant amount and its spatial distribution inside the tablet on the resulting fragment size distribution was tested. The disintegration of the ibuprofen/croscarmellose tablets with varying contents of croscarmellose (1 %, 2 %, and 4 %) was simulated.

3.3. Dissolution model

In the second part of this work, the dissolution model was used to dissolve the individual fragments obtained by DEM simulation. In order to use the data from the disintegration model, the resulting fragments were discretized and superimposed on a square elements grid. Based on the element positions obtained by DEM simulation, each voxel was labelled either as solid (API) or pore. A boundary layer was created around the resulting fragment. The dissolution is modelled as a diffusion rate limited process. During the dissolution simulation, the equilibrium solubility at the solid/pore boundary was assumed and the diffusion transport of the dissolved API between neighbouring elements was calculated. The model can be viewed as an extension of Noyes-Whitney equation for irregular geometries and its details are described in [19]. The course of the dissolution is explained in Fig. 4.

In order to reconstruct the complete dissolution curve of the modelled tablet, 5 fragments from every size class bin were selected (if the bin contained less than 5 fragments then all fragments were selected), the dissolution curves of individual fragments were simulated and an average dissolution curve was calculated for every size class bin. The resulting dissolution curve of the tablet was then constructed as a weighted sum of the fragment dissolution curves according to:

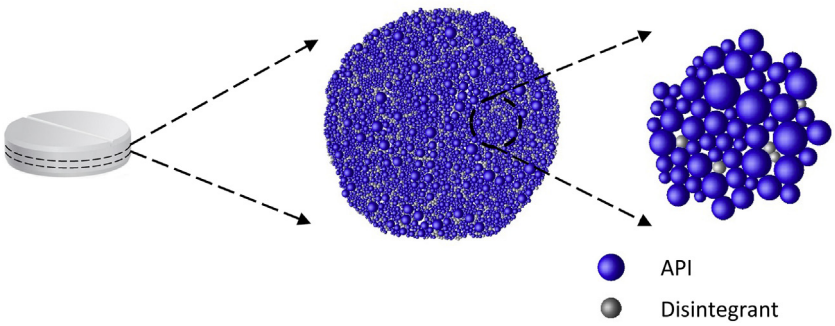

Fig. 2. Schematic representation of modelling domain. Tablets layer consisting of elements of API and disintegrant.

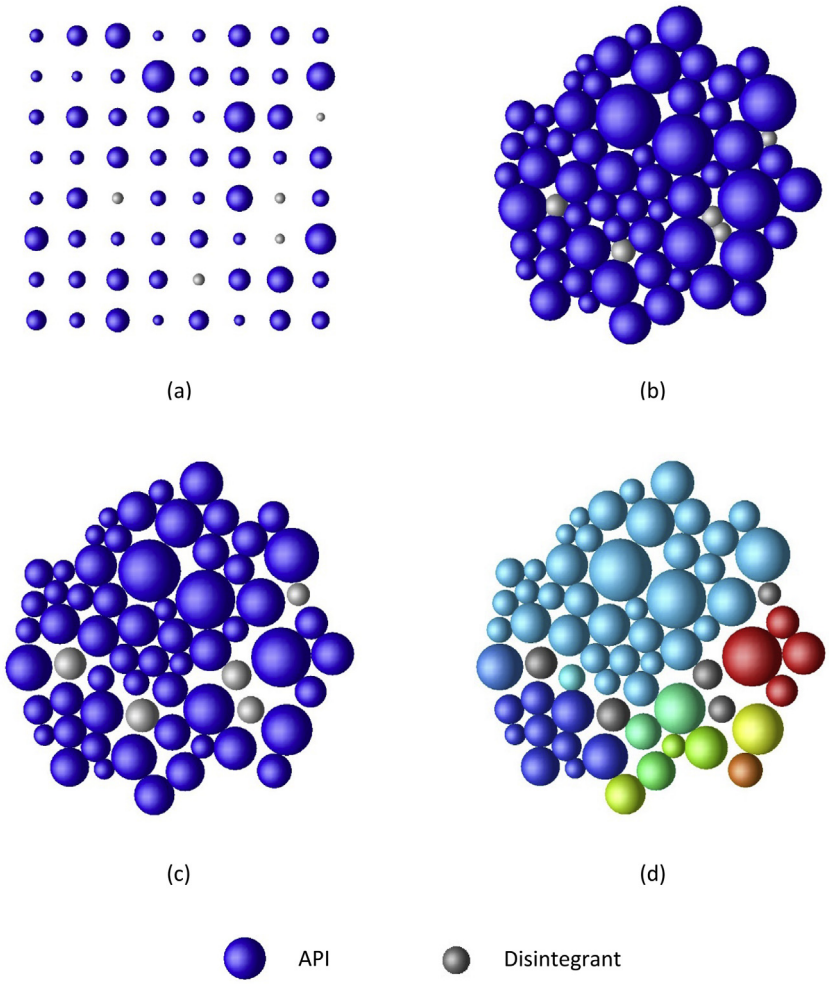

Fig. 3. Schematic of the course of the disintegration model. (a) Initialization of the particle positions, size and type. (b) Formation of the tablet structure. (c) Growth of the disintegrant elements. (d) Identification of the formed fragments.

$$Y(t) = \sum_i w_i y_i(t) \tag{20}$$

where Y is the dissolved fraction of the tablet, y_i is the dissolved fraction of a fragment of particular size i and w_i is the fragment's fraction evaluated from the disintegration model. This calculation is shown schematically in Fig. 5.

4. Results

4.1. Disintegration experiments

The disintegration of tablets was carried out using two types of tablets with different PSD of ibuprofen particles. This was done in order to test the effect of the primary PSD on the resulting fragment size

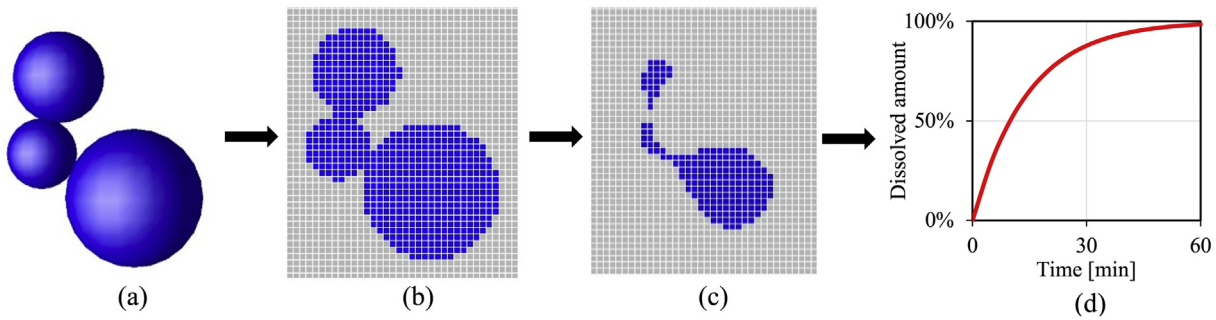

Fig. 4. Course of the dissolution model. (a) Individual fragment chosen from the disintegration model. (b) Fragment meshed onto regular grid. (c) Dissolution of the fragment. (d) Dissolution curve of a fragment obtained.

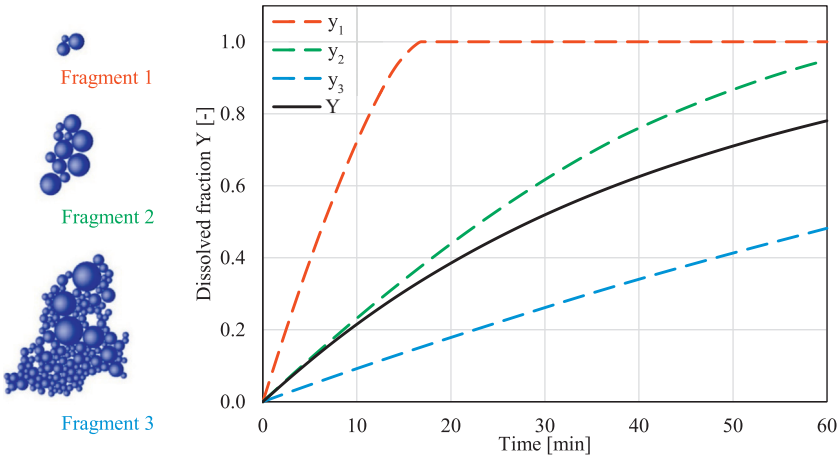

Fig. 5. Schematic of calculation of the dissolution curve of the tablet from the dissolution curves of the individual fragments.

distribution after the tablet disintegration and to verify the presented mathematical model. The difference in PSDs of the ibuprofen particles used for tabletting is shown in Fig. 6.

The final PSDs of the fragments formed by tablet disintegration are shown in Fig. 7 for both types of tablets and for different amounts of disintegration component. The PSD was measured by static light scattering, except for the case of tablets "B" containing 1 % of disintegrant that was measured by optical microscopy due to the large size of resulting fragments.

As can be seen in Fig. 7 the resulting fragment PSD is bimodal. The first peak at around 90 μm visible in all curves is associated with the croscarmellose sodium particles. The height of the peak corresponds roughly to the content of the disintegrant particles in the tablet while its position is the same for all tablets regardless of the disintegrant content. These results show that most of the bonds between the ibuprofen particles and the croscarmellose particles break as the disintegrant grows. The second peak in the distribution, whose position varies with different amount of the disintegrant component in the tablet, is the peak representing the resulting fragments composed from ibuprofen particles. As expected, with increasing amount of the disintegrant in the formulation, the mean size of the resulting fragments becomes smaller. The modes of the individual distributions of fragments for tablets "A" with 1 %, 2 % and 4 % of disintegrant are 1020, 452 and 300 μm, respectively. As can be seen, the shape of PSDs of the fragments is the same for tablets "B" and "A". However, compared to tablets "A", the main peak of PSD of the fragments forming from tablets "B" is shifted to the right, indicating that tablets "B" disintegrate into larger fragments than tablets "A". This relation is interestingly opposite to the relation between the peaks on the primary particles distributions because tablets "B" are compressed from smaller ibuprofene particles than tablets "A". Looking at the difference between fragments resulting from "A" and "B" tablets, the mode of the distribution shifted only slightly from 300 μm to 344 μm for tablets containing 4 % of the disintegrant. For tablets with 2 % and 1 % of the disintegrant, the increase in the mean size of the fragments was more significant: shifting from 452 to 679 μm and from 1020 to approximately 2000 μm, respectively.

The study of fragmentation kinetics was not the focus of the present work; however, the disintegration times were estimated by observing the disintegration experiments. Tablets "A" with 1 %, 2 % and 4 % of disintegrant disintegrated within 21, 9 and 7 min, respectively. The disintegration rate of tablets "B" was much slower: 6 h for tablets with 4 % and more than 24 h for tablets with 1 % and 2 % of disintegrant content. The reason of long disintegration times for tablets "B" might be that smaller and more narrowly distributed ibuprofen particles (cf. Fig. 6) were used for tableting of "B" tablets, making "B" tablets more compact than "A" tablets. The rate of solvent uptake could be slowed down

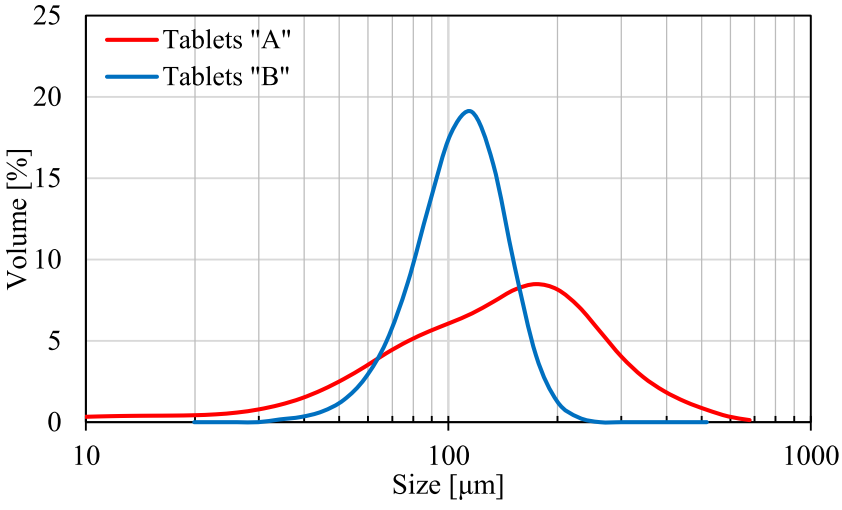

Fig. 6. Particle size distributions of the ibuprofen used for preparation of tablets "A" and "B".

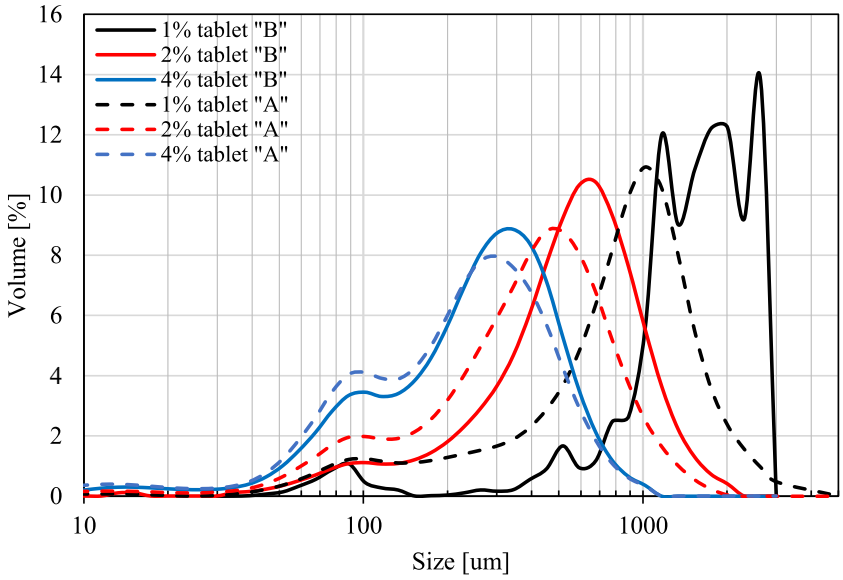

Fig. 7. Disintegration experiments: Particle size distribution of resulting fragments comparing different PSDs of primary particles ("A" and "B" tablets) and different amounts of disintegrant component in tablet formulation (1 %, 2 % and 4 %). Optical microscopy was used to obtain data for a 1 % disintegrant-tablet "B" line, the remaining lines were obtained using static light scattering measurements.

considerably by smaller pores in "B" tablets which would result in longer disintegration times.

4.2. Disintegration modelling

Let us start with a parametric study showing the effect of the attractive force strength coefficient α and the maximum bond strain d_{max}. This will help to determine the values of unknown parameters when the simulation results will be compared with experiments. Ibuprofen tablets "A" with 2 % content of disintegrant were used as the reference. The effect of the parameter d_{max}, which determines the maximum strain before the bond between particles is broken, is shown in Fig. 8a. It can be seen that increasing the parameter d_{max} increases the size of the resulting fragments, as the attractive bond between the particles breaks at larger distance.

The effect of the second parameter α that determines the strength of the attractive force, is shown in Fig. 8b. Increasing the parameter α increases the size of the fragments, as the bond between particles is stronger. Based on the comparison with experimental data, the optimal value for the parameters has been chosen 0.007 kg s^{-2} for α and 4μm for d_{max}. The chosen value of maximum bond strain d_{max} corresponds to

Table 1
Values of parameters used in the simulation.

Parameter	Symbol	Value	Units
Time step	Δt	$2 \cdot 10^{-6}$	s
No. of simulation steps	–	$2 \cdot 10^{6}$	–
No. of particles	–	8100	–
Disintegrant growth speed	Q	$1 \cdot 10^{-5}$	s^{-1}
Global attractive force acceleration	g	10.0	$m \cdot s^{-2}$
Damping force parameter	b	5.0	s^{-1}
Attractive force strength	α	$7 \cdot 10^{-3}$	kg s^{-2}
Maximum bond distance	d_{max}	4	μm

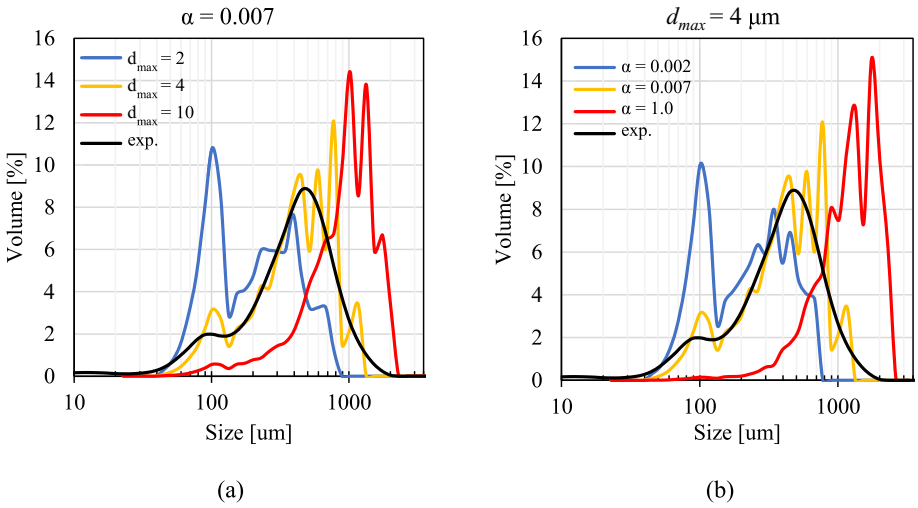

Fig. 8. (a) The effect of the maximum range of the attractive force (d_{max}) on the disintegration for constant α (0.007 kg s^{-2}). (b) The effect of the attractive force strength (α) on the disintegration for constant d_{max} (4 μm).

approximately 10 % of the average particle diameter. The values of other model parameters that were used during simulations are summarized in Table 1.

Once the values of the attractive force strength α and the maximum bond distance d_{max} were determined, the model was used to simulate the disintegration of the ibuprofen tablets with different amounts of disintegrant. This was done firstly using the tablets of type "A", which were used also for the parametric study. The particle size distributions of fragments obtained from the simulation are compared to the experimental results in Fig. 9. The presented distributions were calculated as an average from 20 parallel simulations starting from different random realizations of initial particles positions. Both the differential and cumulative volume distributions for individual tablets are shown in Fig. 9. The relative difference between cumulative PSD curves *z* is 2.4 %, 4.7 % and 5.3 % for tablets containing 1 %, 2 % and 4 % of disintegrant, respectively.

The simulation results are generally in a good agreement with the experimental results. However, the biggest discrepancy between the two resulting distributions is for the tablets containing 4 % of disintegrant. As can be seen, the particle size distribution obtained from the simulation is shifted left from the experimental results, thus the simulation predicts creation of slightly smaller fragments. This is likely caused by higher degree of breaking of the interparticular bonds between ibuprofen particles in close proximity

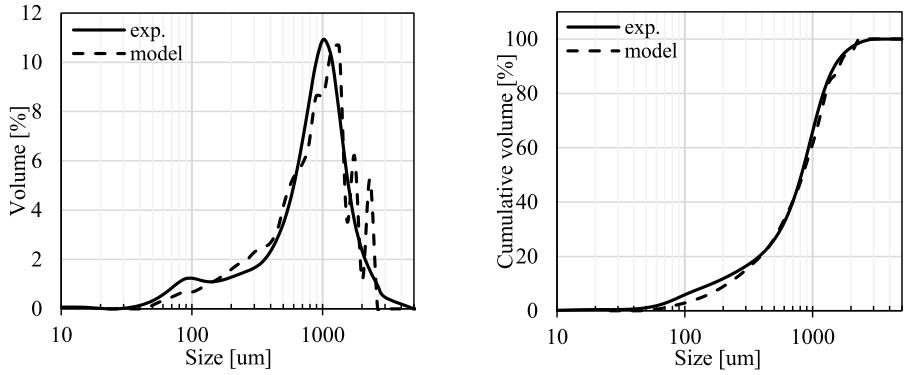

(a) 1% disintegrant

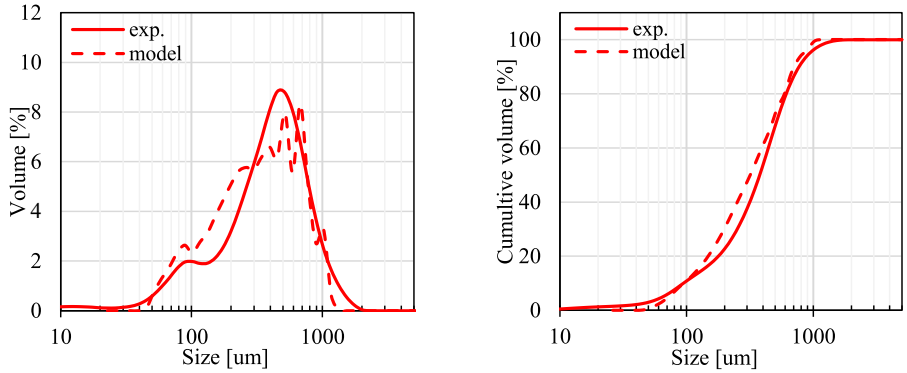

(b) 2% disintegrant

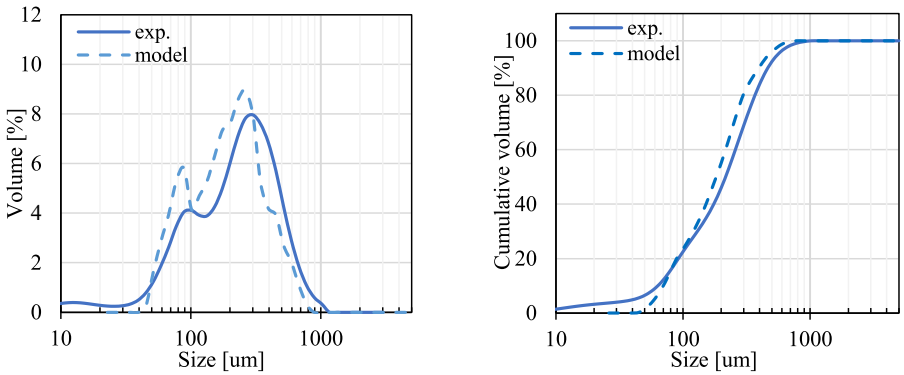

(c) 4% disintegrant

Fig. 9. Comparison of particle size distribution of fragments obtained from experiments and from simulation for tablets "A" with different amount of disintegrant.

of the disintegrant particles, which was observed in the simulation. This causes creation of higher number of single ibuprofen particle fragments, whose size depends on the initial ibuprofen particle size distribution used in the simulation. As Fig. 9 shows, the size of the single ibuprofen particles ranges approximately from 100 to 250 μm, which corresponds to higher percentage of those particles in the simulation results compared to the experiments. Similar effect in smaller scale can be observed for the tablets with 2 % of disintegrant. This issue will be addressed in a future work.

For tablets with 1 % and 2 % of disintegrant, the simulation results show several smaller peaks for the larger ibuprofen fragments. This is caused by the inherent randomness of the simulation, as the number of the largest fragments in the simulation is relatively low due to the smaller domain size. This can be addressed by using larger domain size or by performing higher number of parallel simulations.

4.3. Tablets "B"

In this section, the tablets of type "B" compressed from ibuprofen with smaller d_{50} were modelled. The simulated tablets had the same composition as in the previous case, they contained 90 % of ibuprofen with three different amounts of disintegrant – 1 %, 2 % and 4 %. This second type of tablets was used to test the effect of the initial particle size distribution on the simulation results. The comparison of the experimentally measured distribution of fragments for the tablets "B" to the simulation results is shown in Fig. 10. The distributions were calculated as an average from 20 parallel simulations. The distributions of the individual tablets are shown by volume and also by cumulative volume.

As can be seen, the simulation was successfully able to predict the increase in the mean size of the fragments for tablets "B" made from different particle size distribution of the primary ibuprofen particles. In addition, the size distributions of the fragments obtained from the

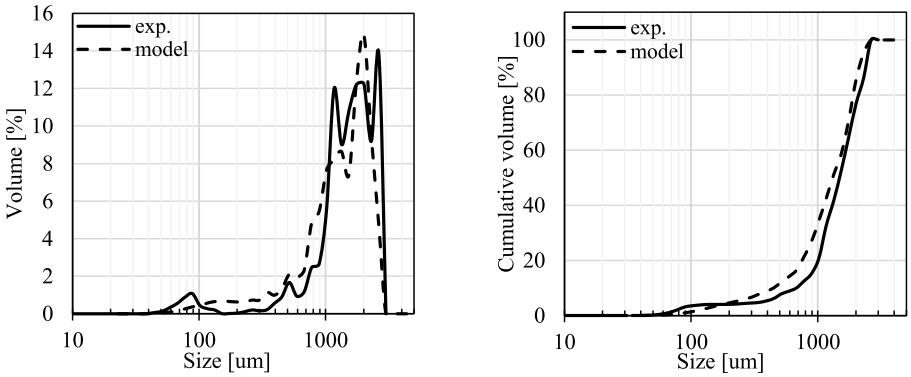

Fig. 10. Comparison of particle size distribution of fragments obtained from experiments and from simulation for tablets "B" with different amounts of disintegrant.

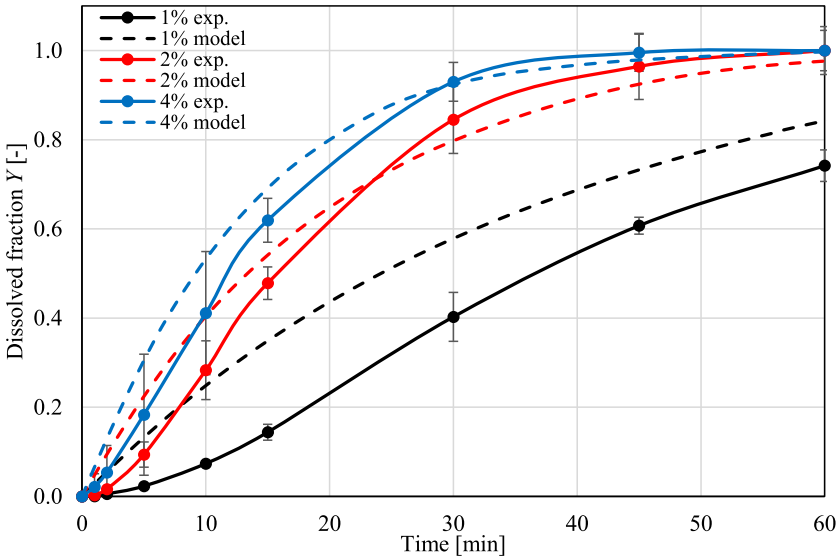

Fig. 11. Comparison of dissolution curves from experiments and simulation for tablets with different content of disintegrant.

simulations are overall in good agreement with the experimentally measured distributions. This shows that the disintegration of the tablets is highly dependent on their composition but also on the particle size distribution of the constituting powders. In Fig. 10, the relative difference between cumulative PSD curves z is 5.6 %, 4.9 % and 5.6 % for tablets with 1 %, 2 % and 4 % of disintegrant, respectively.

The biggest discrepancy between the distributions from simulations and experiments is for the tablets with 4 % of disintegrant, similarly as in the case of tablets "A". There is another peak at around 130 μm, which corresponds to the primary particles of the ibuprofen in the simulation. This is caused again by the higher degree of breaking of the bonds between ibuprofen particles in proximity of the disintegrant, which creates more primary ibuprofen particles. The size distributions of the fragments from tablets with 1 % and 2 % of disintegrant obtained from the simulation fit the experimental data more closely.

4.4. Dissolution modelling

In this section, the simulation that dissolves ibuprofen tablets "A" containing 1 %, 2 % and 4 % of disintegrant component are presented. The fragments obtained from the DEM based disintegration model and their size distribution were used as an input to the dissolution model. The dissolution curves predicted by the simulation are compared to the experimentally measured dissolution curves in Fig. 11.

As can be seen, there are relatively large differences between the experimental results and the simulations, the discrepancy is particularly large for the tablets with 1 % of disintegrant. There is a visible lag phase in the dissolution curve obtained from the experiments that is not reflected in the simulation. This is due to the fact that, in reality, the dissolution is very slow at first due to a compact form of the tablet and therefore disintegration is the rate-limiting step at the very beginning of the tablet dissolution. After the tablet disintegrates, the

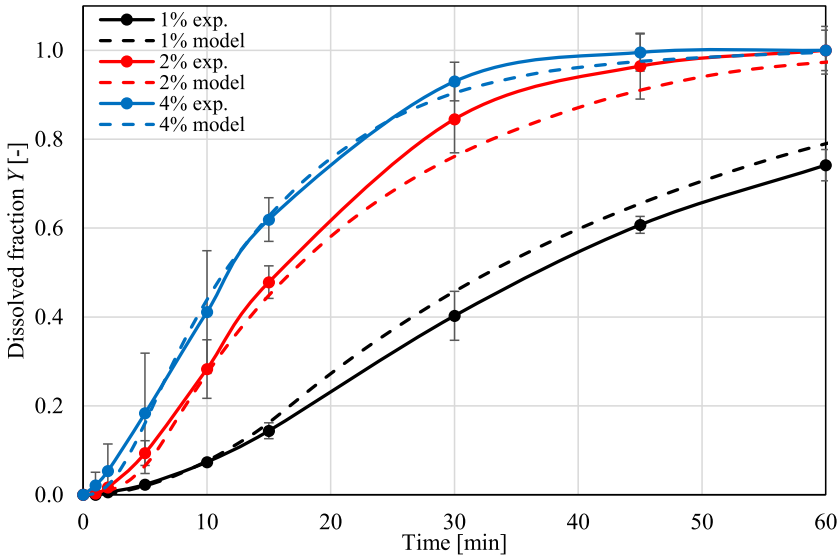

Fig. 12. Comparison of dissolution curves obtained from experiments and simulations considering the disintegration time for tablets with different content of disintegrant.

dissolution rate increases due to the higher surface area of the formed fragments. As the disintegration is the slowest for the tablets with 1 % of disintegrant, their lag phase is the longest. However, the disintegration is assumed to take place instantly in the model. At the moment, the model is not intended to be able to predict the actual disintegration time. The instant disintegration assumption is reasonable in the case of tablets with higher disintegrant content that are able to disintegrate rapidly, however there will be a larger discrepancy between experiment and simulation when the actual disintegration is relatively slow, as can be seen in the case of tablets containing 1 % of disintegrant.

In order to address this issue, the dissolution curves of the individual fragments were shifted by Δt randomly selected from interval $\langle 0, t_{dis} \rangle$ during the calculation of the tablet dissolution curve. The experimentally measured disintegration time of the tablet was used as the interval upper limit value t_{dis}. The dissolution curve of the tablet was therefore modified according to:

$$Y\prime(t) = \sum_i w_i y_i(t + \Delta t) \tag{21}$$

where Y' is the modified dissolved fraction of the tablet. The measured disintegration time t_{dis} was 21, 9 and 7 min for the tablets with 1 %, 2 % and 4 %, respectively. This modification was made in order to approximate the gradual disintegration of the tablet into individual fragments and their subsequent dissolution. The resulting dissolution curves of tablets "A" containing 1 %, 2 % and 4 % of disintegrant obtained by simulation and considering the measured disintegration time are compared to experimental results in Fig. 12.

The comparison shows that, when the modification taking into account also the disintegration time is made, the simulation results become in a much better agreement with the experimental data. Therefore, the dissolution model can be successfully used to calculate the dissolution of the individual fragments created by the disintegration model and the drug release from the tablets with different amounts of disintegrant can be evaluated. The dissolution of the tablets "B" was not measured nor simulated as their disintegration time was too long and therefore the tablet disintegration and fragments dissolution phases could not be treated separately.

5. Conclusions

A mathematical model based on the discrete element method for the disintegration of directly compressed tablets containing API and disintegrant was presented. A parametric study was conducted first: the effect of model parameters on tablet disintegration was investigated and experimental data were used to find the optimal parameter values. Subsequently, the size distribution of fragments formed by the disintegration of tablets containing varying disintegrant content was predicted by numerical simulations. The comparison of the results with experimental data showed a good agreement. Furthermore, the model was used to simulate the disintegration of a second type of tablets containing API with different particle size distribution. The model was able to successfully predict the increase in the mean size of the fragments as well as the shape of the distribution, despite the smaller size of the initial API particles. The actual fragments resulting from disintegration simulation were then used as an input for a modified version of a dissolution model developed in our research group earlier and described in [19]. The dissolution of the individual fragments was simulated, and dissolution curves were constructed and compared with experiments.

Some limitations must be mentioned regarding the predictability of the present model: (i) The parameters α and d_{max} must be calibrated for a chosen material of primary API and disintegrant particles and the values of these parameters will be different in two- and three-dimensional simulations, (ii) the kinetics of the disintegration step is not considered by the model and the disintegration time t_{dis} must be measured in order to correct the calculated dissolution curves in cases when the fragmentation is not instantaneous, and (iii) homogeneous stress distribution and uniform growth rate of disintegrant particles is assumed. It has been demonstrated that, despite these simplifications, the current methodology is able to successfully predict the disintegration and the dissolution behaviour of directly compressed tablets and therefore we believe it could be used as a tool making the design and development of new pharmaceutical tablets more efficient.

List of symbols

b	Damping force parameter [s^{-1}]
d_{max}	Maximum bond distance [m]
E	Young modulus [kg m^{-1} s^{-2}]
F	Force [N]
J	Moment of inertia [kg m^2]
k	Stiffness coefficient [kg $m^{-1/2}$ s^{-2}]
m	Mass [kg]
M	Torque [N m]
m_{eff}	Effective mass [kg]
q	Maximum radius increase [−]
Q	Rate of growth [s^{-1}]
r	Position [m]
R	Radius [m]
R_{eff}	Effective radius [m]
t	Time [s]
v	Velocity [m s^{-1}]
α	Attractive force strength [kg s^{-2}]
ε	Particle overlap [m]
ζ	Displacement [m]
η	Damping coefficient [kg s^{-1}]
μ	Coefficient of friction [−]
ν	Poisson ratio [−]
φ	Euler angles [−]
ω	Angular velocity [rad s^{-1}]

Declaration of Competing Interest

The authors declare that they have no known competing financial interests or personal relationships that could have appeared to influence the work reported in this paper.

Acknowledgements

Support from Czech Science Foundation through grant No. 19-26127X is acknowledged. This work was also supported by The Ministry of Education, Youth and Sports from the Large Infrastructures for Research, Experimental Development and Innovations project "IT4Innovations National Supercomputing Center – LM2015070".

References

[1] R. Eyjolfsson, Design and Manufacture of Pharmaceutical Tablets, Academic Press, 2014.
[2] D. Markl, J.A. Zeitler, A review of disintegration mechanisms and measurement techniques, Pharm. Res. 34 (5) (2017) 890–917.
[3] D. Caccavo, An overview on the mathematical modeling of hydrogels' behavior for drug delivery systems, Int. J. Pharm. 560 (2019) 175–190.
[4] J. Siepmann, F. Siepmann, Mathematical modeling of drug dissolution, Int. J. Pharm. 453 (1) (2013) 12–24.
[5] G. Lamberti, I. Galdi, A.A. Barba, Controlled release from hydrogel-based solid matrices. A model accounting for water up-take, swelling and erosion, Int. J. Pharm. 407 (1–2) (2011) 78–86.
[6] H.L. Zhu, et al., A model for flow and deformation in unsaturated swelling porous media, Transp. Porous Media 84 (2) (2010) 335–369.
[7] P.M. Desai, C.V. Liew, P.W.S. Heng, Review of disintegrants and the disintegration phenomena, J. Pharm. Sci. 105 (9) (2016) 2545–2555.
[8] J. Quodbach, P. Kleinebudde, A critical review on tablet disintegration, Pharm. Dev. Technol. 21 (6) (2016) 763–774.

[9] R. Yokoyama, et al., Modeling of disintegration and dissolution behavior of Mefenamic acid formulation using numeric solution of Noyes-Whitney equation with cellular automata on microtomographic and algorithmically generated surfaces, Pharmaceutics 10 (4) (2018) 17.
[10] F. Bertrand, L.A. Leclaire, G. Levecque, DEM-based models for the mixing of granular materials, Chem. Eng. Sci. 60 (8–9) (2005) 2517–2531.
[11] W.R. Ketterhagen, M.T.A. Ende, B.C. Hancock, Process modeling in the pharmaceutical industry using the discrete element method, J. Pharm. Sci. 98 (2) (2009) 442–470.
[12] W.R. Ketterhagen, et al., Computational approaches to predict the effect of shear during processing of lubricated pharmaceutical blends, Powder Technol. 335 (2018) 427–439.
[13] Z. Grof, J. Kosek, M. Marek, Modeling of morphogenesis of growing polyolefin particles, AICHE J. 51 (7) (2005) 2048–2067.
[14] Z. Grof, J. Kosek, M. Marek, Principles of the morphogenesis of polyolefin particles, Ind. Eng. Chem. Res. 44 (8) (2005) 2389–2404.
[15] B. Horackova, Z. Grof, J. Kosek, Dynamics of fragmentation of catalyst carriers in catalytic polymerization of olefins, Chem. Eng. Sci. 62 (18–20) (2007) 5264–5270.
[16] J.A. Kimber, S.G. Kazarian, F. Stepanek, Modelling of pharmaceutical tablet swelling and dissolution using discrete element method, Chem. Eng. Sci. 69 (1) (2012) 394–403.
[17] J.A. Kimber, S.G. Kazarian, F. Stepanek, DEM simulation of drug release from structurally heterogeneous swelling tablets, Powder Technol. 248 (2013) 68–76.
[18] J.A. Kimber, S.G. Kazarian, F. Stepanek, Formulation design space analysis for drug release from swelling polymer tablets, Powder Technol. 236 (2013) 179–187.
[19] M. Novák, et al., Virtual prototyping and parametric design of 3D-printed tablets based on the solution of inverse problem, AAPS PharmSciTech 19 (8) (2018) 3414–3424.
[20] J. Dvorak, et al., Investigation of tablet disintegration pathways by the combined use of magnetic resonance imaging, texture analysis and static light scattering, Int. J. Pharm. 587 (2020), 119719. https://doi.org/10.1016/j.ijpharm.2020.119719.
[21] J. Tomas, et al., Probing the early stages of tablet disintegration by stress relaxation measurement, Eur. J. Pharm. Sci. 124 (2018) 145–152.
[22] D. Smrcka, et al., Experimental analysis of inter- and intra-batch variation of granule porosity, stiffness and dissolution rate, Chem. Eng. Res. Des. 132 (2018) 1131–1142.
[23] M.P. Allen, D.J. Tildesley, Computer Simulation of Liquids, Oxford university press, 2017.
[24] T. Pöschel, T. Schwager, Computational Granular Dynamics: Models and Algorithms, Springer Science & Business Media, 2005.
[25] P.A. Cundall, O.D. Strack, A discrete numerical model for granular assemblies, Geotechnique 29 (1) (1979) 47–65.
[26] Y. Tsuji, T. Tanaka, T. Ishida, Lagrangian numerical simulation of plug flow of cohesionless particles in a horizontal pipe, Powder Technol. 71 (3) (1992) 239–250.
[27] J. Shäfer, S. Dippel, D. Wolf, Force schemes in simulations of granular materials, J. Phys. I. 6 (1) (1996) 5–20.
[28] J. Rojas, S. Guisao, V. Ruge, Functional assessment of four types of disintegrants and their effect on the spironolactone release properties, AAPS PharmSciTech 13 (4) (2012) 1054–1062.

9.4 The optimization of multi-component tablet internal structure by evolutionary algorithm

Zdeněk Grof
František Štěpánek

Draft of the article that is being prepared for the publication, 2021

The optimization of multi-component tablet internal structure by evolutionary algorithm

Zdeněk Grof, František Štěpánek*

Department of Chemical Engineering, University of Chemistry and Technology, Prague, Technická 5, 166 28 Prague 6, Czech Republic

Abstract

This is the draft of a manuscript which will be submitted

Keywords: tablet dissolution, modelling, genetic algorithm, personalized dosage forms

1. Introduction

Optimization problems can be solved by different methods, but evolutionary algorithms (EA) and their subset, genetic algorithms, are particularly well suited for problems characterized by a vast space of possible solutions [1]. The application area of problems that have been tackled by EA is wide and includes material selection [2], optimum resource allocation as in a travelling thief [3] or a plant design [4, 5] problems, or structural optimization, eg. reinforced concrete beams [6], shock absorbing granular protectors [7] or degradable tissue scaffolds [8] designs. Within pharmaceutical and medicinal communities, an EA is a well known and an irreplaceable part of rational drug design at the molecular level [9–15], however, at the dosage form (i.e. tablet or capsule) level, EA have been rarely used. In the field of release kinetics modeling [16, 17], EA have been employed to optimize the parameter values describing, for example, *in vitro-in vivo* correlation [18], or to train artificial neural networks [19, 20].

*Corresponding author

Email addresses: zdenek.grof@vscht.cz (Zdeněk Grof), frantisek.stepanek@vscht.cz (František Štěpánek)

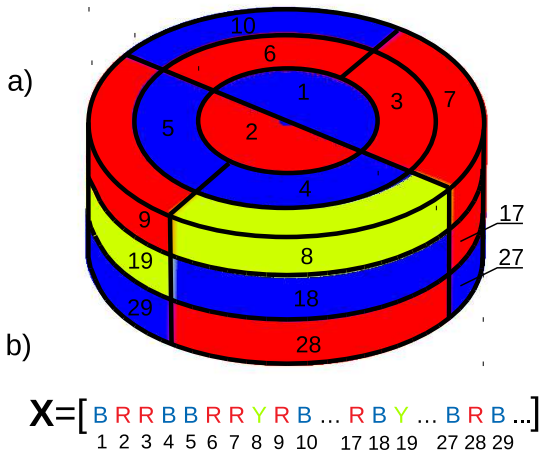

Figure 1: Illustration of tablet structure representation: a) division of the tablet into segments, b) example of tablet structure representation by a sequence $\mathbf{X}$

.

2. Methodology

2.1. The tablet representation

To describe the algorithm solving the inverse problem by finding the appropriate tablet structure, let us start with segments that form the building blocks of a tablet. For a particular design problem, there can be defined several segment types forming a set $\mathcal{L}$. Every segment type $l \in \mathcal{L}$ is described by the intrinsic dissolution rate I_l and the concentrations of individual API components $C_{k,l}$ ($k \in \{\mathrm{API\,1}, \mathrm{API\,2}, \ldots\}$). For example, it is possible to define types containing either API 1 or API 2 component, types with high or low API amount, types consisting of faster or slower dissolving material, and so on; and to form a tablet by arranging these segment types.

Although the presented method is not specific for a particular tablet shape, in this paper we will consider cylindrical tablet with the diameter D and the height H that is comprised of segments. The division of a tablet into segments (cf. Fig 1a) is made as follows: the cylinder is (i) sectioned into M_s stacks with

the height H/M_s, (ii) sectioned into M_a annuli and (iii) sectioned into $M_w(i)$ ($1 \leq i \leq M_a$) equiangular wedges. The inner annuli are usually sectioned into less wedges than the outer annuli and the radial position of the border between neighboring annuli is set in such a way that the volume of all segments is the same. Because the number of segments is

$$M = M_s \sum_{i=1}^{M_a} M_w(i), \tag{1}$$

the placement of every segment within the tablet can be specified by a single integer m, where $1 \leq m \leq M$.

Whenever an evolutionary algorithm (EA) is employed, the genetic representation (i.e. *chromosome*) must be used to specify the tablet structure. In the present situation, tablet structure is specified by a sequence of M elements from the set of segment types $\mathcal{L}$ (cf. Fig 1b). Using EA terminology, the sequence specifying a particular tablet structure i is called *individual* and denoted $\mathbf{X}_i$, while *population* is the set of individuals. In the course of searching for an appropriate tablet structure, EA iteratively creates new individuals by applying genetic operations on selected individuals from the population until the best solution is found.

2.2. Evolutionary algorithm

The pseudo-code of the EA is shown in Tab. 1. Our algorithm follows the structure of a standard genetic algorithm, however it also contains feature that is characteristic for tabu search optimization methods: Each individual offered by crossover or mutation operation is compared with the list of all previously evaluated individuals and only original individuals with no match found in the list are accepted. The selection followed by crossover or mutation operation in step 3 of Tab. 1 is therefore repeated until a required number of *original* individuals is found. (Or, in order to avoid the algorithm being stuck in an infinite loop, until the number of unsuccessful attempts to find original individuals reaches some large threshold value.)

Table 1: Evolutionary algorithm pseudo-code

1. Generate the initial population of the size p.
2. Evaluate the fitness of each individual in the population.
3. Evolve the population:
   - create px_c original individuals by selecting two individuals from the current population and making the crossover operation,
   - create px_m original individuals by selecting an individual from the current population and making the mutation operation,
   - evaluate the fitness of new individuals.
4. Repeat step 3 until the appropriate solution is found.

For the purpose of the design problem, it is important that the total amount of API components remains the same in all tablet structures that evolve during the course of EA. Therefore, all genetic operations must be implemented as count-preserving. In other words, all sequences specifying the tablet structure contain the same number of elements of a particular type and crossover or mutation must not change this number. The initial population is generated by randomly ordering the chosen number of elements of each type.

Crossover: $M/2$ positions in parent sequences $\mathbf{X}_i$ and $\mathbf{X}_j$ are randomly selected and the elements at the selected positions are copied into sub-strings $\mathbf{x}_1$ and $\mathbf{x}_2$. The elements in $\mathbf{x}_1$ and $\mathbf{x}_2$ are swapped at such many positions as possible providing that the number of elements of a particular type in $\mathbf{x}_1$ (and naturally in $\mathbf{x}_2$) does not change. The result of the swap is stored in $\mathbf{x}'_1$ and $\mathbf{x}'_2$. The child sequences $\mathbf{X}_k$ and $\mathbf{X}_l$ originate from $\mathbf{X}_i$ and $\mathbf{X}_j$ where elements at selected positions are replaced by elements from $\mathbf{x}'_1$ and $\mathbf{x}'_2$, respectively. The number of swapped elements during the crossover is a number between 0 and $M/2$: it depends on the actual selected positions and on the number of elements that can be swapped without violating the count preserving condition.

Mutation: Mutation is made by swapping elements between two randomly

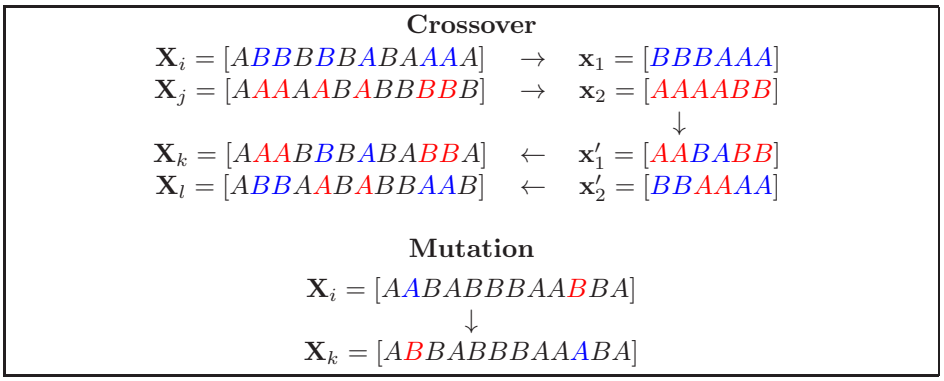

Figure 2: Illustration of the count-preserving crossover and mutation operations.

selected positions in the sequence $\mathbf{X}_i$.

Selection: There exist many possible ways to select individuals used as the input for crossover or mutation in the area of genetic algorithms [21]. In this work, tournament selection method has been used, as it is easy to implement while allowing to adjust the selection pressure by setting the tournament size and the candidate list size parameters t and p, respectively. The list of candidates for the selection contains p best fitted individuals from the population. To select an individual, the "tournament" is run: t individuals from the candidates list are selected at random and the best individual among them is chosen for the subsequent crossover or mutation. Please note that the initial population size is the same as the candidates list size p.

2.3. Fitness evaluation

In order to evaluate the fitness of an individual (the sequence that specifies the tablet structure), the dissolution curve must be obtained by the simulation of the particular tablet dissolution (i.e. by solving a forward problem) and compared with the target dissolution curve. The fitness score quantifies the match of the two dissolution curves.

Target dissolution curve can be written as the table in the form

$$\begin{bmatrix} \tau_1 & y^{\mathrm{t}}_{1,1} & \cdots & y^{\mathrm{t}}_{K,1} \\ \vdots & \vdots & \ddots & \vdots \\ \tau_N & y^{\mathrm{t}}_{1,N} & \cdots & y^{\mathrm{t}}_{K,N} \end{bmatrix} \tag{2}$$

where τ_i is time, $y^{\mathrm{t}}_{k,i}$ is the target fraction of released API component k at time τ_i, K is the number of API components for which the target dissolution curve is specified and N is the number of points on the target dissolution curve. Fitness score f of an individual is

$$f = 100 \left[\frac{1}{NK} \sum_{i=1}^{N} \sum_{k=1}^{K} (y_{k,i} - y^{\mathrm{t}}_{k,i})^2 \right]^{1/2}, \tag{3}$$

where the actual fraction of released component k is

$$y_{k,i} = \frac{m_k(\tau_i)}{m_k(\infty)}. \tag{4}$$

The cumulative amount of the component k that has been released from the tablet until time τ, $m_k(\tau)$, is the result of the simulation using an event-driven erosion algorithm described in the following section. Because the times at which the dissolution curve is recorded during the simulation do not coincide with times specifying the target dissolution curve, $m_k(\tau)$ is obtained by interpolation of recorded values. Better fitted individuals are individuals with lower fitness score f.

2.4. Event-driven erosion algorithm

Computational mesh $\mathcal{V}$ consists of a connected network of finite volumes (voxels) where every voxel $i \in \mathcal{V}$ is characterized by its volume V_i and type $t_i \in \{\mathrm{P}, \mathrm{S}\}$ that is either pore (P) or solid (S); the area between two neighboring (connected) voxels i and j is denoted as A_{ij} $(i, j \in \mathcal{V})$. For every solid voxel i $(i \in \mathcal{V} \,|\, t_i = \mathrm{S})$, the following additional variables must be introduced: intrinsic dissolution rate I_i, concentration of kth API component, $C_{k,i}$ $(k \in \{\mathrm{API}\,1, \mathrm{API}\,2, \ldots\})$, the undissolved solid fraction $\varphi_i \in < 0, 1 >$ and its rate of change $\dot{\varphi}_i$, τ_i representing time at which a complete dissolution of

this solid voxel is anticipated and u_i marking the time when the values of φ_i, $\dot{\varphi}_i$ and τ_i were last updated.

There are also several global variables that are gradually updated in the course of tablet erosion: the cumulative amount of released kth API component, m_k, its actual rate of release $\dot{m}_k$ and the actual time τ. Let us also denote the initial amount of kth API component in the tablet as m_{k0}.

At $\tau = 0$, the erosion algorithm is initialized for all solid voxels i by calculating the initial release rate from the tablet

$$\dot{m}_k = \sum_{i \in \mathcal{B}} C_{k,i}\, \dot{\varphi}_i V_i \qquad \mathcal{B} = \{i \in \mathcal{V} \,|\, t_i = \mathrm{S}\}, \tag{5}$$

where

$$\dot{\varphi}_i = I_i\, a_i / V_i. \tag{6}$$

The area exposed to the solvent a_i is calculated for every solid voxel as the area sum over all neighboring pore voxels

$$a_i = \sum_{j \in \mathcal{D}} A_{ij} \qquad \mathcal{D} = \{j \in \mathcal{V} \,|\, (t_j = \mathrm{P}) \wedge (j \text{ is neighbor of } i)\}. \tag{7}$$

The time τ_i at which the solid voxel completely dissolves, i.e. time at which φ_i drops to zero, is calculated

$$\tau_i = \tau + \varphi_i / \dot{\varphi}_i \tag{8}$$

and voxels are sorted by τ_i in increasing order and inserted into the queue. Also, the total amount of API components m_{k0} is computed

$$m_{k0} = \sum_{i \in \mathcal{B}} C_{k,i} V_i \qquad \mathcal{B} = \{i \in \mathcal{V} \,|\, t_i = \mathrm{S}\}, \tag{9}$$

The queue is processed sequentially. The voxel i with smallest τ_i is removed from the queue, global variables τ, m_k and $\dot{m}_k$ (the voxel i stops releasing API) are updated, the voxel type is changed from S (solid) to P (pore) and one point on the dissolution curve $[\tau,\, m_k/m_{k0}]$ is recorded. The change of a solid voxel into a pore voxel opens up an additional surface area exposed to the solvent which affects all solid voxels j that are neighbors of the voxel i. Therefore local

variables φ_j, $\dot{\varphi}_j$, u_j and τ_j must be modified at voxels j. In turn, the total API release rate $\dot{m}_k$ changes as well. Finally, the neighboring voxels j move forward in the queue because their anticipated time of complete dissolution τ_j decreases.

The steps described in the previous paragraph are repeated until all solid voxels in the queue are processed and the tablet completely dissolves. The pseudo-code of the algorithm is shown in Tab. 2.

Regarding the time complexity of the algorithm, the initial sorting of the voxels in step 2 of Tab. 2 is the most demanding. When self-balancing binary search tree is used for the implementation of queue Q then the process of sorting becomes equivalent to inserting n voxels into the tree leading to $O(n \log n)$ complexity for the sorting. In the step 4, the neighbors of voxel i must be repositioned in the queue. The process of deleting and reinserting voxels into the tree is $O(\log n)$ and step 4 is repeated for n voxels in the queue. Therefore the time complexity of this part and of the whole algorithm remains $O(n \log n)$. This is in a stark contrast with methods involving the integration of differential equations where the time complexity is $O(n^{5/3})$ (When assuming that the stability criterion for the diffusion equation limits the maximum time step in the connection with the actual spatial discretization as $\Delta t \propto \Delta h^2$).

3. Results and discussion

3.1. Validation of event-driven erosion algorithm

The intrinsic dissolution rate I specifies the rate at which the tablet looses its volume V during dissolution:

$$\frac{\mathrm{d}V}{\mathrm{d}\tau} = -IA, \tag{10}$$

where A is the area exposed to the solvent. For a cylindrical tablet that dissolves only through its side, there exists the following analytical solution of Eq. 10:

$$y(\tau) = \frac{V(0) - V(\tau)}{V(0)} = 2k\tau - (k\tau)^2 \qquad k = \frac{2I}{D_0}, \tag{11}$$

where D_0 is the initial tablet diameter and $y(\tau)$ is the fraction of tablet already dissolved at time τ.

Table 2: Event-driven erosion algorithm pseudo-code

1. Generate mesh (voxels and connections), define tablet structure, set initial conditions:
   - calculate A_{ij}, for all voxels $i \in \mathcal{V}$: calculate V_i and set $t_i \in \{\mathrm{P}, \mathrm{S}\}$
   - for all solid voxels $\{i \in \mathcal{V} \,|\, t_i = \mathrm{S}\}$: set I_i and $C_{k,i}$
2. Initialization for all solid voxels $\{i \in \mathcal{V} \,|\, t_i = \mathrm{S}\}$:
   - calculate $\dot{\varphi}_i$ (cf. Eq 6), $\varphi_i \leftarrow 1$, $u_i \leftarrow 0$ and $\tau_i \leftarrow \varphi_i / \dot{\varphi}_i$
   - sort voxels by increasing τ_i and insert them to queue Q
3. Initialize global variables:
   - calculate $\dot{m}_k$ and m_{k0} (cf. Eqs 5 and 9), $m_k \leftarrow 0$ and $\tau \leftarrow 0$
4. i is the voxel with the smallest τ_i in queue Q:
   - $m_k \leftarrow m_k + \dot{m}_k(\tau_i - \tau)$ and $\dot{m}_k \leftarrow \dot{m}_k - C_{k,i}\dot{\varphi}_i V_i$
   - $\tau \leftarrow \tau_i$, record a point on the dissolution curve $[\tau,\, m_k/m_{k0}]$
   - change t_i from S to P, remove voxel i from Q
   - for all voxels j $\{j \in \mathcal{V} \,|\, (t_j = \mathrm{S}) \wedge (j \text{ is neighbor of } i)\}$:
     - $\varphi_j \leftarrow \varphi_j - \dot{\varphi}_j(\tau - u_j)$ and $\dot{\varphi}_j \leftarrow \dot{\varphi}_j + I_j A_{ij}/V_j$
     - $\dot{m}_k \leftarrow \dot{m}_k + C_{k,j} I_j A_{ij}$
     - $u_j \leftarrow \tau$ and $\tau_j \leftarrow \tau + \varphi_j / \dot{\varphi}_j$
     - reposition voxel j in Q (τ_j has changed)
5. If queue Q is not empty, go back to step 4 and process the next voxel from Q. If Q is empty, then the tablet erosion is complete.

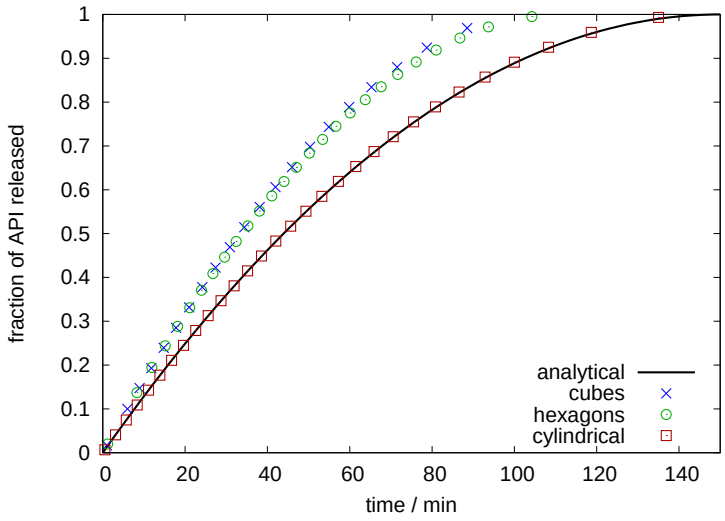

a)

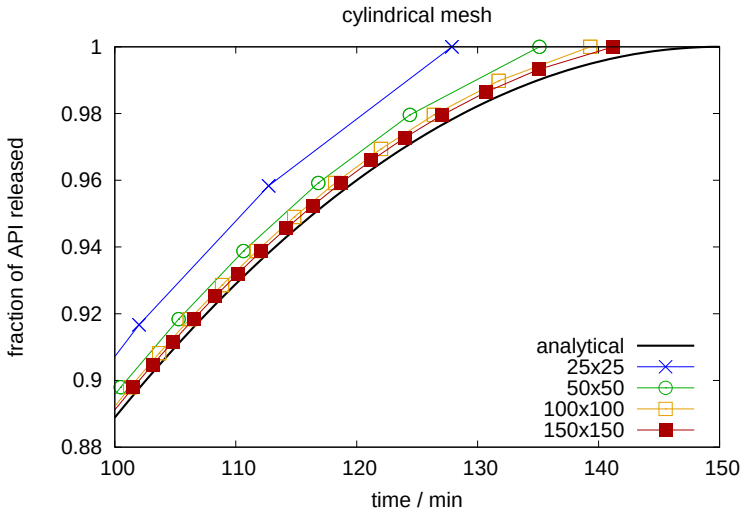

b)

Figure 3: Validation of the erosion algorithm by a two-dimensional dissolution of a cylindrical tablet. Analytical solution comes from Eq. 11: a) the effect of different mesh types, discretization into 150x150 (cubic and cylindrical) or 150x130 (hexagonal) voxels, b) the effect of discretization extent in cylindrical mesh.

The comparison of simulated dissolution curves with the analytical solution Eq. 11 in Fig. 3 enables to validate the erosion algorithm. It is clear that the type of mesh used for the discretization plays an important role for the simulation precision. The following voxel shapes were tested: cubes, hexagonal prisms and volume elements based on cylindrical coordinates. Cubic and hexagonal discretizations overestimate the surface area and predict a dissolution that is faster than the analytical solution. Unfortunately, the precision does not substantially improve even if a finer mesh is used. A calibration that corrects the actual area would be necessary for cubic and hexagonal meshes. On the other hand, cylindrical mesh is best suited for cylindrical tablets, provides results that closely fit the analytical solution even when coarser mesh is used (cf. Fig 3b) and will be therefore used within the rest of the present paper.

An additional disadvantage of cubic mesh is its lack of isotropicity: diagonally oriented erosion fronts move faster than horizontal or vertical fronts. Therefore, as the tablet dissolves, its shape progressively shifts from a circle into a diamond. Similarly, less pronounced but still undesirable shape-shifting can be observed in hexagonal meshes as well. This problem could be solved by using an irregular mesh with randomly oriented elements, for example a mesh resulting from a Voronoi triangulation of irregularly placed points.

Table 3: The values of parameters that define tablet geometry: the number of sections, annuli and wedges

Geometry (M)	M_s	M_a	$M_w(i)$
Base 24	1	5	$(2, 4, 6, 6, 6)$
Base 32	1	6	$(2, 4, 5, 5, 8, 8)$
Base 110	5	5	$(2, 4, 5, 5, 6)$

3.2. Evolutionary algorithm parameters (Scenario I)

After testing the simulation of tablet erosion and the dissolution curve prediction (i.e. the forward problem), let us proceed to the testing of evolutionary algorithm itself. The parameters that define tablet geometry and boundary conditions used for the tests are listed in Table 3. Both the two- and three-dimensional configurations are used: Two dimensional (base 24 and 32) geometries contain only one section and the segments can be placed into 24 or 32 positions. Boundary conditions are set in such a way, that the tablet dissolves through its sides only. Two-dimensional configuration is ideal for testing as the tablet structure and the dissolution progress can be easily observed and pictured. The three-dimensional tablet (base 110) containing 5 sections is placed on the pad so its bottom base is not in the contact with solvent. Therefore the tablet dissolves through its top base and the sides, but not through its bottom base. The segments can be placed into 110 positions within the tablet.

In Scenario I, two segment types are used: those containing the API component (type "a") and those without any API (type "b"). When 16 "a"-segments and 16 "b"-segments in two dimensions and 33 "a"-segments and 77 "b"-segments in three dimensions are used, the number of permutations the segments can be placed in a tablet is

$$J_{2\mathrm{D}} = \frac{32!}{16!\,16!} = 6.01 \cdot 10^8, \tag{12}$$

$$J_{3\mathrm{D}} = \frac{110!}{33!\,77!} = 1.26 \cdot 10^{28}. \tag{13}$$

It is possible to test how fast the algorithm can find a particular permutation sequence, namely the one where all "a"-segments are placed in the tablet center and encapsulated by "b"-segments. The search begins from a population with randomly placed segments. The result for two and three dimensions is illustrated in Figs. 4 and 5, respectively. It can be seen, that for the particular runs, only 207 or 1278 individuals in two or three dimensions, respectively, had to be generated and their dissolution curve tested before the correct sequence was found. These numbers are indeed only a small fraction of the possible number of permutations in Eqs. 12 and 13. The advantage of the evolutionary algorithm over a "brute force" approach based on evaluating all permutations is evident.

The progress of EA toward a target sequence is shown in Fig 6. It can be seen that as the population evolves, the dissolution curve of recently generated individuals moves closer to the target dissolution curve. The figure also illustrates that all possible dissolution curves lie inside the area between the dissolution curves corresponding to the two limiting configurations: with "a"-segments either fully encapsulated inside the tablet or completely placed on the tablet surface.

The effect of the population size p, tournament size t, and the ratio between the number of cross-over and mutation operations (x_c/x_m) has been tested. The curves in Fig. 7 show how the fitness score f of the best individual decreases as new individuals are generated and tested when different values of EA parameters are used. Due to the random nature of the algorithm, the search was repeated several times with the same parameter values. It can be seen that, in general, the effect of parameter values on the number of individuals tested before the solution is found is small and that the variability due to randomness is of the same order of magnitude as the variability due to parameters change. The statistics (mean and standard deviation values) summarized in Tab. 4 confirms that no strong trends in parameter selection exist for this particular scenario. One exception is the effect of switching off the cross-over operation ($x_c = 0$): the algorithm convergence rate slows down considerably when only mutation is used.

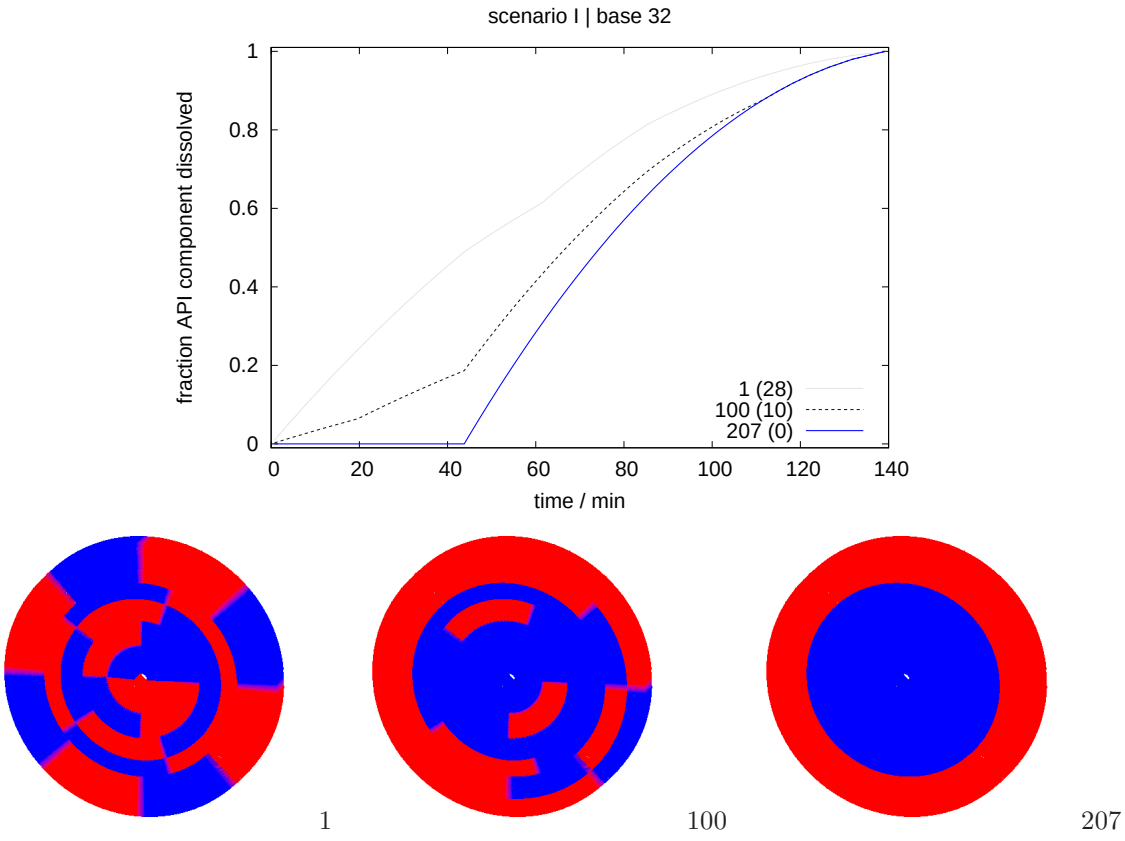

Figure 4: Scenario I: Illustration of tablet structure evolution for a two-dimensional dissolution (32 segments) by EA during the search for an encapsulated structure. The dissolution curve: numbers in the legend correspond to the generated sequence number, the number in parentheses is the fitness score f.

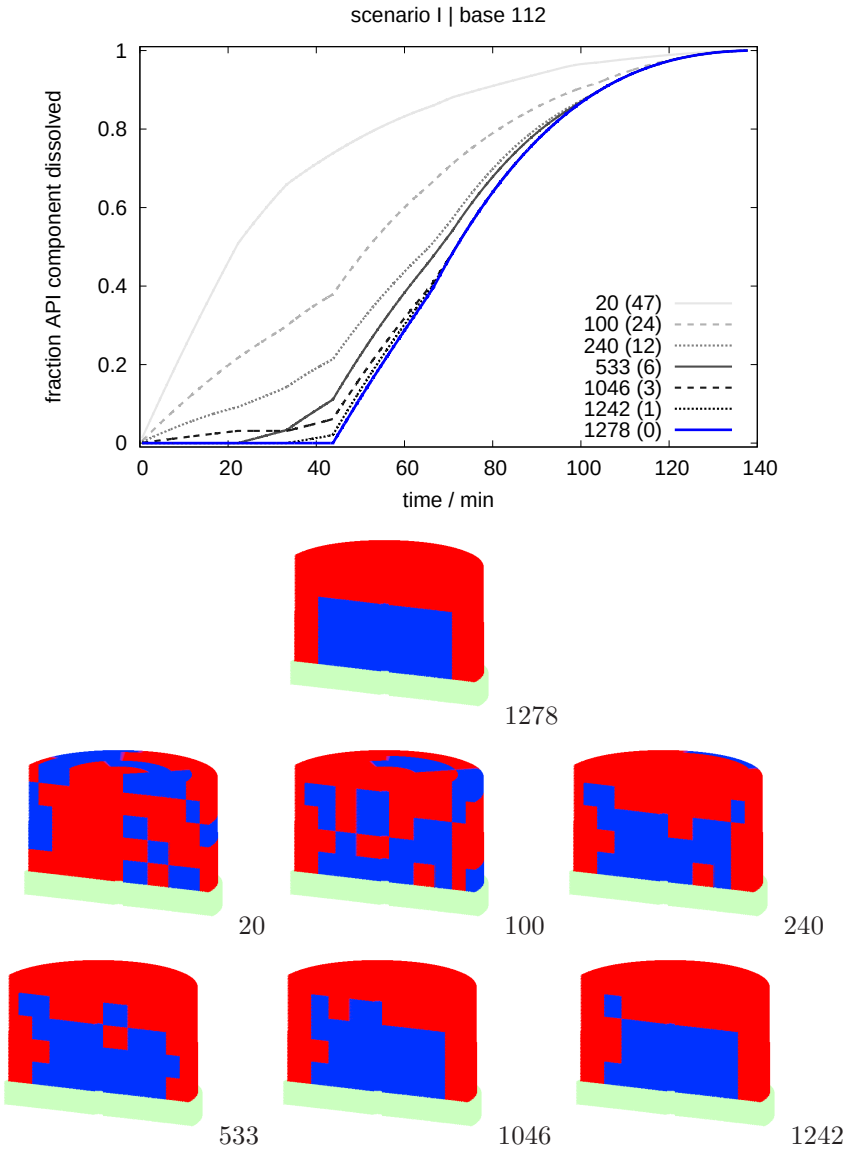

Figure 5: Scenario I: Generation of encapsulated structure (three-dimensional dissolution, 110 segments). Example of structures generated during an EA run. Number corresponds to the generated sequence number, number in parentheses is the fitness score f.

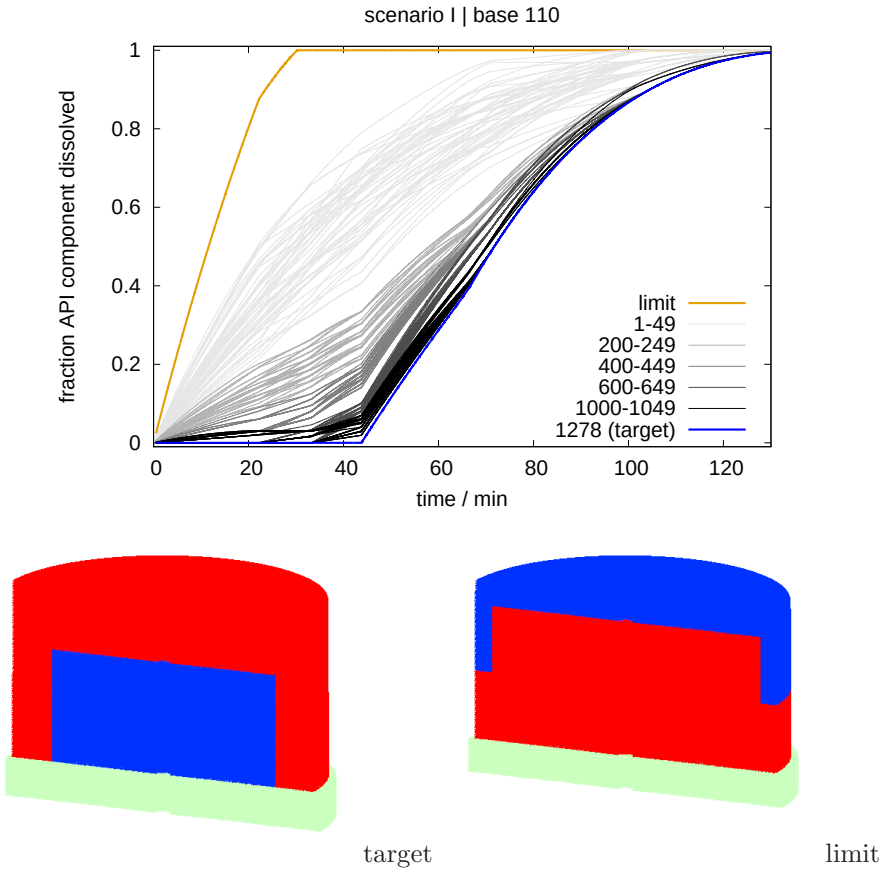

Figure 6: The progress of EA during encapsulated structure generation showing how dissolution curve (DC) evolves toward the target DC. The number intervals in the legend correspond to the sequence number range of generated structures whose DCs are shown. The best and the worst structures in respect to their match with the target DC (limiting configurations) are also shown.

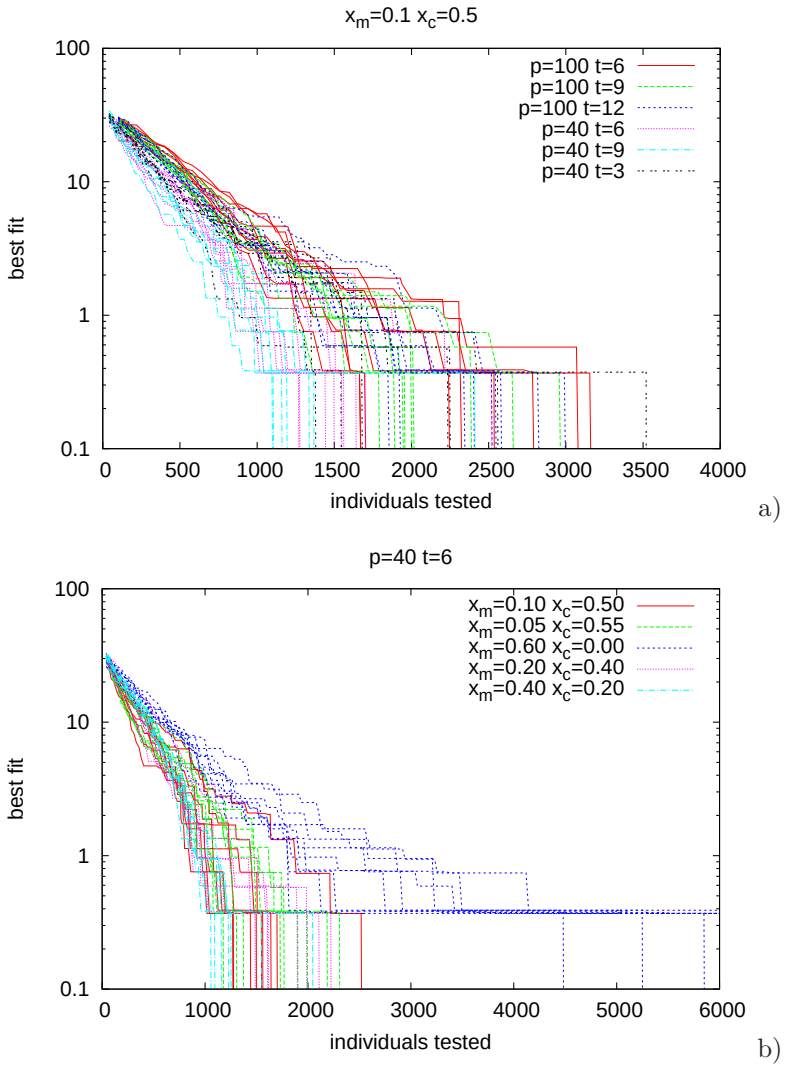

Figure 7: Evolution of best fitness score f with the increasing number of generated sequences: a) the effect of considered population size p and the tournament size t during the selection operation, b) the effect of incidence ratio between crossover (x_c) and mutation (x_m) operations.

Table 4: The mean and the standard deviation of the actual number of generated sequences before the target sequence has been found (8 repetitions).

p	t	x_c	x_m	mean $\pm$ std
100	6	0.50	0.10	2363 ± 630
	9			2117 ± 382
	12			2373 ± 331
40	3			2109 ± 702
	6			1496 ± 156
	9			1407 ± 434
40	6	0.55	0.05	1682 ± 356
		0.50	0.10	1496 ± 156
		0.40	0.20	1845 ± 260
		0.20	0.40	1396 ± 358
		0	0.60	7553 ± 2661

3.3. Fast and slowly dissolving segments (Scenario II)

In the previous section, the single value of intrinsic dissolution rate I has been used for all segment types. However, it is possible to create a tablet consisting of segments that dissolve at different rates. For example, if the erosion front progresses at the rate that primarily depends on the solvent uptake flux, the local dissolution rate can be controlled by the modification of porosity and/or pore size in some parts of the tablet. By allowing intrinsic dissolution rate spatial variability in tablets, the solution space of all possible dissolution curves that can be achieved increases vastly. Unlike an spatially uniform value of I, the dissolution is no longer symmetrical and the percolation phenomena might take effect as well.

The effect of the percolation is illustrated in Fig 8. The structures labeled as "1X" and "2X" were obtained by setting target dissolution curves to $y^{\mathrm{t}}(\tau) = 1$ and $y^{\mathrm{t}}(\tau) = 0$, respectively, and by running an EA. The segment types used for these tests (Scenario IIa) are listed in Table 5. The time, at which the dissolution front reaches the segments containing API whose position was fixed in the tablet center, depends by the great extent on the way the four faster dissolving "B"-segments are placed among the slower dissolving "b"-segments in the tablet ($I_{\mathrm{B}} = 30$ mm/h, $I_{\mathrm{b}} = 3$ mm/h). When all fast dissolving segments (type "B") are placed in different annuli and aligned, the result is an "as soon as possible" API release ("1X" structure). On the other hand, an "as late as possible" API release is obtained when all fast dissolving segments are placed into the outer annulus as can be seen in the structure "2X". Other possible configurations lead to the release time that lies in the interval specified by release times of the two limiting structures "1X" and "2X". This is illustrated by a randomly chosen sample of corresponding dissolution curves in Fig. 8.

Let us now demonstrate the effect of non-uniform intrinsic dissolution rate using a more complex example (Scenario IIb). Four segment types are used: "a"- and "b"-segments dissolving slowly and "A"- and "B"-segments dissolving faster. The API is present at the same concentration in "a"- and "A"-segments ($C_{\mathrm{A}} = C_{\mathrm{a}}$) while there is no API in "b"- and "B" segments. Assuming that

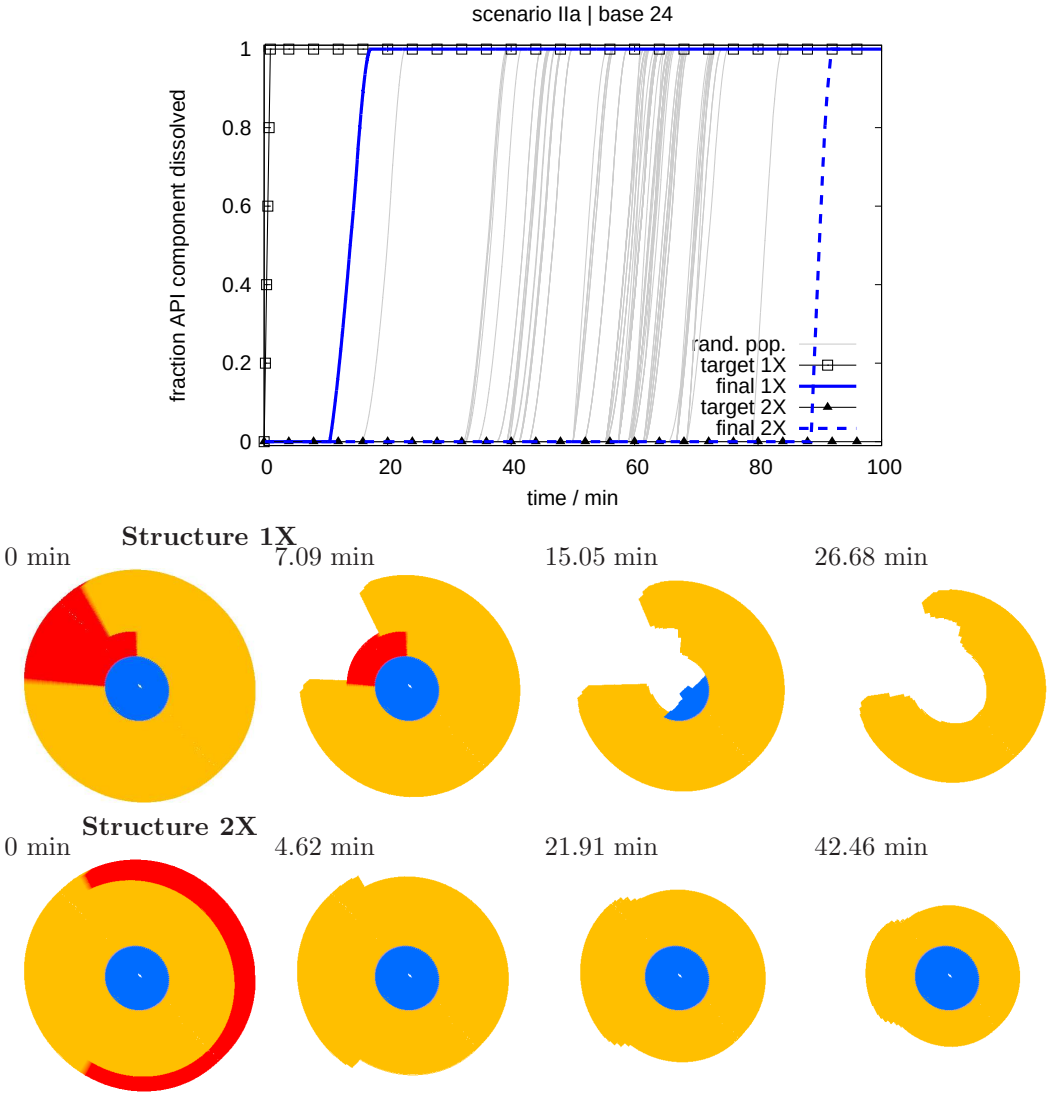

Figure 8: Scenario IIa: Combination of slowly (orange color) and fast (red color) dissolving segments in the tablet. The time at which API (blue color) fixed in the center is released can be controlled by the configuration of red and orange segments. Structure "1X" releases API as soon as possible, structure "2X" releases API as latest as possible. Dissolution curves corresponding to both limiting situations and to other 100 randomly selected structures are shown in the graph. The graph also shows the target dissolution curves used during the search for the limiting configurations.

the number of each segment type in the tablet does not change, the family of achievable dissolution curves together with selected structures that were generated by EA are shown in Figs. 9 and 10. The structures were obtained similarly as in the previous example: target dissolution curve was set and EA was run to find the structure with the best possible fitness score f. The following target DCs were used for particular structures: $y^{\mathrm{t}}(\tau) = 1$ (structure "1"), $y^{\mathrm{t}}(\tau) = 0$ (structures "4a" and "4b") and y^{t} jumping from 0 to 1 at times 13 and 31 min (structures "2" and "3", respectively). For comparison reasons, also structure "4c" has been included as an example of an obvious placement choice.

The dissolution curves in Fig 9 illustrate that the release time and rate can be controlled to some extent by different placement of the same number of API/no-API and fast/slowly dissolving segments in the tablet. Structures suited for an "as fast as possible" release (structure "1"), an "as late as possible" release (structures "4a" and "4b") or the release as close as possible within an arbitrarily chosen time (structures "2" and "3") were suggested by an EA.

Regarding results in Fig. 9, the search for a suitable structure by EA was ended after a specified number of sequences was tested. Because this procedure is a random process, different structures can be found in different EA runs. Also no proof can be made that the resulting structure is the best solution. It cannot be completely excluded that a better solution is found when the number of iterations would be increased or the values of genetic algorithm parameters modified.

All structures "4a"–"4c" have a similar fitness score, but their dissolution curves follow completely different paths. Such solution variability is caused by the fact that the target dissolution function for these structures (target 4) is impossible to achieve given the constrains set for the particular scenario. For example, comparing the "4a" and "4b" dissolution curves in Fig. 9, in respect to the match with the target, the structure "4a" is worse than "4b" in intervals up to 27 min and after 69 min, while "4a" is better than "4b" in the interval between 27 and 69 s. This leads to similar values of fitness score for both structures. Therefore, in situations when it would be necessary to select between different

"4" structures and to reduce the solution variability, the formula for fitness score calculation and the target DC should be modified.

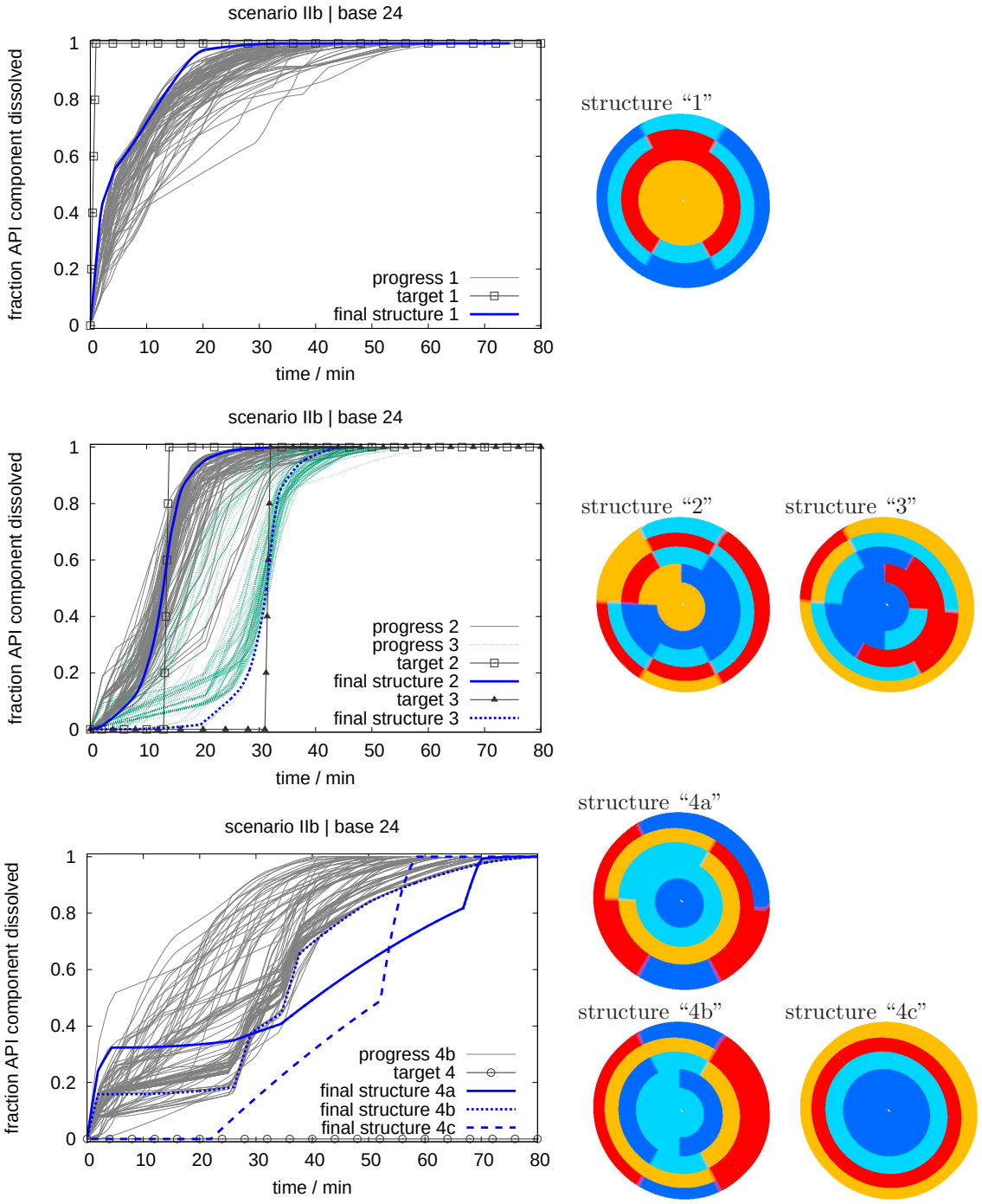

Figure 9: Scenario IIb: Combination of slowly (orange and light blue color) and fast (red and blue color) dissolving segments in the tablet. The release of API component (present in blue and light blue colored segments) can be controlled by segments placement. Target dissolution curves, dissolution curves corresponding to structures generated during the EA search (evaluated) and the resulting structures are shown in graphs.

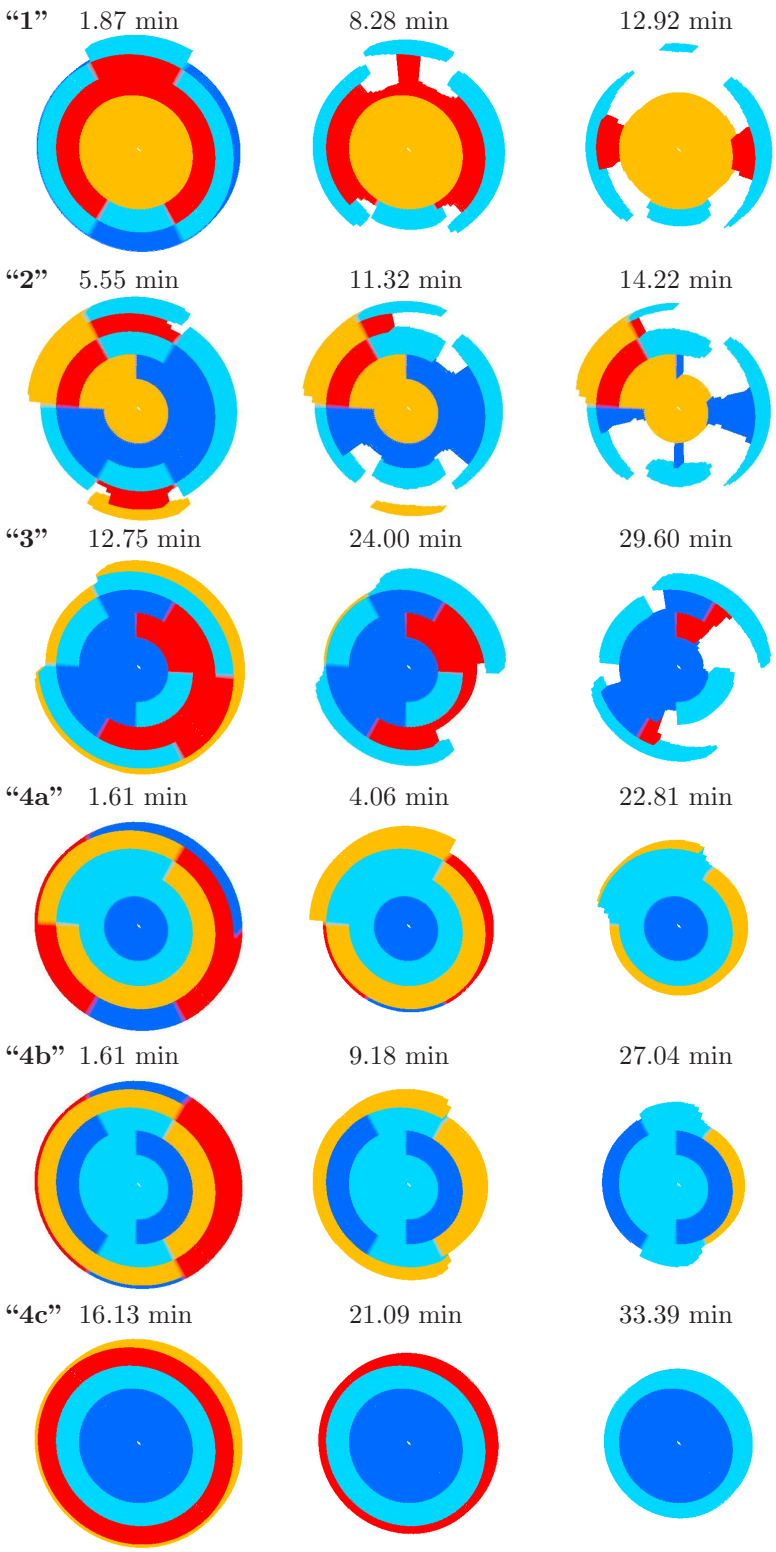

Figure 10: Scenario IIb: The course of dissolution of structures shown in Fig. 9.

Table 5: Overview of segment types used in the paper to demonstrate the inverse problem solution by evolutionary algorithm.

Scenario	Base (M)	Permutations (J)	Segment code[a]	Number of segments	Color	Figs.
I	32	$6.0 \cdot 10^8$	a	16	blue	4
			b	16	red	
	110	$1.3 \cdot 10^{28}$	a	33	blue	5, 6
			b	77	red	
IIa	24	$7.3 \cdot 10^3$	A	2[b]	blue	8
			B	4	red	
			b	18	orange	
IIb	24	$2.3 \cdot 10^{12}$	A	6	blue	9, 10
			a	6	light blue	
			B	6	red	
			b	6	orange	
III	32	$1.5 \cdot 10^{10}$	A	2	blue	11, 12
			B	10	red	
			b	20	orange	
	110	$3.5 \cdot 10^{32}$	A	2	blue	13a, 14[c]
			B	36	red	
			b	72	yellow	

[a] Segments "a" and "A" contain API, segments "b" and "B" do not contain API, segments "A" and "B" dissolve fast ($I_{\mathrm{A}} = I_{\mathrm{B}} = 30$ mm/h), segments "a" and "b" dissolve slowly ($I_{\mathrm{a}} = I_{\mathrm{b}} = 3$ mm/h).

[b] These segments are fixed in the center.

[c] Tablet structures animation attached as supplemental material.

3.4. Piecewise release (Scenario III)

Both the two and three dimensional tablet geometries will be shown in the last example that demonstrates the ability of an EA to suggest a suitable tablet configuration for a particular target dissolution curve (cf. Scenario III in Tab 5). The example problem is to place two segments containing API (type "A") in the tablet composed also of slowly and fast dissolving segments without API (types "B" and "b", respectively) in a way that the API release from the tablet matches the prescribed dissolution curve. The following release modes were specified: an "as soon as possible" release ("target 1"), piecewise release at 19 and 39 s ("target 2"), at 19 and 59 s ("target 3"), at 39 and 59 s ("target 4"), at 19 and 75 s ("target 5"), and an "as late as possible" release ("target 6"). These times were chosen to lie within the time interval originating from the possible solutions space bordered by the two limiting situations ("target 1" and "target 6").

Two dimensional structures found by an EA together with their corresponding dissolution curves and dissolution sequence are shown in Figs. 11 and Figs. 12 It can be seen that all the dissolution curves agree well with the target ones and suitable tablet configurations have been found for all release modes.

Qualitatively same release modes as in two dimensions were used also for EA runs searching suitable three-dimensional structures. The only differences in target dissolution curves are the times defining piecewise release that had to be rescaled because the dissolution time of limiting structures is different in three and two dimensional tablets. The dissolution curves of three-dimensional tablet configurations that were found by an EA are shown in Figs. 13a and 13b and a good agreement with the requirements can be seen.

The fitness score of "structure 5" is slightly worse than in the remaining situations. The "target 5" mode is indeed the most challenging case as it combines earliest release of the first half and latest release of the second half of total API content. It seems that no better solution exists inside the solution space constrained by our arbitrarily chosen numbers of 36 fast (type "B") and 72 slowly (type "b") dissolving segments. However, better solutions were found when

these numbers were modified as is briefly illustrated in Fig 13c. A straightforward modification of cross-over and mutation operations could loosen the constrain of fixed "b"/"B" types ratio. If these operations are changed in such a way that the sum of "b" and "B" segments is preserved (instead of preserving the number of each segment type) also the optimum ratio of different segment types can be searched for in the course of single EA run.

Because it is difficult to visualize three dimensional structures by images, the resulting structures shown Fig 13 are specified using their genetic code in Figs. 14 and 15. Additionally, animations showing the structure and the dissolution of three-dimensional tablet are available in supplemental material.

4. Conclusions

Evolutionary algorithm for optimizing the tablet configuration together with event-driven model of tablet dissolution has been presented. It has been demonstrated that this novel methodology enables to solve the inverse problem of finding a particular internal structure of a multi-component tablet that meets the prescribed dissolution curve. We believe that the algorithm could be adopted as an useful tool in design and development processes in the emerging area of personalized medicine production.

Acknowledgment

Support from the Czech Science Foundation through grant 19-26127X is acknowledged.

Conflict of interest

The authors declare that they have no competing financial interests.

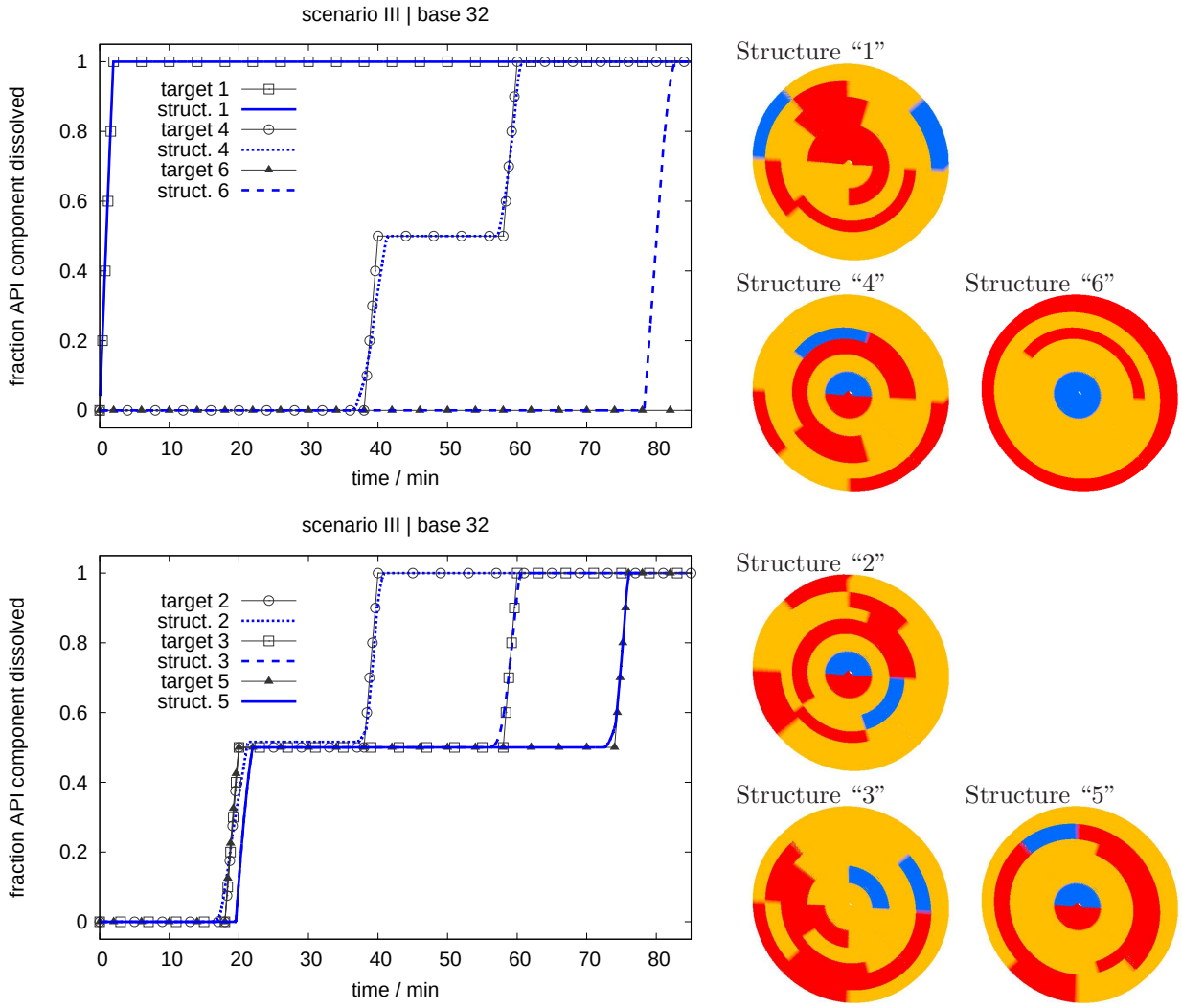

Figure 11: Scenario III / two-dimensional geometry: Example of arbitrarily chosen stepwise dissolution profiles and the corresponding structures obtained by an EA that best fit the targets. The colors in the tablet dissolution sequences correspond to: the fast dissolving (blue) API segments and slowly (orange) and fast (red) dissolving segments without API.

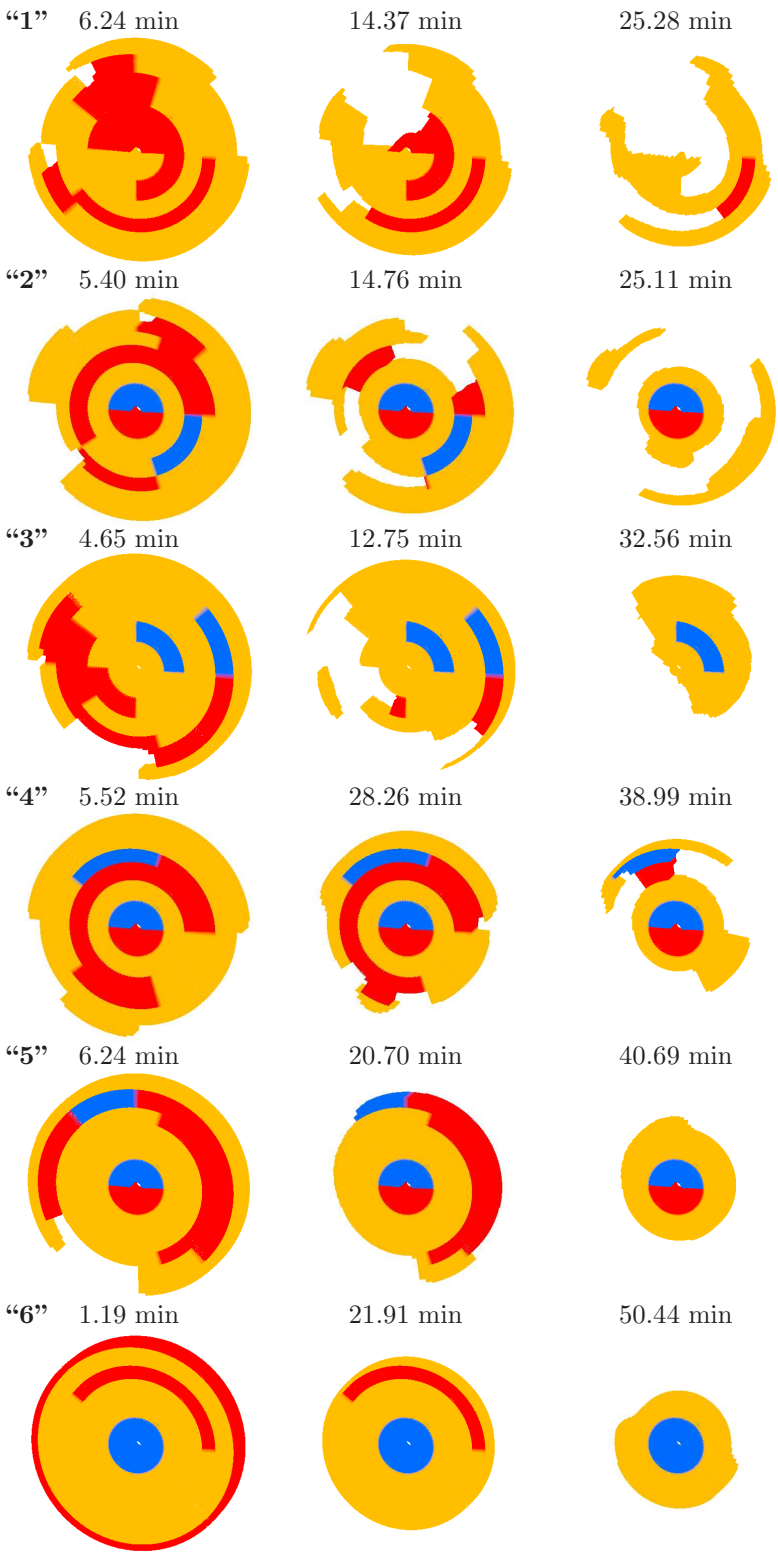

Figure 12: Scenario III: The course of dissolution of structures shown in Fig. 11.

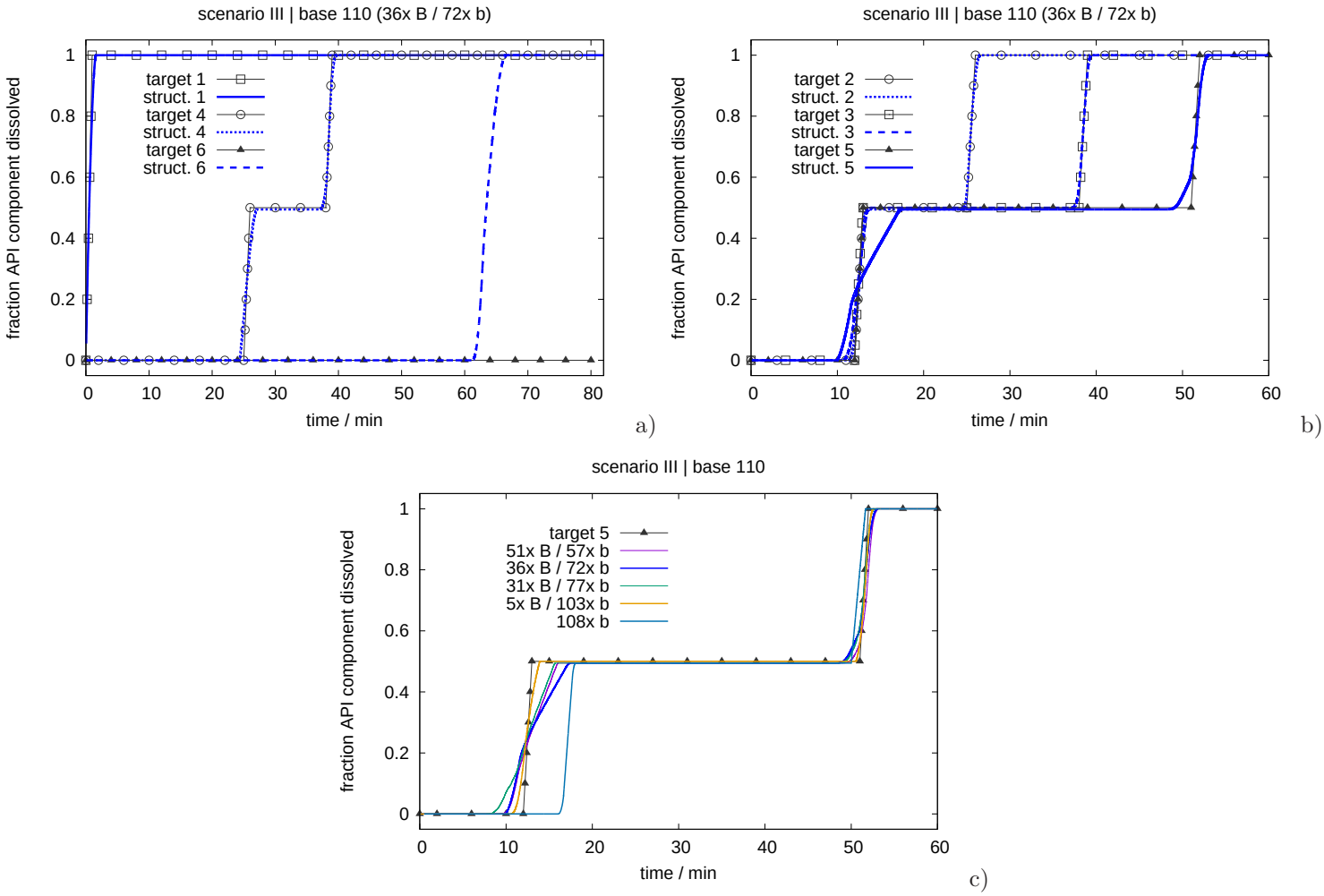

Figure 13: Scenario III / three-dimensional geometry: Dissolution curves corresponding to the three-dimensional structures found by an EA that best match the arbitrarily chosen dissolution profiles. The genetic code of the structures is shown in Figs 14 and 15 and the structures are visualized using animations attached in supplementary material.

sample	fitness	central			outer	
	score	annuli	<---------		annuli	
‘‘1’’	2.109	Bb	BBBB	BBBBB	BBBBb	AABBBb	top section
		BB	BBBB	BBBBB	BBBBB	BBBbbb	|
		bb	bbbb	bbbbb	bbbbb	bbbbbb	|
		bb	bbbb	bbbbb	bbbbb	bbbbbb	|
		bb	bbbb	bbbbb	bbbbb	bbbbbb	bottom sect.
‘‘2’’	1.489	BB	bbbb	bbbBB	BbBbb	bbbbbB	
		bb	BbBb	BBbBb	BBbBb	bbbBbB	
		BB	bBbb	bbBbB	bbBBB	bBbbBB	
		bb	bbbb	bBbbb	bbBbB	bbbbbB	
		bA	bbBB	bAbbb	bbBbb	bBbbbb	
‘‘3’’	2.311	BB	BBbb	BbbBb	BbBbb	BBBBBB	
		Bb	bBbB	bbbbB	bBBbb	bBbBbb	
		bb	bbbb	bBBbb	bbbbb	bbBBbb	
		bB	bBbb	bbbbb	bbbbb	bBBbbb	
		BB	bbBb	bABbA	bbbbb	bBBbbb	
‘‘4’’	2.473	bb	BbBb	Bbbbb	BBbBB	bBBbbb	
		BB	bbbb	bBbbB	bBbbb	bBBBbb	
		bb	bbbb	BBbBb	bBbBb	bBBBbb	
		bb	bbbb	bBbbb	bBbbb	bBBBbb	
		BA	bbbb	bBbBA	bbbbB	bBbBbb	
‘‘5’’	4.903	bB	BbBB	BbBBB	bBbBb	BbbBBB	
		bb	bbbb	bbbbb	bbBbb	BbbBbB	
		bb	bbbb	bBbbb	bbbbb	BbbBBB	
		bb	bbbb	bBbbb	bbbbb	BBbBBB	
		bA	bbbB	bAbbb	bbbbb	BBBBBB	
‘‘6’’	38.439	bb	bbbb	bbbbb	bbbbb	BBBBBB	
		bb	bbbb	bbbbb	bbbbb	BBBBBB	
		bb	bbbb	bbbbb	bBBbb	BBBBBB	
		bb	bbbb	bbbbb	bBBbb	BBBBBB	
		AA	bbbb	bbbbb	bBBbb	BBBBBB	

Figure 14: Genetic code of structures shown in Figs. 13a and 13b.

```
sample fitness central              outer
       score   annuli  <---------> annuli

5/51xB 4.443   BB BBBB BBBbB BBBBB BBBBBB  top section
               bb bbbb bbbbb BBbbB BBBBBB       |
               bb bbbb bbbbb BbbbB BBbbBB       |
               bb bbbb bbbBb BbAbB BBbbBB       |
               Ab bbbb bbbBb BBbBB BBbbbB  bottom sect.

5/31xB 4.494   BB BBBB BBBBB BBbBB bBbbBB
               bb bbbb bbbbb BBbbB bBbbbB
               bb bbbb bbbbb bbbBb bBbBbB
               bb bbbb bBbbb BBbBb bbbbbb
               bA bbbb bbbbb bbbbA bbbbbb

5/5xB 2.723    bb bbbb bbbbb bbbbb bbbbbb
               bb bbbb bbbbb bbbbb bbbbbB
               bb bbbb bbbbb bbbbB bbbbbb
               bb bBbb bbbbB bBbbb bbbbbb
               bb bAbA bbbbb bbbbb bbbbbb

5/0xB 12.50    bb bbbb bbbbb bbbbb bbbbbb
               bb bbbb bbbbb bAbbb bbbbbb
               bb bbbb bbbbb bbbbb bbbbbb
               bA bbbb bbbbb bbbbb bbbbbb
               bb bbbb bbbbb bbbbb bbbbbb
```

Figure 15: Genetic code of structures shown in Fig 13c.

List of symbols

A_{ij}	area between neighboring voxels i and j, m^2
a_i	area of voxel i exposed to the solvent, m^2
$C_{k,i}$	concentration of kth component in voxel i, $\mathrm{mol/m}^3$
$C_{k,l}$	concentration of kth component in segments of type l, $\mathrm{mol/m}^3$
D	tablet diameter, m
f_i	fitness score of individual i
H	tablet height, m
I	intrinsic dissolution rate, $\mathrm{m}^3/(\mathrm{m}^2\ \mathrm{s})$
J	number of permutations
M	number of segments in the tablet
M_a	number of annuli in the tablet
M_s	number of stacks in the tablet
M_w	number of wedges in the tablet
m_k	cumulative amount of released component k, mol
m_{k0}	initial amount of component k, mol
p	population size and selection list size
t	tournament size
t_i	type of voxel i
u_i	variables update time in voxel i, s
V_i	volume of voxel i, m^3
$\mathbf{X}_i$	sequence of segment types for individual i
x_m	fraction of individuals created by mutation in single EA step
x_c	fraction of individuals created by cross-over in single EA step
y	fraction of released component (dissolution curve)
φ_i	undissolved solid fraction in voxel i
τ	time, s
τ_i	expected time of complete solid dissolution in voxel i, s

Appendix A. Supplementary data

Supplementary data to this article can be found online at ***.

References

[1] Tu C. Le and D. A. Winkler. Discovery and optimization of materials using evolutionary approaches. *Chem. Rev.*, 116:6107–6132, 2016. doi:10.1021/acs.chemrev.5b00691.

[2] D. Wolf, O. V. Buyevskaya, and M. Baerns. An evolutionary approach in the combinatorial selection and optimization of catalytic materials. *Appl. Catal. Gen.*, 200:63–67, 2000. doi:10.1016/S0926-860X(00)00643-8.

[3] S. T. Alharbi. A hybrid genetic algorithm with tabu search for optimization of the traveling thief problem. *Int. J. Adv. Comput. Sci. Appl.*, 9(11):276–287, 2018.

[4] Young-Chang Hou and Ying-Hua Chang. A new efficient encoding mode of genetic algorithms for the generalized plant allocation problem. *J. Information Sci. Eng.*, 20:1019–1034, 2004.

[5] A. Dietz, C. Azzaro-Pantel, L. Pribouleau, and S. Domenech. A framework for multiproduct batch plant design with environmental consideration: Application to protein production. *Ind. Eng. Chem. Res.*, 44:2191–2206, 2005. doi:10.1021/ie049499m.

[6] C. A. Coello, A. D. Christiansen, and F. S. Hernandez. A simple genetic algorithm for the design of reinforced concrete beams. *Eng. Comput.*, 13: 185–196, 1997. doi:10.1007/BF01200046.

[7] F. Fraternali, M. A. Porter, and C. Daraio. Optimal design of composite granular protectors. *Mech. Adv. Mater. Struct.*, 17:1–19, 2010. doi:10.1080/15376490802710779.

[8] M. K. Heljak, K. J. Kurzydlowski, and W. Swieszkowski. Computer aided design of architecture of degradable tissue engineering scaffolds. *Comput. Meth. Biomech. Biomed. Eng.*, 20(15):1623–1632, 2017. doi:10.1080/10255842.2017.1399263.

[9] P. Schneider and G. Schneider. De novo design at the edge of chaos. *J. Med. Chem.*, 59:4077–4086, 2016. doi:10.1021/acs.jmedchem.5b01849.

[10] Che-Lun Hung and Chi-Chun Chen. Computational approaches for drug discovery. *Drug Dev. Res.*, 75:412–418, 2014. doi:10.1002/ddr.21222.

[11] R. Vasundhara Devi, S. Siva Sathya, and Mohane Selvaraj Coumar. Evolutionary algorithms for de novo drug design a survey. *Applied Soft Computing*, 27:543–552, 2015. doi:10.1016/j.asoc.2014.09.042.

[12] D. Douguet, E. Thoreau, and G. Grassy. A genetic algorithm for the automated generation of small organic molecules: Drug design using an evolutionary algorithm. *J. Comput. Aided Mol. Des.*, 14:449–446, 2000. doi:10.1023/A:1008108423895.

[13] G. Schneider, Man-Ling Lee, M. Stahl, and P. Schneider. De novo design of molecular architectures by evolutionary assembly of drug-derived building blocks. *J. Comput. Aided Mol. Des.*, 14:487–494, 2000. doi:10.1023/A:1008184403558.

[14] Venkat Venkatasubramanian, King Chan, and James M. Caruthers. Evolutionary design of molecules with desired properties using the genetic algorithm. *J. Chem. Inf. Comput. Sci.*, 35:188–195, 1995. doi:10.1021/ci00024a003.

[15] S. Golla, B. J. Neely, E. Whitebay, S. Madihally, R. L. Robinson Jr, and K. A. M. Gasem. Virtual design of chemical penetration enhancers for transdermal drug delivery. *Chem. Biol. Drug. Des.*, 79:478–487, 2012. doi:10.1111/j.1747-0285.2011.01293.x.

[16] J. Siepmann and F. Siepmann. Mathematical modeling of drug delivery. *Int. J. Pharm.*, 364:328–343, 2008. doi:10.1016/j.ijpharm.2008.09.004.

[17] C. Mircioiu, V. Voicu, V. Anuta, A. Tudose, C. Celia, D. Paolino, M. Fresta, R. Sandulovici, and I. Mircioiu. Mathematical modeling of release kinetics from supramolecular drug delivery systems. *Pharmaceutics*, 11(3):140, 2019. doi:10.3390/pharmaceutics11030140.

[18] F. Yamashita, A. Fujita, X. Zhang, Y. Sasa, K. Mihara, and M. Hashida. Computer-based evolutionary search for a nonlinear conversion function for establishing in vitroin vivo correlation (ivivc) of oral drug formulations. *Drug Metab. Pharmacokinet.*, 27(3):280–295, 2012. doi:10.2133/dmpk.DMPK-11-RG-075.

[19] A. Ghaffari, H. Abdollahi, M. R. Khoshayand, I. Soltani Bozchalooi, A. Dadgar, and M. Rafiee-Tehrani. Performance comparison of neural network training algorithms in modeling of bimodal drug delivery. *Int. J. Pharm.*, 327:126–138, 2006. doi:10.1016/j.ijpharm.2006.07.056.

[20] M. Maleki, M. Amani-Tehran, M. Latifi, and S. Mathur. Drug release profile in coreshell nanofibrous structures: A study on peppas equation and artificial neural network modeling. *Comput. Meth. Programs Biomed.*, 113:92–100, 2014. doi:10.1016/j.cmpb.2013.09.003.

[21] T. Blickle and L. Thiele. A comparison of selection schemes used in evolutionary algorithms. *Evolutionary Computations*, 4(4):361–394, 1996. doi:10.1162/evco.1996.4.4.361.

This page has been intentionally left blank in order to mark the last page of the thesis